(NASA-CR-157110) THE DEEP SPACE NETWORK Progress Report, Jan. - Feb. 1978 (Jet Propulsion Lab.) 319 p HC A14/MF A01 CSCL 22D

N78-24212 THRU N78-24244 Unclas G3/12 21439

The Deep Space Network Progress Report 42-44

January and February 1978

National Aeronautics and Space Administration

Jet Propulsion Laboratory
California Institute of Technology
Pasadena California 91103

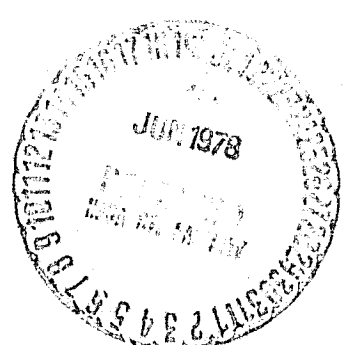

The Deep Space Network Progress Report 42-44

January and February 1978

April 15, 1978

National Aeronautics and
Space Administration

Jet Propulsion Laboratory
California Institute of Technology
Pasadena California 91103

Preface

Beginning with Volume XX, the Deep Space Network Progress Report changed from the Technical Report 32- series to the Progress Report 42- series. The volume number continues the sequence of the preceding issues. Thus, Progress Report 42-20 is the twentieth volume of the Deep Space Network series, and is an uninterrupted follow-on to Technical Report 32-1526, Volume XIX.

This report presents DSN progress in flight project support, tracking and data acquisition (TDA) research and technology, network engineering, hardware and software implementation, and operations. Each issue presents material in some, but not all, of the following categories in the order indicated.

Description of the DSN

Mission Support
- Ongoing Planetary/Interplanetary Flight Projects
- Advanced Flight Projects

Radio Astronomy

Special Projects

Supporting Research and Technology
- Tracking and Ground-Based Navigation
- Communications–Spacecraft/Ground
- Station Control and Operations Technology
- Network Control and Data Processing

Network and Facility Engineering and Implementation
- Network
- Network Operations Control Center
- Ground Communications
- Deep Space Stations
- Quality Assurance

Operations
- Network Operations
- Network Operations Control Center
- Ground Communications
- Deep Space Stations

Program Planning
- TDA Planning

In each issue, the part entitled "Description of the DSN" describes the functions and facilities of the DSN and may report the current configuration of one of the five DSN systems (Tracking, Telemetry, Command, Monitor & Control, and Test & Training).

The work described in this report series is either performed or managed by the Tracking and Data Acquisition organization of JPL for NASA.

Page intentionally left blank

Contents

DESCRIPTION OF THE DSN

DSN Functions and Facilities 1
N. A. Renzetti

DSN Test and Training System, Mark III-77 4
H. C. Thorman
NASA Code 311-03-43-10

MISSION SUPPORT

Ongoing Planetary/Interplanetary Flight Projects

Voyager Support 16
R. Morris
NASA Code 311-03-22-20

Viking Extended Mission Support 34
T. W. Howe
NASA Code 311-03-21-70

Pioneer Mission Support 44
T. P. Adamski
NASA Code 311-03-21-90

Helios Mission Support 50
P. S. Goodwin, W. N. Jensen, and G. M. Rockwell
NASA Code 311-03-21-50

SUPPORTING RESEARCH AND TECHNOLOGY

Tracking and Ground-Based Navigation

An Alternate Technique for Near-Sun Ranging 54
J. W. Layland
NASA Code 310-10-61-08

The Tone Generator and Phase Calibration in VLBI Measurements 63
J. B. Thomas
NASA Code 310-10-60-06

An Analysis of Viking S-X Doppler Measurements of Solar Wind Columnar Content Fluctuations 75
P. S. Callahan
NASA Code 310-10-60-05

A Method for Measuring Group Time Delay Through a Feed Horn 82
T. Y. Otoshi, R. B. Lyon, and M. Franco
NASA Code 310-10-61-08

Communications—Spacecraft/Ground

An Analysis of Alternate Symbol Inversion for Improved Symbol Synchronization in Convolutionally Coded Systems 90
L. D. Baumert, R. J. McEliece, and H. van Tilborg
NASA Code 310-20-67-11

A Prototype DSN X-S Band Feed: DSS 13 First Application Status 98
W. F. Williams
NASA Code 310-20-65-05

LAASP 100-m Antenna Wind Performance Studies 104
R. Levy and M. S. Katow
NASA Code 310-20-65-13

A Public-Key Cryptosystem Based On Algebraic Coding Theory 114
R. J. McEliece
NASA Code 310-10-67-11

Tracking Loop and Modulation Format Considerations for High Rate Telemetry 117
J. R. Lesh
NASA Code 310-20-67-13

Station Control and Operations Technology

Development Support—DSS 13 S-X Unattended Systems Development 125
E. B. Jackson
NASA Code 310-30-68-10

Network Control and Data Processing

The DSN Standard Real-Time Language 131
R. L. Schwartz, G. L. Fisher, and R. C. Tausworthe
NASA Code 310-40-72-05

NETWORK AND FACILITY ENGINEERING AND IMPLEMENTATION

Network

On Decoding of Reed-Solomon Codes Over *GF*(32) and *GF*(64) Using the Transform Techniques of Winograd 139
I. S. Reed, T. K. Truong, and B. Benjauthrit
NASA Code 311-03-42-95

Electron Density and Doppler RMS Phase Fluctuation in the Inner Corona 172
A. L. Berman
NASA Code 311-03-43-10

The DSS Radio Science Subsystem—Real-Time Bandwidth Reduction and Wideband Recording of Radio Science Data 180
A. L. Berman
NASA Code 311-03-43-10

Solar Wind Density Fluctuation and the Experiment to Detect Gravitational Waves in Ultraprecise Doppler Data 189
A. L. Berman
NASA Code 311-03-43-10

Solar Wind Turbulence Models Evaluated via Observations of Doppler RMS Phase Fluctuation and Spectral Broadening in the Inner Corona 197
A. L. Berman
NASA Code 311-03-43-10

On the Suitability of Viking Differenced Range to the Determination of Relative Z-Distance 203
F. B. Winn
NASA Code 311-03-42-54

Ground Communications

CCIR Papers on Telecommunications for Deep Space Research 211
N. F. deGroot
NASA Code 311-06-50-00

Deep Space Stations

Development of a Unified Criterion for Solar Collector Selection 224
F. L. Lansing
NASA Code 311-03-41-08

Implementation of Automated Fault Isolation Test Programs for Maximum Likelihood Convolutional Decoder (MCD) Maintenance 236
M. E. Alberda
NASA Code 311-03-44-11

Performance of Solar-Powered Vapor-Jet Refrigeration Systems with Selected Working Fluids 245
V. W. Chai and F. L. Lansing
NASA Code 311-03-41-08

OPERATIONS

Network Operations

Voyager Near Simultaneous Ranging Transfers. 252
G. L. Spradlin
NASA Code 311-03-13-20

Some Data Relationships Among Diverse Areas of the DSN and JPL 260
R. M. Smith
NASA Code 311-03-13-25

A New, Nearly Free, Clock Synchronization Technique 268
W. H. Hietzke
NASA Code 311-03-13-20

Deep Space Stations

Tracking Operations During the Voyager 2 Launch Phase. 273
J. A. Wackley and G. L. Spradlin
NASA Code 311-03-13-20

PROGRAM PLANNING

An Effective Procurement and Financial Management Reporting System 283
J. B. Rozek and F. R. Maiocco
NASA Code 311-03-32-10

N78-24213

Network Functions and Facilities

N. A. Renzetti
Office of Tracking and Data Acquisition

The objectives, functions, and organization of the Deep Space Network are summarized; deep space station, ground communication, and network operations control capabilities are described.

The Deep Space Network was established by the National Aeronautics and Space Administration (NASA) Office of Space Tracking and Data Systems and is under the system management and technical direction of the Jet Propulsion Laboratory (JPL). The network is designed for two-way communications with unmanned spacecraft traveling approximately 16,000 km (10,000 miles) from Earth to the farthest planets and to the edge of our solar system. It has provided tracking and data acquisition support for the following NASA deep space exploration projects: Ranger, Surveyor, Mariner Venus 1962, Mariner Mars 1964, Mariner Venus 1967, Mariner Mars 1969, Mariner Mars 1971, and Mariner Venus-Mercury 1973, for which JPL has been responsible for the project management, the development of the spacecraft, and the conduct of mission operations; Lunar Orbiter, for which the Langley Research Center carried out the project management, spacecraft development, and conduct of mission operations; Pioneer, for which Ames Research Center carried out the project management, spacecraft development, and conduct of mission operations; and Apollo, for which the Lyndon B. Johnson Space Center was the project center and the Deep Space Network supplemented the Manned Space Flight Network, which was managed by the Goddard Space Flight Center. The network is currently providing tracking and data acquisition support for Helios, a joint U.S./West German project; Viking, for which Langley Research Center provides the project management, the Lander spacecraft, and conducts mission operations, and for which JPL provides the Orbiter spacecraft; Voyager, for which JPL provides project management, spacecraft development, and conduct of mission operations; and Pioneer Venus, for which the Ames Research Center provides project management, spacecraft development, and conduct of mission operations. The network is adding new capability to meet the requirements of the Jupiter Orbiter Probe Mission, for which JPL provides the project management, spacecraft development and conduct of mission operations.

The Deep Space Network (DSN) is one of two NASA networks. The other, the Spaceflight Tracking and Data Network (STDN), is under the system management and technical direction of the Goddard Space Flight Center (GSFC). Its function is to support manned and unmanned Earth-orbiting satellites. The Deep Space Network supports lunar, planetary, and interplanetary flight projects.

From its inception, NASA has had the objective of conducting scientific investigations throughout the solar system. It was recognized that in order to meet this objective, significant supporting research and advanced technology development must be conducted in order to provide deep space telecommunications for science data return in a cost effective manner. Therefore, the Network is continually evolved to keep pace with the state of the art of telecommunications and data

handling. It was also recognized early that close coordination would be needed between the requirements of the flight projects for data return and the capabilities needed in the Network. This close collaboration was effected by the appointment of a Tracking and Data Systems Manager as part of the flight project team from the initiation of the project to the end of the mission. By this process, requirements were identified early enough to provide funding and implementation in time for use by the flight project in its flight phase.

As of July 1972, NASA undertook a change in the interface between the Network and the flight projects. Prior to that time, since 1 January 1964, in addition to consisting of the Deep Space Stations and the Ground Communications Facility, the Network had also included the mission control and computing facilities and provided the equipment in the mission support areas for the conduct of mission operations. The latter facilities were housed in a building at JPL known as the Space Flight Operations Facility (SFOF). The interface change was to accommodate a hardware interface between the support of the network operations control functions and those of the mission control and computing functions. This resulted in the flight projects assuming the cognizance of the large general-purpose digital computers which were used for both network processing and mission data processing. They also assumed cognizance of all of the equipment in the flight operations facility for display and communications necessary for the conduct of mission operations. The Network then undertook the development of hardware and computer software necessary to do its network operations control and monitor functions in separate computers. A characteristic of the new interface is that the Network provides direct data flow to and from the stations; namely, metric data, science and engineering telemetry, and such network monitor data as are useful to the flight project. This is done via appropriate ground communication equipment to mission operations centers, wherever they may be.

The principal deliverables to the users of the Network are carried out by data system configurations as follows:

- The DSN Tracking System generates radio metric data, i.e., angles, one- and two-way doppler and range, and transmits raw data to Mission Control.
- The DSN Telemetry System receives, decodes, records, and retransmits engineering and scientific data generated in the spacecraft to Mission Control.
- The DSN Command System accepts spacecraft commands from Mission Control and transmits the commands via the Ground Communication Facility to a Deep Space Station. The commands are then radiated to the spacecraft in order to initiate spacecraft functions in flight.
- The DSN Radio Science System generates radio science data, i.e., the frequency and amplitude of spacecraft transmitted signals affected by passage through media such as the solar corona, planetary atmospheres, and planetary rings, and transmits this data to Mission Control.

The data system configurations supporting testing, training, and network operations control functions are as follows:

- The DSN Monitor and Control System instruments, transmits, records, and displays those parameters of the DSN necessary to verify configuration and validate the Network. It provides the tools necessary for Network Operations personnel to control and monitor the Network and interface with flight project mission control personnel.
- The DSN Test and Training System generates and controls simulated data to support development, test, training and fault isolation within the DSN. It participates in mission simulation with flight projects.

The capabilities needed to carry out the above functions have evolved in three technical areas:

(1) The Deep Space Stations, which are distributed around Earth and which, prior to 1964, formed part of the Deep Space Instrumentation Facility. The technology involved in equipping these stations is strongly related to the state of the art of telecommunications and flight-ground design considerations, and is almost completely multimission in character.

(2) The Ground Communications Facility provides the capability required for the transmission, reception, and monitoring of Earth-based, point-to-point communications between the stations and the Network Operations Control Center at JPL, Pasadena, and to the JPL Mission Operations Centers. Four communications disciplines are provided: teletype, voice, high-speed, and wideband. The Ground Communications Facility uses the capabilities provided by common carriers throughout the world, engineered into an integrated system by Goddard Space Flight Center, and controlled from the communications Center located in the Space Flight Operations Facility (Building 230) at JPL.

The Network Operations Control Center is the functional entity for centralized operational control of the Network and interfaces with the users. It has two separable functional elements; namely, Network Operations Control and Network

Data Processing. The functions of the Network Operations Control are:

- Control and coordination of Network support to meet commitments to Network users.
- Utilization of the Network data processing computing capability to generate all standards and limits required for Network operations.
- Utilization of Network data processing computing capability to analyze and validate the performance of all Network systems.

The personnel who carry out the above functions are located in the Space Flight Operations Facility, where mission operations functions are carried out by certain flight projects. Network personnel are directed by an Operations Control Chief. The functions of the Network Data Processing are:

- Processing of data used by Network Operations Control for control and analysis of the Network.
- Display in the Network Operations Control Area of data processed in the Network Data Processing Area.
- Interface with communications circuits for input to and output from the Network Data Processing Area.
- Data logging and production of the intermediate data records.

The personnel who carry out these functions are located approximately 200 meters from the Space Flight Operations Facility. The equipment consists of minicomputers for real-time data system monitoring, two XDS Sigma 5s, display, magnetic tape recorders, and appropriate interface equipment with the ground data communications.

N78-24214

DSN Test and Training System, Mark III-77

H. C. Thorman
TDA Engineering Office

Implementation of the DSN Test and Training System, Mark III-77, throughout the network is nearing completion. The Mark III-77 system is configured to support DSN testing and training for the Pioneer-Venus 1978 mission and all on-going, in-flight missions. DSN Test and Training System capabilities include functions performed in the Deep Space Stations, Ground Communications Facility, and Network Operations Control Center.

I. System Definition

A. General

The DSN Test and Training System is a multiple-mission system which supports Network-wide testing and training by inserting test signals and data into subsystems of the Deep Space Stations (DSS), the Ground Communications Facility (GCF), and the Network Operations Control Center (NOCC). The system includes capabilities for:

(1) On-site testing of the DSS portion of each DSN system.

(2) Local testing of the NOCC portion of each DSN system.

(3) End-to-end testing of each DSN system, including DSS, GCF, and NOCC functions.

Figure 1 describes the functions, elements, and interfaces of the system. This article updates the system description published in Ref. 1.

B. Key Characteristics

Design goal key characteristics of the DSN Test and Training System are:

(1) Capability to function without alteration of DSN operational configuration.

(2) Utilization of mission-independent equipment for DSN testing and training functions.

(3) Capability to exercise NOCC, GCF, and DSS simultaneously, for end-to-end testing of each DSN system.

(4) Capability to supply test data to all DSN systems simultaneously.

(5) Capability to load Network with combination of actual and simulated data streams.

(6) Accommodation of flight-project-supplied simulation data via GCF.

(7) Accommodation of other data sources, as follows:

(a) Spacecraft test data via JPL Compatibility Test Area (CTA 21).

(b) Spacecraft prelaunch data via Merritt Island, Florida, Spacecraft Compatibility-Monitor Station (STDN (MIL 71)).

C. System Usage

Major testing and training activities supported by the DSN Test and Training System are summarized below:

(1) Prepass and pretest calibrations, readiness verifications, and fault isolation.

(2) DSN implementation activities and performance testing of DSN systems, DSS subsystems, and NOCC subsystems.

(3) DSN operational verification tests to prepare for mission support.

(4) Flight project ground data system tests and mission simulations.

II. Mark III-77 System Implementation

A. Status

A functional block diagram showing the data-flow and signal-flow paths of the DSN Test and Training System, Mark III-77, is shown in Fig. 2. Implementation of the Mark III-77 system throughout the network will have been completed when DSS 11 returns to operation in the latter part of March, 1978.

Upgrading of the DSS portions of this system has been a part of the DSN Mark III Data Subsystems (MDS) implementation project, which began in 1976.

B. Mission Set

The Mark III-77 configuration of the DSN Test and Training System includes all elements of the system required for support related to the following mission set:

(1) Viking Orbiters 1 and 2 and Viking Landers 1 and 2 (extended mission).

(2) Pioneers 6 through 9.

(3) Pioneers 10 and 11.

(4) Helios 1 and 2.

(5) Voyagers 1 and 2 (including planetary encounters).

(6) Pioneer-Venus 1978 (PV '78) Orbiter and Multiprobe.

C. New Capabilities

The following modifications and additions upgraded the system to the Mark III-77 configuration:

(1) Modification of the DSS Simulation Conversion Assembly (SCA) to provide capability for short-constraint-length convolutional coding of simulated Voyager telemetry data and long-constraint-length convolutional coding of simulated PV '78 telemetry data, as described in Ref. 2.

(2) Additional program software for the XDS-910 Simulation Processor Assembly (SPA), to control new SCA equipment, to generate simulated Voyager and Pioneer-Venus telemetry data patterns, and to convert project-supplied data from GCF high-speed and wideband data blocks into serial data streams, as described in Ref. 2.

(3) New program software to perform the System Performance Test (SPT) functions of on-site closed-loop performance testing and validation of the Tracking, Telemetry, Command, and Monitor and Control Systems.

(4) Configuring of the GCF Communications Monitor and Formatter (CMF) backup minicomputer to provide interfaces required for the SPT functions.

(5) Implementation of the Network Control Test and Training Subsystem in the Network Operations Control Center (Block III).

(6) Implementation of special test and training equipment in the Receiver-Exciter Subsystem at DSS 14 and 43, to generate four carriers simulating the expected doppler profile and sequence characteristics of the carriers to be received from the Pioneer-Venus atmospheric entry probes. The design of this simulator is described in Ref. 3.

III. Deep Space Station Functions

A. DSS Test and Training Subsystem

The functions of the DSS Test and Training Subsystem and the related interfaces are shown in Fig. 3.

(1) Telemetry simulation and conversion. The telemetry simulation and conversion functions are performed by

the Simulation Processor Assembly and the Simulation Conversion Assembly, as diagrammed in Fig. 4. Digital and analog capabilities are itemized in Tables 1 and 2, respectively.

(2) System performance test functions. The system performance test functions are performed by the SPT Software Assembly, as diagrammed in Fig. 5.

B. Receiver-Exciter Subsystem

The Receiver-Exciter Subsystem provides the following test and training functions:

(1) Generation of simulated S-band and X-band downlink carriers.

(2) Modulation of telemetry subcarriers from the SCA onto simulated carriers.

(3) Variable attenuation of simulated downlink carrier signal level under control of the SPA.

(4) Translation of S-band exciter uplink frequencies to S-band and X-band downlink frequencies, for Tracking System calibrations and performance testing.

(5) Generation of simulated Pioneer-Venus entry probe carriers at DSS 14 and 43.

C. Antenna Microwave Subsystem

The Antenna Microwave Subsystem provides the following test and training functions:

(1) Routing of simulated downlink carriers to masers and/or receivers.

(2) Mixing of simulated S-band downlink carriers.

D. Transmitter Subsystem

The Transmitter Subsystem includes provision for feeding the transmitter output into a dummy load to support Command System and Tracking System test operations.

E. Frequency and Timing Subsystem

The Frequency and Timing Subsystem provides the following support functions to the DSS Test and Training Subsystem:

(1) Time code and reference frequencies.

(2) Generation and distribution of a simulated time signal which can be substituted for the true GMT input to the various DSS subsystems. This capability is provided for realistic mission simulations in support of flight project testing and training activities.

IV. Ground Communications Facility Functions

The DSN Test and Training System utilizes the Ground Communications Facility Subsystems for communicating data and information between the Network Operations Control Center (NOCC) or any Mission Operations Center (MOC) and the Deep Space Stations.

A. High-Speed Data Subsystem

The High-Speed Data Subsystem provides the following:

(1) Transmission of text messages, control messages, low- to medium-rate simulated telemetry data, and simulated command data to any DSS from the NOCC or from any MOC.

(2) On-site loop-back of test data for systems performance testing and readiness verifications in the DSS.

B. Wideband Data Subsystem

The Wideband Data Subsystem provides the following:

(1) Transmission of simulated high-rate telemetry data to the 64-m subnet (DSSs 14, 43, and 63), the Compatibility Test Area (CTA 21), in Pasadena, California, and STDN (MIL 71) at Merritt Island, Florida, from the NOCC or from any MOC having wideband capability.

(2) On-site loop-back of test data for telemetry system performance testing and readiness verification in those Deep Space Stations which have wideband capability.

C. Teletype and Voice Subsystems

The Teletype and Voice Subsystems provide communication of information for purposes of test coordination and monitoring of the DSN Test and Training System status.

V. Network Operations Control Center Functions

A. NOCC Test and Training Subsystem

Functions and interfaces of the NOCC Test and Training Subsystem are shown in Fig. 6. Subsystem data flow is diagrammed in Fig. 7. Test and training capabilities presently implemented in the Network Operations Control Center are as follows:

(1) Selection of stored data blocks and output to the DSS for system readiness verification.

(2) Off-line generation of recordings of high-speed data blocks for testing of the real-time monitors in the

NOCC Tracking, Telemetry, Command, and Monitor Subsystems.

(3) Output of text and control messages to the DSS for remote configuration and control of the SPA and SCA in support of DSN Operational Verification Tests.

B. DSN Test and Training System Control Console

A DSN Test and Training System Control Console in the Network Data Processing Area provides keyboard, card reader, magnetic tape unit, volatile display, and character printer for operation of the Test and Training System separate from the operations of the other DSN Systems.

References

1. Thorman, H. C., "DSN Test and Training System, Mark III-77," in *The Deep Space Network Progress Report 42-38*, pp. 4-15, Jet Propulsion Laboratory, Pasadena, California, April 15, 1977.

2. Yee, S. H., "Modification of Simulation Conversion Assembly for Support of Voyager Project and Pioneer-Venus 1978 Project," in *The Deep Space Network Progress Report 42-39*, pp. 100-108, Jet Propulsion Laboratory, Pasadena, California, June 15, 1977.

3. Friedenberg, S. E., "Pioneer Venus 1978 Multiprobe Spacecraft Simulator," in *The Deep Space Network Progress Report 42-38*, pp. 148-151, Jet Propulsion Laboratory, Pasadena, California, April 15, 1977.

Table 1. DSS Test and Training Subsystem digital telemetry simulation capabilities

Capability	26-meter DSS, MIL 71	64-meter DSS, CTA 21
Maximum number of simultaneous real-time data streams	2 channels	Viking extended mission, 4 channels Other missions, 3 channels
Bi-orthogonal (32, 6) comma-free block coding	Viking, 2 channels Other missions, none	Viking, 3 channels Other missions, none
Short-constraint-length convolutional coding (k=7, r=1/2 or 1/3)	Mariner Jupiter-Saturn, rate = 1/2, 2 channels Future missions, rate = 1/3, 1 channel	Mariner Jupiter-Saturn, rate = 1/2, 3 channels Future missions, rate = 1/3, 2 channels
Long-constraint-length convolutional coding (k=32, r=1/2)	Helios, 1 channel Pioneer 10/11, 2 channels Pioneer Venus, 2 channels	Helios, 1 channel Pioneer 10/11, 2 channels Pioneer Venus, 3 channels
Variable rate control	1 bps to 600 ksps on 1 channel 1 bps to 190 ksps on 1 additional channel	1 bps to 600 ksps on 2 channels 1 bps to 190 ksps on 1 additional channel
Selection of discrete rates	8-1/3, 33-1/3 bps on each of 2 channels (for Viking)	8-1/3, 33-1/3 bps on each of 3 channels (for Viking)

Table 2. DSS Test and Training Subsystem analog telemetry simulation capabilities

Capability	26-meter DSS, MIL 71	64-meter DSS, CTA 21
Data and subcarrier signal conditioning, phase-shift keyed modulation	2 subcarriers	Viking extended mission, 4 subcarriers Other missions, 3 subcarriers
Subcarrier frequency output	512 Hz to 1.25 MHz, 1/4-Hz resolution	512 Hz to 1.25 MHz, 1/4-Hz resolution
Modulation-index angle control	Controllable from 0 to 89 deg on each subcarrier	Controllable from 0 to 89 deg on each subcarrier
Subcarrier mixing and downlink carrier biphase modulation	Single or dual subcarriers onto each of 2 S-band test carriers or 1 S-band and 1 X-band	Single or dual subcarriers onto each of 3 test carriers or 2 S-band and 1 X-band
Downlink carrier signal level	Attenuation of 0 to 40 dB on each test carrier output	Attenuation of 0 to 40 dB on each test carrier output

ORIGINAL PAGE IS
OF POOR QUALITY

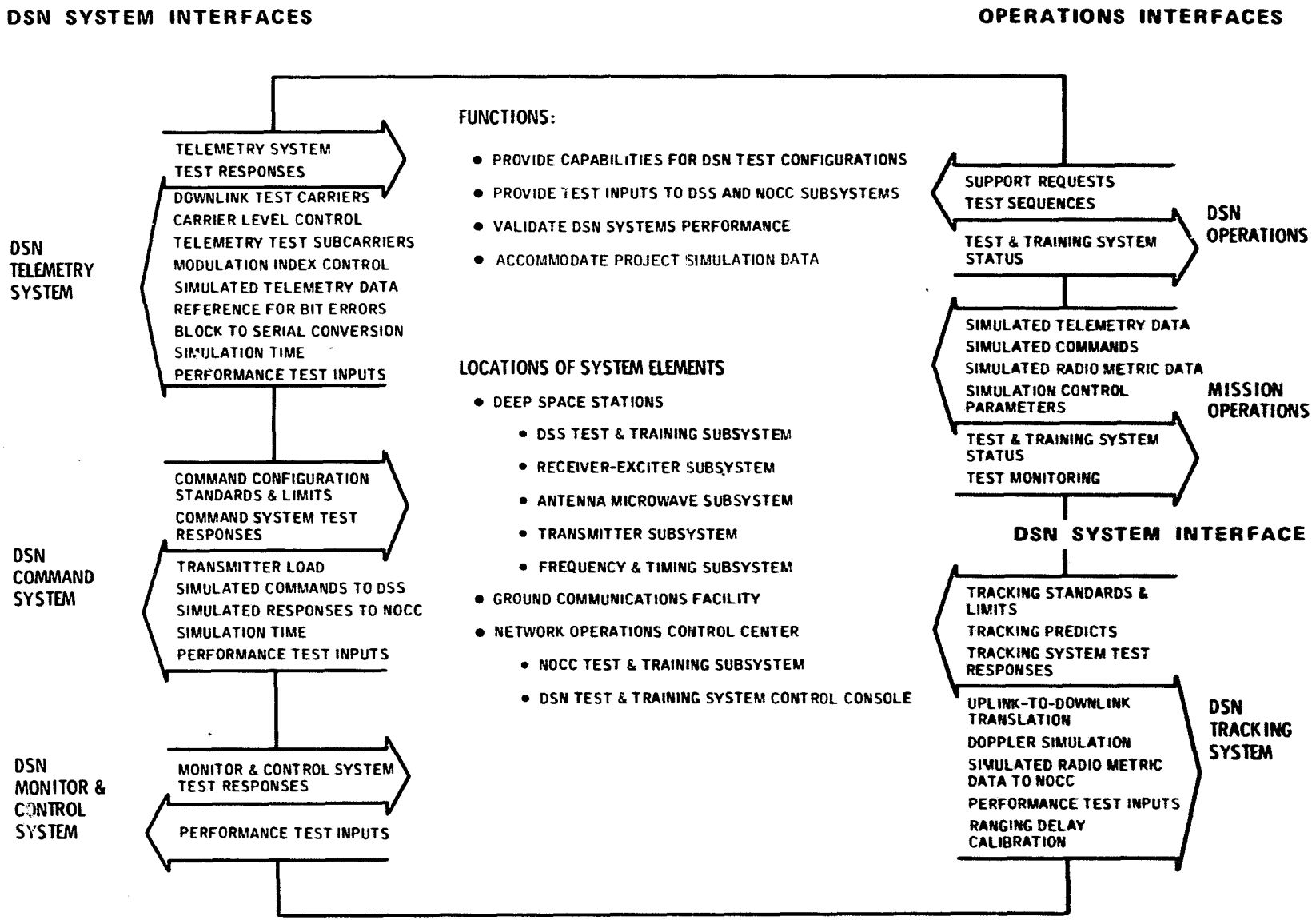

Fig. 1. DSN Test and Training System functions and interfaces

ORIGINAL PAGE IS
OF POOR QUALITY

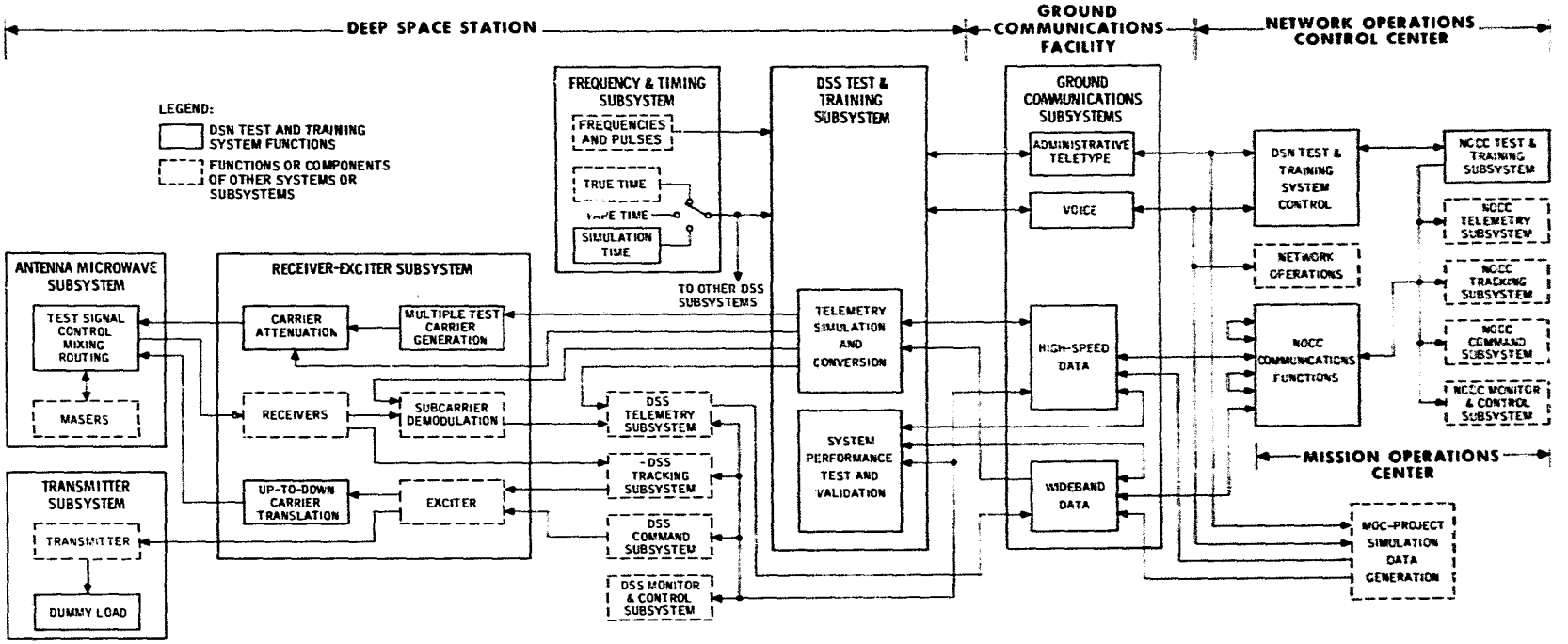

Fig. 2. DSN Test and Training System, Mark III-77, functional block diagram

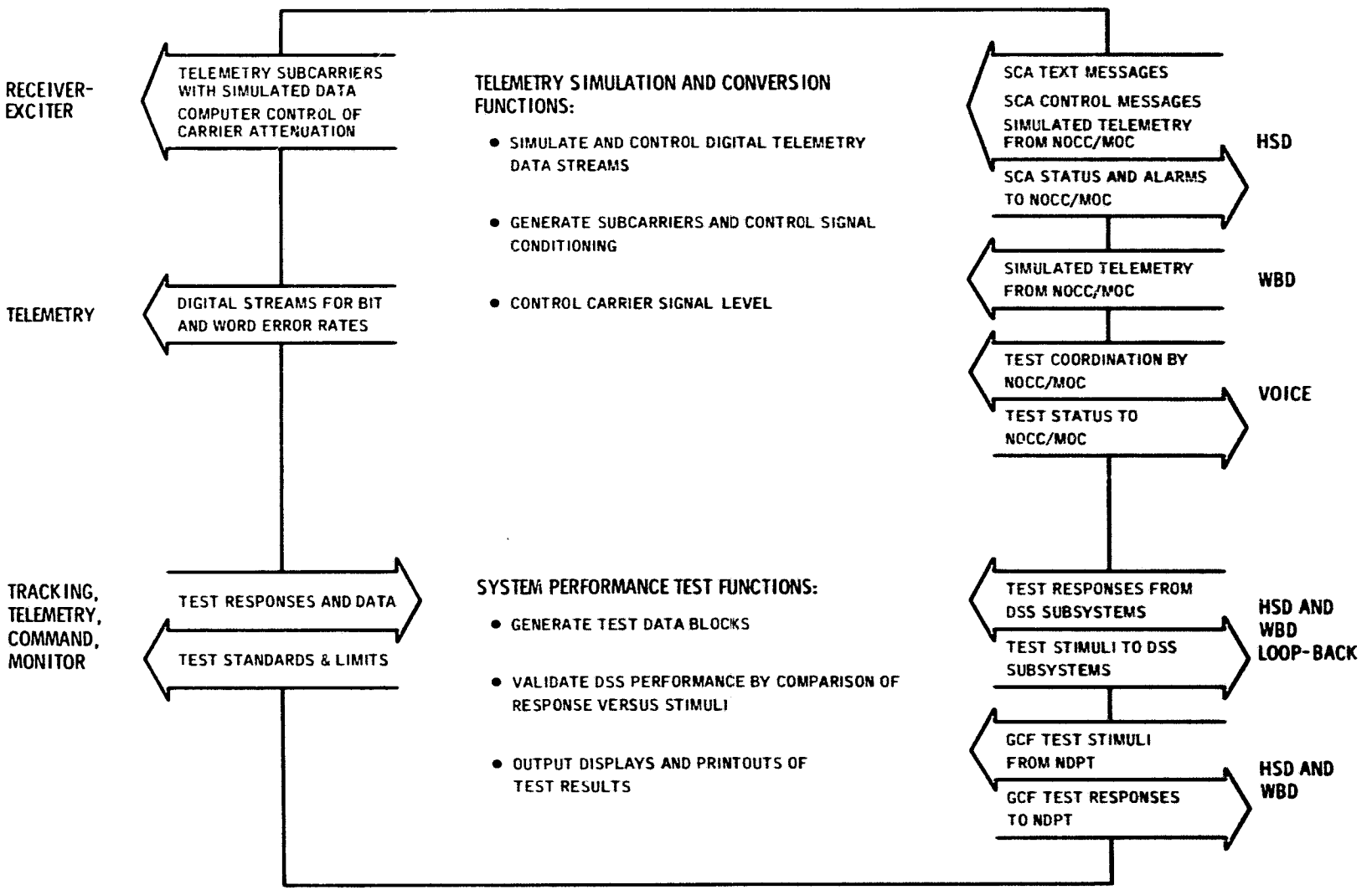
DSS SUBSYSTEM INTERFACES
GCF SUBSYSTEM INTERFACES
RECEIVER-EXCITER
TELEMETRY SUBCARRIERS WITH SIMULATED DATA
COMPUTER CONTROL OF CARRIER ATTENUATION
TELEMETRY
DIGITAL STREAMS FOR BIT AND WORD ERROR RATES
TRACKING, TELEMETRY, COMMAND, MONITOR
TEST RESPONSES AND DATA
TEST STANDARDS & LIMITS
TELEMETRY SIMULATION AND CONVERSION FUNCTIONS:
• SIMULATE AND CONTROL DIGITAL TELEMETRY DATA STREAMS
• GENERATE SUBCARRIERS AND CONTROL SIGNAL CONDITIONING
• CONTROL CARRIER SIGNAL LEVEL
SYSTEM PERFORMANCE TEST FUNCTIONS:
• GENERATE TEST DATA BLOCKS
• VALIDATE DSS PERFORMANCE BY COMPARISON OF RESPONSE VERSUS STIMULI
• OUTPUT DISPLAYS AND PRINTOUTS OF TEST RESULTS
SCA TEXT MESSAGES
SCA CONTROL MESSAGES
SIMULATED TELEMETRY FROM NOCC/MOC
HSD
SCA STATUS AND ALARMS TO NOCC/MOC
SIMULATED TELEMETRY FROM NOCC/MOC
WBD
TEST COORDINATION BY NOCC/MOC
TEST STATUS TO NOCC/MOC
VOICE
TEST RESPONSES FROM DSS SUBSYSTEMS
TEST STIMULI TO DSS SUBSYSTEMS
HSD AND WBD LOOP-BACK
GCF TEST STIMULI FROM NDPT
GCF TEST RESPONSES TO NDPT
HSD AND WBD

Fig. 3. DSS Test and Training Subsystem functions and interfaces

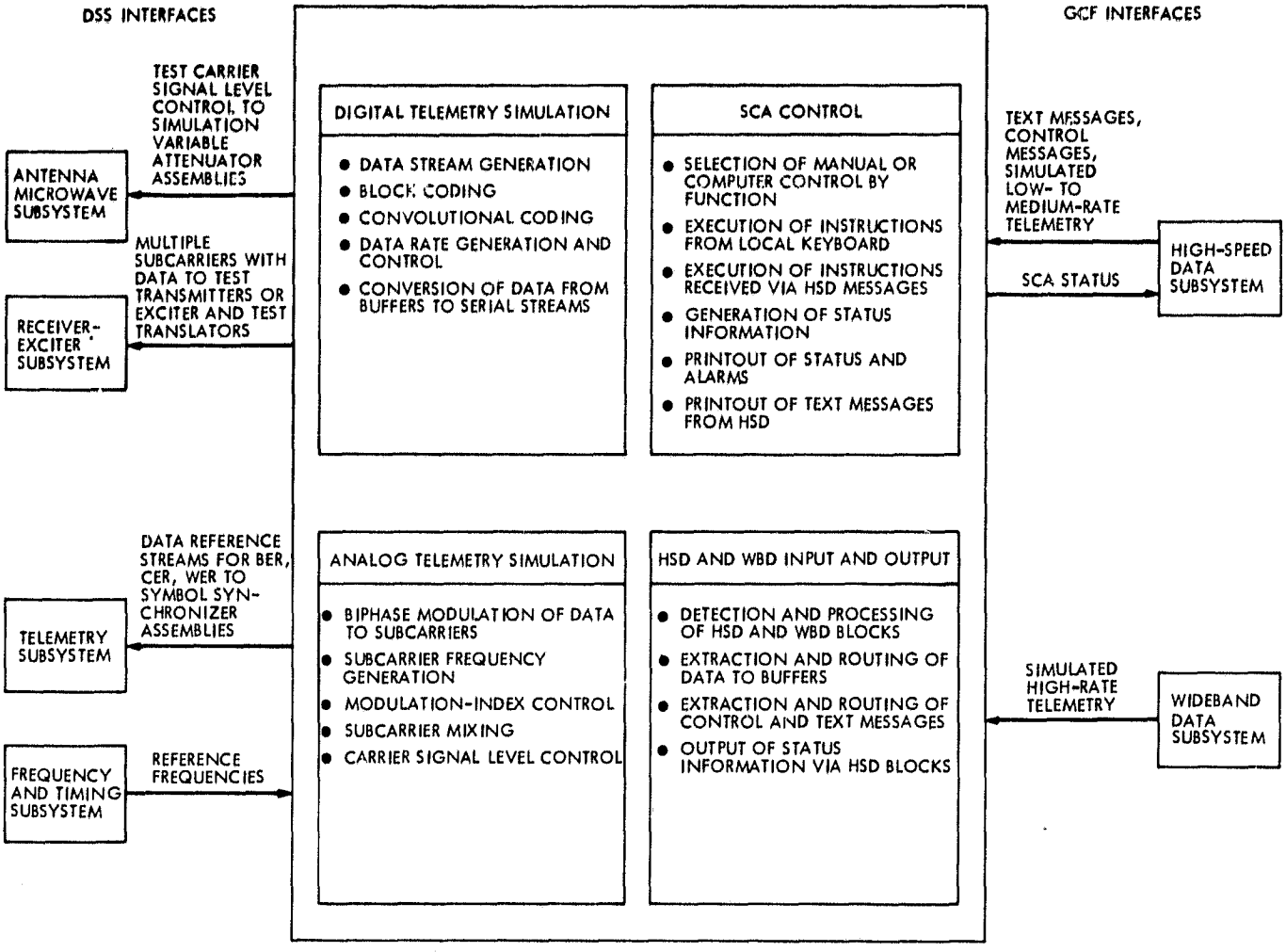
DSS INTERFACES
GCF INTERFACES
TEST CARRIER SIGNAL LEVEL CONTROL TO SIMULATION VARIABLE ATTENUATOR ASSEMBLIES
ANTENNA MICROWAVE SUBSYSTEM
MULTIPLE SUBCARRIERS WITH DATA TO TEST TRANSMITTERS OR EXCITER AND TEST TRANSLATORS
RECEIVER-EXCITER SUBSYSTEM
DIGITAL TELEMETRY SIMULATION
DATA STREAM GENERATION
BLOCK CODING
CONVOLUTIONAL CODING
DATA RATE GENERATION AND CONTROL
CONVERSION OF DATA FROM BUFFERS TO SERIAL STREAMS
SCA CONTROL
SELECTION OF MANUAL OR COMPUTER CONTROL BY FUNCTION
EXECUTION OF INSTRUCTIONS FROM LOCAL KEYBOARD
EXECUTION OF INSTRUCTIONS RECEIVED VIA HSD MESSAGES
GENERATION OF STATUS INFORMATION
PRINTOUT OF STATUS AND ALARMS
PRINTOUT OF TEXT MESSAGES FROM HSD
TEXT MESSAGES, CONTROL MESSAGES, SIMULATED LOW- TO MEDIUM-RATE TELEMETRY
SCA STATUS
HIGH-SPEED DATA SUBSYSTEM
DATA REFERENCE STREAMS FOR BER, CER, WER TO SYMBOL SYNCHRONIZER ASSEMBLIES
TELEMETRY SUBSYSTEM
ANALOG TELEMETRY SIMULATION
BIPHASE MODULATION OF DATA TO SUBCARRIERS
SUBCARRIER FREQUENCY GENERATION
MODULATION-INDEX CONTROL
SUBCARRIER MIXING
CARRIER SIGNAL LEVEL CONTROL
HSD AND WBD INPUT AND OUTPUT
DETECTION AND PROCESSING OF HSD AND WBD BLOCKS
EXTRACTION AND ROUTING OF DATA TO BUFFERS
EXTRACTION AND ROUTING OF CONTROL AND TEXT MESSAGES
OUTPUT OF STATUS INFORMATION VIA HSD BLOCKS
SIMULATED HIGH-RATE TELEMETRY
WIDEBAND DATA SUBSYSTEM
FREQUENCY AND TIMING SUBSYSTEM
REFERENCE FREQUENCIES

Fig. 4. Telemetry simulation and conversion functions and data flow

ORIGINAL PAGE IS
OF POOR QUALITY

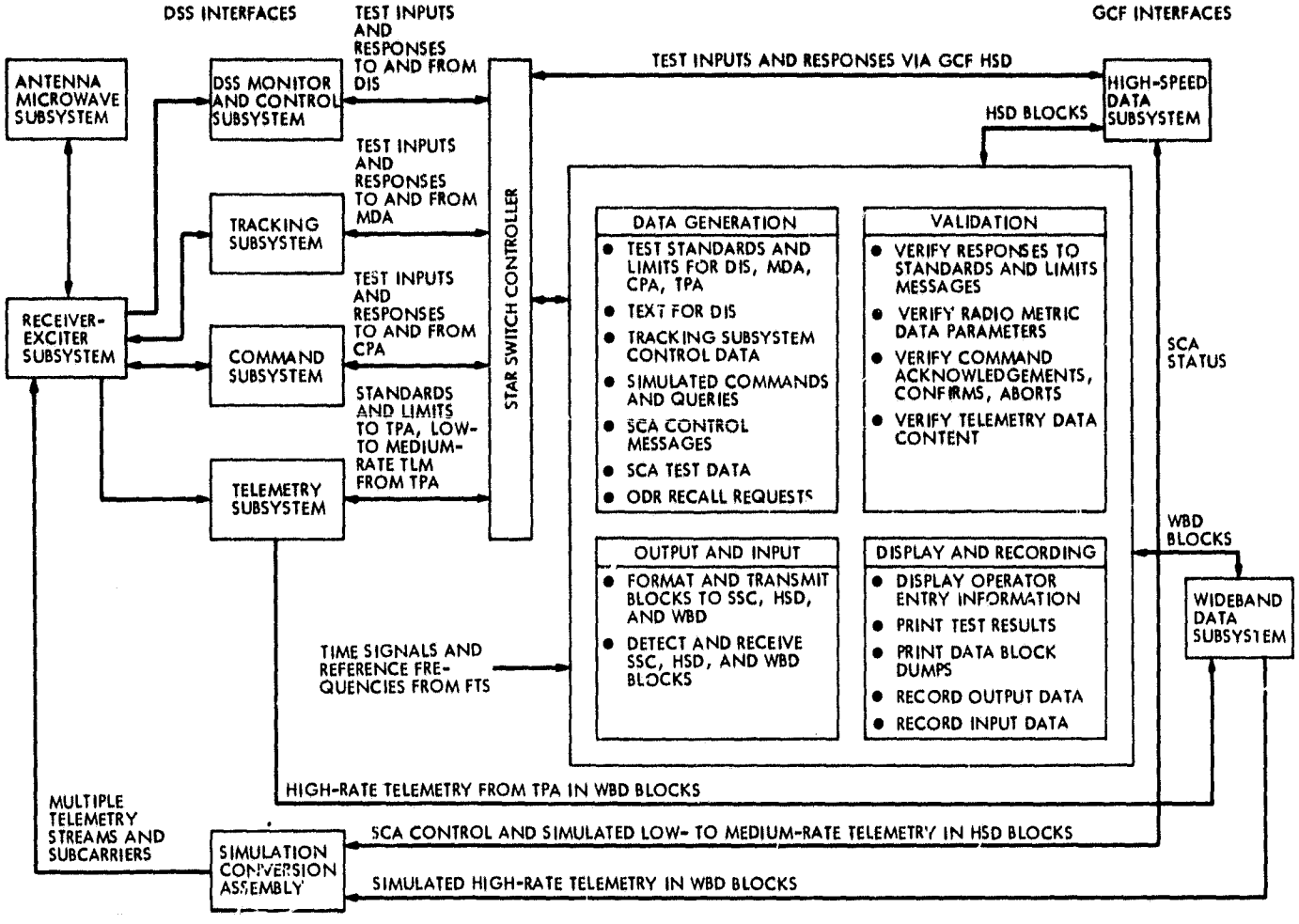
DSS INTERFACES
TEST INPUTS AND RESPONSES TO AND FROM DIS
GCF INTERFACES
ANTENNA MICROWAVE SUBSYSTEM
DSS MONITOR AND CONTROL SUBSYSTEM
TEST INPUTS AND RESPONSES VIA GCF HSD
HIGH-SPEED DATA SUBSYSTEM
HSD BLOCKS
TEST INPUTS AND RESPONSES TO AND FROM MDA
TRACKING SUBSYSTEM
STAR SWITCH CONTROLLER
DATA GENERATION
TEST STANDARDS AND LIMITS FOR DIS, MDA, CPA, TPA
TEXT FOR DIS
TRACKING SUBSYSTEM CONTROL DATA
SIMULATED COMMANDS AND QUERIES
SCA CONTROL MESSAGES
SCA TEST DATA
ODR RECALL REQUESTS
VALIDATION
VERIFY RESPONSES TO STANDARDS AND LIMITS MESSAGES
VERIFY RADIO METRIC DATA PARAMETERS
VERIFY COMMAND ACKNOWLEDGEMENTS, CONFIRMS, ABORTS
VERIFY TELEMETRY DATA CONTENT
TEST INPUTS AND RESPONSES TO AND FROM CPA
RECEIVER-EXCITER SUBSYSTEM
COMMAND SUBSYSTEM
SCA STATUS
STANDARDS AND LIMITS TO TPA, LOW- TO MEDIUM-RATE TLM FROM TPA
TELEMETRY SUBSYSTEM
WBD BLOCKS
OUTPUT AND INPUT
FORMAT AND TRANSMIT BLOCKS TO SSC, HSD, AND WBD
DETECT AND RECEIVE SSC, HSD, AND WBD BLOCKS
DISPLAY AND RECORDING
DISPLAY OPERATOR ENTRY INFORMATION
PRINT TEST RESULTS
PRINT DATA BLOCK DUMPS
RECORD OUTPUT DATA
RECORD INPUT DATA
WIDEBAND DATA SUBSYSTEM
TIME SIGNALS AND REFERENCE FREQUENCIES FROM FTS
HIGH-RATE TELEMETRY FROM TPA IN WBD BLOCKS
MULTIPLE TELEMETRY STREAMS AND SUBCARRIERS
SIMULATION CONVERSION ASSEMBLY
SCA CONTROL AND SIMULATED LOW- TO MEDIUM-RATE TELEMETRY IN HSD BLOCKS
SIMULATED HIGH-RATE TELEMETRY IN WBD BLOCKS

Fig. 5. System performance test functions and data flow

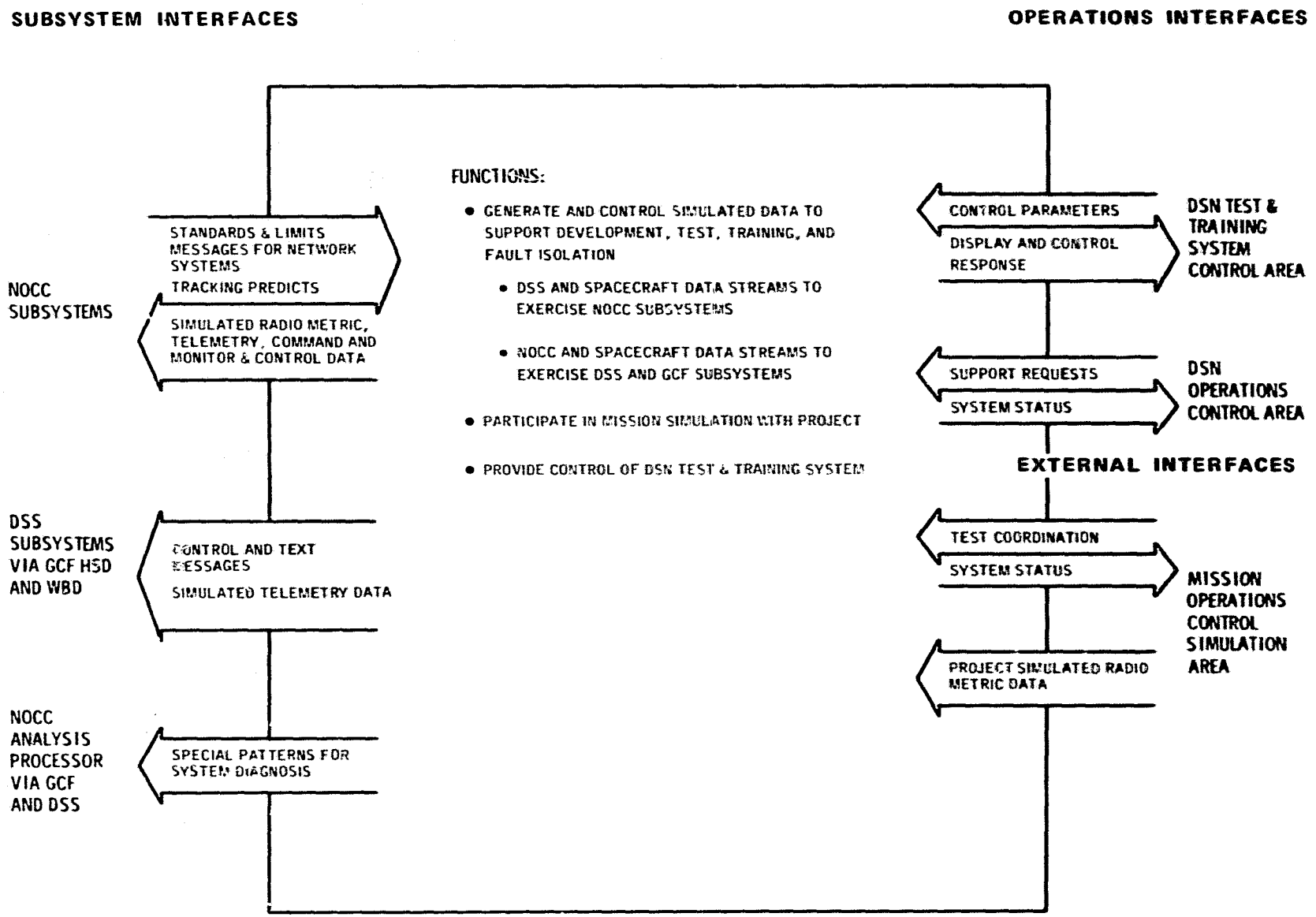
SUBSYSTEM INTERFACES
OPERATIONS INTERFACES
FUNCTIONS:
• GENERATE AND CONTROL SIMULATED DATA TO SUPPORT DEVELOPMENT, TEST, TRAINING, AND FAULT ISOLATION
• DSS AND SPACECRAFT DATA STREAMS TO EXERCISE NOCC SUBSYSTEMS
• NOCC AND SPACECRAFT DATA STREAMS TO EXERCISE DSS AND GCF SUBSYSTEMS
• PARTICIPATE IN MISSION SIMULATION WITH PROJECT
• PROVIDE CONTROL OF DSN TEST & TRAINING SYSTEM
NOCC SUBSYSTEMS
STANDARDS & LIMITS MESSAGES FOR NETWORK SYSTEMS
TRACKING PREDICTS
SIMULATED RADIO METRIC, TELEMETRY, COMMAND AND MONITOR & CONTROL DATA
DSS SUBSYSTEMS VIA GCF H5D AND WBD
CONTROL AND TEXT MESSAGES
SIMULATED TELEMETRY DATA
NOCC ANALYSIS PROCESSOR VIA GCF AND DSS
SPECIAL PATTERNS FOR SYSTEM DIAGNOSIS
CONTROL PARAMETERS
DISPLAY AND CONTROL RESPONSE
DSN TEST & TRAINING SYSTEM CONTROL AREA
SUPPORT REQUESTS
SYSTEM STATUS
DSN OPERATIONS CONTROL AREA
EXTERNAL INTERFACES
TEST COORDINATION
SYSTEM STATUS
MISSION OPERATIONS CONTROL SIMULATION AREA
PROJECT SIMULATED RADIO METRIC DATA

Fig. 6. NOCC Test and Training Subsystem functions and interfaces

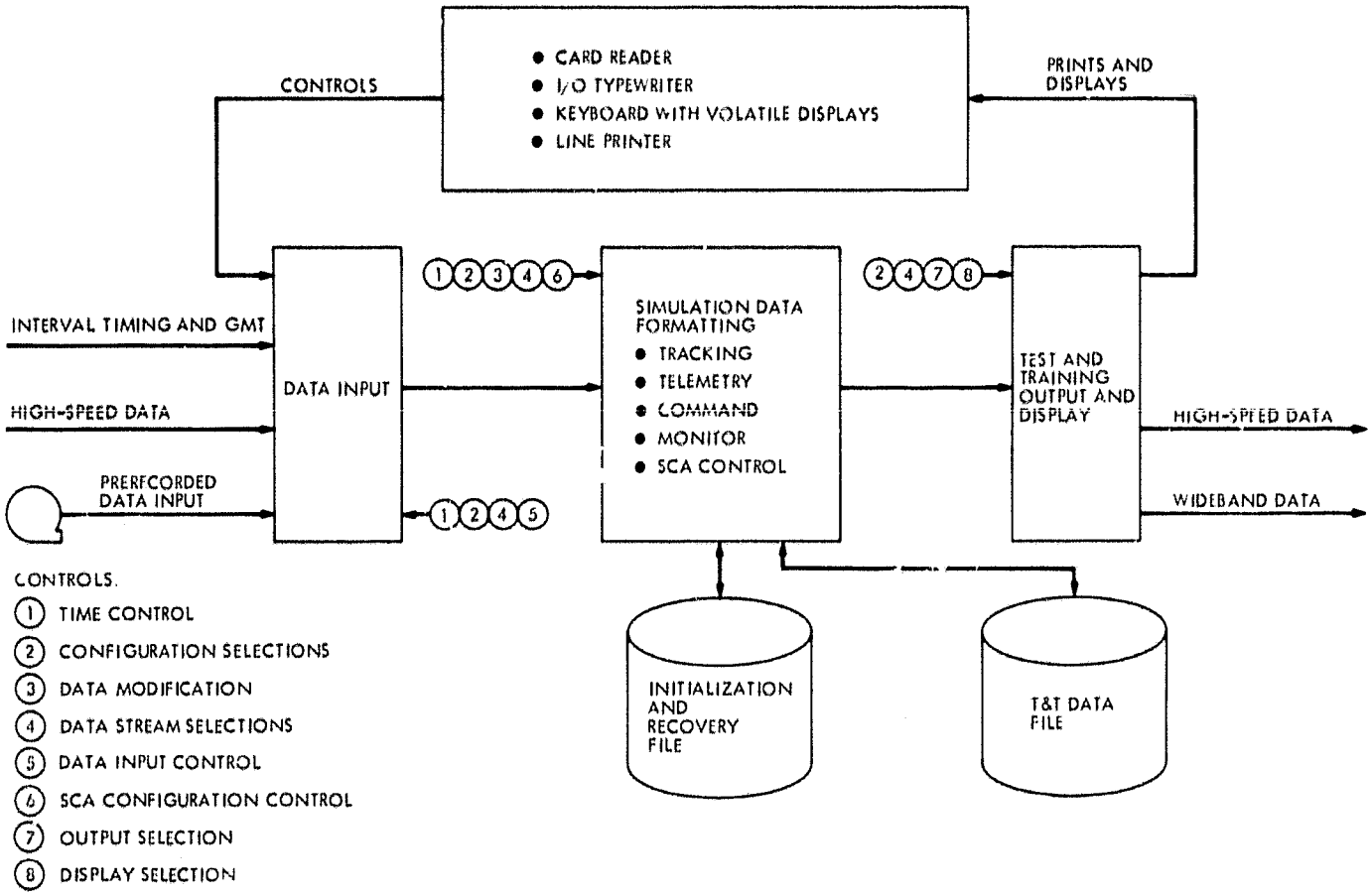

Fig. 7. NOCC Test and Training Subsystem data flow

N78-24215

Voyager Support

R. Morris
DSN Operations Section

This is a first in a series of Deep Space Network reports on Tracking and Data Acquisition support for Project Voyager. This report covers the Network's pre-launch preparations and flight support through 31 December 1977.

I. Introduction

This is the first in a series of articles which will cover Deep Space Network operational support for Project Voyager. The purpose is to summarize tracking and data acquisition activities and the Network's performance in meeting commitments throughout the mission. Significant new capabilities were implemented for Voyager as part of the DSN Mark III 1977 Data Subsystem Implementation Project (MDS).[1] Consequently, network pre-launch test and training activities were extensive as described herein. Also, since this is the initial article, a brief mission--spacecraft description is provided for reference. Additional information on the mission is provided in Ref. 1.

II. General Mission Description

The objectives of the Voyager Project are to conduct exploratory investigations of the Jupiter and Saturn planetary systems, and the interplanetary medium between Earth and Saturn. This will be accomplished by two spacecrafts launched in 1977 on flyby trajectories that will employ Jupiter's gravitational assist to reach Saturn. Although not a formal objective, the Voyager mission design will not preclude one spacecraft from using a Saturn gravity assist to go on to a Uranus flyby.

A. Mission Design

The primary science objectives are to conduct comparative studies of the planetary systems of Jupiter and Saturn, including their environment, atmosphere, surface, and body characteristics. Also, objectives include the investigation of one or more satellites of each planet, the nature of Saturn's rings, and the interplanetary and interstellar media throughout the cruise phase of the mission.

Science instruments which have been selected for the Voyager mission are as follows: imaging television cameras; infrared interferometer, spectrometer, and radiometer; ultraviolet spectrometer, plasma wave analyzer, magnetometers, low-energy charged particle detectors, cosmic ray detectors, plasma detector, planetary radio astronomy receivers, photopolarimeter, and the spacecraft radio frequency communications link for celestial mechanics and radio science investigations.

The interplanetary cruise activities will gather data on the fields and particles environments of the Solar System as the

[1]The MDS Project has been described in numerous, previous Progress Report Articles.

mission modules move away from the sun. In addition, the pointing and stabilization capability of the mission modules will allow detailed observations of targets of opportunity that include comets, asteroids, stars, etc., that have not been possible on previous outer planet missions.

The second launched mission module (Voyager 1) will arrive first at Jupiter with closest approach on March 5, 1979, at about 5 Jupiter radii. The encounter geometry is illustrated in Figures 1 and 2. The second arriving mission module (Voyager 2) will have closest approach at Jupiter on July 9, 1979, at about 10 Jupiter radii. The encounter geometry is illustrated in Figures 1 and 3. Although the critical period for each encounter is measured in terms of a few days, the total encounter period of each mission module is approximately four months long. Planetary remote observations will be taken during this period and will provide many repeated cycles of total planetary mapping in the visual, ultraviolet and infrared wavelengths. At the same time, the fields and particles experiments will increase their activity to investigate the total planet-satellite environment. The first mission module will arrive at Saturn in late 1980, with the second arriving some nine months later as illustrated in Figures 4 and 5, respectively. Again, multiple satellite encounters are planned. The first mission module will also be targeted to occult the Rings of Saturn.

If the first mission module achieves its scientific objectives for the Saturn system, and if the second arriving mission module is operating satisfactorily, a decision could be made in early 1981 to target the second mission module for a Saturn aim point permitting an encounter with Uranus in 1986. Otherwise, the second mission module would be targeted to optimize Saturn-related science, including a close flyby of Titan prior to Saturn encounter. In either case, planetary observations of the Saturn system would last for about four months for each mission module.

By designing the mission modules to assure nominal operation out to Saturn, they are quite likely to continue to operate well beyond encounter with that planet. Following the Saturn flyby, both mission modules escape the Solar System with a heliocentric velocity of approximately 3 AU per year. Since departure is in the general direction of the Solar Apex, the spacecraft may return data (as a part of an extended mission) from the boundary between the solar wind and the interstellar medium. If an Uranus option is exercised for the second arriving mission module at Saturn, observations of the Uranus system would occur in 1986 over a time period from about three months before to one month after Uranus encounter. General design of the Uranus encounter phase observations would be similar to that at Jupiter and Saturn, except for the reduced data rates from a distance of 20 AU.

B. Earth-To-Jupiter Mission Phases

While Voyager flies on toward Jupiter, work continues on Earth for the planetary and satellite encounters to come. Figure 6 shows the planned Earth-to-Jupiter phases for both missions; dates and times given are for Voyager 1, launched September 5, 1977.

The early cruise phase lasted from post-launch to about 95 days into the flight. One trajectory correction maneuver (TCM) and a "clean-up" TCM were executed during the early cruise phase.

The cruise phase officially began when the high-gain antenna was turned toward Earth to remain in that position for most of the mission. The antenna must point toward Earth for communications. During the long cruise phase, nearly a year, one TCM is planned. In December 1978, during the last three days of the cruise phase, the near encounter test (NET) will be performed. The NET will be an actual performance of the activities scheduled for the period of closest approach to Jupiter.

Eighty days and approximately 80 million kilometers (50 million miles) from the Giant Planet, the Jupiter observatory phase will begin, about January 5, 1979. Following a quiet period over the holidays, periodic imaging with the narrow-angle camera will begin later in January, 1979. A third TCM is planned during this period. In early February 1979, a four-day movie sequence will record 10 revolutions of the planet, photographing the entire disk.

Following the movie phase will be the far encounter phases, as the spacecraft zeroes in on the planet, closing to 30 million kilometers (18.6 million miles) at 30 days out. The far encounter phases, from early February to early March, 1979, will provide unique observation opportunities for the four largest satellites – Lo, Europa, Ganymede and Callisto – and a crossing of the bow shock of the Jovian magnetosphere, of great interest to all of the fields and particles instruments. One TCM is planned during the far encounter phase.

For Voyager 1, near encounter will be a 39-hour period packed with close-range measurements by the spacecraft's 11 science experiments. On the outbound leg, five Jovian satellites – Amalthea, Io, Europa, Ganymede, and Callisto – will also receive close-range scrutiny by the various science instruments. Passing 280,000 kilometers (174,000 miles) from the visible surface of Jupiter, Voyager 1 will then whip around the backside of the planet, passing out of view of the Earth for a brief two hours.

The post encounter phases, from the end of near encounter to about 35 days later, will continue observations as the planet

ORIGINAL PAGE IS
OF POOR QUALITY

is left behind. Using the gravity of Jupiter to slingshot it on its way, Voyager 1 will flash onward toward the ringed planet Saturn, about 800 million kilometers (500 million miles) and 19 months distant. Voyager 1 will study Saturn from August through December 1980. Voyager 2 follows Voyager 1 through the same phases described except that a longer cruise to Jupiter and Saturn is involved for near-encounters on 9 July 79 and 27 Aug 1981 respectively.

III. Spacecraft Description

The Voyager Spacecraft embodies the Mission Module (MM) and the Propulsion Module (PM). The PM provides the final injection velocity on the desired flight path. The MM electronic and inertial reference components are used for PM control. The PM was separated from the MM after injection into the planetary transfer trajectory. The Mission Module is a three-axis stabilized craft based on previous Mariner and Viking Orbiter designs and experience, with modifications to satisfy the specific Voyager Mission requirements on long-range communications, precision navigation, solar-independent power, and science instrumentation support.

The current spacecraft configuration is shown in Figure 7. The 3.66 meter (12 feet) diameter high gain antenna (HGA) provides S- and X-band communication. The X-band antenna dichroic subreflector structure serves as a mounting platform for the low gain antenna (LGA) and the HGA S-Band focal point feed. The bi-stable Sun sensors in conjunction with the Canopus tracker (mounted on the electronic compartment) provides the celestial reference for three-axis stabilized attitude control of the Mission Module. Hydrazine thrusters mounted on the MM provide both reaction-control torque for MM stabilization and thrust for Trajectory Correction Maneuvers (TCMs).

IV. DSN Operational Test and Training

For pre-launch, launch, and early-mission support, the DSN committed readiness of Network Stations as follows: (1) CTA-21 for spacecraft-network compatibility tests and DSN development, (2) STDN MIL-71 for spacecraft-network compatibility verifications and near-earth launch support, (3) one 26 meter subnet of three stations: DSS 12 (Goldstone CA), DSS 44 (Australia), and DSS 62 (Spain) for cruise support, and (4) one 64 meter station, DSS 14, for periodic high-rate data acquisition and S-X band radio metric data generation. Most of the Voyager compabilities required were provided through the DSN Mark III '77 Data Subsystem (MDS) Implementation Project per the schedule shown in Fig. 8. Mission-dependent network tests and training activities following the MDS implementation were key factors in achieving DSN operational readiness prior to Voyager launch.

The training problem associated with the MDS conversions were two-fold. First, the DSN was supplied with new hardware and software and second, Voyager procedures and configurations were new. The first problem was to familiarize DSN personnel with the new MDS equipment and associated software procedures.

DSN testing for Voyager centered on the prime 26 meter DSN stations to be used for launch and cruise; DSS-12, DSS 44, and DSS 62. DSS-12 was the first of these to receive the MDS update Operational Verification Tests (OVTs) were started immediately after all SPT's were completed. This being the first Goldstone Complex station to be converted to MDS, it was used as the testbed for all complex MDS training. The objectives of the Voyager mission-dependent training was to:

(1) Familiarize the station and NOCT personnel with the Mark III Data System pertaining to the support of the Voyager mission.

(2) To provide experience with the MDS equipment and Voyager configurations and operational procedures.

(3) To ensure that all network operational personnel were adequately trained to support all Voyager mission activities.

Problems experienced at DSS-12 were numerous. Growing pains of new hardware, new software, and operational personnel unfamiliarity with both, plagued the first few Operational Verification Tests (OVT's). Approximately 30 percent of the OVT's performed at station 12 produced more problems than training benefit. (A total of 10 OVT's were run with DSS-12.) It was not until half of these tests were completed before results of the training could be seen. This was not altogether unexpected, and the problems experienced with station 12 led to identifying, documenting, and eventual corrections of hardware configurations, software and procedures. Further DSN tests with CTA-21 and MIL-71 also contributed to this effort.

By the time DSS-62 DSN testing (OVT's) were begun new CMD, TLM, and CMF software versions (Ver. A) were at the station. Test results began to improve. All OVT's performed with DSS-62 were successful. Minor problems which did occur, were usually corrected before the next test.

Software reliability and operational procedures continued to improve by the time DSS-44 testing began. Only one of nine OVT's at DSS-44 was unsuccessful, and it was due to equipment outage. With the highly successful completion of DSS-44 testing the 26 meter subnet required for Voyager launch phase and early cruise was ready for support.

Because of the Voyager launch trajectory DSS-12 was selected as the initial acquisition station (this was the first time

a Goldstone station has been used for initial acquisition). Special Initial Acquisition OVT's were run to familiarize station personnel with Initial Acquisition procedures. These tests went very smoothly. Several tests using a GEOS satellite (fast moving) were conducted by DSS-12 to practice Initial Acquisition procedures and acquire much needed experience.

As the MDS schedule shows, there was little time to achieve DSS 14 operational readiness prior to launch. However, Viking support requirements dictated the downtime schedule, and Voyager had to live with the limited test and training risks.

The first test with DSS-14 was on 27 June 77. The test failed due to station air conditioning problems and a NDPA software failure. Approximately one-half of the DSS-14 OVT's experienced major difficulties; mostly hardware in nature. Problems with DSS-14 continued into the first MOS* tests. As the MOS and special testing continued the problems at DSS-14 decreased but never diminished altogether. Because DSS-14 would play an important role on the initial pass over Goldstone, special tests were designed to further test the equipment and provide additional training to station personnel. By the first Operational Readiness Test (ORT) DSS-14's performance had vastly improved. The ORT was a success with only minor problems. Three Science and Mission Plans Leaving Earth Region (SAMPLER) OVT's were conducted with DSS-14 which provided additional training. (SAMPLER was cancelled by project before launch.)

In the last three weeks before launch of Voyager 2 several MOS tests were conducted, with the spacecraft (at Cape Canaveral) providing the TLM data. Although several stations were involved in these tests, MIL-71 was engaged in all of them. For the most part, MIL-71's performance was outstanding.

ORT number 2 was conducted on 14/15 August, 1977. Stations participating in this test were MIL-71, DSS-11, -12, -14. Both DSS-12 and -14 experienced some equipment and operations anomalies, however it was felt that they could be corrected before launch.

Since DSS-44 had not been active on Voyager in about two months, an OVT was performed on 17 August to insure personnel proficiency. The station's performance was excellent.

Station Configuration Verification Tests (CVT) were conducted with MIL-71, DSS-11, -12, -14, -44, and -62 on 17, 18, 19 August 1977. With these CVT's the stations were placed under configuration control for Voyager 2 launch. (Table 1 gives a summary of all prelaunch tests conducted.)

*Mission Operational System.

Voyager 2 launch occurred on 20 August 1977 at the launch window opening.

Between Voyager 2 launch and Voyager 1 launch (5 September) the recertification of DSS-14 was ensured by performing a CVT on 4 September. DSS's-12, 44, 62 had been tracking the Voyager 2 spacecraft daily, so their configuration was still validated. The second CVT at DSS-14 was very successful and the station was placed under configuration control for the Voyager 1 launch.

The first conjoint Deep Space Station (42/43) was taken down in July 1977 for the Mark III Data system conversion. The 42/43 combined system test was conducted on 24 September 1977, signaling the end of System Performance Testing (SPT's) and the start of the 2 month DSN testing phase.

Being a conjoint station, DSS-42/43 presented further problems in that one CMF is used to transmit data from both stations simultaneously. Although it is a minor change to the basic 64/26m MDS configuration we did not fully understand the impact to operations or what to expect in the way of interaction.

At the request of DSS-42/43 management a new testing technique was used. The first day was scheduled for on-site training, followed by Viking Operational Verification Testing (16 hours per day) completing the first week. Viking was selected because it was a project the operational personnel would be familiar with rather than starting with a new project (like Voyager or Pioneer Venus).

The first Voyager OVT was conducted on 1 October 1977. This OVT was very successful and set the pattern for the rest of the DSN testing at DSS 42/43. Two OVT's per crew were conducted during the month of October. All but one OVT was very successful. Station operational personnel were highly motivated and their performance for the most part was excellent. On the 31st of October the station was placed on operational status for Voyager support.

The Spanish complex at DSS-61/63 was converted to the MDS system during the period of 15 Oct. through December 1977. DSN Operational testing started in early January, 1978. Again, a minimum of two OVT's were conducted with each operational crew. Simulation Conversion Assembly (SCA) and comm equipment problems plagued the first half of testing. After these problems were cleared the remaining tests were smooth. The station became operational on 31 January 1978.

Deep Space Station 11, the last of the network to be converted, was taken down on schedule (mid January) and is not covered by this report.

V. Spacecraft Operations

A. Prelaunch Activities

Three spacecraft were built for the Voyager Mission, one (VGR77-1) was designated the Proof Test Model (PTM) and subjected to extensive testing in simulated deep space conditions to test the spacecraft design, construction, and durability. VGR77-2 and VGR77-3 were designated flight spacecraft and subjected to less arduous testing to save them for flight conditions.

Failures in the Attitude and Articulation Control Subsystem (AACS) and Flight Data Subsystem (FDS) on the VGR 77-2 spacecraft, planned to be launched first on August 20, 1977, resulted in a decision to interchange the two flight spacecraft. The VGR77-3 spacecraft was redesignated Voyager 2 and launched first.

The decision to switch the flight spacecraft necessitated switching of the Radioisotope Thermoelectric Generators (RTG's) as well. Since the first launch trajectory includes the option to extend the mission to Uranus, a distance of 19 Astronomical Units (AUs) from the sun, the higher power output RTG's previously installed on VGR77-2 were removed and reinstalled on VGR77-3.

B. Voyager 2 Operations

Voyager 2, aboard a Titan IIIE/centaur launch vehicle, lifted off launch complex 41, Air Force Eastern Test Range (AFETR), Cape Canaveral, Florida at 14:29:45 GMT, August 20, 1977. The time was less than 5 minutes into the launch window on the first day of a 30 day launch period. The countdown progressed smoothly except for a brief unscheduled hold at launch minus five minutes to determine the open/closed status of a launch vehicle valve. Minutes after launch, however, several problems were noted.

These problems included a suspected gyro failure, incomplete data transmission, and uncertainty as to the deployment of the science platform boom. The gyro failure and data transmission problems cleared. The boom supporting the science platform was to be released and deployed about 53 minutes into the flight, but initial data gave no confirmation that the boom was extended and locked. (When the boom is within 0.05 degrees of normal deployment, a microswitch on the folding boom opens.) Confirmation of the microswitch position was not received.

On August 26 the spacecraft was programmed to execute a pitch turn and simultaneously jettison the dust cover on the infrared interferometer spectrometer (IDIS) in hopes that enough jolt would be provided to open the boom hinge and slow the locking pin to drop into position. However, the sequence was aborted by the spacecraft before the events could take place. (The spacecraft is programmed to think such a maneuver is an emergency and will safe itself, aborting the maneuver.) It is still not certain that the science boom aboard Voyager 2 is latched, but data indicates that the hinge is only fractions of a degree away from being locked and should present no problems in maneuvering the scan platform.

The boom is stiff enough to prevent wobbling when the scan platform, perched at its tip, is maneuvered, and should stiffen further as the spacecraft travels farther from the sun into the colder regions of deep space.

Shortly after separation of the spacecraft booster motor from the bus the spacecraft experienced what was later to be known as "a bump in the night" – an erratic gyration of the spacecraft. It was first thought that the spacecraft's separated rocket motor was possibly traveling alongside and "bumping" the spacecraft. But after sifting through puzzling launch data recorded by Voyager 2, the controllers concluded that the gyrations were caused by the spacecraft's attitude stabilizing system. The system stabilized itself and is now in stable condition.

By September 1, Voyager 2 was in interplanetary cruise and on September 2 was "put to bed" to allow flight controllers to concentrate on the launch activities of Voyager 1. The computer program was placed in a "housekeeping" sequence designed to automate the craft until September 20. In this condition various measurements were taken during this period, and tape recorded aboard the spacecraft for later playback to earth. All but one of the science instruments had been turned on and were functioning normally.

On September 23, Voyager 2 experienced a failure in the Flight Data Subsystem (FDS) circuitry which resulted in the loss of 15 engineering measurements sent to earth. An effort to reset the FDS tree switch was performed on October 10th, but was unsuccessful. The problem is now considered a permanent hardware failure and "work around" alternatives are being used.

This failure affects 15 separate engineering measurements, an internal FDS measurement and four redundant measurements. Voyager 2's first trajectory correction maneuver (TCM) was performed on October 11, achieving the desired correction to within one percent.

In anticipation of experiencing a similar thruster plume impingement to that observed on Voyager 1's first TCM (later in this article), an overburn and pitch turn adjustments were factored into the Voyager 2 sequence.

This TCM slightly adjusted the aiming point for the Jovian satellite Ganymede. Voyager 2's closest approach to Ganymede is now planned for about 60,000 kilometers (37,000 miles) rather than 55,000 kilometers (34,000 miles) on July 9, 1979.

On October 31, Voyager 2 was commanded to acquire the star Deneb as a celestial reference point. Deneb lies on the opposite side of the spacecraft from Canopus (the normal celestial reference). Acquiring Deneb effectively required turning the spacecraft upside down. This was done to minimize the effects of the solar pressure which was contributing to the frequent attitude control thruster firings to steady the ship and also to allow an earlier pointing of the high gain antenna to the Earth. Voyager 2 stayed on Deneb until 29 November 1977, when Canopus was again returned to as celestial reference.

Voyager 2 was put through some sequence verification tests December 5, 7, and 8, performing flawlessly. Then on December 27, 28 the spacecraft performed a cruise science maneuver. This maneuver allows calibration of several instruments by turning the spacecraft to look at the entire sky. The scan platform instruments are able to map the sky as the spacecraft rolls, and the ultraviolet spectrometer and photopolarimeter make their observations against the total sky background. The magnetometer and plasma instrument also obtain calibration data.

The cruise science maneuver consists of rolling the spacecraft in one direction for about 5 hours (10 yaw turns) and rolling it about the roll axis for about 12 hours (26 roll turns). The last roll turn was finished 20 seconds earlier than the computer expected, activating a "safing sequence" aboard the spacecraft. The result of this anomaly included loss of approximately 4 out of 20 hours of the cruise science maneuver data and loss of a subsequent slew to observe Mars.

A degradation of the S-band radio solid-state amplifier in the high power mode has been noted. The amplifier has been switched to the lower power mode and is being monitored. The radio system has built-in redundancy, using both solid state amplifier and a traveling wave tube amplifier.

On 2 February 1978, at 1104 GMT, while being tracked by DSS-44 the spacecraft downlink was lost. This was near the end of DSS-44's view period. When DSS-62 failed to acquire the downlink a spacecraft emergency was declared at 1407 GMT and DSS-63 was released by the Viking project to answer the Voyager emergency. Preliminary evaluation of the situation was that the spacecraft had lost Canopus lock. During the end of the DSS-44 view period the stations' data was marginal due to low elevation angle and high data rate. A Canopus sensor alarm occurred that was masked by the marginal data. (The alarm may have been caused by a dust particle passing through the Canopus sensor's view.) This set a flag in the spacecraft's computer indicating that a timer had been set counting down 6 hours, by which time the flight team could determine if the sensor was still on Canopus. But the spacecraft flight team had begun their unmanned period with DSS-44 end of track. The timer ran down and the computer "safed" the spacecraft by switching to low gain antenna. This dropped the downlink by 29dB (below TLM threshold). The spacecraft team was called in and, after studying the problem, commanded the spacecraft back to HGA, acquired Canopus and reset the Canopus sensor cone angle to center Canopus in the tracker. After a computer readout was performed, confirming normal configuration, the spacecraft emergency was terminated at 2125 GMT, same day.

Voyager 2 continues in cruise mode.

C. Voyager 1

Due to the problems experienced with Voyager 2's science boom it was decided to de-encapsulate Voyager 1 (VGR77-2) on 20 August for inspection of the science boom, and installation of stiffer coil springs to assure proper boom deployment and locking.

Engineers had conducted several tests on the mechanical configuration of the VGR77-1 (PTM) science boom, including torque tests on the microswitch and stiffness test of the boom.

The Centaur shroud was placed over the spacecraft on August 29, and post-encapsulation electrical test was conducted in preparation for mating to the launch vehicle. Movement to the launch pad occurred on 31 August 1977.

Voyager 1, aboard a Titan III E/Centaur launch vehicle, lifted off launch complex 41 at the Air Force Eastern Test Range (AFETR), at 12:56:01 GMT, September 5, 1977, sixteen days after its twin. The launch countdown went smoothly with no unscheduled holds.

None of the attitude control problems encountered during the launch of Voyager 2 were experienced. A switch to the secondary thruster system was noted during the magnetometer boom deployment; a reset to initial conditions was commanded about 12 hours after launch.

Voyager 1, due to the alignment of the planets at the time of launch, will fly a faster trajectory relative to the Sun and will arrive at Jupiter 4 months ahead of Voyager 2. The Jupiter observation phase will begin the 1st week in January, 1979. The spacecraft will travel a total of 998 million kilometers (620 million miles) to Jupiter, its first destination.

Voyager 1 completed its first trajectory correction maneuver (TCM) in two parts on September 11 and 13. An analysis of the TCM data indicated a 20 percent under-velocity resulting from each part of the maneuver. The suspected cause was impingement of the thruster exhaust on the spacecraft structural support struts. The ungained velocity was planned to be compensated for during the next scheduled TCM. The maneuver was considered successful and included calibration sequences of the dual frequency communications links and the high-gain antenna S- and X-bands. During these sequences, the 3.7 meter (12-foot) diameter high-gain antenna dish was pointed towards Earth and the S-band and X-band radio links were calibrated over DSS-14 at the Goldstone complex near Barstow, California.

These periodic flight path adjustments are necessary to assume precise arrival times of the spacecraft at their objectives, maximizing science data return. As a result of the trajectory adjustment, Voyager 1 will arrive (closest approach) at Jupiter March 5, 1979, studying the interactive region between Jupiter and its satellite IO.

The spacecraft began its Earth-Jupiter cruise phase on September 15, 1977, having completed all planned near-Earth activities.

A recorded Earth-Moon video and optical navigation data sequence was conducted on September 18, in which dramatic pictures of the Earth and moon were recorded from the spacecraft 11.66 million kilometers (7.25 million miles) from Earth. The video playbacks of these pictures were conducted on 7 and 10 October 1977.

The second trajectory correction maneuver was executed on October 29, 1977. The maneuver was successful, with pointing accuracies and undervelocity resulting during the first trajectory maneuver on September 11 and 13 being accounted for in the sequence.

On December 13, Voyager 1 conducted a fairly extensive mapping of the Orion nebula with the ultraviolet spectrometer (UVS) and photopolarimeter (PPS) instruments.

Voyager 1, on December 15, 1977, earned its title when it took over the lead from Voyager 2 and is now farther away from Earth and Sun.

Presently Voyager 1 is in Earth-Jupiter cruise with all subsystems and experiments in good working condition.

VI. Tracking and Data Acquisition

From the moment of launch, the Voyager spacecrafts have been under alternating surveillance by a world-wide tracking and data system which includes elements of the NASA/JPL Deep Space Network, the Air Force Eastern Test Range (AFETR), and the NASA Spaceflight Tracking and Data Network (STDN).

A. Near-Earth Launch Support

The Near-Earth coverage, from launch through the propulsion module burn which boosted the spacecrafts into the Jupiter-bound trajectories, was accomplished by the near-Earth facilities. These consist of the AFETR stations downrange elements of the STDN, ARIA (Advanced Range Instrumented Aircraft), and a tracking communications ship at sea, the USNS Vanguard.

For the first launch, Voyager 2, coverage, data acquisition, and real-time acquisition were excellent. Resources proved to be in the right place at the right time to preclude unplanned data outages. The near-Earth non-real-time data return plan was executed resulting in practically all near-Earth data available to project.

The Voyager 1 launch support on 5 September went very smoothly. The near-Earth facilities again turned in an excellent performance retrieving the data in a timely manner to the Voyager project.

B. Deep Space Network (DSN) Support

Tracking and data acquisition communications with the Voyager spacecrafts from injection into the Jupiter trajectories, about one hour after launch, until the end of the mission is conducted by the Deep Space Network (DSN).

Initial acquisition of both Voyager spacecraft was conducted by DSS-12, with backup being provided by DSS-11 and DSS-14. Both initial acquisitions went according to plans.

On the first launch (Voyager 2), DSS-14 was prime for the 7.2 kb/s telemetry data, which occurred shortly after initial acquisition. Due to an operations procedural error in frequency predictions sent to the station, DSS-14 was 25 minutes late acquiring the spacecraft signal. There would have been a loss of data if MILA/MIL-71 had not acquired the 7.2 kb/s data on time and made it available to the Voyager Project.

MILA/MIL-71 again came to the rescue, when at 1638Z (same day) the spacecraft failed to acquire the Sun, and went into the failure recovery mode–switching data rates from 7.2 kb/s to 40 bps. MILA/MIL-71 immediately detected this

change, locked up on the data and alerted the network. All stations responded quickly and data outage was negligible.

Upon launch of Voyager 1, DSS-11 acquired the spacecraft about 2 minutes before DSS-14 and DSS-12. Since DSS-11's (not a MDS station) data was record only, the project chose to process DSS-14's telemetry as prime from Goldstone. Telemetry from DSS-14 continued without problems until LOS. DSS-12 experienced some difficulty reacquiring the spacecraft downlink after going two-way. The difficulty was caused by a 12 Hz filter failure.

Both spacecraft are presently in the cruise phase of their Earth-Jupiter trajectories. This phase was planned to be relatively quiet and routine, broken by an occasional spacecraft maneuver or special calibration procedure. However, support activities have been anything but routine. Spacecraft anomalies have dictated real time commands, special maneuvers calibration sequences and tests not originally planned for the cruise phase. The DSN has responded in real time to satisfy all project requirements where resources have allowed. Additionally, special tests and procedures to support these tests and calibration sequences were developed and implemented as required.

C. Weilheim Tracking Support

The Voyager and Helios Projects decided to take advantage of an alignment of their respective spacecraft and the Earth which during the period between Oct. 15 and late Dec., 1977, provided unique data on solar related field and particle phenomena. To augment data acquisition in this interval, the Weilheim 30 meter tracking station under the direction of the German Space Operations Center (GSOC) tracked the Voyager spacecrafts. In order for the Weilheim station to track the Voyager spacecrafts, the DSN provided tracking predicts (state vectors) and a Communications decoder for interfacing with the NASCOMM high speed data lines. Several successful tests were run and, as a result, the first live track of the Voyager spacecraft by the Weilheim station was during the week of Oct. 17.

Weilheim continued to gather the Voyager spacecraft data until 31 December 1977 when support was terminated; the period of radial alignment having passed. A spiral alignment of the two spacecraft will occur in April 1978 and Weilheim is again expected to track Voyager.

VII. DSN Performance

A. Tracking

The Voyager 2 launch and near-Earth phases were marked by spacecraft and data acquisition anomalies resulting in a less than smooth beginning for the Voyager 2 mission. DSN tracking procedures, conservatively designed to encompass launch contingencies, contributed to the successful completion of this phase of the Voyager mission. The launch of the Voyager 1 spacecraft proceeded very smoothly, with none of the problems of predict generation, station reception or spacecraft anomalies, as experienced with the earlier launch.

The unique geometry (zero declination) which will exist at Saturn encounter for both Voyager spacecraft will make impossible the determination of spacecraft declination by Doppler fitting techniques. An alternate method of determining declination requires that range data be taken nearly simultaneously from stations at widely separated latitudes and triangulating to solve for the declination angle. This method, Near Simultaneous Ranging (NSP), requires very accurate range measurements and delay calibration data be furnished to the spacecraft navigator and the radio scientists. The acquisition of NSR data also requires that the up and down link signals remain phase coherent during station transfers. Since this is not possible using the standard DSN transfer technique, a new transfer technique which enables two stations to maintain the necessary phase coherence during transfers was devised and implemented during NSR passes, occurring approximately every 14 days.

B. Command

Due to spacecraft anomalies and additional instrument calibration requirements, more spacecraft commands have been sent to date than originally planned prior to launch. A total of 11,255 commands to Voyager 1 and 12,977 commands to Voyager 2 were transmitted by the end of December 1977. During the cruise mission phase a command load was planned about once a month; however, actual activities have been close to weekly plus real-time commanding to meet real-time situations.

Several command anomalies have occurred since launch. Two of the most significant failures were software related and were eventually corrected with a new Command Processor Assembly (CPA) software version (DMC-5084-OP-C). These were 1) loss of response from a stations CPA, because the CPA Temporary Operational Data Record (TODR) would write past its partitioned space, destroying a portion of the CPA program, and 2) random inability to access either CPA, caused by a software anomaly in the CPA timing.

C. Telemetry

All critical mission activities such as TCM's, celestial reference changes, cruise science maneuvers, special calibrations, spacecraft emergencies, etc. require accurate telemetry link predictions to guarantee any measure of success. The telecom-

munications links have been accurately predicted in most all instances by both the DSN and project spacecraft and telecomm teams. These have greatly influenced the successful support provided by the DSN in all such critical mission phases.

S-band link residuals through December 1977 show that downlink AGC values for both spacecraft are near nominal while symbol Signal-to-Noise Ratios (SNR) are about +2dB. X-band performance for Voyager 2 is also within 0.5dB of predicts.

Intermediate Data Records (IDR's) have been provided on each pass. The DSN commitment of at least 96 percent has been exceeded, usually averaging approximately 99.6 percent of all data received.

Acknowledgments

The authors wish to thank the following members of the Network Operations Analysis Group for their contribution of periodic Network Performance Reports.

Tracking: G. Spradlin, J. Wackley, L. G. Chandler, K. Weld.

Command: D. Lopez, W. Tucker

Reference

1. Voyager mission status bulletins 1 through 14, published by the Jet Propulsion Laboratory (JPL internal documents).

Table 1. Summary of prelaunch VGR test activities (15 Nov. 76 through 19 Aug. 77)

Test	CTA-21	MIL-71	*DSS-11	DSS-12	DSS-14	DSS-44	DSS-62
DFT	0	1	0	2	1	1	1
OVT	0	9	0	10	7	9	7
PDT	0	1	0	1	1	1	1
CVT	0	1	1	1	1	1	1
MEIVT/DEIVT	9	3	0	2	3	1	1
GDS	7	2	0	5	1	1	1
INIT. ACQ.	0	0	0	5	0	0	0
Special Tests	6	15	3	4	10	0	0
S/C Monitor	0	6	0	0	0	0	0
MOS	0	4	0	4	7	1	2
ORT	0	2	2	2	2	1	1

*Non MDS Station

DFT = Data flow test
OVT = Operational verification test
PDT = Performance demonstration test
CVT = Configuration verification test
MEIVT = MCCC external interface verification test
DEIVT = DSN external interface verification test
GDS = Ground data system test
MOS = Mission operation systems test
ORT = Operational readiness test

ORIGINAL PAGE IS
OF POOR QUALITY

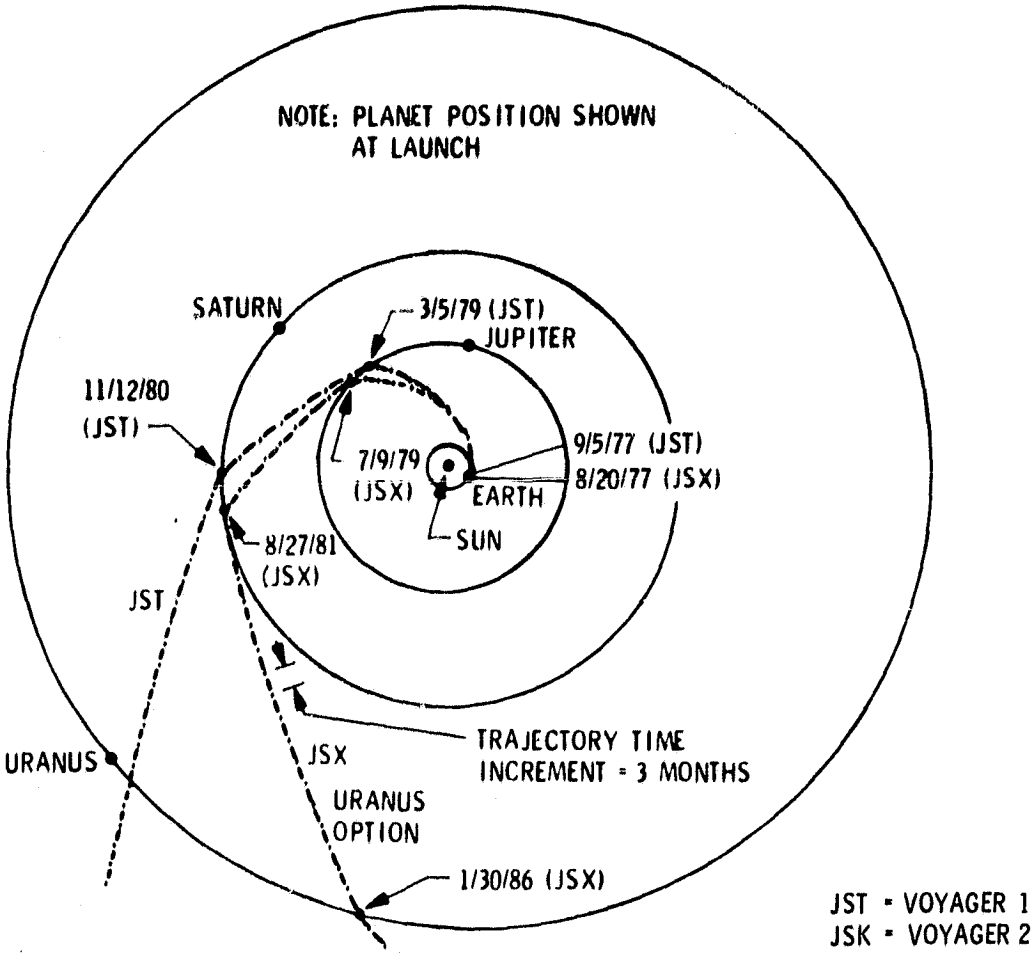

Fig. 1. Trajectories JST and JSX

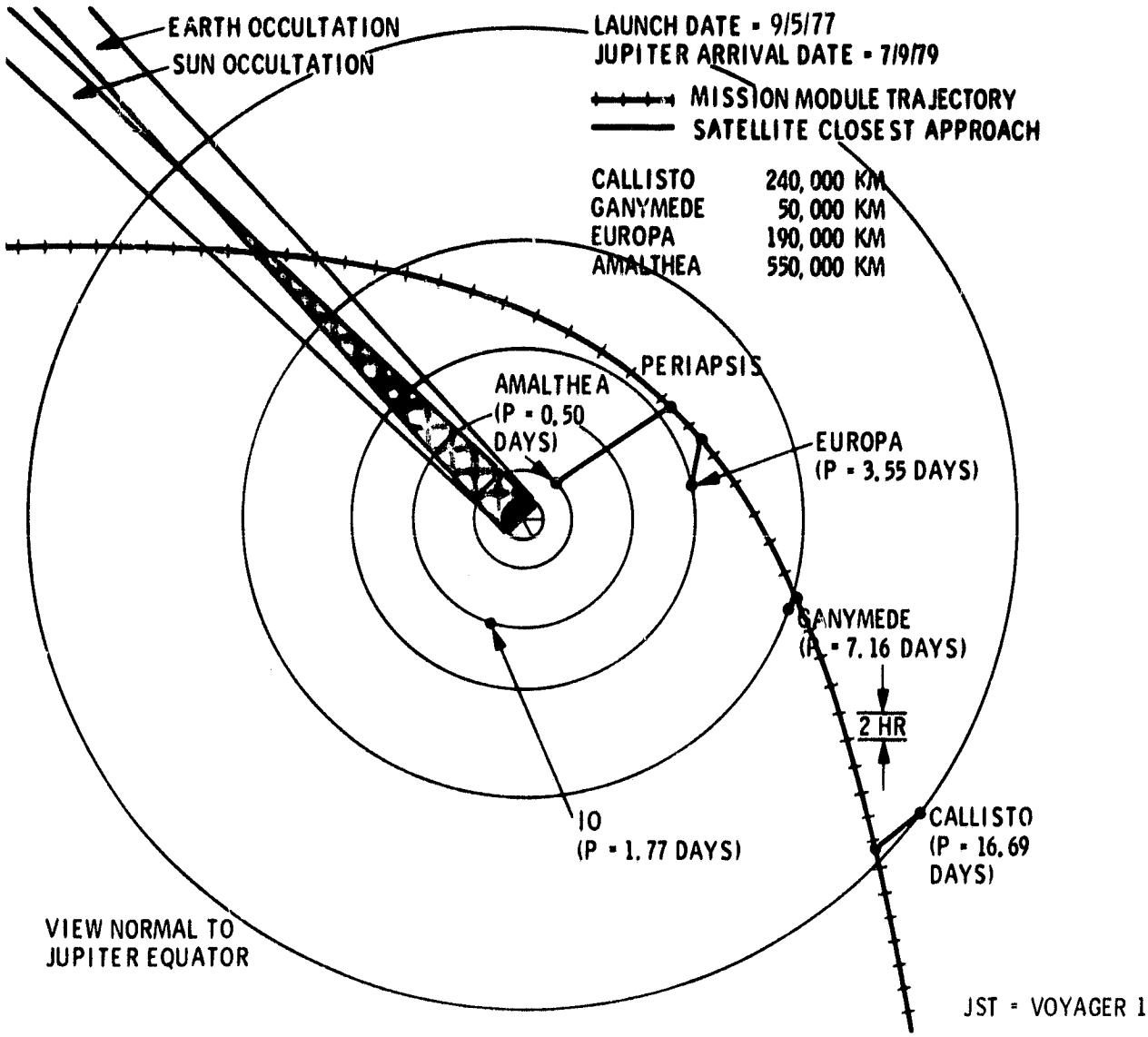

Fig. 2. JST Jupiter encounter at 4.9R_J

ORIGINAL PAGE IS
OF POOR QUALITY

ORIGINAL PAGE IS
OF POOR QUALITY

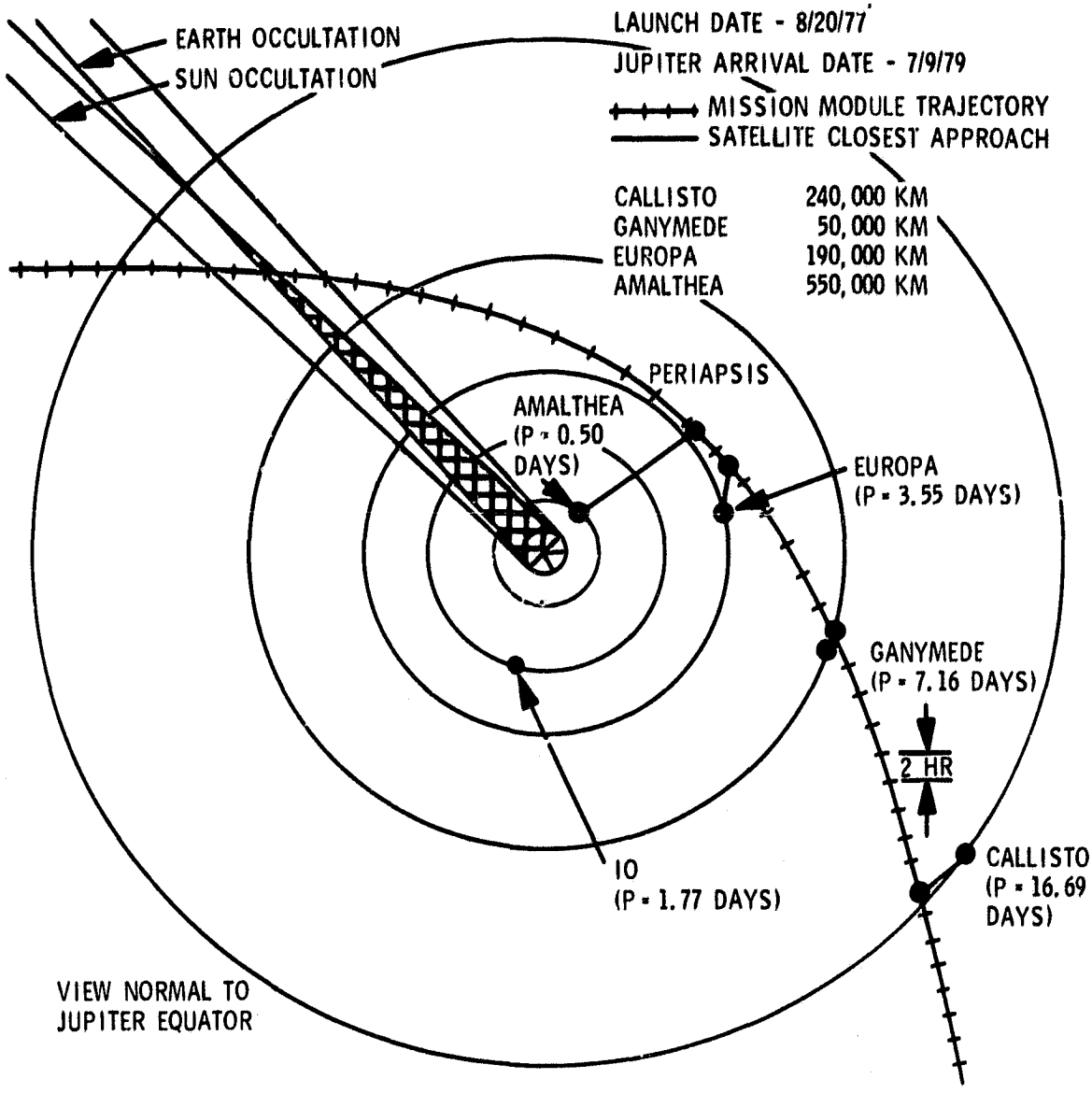

Fig. 3. Voyager 2 Jupiter encounter at $10R_J$

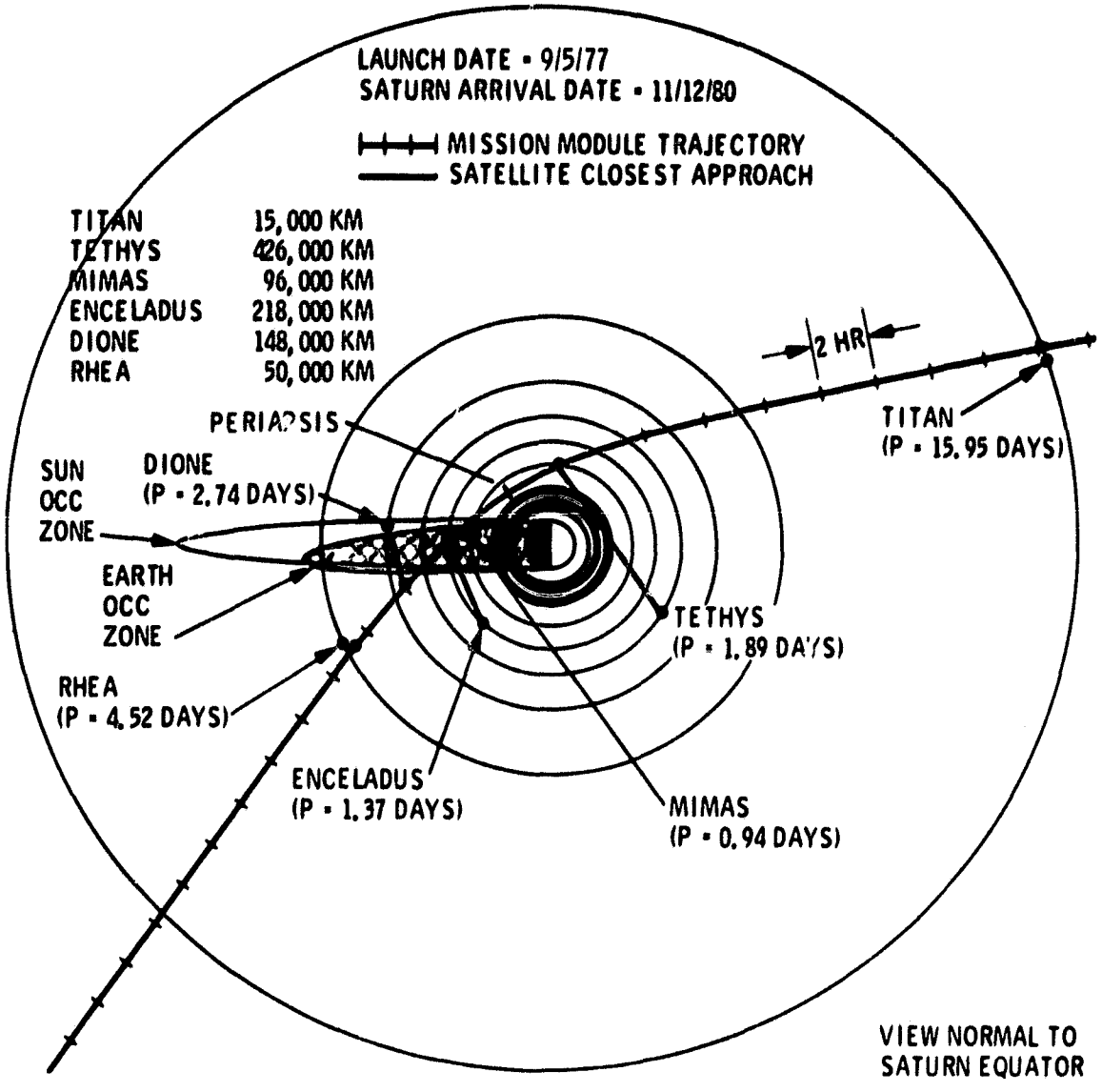

Fig. 4. Voyager 1 Saturn encounter at 3.3R_S

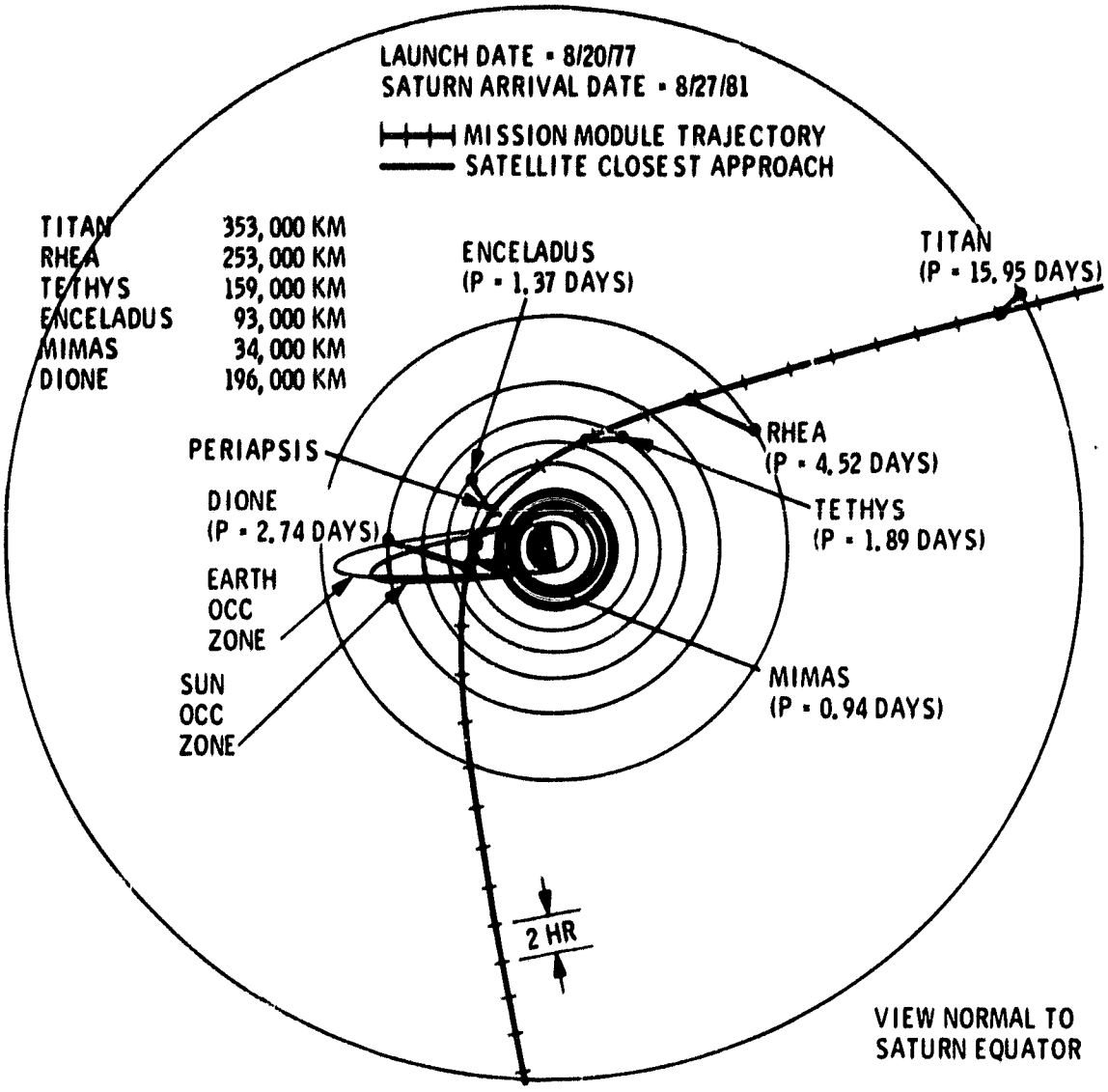

Fig. 5. Voyager Saturn encounter at 2.7R_S

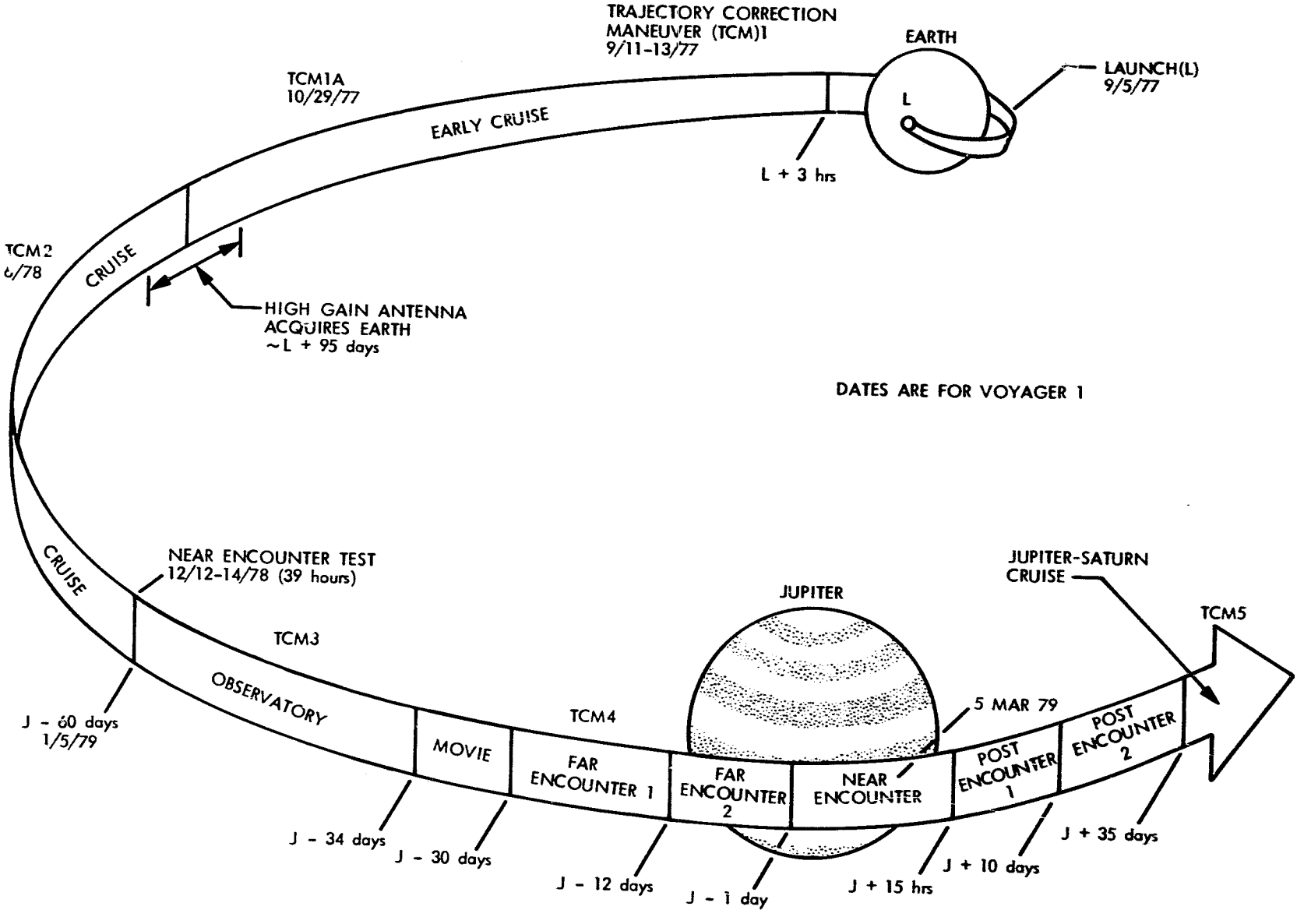

Fig. 6. Voyager 1 mission phases, Earth to Jupiter

ORIGINAL PAGE IS
OF POOR QUALITY

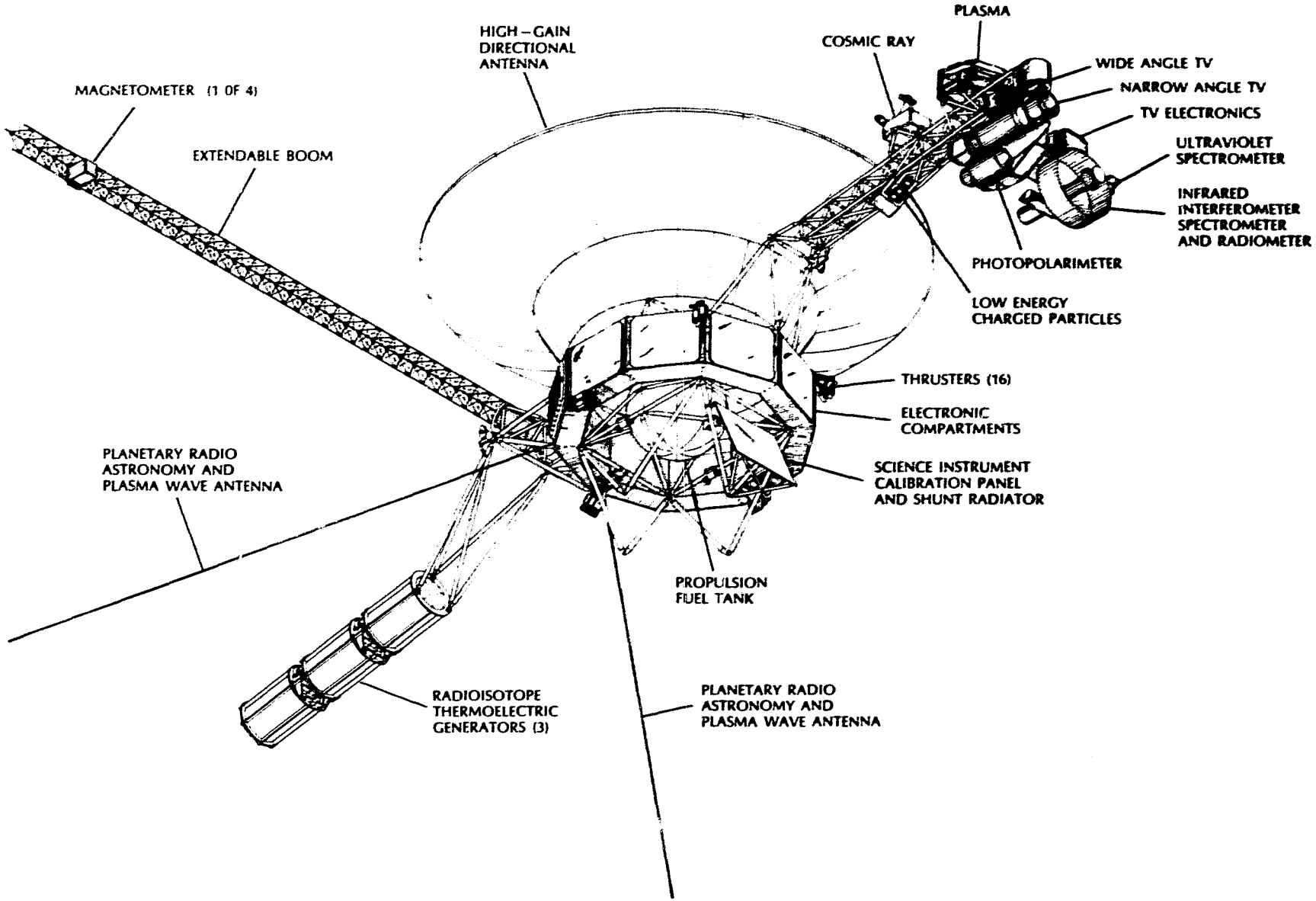

Fig. 7. Voyager spacecraft configuration

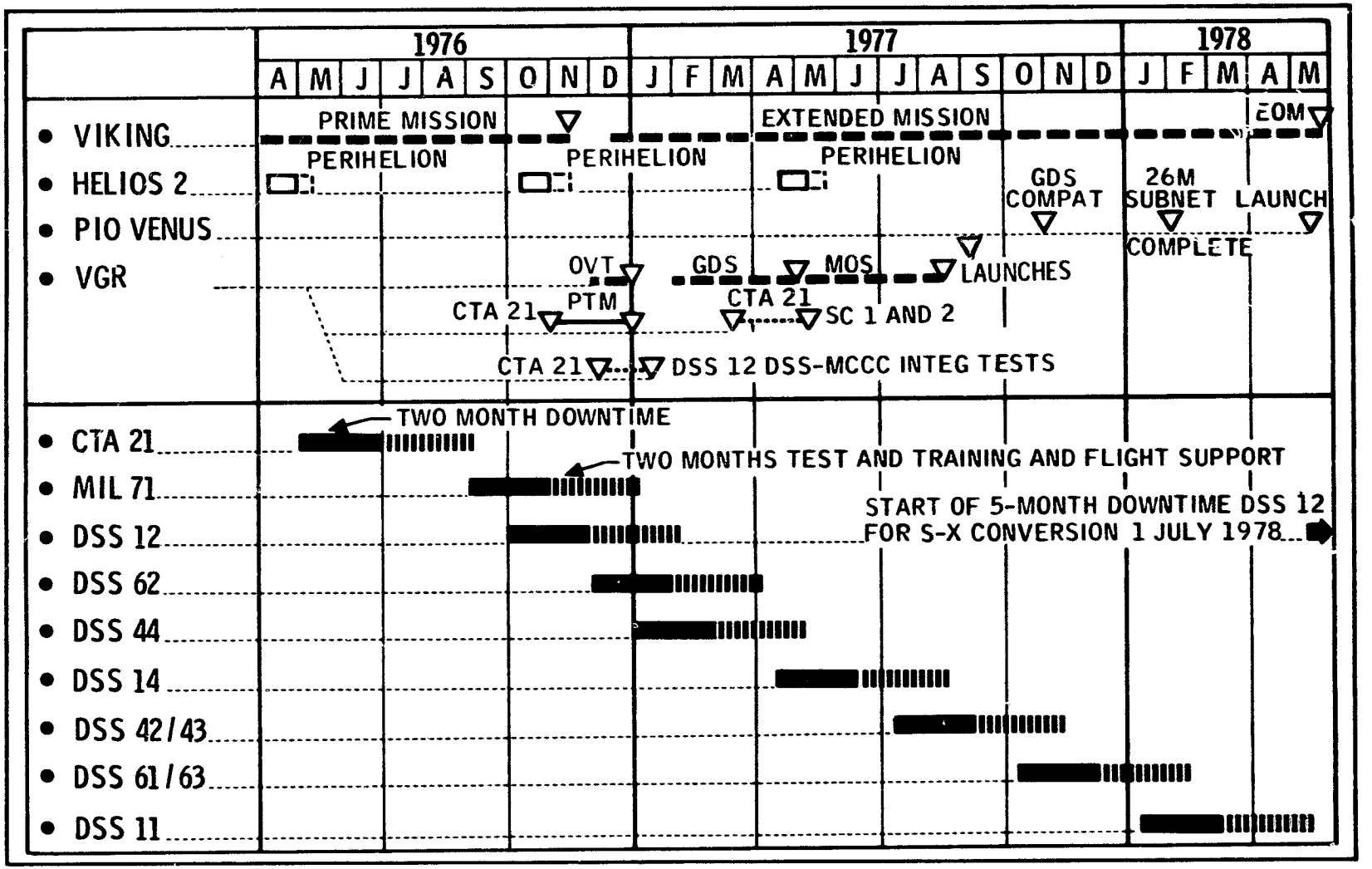

Fig. 8. Mark III-DSN Data Subsystems Implementation Project schedule

ORIGINAL PAGE IS
OF POOR QUALITY

N78-24216

Viking Extended Mission Support

T. W. Howe
Deep Space Network Operations Section

This report covers the period from 1 November through 31 December 1977. It reports on DSN support of Viking spacecraft activities during the period and continues reporting on the DSN Discrepancy Reporting System, Viking Command support and Tracking support. It also continues the reports on the status of Viking DSN Mark III Data Subsystem Implementation Project (MDS) related testing.

I. Viking Operations

A. Status

The two Viking Orbiters continued to make detailed photo maps of Mars during this reporting period. In addition they measured the temperature and water vapor content of the Martian atmosphere. Cloud patterns were checked to see how weather and storms develop. The Orbiters continue to act as relay stations for Viking Lander data transmission.

Spring equinox occurred in the northern hemisphere of Mars during early November. The frost seen earlier in Lander photos has disappeared and the polar hood clouds were breaking up. A record gust of wind of 122 km/h was recorded by Lander 2. The Landers continued to take soil samples for analysis.

The received signal level continued to improve by 0.5 dBm per week because of the shortening distance between Mars and Earth. December telecommunication links had improved to a point 10 dB stronger than levels recorded one year earlier. The December performance is summarized as follows:

Orbiter link quantity (high-gain antenna)	Dec. 1976	Dec. 1977
Uplink AGC, 64-meter, 20 kw, no modulation	−109 dBm	−99 dBm
Downlink AGC, 64-meter, single subcarrier	−143 dBm	−133 dBm
X-band downlink AGC, 64-meter	−153 dBm	−143 dBm

B. Spacecraft Problems

The Viking project declared a spacecraft emergency on November 1, when Orbiter 2 indicated a leaking yaw-axis attitude control jet. The Deep Space Station in Spain (DSS 62) was brought up to fill a tracking gap between DSS 43 (Australia) and DSS 11 (Goldstone). The leak was stopped by sending commands to perform a yaw turn and clear the leaky valve and then the Reaction Control Assembly (RCA) was commanded off.

Viking Orbiter 1 (VO-1) showed a small roll axis gas leak on November 18. DSS 62 was released early by the Voyager project so that data could be obtained to check the gas leak. When

data came into lock, telemetry indicated that the leak had cleared itself. Monitoring continued for the next two days and performance was normal. It was thought that this particular gas leak was caused by a particle which cleared itself.

On November 25, VO-1 again showed a possible gas leak in the yaw-axis. DSS 62 was obtained to monitor the data. Analysis determined that the leak indications were not caused by a microleak but were due to a strong and variable gravity gradient torque experienced near periapsis, with Arcturus as the reference star. The effect was later confirmed using a computer model.

A problem first noticed during the interplanetary cruise phase of the mission was noted again in mid-October and continued sporadically throughout this reporting period. The Viking Orbiter highrate data content interferes with the low-rate signal-to-noise ratio. When either Orbiter is in the dual subcarrier mode at a data rate of 8 kbps or 16 kbps the 33.333 bps low-rate SNR is seen to fluctuate by several dB. The effect is most notable during an all zeros data condition. Sidebands of the high-rate channel occur near the 24-kHz low-rate subcarrier and in some cases are strong enough to cause the stations Subcarrier Demodular Assembly to lose lock.

C. Maneuvers

There were no propulsive maneuvers during this reporting period. Nonpropulsive maneuvers continued to occur on both Orbiters in order to take pictures and to support the Bistatic Radar experiment.

D. Radio Science

Radio Science activities and experimentation continued during November and December. There were 7 Near Simultaneous Lander/Orbiter Ranging passes during the period. Gravity Field experiment data taking occurred nearly every day during the period.

Occultation data was collected during the period except during the times in which there was no DSN coverage, a Bistatic Radar pass, Viking Lander Ranging, or a spacecraft roll maneuver.

Viking Orbiter 2 occultations began on November 19 and will continue through January of 1978.

Differential VLBI coverage occurred on 7 days during the period. The Owens Valley Radio Observatory and the Haystack Observatory in Massachusetts supported this experiment using Viking Orbiter 1 data.

Two new Radio Science experiments began during this reporting period. The Gravity Wave Experiment, using DSS's 14 and 43 and Orbiters 1 and 2, was conducted on 12, 14, 23, and 29 December.

This experiment requires six hours of closed-loop two-way, S/X-band doppler, taken at a sample rate of one sample per second. It also requires simultaneous two station tracking with two and three way S/X doppler for one hour taken at the one sample per second rate.

The second new experiment which began during this period was Bistatic Radar (BSR). The Bistatic Radar experiment requires the Viking Orbiter high-gain antenna to be pointed at the Martian surface. The transmitted signal is reflected off the surface of Mars and received and recorded on the occultation open-loop receivers and analog recorders at DSS 14 and/or 43.

There are two types of observations. During a "Specular Reflection" pass the Orbiter high-gain antenna pointing is maintained for an angle of incidence equal to the angle of reflection towards Earth. The reflection point scans the surface of Mars because of orbital motion. Figure 1 illustrates the geometry of a Specular Reflection pass. Of primary interest during these BSR passes are the northern, middle, and polar latitudes of Mars, which cannot be studied from Earth.

For "Fixed Target" passes, the high-gain antenna is pointed at a fixed location on Mars. Figure 2 shows a Fixed Target pass. This type of BSR pass will investigate the equatorial region of Mars to develop information on known sites of interest.

Table 1 lists potential Bistatic Radar targets.

Figure 3 shows the station configuration for this experiment. The reflected signal contains information about Martian surface roughness and electrical properties. Similar experiments have been conducted using earth based transmitters for radar studies of Mars. Bistatic Radar passes took place beginning November 8. A total of 10 passes were used during this reporting period.

Stations have been able to maintain some closed loop receiver lock during Bistatic Radar passes. This is believed to be lock on a sidelobe of the Orbiter high-gain antenna. Although the received signal level is relatively weak, at times it increased to the point at which telemetry lock was achieved.

E. Spacecraft Tests

Routine spacecraft testing continued during November and December. Orbiter Command Detector Unit (CDU) signal-to-noise ratio estimator (SNORE) tests were conducted on an

average of two per week. High-gain antenna calibrations were also performed.

Effective December 7, the routine CDU SNORE checks were cancelled. Stations were having difficulties setting low output transmitter power levels with the provided calibration time. Without accurate settings, the SNORE test results were questionable. Future tests will be scheduled periodically and appropriate precalibration time provided to insure valid output power levels.

II. Network Support

Table 2 shows the Viking Extended Mission (VEM) Tracking Support for 1977. Noticeable during this period is the fact that December produced more tracking passes than November but had less tracking hours. This resulted from shorter passes throughout the network.

Table 3 gives the total number of commands transmitted by the DSN for the Viking project during 1977. The monthly total number of commands has declined since the record amount transmitted during September of this year. Fewer commands were sent in November than any other month of 1977.

Table 4 identifies the DSN VEM Discrepancy Reports generated during the period and 1977. The total number of open discrepancy reports has been on the increase since September.

A. Operational Use of Ampex FR-2000A Recorders

Ampex FR-2000A analog recorders were installed at each of the 64-meter DSN stations under engineering change order 75.291 early in 1976. These machines were used for playback of baseband analog data previously recorded on FR-1400 type of recorders.

Data was available from either Subcarrier Demodular Assembly (SDA) detected data output or from receiver baseband.

Following the MDS implementation, SDAs at 64-meter stations were reduced from six to four and of these four, only two detected data outputs were recorded on analog tape. This coupled with the requirement to record the third RF carrier when more than two spacecrafts were being tracked caused more reliance on baseband recovery.

By September 1977, the analog baseband record and replay capability had deteriorated below acceptable operational levels of performance and impacted the quality of operational Viking support. Attempts at corrective action did not improve the overall situation.

The Viking Tracking and Data Acquisition Manager established a task team on September 16, 1977 to coordinate the work necessary to reestablish analog baseband record and replay as a dependable operational capability.

The task team determined that reliable analog record and replay could be accomplished by:

(1) Recording and replaying data on the FR-2000A recorders.

(2) Changing track assignments to effect better replay characteristics by reducing interference between adjacent tracks (see Tables 5 and 6).

(3) Recording baseband data only.

The conditions underwhich this capability could be made available for operational use are as follows:

(1) A 5-minute gap in recording every 30 minutes was required to change tapes since only one FR-2000A recorder had been implemented at each 64-meter station.

(2) An additional 30 minutes of prepass preparation time was required to set up the tape machines.

(3) Analog recordings would only be made if the minimum specified signal-to-noise ratios were met.

(4) A failure of the prime recorder would result in a loss of analog data since no backup existed.

Successful demonstrations of the analog baseband record and replay capability were run with DSS 14 on November 18, and with DSS 43 on November 25. DSS 63 was down for the MDS reconfiguration and no demonstrations were possible with this station.

The Viking Project Manager approved this new plan on November 22 with the single qualification that the project might choose the time at which the recording gaps would occur so as to minimize the loss of critical data.

The FR-2000A recorders were authorized for use for all project support on December 2, 1977. The Network Operations Plans for each project were revised to show the new analog recorder configuration.

III. DSN Mark III Data Subsystem Implementation MDS Testing and Status

Except for DSSs 11, 61, and 63, all stations had completed the MDS implementation and testing prior to this reporting period. DSS 61/63 was released from tracking support on 15 October 1977 to begin it's implementation phase. The testing phase is scheduled to begin on 1 January 1978. DSS 11 will begin the MDS upgrade on 15 January 1978.

Table 1. Potential Bistatic-Radar targets

	Target	Prior radar inferences	Other information	Questions
A	Chryse Basin	Above average dielectric constant and roughness	Large number of surface rocks; Viking 1 site	Basin Characteristics Are surface rocks detectable?
B	Utopia	No data	Large number of surface rocks; Viking 2 site	Are surface rocks detectable?
C	Apollinares-Memnonia C site area	Variable echoes, generally weak; high diffuse-to-specular ratio	Low plains with little relief; surface features subdued	Nature of high angle scattering
H	Hellas	No data	Southern basin; few features	Basin Characteristics?
Pl	Plateau	Strong, sharp echoes; average dielectric constant; unusually smooth	Massive (recent?) flows; low crater counts	Scattering function in very specular region?
Po	Polar regions	No data	Ice forms, terracing, sculpturing	Polar characteristics?
T	Tharsis	Weak, diffuse echoes	Volcanic ridge and flanks	Nature of weak scattering?
S	Soviet landing sites	No data	Cratered uplands; basin	Possible clues to mission failures
SM	Syrtis Major	Strong echoes; smooth surface	Wind-blown surface; variable albedo	Basin characteristics?

Table 2. VEM tracking support 1977

DSS	Jan	Feb	Mar	Apr	May	Jun	Jul	Aug	Sept	Oct	Nov	Dec	1977 Total
	Tracks[a] / h												
11	23 135	22 142	10 100	17 118	38 228	40 289	44 322	42 343	26 210	40 408	35 310	42 320	379 2925
12	4 11	1 6	—	24 176	17 119	1 4	1 1	1 7	—	—	—	—	49 324
14	52 341	59 392	50 368	20 176	—	—	10 46	16 128	28 363	43 329	41 358	45 254	364 2753
42	21 247	25 226	58 453	17 138	17 162	14 112	10 69	—	—	14 100	18 116	20 126	214 1749
43	68 721	62 627	—	63 603	60 521	57 486	31 238	—	1 01	24 141	36 214	48 196	450 3748
44	—	—	7 7	1 4	—	—	16 99	26 166	6 22	12 51	—	—	68 349
61	35 261	29 227	12 72	40 317	54 461	51 475	37 337	35 322	38 345	22 203	—	—	353 3020
62	—	2 7	4 22	9 55	3 14	2 7	—	—	—	3 23	5 28	9 36	37 192
63	38 327	28 202	66 525	15 78	23 186	15 136	40 399	64 590	57 590	15 136	—	—	361 3169
Total	241 2043	228 1829	207 1547	206 1665	212 1691	180 1509	189 1511	184 1554	156 1531	173 1391	135 1026	164 932	2275 18229

[a]Number of tracks represent the summation of all Viking spacecraft tracked. Track time, in hours, represents scheduled station support.

ORIGINAL PAGE IS
OF POOR QUALITY

Table 3. Number of commands transmitted in Viking Extended Mission during 1977

DSS	Jan	Feb	Mar	Apr	May	Jun	Jul	Aug	Sept	Oct	Nov	Dec	1977 Total
	CMDS												
11	1,521	1,394	1,027	117	811	-0-	1	795	2,028	3,687	3,064	4,746	19,191
12	-0-	-0-	-0-	1,314	721	-0-	-0-	-0-	-0-	-0-	-0-	-0-	2,035
14	769	1,404	1,206	274	-0-	-0-	74	108	2,704	2,108	1,134	1,589	11,370
42	2,072	953	1,778	8	1,886	1,619	-0-	-0-	-0-	18	1,250	-0-	9,589
43	919	2,523	-0-	2,094	1,447	972	1,190	-0-	-0-	456	656	491	10,748
44	-0-	-0-	2	1	-0-	-0-	-0-	5	19	2	-0-	-0-	29
61	605	1,116	1,328	1,925	1,922	3,838	4,257	5,589	5,256	1,371	-0-	-0-	27,207
62	-0-	-0-	1	1,991	-0-	496	-0-	-01	-0-	-0-	14	5	2,507
63	795	472	2,039	381	675	383	2,579	2,318	1,610	847	-0-	-0-	12,099
Total	6,681	7,862	7,381	8,105	7,462	7,308	8,101	8,815	11,617	8,489	6,118	6,831	94,770

Table 4. DSN VEM discrepancy reports

DSS	Jan	Feb	Mar	Apr	May	Jun	Jul	Aug	Sept	Oct	Nov	Dec
	0[a] / C[b]											
11	4 / 0	3 / 4	4 / 6	1 / 3	2 / 3	2 / 6	2 / 7	1 / 7	1 / 1	1 / 3	2 / 2	1 / 4
12	4 / 0	0 / 0	0 / 0	5 / 2	7 / 5	0 / 7	0 / 0	0 / 0	0 / 0	0 / 0	0 / 0	1 / 0
14	14 / 2	11 / 19	4 / 33	3 / 9	2 / 2	0 / 2	6 / 2	4 / 18	5 / 14	10 / 24	14 / 13	7 / 16
42	0 / 1	2 / 3	0 / 7	0 / 2	0 / 0	0 / 0	0 / 0	0 / 0	0 / 0	1 / 0	3 / 2	3 / 3
43	10 / 13	11 / 10	0 / 12	9 / 11	8 / 17	2 / 14	1 / 6	0 / 1	0 / 0	0 / 5	3 / 7	11 / 14
44	0 / 0	0 / 0	0 / 2	0 / 1	0 / 0	0 / 0	1 / 0	1 / 4	0 / 1	0 / 0	0 / 0	0 / 0
61	1 / 9	1 / 6	0 / 3	0 / 1	1 / 2	0 / 6	1 / 4	0 / 7	0 / 4	0 / 4	0 / 0	0 / 0
62	0 / 0	0 / 8	1 / 2	2 / 1	0 / 2	0 / 1	0 / 0	0 / 0	0 / 0	2 / 0	0 / 2	2 / 0
63	1 / 4	7 / 3	1 / 18	0 / 6	4 / 4	3 / 12	4 / 4	9 / 17	8 / 17	4 / 7	1 / 5	0 / 1
Others[c]	4 / 3	3 / 0	2 / 10	4 / 7	7 / 12	10 / 13	8 / 16	5 / 9	7 / 8	10 / 15	13 / 21	13 / 13
Total	38 / 32	38 / 62	12 / 93	24 / 43	31 / 47	17 / 61	23 / 39	20 / 63	21 / 45	28 / 58	36 / 52	39 / 51

[a]0 = Number remaining open at end of month.

[b]C = Number closed during month.

[c]Other = DSN, NDPA, NOCA, GCF.

Table 5. FR-1400 analog recorder configuration showing high-density track assignments leading to interference between adjacent channels[a]

Track	Data		
	IRIG channel	Function	VCO center frequency kHz
1	5	RCVR 1 DAGC	1.30
	6	RCVR 2 DAGC	1.70
	7	RCVR 3 DAGC	2.30
	8	RCVR 4 DAGC	3.00
	A	Voice	22.00
	C	CMA 1	40.00
	18	CMA 2	70.00
	19	NASA time	93.00
2		RCVR 3 baseband	Direct
3		RCVR 1 baseband	Direct
4		RCVR 4 baseband	Direct
5		RCVR 2 baseband	Direct
6		Speedlock (100 kHz)	Direct
		SDA 2 output	525.00
7		Speedlock (100 kHz)	Direct
		SDA 1 output	13.50

[a]Tape speed to be 1.52 m/s (60 in./s).

Table 6. FR-2000 analog recorder configuration showing reallocation of track assignments to reduce adjacent track interference[a]

Track	Data		
	IRIG channel	Function	VCO center Frequency kHz
1	19	NASA time	93.00
2		RCVR 3 baseband	Direct
3		RCVR 1 baseband	Direct
4		Speedlock (100 kHz)	Direct
5		Speedlock (100 kHz)	Direct
6		RCVR 4 baseband	Direct
7		RCVR 2 baseband	Direct

[a]Tape speed to be 1.52 m/s (60 in./s).

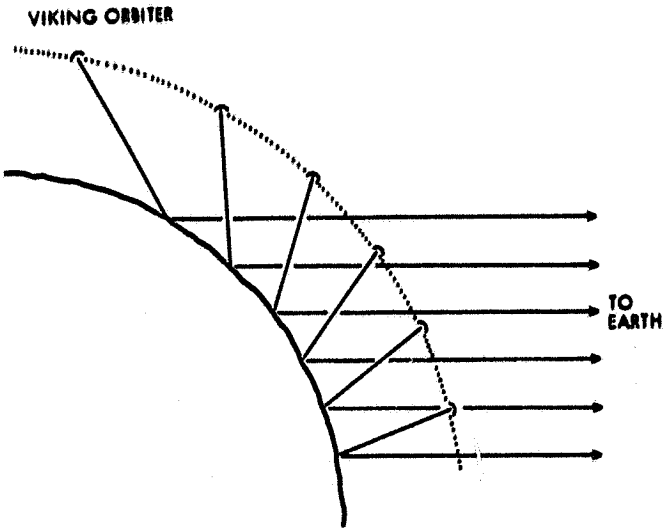

Fig. 1. Specular reflection pass

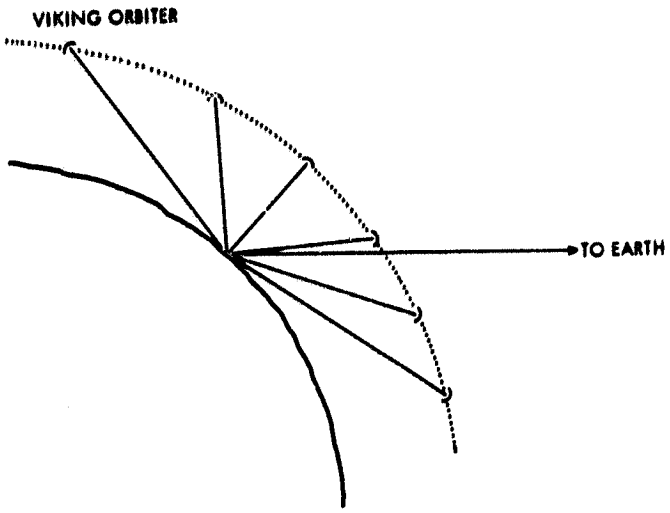

Fig. 2. Fixed target pass

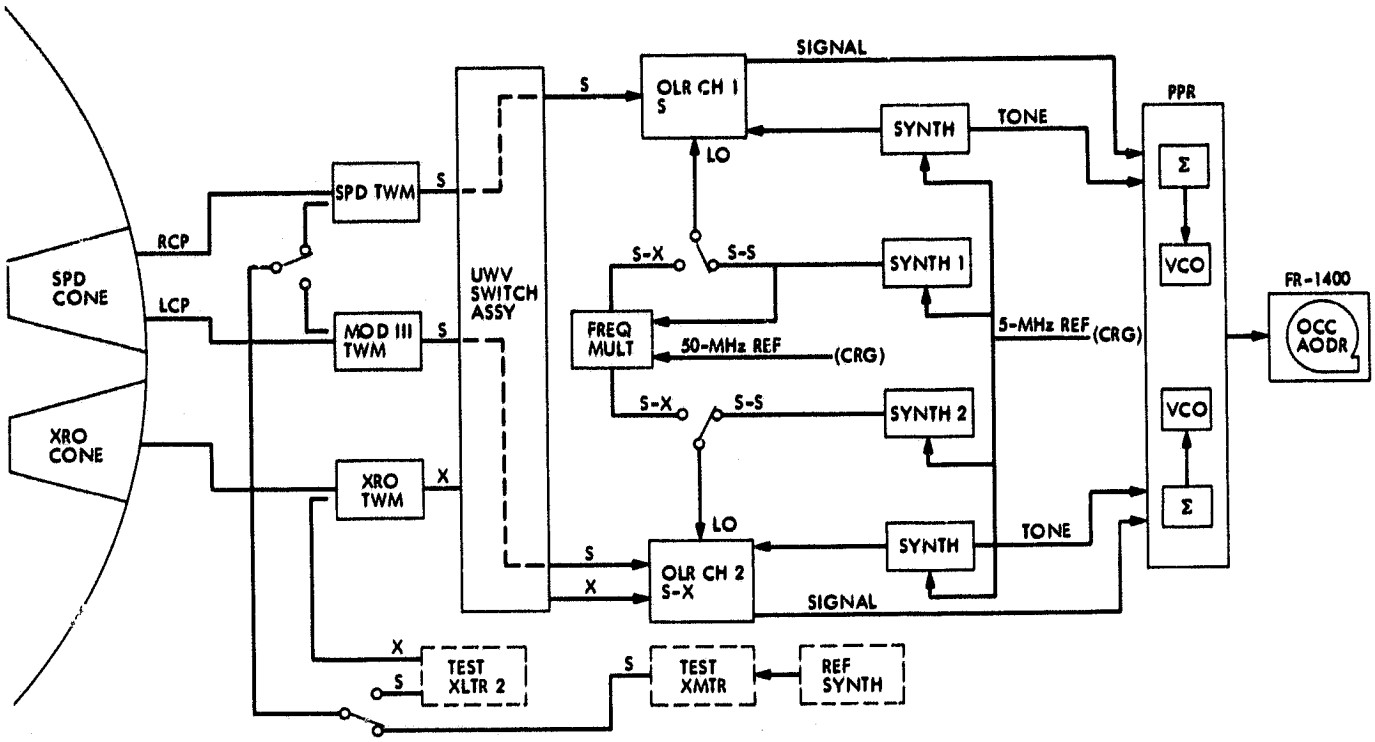

Fig. 3. Bistatic Radar DSN station configuration

ORIGINAL PAGE IS
OF POOR QUALITY

N78-24217

Pioneer Mission Support

T. P. Adamski
DSN Operations Section

This article reports on activities within the Deep Space Network in support of the Pioneer Project's in-flight spacecraft during the period August 1977 through January 1978. The amount of tracking coverage provided by the Network and a summary of operational testing of the Mark III Data Subsystems at DSSs 42/43 and 61/63 are presented.

I. Pioneers 6, 7, 8, and 9

As indicated by Table 1, coverage of these spacecraft has decreased from the levels of the last reporting period (Ref. 1). A total of 26 tracks were conducted during August, primarily for the acquisition of radio metric data to be used for trajectory updating. In the following months, coverage was minimal due principally to increased Network loading in support of higher priority users. Tracks in the months subsequent to August were used primarily to verify Mark III Data Subsystem (MDS) performance at the Deep Space Stations.

All of these spacecraft celebrated launch anniversaries during this reporting period. Pioneer 7 was eleven years old on 17 August, Pioneer 9 was nine years old on 8 November, Pioneer 8 was ten years old on 13 December, and Pioneer 6 was twelve years old on 16 December. In general, all four spacecraft have continued operating normally. The principal exception was Pioneer 8 which experienced a severe degradation in one of its sun sensors. The extent of the degradation will not be known until the spacecraft reaches perihelion when the sensor may be able to detect the sun.

The degraded sensor provided the spacecraft roll reference and sun pulse. Without the sun pulse, most scientific data are useless as the instruments have no pointing information with which to correlate their measurements. As a consequence, all instruments have been powered down; the plasma analyzer will be turned on whenever the spacecraft is tracked since data may be recovered from this instrument even in the absence of the sun pulse.

II. Pioneers 10 and 11

Pioneer 10 continues to operate satisfactorily. The spacecraft is now almost 15 astronomical units (AU) from the earth and the round trip light time is over four hours. Tracking coverage has remained fairly constant since the last report. Coverage by the 26-metre stations has declined sharply as the spacecraft is approaching threshold for those facilities. Tracking coverage for the last six months is tabulated in Table 1 and coverage for the last twelve months is shown graphically in Fig. 1.

Pioneer 11 is also operating normally. Earth-spacecraft range is now approximately 5.5 AU and the round-trip light time is over one and one-half hours. Tracking coverage is shown in Table 1 and Fig. 2 for the past six months and twelve months, respectively.

On 3 August, the spacecraft passed through its fourth superior conjunction at a minimum earth-Sun-probe angle of 9.°05 (approximately 33.3 $R_{\odot}$). No significant telemetry degradation was observed at this great an angular separation. Some increase in Doppler noise was experienced, as shown in Fig. 3, but this enhancement was somewhat less than that expected.

The plasma analyzer on Pioneer 11, which ceased operation in April 1975, began to output data again on 4 December. Since that date, the instrument has responded to ground commands and appears to be fully operational. This experiment should provide much valuable data during the Saturn encounter in September 1979.

A Saturn targeting maneuver, scheduled for late January, has been delayed until mid-year in order to decrease the amount the spacecraft must be turned off earth-pointing. Current plans are for Saturn periapsis to occur outside the visible rings, but an option remains for a passage between the planet and its rings.

III. Mark III Data Subsystems Support of Pioneer

Since the previous report, Mark III Data Subsystem (MDS) verification testing for Pioneers 6 through 11 has been completed at DSSs 42/43 and 61/63. A total of nine demonstration tracks of the Pioneer spacecraft were conducted at DSS 42/43 between the date the station was returned to service (26 September) and the date of configuration control application (18 October). DSS 61/63 participated in 21 Pioneer demonstration passes during the period 3 January (return to service) and 31 January (configuration control application).

No significant, MDS-related anomalies were experienced throughout either period of verification testing. The majority of the minor anomalies encountered were related to operator training and familiarization. These problems decreased as operations personnel became more proficient and more knowledgeable of the new systems.

DSS 11 is currently undergoing upgrading to an MDS configuration. Verification testing of this station will begin in March and will follow the same pattern of demonstration passes as was used for the other stations of the Network. A future article will report on this testing.

Reference

1. Adamski, T. P., "Pioneer Mission Support," in *The Deep Space Network Progress Report 42-41*, pp. 33-38, Jet Propulsion Laboratory, Pasadena, Calif., October 15, 1977.

Table 1. Pioneer tracking coverage

Month	Spacecraft	Station Type	Tracks	Tracking Time hr:min
August	Pioneer 6	26 m	6	36:00
	Pioneer 7	26 m	12	69:56
	Pioneer 9	26 m	8	42:41
	Pioneer 10	26 m	1	4:35
		64 m	27	195:07
	Pioneer 11	26 m	85	527:38
		64 m	1	6:28
September	Pioneer 10	26 m	2	11:12
		64 m	29	225:50
	Pioneer 11	26 m	50	396:56
		64 m	2	14:00
October	Pioneer 7	26 m	4	18:21
	Pioneer 8	64 m	1	3:37
	Pioneer 10	26 m	1	4:35
		64 m	33	237:37
	Pioneer 11	26 m	49	315:51
		64 m	8	59:01
November	Pioneer 10	64 m	37	265:57
	Pioneer 11	26 m	47	364:06
		64 m	2	16:03
December	Pioneer 10	26 m	1	0:50
		64 m	40	267:53
	Pioneer 11	26 m	36	289:09
		64 m	5	28:33
January	Pioneer 6	26 m	1	7:40
	Pioneer 8	64 m	1	6:18
	Pioneer 9	26 m	1	5:34
	Pioneer 10	64 m	32	223:58
	Pioneer 11	26 m	50	341:38
		64 m	2	11:11

ORIGINAL PAGE IS
OF POOR QUALITY

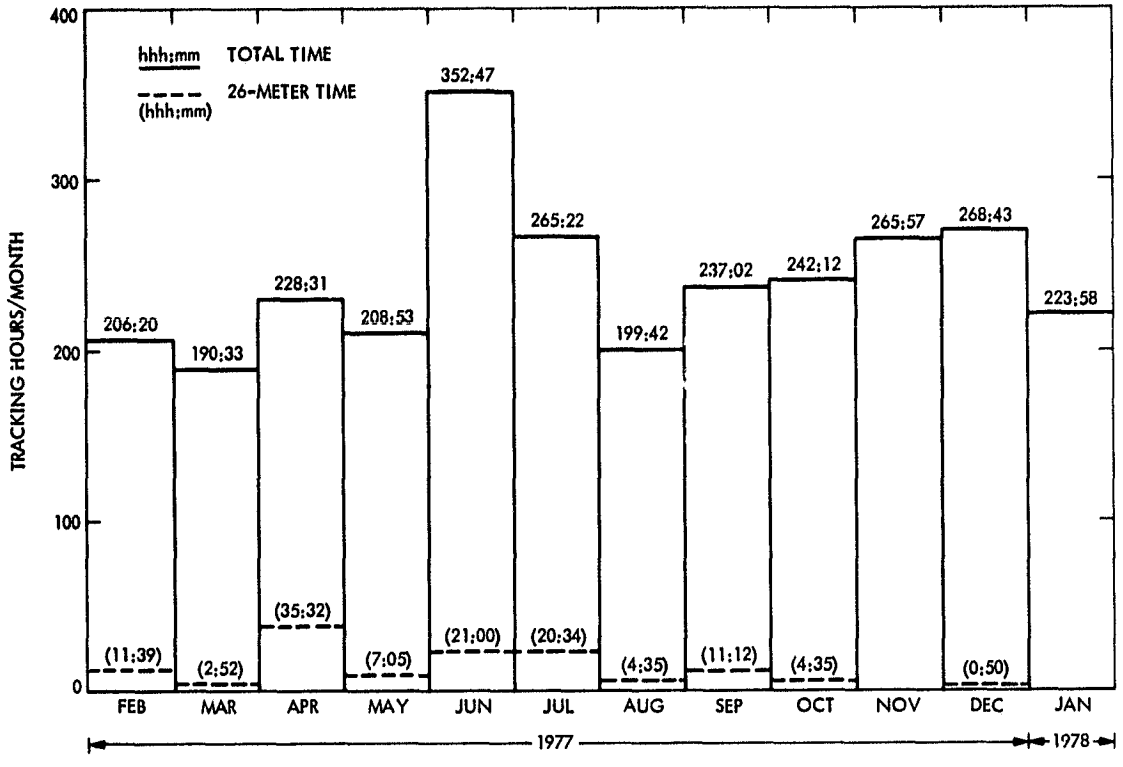

Fig. 1. Pioneer 10 tracking times

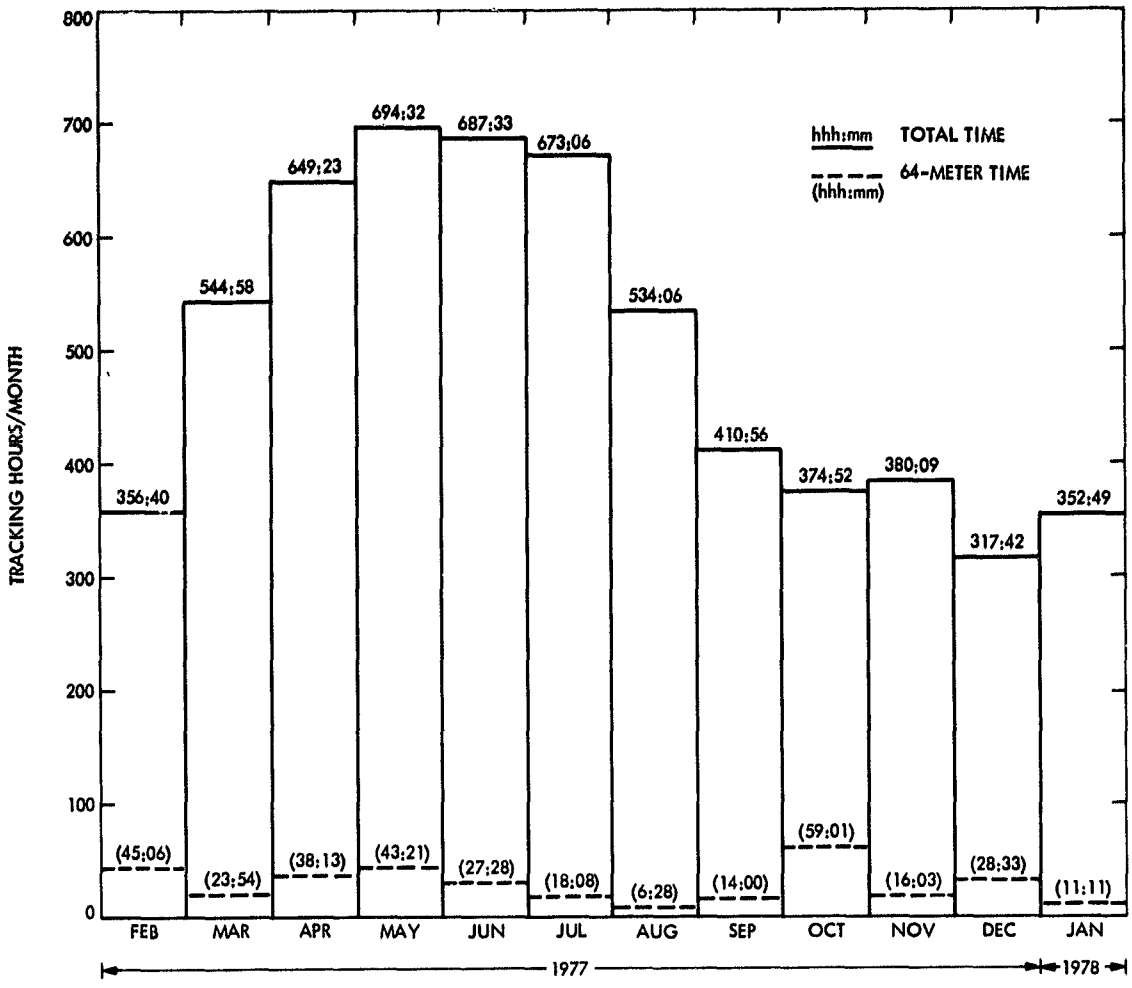

Fig. 2. Pioneer 11 tracking times

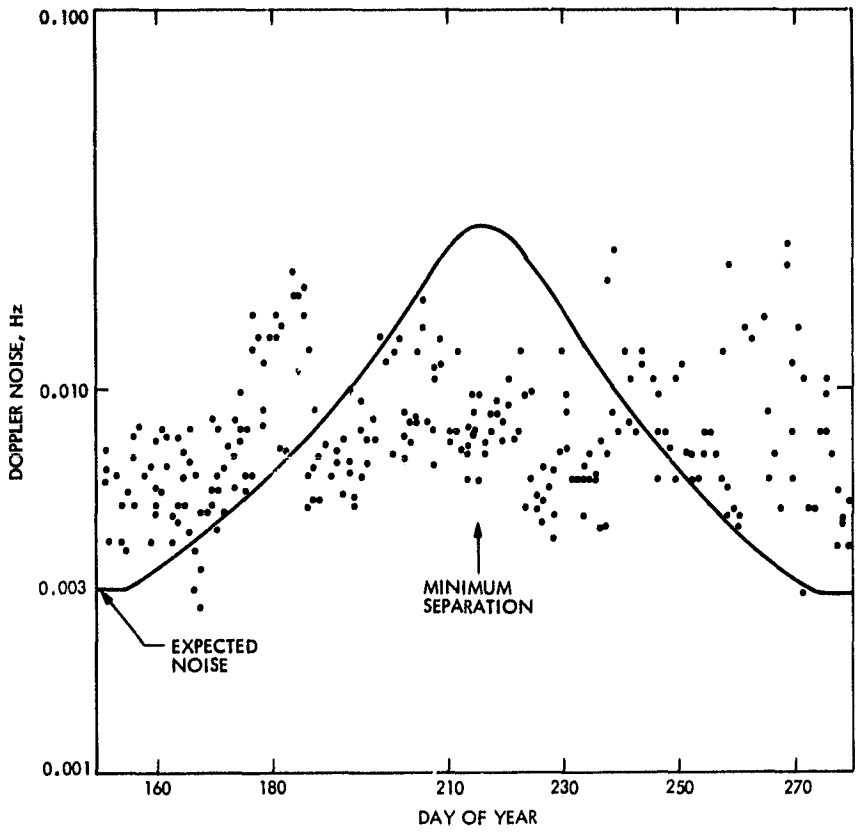

Fig. 3. Doppler noise during Pioneer 11 superior conjunction

N78-24218

Helios Mission Support

P. S. Goodwin
TDA Mission Support Office

W. N. Jensen and G. M. Rockwell
DSN Operations Section

This article reports on activities of the DSN Network Operations Organization in support of the Helios Project from 15 December 1977 through 15 February 1978.

I. Introduction

This article is the twentieth in a continuing series of reports that discuss Deep Space Network support of Helios Mission Operations. Included in this article is information on Mark III Data Subsystems (MDS) testing at the conjoint Deep Space Station 61/63 (Madrid, Spain) and other mission-related activities.

II. Mission Operations and Status

The Helios-1 spacecraft experienced an anomaly over DSS 43 (Canberra, Australia) on January 2, 1978. DSS 43 lost the downlink, and at first the station suspected a maser problem but after investigating this possibility all station systems checked normal. DSS 44 (Honeysuckle Creek, Australia) was then asked to track the spacecraft, but no signal was observed. The spacecraft was then blind-commanded to its original configuration and carrier lock was achieved on DSS 43's receiver, but no telemetry data lock was obtained. Additional commands were transmitted to configure the spacecraft to 512 bits per second (bps) coded telemetry in Format 4. At 04:34 UTC, DSS 43 reported data lock. The reason for the anomaly was subsequently traced to a spacecraft regulator switch causing a power drop, which knocked the high-gain antenna off point resulting in a loss of downlink signal. Later, the data rate was changed to 256 bps to improve the signal-to-noise ratio (SNR).

On January 24, 1978, at 04:16 UTC, Helios-2 passed through its sixth aphelion with no scheduled ground station support. Last support prior to aphelion was over DSS 12 (Goldstone, California), which had LOS at 21:05 UTC on 23 January. The next support after aphelion was over DSS 67 (Germany). The spacecraft was in a medium power mode and only Experiments E-5A, E-5C and E-8 were on.

On January 15, 1978, DSS 42 (Canberra, Australia) lost Helios-2's downlink due to lunar occultation. Because the predicts did not show this event occurring, 1.4 hours of data were lost which could have been stored on board the spacecraft for future recovery. As a result, the appropriate parties have been notified and hopefully this type of oversight will not occur in the future.

A special Helios-2 de-spin maneuver over DSS 42 was conducted on January 16, 1978. Two attempts were required because the spacecraft's power regulator No. 1 switched on the first attempt, causing a maneuver abort.

ORIGINAL PAGE IS
OF POOR QUALITY

On January 27, 1978, the Helios-2 spacecraft passed through its fourth aphelion. Ground station coverage was provided by DSS 42 (Canberra, Australia). The spacecraft was configured in medium power mode with all experiments on, except for E-3 and E-9. Overall coverage of both Helios-1 and Helios-2 for this period is listed in Table 1.

III. Special Activities

A. DSN Mark III Data Subsystems (MDS) Update

As reported earlier (Ref. 1), DSS 61/63 (Madrid, Spain) began MDS implementation on October 16, 1977. The Complex began its test and training phase on January 1, 1978. The Helios training consisted of demonstration tracks being conducted with DSS 61 (the 26-meter side) and DSS 63 (the 64-meter side). The first demonstration track was successfully performed on January 14, 1978. A total of six demonstration tracks were performed with DSS 61/63 with no major difficulty.

The DSS 61/63 Complex was placed under configuration control to support all flight projects on January 31, 1978.

On January 15, 1978, DSS 11 (Goldstone, California) was deactivated for MDS implementation. This is the last DSN facility to undergo modification and will complete the network's MDS upgrade. The MDS configuration for DSS 11 is shown in Figure 1. A report on DSS 11 will appear in the next article.

B. Support of On-Board and Ground Experiments

In the last article, it was hoped that some results of the Experiment 12 (Faraday Rotation) data analysis would be available for this article, but this is not the case. As of this time, no data have been released for publication. As was stated before, due to the large amount of data collected, processing is taking longer than expected. As soon as results become available, they will be summarized in the next sequential article.

Reference

1. Goodwin, P. S., Rockwell, G. M., "Helios Mission Support", in *The Deep Space Network Progress Report 42-43*, pp. 24-46, Jet Propulsion Laboratory, Pasadena, California, December 15, 1977.

Table 1. Helios Tracking Coverage

Month	Spacecraft	Station Type	Number of Tracks	Tracking time (Hours, Min.)
December	Helios 1	26 Meter	56	185:14
		64 Meter	9	60:43
	Helios 2	26 Meter	26	191:31
		64 Meter	0	0:00
January	Helios 1	26 Meter	45	332:52
		64 Meter	2	11:56
	Helios 2	26 Meter	42	312:37
		64 Meter	7	51:30

ORIGINAL PAGE IS
OF POOR QUALITY

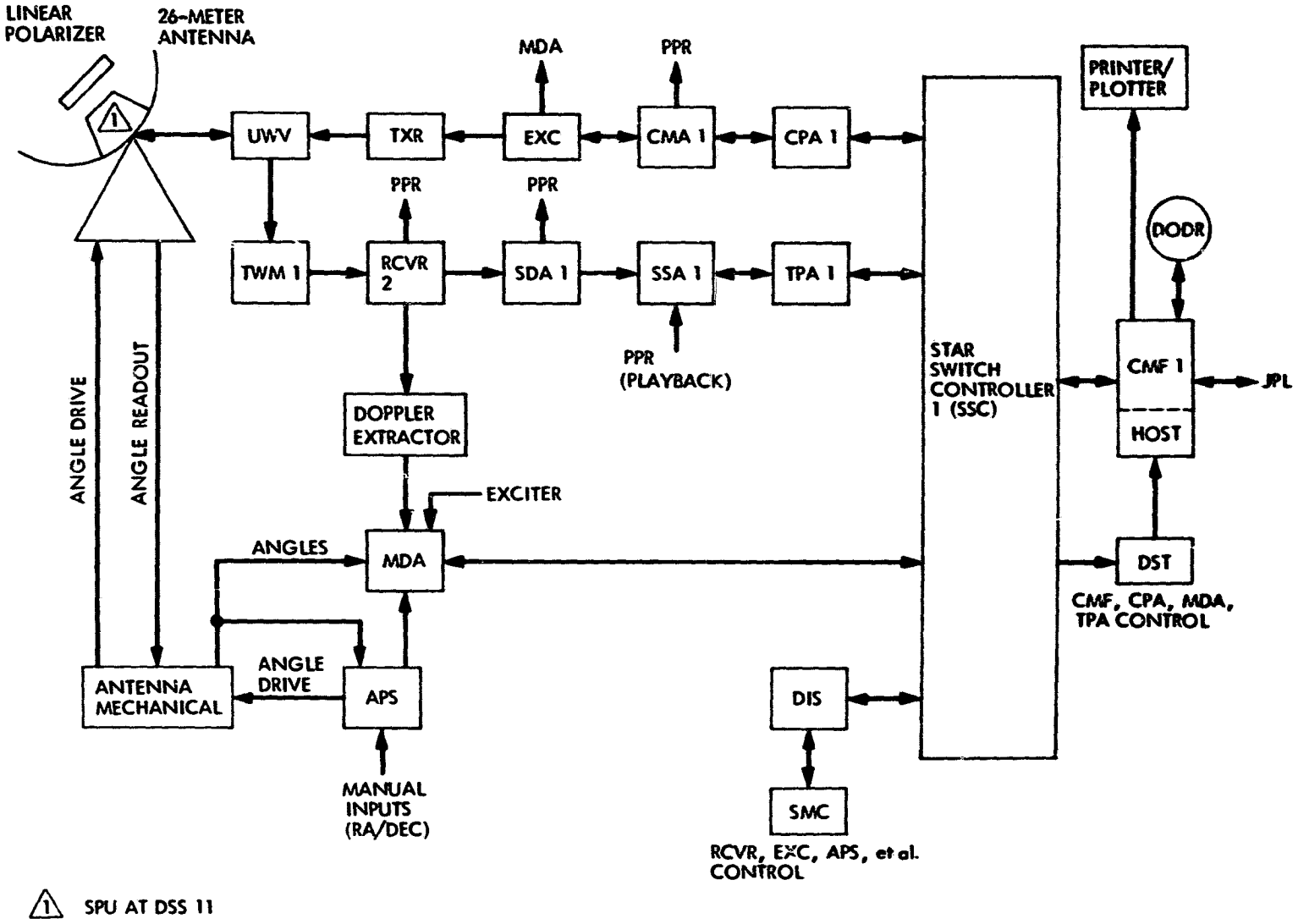

Fig. 1. Standard Helios configuration for DSS 11

N78-24219

An Alternate Technique for Near-Sun Ranging

J. W. Layland
Communications Systems Research Section

Measurement of the round-trip propagation time to a spacecraft when the signal path passes close by the sun is a severe challenge because of the high noise and time-varying signal delay encountered. Scintillation in the solar corona widens the spectrum of the received carrier signal so that it can not be efficiently tracked by the conventional phase locked receivers of the DSN. A substantial improvement in performance can be achieved by matching the processing bandwidth to the dynamical conditions of the near-Sun signal path. This processing can be performed off-line with software after the signal is open loop digitized and recorded. This article gives a detailed description and estimates the performance of such a system.

I. Introduction

Measurement of round-trip propagation time to a spacecraft when the signal path passes close by the Sun is interesting for the physics that it measures and for the challenge it represents to communications. Zygielbaum (Ref. 1) has recently described the techniques that are currently being used successfully to make such measurements. In the light of his review, it is incumbent upon us to ask if there are any alternate techniques which can improve the quality of results. The answer appears to be a substantial yes when we match our processing bandwidths and probing waveforms precisely to the dynamical conditions of the near-Sun signal path.

II. The Receiver Structure

Figure 1 is a rough block diagram showing the geometry and the real-time portions of the near-Sun ranging system. The transmitter portion is identical to that of our current ranging systems with the possible exception of the range-code bandwidths, which will be discussed later. The receiver portion is based upon that of our current ranging systems, but some operations are deferred to nonreal-time by sampling and recording after the signal bandwidth is reduced to that of the spectral spreading caused by the near-Sun environment. Some items of equipment are needed which are not part of the current R&D ranging system (MU-II) or the Operational Ranging System. The more significant of these are indicated in Figure 1.

The receiver Local Oscillator (LO) is driven by a programmed oscillator, or (optionally) by a frequency tracking loop to place the middle of the received carrier spectrum essentially at the middle of IF passband. The LO frequency should be stable enough and precise enough that the bandwidth of the carrier signal at IF (as measured from the IF passband center) is indistinguishable from the bandwidth of the RF carrier as received. This cannot be accomplished by a conventional phase locked loop which must have a bandwidth comparable to the spectral spread in the received carrier.

Extraction of the carrier reference phase for coherent detection of the range-code sidebands can be performed in a near-optimal manner from the recorded quadrature samples of the carrier signal.

The receiver coder is not rate-aided by the estimate of its doppler frequency in real time, so that once synchronized with the transmitter, it remains so throughout the tracking operation. The range-code doppler should in all cases be much less than the spread-carrier bandwidth, so that correction for the range-code doppler can be applied without loss to the recorded quadrature samples of the detected range code.

We expect two principal benefits with the nonreal-time processing: (1) the carrier phase reference for the i^{th} sample can be extracted from an optimally weighted sum of the j^{th} carrier samples for all j in the range $i - k \leq j \leq i + k$, where the weighting values, and the memory-limit k depend upon the autocorrelation function (hence bandwidth) of the received carrier phase. Since this carrier reference is constructed using the j^{th} samples for $j > i$, as well as for $j < i$, there is potentially a 3-dB improvement in the SNR of this phase reference relative to an ideally matched phase-locked loop which must depend only upon signal received prior to the sample of interest, i.e., for $j < i$ only. In addition, the nonreal-time phase reference need not suffer the 1-dB limiter suppression factor present in the DSN tracking loops. While such small factors would not be important if the phase-reference had high SNR, they add directly to data SNR when the phase reference has below unity SNR.

(2) The phase of the range coders can be completely accounted for throughout the tracking pass. This means that if it is necessary, data from the entire pass can be accumulated to provide one range acquisition, rather than depending upon a complete short acquisition falling within favorable signal conditions. DRVID can be obtained by postprocessing whenever the signal is strong enough for the doppler data to be valid, and strong enough for the received range code phase to be tracked as a function of time.

Without the rate-aiding of the range coders from doppler data, the bandwidth of the range code used need only be set low enough to accommodate changes in group delay which result from charged particle density changes. Were rate-aiding by doppler to be used, the allowed range code bandwidth would be reduced by 1/2 to accommodate changes in the difference between group delay and phase delay.

III. Nonreal-Time Processing

The equations which follow describe the nonreal-time processing. Let the signal as received at the antenna be $r(t)$:

$$r(t) = n(t) + \alpha \sin \left\{ \omega_c [t - \eta(t)] + m \square \cos \left(\omega_m [t - \eta'(t)] + \phi_m \right) + \phi_c \right\} \quad (1)$$

In Equation (1), $n(t)$ is additive noise, α is signal amplitude, ω_c is carrier frequency, $\eta(t)$ is the time-varying phase delay, m is the range-code modulation index, ω_m is the range-code frequency, $\eta'(t)$ is the time varying group delay, and ϕ_m and ϕ_c are arbitrary phase-shifts on modulation and carrier. Let the code-reference waveforms be unit power sinusoids: $\sqrt{2}$ {sin/cos} $(\hat{\omega}_m t)$; and let the carrier-reference waveforms be unit power sinusoids: $\sqrt{2}$ {sin/cos}$(\hat{\omega}_c t)$. With no code rate-aiding, $\hat{\omega}_m$ will differ from ω_m primarily by the doppler on ω_m; $\hat{\omega}_c$ should differ from ω_c by the error in predicting (tracking) carrier doppler.

Only the difference-frequency terms of the cross products between $r(t)$ and the reference signals will be considered because sum-frequency terms are filtered out in processing. The low-frequency terms which appear integrated at points a and b of Figure 1 are

$$\frac{\alpha}{\sqrt{2}} \cos(m) \begin{Bmatrix} \sin \\ \cos \end{Bmatrix} ([\omega_c - \hat{\omega}_c]\, t - \omega_c \eta(t) + \phi_c) + \begin{Bmatrix} n_{1c}(t) \\ n_{1s}(t) \end{Bmatrix} \quad (2)$$

The low-frequency terms which appear integrated at points c through f of Figure 1 are

$$\frac{\alpha}{2} \sin(m)\, \xi \begin{Bmatrix} \cos \\ \sin \end{Bmatrix} ([\omega_m - \hat{\omega}_m]\, t - \omega_m \eta'(t) + \phi_m) \times \begin{Bmatrix} \cos \\ \sin \end{Bmatrix} ([\omega_c - \hat{\omega}_c]\, t - \omega_c \eta(t) + \phi_c) \quad (3)$$

$$+ \begin{Bmatrix} n_{cc}(t) \\ n_{cs}(t) \end{Bmatrix} \text{ or } \begin{Bmatrix} n_{sc}(t) \\ n_{ss}(t) \end{Bmatrix}$$

The factor ξ is the amplitude of the sine-wave fundamental of a squarewave. If $n(t)$ can be assumed to be white and Gaussian with spectral density N_0, the six noise terms in Equations (2) and (3) are also white, Gaussian, and independent, with density N_0. By earlier assumption, the bandwidths of the signal terms in Equations (2) and (3) are the same as the bandwidth

ORIGINAL PAGE IS
OF POOR QUALITY

of the spread-carrier. These signals are integrated (or low-pass filtered) suitably for that bandwidth and then sampled and recorded for final processing later.

If the one-sided half-power bandwidth of the carrier spectrum is 120 Hz, we should be able to recover virtually all of the signal power by filtering each of the six signals to 250 Hz and sampling at 500 Hz. Since these signals are composed predominantly of Gaussian noise, quantization to 8 bits for each sample is more than adequate. This yields a recording rate of about 25 kb/s, so that a standard 730-m (2400-ft) reel of magnetic tape could record in excess of an hour of data. This record rate could probably be cut by a factor of four, through coarser quantization or narrow filtering, with only minor degradation.

For simplicity of exposition in what follows, the sampled signals will be assumed to be Nyquist-rate samples of both noise and signal processes. Modifications necessary to account for the actual spectrum of the carrier are straight-forward and not discussed. Let $\Psi_{ci} = [\omega_c - \hat{\omega}_c]\ t_i - \omega_c \eta\ (t_i) + \phi_c$ be the carrier phase at time t_i, $\Psi_{mi} = [\omega_m - \hat{\omega}_m]\ t_i - \omega_m \eta'(t_i) + \phi_m$ be the range-code phase at time t_i, and denote the various noises at time t_i by $n_{xi} = n_x(t_i)$ where x ranges over the various noise subscripts in Equations (2) and (3). The sequence $\{\Psi_{mi}\}$ contains the desired range information. The sequence $\{\Psi_{ci}\}$ contains little or no useful information because of the fluctuations in $\eta(t)$. The six samples at time t_i (subscript i assumed) are

$$\begin{aligned}
\beta_{1c} &= \frac{\alpha}{\sqrt{2}} \cos(m) \sin(\Psi_c) + n_{1c} \\
\beta_{1s} &= \frac{\alpha}{\sqrt{2}} \cos(m) \cos(\Psi_c) + n_{1s} \\
\beta_{cc} &= \frac{\alpha}{2} \sin(m)\, \xi \cos(\Psi_m) \cos(\Psi_c) + n_{cc} \\
\beta_{cs} &= \frac{\alpha}{2} \sin(m)\, \xi \cos(\Psi_m) \sin(\Psi_c) + n_{cs} \\
\beta_{sc} &= \frac{\alpha}{2} \sin(m)\, \xi \sin(\Psi_m) \cos(\Psi_c) + n_{sc} \\
\beta_{ss} &= \frac{\alpha}{2} \sin(m)\, \xi \sin(\Psi_m) \sin(\Psi_c) + n_{ss}
\end{aligned} \tag{4}$$

Information about the sequence $\{\Psi_{ci}\}$ can be conveniently destroyed by taking cross products of the βs.

$$\begin{aligned}
\beta'_c &= \beta_{cc} \cdot \beta_{1s} + \beta_{cs} \cdot \beta_{1c} \\
\beta'_s &= \beta_{sc} \cdot \beta_{1s} + \beta_{ss} \cdot \beta_{1c}
\end{aligned} \tag{5}$$

Taking expected values,

$$\begin{aligned}
\langle \beta'_c \rangle &= \frac{\alpha^2}{2\sqrt{2}}\, \xi \sin(m) \cos(m) \cos(\Psi_m) \\
\langle \beta'_s \rangle &= \frac{\alpha^2}{2\sqrt{2}}\, \xi \sin(m) \cos(m) \sin(\Psi_m)
\end{aligned} \tag{6}$$

and if V denotes $\langle n_x^2 \rangle$ for any of the noise terms,

$$\begin{aligned}
\text{Variance}\ \{\beta'_c\} &= 2 \cdot V^2 + V \cdot \frac{\alpha^2}{4} \xi^2 \sin^2(m) \cos^2(\Psi_m) \\
&\quad + V \cdot \frac{\alpha^2}{2} \cos^2(m) \\
\text{Variance}\ \{\beta'_s\} &= 2 \cdot V^2 + V \cdot \frac{\alpha^2}{4} \xi^2 \sin^2(m) \sin^2(\Psi_m) \\
&\quad + V \cdot \frac{\alpha^2}{2} \cos^2(m)
\end{aligned} \tag{7}$$

The β'_c, β'_s cross products are accumulated for as long as the variations in Ψ_m will permit in order to estimate the range information which is in Ψ_m. The amplitude SNR of β'_c is

$$\rho'_c = \frac{\frac{\alpha \cos(m)}{\sqrt{2V}} \cdot \frac{\alpha \sin(m)}{\sqrt{4V}}\, \xi \cos(\Psi_m)}{\sqrt{2 + \frac{(\alpha \cos(m))^2}{2V} + \frac{(\alpha \sin(m)\, \xi)^2}{4V} \cos^2(\Psi_m)}} \tag{8}$$

while that for ρ'_s is similar. If the carrier signal is strong relative to the noise, and the modulation index m is small, then ρ'_c converges to

$$\rho_c' \approx \frac{\alpha}{2\sqrt{V}} \sin(m) \cdot \xi \cdot \cos(\Psi_m) \quad \text{if } \alpha \cos(m) \gg \sqrt{V} \tag{9}$$

This result is identical to the comparable result for coherent detection when a strong carrier is tracked by a phase locked loop. If the total signal is weak relative to the noise, then ρ_c' is approximately

$$\rho_c' \approx \left(\frac{\alpha}{2\sqrt{V}}\right)^2 \cdot \cos(m) \cdot \sin(m) \cdot \xi \cdot \cos(\Psi_m) \quad \text{if } \alpha \ll \sqrt{V} \tag{10}$$

When a conventional phase locked loop tracks $\Psi_c(t)$, the loop SNR, R_L should be given by

$$R_L = \eta \frac{\alpha^2 \cos^2(m)}{2V} \tag{11}$$

Where η is a correction factor for the relative bandwidths of the tracking loop and the samples to be recorded (cf. Eq. (4)). By the bandwidth assumptions, $\eta < 1$. The information on cos (Ψ_m) is now contained in β_{cc}, which has expected value

$$\langle \beta_{cc} \rangle \approx \frac{\alpha}{2} \sin(m)\, \xi \cos(\Psi_m) \left[I_1(R_L)/I_0(R_L) \right] \tag{12}$$

The modified Bessel functions $I_i(\cdot)$ derive from the tracking error of a first-order phase locked loop following $\Psi_c(t)$. The weak-signal asymptote for the amplitude SNR of β_{cc} is:

$$\rho_{cc} \approx \left(\frac{\alpha}{2\sqrt{V}}\right)^3 \cdot \eta \cdot \sin(m) \cdot \xi \cdot \cos^2(m) \cdot \cos(\Psi_m) \quad \text{if } \alpha \ll \sqrt{V} \tag{13}$$

which may be very much less than ρ_c' for small α. The nonreal-time processing should thus perform much better than real-time coherent detection when the signal is weak, and at least as well when the carrier signal is strong.

IV. Ranging Link Design

Using the receiver structure described above, ranging link design is completed by specifying the bandwidth within which the signal must be measured to ensure reliable operation, and from this and the spectral broadening information, the bandwidth of the range code itself. Data from previous solar conjunctions will be used as a guide.

The three primary degradations are shown approximated in Figure 2 as a function of $\rho = R/R_\odot$, the distance from the Sun of the signal ray path at its closest approach, given in units of the solar radius. The approximations shown are slight over-estimates to actual data for $\rho > 1.7$. They are of dubious value for $\rho < 1.7$ where no data was found.

The receiver system temperature increases drastically as the antenna beam approaches the Sun's disk. Rockwell (Ref. 2) developed an approximation to the system temperature increase caused by close approach to the Sun which is

$$T_{SUN} \approx 5.6 \exp\{16.3/(\rho + 1)\}$$

when written in terms of ρ. His approximation is conveniently overestimated by

$$T'_{SUN} \approx 20 \cdot \left(\frac{\rho}{10}\right)^{-1.5} + 3 \cdot \left(\frac{\rho}{10}\right)^{-4} \tag{14}$$

This form is convenient for graphic display and "calculation" since it is representable as the sum of straight line segments on a log-log plot. In Figure 2, the asymptotes are shown for T_{SUN} in dB degradation relative to a nominal system temperature of 20 K.

Spectral spreading data has been presented by Woo (Ref. 3). This data is for one-way transmission at S-band with a variety of spacecraft, and a variety of ρ. The carrier spectrum is spread by scintillation into an almost Gaussian shape. The half-power bandwidth of this spread carrier is slightly overestimated by the function

$$B \approx 2 \left(\frac{\rho}{10}\right)^{-1.5} + 0.25 \left(\frac{\rho}{10}\right)^{-3.5} \tag{15}$$

This form is again chosen for graphic convenience. In Figure 2, B is shown in dB relative to 1 Hz.

Angular broadening of the ray-path from the Helios I spacecraft was inferred by Woo (Ref. 3) at $\rho = 1.7$. Assume that this

measurement is consistent with prior determinations at much larger ρ, at a similar "quiet" Sun condition. Then the factor by which the beam cross-section of the DSN 64-m antenna is exceeded is approximately

$$\text{Beam Overspread} \approx 10^3 \times \rho^{-9} + 1 \qquad (16)$$

when a 'moderate' solar activity is assumed. The S-band signal power loss due to this beam spreading is shown in dB in Figure 2.

Amplitude scintillations can also cause severe short-term degradation. However, most available literature seems to imply that the overall long-term effect can be almost negligible, so it is tentatively ignored here.

For the ranging link calculations, the bandwidths of the spread spectrum of the range code is proportional to that of the carrier on which it resides, but reduced by the ratio of the range code frequency to the carrier frequency. For two-way S-band transmission, the spectral spreading should be $\sqrt{2}$ times that for one-way S-band transmission.

For two-way S-band up/X-band down transmission, the spectral broadening takes place almost entirely on the S-band uplink. The received X-band carrier bandwidth will be 11/3 times that of the one-way S-band link as a result of the multiplication to the S-band frequency in the transponder. The range-code bandwidth will be essentially the same as for the one-way S-band link. The angular beam-spreading loss, which pertains to the down-link only, is reduced for X-band to $(3/11)^2$ times its S-band value.

An example link calculation has been carried out using power assumptions pertinent to the recent past Viking solar superior conjunction. Then, the undegraded down-link carrier power was approximately - 143 dBm, and the ranging sideband power was approximately - 153 dBm. These ranging sidebands consist mostly of a turned-around copy of the uplink range code whenever the S-band uplink is suitably strong relative to thermal noise at the spacecraft. Using these parameters, and a "strong uplink" assumption, the ranging link SNR is as shown in Figure 3 as a function of ρ for a two-way S-band link. Only the straight line asymptotes are shown. The ranging sideband power-to-noise density ratio (P_r/N_0) is shown in dB-Hz. When the solar impact parameter ρ is moderately large ($\rho > 10$), this ratio is approximately the same as it is far from the Sun. As ρ decreases below 10, the increased system temperature and beam-spreading losses cause severe degradation. The carrier sample SNR ($P_c/N_0 \cdot W_c^s$) is shown in dB. The sample bandwidth is the two-way counterpart of the half-power bandwidth displayed in Figure 2, so that there is a 3-dB direct signal power loss incurred. As ρ decreases, the increase in sample bandwidth joins with increased system temperature and beam spreading losses to degrade the SNR as shown. The detected P_r/N_0 is that to be obtained through the quasi-coherent scheme described above, as represented by Eq. (8).

A ranging measurement SNR of +20 dB can be achieved at $\rho \approx 1.85$ by filtering this measurement to 10^{-2} Hz if significant power is not to be lost. From Figure 2, the half-power bandwidth of the S-band (2.3×10^9 Hz) carrier at $\rho = 1.85$ is 19.5 dB-Hz one-way (21 dB-Hz two-way). This spectral spread on a range code of 10^5 Hz or less will fit within a 10^{-2} Hz measurement bandwidth. For an S-band uplink/X-band downlink, the ranging link is as shown in Figure 4, as a function of ρ. This link appears to be operable at a somewhat smaller value of ρ than the two-way S-band link because the carrier bandwidth expansion due to frequency multiplication to X-band is more than counterbalanced by the lessened degradation of the X-band downlink.

The value of ρ for which ranging appears to become unworkable is in the vicinity of 1.8 to 1.9 with the assumptions used. The actual value will vary from this depending upon the activity level of the Sun, and the validity of the various assumptions and approximations. In particular, the assumed "strong" uplink is probably also degrading as ρ decreases, and this degradation would be reflected in a reduced P_r/N_0 in the downlink. This effect needs to be examined, but should not dramatically change the threshold value for ρ.

For conventional phase locked loop carrier tracking and coherent detection, and the assumptions of Figure 3 and Figure 4, the value of ρ for which ranging appears to become unworkable is in the vicinity of 2.0 for both S/S and S/X ranging links. In fact, the closest range point achieved to date was at $\rho = 2.0$ ($< \text{SEP} = 0.55°$) using the conventional DSN receiving equipment in conjunction with the Mu-II ranging system (Ref. 1).

V. Signaling Strategy

In practice, only a part of the ranging signal energy can be placed into the highest frequency code to be used. The remainder must be transmitted as lower frequency tones in order to resolve ambiguities in the measured range to at least the a priori uncertainty in that measurement. Suppose that overall one half of the signal energy is to be allocated to the highest frequency code for which spectral spreading is within the measurement bandwidth, and the other half allocated to

resolving ambiguities. This can be achieved conveniently in a sequential component system by dividing time into equal-length segments, e.g. 30 sec, and using every other segment for the high frequency code component. A signal received in several segments can be combined together as allowed by spectral spreading of that code component, and as needed from SNR considerations.

The remaining segments should be allocated to lower frequency range code components such that the entire measurement strategy is robust in the face of larger-than-expected variations in the plasma delay, and such that the a priori ambiguities can be resolved reliably. Let C_1 denote the highest frequency code component, and let C_1 be assigned to all even-numbered time segments. Two feasible signalling strategies for the odd-numbered segments are as shown in Table I, under the assumption that ambiguity can be resolved with only five code components. Note that at no time is a code "chopped" by a higher frequency code. The linear strategy is analogous to an acquisition as performed by current ranging systems, while the logarithmic strategy should be somewhat more tolerant of unexpected delay variations.

VI. Discussion

From the information in the preceding sections, it is clear that we can improve the performance of near-Sun ranging operations by quasi-optimal detection techniques that are possible with nonreal-time processing. This improvement would at least manifest itself by an increase in the reliability with which range data is obtained when the spacecraft signal passes to within a few solar radii of the Sun. Optimistically, we may be able to reduce the value of R at which ranging is accomplished to about 1.8 solar radii.

As dual-frequency range is a measure of the total charged particle content in the signal path, and the concurrent doppler or spectral spreading data provide a measure of the variations in that charged particle content, we will be testing very close to the Sun the often used assumption that the total charged particle content of the solar corona is directly proportional to its variation. Furthermore, since the data acquisition process "just runs" without the hectic scheduling activity normally associated with near-Sun ranging, the amount of operational trauma associated with solar-superior conjunction experiments should be greatly reduced.

References

1. Zygielbaum, A. I., "Near-Sun Ranging" DSN-PR 42-41, pp. 43-50, October 15, 1977. Jet Propulsion Laboratory, Pasadena, Calif.
2. Rockwell, S. T., "A model of SNR Degradation during Solar Conjunction", DSN-PR 42-38, pp. 187-198. April 15, 1977. Jet Propulsion Laboratory, Pasadena, Calif.
3. Woo, R. "Radial Dependence of Solar Wind Properties Deduced from Helios 1/2 and Pioneer 10/11 Radio Scattering Observations" (Preprint) 1977. *Astro Physics Journal*, January 1978.

Table 1. Signalling strategies

Time segment No.	1	3	5	7	9	11	13	15
Linear strategy	C_2	C_3	C_4	C_5	···	REPEAT	···	
Logarithmic strategy	C_2	C_3	C_2	C_4	C_2	C_3	C_2	C_5···

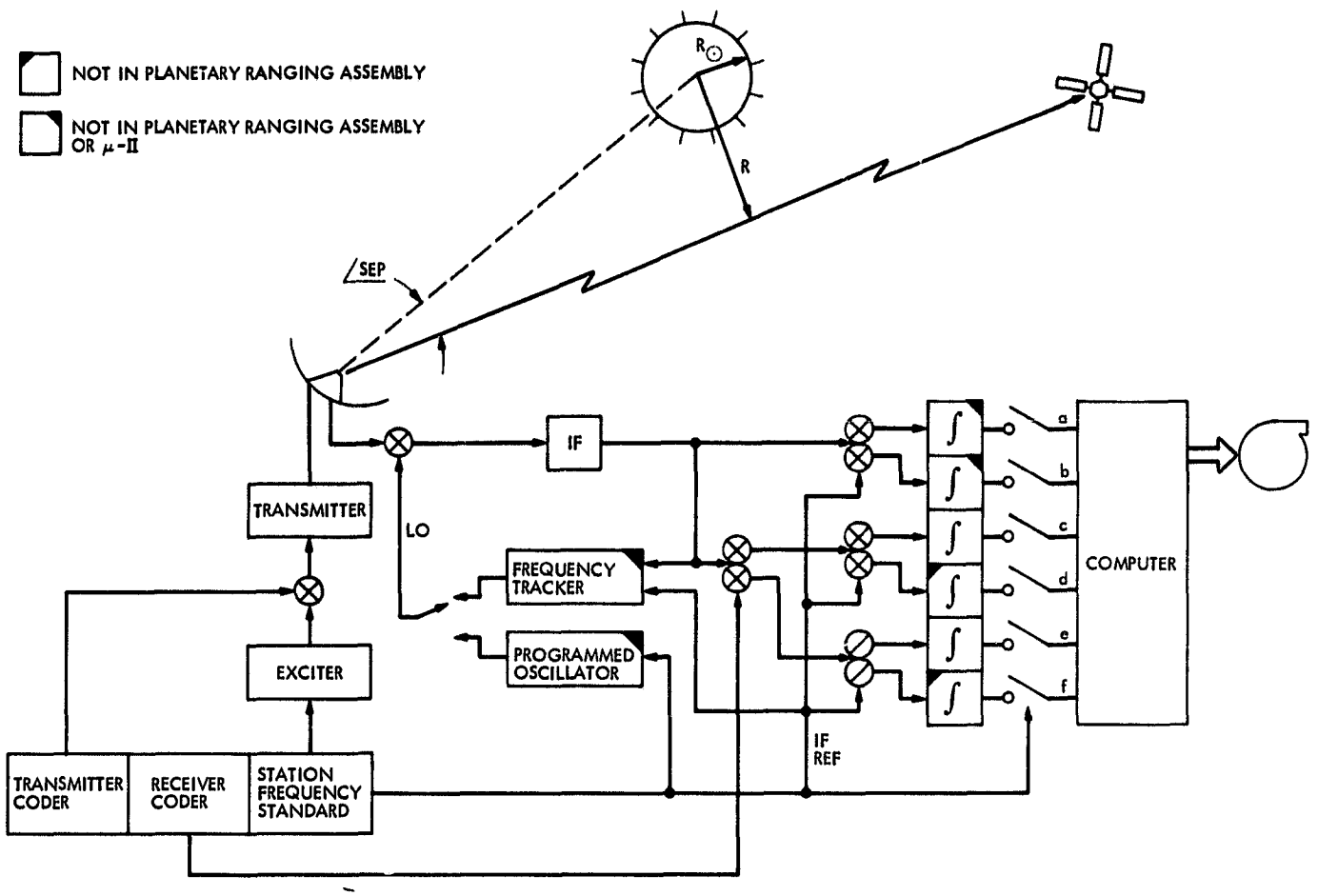

Fig. 1. Block diagram of near-Sun ranging system

ORIGINAL PAGE IS
OF POOR QUALITY

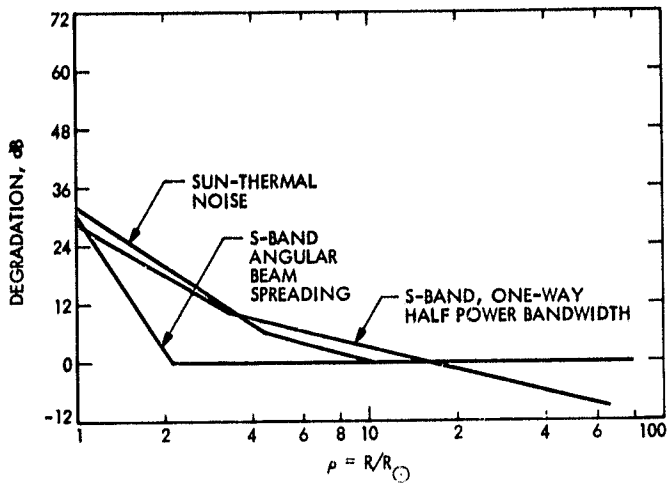

Fig. 2. Degradation terms for near-Sun ranging

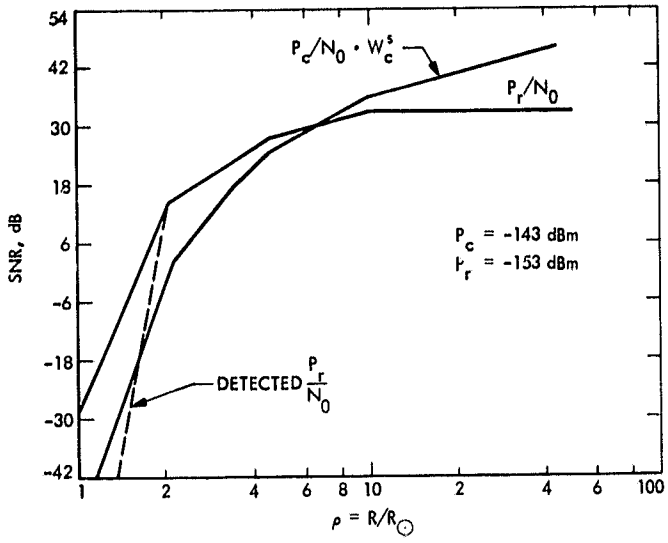

Fig. 3. Ranging link parameters two-way S/S

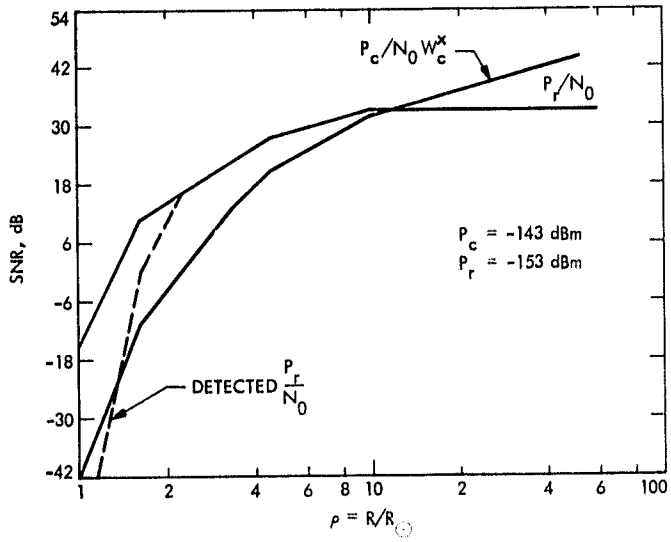

Fig. 4. Ranging link parameters two-way S/X

N78-24220

The Tone Generator and Phase Calibration in VLBI Measurements

J. B. Thomas
Tracking Systems and Applications Section

In very long baseline interferometry (VLBI) applications, the measurements of geophysical/astrometric quantities and clock synchronization are degraded by unknown and unstable phase effects due to instrumentation. Most of these phase effects can be removed through the use of a tone generator that injects near the front of the instrumentation a set of tones derived from the station frequency standard. When properly used, such a calibration technique will not only remove post-injection instrumental phase instabilities, but will also allow absolute calibration of interferometer phase so that clock synchronization is possible. As implied, these advantages of the tone generator pertain only to instrumental effects after the injection point. This report presents a nonrelativistic mathematical model to describe the calibration signal, its processing, and its use in removing instrumental effects from interferometer phase.

I. Introduction

In very long baseline interferometry (VLBI) measurements, the measured delays are corrupted by unknown and unstable phase shifts due to instrumentation. Such phase effects can degrade the accuracy of geophysical measurements and complicate measurements of clock synchronization. Most of these instrumental effects in VLBI measurements can be removed through the use of a phase calibrator. The commonly used approach, pioneered by A. E. E. Rogers (Ref. 1), is to inject at a point near the front of the instrumentation a calibration signal consisting of a set of tones, equally spaced in frequency and derived from the station frequency standard. When properly used, such a calibration technique will not only correct for system phase instabilities, but will also allow absolute calibration of interferometer phase so that clock synchronization is possible. Phase calibration hardware, suitable for use in the Deep Space Network, is currently being developed at the Jet Propulsion Laboratory in Division 33 (R. L. Sydnor's group).

It should be noted that the aforementioned advantages of phase calibration pertain only to instrumental effects after the calibrator injection point and that other measures must be taken to account for instrumental effects before that point. This report will ignore the important issue of calibration before the injection point.

As implied above and indicated in the text, the goal of phase calibration is to remove from the phase all instrumental effects after the injection point so that the measured values of delay and delay rate are left in their ideal form: a sum of geometric delay and clock offset terms. (For simplicity, transmission media terms will be ignored). In this report, a nonrelativistic model is developed to describe the tone signal, its processing, and its use in removing instrumental effects.

The sections dealing with phase analysis are similar to an analysis by Fanselow (Ref. 2), but are more detailed. Further, material has been added that deals with clock modeling, tone amplitude, and tone SNR.

The sections in this report have been organized as follows: Section II models the calibrator signal including power level, clipping, tone-stopping, and stopped-tone SNR. Section III presents fundamental definitions in clock modeling. Section IV develops a detailed model for the amplitude and phase of the calibrator signal in terms of basic instrumental effects. Section V presents a heuristic derivation of interferometer phase in terms of basic instrumental effects. Section VI demonstrates formally how the calibration process removes instrumental effects from interferometer phase. Section VII summarizes areas where work remains to be done.

II. Phase Calibrator Signal

This section treats the phase calibrator signal and includes an analysis of: (a) tone power (b) the effect of bilevel clipping on the recorded signal (c) tone stopping (d) stopped-tone SNR. Since it is not necessary for these topics, this section will not decompose tone phase and amplitude into more fundamental quantities but will treat each of them as a single variable. Section IV will deal with the more complicated problem of expressing tone amplitude and phase in terms of contributing instrumental factors.

The phase calibrator injects near the front of the instrumentation an equally spaced set of tones that have all been derived from the same frequency standard. The phases of these tones are expected to be stable at the 10-picosecond level and calibrated absolutely to the nanosecond level. Each channel bandpass will probably contain more than one tone, but determination of the optimum number will require a thorough study of bandpass characteristics, a task outside the scope of this report. The calibrator signal will be injected into the system at a low power level and thus imbedded in the radio source data. The Mark II system digitally records the signal in a bilevel mode at 4 Mbits/sec. Each tone will be extracted at the correlator by mixing the bit stream digitally with a frequency that closely approximates the baseband frequency for that tone.

The analog baseband signal (before clipping) can be represented in the form

$$V(t) = S(t) + \sqrt{T_s}\, W(t) \tag{1}$$

$$= \sum_n A_n \cos \phi_n(t) + \sqrt{T_s}\, W(t) \tag{2}$$

where the calibrator signal (S) has been decomposed in the second equation into its constituent tones. As implied above, the baseband phase (ϕ_n) of each tone will be essentially linear in time. We have normalized the noise term W, which contains both system noise and radio source noise, to unity [i.e., $\langle W^2 \rangle = 1$]. The factor T_s is the (average) system temperature contributed by W.

Total power of the signal will be given by

$$P \propto \langle V^2 \rangle = \frac{1}{2} \sum_n A_n^2 + T_s \tag{3}$$

If we specify total calibrator power relative to total noise power, we can express the tone amplitude in terms of T_s. That is, if the ratio of total calibrator power to total noise power is ϵ, then the ratio (SNR) of tone amplitude to rms noise voltage becomes

$$\boxed{\frac{A}{\sqrt{T_s}} \approx \sqrt{\frac{2\epsilon}{N_c}}} \tag{4}$$

where N_c is the number of tones in the passband, and A is the (virtually constant) tone amplitude within the passband. (It is unnecessary for our purposes to resolve the minor ambivalence involving tones on the bandpass edges.) We currently plan to keep the total calibrator power low – say, 2% of the system noise. Thus, if there are 3 tones in the passband, the SNR for a tone becomes

$$\frac{A}{\sqrt{T_s}} \approx \sqrt{\frac{2 \times 0.02}{3}} \approx 0.12 \tag{5}$$

(For the sake of numerical example, we will assume a nominal system with a 2% power level and 3 tones/passband. It is outside the scope of this work to determine optimum values for these parameters.) It is worth noting here that this "single-sample" SNR is large compared to typical intercontinental cross-correlation amplitudes, which are usually in the range 0.001 to 0.04. The tone SNR in Eq. 4 will be modified slightly below when two-level sampling is taken into account and will increase when many bits are collected in the tone-stopping process.

The maximum value of the total tone signal S will occur whenever all tones are in phase and is given by

$$\frac{S_{max}}{\sqrt{T_s}} \approx N_c \frac{A}{\sqrt{T_s}} \tag{6}$$

This maximum value occurs, of course, every time a calibrator pulse (see Section IV) reaches the recorder and equals about 0.35 for the example above. (The pulse width at baseband is approximately equal to inverse of the system bandwidth when a number of tones are in the passband.)

We are now prepared to analyze tone-stopping in the correlator. Let $\tilde{V}_k$ be the recorded signal at time t_k, where the tilde denotes bilevel sampling. For a given station the correlator will counter-rotate (tone-stop) a given tone as follows

$$V_{sn} = \frac{1}{N_t} \sum_{k=1}^{N_t} \tilde{V}_k \exp -i\psi_{nk} \tag{7}$$

where ψ_{nk} is the model phase for the n^{th} tone at time t_k. (In this report, we will not take into account the fact that the Mark II correlator uses a trilevel quantized model for the stopping sinusoids. Such trilevel quantization has only two minor effects: a slight decrease in SNR and a change in stopped-fringe (or tone) amplitude. In tone analysis, these changes are not significant in most applications. However, if absolute calibration of tone amplitude is desired, this amplitude effect must be considered. Overall phase is not affected by such quantization.)

We will now calculate the expectation value of the stopped tone given in Eq. 7. Unlike interferometric cross-correlation where both the signal and noise are random, the tone signal is deterministic and the "noise" $W(t)$ is random (see Eq. 1). The expectation of Eq. 7 becomes

$$\langle V_{sn} \rangle = \frac{1}{N_t} \sum_{k=1}^{N_t} \langle \tilde{V}_k \rangle \exp(-i\psi_{nk}) \tag{8}$$

The expectation for a single sample point $\tilde{V}_k$ can easily be calculated as follows:

$$\langle \tilde{V}_k \rangle = \int_{-\infty}^{\infty} Q(V)P(V)dV \tag{9}$$

where

$$Q(V) = +1, \; V > 0$$

$$= -1, \; V < 0$$

and where the probability distribution of V (about S) is given by

$$P(V) = \frac{1}{\sqrt{2\pi T_s}} \exp\left[-(V-S)^2/2T_s\right] \tag{10}$$

The tone signal S is defined in Eq. 1. This integral can be shown to equal

$$\langle \tilde{V}_k \rangle = \sqrt{\frac{2}{\pi}} \int_o^{S/\sqrt{T_s}} \exp(-z^2/2)\, dz \tag{11}$$

$$\approx \sqrt{\frac{2}{\pi}} \left[\frac{S}{\sqrt{T_s}} - \frac{1}{6}\left(\frac{S}{\sqrt{T_s}}\right)^3 + \cdots \right] \tag{12}$$

$$\approx \sqrt{\frac{2}{\pi}} \frac{S}{\sqrt{T_s}} \tag{13}$$

if one neglects higher order terms. As indicated above, the maximum of $S/\sqrt{T_s}$ in our nominal system will be about 0.35 so that the maximum of the cubic term will be of the order of 2% relative to the first term (before tone stopping). This cubic term can be represented as a sum of three-tone beat notes. During tone-stopping, a given three-tone beat note will clearly be reduced to an insignificant level provided it possesses a different frequency than the original tone frequencies. If this last condition is not satisfied, a given offending three-tone beat note in a system with $A/\sqrt{T_s} = 0.12$ would fractionally contribute in amplitude:

$$\frac{1}{8} * \frac{1}{6}\left(\frac{A_n}{\sqrt{T_s}}\right)^2 \lesssim 0.0003 \tag{14}$$

or 0.03% to the tone under consideration. Although this is not much by itself, many equally spaced tones can generate many three-tone beat notes equal to a given original tone frequency.

Thus the combined effect might be non-negligible when there are many tones in the passband. This problem will deserve more thorough study if many tones are ever used.

Based on Eq. 13 and the decomposition of S in Eq. 2, the stopped tone in Eq. 8 thus becomes

$$\langle V_{sn} \rangle = \frac{1}{\sqrt{2\pi}} \frac{A_n}{\sqrt{T_s}} \exp\left[i(\phi_n - \psi_n)\right] \qquad (15)$$

if we assume the other tones sum to negligible levels. The phase difference $\phi_n - \psi_n$, presumed to be nearly constant, is the phase difference at the middle of the sum interval. (We will assume stopped-tone frequency is negligibly small. If it is not, there are straightforward, simple ways to overcome the difficulty).

The noise on the stopped tone due to system noise can be calculated as follows:

$$\sigma_V^2 = \left\langle \left(V_{sn}^R - \langle V_{sn}^R \rangle \right)^2 \right\rangle \qquad (16)$$

where V_{sn}^R is the real part of the stopped tone in Eq. 7. Using Eq. 7, one obtains

$$\sigma_V^2 = \frac{1}{N_t^2} \sum_{k\ell} \left[\langle \tilde{V}_k \tilde{V}_\ell \rangle - \langle \tilde{V}_k \rangle \langle \tilde{V}_\ell \rangle \right] \cos \psi_{nk} \cos \psi_{n\ell} \qquad (17)$$

These expectation values can be evaluated to obtain

$$\sigma_V^2 \approx \frac{1}{2N_t} \left[1 + \frac{2}{\pi} \sum_{\tau \neq 0} R(\tau) \cos 2\pi \nu_n \tau \right] \qquad (18)$$

where $R(\tau)$ is the bitstream autocorrelation function, and ν_n is the baseband frequency of the n^{th} tone. The derivation of this expression assumes that interbit correlations of system noise are small. The first term represents the noise that would be present if there were no correlation between bits. The second term accounts for small correlations between bits and will be of the order of 10% or less, but the exact size depends on the shape of the bandpass, the sample rate relative to bandwidth, and the value of the baseband tone frequency ν_n. Note that, if the small second term is neglected, the tone noise is the same for all tones.

We can now calculate the stopped tone SNR using Eqs. 4, 15, and 18. The SNR will be defined as the maximum amplitude (modulus) of the stopped tone divided by the rms noise:

$$\mathrm{SNR} = \frac{1}{\sqrt{2\pi}} \frac{A_n}{\sqrt{T_s}} \frac{1}{\sigma_V} \qquad (19)$$

$$\boxed{\mathrm{SNR} \approx \sqrt{\frac{2\epsilon N_t}{\pi N_c}}} \qquad (20)$$

where we have neglected the small interbit-correlation term in Eq. 18. In analogy with fringe phase calculations, the system noise error in the calibration phase will be

$$\sigma_\phi = \mathrm{SNR}^{-1} \qquad (\mathrm{SNR} \gg 1) \qquad (21)$$

The following example will help illustrate the size of the system noise error in the phase calibrator corrections. As assumed above, suppose we have a 2% total power level for the calibrator signal with 3 tones across the passband. When 4 seconds of MKII data (record rate = 4 Mbs) are reduced for a given tone, we obtain from Eq. 20

$$\mathrm{SNR} \approx \sqrt{\frac{2 \times .02 \times 4 \times 4 \times 10^6}{3\pi}} \approx 260 \qquad (22)$$

The associated phase error will be

$$\sigma_\phi \approx \frac{1}{260} \mathrm{rad} = 0.0006 \text{ cycle} \qquad (23)$$

This phase error would be the system noise error in the phase from one tone. When fringe phase is calibrated, a number of tones (N_u) in the passband will probably be used, in which case the system noise error in the overall phase would be

$$\boxed{\sigma_\phi^T \approx \frac{\sigma_\phi}{\sqrt{N_u}} \approx \sqrt{\frac{\pi}{2N_t\epsilon} \frac{N_c}{N_u}}} \qquad (24)$$

For our numerical example, the overall phase error becomes

$$\sigma_\phi^T \approx 0.00035 \text{ cycle} \tag{25}$$

if all 3 tones are used. For a 40-MHz spanned bandwidth in a bandwidth-synthesis delay measurement, the corresponding delay error will be

$$\sigma_\tau = \frac{\sqrt{2} \times 0.00035 \text{ cycle}}{40 \text{ MHz}} = 0.012 \text{ nsec} = \frac{0.36 \text{ cm}}{c} \tag{26}$$

The factor of $\sqrt{2}$ is a result of the combination of two channels in the BWS process.

III. Clock Model

Before proceeding to detailed calibrator analysis, it is advisable to specify some rather trivial time-keeping terms that are a potential source of confusion if left undefined. First, we will define the following symbols:

t = true (universal) time

t_c = station (universal) time (station clock)

ω_o = true oscillator frequency (in terms of true time)

ω_c = nominal oscillator frequency (e.g., 5 MHz)

The phase ϕ_c of the station oscillator is the quantity that physically exists and is measured for the purpose of timekeeping. By definition, the oscillator phase at the selected clock reference point will be given in terms of true time and frequency by

$$\phi_c = \omega_o (t - t_o) \tag{27}$$

where t_o is a reference time. By design, clock synchronization will be referred to this point.

When the phase ϕ_c of the station oscillator is measured at this point, station time can be operationally defined and determined by

$$t_c \equiv \phi_c / \omega_c \tag{28}$$

We assume here that t_c is zero when ϕ_c is zero. This is possible since a particular zero crossing can be defined to be UT = 0.

If the nominal frequency is related to the true frequency by

$$\omega_o = \omega_c + \Delta\omega_c \tag{29}$$

then station time is related to true time by

$$t_c = t + \tau_c \tag{30}$$

where the clock error τ_c for that station is given by

$$\tau_c = \frac{\Delta\omega_c}{\omega_c} (t - t_o) - t_o \tag{31}$$

Usually the difference between ω_c and ω_o is small, less than a part in 10^{11}.

The following analysis will use some simple time relations that should be explicitly specified. Let t_{bj} represent the time marked off on the tape by the bits at station j and let τ_{rj} represent the cable delays, etc., from the clock to the sampler. Then bit time is related to station time by

$$t_{bj} = t_{cj} - \tau_{rj} \tag{32}$$

and, based on Eq. 30, to true time by

$$t_{bj} = t_j + \tau_{bj} \tag{33}$$

where

$$\tau_{bj} \equiv \tau_{cj} - \tau_{rj} \tag{34}$$

(We should note here that we have simplistically assumed that the timing signal for the sampler originates at the clock reference point discussed above. The fact that this will not necessarily be the case is not important as far as phase calibration is concerned. A separate point of origin for the sampler timing signal would simply result in a different value for timing signal delay τ_r. As we shall see, τ_r, whatever its origin or value, is removed in phase calibration.)

IV. Detailed Model for Tone Amplitude and Phase

In this section, calibrator phase is broken down in terms of the various effects that enter the calibrator signal in

transit from the clock through the instrumentation and then through the data reduction procedure. Since the analysis will be based on an "ideal" model for the system, extra effort might be required to account for some deviations from ideal behavior. It is beyond the scope of this report to assess all complications – as we shall see, even the analysis of the ideal system is fairly involved.

The analysis that follows develops the model for the calibrator signal in the following sequence: it models effects on the signal (a) from the clock to the injection point, (b) from the injection point to the recorder and (c) through the data reduction procedure. The simplified block diagram of the instrumentation shown in Fig. 1 will be useful in tracing the signal through the instrumentation.

First, for step (a), the phase of the signal at the clock reference point (i.e. the output of the cable stabilizer in Fig. 1) will be given in terms of true time and nominal frequency by

$$\phi_c = \omega_c(t + \tau_c) \tag{35}$$

as indicated by Eqs. 28 and 30. We have chosen to represent calibration phase in this way since a) the clock error τ_c is explicitly shown b) true time t is a scale common to both stations, and c) tone frequencies will be calculated by the correlator operator on the basis of the nominal frequency ω_c. The clock signal will experience a cable delay (τ_u) so that its phase entering the tone generator will be given by

$$\phi_c = \omega_c(t + \tau_c - \tau_u) \tag{36}$$

The "ideal" tone generator will detect the zero crossings of the input signal and convert the positive-going zero crossing into rectangular pulses as schematically indicated in Fig. 2. We currently plan to make the width (τ_p) of the output pulses equal to about 20 psec. Different (slower than ω_c = 5 MHz) repetition rates will be obtained by blanking pulses. For example, by passing every 10th pulse, the pulse repetition rate would be 500 kHz. The passed repetition rate will be denoted by ω_p. As indicated below, the tone frequencies will be the harmonics of the fundamental repetition rate ω_p.

In practice, there will be deviations from the ideal waveforms shown in Fig. 2, deviations such as delays, phase shifts and an amplitude distortion, arising in both the tone generator and connecting elements. For example, we have assumed that a zero crossing is at the center of a rectangular pulse. In practice, this is not necessarily precisely the case but can be accounted for. Further, the pulse shapes will not be perfect rectangles. This report will not consider such deviations but will note that most of these effects can be formally included by making a complex Fourier expansion rather than the cosine expansion presented below. However, we will note here that a constant deviation from rectangularity will cause clock synchronization measurements to be biased by a constant error that is less than the pulse width. Further, a constant deviation will cause no error in geophysical/astrometric measurements.

The ideal calibrator signal in Fig. 2 can be Fourier decomposed to give

$$S(t) = C \sum_{n=1}^{\infty} F_p(\omega_n) \cos [\omega_n (t + \tau_c - \tau_u)] \tag{37}$$

where, for simplicity, we have neglected a constant term that is of no importance due to subsequent filtering. The tone frequency ω_n is a multiple ($n\omega_p$) of the nominal pulse rate ω_p. The function F_p is the Fourier transform of an individual rectangular pulse and is given by

$$F_p(\omega) = \frac{\sin \omega\tau_p/2}{\omega\tau_p/2} \tag{38}$$

Note that the phase of the Fourier components is consistent with the placement of the positive-going zero crossings at the rectangle centers. With a pulse width of 20 psec, the tone amplitude at X-band (8.4 GHz) will fall off to about

$$F_p(\omega_x) \approx 1 - \frac{(\omega_x\tau_p/2)^2}{6} \approx 0.95 \tag{39}$$

or a loss of about 5% relative to the maximum amplitude at lower frequencies. The amplitude change across the passband at S- or X-band will be even smaller. For example, if the passband is 100 MHz, the amplitude change will be about 0.1% across the band at X-band. Thus, changes in tone amplitude across the passband due to pulse shape appear to be negligible.

We are now prepared to model effects on calibrator phase in transit from the injection point to the recorder and then through the tone-stopping process. As indicated in Eq. 37, the tone phase at the injection point will be given by

$$\phi_n = \omega_n(t + \tau_c - \tau_u) \tag{40}$$

We have not explicitly represented the small delays from the input of the tone generator to the injection point since these can be included in τ_u.

After injection, the signal at station j passes through various filters and is heterodyned to baseband under the combined effect of various mixing signals. The phase effects of all of the intervening components can be divided into three major categories. First, the overall effect of the mixing signals can be described as one total mixing signal, to be represented by $\omega_{hj} t_j + \phi_{hj}$, where ω_{hj} is the total mixing frequency and ϕ_{hj} accounts for a constant phase term as well as variations in mixing phase that are nonlinear in time. All group delays, including effective group delays through filters, will be represented by one total delay τ_{lj}. All phase shifts (except those from group delays) will be represented by one total shift ϕ_{lj}. Given these definitions, the tone phase at baseband will be equal to the injection phase (Eq. 40) combined with these three terms:

$$\phi_{nj}(t_{bj}) = \omega_n(t_j + \tau_{lj}) - \omega_{hj} t_j - \phi_{hj} - \omega_n \tau_{lj} - \phi_{lj}(\omega_n) \tag{41}$$

where

$$\tau_{tj} \equiv \tau_{cj} - \tau_{uj} \tag{42}$$

and where t_j is the true time corresponding to bit time t_{bj}. Fig. 1 schematically shows these modifications to calibrator phase on a step-by-step basis as the signal progresses through the instrumentation from clock to recorder. For clarity, however, the block diagram has been simplified to involve only one element of a given type and token phase shifts and group delays. Nevertheless, Eq. 41 is quite general if the variables are properly defined to account for lumped effects of all the elements in an actual system. At the correlator the operator will use a best estimate for the baseband frequency of each calibrator tone to separately "fringe-stop" each tone in a given bitstream. That is, in effect, the correlator will subtract from the phase of the n^{th} tone the phase

$$\psi_{nj} = (\omega_n - \omega'_{hj}) t_{bj} \tag{43}$$

$$= (\omega'_n - \omega'_{hj}) (t_j + \tau_{bj}) \tag{44}$$

where ω'_{hj} is the best (nominal) estimate for the heterodyne frequency and t_{bj} is bit time (Eq. 33) at station j.

The stopped calibrator phase (Eq. 15) at station j becomes

$$\Delta\phi_j(\omega_n) = \phi_{nj} - \psi_{nj} \tag{45}$$

$$= \omega_n(\tau_{tj} - \tau_{bj}) - \omega_n \tau_{lj} - \phi_{lj}(\omega_n) - \Delta\phi_{hj} \tag{46}$$

where the "stopped" heterodyne phase is given by

$$\Delta\phi_{hj} = \omega_{hj} t_j + \phi_{hj} - \omega'_{hj} t_{bj} \tag{47}$$

This puts the stopped-tone phase in the form we want, expressed in detail in terms of contributing effects due to instrumentation and data reduction.

V. Interferometer Phase

This section derives a theoretical expression for interferometer phase that includes most of the terms that enter VLBI measurements. However, since a full treatment of interferometry theory would exceed the scope of this report, we will only present a heuristic derivation based on a deterministic analog model for a single frequency component. As in the case of the calibrator signal, one can use the schematic block diagram in Fig. 1 as an aid in understanding the instrumental effects described below.

When the following sections deal with some instrumental terms, the same symbol will be used to denote the difference between stations as was used to denote the single station effect [e.g. τ_c and τ_u]. Consideration of the context of the equation should prevent confusion in interpretation.

Let the radio signal received at the calibrator injection point at station i be given by

$$V_i \propto \cos(\omega t + \theta) \tag{48}$$

where t is true time and ω is the radio frequency. The corresponding phase at station j will be delayed by a geometric delay τ'_g (referenced to the tone injection points) and will be given by

$$V_j \propto \cos[\omega(t - \tau'_g) + \theta] \tag{49}$$

As in the case of the calibration signals (Eq. 41), the instrumentation will contribute various phase terms in bringing these two signals to baseband:

$$V_i \propto \cos[\omega t + 0 - \omega_{hi} t - \phi_{hi} - \omega\tau_{Ii} - \phi_{Ii}] \quad (50)$$

$$V_j \propto \cos[\omega(t - \tau'_g) + 0 - \omega_{hj} t - \phi_{hj} - \omega\tau_{Ij} - \phi_{Ij}] \quad (51)$$

These signals are then sampled and recorded on magnetic tape at each station on the basis of the recorder timing (i.e. bit time). When the tapes are brought together for processing, the correlator will offset the signal at station j by a model delay τ_m and then multiply the two signals together to obtain

$$V_i(t_{bi}) V_j(t_{bj} + \tau_m) \propto \quad (52)$$

$$\cos[\omega(\tau'_g + \tau_b + \tau_I - \tau_m) + \phi_I + \Delta\theta_h + \omega_{hj}\tau_m]$$

where

$$\Delta\theta_h = \omega_{hj} t_j + \phi_{hj} - \omega_{hi} t_i - \phi_{hi} \quad (53)$$

$$\tau_I = \tau_{Ij} - \tau_{Ii} \quad (54)$$

$$\phi_I = \phi_{Ij} - \phi_{Ii} \quad (55)$$

$$\tau_b \equiv t_i - t_j = \tau_{bj} - \tau_{bi} \quad (56)$$

and where t_k is the true time corresponding to bit time t_{bk} at station k (see Eq. 33). The relation for $t_i - t_j$ depends on the correlator-enforced assumption that nominal bit times are correct (i.e. $t_{bi} = t_{bj}$). In this expression, we have only retained the difference-phase term in the cosine product rule since the sum-phase term will possess a high frequency and will average to negligible levels in subsequent time averaging. We should note that the reason for offsetting by τ_m in the above product is not obvious in the deterministic single-frequency derivation described here. A more general derivation would show (e.g. Ref. 3) that when the signals are derived from a random broadband process, they must be aligned in time to produce a correlated output.

After multiplication, the correlator will digitally heterodyne (counter-rotate or fringe-stop) the product signal (fringes) and thereby subtract a model phase given by

$$\phi_m = \omega'_{hj} t_{bj} - \omega'_{hi} t_{bi} + \omega'_{hj} \tau_m \quad (57)$$

The stopped signal will thus possess very low frequency ($\leq$50 mHz) and can be averaged over relatively large time intervals (0.1 - 1.0 sec). These stopped and averaged fringes will be given by

$$\sum_t V_i(t_{bi}) V_j(t_{bj} + \tau_m) \cos\phi_m$$

$$\propto \cos[\omega(\tau'_g + \tau_b + \tau_I - \tau_m) + \phi_I + \Delta\phi_h] \quad (58)$$

where

$$\Delta\phi_h \equiv \Delta\phi_{hj} - \Delta\phi_{hi}$$

and where we have assumed the sum-phase term averages to zero. Phase-tracking is then used to extract the fringe phase, given by

$$\boxed{\psi_f = \omega(\tau_g + \tau_a + \tau_b + \tau_I - \tau_m) + \phi_I + \Delta\phi_h} \quad (59)$$

where we have now represented the geometric delay in the customary fashion, $\tau'_g = \tau_g + \tau_a$. This redefines the geometric delay in terms of arrival times at the intersection of axes (i.e. τ_g) and adds a compensating term (τ_a) to account for the difference in pathlength for the radiowave in its actual propagation to the tone injection point and its theoretical propagation to the intersection of axes.

VI. Calibration of Interferometer Phase

This section demonstrates how the tone phase can be used to remove post-injection instrumental effects from the phase measured by the interferometer. As suggested in Fig. 1, the essence of phase calibration with tones is that all of these instrumental terms (except for τ_a) enter the tone phase in the same way that they enter the radio phase since both signals pass simultaneously through the same instrumentation and are simultaneously recorded by the same recorders. Thus, by subtracting the tone phase from interferometer phase, we can remove these instrumental terms.

Phase calibration will be applied as follows. For each station, tone phase is extracted from the stopped tones given by Eq. 15 (for example, by computing the inverse tangent of the ratio of real and imaginary parts). If we difference the measured tone phase between stations, we obtain

$$\phi_t(\omega) \equiv \Delta\phi_i(\omega) - \Delta\phi_j(\omega) \tag{60}$$

which, according to Eq. 46, is given theoretically by

$$\phi_t(\omega) = \omega(\tau_b + \tau_I - \tau_t) + \phi_I + \Delta\phi_h \tag{61}$$

where

$$\tau_t = \tau_{t_j} - \tau_{t_i}$$

We have assumed here that the calibration phase at a given frequency ω can be obtained by interpolation (or some other process) from the measured phases of the tones. Further, we neglect small doppler-shift effects, which produce frequency shifts of the order of a hundredth of a bandwidth but can be accounted for. When this calibration phase is subtracted from the fringe phase (Eq. 59), we obtain

$$\psi(\omega) = \psi_f - \phi_t \tag{62}$$

which is given theoretically by

$$\boxed{\psi(\omega) = \omega(\tau_g + \tau_c + \tau_a - \tau_u - \tau_m)} \tag{63}$$

where we have used Eq. 42 to show explicitly the clock-synchronization offset τ_c and the cable delay τ_u. We have now obtained a measurement of interferometer phase that is free of the instrumental terms calibrated by tone phase.

Once the interferometer phase has been corrected with tone phase, one can readily obtain the delay by the bandwidth synthesis (BWS) technique of taking the difference between the phases at frequencies ω_a and ω_b:

$$\tau'_{BWS} = \frac{\psi(\omega_a) - \psi(\omega_b)}{\omega_a - \omega_b} \tag{64}$$

which is given theoretically by

$$\tau'_{BWS} = \tau_g + \tau_c + \tau_a - \tau_u - \tau_m \tag{65}$$

Station calibration will provide measurements of the cable delay τ_u and intersection-of-axis delay τ_a so that they can be removed. The model delay τ_m is very accurately known, of course, and can be removed exactly. Thus, we finally obtain the desired quantity – a measured delay containing only geometric delay and clock offset:

$$\tau_{BWS} = \tau'_{BWS} - \tau_a + \tau_u + \tau_m \tag{66}$$

which is given theoretically by

$$\boxed{\tau_{BWS} = \tau_g + \tau_c} \tag{67}$$

The clock offset τ_c is the only remaining instrumental term. This term represents the synchronization offset between station clocks (τ_{cj}-τ_{ci}) and pertains to the clock reference points, established by the definition and removal of the cable delays, τ_u.

(We should note here that the aforementioned DSN calibrator system will have the capability of compensating on-site for the cable delay up to the tone generator by applying a calibrated advance to the phase leaving the cable stabilizer. In this case, τ_u in earlier equations would be equal to the small delay through the tone generator up to the injection point.)

As indicated previously, certain conditions must be met for this calibration analysis to be valid. First, the model for the heterodyne phase must be identical in the model phases used for fringe-stopping and tone-stopping. The calibrator signal must possess a low fractional power level. Tone frequencies must be chosen to handle phase variations across each channel passband, if such variations are present at a significant level.

In the calibration process described above, a subtle point has been neglected. Only the fractional part (in cycles) of both the interferometer phase and tone phase can be determined when phase is extracted after counter-rotation. The integer-cycle part of phase can not be determined by this process alone. Thus, when tone phase is subtracted from interferometer phase, the subtraction actually denotes removal of the fractional part of instrumental phase. We can ignore all integer cycle errors at this point since we realize that there are integer cycle ambiguities due to delay modeling that must be resolved later in the BWS process. The BWS process only requires as input precise values for the fractional part of phase, free of unwanted instrumental phase (fractional part). The integer-cycle part (due to τ_g and τ_c) is then added in a recursive process to be described in a later report. The output is a delay measurement free of post-injection instrumental

effects. It is a peculiarity of this technique that, even though delay and interferometer phase can be ultimately calibrated absolutely with regard to instrumental effects, instrumental phase, including integer cycles, is never absolutely measured.

VII. Remaining Work

Some important issues related to system calibration remain to be considered. For lack of adequate information concerning system characteristics (e.g., phase ripple and variability), this report has made no effort to assess the accuracy with which system calibrations can be carried out. This is obviously a crucial question that should be addressed as soon as possible. Such an accuracy analysis would have to consider the approximations, if any, that are imposed by practical considerations during implementation and will be intimately connected with the determination of the optimum number of tones and power level.

References

1. A. E. E. Rogers, "A Receiver Phase and Group Delay Calibrator for Use in Very Long Baseline Interferometry," Haystack Observatory Technical Note 1975-6.
2. J. L. Fanselow, "The Use of a Phase Calibrator in VLBI to Remove Receiving System Phase Shifts," JPL IOM 315.2.011 (an internal document), Oct. 1976.
3. J. B. Thomas, "An Analysis of Long Baseline Radio Interferometry," JPL DSN Progress Report 32-1526, Vol. V (1971).

ORIGINAL PAGE IS
OF POOR QUALITY

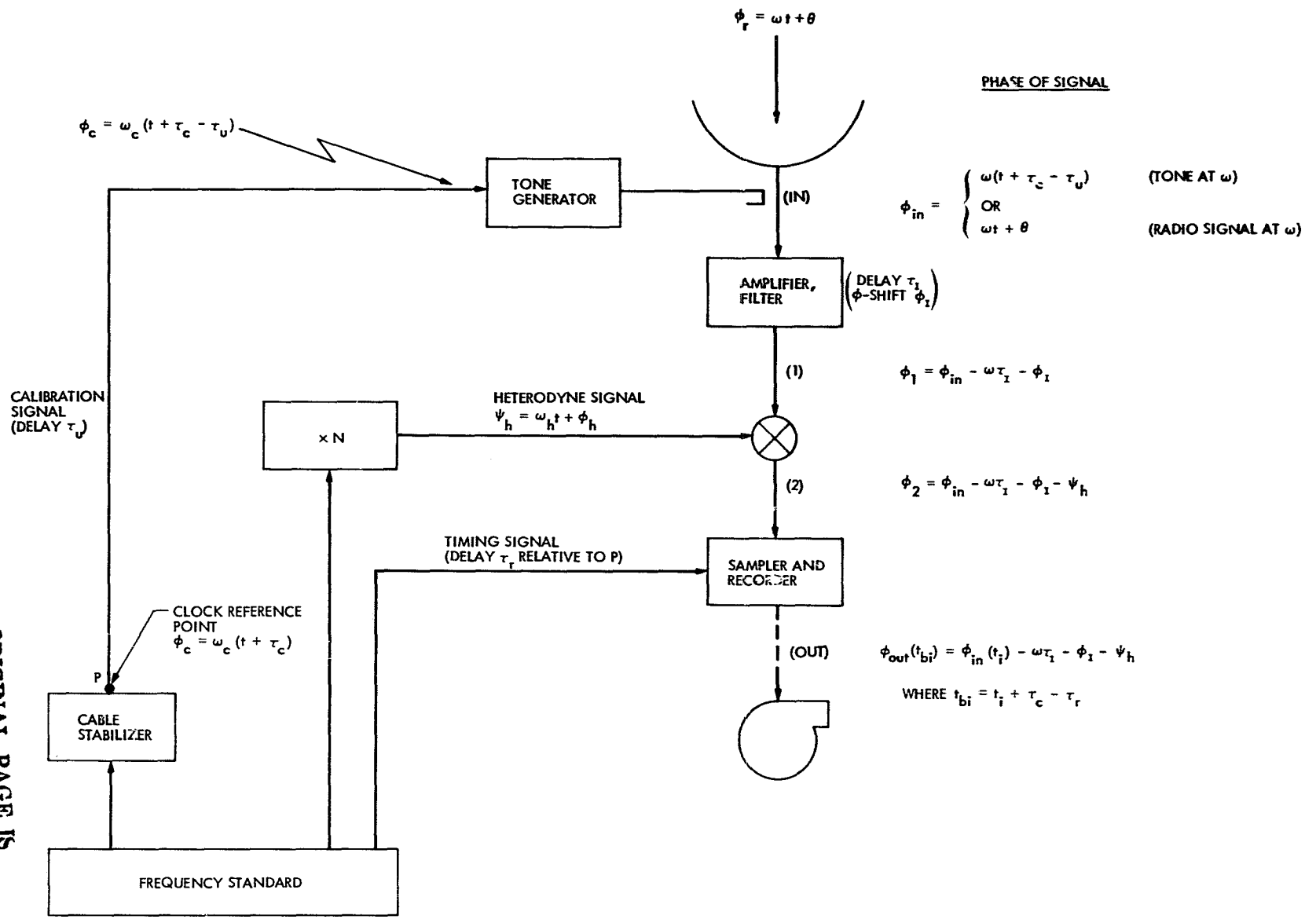
$\phi_r = \omega t + \theta$
PHASE OF SIGNAL
$\phi_c = \omega_c (t + \tau_c - \tau_u)$
TONE GENERATOR
(IN)
$\phi_{in} = \begin{cases} \omega(t + \tau_c - \tau_u) & \text{(TONE AT } \omega\text{)} \\ \text{OR} \\ \omega t + \theta & \text{(RADIO SIGNAL AT } \omega\text{)} \end{cases}$
AMPLIFIER, FILTER
(DELAY τ_I, ϕ-SHIFT ϕ_I)
(1)
$\phi_1 = \phi_{in} - \omega\tau_I - \phi_I$
CALIBRATION SIGNAL (DELAY τ_u)
HETERODYNE SIGNAL
$\psi_h = \omega_h t + \phi_h$
× N
(2)
$\phi_2 = \phi_{in} - \omega\tau_I - \phi_I - \psi_h$
TIMING SIGNAL (DELAY τ_r RELATIVE TO P)
SAMPLER AND RECORDER
CLOCK REFERENCE POINT
$\phi_c = \omega_c (t + \tau_c)$
(OUT)
$\phi_{out}(t_{bi}) = \phi_{in}(t_i) - \omega\tau_I - \phi_I - \psi_h$
WHERE $t_{bi} = t_i + \tau_c - \tau_r$
P
CABLE STABILIZER
FREQUENCY STANDARD

Fig. 1. Simplified illustration of VLBI instrumentation

ORIGINAL PAGE IS
OF POOR QUALITY

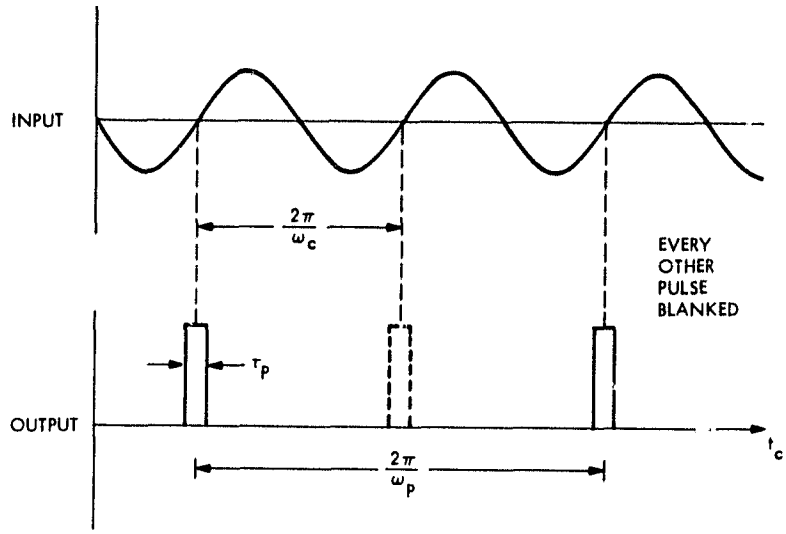

Fig. 2. Input and output signals for an ideal tone generator

N78-24221

An Analysis of Viking S-X Doppler Measurements of Solar Wind Columnar Content Fluctuations

P. S. Callahan
Tracking Systems and Applications Section

More than 320 passes of Viking S-X Doppler data have been used to investigate columnar content fluctuations in the solar wind from 19 August, 1976 to 28 February, 1977. These data are used to estimate the power spectrum and radial dependence of solar wind density fluctuations. It is found that: (1) the electron density fluctuations decline with heliocentric distance as $r^{-1.8 \pm 0.1}$*; (2) the power spectrum depends on fluctuation frequency as* $\nu^{-2.5 \pm 0.2}$*. These results are used to predict range change as a function of time scale and sun-earth-probe angle. Changes of interest for advanced navigation techniques are found to be likely.*

I. Introduction

There is continuing interest in the errors introduced into radio metric tracking by the solar wind (SW) plasma. In order to estimate these errors a large amount of Viking S-X Doppler data measuring the change in electron columnar content has been analyzed. Because the density fluctuations (DF) are of a random nature the analysis has been done in terms of the power spectrum and the changes in spectral amplitude with heliocentric distance extracted.

A long term goal for the DSN is a predictive model of radio metric data quality. This analysis is a major first step in building that model as it provides the large-scale radial and time variations of the SW plasma. It remains to compare the residuals from these large-scale models to solar surface and other SW data to develop the detailed predictive model.

A preliminary report of the present analysis (but with only half the amount of data) was given in Ref. 1. The major differences between the findings there are (1) a revision of the spectral index from -3.0 to -2.5; and (2) a deletion of the discussion of sunspot cycle effects. It has become clear that a longer time base of measurements will be needed to discuss sunspot cycle effects.

The data coverage for this analysis is described in Section II. The analysis procedures are outlined in Section III. Section IV gives the results and discusses the implications for radio metric data.

II. Data Coverage

The data coverage for this analysis is shown in Table 1. The data are given in the groups in which they were averaged to determine the radial dependence of the power spectrum. The dates are in the format YYMMDDHH (year, month, day, hour at beginning of pass). Superior conjunction was taken to be 1976 November 25, 00 hours.

All of the passes used in this analysis were at least 5 hours long and contained at least 275 points. Thus, some gaps were allowed, but none exceeding 1 hour. Most of the data were 1-minute samples, but stretches of 10-second data occur in some passes. The net average sample spacings ranged from about 55 to 65 seconds. Individual passes lasted up to 12 hours. Near and after conjunction 10-second and some 1 second data were obtained in large amounts. Ten second data from 8 to 15 December 1976 have been included in this analysis by averaging the data to 30-second sample times and then treating the data to give the same spectral resolution as the 60 second passes. The 10 and 1 second data have been examined and show that the power spectrum continues smoothly to higher frequencies.

The coverage of one or both spacecraft is often continuous. When the doppler data overlap, it is possible to continue the record by continuing to add the change in columnar content at each step. Records up to 32 hours (typically 15-20 hours) have been constructed in this way. The spectra from these longer records have been averaged in the same way as the results presented here. These data show that the power spectrum also continues smoothly to lower frequencies.

Altogether more than 320 passes of S-X Doppler data ($\gtrsim$3000 hrs) have been analyzed. These data span ±95 days around superior conjunction and cover the range of heliocentric distances of closest approach of 0.031 to 0.487 AU. Continuous data records up to 32 hr and sample rates as fast as 1 per sec allow highly reliable estimates of the power spectrum in the frequency range 1×10^{-4} to 2×10^{-1} Hz.

III. Data Analysis

In order to investigate the columnar content changes under a wide range of conditions, it is necessary to have an objective measure of these changes. The power spectra of the data provide such a measure. The spectra give the mean squared fluctuation per unit frequency interval in a range of frequencies. Thus, given the power density at some frequency, $P_{\Delta I}(\nu)$, the expected change in the columnar content on a time scale $t_I = 1/\nu$ is

$$\Delta I(t_I) \cong (P_{\Delta I}(\nu)^* \nu)^{1/2} \qquad (1)$$

where for rapidly falling spectra at low frequencies we have approximated the frequency interval $\Delta\nu$ (spectral resolution) by ν.

The frequencies over which one can obtain reliable estimates of the spectrum from discretely sampled records of limited length are $1/4\ \Delta t \geqslant \nu \gtrsim 10/T$, where Δt is the sample rate, and T is the length of the record. For most of the data used here 3×10^{-4} Hz $\lesssim \nu \lesssim 4 \times 10^{-3}$ Hz, corresponding to times scales of 4 minutes $\lesssim t_1 \lesssim$ 1 hour. The longer records produced by tying passes together permit the investigation of time scales of up to 3 hours, while 10-second data extend the time scale down to 40 seconds ($\nu \sim 2 \times 10^{-2}$ Hz), and 1-sec data to 4 sec ($\nu \sim 2 \times 10^{-1}$ Hz).

For some purposes (near-simultaneous ranging or the error of making uplink calibrations using a downlink-only measurement) the change of the columnar content on various time scales is of most interest. In other cases (two-station tracking or single station tracking of two separated spacecraft) the change of the SW density on various cale sizes is more important. The latter can be obtained from the former if the SW velocity is known. A typical SW velocity is 350-450 km s^{-1}. Since our data have no direct measurement of the velocity, scale sizes inferred using 400 km s^{-1} could be in error by up to 50 percent sir :e the range of velocities is ~300-700 km s^{-1}. The results here are in terms of frequency.

The results below were obtained through the following steps:

(1) The columnar content change records from each pass were autocorrelated to 60 lags (~1 hour). The 10 second data were summed to ~30-second intervals and autocorrelated to 80 lags (~40 minutes).

(2) The cosine transform of the autocorrelation, smoothed with the Hanning window, was used to give the power spectrum.

(3) The individual power spectra were averaged in groups of 5 to 12. The data were grouped by the distance of the ray path's closest approach to the sun, Q. The lowest value of all the averaged points was subtracted to remove the noise.

(4) The slopes of the averaged spectra were obtained by hand. A number of estimates were made for each spectrum to determine the possible range. It is typically ±0.2. Account was taken of the fact that the spectral estimation program overestimates the power at low frequencies by a factor of 2 to 4.

None of the data have been corrected for the change in ionospheric columnar content. This change is generally $\lesssim$1.5 meters over a pass and so is much less ($\lesssim$10 percent) than the observed changes, except for some passes in August and September. Neglect of this correction is not thought to signifi-

cantly affect any of the final results. Care was taken, especially for data taken very near the sun, to insure that slipped cycles were not added to the columnar content change. Apparent columnar content changes greater than 2m/min were never allowed and in most cases tighter limits were imposed.

In addition to the power spectrum analysis, the individual and long records were examined for rms variation about the mean, peak-to-peak change, maximum rate of change, and character (slope, single or multiple "humps," and time scale of significant change) of the change. The numerical indices are all closely related to the power spectrum. The character of the change allows some investigation of changes on longer time scales than can be done formally with the power spectrum.

IV. Results and Discussion

From the general character of the columnar content changes, especially those seen on the long (tied) passes, one can see that the power spectra extend to low enough frequencies to pick up most of the important changes. Occasionally, there are slopes or "humps" with time scales of 8-12 hours, but these occur only about once per month. At the fastest sample rates, the character of the columnar content is very similar, though of reduced amplitude. Thus, the data from the power spectra provide a fairly complete and realistic description of the columnar content changes for time scales from 2 seconds to several hours.

The spectral index range for each averaged spectrum is given in the last column of Table 1. The indices were estimated by hand on plots of the averaged spectra. The average and standard deviation of the upper and lower estimates are respectively $\beta_u = 2.63 \pm 0.18$, $\beta_L = 2.40 \pm 0.16$. The value $\beta = 2.5 \pm 0.2$ will be adopted for the spectral index of columnar content fluctuations. It is in good agreement with Ref. 2 and 3 and other recent work on SWDF. Examination of averaged spectra of data records in which passes were tied together to give total record lengths of 20-30 hr show that this spectral index is maintained down to $\nu \cong 1 \times 10^{-4}$ Hz. As discussed above the spectral estimation program overestimates the power at low frequencies. This effect is important, (approximately a factor of 2) at 3×10^{-4} Hz for single pass records. Thus, for reliable results the scaling law $\nu^{-2.5}$ should only be applied to $P(F2 = 6 \times 10^{-4}$ Hz) data in Table 1.

Data sampled at once per second and once per 10 sec were used to investigate the high frequency portion of the spectrum. It was found that at the highest frequencies, $1 \times 10^{-2} \lesssim \nu \lesssim 2 \times 10^{-1}$, the spectrum flattened somewhat to $2.1 \lesssim \beta \lesssim 2.3$. Below $\nu \cong 1 \times 10^{-2}$ Hz the spectral index remained at $\beta \cong 2.5$. Three sets of 1 sec. data (of 6 obtained) showed discrete spectral features at frequencies of about 1.5×10^{-1} Hz. The periodic (period $\cong 7$ sec) disturbances lasted for about 1 hour in each case. The spectral amplitude indicates columnar content changes of about 9×10^9 cm^{-2} $\approx 8 \times 10^{-4}$ m(!) of one-way S-band range change. The explanation of the features has not been found.

In Fig. 1, the averaged power density 3×10^{-4} Hz is plotted against Q, the distance of the ray path's closest approach to the sun. The line through the points has slope 2.6. Note that the Mariner points generally lie above the Viking points. The points at large Q may be biased upward by the ionosphere. These data overestimate the true spectral amplitude by a factor of 2.

To investigate the radial dependence more quantitatively, a computer program was used to find the RMS deviation about a series of models characterized by a radial exponent, γ and an ellipticity ϵ. The ellipticity was included because the solar corona is known to be reduced near the poles at sunspot cycle minimum. The model used was

$$P^{(\nu)}_{\text{scaled}} = P^{(\nu)}_{\text{obs}} \, (\text{Q}/0.1 \text{ AU})^{(3+2\gamma)} (1 + \epsilon \sin (\text{Lat}))^2 \tag{2}$$

where Q is the distance of closest approach (column 5 of Table 1) and Lat is the heliographic latitude of the point of closest approach (column 6 of Table 1). The parameters which produce the smallest RMS of the scaled spectral estimates about their average were $\gamma = -0.2 \pm 0.1$ and $\epsilon = 0.6 \pm 0.6$. The data show no strong preference for any value of ϵ, but do clearly show that γ is less than 0.

A decline of the spectral amplitudes of $Q^{-2.6}$ implies (for an approximately constant radial SW velocity) that SWDF decline as $\delta n \propto r^{-1.8 \pm 0.1}$. This result is also found in an analysis of Doppler Noise data (Ref. 3 and 4). It implies that the relative density changes become larger with radius, (since n declines at least as fast as r^{-2}), although this conclusion may be modified somewhat by including the acceleration of the SW near ($r \sim 3$ to $30\, R_\odot = 0.015$ to 0.15 AU) the sun.

The data in Table 1 are well-summarized by the function

$$P(\nu,Q) = (4.0 \pm 2.0) \times 10^{30} \left(\frac{Q}{0.1 \text{AU}}\right)^{-2.6 \pm 0.1} \left(\frac{\nu}{3 \times 10^{-4}}\right)^{-2.5 \pm 0.2} \text{cm}^{-4}\text{Hz}^{-1} \tag{3}$$

where Q is the distance of the ray path's closest approach to the sun, and ν is the frequency of the fluctuations in the columnar content, for $1 \times 10^{-4} \lesssim \nu \lesssim 1 \times 10^{-2}$ Hz, $0.03 \lesssim Q \lesssim 0.5$ AU. By using Eq. (1), one may easily deduce the rms change in columnar content from Eq. (3). The result in one-way meters of S-band range change is

$$\Delta I_{rms}(\tau,Q) = (0.039 \pm 0.019)\left(\frac{Q}{0.1\ \text{AU}}\right)^{-1.3}\left(\frac{\tau}{10\ \text{sec}}\right)^{0.75}\ \text{m} \tag{4}$$

where $\tau = 1/\nu$ is the time scale of changes.

Values of this expression for several values of τ and Q are given in Table 2. The distance scales ϱ in Table 2 are obtained by multiplying τ by a typical SW velocity of 400 km s^{-1}

The range changes in Table 2 could be significant for advanced navigation techniques. As the data of Table 1 and Fig. 1 show, the amplitude of the power spectrum is highly variable. Values 2 to 3 times those in Table 2 are possible on occasion (once per week to once per month). Furthermore, peak-to-peak changes between adjacent samples are $\simeq 3\Delta I_{rms}$. Thus, overall changes between data points separated in time or from ray paths separated in space could be 3 to 10 times the values in Table 2. At SEP angles of 15° one might expect differences of 1.0 to 3.7 m on alternate range points separated by 15 min and of 0.03 to 0.1 m in VLBI data on a single source.

The differences expected in ΔVLBI will be $\sim \sqrt{2}$ greater than those for VLBI of a single source independent of the separation of the two sources in the sky because of the small error between the two ray paths to each source. The error introduced into alternate ranging could be significant, while the SW is virtually eliminated as an error source by ΔVLBI.

Reference

1. Callahan, P. S., "A Preliminary Analysis of Viking S-X Doppler Data and Comparison to Results of Mariner 6, 7, and 9 DRVID Measurements of the Solar Wind Turbulence," in the Deep Space Network Progress Report, 42-39, pp. 23-29; 1977, June 15.
2. Woo, R., "Radial Dependence of Solar Wind Properties Deduced from Helios 1/2 and Pioneer 10/11 Radio Scattering Observations," Astrophys, J., *219*, 727; 1978, January 15.
3. Callahan, P. S., "A First-Principles Derivation of Doppler Noise Expected from Solar Wind Density Fluctuations," in the Deep Space Network Progress Report 42-42, pp. 42-53; 1977, December 15.
4. Berman, A. L., "Viking S-Band Doppler RMS Phase Fluctuations Used to Calibrate the Mean 1976 Equatorial Corona," in the Deep Space Network Progress Report 42-38, p. 152.

ORIGINAL PAGE IS
OF POOR QUALITY

Table 1. Averaged spectra of Viking S-X doppler data*

First Date	Last Date	No. Avg	SC	Q Avg (0.1AU)	Avg Lat	Obs P(F1) [a]	Obs P(F2) [b]	Days from Sup. Conjunction First	Last	Avg	P(F1), Scaled for Radial	Radial + Lat	P(F2), Scaled for Radial	Radial + Lat	β
76082116.	76082616.	10.	30.	4.870	3.0	.137•30	.124•29	-95.33	-90.33	-92.83	.4096•30	.3668•30	.3787•29	.3320•29	2.55-2.65
76082708.	76090100.	11.	30.	4.590	3.4	.788•29	.710•28	-89.67	-85.00	-87.33	.2044•30	.1846•30	.1862•29	.1682•29	2.7 -2.9
76090117.	76090616.	10.	30.	4.300	3.8	.168•30	.180•29	-84.29	-79.33	-81.81	.3637•30	.3315•30	.3902•29	.3638•29	2.5 -2.7
76090708.	76091016.	6.	30.	4.070	4.1	.142•30	.115•29	-78.67	-75.33	-77.00	.2760•30	.2533•30	.2235•29	.2052•29	2.5 -2.7
76090916.	76091522.	12.	27.	3.830	4.4	.698•29	.649•28	-76.33	-70.08	-73.21	.1159•30	.1071•30	.1090•29	.1008•29	2.3 -2.6
76091700.	76092121.	11.	27.	3.500	4.8	.446•30	.452•29	-69.00	-64.12	-66.56	.6035•30	.5627•30	.6116•29	.5703•29	2.3 -2.55
76101808.	76102721.	8.	30.	1.690	6.2	.229•31	.323•30	-37.67	-28.13	-32.90	.5390•30	.5194•30	.7615•29	.7326•29	2.5 -2.75
76102011.	76103111.	8.	27.	1.490	6.2	.136•31	.103•30	-35.54	-24.54	-30.04	.2378•30	.2278•30	.1795•29	.1720•29	2.3 -2.7
76110106.	76111320.	9.	30.	.960	5.4	.536•31	.506•30	-24.00	-11.17	-17.58	.3252•30	.3071•30	.3078•29	.2899•29	2.4 -2.6
76110121.	76110721.	7.	27.	1.070	5.9	.609•31	.638•30	-23.12	-17.12	-20.12	.4704•30	.4578•30	.5022•29	.4796•29	2.35-2.65
76112619.	76120220.	7.	20.	.280	-22.9	.113•33	.127•32	1.79	7.83	4.81	.3749•30	.5244•30	.4214•29	.5890•29	2.25-2.35
76120800.	76121522.	8.	20.	.908	-12.1	.187•32	.677•30	13.00	20.92	16.96	.9927•30	.1092•31	.3594•29	.3953•29	2.6 -2.8
76123119.	77010503.	6.	30.	1.910	-10.2	.153•31	.214•30	36.79	41.12	38.96	.4839•30	.5092•30	.6768•29	.7122•29	2.6 -2.85
77010416.	77010901.	5.	30.	2.040	-10.0	.226•31	.205•30	40.67	45.04	42.85	.8371•30	.8769•30	.7593•29	.7958•29	2.6 -3.0
77010518.	77010803.	5.	27.	2.060	-10.0	.570•30	.800•29	41.75	44.12	42.94	.2161•30	.2264•30	.3035•29	.3178•29	2.3 -2.4
77011100.	77011205.	5.	27.	2.280	-9.7	.457•30	.515•29	47.00	48.21	47.60	.2211•30	.2308•30	.2491•29	.2592•29	2.4 -2.7
77011218.	77011516.	5.	30.	2.360	-9.6	.121•30	.112•29	48.75	51.75	50.25	.6358•29	.6668•29	.5805•28	.6109•28	2.35-2.5
77011823.	77012014.	5.	30.	2.620	-9.2	.357•30	.311•29	54.96	56.58	55.77	.2411•30	.2679•30	.2100•29	.2160•29	2.3 -2.45
77013122.	77020818.	8.	27.	3.330	-8.0	.134•31	.282•29	67.92	75.75	71.83	.1009•31	.1610•31	.3386•29	.3388•29	2.35-2.6
77021518.	77022315.	8.	27.	3.870	-6.8	.630•30	.510•29	82.75	90.63	86.69	.1085•31	.1058•31	.8921•29	.8696•29	2.1 -2.3
77022200.	77022818.	7.	27.	4.070	-6.3	.135•30	.278•29	89.00	95.75	92.37	.2e24•30	.2530•30	.5403•29	.5209•29	2.1 -2.4

a) F1 = 3×10^{-4} Hz

b) F2 = 6×10^{-4} Hz

*The scaled spectral estimates have been scaled by $(Q/0.1\ AU)^{2.6}$ and/or $(1 + 0.6 \sin(Lat))^2$ and then divided by the average of these factors (19.46 and 1.19) for the whole data set.

Table 2. Δl_{rms} (τ, Q) in one-way S-band meters.
$\ell = \tau \times 400$ km/sec

τ(sec) =		3000	1000	100	30	10	3
ℓ(km) =		1.2^{+6}	4^{+5}	4^{+4}	1.2^{+4}	4^{+3}	1.2^{+3}
Q(AU)	SEP	Δl_{rms} (m)					
.05	2.9	6.86	3.01	.535	.217	.0952	.0386
.10	5.7	2.79	1.22	.217	.0881	.0386	.0157
.15	8.6	1.64	.721	.128	.0520	.0228	.0092
.20	11.5	1.13	.496	.0883	.0358	.0157	.0064
.25	14.5	.846	.371	.0660	.0268	.0117	.0048
.30	17.5	.668	.293	.0521	.0211	.0093	.0038
.40	23.6	.459	.201	.0358	.0145	.0064	.0026
.50	30.0	.344	.151	.0268	.0109	.0048	.0019

ORIGINAL PAGE IS
OF POOR QUALITY

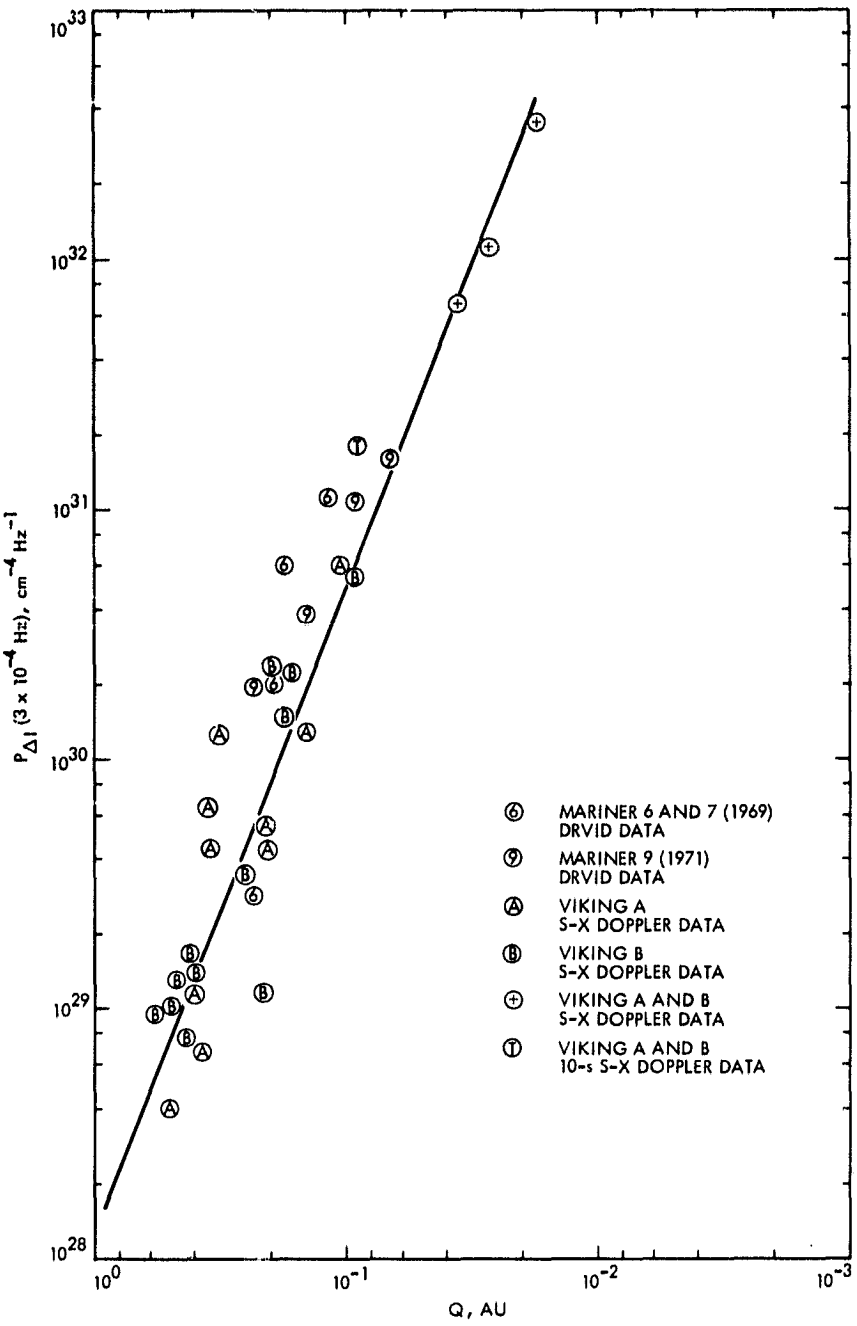

Fig. 1. Averaged spectral amplitudes

C-2

N78-24222

A Method for Measuring Group Time Delay Through a Feed Horn

T. Y. Otoshi, R. B. Lyon, and M. Franco
Radio Frequency and Microwave Subsystems Section

A technique is described for measurement of time delay through a feed horn. The technique consists of measuring the time delay between the input and output ports of two identical horns separated by a known airpath distance. Ground multipath signals, which normally produce errors in this type of measurement, were identified and eliminated by using a time domain technique. Experimental results at 2113 MHz showed good agreement with calculated values.

I. Introduction

Ground station delays for 64-m antenna Deep Space Stations (DSS) are currently being calibrated by the Translator Method. As described in References 1 and 2, the major portion of the ground station delay is measured during pre- and post-track calibrations by this method. The remaining (smaller) portion of station delay is calculated and assumed to be time and frequency invariant. One of the more difficult components for which delays are calculated is a complex feed horn assembly. The current feed horn assembly used in the S-Band Polarization Diversity (SPD) Cone used on 64-m antennas consists of orthomode transducers, quarter wave plates, mode generator, and a corrugated horn. Calculated delay values for these components have been reported in Reference 3. The monopulse feed horn assembly used in DSN 26-m antenna systems is even more complex and no simple method is currently known to the authors for calculating delays of monopulse feeds. The current use of dish-mounted zero delay devices (Ref. 1) for ranging has made it unnecessary to determine the delay of the monopulse feed. However, it may become important to determine 26-m antenna monopulse feed horn delays in the near future for such projects as the VLBI Time Sync Experiment and VLBI Validation Project.

This article presents a method which can be used to experimentally determine the delay through a feed horn assembly. The technique was used on simple standard gain horns, but can be extended to complex feeds.

II. Test Setup

The method to be described is very similar to the antenna gain measurement method discussed by Silver (Ref. 4) and Beatty (Ref. 5). The method consists of using an antenna range where two horns (or antennas) are separated by a known physical distance R as shown in Fig. 1. Figure 2 shows the actual test setup on the antenna range located on the South End of the JPL Mesa Facility. The standard gain horns are

mounted on two antenna towers, one of which is rotatable and can be moved axially on a rail in the direction of the main beam. The second tower is stationary but permits a mounted horn to be adjusted in a vertical direction. Both horns were mounted at a height of 5.55-m above the ground and 1-m above the top of the roof of Mesa Building 212. The horns being tested are Scientific Atlanta Model (12-1.7) pyramidal horns. The horns were separated at distances varying from 152.4 cm (5 ft) to 1676.4 cm (55 ft) in 152.4 cm (5 ft) increments. The smallest and largest separation distances correspond to $1.6D^2/\lambda$ and $17.5D^2/\lambda$, respectively, where D is the widest opening of the horn equal to 36.88 cm (14.52 inch) and λ is the free space wavelength of the test frequency of 2113 MHz.

The basic instrument used to measure delay was a Scientific Atlanta Fault Locator Model 1691 shown in Fig. 3. This instrument was developed to be portable for field use and is normally used as a high resolution time domain reflectometer to locate discontinuities (faults) in microwave antenna transmission lines. For the results of this article, this instrument was temporarily modified to measure transmission time delay. The absolute accuracy of the modified instrument is estimated to be better than ±2 ns and the resolution is about ±0.2 ns. The main advantage of this instrument is in its time domain logic whereby the time delay of the primary (desired) signal can be isolated and measured separately from the effects of other undesired signals such as from ground multipath.

Figure 4 shows typical X-Y recording of this instrument for horn separation distances of 152.4 cm (5 ft) and 304.8 cm (10 ft).* The recordings show only primary signals because multipath signals were at least 35 dB down from the main signal amplitude in the particular test setup used. The basic measurement technique is described as follows. As indicated by the block diagram of the test set-up shown in Fig. 1, measurement of the time delay is made of the total system which includes the delays of the two horns, airpath, cables, amplifier and the Fault Locator instrument. Then a reference measurement is taken by disconnecting the cables at the input and output of the coax-to-waveguide transitions and then connecting the cables together with a coaxial adapter or pad inserted between them. Subtraction of this reference measurement from the test measurement values results in the delays of only the two horns plus waveguide transitions plus airpath. After further subtraction of (1) the airpath delays, (2) the delays of the waveguide-to-coax transitions, and (3) making a small correction for coaxial adapters used, then one arrives at the delays of the two horns only. If the two horns are identical, the delay of a single horn is obtained by dividing the result by 2.

*The use of the Fault Locator in a transmission mode rather than the reflectometer mode required that the indicated instrument readings be multiplied by 2 as shown in the table in Fig. 4.

The airpath delays are easily calculable from precise measurements of the physical separation distance R between the horn apertures using a plumb bob and a steel tape measure. The delays of the two waveguide transitions are determined by measuring them separately at the same test frequency by use of a network analyzer.

III. Test Results

Table 1 shows test results of measurements made at 2113 MHz. It can be seen that the horn delay measured at the largest separation $17.5D^2/\lambda$ does not differ from the measured value at the smallest separation $1.6D^2/\lambda$ by more than 0.41 ns. At very close distances, multiple reflections between horns cannot be isolated by the Fault Locator. Figure 5 shows the theoretical calculated delay for a single horn at 2113 MHz. This calculated delay of 1.39 ns is based on the theoretical group velocities in the constant and tapered section of the horn at 2113 MHz. It can be seen that the calculated and measured delays in Table 1 are in agreement to within ±0.3 ns.

The entire set of measurements was again repeated with absorbers placed on the ground midway between the horns at each separation distance. A slight (but non-significant) improvement in agreement was obtained between theoretical and measured values. It was concluded that absorbers would not generally be needed for most test setups.

Although the Fault Locator instrument is not intended to be used for accurate gain measurements, relative amplitude data accurate to ±0.5 dB is simultaneously available and can be used to provide a good cross check on the experimental setup. Amplitude data obtained from recordings such as the one shown in Fig. 4, were used to calculate horn gain. For the various separation distances shown in Table 1, the measured horn gains agreed to within 1 dB of the theoretical value of 15.95 dB at 2113 MHz.

IV. Conclusions and Future Application

A technique has been presented for the measurement of time delays of a feed horn. The technique presented in this article involves the measurement of the time delay of a pyramidal standard gain horn. This technique can be extended to make measurements of corrugated standard gain horns, spacecraft antennas, and most non-dispersive types of complex feed assemblies used in the DSN. Two identical feeds are not required if the delay of a simpler horn of the same polarization has already been determined.

The measurement technique is not necessarily restricted to the use of a Fault Locator (such as described in this article) provided that it is already known that the antenna range is free

from multipath errors. In such a case, a network analyzer can be used and possibly give more accurate time delay measurements over frequency intervals (spanned bandwidths) of about 20 to 40 MHz. However in most cases, the sources of ground multipath and multiple reflection are generally not known and special time consuming techniques must be employed to minimize or identify their effects. The Fault Locator time domain instrument provides a simple method for quickly identifying and making a direct measurement of the time delay of only the desired primary signal to accuracies of about ±1 ns.

Acknowledgement

The modification of the Fault Locator was suggested and accomplished by A. Ray Howland, JPL consultant and President of the Howland Company at Atlanta, Georgia.

References

1. Komarek, T., and Otoshi, T., "Terminology of Ranging Measurements and DSS Calibrations," in the *Deep Space Network Progress Report* 42-36, pp. 35-40, Jet Propulsion Laboratory, Pasadena, Ca., Dec. 15, 1976.

2. Otoshi, T. Y. et al, "Calibration of Block 4 Translator Path Delays at DSS 14 and CTA 21," *DSN Progress Report* 42-37, pp. 188-197, Feb. 15, 1977.

3. Otoshi, T. Y., Wallace, K. B., and Lyon, R. B., "Dual Coupler Configuration at DSS 14 for the Voyager Era," *DSN Progress Report* 42-42, pp. 184-195, Dec. 15, 1977.

4. Silver, S., "Microwave Antenna Theory and Design," Radiation Laboratory Series, Vol. 12 McGraw Hill, 1949, pp. 582-585.

5. Beatty, R. W., "Discussion of Errors in Gain Measurements of Standard Electromagnetic Horns," *NBS Technical Note 351*, National Bureau of Standards, March 1967.

Table 1. Scientific-Atlanta Model 12-1.7 Standard Gain Horn Delay measurement results at 2.113 GHz

Horn separation			①	②	③	④	⑤
R, ft	R, cm	$\frac{R\lambda}{D^2}$	Airpath delay t_R, ns	Net measured delay,[a] ns	Waveguide transition pair delay, ns	Two horn delay,[b] ns	Single horn delay, ns
55	1676.4	17.5	55.92	60.39	1.44	3.03	1.52
50	1524.0	15.9	50.84	55.11	1.44	2.83	1.42
45	1371.6	14.3	45.75	50.02	1.44	2.83	1.42
40	1219.2	12.8	40.67	44.73	1.44	2.62	1.31
35	1066.8	11.2	35.58	39.45	1.44	2.43	1.22
30	914.4	9.6	30.50	34.97	1.44	3.03	1.52
25	762.0	8.0	25.42	29.48	1.44	2.62	1.31
20	609.6	6.4	20.33	24.40	1.44	2.63	1.32
15	457.2	4.8	15.25	19.11	1.44	2.42	1.21
10	304.8	3.2	10.17	14.03	1.44	2.42	1.21
5	152.4	1.6	5.08	8.74	1.44	2.22	1.11

[a]Net delay results from subtracting Fault Locator reference reading from test reading in units of feet and converting the result into transmission delay in units of nanoseconds.

[b]Delay of two horns = column ② data – (column ① + column ③ data).

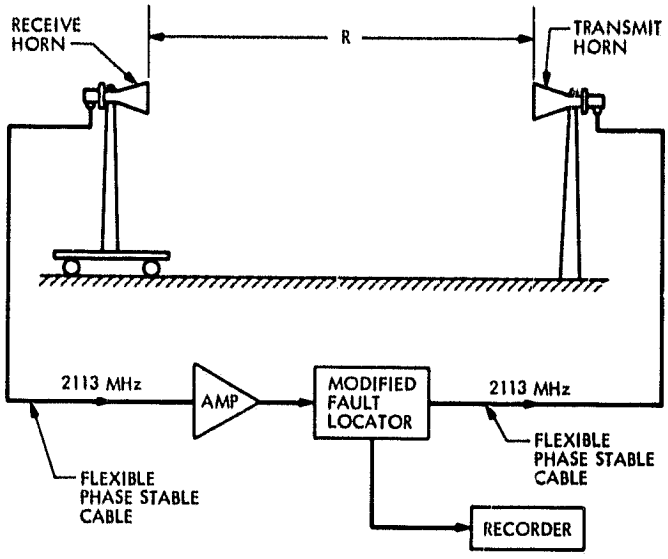

Fig. 1. Block diagram of test setup for antenna time delay measurements using a Fault Locator

Fig. 2. Test Setup at JPL Antenna Range Facility. Horns are 152.4 cm (5 ft) apart

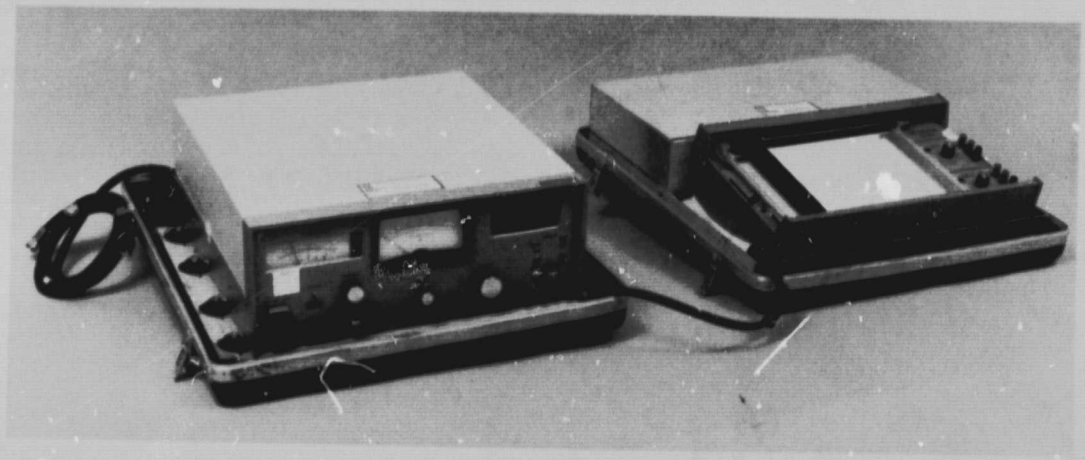

Fig. 3. Scientific Atlanta Fault Locator Model 1691 and Recorder

ORIGINAL PAGE IS
OF POOR QUALITY

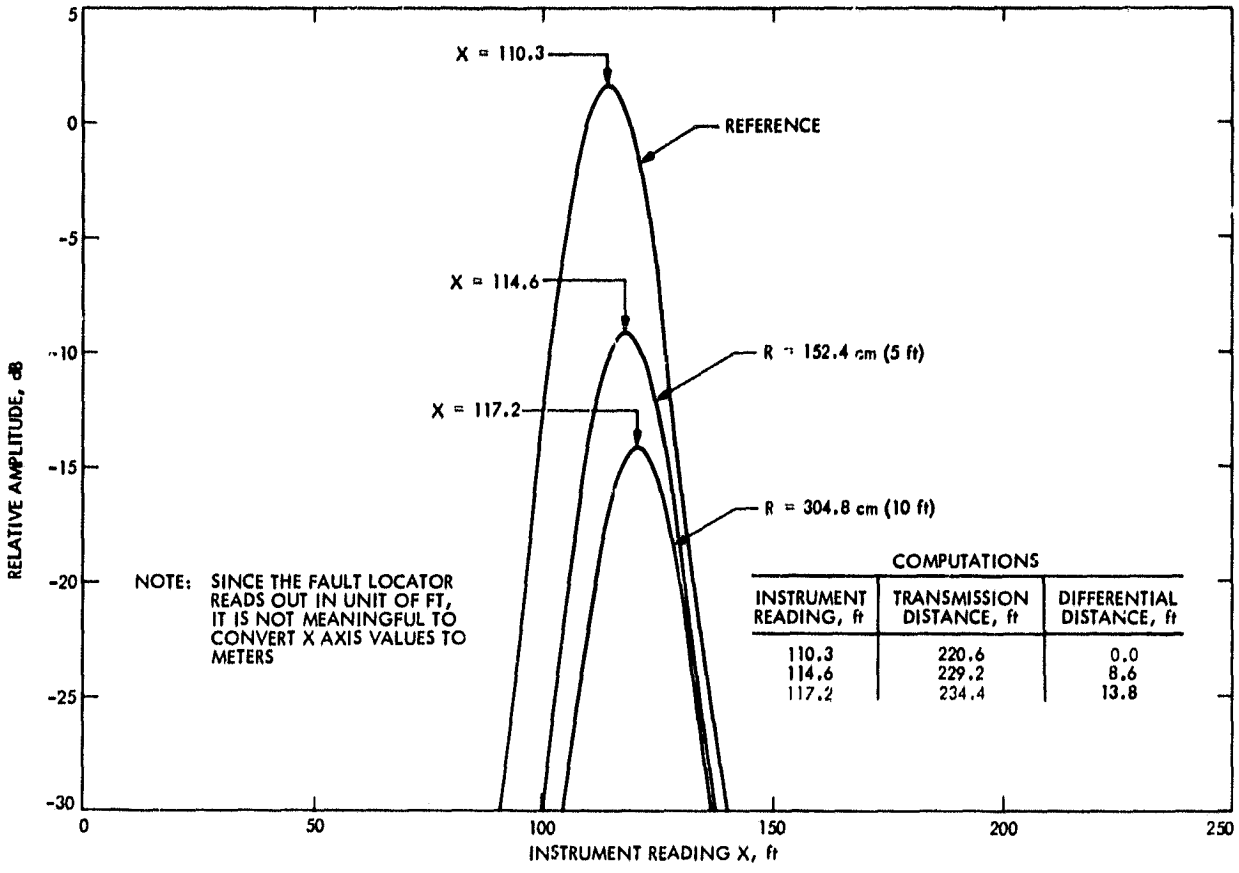

Fig. 4. Sample recording of transmission distance measurement using Fault Locator

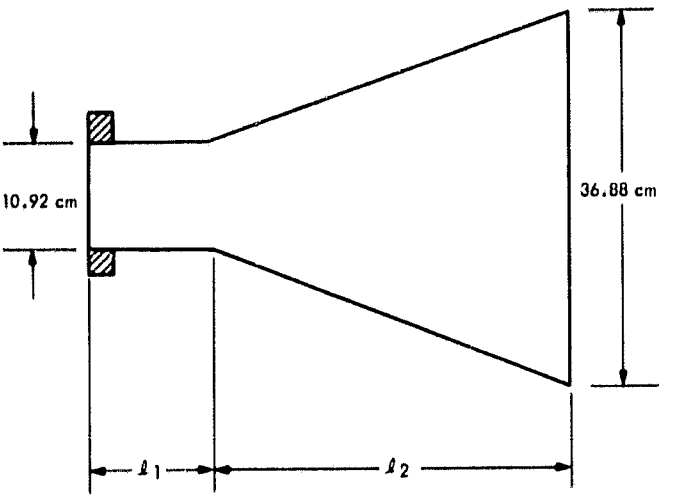

$$t_{gl} = \frac{1}{c} \int_0^{\ell_l} \frac{\lambda_0 \, dx}{\sqrt{\left[\lambda_c(x)\right]^2 - \lambda_0^2}}$$

WAVEGUIDE SECTION	λ_c, cm	ℓ_l, cm	t_{gl}, ns
CONSTANT WR430 SECTION	21.84	10.08	0.44
TAPERED HORN SECTION	21.84 → 73.76	26.49	0.95
		TOTAL	1.39

Fig. 5. Calculated time delay of standard gain pyramidal horn (Scientific Atlanta Model 12-1.7) at 2113 MHz

N78-24223

An Analysis of Alternate Symbol Inversion for Improved Symbol Synchronization in Convolutionally Coded Systems

L. D. Baumert and R. J. McEliece
Communications Systems Research Section

H. van Tilborg
Technological University, Eindhoven, The Netherlands

In the current NASA Planetary Program Flight/Ground Data System Standard, it is proposed that alternate symbols of the output of a convolutional encoder be inverted in order to guarantee the symbol synchronizer a certain richness of symbol transition.

In this paper we analyze this technique; in particular we characterize those convolutional codes with the property that even if alternate symbols are inverted, arbitrarily long transition free symbol streams may occur. For codes which do not exhibit this pathological behavior, we give an upper bound on the largest possible transition-free run.

I. Introduction

Many modern digital communication systems derive symbol synchronization from the data itself rather than from a separate synchronization channel. A common type of symbol synchronizer, and one that has become a NASA standard, is one that includes a clock whose phase and frequency are governed by timing estimates derived from the received data. The performance of this kind of symbol synchronizer depends in part on the "richness" of symbol transitions in the received data. An unusually long sequence of all 0's or all 1's, for example, could cause the local clock to lose synchronization, and so also data, temporarily.

If the data were uncoded, one possible method of increasing the transition density would perhaps be to add the sequence $\cdots 10101010 \cdots$ to the data stream, i.e., by inverting alternate symbols. The new data stream would then contain a long transition-free string only if the original data stream contained a long alternating string. Presumably a long alternating string is less likely than a long constant string, and so this method would probably have the desired effect.

If the data is encoded prior to transmission, one could again try to increase the transition density by inverting alternate symbols, and indeed this symbol inversion is now part of NASA's data system standards (Ref. 3). And whereas for uncoded data one can only assert that symbol inversion will tend to increase the transition density, for convolutionally encoded data a much stronger statement can be made: Provided the code does not suffer from a certain improbable property, there is an absolute upper bound one can place on

the length of the largest possible transition-free symbol run from the encoder, independent of the data being encoded. For example, the NASA standard rate 1/2 constraint length 7 has maximum run 14; the rate 1/3, constraint length 7 has maximum run 12.

In this paper we shall give a general approach to the problem of finding the largest possible encoded output of the form $\cdots 10101010 \cdots$ from any convolutional code. In Section 2 we will classify all codes which admit an infinite run of this type; in Section 3 we will give an upper bound on the largest runs for codes which do not admit an infinite run; in Section 4 we work some specific examples; and in the Appendix we collect some known results about convolutional codes which we need to derive our results.

Finally, a word about notation is needed. The convolutional encoders of concern operate on binary sequences of the form

$$a = (\cdots, a_{-1}, a_0, a_1, \cdots)$$

which, theoretically at least, extend infinitely in both directions. The index refers to discrete time intervals. In practice, however, each sequence "starts" at some finite time; i.e., there is an index s such that $t < s$ implies $a_t = 0$. The codewords produced by the encoder are of the same type; indeed some are also of finite length ($a_t = 0$ for $t > m$). Using x as a place holder it is sometimes convenient to write

$$a = \sum_{-\infty}^{\infty} a_t x^t = \sum_{s}^{\infty} a_t x^t$$

We also use certain algebraic properties of these formal power series, e.g., $x^r + x^{r+1} + \cdots = x^r/(1+x)$.

II. Convolutional Codes with an Infinite Run of Alternating Symbols

Theorem 1. Let C be an (n, k) convolutional code over $GF(2)$ with basic generator matrix G. Then C contains a codeword with an infinite run of alternating symbols if and only if there exists a linear combination $\nu = [\nu_1, \cdots, \nu_n]$ of the rows of G such that

$$[\nu_1, \cdots, \nu_n] \equiv \begin{cases} [0, 1, \cdots, 0, 1] \quad \text{or } [1, 0, \cdots, 1, 0] \\ \text{modulo } 1 + x, \ n \text{ even} \end{cases}$$

$$[\nu_1, \cdots, \nu_n] \not\equiv \begin{cases} [1, x, \cdots, x, 1] \quad \text{or } [x, 1, \cdots, 1, x] \\ \text{modulo } 1 + x^2, \ n \text{ odd} \end{cases}$$

Proof. We prove sufficiency first. When n is even consider the codeword produced by the inputs $X_t = a_t/1 + x$ applied to each of the generators g_i, where $\nu = \Sigma\, a_i g_i$. After an initial transient the output will be $\nu_1(1), \nu_2(1), \cdots, \nu_n(1)$ and since $\nu_i(1) \equiv \nu_i(x)$ modulo $1 + x$ the result follows. For n odd note that $\nu_i(x) \equiv x$ modulo $1 + x^2$ means that the sum of its even coefficients is 0 and the sum of its odd coefficients is 1, whereas the situation is reversed for $\nu_i(x) \equiv 1$ modulo $1 + x^2$. Thus after an initial transient the input sequences $X_t = a_t/1 + x^2$ will produce an infinite run of alternating symbols.

We now prove necessity. When n is even an infinite run of alternating symbols results from the juxtaposition of n-tuples of the form $10\ldots10$ or $01\ldots01$. For definiteness, assume the former occurs. Then, if a codeword of C contains such an infinite run, there exists a codeword c and input sequences $X_1, \cdots, X_k$, none starting earlier than $t = 0$, such that

$$X_1 g_1 + \ldots + X_k g_k = h + \frac{x^s}{1+x}[1, 0, \ldots, 1, 0] \quad s \geq 0$$

Here g_i is the i^{th} row of G and h is an n-tuple of polynomials (of degrees $< s$) which describes the initial segment of c. Since G is a basic encoder, there exists a basis for the module of n-tuples of polynomials over $GF(2)$ which is of the form $\{g_1, \cdots, g_k, g_{k+1}, \cdots, g_n\}$. Let $\{g_j^{\perp}\}$ be the dual basis, i.e., the $g_j^{\perp}$ are n-tuples of polynomials such that $g_i \cdot g_j^{\perp} = 0$ unless $i = j$ and $g_i^{\perp} \cdot g_i = 1$. Taking inner products on both sides of the equation yields

$$X_j = h \cdot g_j^{\perp} + \frac{x^s}{1+x}[1, 0, \cdots, 1, 0] \cdot g_j^{\perp} = A_j + \frac{\epsilon_j}{1+x}$$

where A_j is a polynomial and $\epsilon_j = 0$ or 1. Thus $X_1 g_1 + \cdots + X_k g_k$ is

$$\sum_{j=1}^{k} \left\{ A_j g_j + \frac{\epsilon_j g_j}{1+x} \right\} = h + \frac{x^s}{1+x}[1, 0, \cdots, 1, 0]$$

Multiplying through $1 + x$ and reducing modulo $1 + x$ yields

$$\Sigma\, \epsilon_j g_j \equiv [1, 0, \cdots, 1, 0] \text{ modulo } 1 + x$$

so this is the vector v as promised.

Similarly, for n odd,

$$\Sigma X_j g_j = h + \frac{x^s}{1+x^2}\,[1, x, \cdots, x, 1]$$

$$X_j = A_j + \frac{\epsilon_j}{1+x^2}$$

where A_j is a polynomial and $\epsilon_j = 0, 1, x$ or $1+x$. As before, this yields

$$\Sigma \epsilon_j g_j \equiv x^s\,[1, x, \cdots, x, 1] \text{ modulo } 1+x^2$$

and the proof is complete. [Q.E.D.]

In the proof above the condition that G be basic was not required for sufficiency; thus if the congruence is satisfied an infinite run of alternating symbols does indeed occur in the code. Note that since the ϵ_j are restricted at most 2^k (resp., 4^k) linear combinations need be tried when n is even (resp., n is odd). For modest values of k this is not too large a task.

The case $k = 1$ is particularly important. Here, basic just means that the n polynomials making up the single generator g_1 have no common polynomial divisor and the test amounts to reducing g_1 modulo $1+x$ or $1+x^2$.

It is also possible to test for the presence of an infinite alternating run in terms of the dual code (see Corollary to Theorem 2 below). Of course one does not usually have a generator matrix for the dual code at hand, but when such is available the test is simpler than the one above, for large k. (A generator matrix for the dual code can always be computed, however; see the appendix for this).

Theorem 2. Suppose an $(n, n-1)$ convolutional code C over $GF(2)$ is given and $f = [f_1, \cdots, f_n]$ generates the dual code, where g.c.d. $(f_1, \cdots, f_n) = 1$. Then there is an infinite run of alternating symbols in some codeword of C if and only if

(n even) $\Sigma f_{2i+\alpha} \equiv 0$ modulo $1+x$ for $\alpha = 0$ or $\alpha = 1$

(n odd) $\Sigma f_{2i} + x\Sigma f_{2i+1} \equiv 0$ modulo $1+x^2$

Proof. Since $(f_1, \cdots, f_n) = 1$ all codewords of the dual code are multiples of

$$\cdots 0 f_{10} f_{20} \cdots f_{n0} f_{11} f_{21} \cdots f_{n1} \cdots f_{1d} f_{2d} \cdots f_{nd} 0 \cdots$$

where $d = \max(\deg f_i)$. Thus it is sufficent to check the inner products of this codeword of $C^{\perp}$ with an infinite alternating run.

n even.

$$\cdots 0\ 1\ 0\ 1\ 0\ \cdots 0\ 1\ 0\ 1\ 0\ \cdots$$

($\alpha = 1$) $\quad f_{10} f_{20} f_{30} f_{40} \cdots f_{n0} f_{11} f_{21} f_{31} f_{41} \cdots$

($\alpha = 0$) $\quad f_{10} f_{20} f_{30} \cdots \quad f_{n0} f_{11} f_{21} f_{31} \cdots$

n odd:

$$\cdots 0\ 1\ 0\ 1\ 0\ \cdots 1\ 0\ 1\ 0\ 1\ \cdots 0\ 1\ 0\ 1\ 0\ \cdots$$

(coef. of x)

$$f_{10} f_{20} f_{30} f_{40} \cdots f_{n0} f_{11} f_{21} f_{31} f_{41} \cdots f_{n1} f_{12} f_{22} f_{32} f_{42} \cdots$$

(constant) $\quad f_{10} f_{20} f_{30} f_{40} \cdots f_{n0} f_{11} f_{21} f_{31} f_{41} \cdots$

In both cases the necessity of the above conditions is immediate. (For n odd the coefficients referred to are a, b from

$$\Sigma f_{2i} + x\Sigma f_{2i+1} \equiv ax + b \text{ modulo } 1+x^2$$

On the other hand the above conditions obviously guarantee the existence of a codeword $(\cdots 1010 \cdots 10 \cdots)$ extending infinitely in both directions. However only codewords "starting" at some finite time are of concern and it remains to be shown that such a codeword is in the code. But this is trivial; it amounts to using the same input sequences truncated to start at some time t_0 each preceded by a finite number of initial symbols which set the encoder's memory units properly.

[Q.E.D.]

Suppose an (n, k) convolutional code C over $GF(2)$ with generator matrix F for its dual code is given. Suppose F is a basic encoder, i.e., the g.c.d. of its $n-k$ by $n-k$ subdeterminants is 1, then, if $[f_1, \cdots, f_n]$ is any row of F it follows that $(f_1, \cdots, f_n) = 1$.

Let C_i $(i = 1, \cdots, n-k)$ be the $(n, n-1)$ convolutional code dual to the i^{th} row of F. Clearly

$$C = \bigcap_{i=1}^{n-k} C_i$$

and the maximum run of alternating symbols n any codeword of C has length $L = L(C) \leqslant \min L(C_i)$.

Corollary. When n is odd an (n, k) convolutional code C over $GF(2)$ contains a codeword with an infinite run of alternating symbols if and only if every row of a basic generator matrix F for $C^{\perp}$ satisfies the congruences of Theorem 2. When n is even it is further necessary that this be true for the same value of α (0 or 1).

Note. Suppose n is even and $L(C_i) = L(C_j) = \infty$ with $\alpha \neq 1$ for C_i and $\alpha \neq 0$ for C_j. Add row j to row i in F; this gives an equivalent basic encoder which has $L(C_i) < \infty$.

III. Bounds For Finite Runs of Alternating Symbols

If no codeword contains an infinite run of alternating symbols the question arises as to the maximum length L of such a finite run. It is easy to give a bound for L in terms of the generators for the dual code. From this bound it is possible to derive another bound (in general, weaker) which has the advantage that it can be applied directly without knowledge of the dual (see the Corollary to Theorem 3, below). In Section 4 these bounds are applied to some specific examples.

Suppose $[f_1, \cdots, f_n]$ is a generator matrix for an $(n, 1)$ convolutional code C over $GF(2)$ with $d = max\ (\deg f_i)$, then

$$f_{10}f_{20} \cdots f_{n0}f_{11}f_{21} \cdots f_{n1} \cdots f_{1d}f_{2d} \cdots f_{nd}$$

is its associated bit pattern. Let s be the number of symbols occurring between the first and last nonzero symbols f_{ij} inclusively. If $(f_1, \cdots, f_n) = 1$, s is the minimum length of any nonzero codeword of C and

$$n(d-1) + 2 \leqslant s \leqslant n(d+1)$$

Theorem 3. Let C be an $(n, n-1)$ convolutional code over $GF(2)$ with generator matrix for its dual code given by $[f_1, \cdots, f_n]$, where $(f_1, \cdots, f_n) = 1$. Suppose no codeword of C contains an infinite run of alternating symbols then the maximum run of alternating symbols in any codeword of C has length $L = s + n - 2$ when n is even or when n is odd and

$$h(x) = \Sigma f_{2i} + x \Sigma f_{2i+1} \equiv 1 + x \text{ modulo } 1 + x^2$$

If n is odd and $h(x) \equiv 1$ or x modulo $1 + x^2$ the maximum run of alternating symbols has length $L = s + 2n - 2$.

Combining this with the limits given above for s yields

$$\left.\begin{matrix} nd \\ \\ n(d+1) \end{matrix}\right\} \leqslant L \leqslant \begin{cases} n(d+2) - 2 & n \text{ even or } n \text{ odd}, \\ & h(x) \equiv 1 + x \\ \\ n(d+3) - 2 & n \text{ odd}, h(x) \equiv \\ & 1 \text{ or } x \end{cases}$$

Proof. Suppose n is even. Then from Theorem 2 above $\Sigma f_{2i} \equiv \Sigma f_{2i+1} \equiv 1$ modulo $1 + x$. If there were an alternating run of length $\geqslant s + n - 1$ it would have s consecutive symbols which would have inner product zero with the bit pattern of the f's. This contradicts $\Sigma f_{2i} \equiv \Sigma f_{2i+1} \equiv 1$, so $L \leqslant s + n - 2$. On the other hand consider an alternating run of length $s + n$. Change the first and last of these symbols; the inner products will be correct provided that they match up with the symbols $1, \cdots, s$ and $n + 1, \cdots, n + s$. Clearly this run can be extended to the right and the left to form a codeword of C; it is merely a matter of selecting symbols $1 \pm jn$ so that the inner products are zero. Such a codeword could conceivably extend infinitely in both directions; however using the same argument as at the end of Theorem 2 it follows that there is a finite codeword with an alternating run of this length.

If n is odd then, from Theorem 2, $h(x) \not\equiv 0$ modulo $1 + x^2$. If $h(x) \equiv 1 + x$ the proof above applies, so $L = s + n - 2$. If $h(x) \equiv 1$ or x then one of the inner products is zero but the other is not (see the display shown in the proof of Theorem 2). If there were a run of length $\geqslant s + 2n - 1$ there would have to be a run of s consecutive symbols where the inner product was zero. On one side or the other of these s symbols there would have to be n more symbols from the alternating run of size $s + 2n - 1$. These n symbols together with $s - n$ of the original s symbols would also have to have inner product zero contrary to the hypothesis.

So $L \leqslant s + 2n - 2$. As above a finite codeword of C can be constructed containing an alternating run of length $L = s + 2n - 2$. It is merely necessary that positions $n, \cdots, n + s - 1$ of this run have inner product zero with the bit pattern of the f's. [Q.E.D.]

Recall from the previous section the codes C_i [$(n, n-1)$ convolutional codes dual to the rows of F, where F was a basic generator matrix for $C^{\perp}$] and the obvious property

$$C = \bigcap_{i=1}^{n-k} C_i$$

from which it follows that the maximum run of alternating symbols in any codeword of C has length $L = L(C) \leq \min L(C_i)$. Suppose $L(C_i)$ is finite for at least one value of i. Then if d is the maximum degree of any element in the i^{th} row of F it follows that

$$L(C) \leq L(C_i) \leq \begin{cases} n(d+2) - 2 & n \text{ even} \\ n(d+3) - 2 & n \text{ odd} \end{cases}$$

Corollary. Suppose an (n, k) convolutional code C over $GF(2)$ is given with basic generator matrix G. Let μ be the maximum degree of the $k \times k$ subdeterminants of G. Then either $L = L(C) = \infty$ or

$$L \leq \begin{cases} n(\mu+2) - 2 & n \text{ even} \\ n(\mu+3) - 2 & n \text{ odd} \end{cases}$$

Proof. Under these conditions $C^{\perp}$ has a generator matrix F (a so-called minimal encoder for $C^{\perp}$) all of whose entries are of degree $\leq \mu$. Thus the result follows immediately except when n is even and $L(C_i) = \infty$ for $i = 1, \cdots, n-k$. Here if L is finite, a finite bound for it can be determined by replacing row i of F in turn by the sum of row i and row j, for $j = 1, \cdots, n-k$ $(j \neq i)$. Of course, in general, all this work will not be required but the point is that such transformations do not increase the maximum degree of the elements of the dual encoder and so the bound given above is valid here also.

IV. Some Examples

Consider the (3, 2) code C generated by the encoder G:

$$\begin{bmatrix} x^3+x & x^3+1 & x^4+x^2+x+1 \\ x^2 & x^3+x+1 & x^3+x^2+1 \end{bmatrix} \equiv$$

$$\begin{bmatrix} 0 & x+1 & x+1 \\ 1 & 1 & x \end{bmatrix} \pmod{1+x^2}$$

Note that the sum of its rows is congruent to $[1, x, 1]$ modulo $1 + x^2$ thus, by Theorem 1, C contains a codeword with an infinite run of alternating symbols. As mentioned in Section 2 this conclusion is valid even though G is not a basic encoder ($x + x^2$ divides its 2×2 subdeterminants). Applying Theorem 2 to the dual encoder $F = [x^5 + x^3 + x^2 + x, x^3 + x^2 + 1, x^4 + x + 1]$ note that $(f_1, f_2, f_3) = 1$ and that $f_2 + xf_1 + xf_3 = x^6 + x^5 + x^4 + x^2 + x + 1 \equiv 0$ modulo $1 + x^2$ so that again the existence of a codeword in C with an infinite run of alternating symbols is assured. $C^{\perp}$ does not contain such a codeword since F is a basic encoder and $F \equiv [1 + x, x, x]$ modulo $1 + x^2$.

As a second example consider the (4, 1) code C with generator F' of its dual code given by

$$\begin{bmatrix} x & x^3+x+1 & x+1 & x^2+x+1 \\ x^2+x+1 & x^3+1 & x^3 & x^2+1 \\ x^2 & x^2+x+1 & x^2 & x^3+1 \end{bmatrix} \equiv$$

$$\begin{bmatrix} 1 & 1 & 0 & 1 \\ 1 & 0 & 1 & 0 \\ 1 & 1 & 1 & 0 \end{bmatrix} \begin{matrix} \alpha = 0 \\ \alpha = 0, 1 \\ \alpha = 1 \end{matrix}$$

Thus each row of F' satisfies the congruences of Theorem 2 for some value of α. But row 1 satisfies the congruence only for $\alpha = 0$ and row 3 only for $\alpha = 1$. Thus C does not contain a codeword with an infinite run of alternating symbols. In fact since the sum of rows 1 and 3 of F' has degree $d = 3$ it follows that the maximum run of alternating symbols in any codeword of C is bounded above by $n(d+2) - 2 = 18$. A basic generator for C is $[1 + x^2 + x^4 + x^5 + x^6 + x^7 + x^8, x^3 + x^4 + x^5 + x^9, x + x^7 + x^8, x + x^2 + x^3 + x^6 + x^7 + x^8 + x^9]$ thus $\mu = 9$ and the Corollary to Theorem 3 gives only the weaker bound $n(\mu + 2) - 2 = 42$.

Up to this point the distinction (mentioned in the appendix) between the dual generators F and F' has been overlooked. Actually it is F' that is used in the proofs of Theorems 2 and 3. There is no problem with this because either F and F' both satisfy the congruences of Theorem 2 or they

ORIGINAL PAGE IS
OF POOR QUALITY

both do not. Similarly in Theorem 3 $h(x) \equiv 1 + x$ for F if and only if $h(x) \equiv 1 + x$ for F'. However if the actual value of s is to be used to establish a bound the bit patterns of F' should be examined as s can differ for corresponding rows of F and F'. In the case at hand the sum of rows 1 and 3 of F' has $s = 14$; so $L \leqslant s + n - 2 = 16$.

In the example above the Corollary to Theorem 3 was a little disappointing in that it gave a bound of 42 whereas more careful examination yielded $L \leqslant 16$. (Even 16 may be too high; a cursory examination of the bit pattern associated with the basic generator for C given above indicates that 13 may be the answer). When $k = n - 1$ it is clear from Theorem 3 that encoders do exist for which the bound given by the Corollary is tight. In general there are minimal encoders whose codes have no infinite alternating run but do possess codewords with finite alternating runs of length $n\mu + k + 1$ which compares reasonably well with the bounds given by the Corollary. E.g., consider the (n, k) convolutional encoder

$$G = \left[\begin{array}{c|c} I & 0' \\ \hline 0 \cdots 0 & p\ q\ p\ q \cdots \end{array}\right]$$

where I is an identity matrix of order $k - 1$ and $0'$ is a $k - 1$ by $n - k + 1$ matrix of zeros.

Here $p = p(x) = 1 + x + x^\mu$ and for n even $q = q(x) = 1 + x^2 + x^\mu$ $(\mu \geqslant 3)$ while for n odd $q(x) = 1 + x^3 + x^\mu$ $(\mu \geqslant 4)$. G is obviously basic and minimal. Further Theorem 1 guarantees that no codeword generated by G contains an infinite run of alternating symbols. That G generates a codeword with a run of alternating symbols of length $n\mu + k + 1$ can be confirmed by selecting the inputs $X_1, \cdots, X_k$ properly. E.g., let $n = 8, k = 4$ and $\mu = 3$ then the bit pattern associated with the bottom row of G is

00011111 00010101 00001010 00011111

So if $X_4 = 1 + x^2 + x^3$ $(= 10110 \cdots)$ and $X_2 = x + x^2 + x^3 + x^4$ with $X_1 = X_3 = 0$, the codeword generated by G is

00011111 01010101 01010101 01010101 010111 $\cdots$

which starting with its 8th symbol has an alternating run of length $29 = 8 \cdot 3 + 5$. Obviously $X_1, \cdots, X_{k-1}$ can always be adjusted to fill in the first $k - 1$ symbols of each block of n symbols in the proper fashion. So the input X_k is the critical one. For n even, k even and μ odd $X_k = 1 + x^2 + x^4 + \cdots + x^{\mu-1} + x^\mu$. Similar formulas exist for the other cases-when n is odd these vary with μ modulo 4.

As final examples consider the NASA Planetary Standard encoders of rates 1/2 and 1/3 (Ref. 3). Here $G = [g_1, g_2]$ or $[g_1, g_2, g_3]$ with $g_1 = 1 + x^2 + x^3 + x^5 + x^6, g_2 = 1 + x + x^2 + x^3 + x^6, g_3 = 1 + x + x^2 + x^4 + x^6$. These both are basic minimal encoders which do not possess infinite alternating runs in any codeword as Theorem 1 easily shows. (Note that $[g_1, g_3, g_2]$ and $[g_2, g_3, g_1]$ do possess such runs, thus if infinite alternating runs are to be avoided the outputs in $[g_1, g_2, g_3]$ must be interleaved properly). For the rate 1/2 code the Corollary of Theorem 3 yields $L \leqslant 2 \cdot 8 - 2 = 14$ and Theorem 3 itself guarantees the existence of finite codewords with alternating runs of this length, since $s = 14$ in this case. The rate 1/3 code has a dual generator F' given by

$$F' = \left[\begin{array}{ccc} x & 1 + x^2 + x^3 & 1 + x + x^2 + x^3 \\ 1 + x^3 & x^3 & 1 + x + x^2 \end{array}\right] \begin{array}{l} h(x) \equiv 1 + x \\ h(x) \equiv 0 \end{array}$$

Apply Theorem 3 to the first row of F'. Here $s = 11$ so $L \leqslant s + n - 2 = 12$. A finite codeword with an alternating run of length 12 is generated from G by the input $X_1 = 1 + x + x^2 + x^4 + x^7$ $(= \cdots 0111010010 \cdots)$; so this bound is achieved.

Appendix

Convolutional Encoders

Proofs of most of the results mentioned here may be found in Forney (Ref. 1). Computations are restricted to $GF(2)$; however everything is easily generalized to any finite field.

A $k \times n$ matrix G of polynomials g_{ij} determines a rate k/n ($k \leq n$) convolutional encoder with input sequences X_i ($i = 1, \cdots, k$) and output sequences Y_j ($j = 1, \cdots, n$), where

$$Y_j = \sum_{i=1}^{k} X_i g_{ij}$$

provided that G is of rank k. These output sequences Y_j are interleaved to produce a single codeword

$$Y_{11}\ Y_{21} \cdots Y_{n1}\ Y_{12}\ Y_{22} \cdots Y_{n2} \cdots$$

The collection of all such codewords (i.e., the "row space" of G) is the rate k/n convolutional code generated by G. Such an encoder may be realized by k shift registers the i^{th} of which contains ν_i memory units where $\nu_i = \max_j(\deg g_{ij})$; ν_i is called the constraint length of the i^{th} register. This is said to be the obvious realization of the encoder G and thus requires $\nu = \Sigma\, \nu_i$ memory units in all (ν is the overall constraint length of the realization).

Two convolutional encoders are equivalent if they generate the same code. An encoder is called basic if there is no polynomial h ($\deg h \geq 1$) which divides all the $k \times k$ subdeterminants of G. Basic encoders do not suffer from catastrophic error propagation and thus they are preferred over others. Fortunately every code can be generated by some basic encoder. I.e., there exists a basic encoder equivalent to any given encoder G.

In general a basic encoder that has maximum degree μ among its $k \times k$ subdeterminants requires at least μ memory units for its implementation. Sometimes it requires more. When μ is obviously sufficient, i.e. when $\mu = \Sigma\, \nu_i$, the encoder is said to be a minimal encoder. Since equivalent basic encoders have the same value of μ, a minimal encoder requires as few memory units as any equivalent basic encoder. In fact, a minimal encoder requires as few memory units as any equivalent encoder, basic or not. Again, every encoder is equivalent to some minimal encoder. So, theoretically at least, there is no loss in assuming that any particular code at hand is generated by a minimal encoder. (Finding a minimal encoder equivalent to a given encoder can be a computational chore however; see below). It is a direct consequence of the minimality condition that any linear combination of the generators of a minimal convolutional encoder has degree greater than or equal to the degrees of all the generators occurring in the combination. This implies that equivalent minimal encoders not only have the same overall constraint length $\nu = \Sigma\, \nu_i$, but that they also have the same number of generators of each degree. I.e., the set of degrees ν_i ($i = 1, \cdots, k$ with multiplicities counted) is an invariant of minimal encoders under equivalence. Closely related to these last two comments is a property of minimal encoders called the predictable degree property which allows easy ennumeration of the short codewords generated by a minimal encoder, see Ref. 1.

Associated with any (n, k) convolutional code C is its dual code $C^{\perp}$. $C^{\perp}$ is the $(n, n-k)$ convolutional code which consists of all sequences orthogonal to every codeword of C. If C is generated by a minimal encoder with overall constraint length ν then $C^{\perp}$ can also be generated by a minimal encoder of the same overall constraint length.

If $[g_1, \cdots, g_n]$ is a generator matrix for the $(n, 1)$ code C and if $\Sigma f_i g_i = 0$ for polynomials $f_1, \cdots, f_n$ it is algebraically convenient to consider $[f_1, \cdots, f_n]$ as a row of a generator matrix F for $C^{\perp}$. But if one considers the codewords the coefficients of the f_i's must be reversed. For example, let $n = 2$; then one codeword of C is

$$\cdots 0\ g_{10}\ g_{20}\ g_{11}\ g_{21}\ g_{12}\ g_{22} \cdots$$

This codeword is orthogonal to the symbol sequences

$$\cdots f_{10}\ f_{20}\ 0 \cdots \qquad \ell = 0$$

$$\cdots f_{11}\ f_{21}\ f_{10}\ f_{20}\ 0 \cdots \qquad \ell = 1$$

$$\vdots \qquad\qquad \vdots$$

since the respective inner products are the coefficient of x^{ℓ} in $\Sigma f_i g_i = 0$. Thus each f in F should be replaced by $x^{\sigma} f(1/x)$ where σ is the maximum degree of any element of F. An

equivalent generator matrix F' is given by $x^{\nu_i} f(1/x)$ where ν_i is the maximum degree of any element in row i of F. If F is a minimal encoder then so is F'. The sequence $\{\nu_i\}$ of maximum degrees of the rows is the same for F and F', thus they have the same overall constraint length also. Thus for most purposes F can be taken to be the generator matrix of the dual code $C^{\perp}$.

Every generator matrix G has an invariant factor decomposition $G = A\Gamma B$. Here A and B are square matrices of determinant 1 with polynomial elements. A is $k \times k$ and B is $n \times n$. Γ is a $k \times n$ diagonal matrix whose diagonal elements γ_i ($i = 1, \cdots, k$) are nonzero polynomials. The γ_i are called the invariant factors of G and γ_i divides γ_{i+1}. Over $GF(2)$ an encoder is basic if and only if $\gamma_k = 1$. This decomposition of G can be produced by elementary row and column operations on G; see, for example, Gantmacher (Ref. 2). Now the first k rows of B constitute a basic encoder equivalent to G. Furthermore B^{-1} exists and has polynomial elements. If F^T denotes the last $n - k$ columns of B^{-1}, then F is a $n - k \times n$ polynomial matrix which is a basic encoder for the dual code $C^{\perp}$.

Thus given any encoder G it is possible to find an equivalent basic encoder by computing the invariant factor decomposition. However simpler methods often suffice. If G is not basic, i.e., if the greatest common divisor of the $k \times k$ subdeterminants of G is a polynomial h of degree ≥ 1, let ψ be any irreducible polynomial dividing h. Then some linear combination of the rows of G is divisible by ψ. By performing a row reduction of G modulo ψ one determines a transformation matrix T of determinant 1 such that TG has a row divisible by ψ. Divide this row by ψ; this produces an encoder equivalent to G with h replaced by h/ψ. Eventually this process terminates in an encoder equivalent to G with $h = 1$; i.e., an equivalent basic encoder.

Similarly, if G is basic but not minimal the matrix of ν_i^{th} order terms of G will have rank less than k; thus a row reduction of this matrix leads to a transformation T of determinant 1 such that TG has smaller overall constraint length than G. Clearly, after at most $\Sigma \nu_i - \mu$ of these steps a minimal encoder equivalent to G will be produced.

An alternate method of finding generators for the dual code also exists. After all, any $n - k$ linearly independent vectors orthogonal to G will form such a generator matrix, so the following process can be used to produce them one at a time. Suppose an (n, k) encoder G is given. Since G has rank k some $k \times k$ subdeterminant is not zero. Let H be the matrix formed from these k columns plus one other. Then H has dimension $k \times k + 1$ and is of rank k. Consider the $k + 1 \times k + 1$ matrix H' whose first k rows are H and whose $k + 1^{\text{st}}$ row is row i of H. Expanding $|H'|$ in terms of this last row shows that the vector of cofactors is orthogonal to every row of H, since $|H'| = 0$. Thus using this vector of cofactors to specify $k + 1$ components and setting the other components equal to zero we have a generator for the dual. Adjoin this generator to G and repeat the process until $n - k$ generators have been found. These $n - k$ generators will generate the dual code. Note that after j rows have been added to G it will have rank $k + j$ so the process does not break down. Further, in the special case where $k = n - 1$, the single generator for the dual code will be basic if G was. (In general this will not be the case for $k < n - 1$ however).

Acknowledgement

The authors wish to thank M. K. Simon and J. G. Smith for bringing this problem to their attention and for suggesting several possible approaches.

References

1. G. D. Forney, Jr., "Convolutional Codes I: Algebraic Structure", *IEEE Trans. Inform. Theory*, Vol. IT-16, November 1970, pp. 720-738 (See also correction: same journal, May 1971, page 360).

2. F. R. Gantmacher, *The Theory of Matrices*, Chelsea, New York, 1959.

3. *NASA Planetary Program Flight/Ground Data System Standards.* Revision 5, June 1, 1977. National Aeronautics and Space Administration, Washington, D.C.

N78-24224

A Prototype DSN X-S Band Feed: DSS 13 First Application Status

W. F. Williams
Radio Frequency and Microwave Subsystems Section

This article discusses a new prototype X-S band horn feed for future use at various DSN sites. This project was undertaken to more nearly optimize the X-band performance of these stations. This feed is a corrugated horn with extremely deep corrugation grooves that are suitable for both the X-band and S-band. The horn is very large, becoming gain limited, so that it performs about equally in both bands. A one-half scale model was fabricated and the measurement results were good reproductions of theoretical predictions. A full scale item has now been completed and will be tested at DSS 13.

I. Introduction

The reflex dichroic S-X band feed has been in successful operation on the 64-meter antennas for a number of years, and was selected for implementation in the 34 meter subnet upgrade project. This feed permits full high performance for telemetry within S-band while at the same time allowing for operation in the new telemetry frequencies within X-band. Although the X-band corrugated horn used with this reflex feed is very good, it is also true that the use of the dichroic plate in the system and the large asymmetric feed structure results in about 0.5 dB G/T compromise of X-band performance. This is because of some small loss in the dichroic plate and some back scatter at X-band resulting in an increase (2-3 Kelvins) in the X-band antenna noise temperature.

In the future, the use of X-band telemetry is to be emphasized, at the expense of S-band if necessary and also fully symmetric antennas are desired. It was decided to develop an alternate feeding technique that would more nearly optimize X-band performance, perhaps with some degradation of S-band performance.

It is evident that if the dichroic plate is to be removed, then the two bands must operate concentrically or coaxially from the same or coaxial apertures. Some obvious approaches to accomplish this are: (1) an X-band horn within (coaxial with) the S-band horn, (2) an X-band end fire element (disc-on-rod or helix) within the S-band horn, and (3) an array of four or more S-band horns surrounding the X-band radiator, much like a monopulse system. These approaches all would result in a considerable S-band performance compromise (say 2 dB), and the use of anything but a good horn for X-band might well have as much loss as the dichroic plate. The only obvious approach available is to actually use the same horn with both bands and develop a technique that will result in acceptable illumination functions in both of these widely separated frequencies.

This has been accomplished by using a very large corrugated horn, operable in both bands, and operating in a "beamwidth saturation" mode at X-band so that the two radiation patterns are very similar. A unique characteristic of this horn is that the phase center has moved back, clear into the throat of the horn, in contrast to previous JPL horns.

II. The Horn Concept

Jeuken (Ref. 1) suggested this technique of operation in different frequency bands. The corrugated horn derives its operating characteristics from the fast wave structure of the horn walls. This structure forces the fields from the walls and reduces wall currents. In this manner, the final aperture illumination is well tapered, the electric fields being zero at the edges. This characteristic is obtained by grooving the walls perpendicular to power flow so that the surface impedance becomes capacitive. For this to occur, the grooves must be between $\lambda/4$ and $\lambda/2$ deep (λ = wavelength) at the operating frequency, or in the range

$$\lambda\left\{\frac{2N-1}{4}\right\} \quad \text{to} \quad \lambda\left\{\frac{2N}{4}\right\},$$

where N may assume any integer value. Usually five or more grooves per wavelength are sufficient.

As a horn with fixed flare angle becomes longer, the aperture becomes larger and radiation patterns become narrower. A point is reached however when additional size does not make the pattern narrower nor the horn to develop higher gain, generally because of total phase error in the aperture. For this discussion we may call this "saturated operation." As size is further increased, some change in pattern texture may be detected; however, the pattern remains essentially unchanged.

One now sees the possibilities. A groove depth can be chosen which satisfies the depth requirement above within two (or more) frequency bands for proper corrugated horn operation, and sufficiently large to just be "saturated" in the lowest band so that the higher bands would be operating well above this point for nearly equal pattern characteristics. The beamwidth for these "saturated" conditions is a function only of the horn flare angle, and *not* the aperture size. Narrower flares result in narrower saturated beamwidths, with consequent longer horn lengths.

In this saturated operation, the pattern phase center has moved back into the throat of the horn, approximately at the horn vertex, instead of its usual position near the aperture face. This will give a somewhat unusual appearance to the Cassegrain system because the horn will extend a large distance away from the feedcone-centered hyperboloid focal point, towards the hyperboloid.

III. Calculations

Potter (Ref. 2) has prepared a generalized computer program for the calculation of the performance of corrugated horns. This program was used at length in the calculations of horn patterns for various flare angles from 20 to 40 degrees. Figure 1 represents a compilation of the calculations for a horn of 36 degree flare angle (18° half flare). This figure depicts the 10 dB beamwidth of the horn as it is made larger (longer) through the saturation point. This beamwidth (10 dB) is chosen since it represents in general the taper level in illuminating the hyperboloid subreflector. One notes here that the 10 dB beamwidth reduces to about 27 degrees and holds this level for much larger horns. This "saturation" aperture size is about 7.5 wavelengths, or 0.98 meters for 2.295 GHz. At 8.400 GHz, the aperture is 27.8 wavelengths, and still in the same beamwidth range.

Figures 2 and 3 show the calculated patterns for a horn of 34.2° flare angle and 1.067 meters aperture, using 5.093 cm grooves. This horn has been fabricated for tests and possible use at DSS 13. One notes here that the aperture is 8.16 wavelengths at S-band and 30.0 wavelengths at X-band. The 5.093 cm grooves represent depths of 0.34 λ to 0.403 λ from 2.0 GHz to 2.4 GHz and 1.21 λ to 1.44 λ from 7.1 GHz to 8.5 GHz. Operation slightly below the 1.25 λ limit is due to some unexplained effect.

The 10 dB beamwidths are nearly the same for the two bands. However, there is an obvious difference in the structure of these two patterns. The S-band pattern flares out much more resulting in more spillover energy beyond the normal illumination point of -10 dB taper. Calculated efficiencies of the horn as an equivalent paraboloid prime focus illuminator are as follows, at the polar angle of 13.4°, and 8.150 GHz.

η_s (spillover)	=	0.94744
η_i (illumination)	=	0.88746
η_p (phase)	=	0.99870
η_t (total)	=	0.83972

The X-band phase center is about 1.7 meters behind the aperture. When the S-band pattern is calculated about this same point, the following calculated efficiencies result at the polar angle of 13.4° and 2.295 GHz.

η_s (spillover)	=	0.86323
η_i (illumination)	=	0.88577
η_p (phase)	=	0.98652
η_t (total)	=	0.75432

indicating that X-band is being optimized at some expense to S-band performance. For reference, the same calculations can

be made using the present DSN corrugated horns as used in an equivalent paraboloid system. Those results are:

$$\eta_s \text{ (spillover)} = 0.91454$$
$$\eta_i \text{ (illumination)} = 0.89114$$
$$\eta_p \text{ (phase)} = 0.99836$$
$$\eta_t \text{ (total)} = 0.81365$$

This shows the new feed, as applied in a conventional paraboloid/hyperboloid system gains 2.6% at X-band and losses 5.9% at S-band, as a direct substitute.

Probably one of the most valuable and unexpected results from this type of horn is the complete lack of any sort of sidelobe. Note that the level scale is for a 60 dB range, and at X-band the main lobe reduces to this level and does not reappear. This makes the horn very attractive in the proposed dual reflector antenna shaping applications since it will improve spillover efficiency even more and possibly aid in the further reduction of total antenna noise.

IV. The Half Scale Model

Figure 4 is a photograph of the one half scale model that was constructed and measured during this development. This model had a 34.2° flare angle, a 53.34 cm aperture, and 2.548 cm grooves. Measurements were then made throughout the appropriate frequencies to verify predicted performance. Figures 5 and 6 are these measured patterns at two frequencies, 16.3 GHz and 4.4 GHz. These measurements indicate an excellent agreement with theory. The 10 dB beamwidths are about the same and as expected, sidelobes do not exist.

A full scale version is being constructed for tests and possible other uses at DSS 13, such as VLBI. Figure 7 depicts this installation at DSS 13, indicating the relative horn positions. This figure indicates, as was mentioned above, that the new X-S horn will extend much farther toward the hyperboloid from its feed cone location than the present installation.

References

1. E. J. Jeuken and V. J. Vokurka, "Multi-Frequency Band Corrugated Conical Horn Antenna," 1973 European Microwave Conference Proceedings, Vol. 2, Sept. 4-7, 1973, Brussels University, Brussels, Belgium.
2. P. D. Potter, "Efficient Antenna Systems: A New Computer Program for the Design and Analysis of High Performance Conical Feedhorns," JPL Technical Report 32-1526, Vol. XIII, pp. 92-107, Feb. 15, 1973.

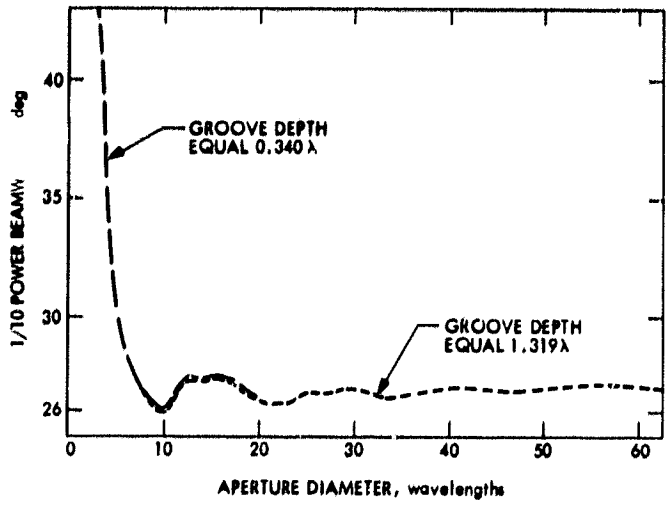

Fig. 1. The "saturated" 36° corrugated horn

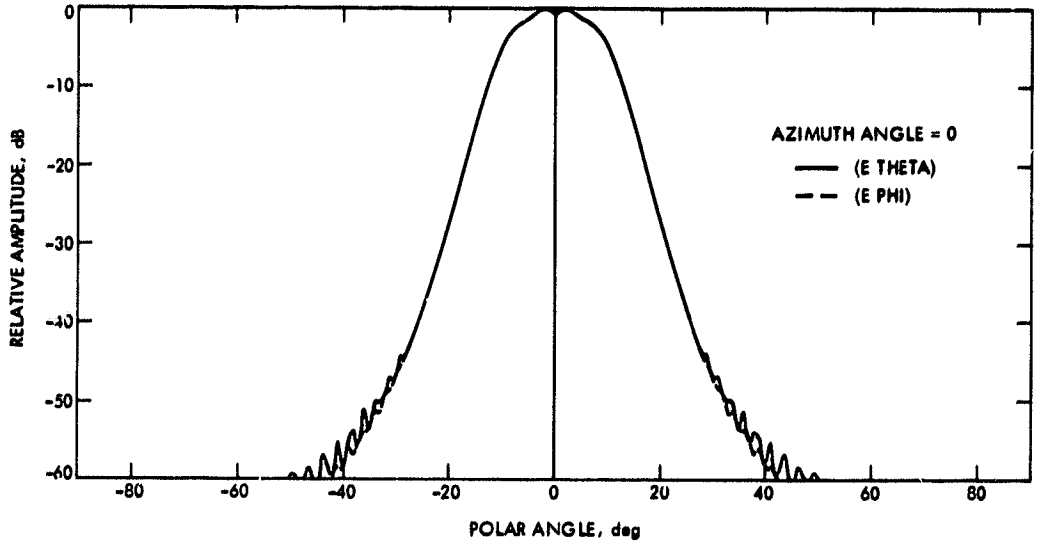

Fig. 2. Amplitude pattern for the 17.1 deg horn, 1.067 meter aperture, 5.093 cm grooves, freq. = 8.150 GHz

ORIGINAL PAGE IS
OF POOR QUALITY

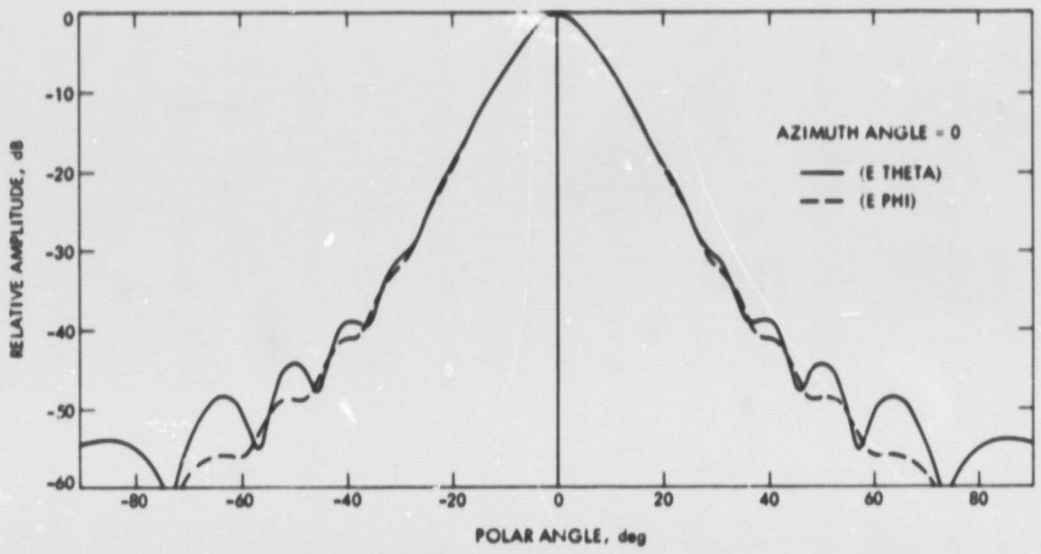

Fig. 3. Amplitude pattern for the 17.1 deg horn, 1.067 meter aperture, 5.093 cm grooves, freq. = 2.200 GHz

Fig. 4. The half scale model

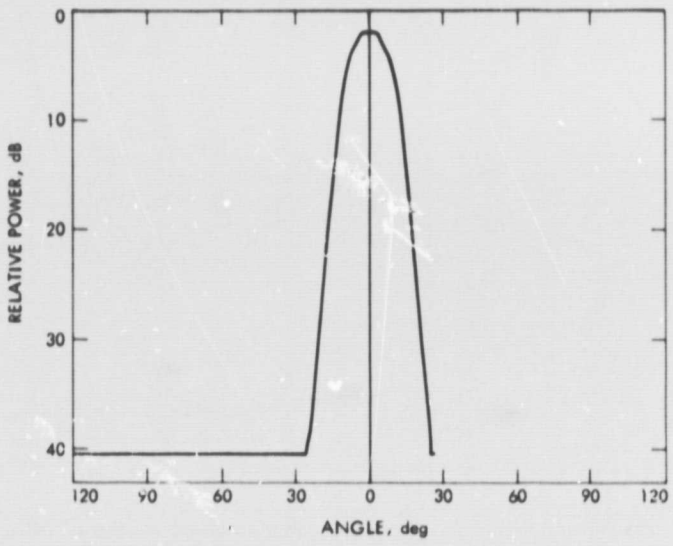

Fig. 5. Measured pattern of a (34.2) 17.1 deg horn, 53.34 cm aperture, 2.548 cm grooves, freq. = 16.3 GHz H-plane

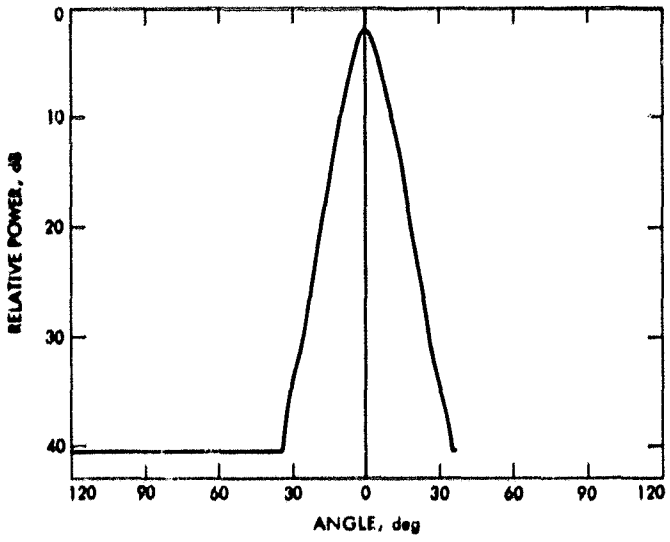

Fig. 6. Measured pattern of a (34.2) 17.1 deg horn, 53.34 cm aperture, 2.548 cm grooves, freq. = 4.400 GHz H-plane

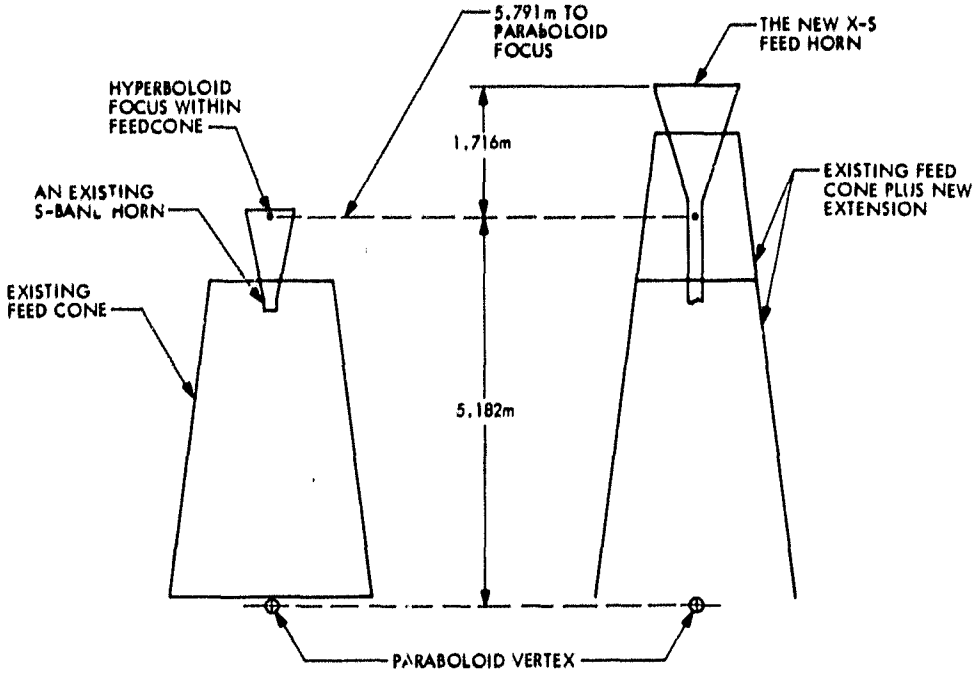

Fig. 7. Comparison of DSS 13 installations

N78-24225

LAASP 100-m Antenna Wind Performance Studies

R. Levy and M. S. Katow
DSN Engineering Section

Structural design procedures are described for the LAASP antenna system to meet performance requirements under gravity and wind loading. A computational method is shown for the evaluation of performance in response to wind loading. Cumulative probability distribution curves for wind loading gain reductions for 100-m-diameter antennas are developed to compare a relatively heavy baseline reflector backup structure with two lighter-weight structures; all have equivalent, acceptable performance for gravity loading.

I. Introduction

Design studies for the Large Antenna Station Project (LAASP) paraboloidal antenna structures are undertaken to derive cost and performance tradeoffs associated with a number of configuration alternatives. Both cost and performance can be characterized by any of a number of quantitative measures, while configuration alternatives also are conceptually limitless. Consequently, to expedite timely completion of any study, some restrictions on the scope are essential. Nevertheless, within a framework of practical and reasonable restrictions, it is feasible to develop significant parametric study information for a comprehensive range of antenna structure designs within a given diameter class.

Within the context of the present discussion, cost will be measured by the structure weight. It is well known that weight is an imperfect measure of structure cost when a wide variety of configurations with diverse fabrication, material, and installation requirements are contemplated. However, when alternative configurations are similar in concept, structure weight is a convenient and acceptable cost measure. Performance will be measured by the antenna radio frequency (RF) gain reduction, which depends upon the structural deformations caused by gravity and wind loading.

Gravity loading, which is always present on antenna structures, is deterministic and well understood. Wind loading is statistical, and the assessment of related response is more complex. Depending upon the location, wind can have a significant effect upon performance. Other loadings such as thermal, shock, and earthquake are primarily stochastic, difficult to quantify, and of relatively short duration. These loadings can be treated as constraints on the design to maintain structure integrity and survivability but are not included for evaluation of operating performance.

Configuration studies will be limited to be within one particular reflector class: The traditional structural format of radial rib trusses braced by circumferential hoop ring trusses. Within this format class, nevertheless, there are many possible variations of the geometrical arrangement, such as proportions, numbers and spacing of trusses, and the configuration of the external supporting structures. Several of these variations are

examined early in the present study but, for brevity, the designs to be described here will include only the preferential geometry as previously developed.

Here the emphasis will be placed upon the relationships between weight and performance for wind loading. The calculational procedure and results obtained will be described for a proposed 100-m-diameter antenna reflector system illustrated in Fig. 1. This system is intended to operate at the X-band frequency of 8.5 GHz. Cumulative probability distribution curves of gain reduction for wind loading will be shown for three alternative reflector designs for this system. These designs have the same geometry and differ only in the cross sectional areas of the bars chosen for the reflector backup structure. They represent a baseline design and two lighter variations with weight reductions of up to 30%. All three designs are constrained to have equivalent performance in the absence of wind loading. The maximum gain reduction due to gravity loading is less than 10% of the total gain reduction from all sources. Those consist of manufacturing and surface alignment errors and subreflector and quadripod blockage.

II. Sources of Gain Reduction

Table 1 is a summary of the sources of gain reduction that have been considered for gravity or wind loading. Two categories are identified: the deformation-type category includes pathlength phase errors of the radiofrequency (RF) beam; the beam-deformation-type category covers pointing misalignment losses of the main beam with respect to the target.

Referring to the table, backup structure contribution is computed with respect to the paraboloid that best fits the deflected surface. Surface panel contributions are also considered with respect to a best-fitting surface. The subreflector offsets are the axial and lateral mismatches of the subreflector position from the focal point of the best-fitting paraboloid. For computational purposes, these offsets can be converted to equivalent additional backup structure deformations (Ref. 1). For gravity loading, which is repeatable and calibratable, the subreflector can be repositioned to the actual focal point, and thus the offsets produce no gain reduction. Subreflector surface deflections are another source of deformation-type losses. However, these will be disregarded because appropriate design can make them small.

The wind speeds are represented by the conventional model of a slowly varying, quasi-steady component and a superimposed gust turbulence. Beam deviation error that results from the steady component of the wind speed is corrected by a programmed pattern search that removes these low-frequency pointing errors. We make a conservative assumption, however, that the pattern search is too slow to overcome the gust effects, so that gust loading always produces gain reductions through beam deviations. The pointing errors from gravity loading can be overcome by calibration that compensates the input command signal. The servo loop error occurs because the servo system is not fully effective in compensating for the higher-frequency components of the gust disturbance torque. The ability of the servo system to compensate depends upon the servo loop transfer function in conjunction with the wind gust spectrum. Calculations for typical antenna systems show that from 75% to 90% of the angular errors detected at the encoders can be removed by compensation. To be conservative, calculations here assume compensation of only 75% of these error magnitudes.

III. Reflector Design Synthesis

The baseline reflector backup structure design was developed by an evolutionary process. Although the JPL-IDEAS computer program (Ref. 2) was used as a pivotal design tool to perform analysis and optimization of member cross-sectional area selection, no software was available to optimize the geometrical proportions for this structure. Consequently these proportions were developed from a sequence of trial variations of the geometry. The variations were tested by analysis and member area redesign within the IDEAS program to assess their ultimate potential.

The ordinarily laborious and time-consuming task of preparing the extensive data card sets required for structural computer analysis was expedited by a program that automatically generated these cards for each variation. This program supplies almost all of the card images needed to describe reflector backup structures of the conventional radial rib truss and circumferential hoop type of construction. The sequence of trial geometry generation and subsequent testing entails generation and processing of an extensive data bank; nevertheless, it is executed rapidly. Furthermore, only a limited amount of effort by the engineer is needed. His participation is required primarily for decision-making to guide the operations and to select from among the many options available to him, with only a small requirement for time to be spent on clerical tasks.

The root mean square (rms) pathlength deviation of the reflector surface from the best-fitting paraboloid was selected as the performance measure for design evaluation. The goal was to achieve a reasonable balance between response to gravity loading and response to wind loading. For the gravity loading, the objective response was the average of the rms values over the elevation angle range weighted by tracking mission probabilities (Ref. 3) associated with the elevation angles A criterion wind-loading case was established to represent the condition of the antenna at the 60-deg elevation angle

with a rear wind at an arbitrary reference speed of 13.4 m/sec (30 mph). Previous experience with similar antennas indicated that this wind orientation was likely to be the most severe. During all of the redesign iterations, member area selections were subjected to constraints on stress and buckling for the gravity loading, for the criterion wind loading, and for additional wind loadings that represented the most severe operational wind (31.3 m/sec) and the survival wind (44.7 m/sec).

The geometry evolved for the baseline design resulted in a nearly homologous response (Ref. 4) for gravity loading and a very good surface rms (0.69 mm) for the criterion wind loading. Two lighter-weight variations of the basic design were developed by permitting a degeneration of performance for the criterion wind loading but at the same time retaining the stress and buckling constraints for all loads and by invoking a new constraint that maintained the performance for the gravity loading. The weight of the backup structure and counterweight for the baseline design was 1210 tons, and the lighter designs produced reductions of 200 and 335 tons with the wind criterion loading rms values of 0.86 mm and 0.93 mm respectively.

The alidade comprises a much less complex analytical model than the reflector. The few data cards required for analysis and redesign were hand-generated. The final geometry also entailed evolutionary proportioning to achieve a favorable arrangement. Analysis and member redesign were performed by the IDEAS program using an option invoked to maximize stiffness with respect to pointing accuracy for wind loading. Only one alidade design was developed, and this is used to support all three of the backup structures.

The alidade model was eventually converted for analysis by the NASTRAN program (Ref. 5). This was done for the convenience of having a direct output of specific internal rotation angles related to the servo loop wind gust error. The NASTRAN program analysis included the bending stiffness of the alidade bars, which is presently not possible within the IDEAS program. Nevertheless, responses from the two programs agreed closely, indicating that the bending rigidity is not significant.

IV. Computational Model for Wind Loading Gain Reduction

A multidimensional four-component statistical model was used for computation of gain reduction due to wind loading. The four random components were (1) V, the mean wind speed; (2) v, a superimposed gust turbulence; (3) AZ, the azimuth of the wind relative to the antenna pointing direction; (4) EL, the elevation of the antenna relative to the horizon.

The mean speed has slow variations that comprise periodic components measured by hours or days. Statistics of the mean speed obtained for the same site (Goldstone, California) as the proposed 100-m antenna have been tabulated in Ref. 6.

The gust speed was described by the conventional model, which represents the gusts as gaussian, with zero mean and standard deviation σ_v proportional to the mean speed; e.g.,

$$\sigma_v = CV \tag{1}$$

The tabulated mean speeds are based upon observations at a 46-m (150-ft) height above ground. For convenience, the mean speeds here are also considered at the same height. Estimating the surface drag coefficient at 0.006 for the proposed terrain and using the computed power law coefficient for speed variations with height equal to 0.1405 (Ref. 6), we find $C = 0.1533$.

Gusts are the dynamic component of the wind speed. Spectral decompositions according to conventional models (Refs. 7, 8) show that the predominant fluctuations are characterized by periods in the order of several seconds to minutes. The natural frequency of the antenna-reflector system of Fig. 1 will be at least 1 Hz for the slowest natural mode. The response of such a system to both the mean speed and the gust speed is essentially the same as for static load application. Consequently the structural response can be computed as a static response to total wind loading $\underline{V}$ where

$$\underline{V} = V + v \tag{2}$$

Wind tunnel test data on antenna reflector and alidade components (Refs. 9, 10) were used to convert from wind speeds to pressure loadings on the proposed reflector and alidade structures. Wind tunnel tests are a logical and reasonable basis for deriving the pressures and forces for the mean components of the wind speeds. Nevertheless, it is recognized that using the same type of conversion for gust effects is a major assumption and simplification of this model. The gust speeds actually have a three-dimensional spatial correlation for which theoretical models require further development. A possible approach to providing a better estimate of the gust loading is available through computer simulation (Ref. 11). However, it was estimated that the application of this approach would have entailed a major additional computational effort and also more wind tunnel test data than is currently available. Nevertheless, despite the simplified representation for gust loading, the present work employs the same formulation to compare alternative designs and should furnish a reasonable basis for comparison.

The distribution of wind azimuths relative to the antenna was also simplified in this model by assuming a uniform distribution in the range of azimuths from 0 to 360 deg. Because of symmetry, only half of this range is considered in the calculations. Had statistics been availabe to describe the distribution of wind azimuths at the proposed site, it would have been possible to determine a more accurate distribution of relative wind azimuths in conjunction with analysis of the statistics of proposed antenna targets. The related uncertainty in the assumption of uniform relative azimuths does not appear to be sufficient to undertake the additional computational complexity.

The distribution of antenna elevations was considered for elevations in the range of 0 to 90 degrees. Probability densities of the elevation angles were available from analysis of composite statistics of planetary tracking missions (Ref. 3).

For computational purposes, discretization of the four random components into specific class marks and class intervals was as follows:

1. Mean speed, V; 0 to 22.35 m/sec (50 mph) at intervals of 2.235 m/sec (5.0 mph). 10 terms.
2. Gust speed, v; −4 to +4 standard deviations. 19 terms unevenly spaced with finest resolution in the vicinity of 0 standard deviations.
3. Relative azimuth, AZ; 0, 30, 60, 90, 120, 150, 180 deg. 7 terms.
4. Antenna elevation, El; 0, 30, 60, 90 deg. 4 terms.

The computational results are represented by cumulative probability distributions of gain reduction. The distributions cover the range of 0 to 4 decibels (dB) at 100 discrete increments of 0.04 dB. Conditional distributions (10 × 7 × 4 = 280) were developed for each combination of mean speed (including the related gust probability), azimuth, and elevation angle. The final distributions were the composite of the conditional distributions weighted by the probability associated with the mean speed, azimuth, and elevation class marks. This very simple method of combining the conditional distributions is permissible from the assumption of independence of wind speed, azimuth, and elevation angles.

V. Computation of Gain Reduction Distribution

The computational method used to compute a typical gain reduction conditional probability distribution will be described here. Each of these distributions represents the random effects of wind gusts and is conditioned upon specific values of mean wind speed, wind azimuth, and antenna elevation.

With reference to gain reduction categories A and B of Table 1, the wind pressures, and consequently the forces, are proportional to the square of the wind speed. The deformations and deviations (pointing angle errors) are proportional to the forces. Gain reductions for category A are proportional to the squares of the deformation. Gain reductions for category B are proportional to the squares of the differences in deviations for the total wind speed minus the deviations for the mean wind. Consequently the gain reductions for these two categories can be represented as

$$G_A = G_R(\underline{V}/V_0)^4 \tag{3}$$

$$G_B = G_P(\underline{V}^2 - V^2)^2/V_0^4 \tag{4}$$

in which

G_A, G_B = category A, B, gain reduction

V_0 = reference mean wind speed

$\underline{V}$ = total (mean + gust) speed

V = mean speed

G_R = category A gain reduction at reference speed

G_P = category B gain reduction computed for V_0 and not allowing correction for the mean speed. Thus G_P is equivalent to a "blind pointing" loss for V_0.

To obtain a convenient computational formula, the gust speed v is replaced by a standardized normal variate Z such that

$$Z = v/\sigma_v \tag{5}$$

Then from Eq. 1

$$v = CZV \tag{6}$$

and from Eq. 2

$$\underline{V} = V(1 + CZ) \tag{7}$$

From these relationships, Eqs. 3 and 4 can be combined so that the total gain reduction G_T, which is the sum of G_A and G_B, can be expressed as

$$G_T = (G_R f_R + G_P f_P) \cdot (V/V_0)^4 \tag{8}$$

where

$$f_R = 1 + 4\,CZ + 6(CZ)^2 + 4(CZ)^3 + (CZ)^4 \tag{9}$$

$$f_P = 4(CZ)^2 + 4(CZ)^3 + (CZ)^4 \tag{10}$$

The conditional distribution for gain reduction, $F(G_T)$, can then be obtained from Eq. 8, using the relationships of Eqs. 9 and 10. Although the procedure is automated within a digital computer program, equivalent operations can be illustrated graphically with respect to Fig. 2 as follows:

① Compute G_T for a set of values of Z in the range (−4, +4) and plot G_T vs Z, as in Fig. 2a.

② At a selected value of gain reduction G_{Tl}, find the intersections of G_{Tl} with the curve in ①.

③, ④ Project the intersections down to the curve in Fig. 2b. This curve is constructed to be the standard normal cumulative probability distribution of Z. Read the ordinates where the projections intersect the curve.

⑤ The value of the distribution of gain reduction at G_{Tl} is the difference in the ordinates read from the curve of Fig. 2b.

VI. Computational Procedure

Figure 3 contains a schematic diagram of the complete computational procedures used to derive the gain reduction distribution for wind loading. The following notes apply to the labeled blocks of the figure:

Block 1. Wind tunnel pressure distribution data for specific relative wind attitudes with respect to the antenna are converted to the force data required as input for reflector analysis. The forces are represented by the three Cartesian coordinates at each node and are derived from the interpolated wind pressures, the surface area tributary to the node, and the components of the unit vector normal to the surface. Development of force data, except for the interpolation, is automated. Wind loading on the structural members of the alidade is also developed from wind tunnel data. For both reflector and alidade, sets of loads are developed to correspond with the discretization of wind azimuth and antenna elevation.

Block 2. The reflector is analyzed by the IDEAS program to supply the responses to the wind loadings. The program is used here for analysis only, by specifying no redesign cycles.

Block 3. The alidade is analyzed by the NASTRAN program to find the response for the wind loadings. Wind reactions of the reflector on the alidade are included.

Block 4. Computation of pathlength deviations from the best-fitting paraboloid are automated within IDEAS.

Block 5. Gain reductions for subreflector offsets are calculated by hand, using results from the reflector analysis.

Block 6. Reflector contributions to the pointing errors are automated within a separate computer program. Results are assembled within a matrix (4 elevations × 7 azimuths).

Block 7. Alidade contributions to pointing error and to servo loop are hand-computed (presently) and assembled within matrices.

Block 8. The category A (deformation-type) gain reductions are combined by hand calculation. These individual G_R terms (Eq. 3) are assembled within a matrix.

Block 9. A compute program derives a matrix containing the G_P terms (Eq. 4). In the preceding blocks, the alidade and reflector pointing deviations have been computed with separate components for the elevation and cross-elevation axes. Vector addition is required to combine the separate components.

Block 10. The G_R and G_P matrices are input. A computer program develops conditional distributions for gain loss, described previously, for all 280 combinations of mean wind speed, wind azimuth, and antenna elevation.

Block 11. The computer program of Block 10 applies probability weighting factors for mean speed, wind azimuth, and antenna elevation to the conditional distributions and assembles the composite distribution of gain reduction for wind loading.

VII. Results and Conclusions

Figure 4 shows the distribution of gain reduction for wind loading for the baseline 100-m antenna system and the

two alternative designs with lighter reflector backup structures. As stated previously, all designs provide equivalent high performance for gravity loading.

For ready reference, Fig. 4 tabulates reductions at a few selected percentiles of the distribution. It can be noted, for example, that the reduction in weight of 335 tons for the lightest structure is achieved with a reduction in performance of 0.37 dB (8% loss in efficiency) at the 98th percentile, and with much smaller reduction at lower percentiles. On the average, the table shows this design to be only 0.04 dB worse than the baseline.

Whether or not the lightest design shown, or possibly a design lighter than any of these, will be adopted must be considered in view of the performance requirements for the entire system. Tracking mission requirements and desired reliability in conjunction with other sources of gain reduction must be integrated within this type of evaluation.

References

1. Katow, M. S., "Evaluating Computed Distortions of Parabolic Reflectors," *Mechanical Engineering in Radar Symposium,* Nov. 8-10, 1977, Washington D.C.
2. Levy, R., "Computer-Aided Design of Antenna Structures and Components," *Computers and Structures,* Vol. 6, pp. 419-428, Pergamon Press, 1976.
3. Levy. R., "Antenna Bias Rigging for Performance Objective," *Mechanical Engineering in Radar Symposium,* Nov. 8-10, 1977, Washington D.C.
4. Von Hoerner, S. "Homologous Deformations of Tiltable Telescopes," *J. Struct Div., Proc. ASCE 93(ST-5),* Proc. Paper 5529, pp. 461-485.
5. *The NASTRAN User's Manual,* NASA SP-222(01), C. W. McCormick, editor, May 1973.
6. Levy, R., and McGinness, H., *Wind Power Prediction Models, JPL TM 33-802,* Jet Propulsion Laboratory, Pasadena, California, Nov. 1976.
7. Davenport, A. G., "The Spectrum of Horizontal Gustiness Near the Ground in High Winds," *Quarterly Journal of the Royal Meteorological Society, London, Vol. 87, Aug. 1961, pp. 194-211.*
8. Hino, M., "Spectrum of Gusty Wind," *Proceedings of the Third Conference on Wind Effects on Buildings and Structures,* Tokyo, Japan, Sept. 6-11, 1971, pp. 69-78.
9. Fox, N. L., *Load Distributions on the Surface of Paraboloidal Reflector Antennas,* Internal Memorandum JPL-CP 4, Jet Propulsion Laboratory, Pasadena, California, July 1962 (JPL internal document).
10. Blaylock, R. B., *Aerodynamic Coefficients for "A Model of A Paraboloidal-Reflector,"* Internal Memorandum JPL-CP6, Jet Propulsion Laboratory, Pasadena, California, May 1964 (JPL internal document).
11. Shinozuka, M. S., and Levy, R., "Digital Generation of Alongwind Velocity Field," *J. Engineering Mechanics Div.,* Proc. ASCE 103 (EM-4), Proc. Paper 13159, Aug. 1977, pp. 689-700.

Table 1. Gravity and wind loading contributions to gain reduction

Source	Gravity loading[a]	Wind loading	
		Steady wind	Gust wind
A. Deformation type			
Backup structure deflection	Contr	Contr	Contr
Surface panel deflection	Contr	Contr	Contr
Subreflector offsets	Comp	Contr	Contr
B. Beam deviation type			
Backup structure pointing error	Calib	Corr	Contr
Alidade pointing error	Calib	Corr	Contr
Servo loop error	None	None	Contr

[a]Contr – Contributes to gain reduction
Comp – Compensated by subreflector repositioning
Calib – Calibration used to modify the commanded position
Corr – Corrected by programmed pattern search

ORIGINAL PAGE IS
OF POOR QUALITY

ORIGINAL PAGE IS
OF POOR QUALITY

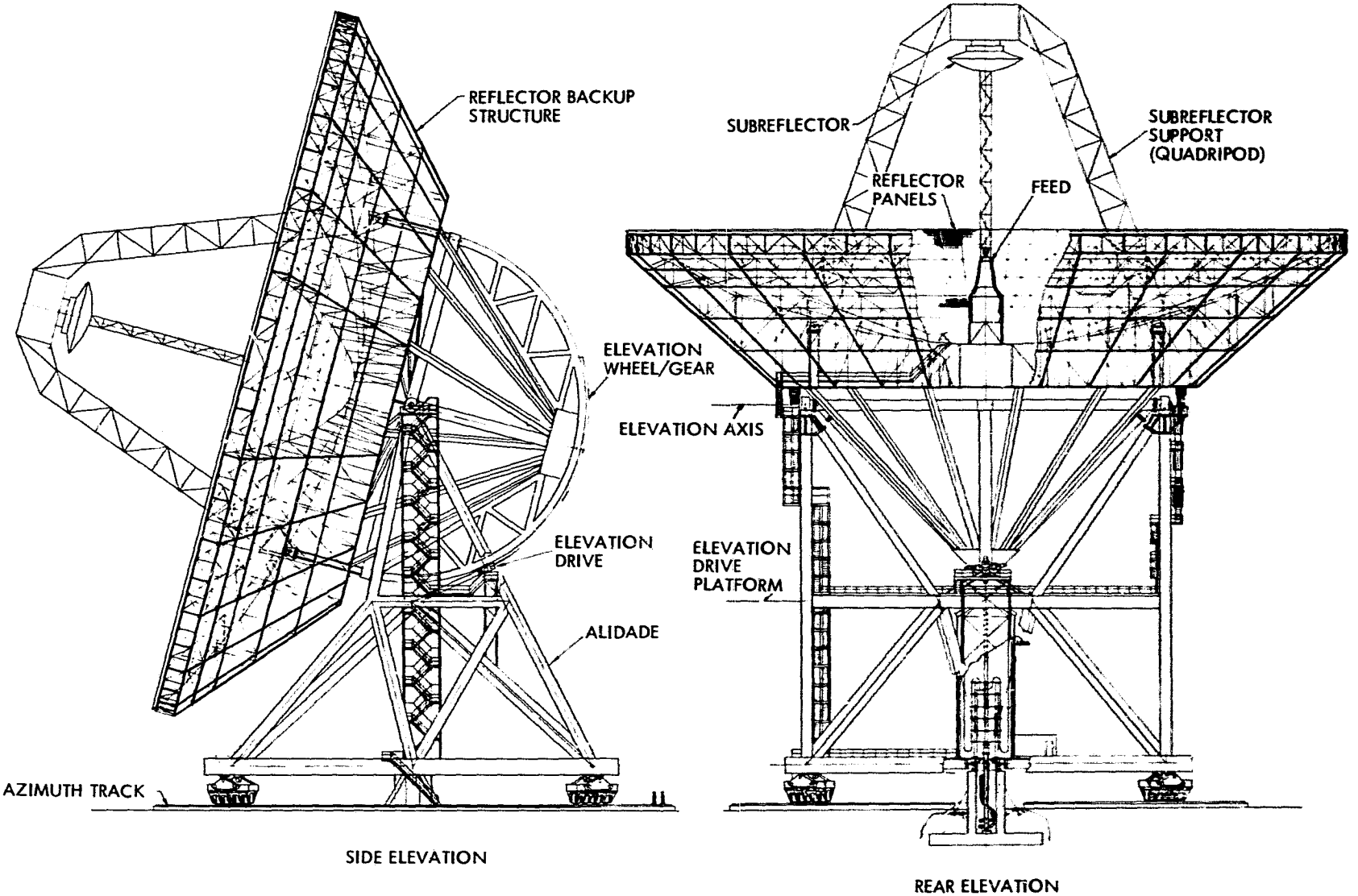

Fig. 1. Configuration of 100-m-diameter antenna system

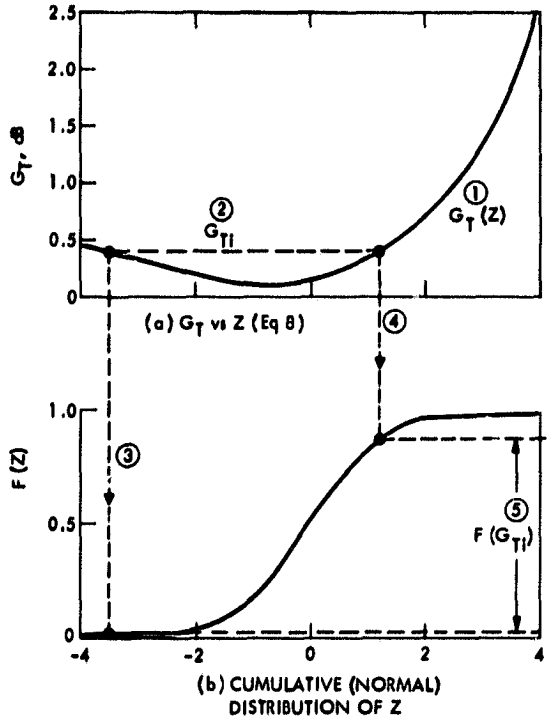

Fig. 2. Development of cumulative distribution of G_T

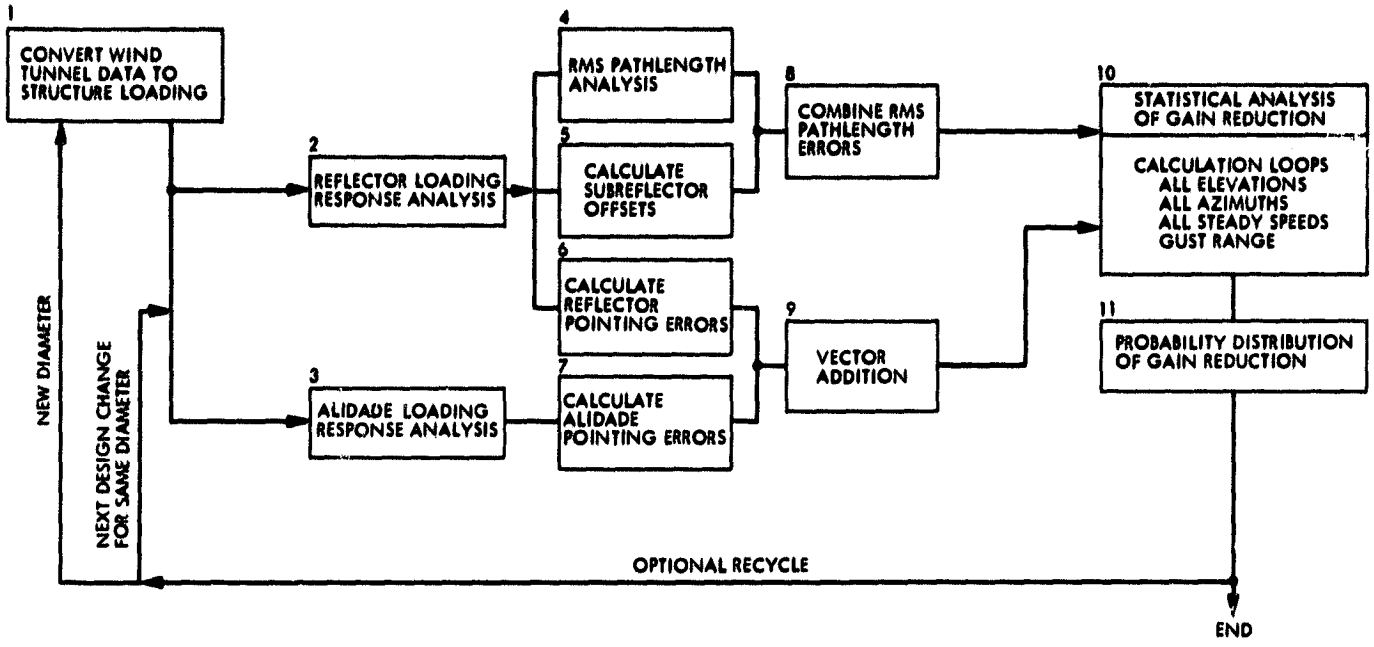

Fig. 3. Computational procedure

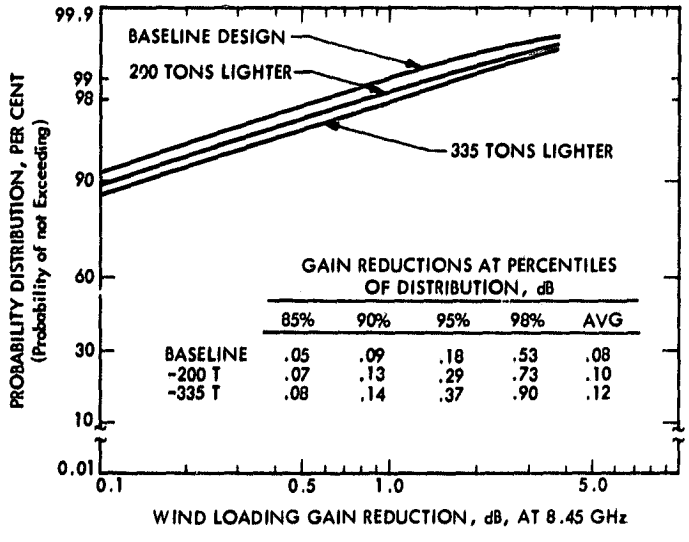

Fig. 4. Gain reduction for 100-m design variations

N78-24226

A Public-Key Cryptosystem Based On Algebraic Coding Theory

R. J. McEliece
Communications Systems Research Section

Using the fact that a fast decoding algorithm exists for a general Goppa code, while no such exists for a general linear code, we construct a public-key cryptosystem which appears quite secure while at the same time allowing extremely rapid data rates. This kind of cryptosystem is ideal for use in multi-user communication networks, such as those envisioned by NASA for the distribution of space-acquired data

I. Introduction

Recently, Diffie and Hellman (Ref. 3) introduced the notion of a *public-key cryptosystem* in which communication security is achieved without the need of periodic distribution of a secret key to the sender and receiver. This property makes such systems ideal for use in multi-user communication networks, such as those envisioned by NASA for the distribution of space-acquired data (Ref. 4). Later, Rivest, Shamir and Adleman (Ref. 7) explicitly exhibited such a system, using facts from number theory, and Merkle and Diffie (Ref. 6) exhibited one based on the known difficulty of the integer-packing "knapsack" problem. In this paper we propose a public key cryptosystem which is based on the theory of algebraic codes.

II. Description of the System

We base our system on the existence of *Goppa codes*. For the full theory of such codes the reader is referred to (Ref. 5, Chapter 8), but here we summarize the needed facts.

Corresponding to each irreducible polynomial of degree t over $GF(2^m)$, there exists a binary irreducible Goppa code of length $n = 2^m$, dimension $k \geq n - tm$, capable of correcting any pattern of t or fewer errors. Moreover, there exists a fast algorithm for decoding these codes. [Algorithm due to Patterson. See Ref. 5, problem 8.18. The running time is $O(nt)$].

Suppose the system designer picks a desirable value of n and t, and then randomly selects an irreducible polynomial of degree t over $GF(2^m)$. Since the probability that a randomly chosen polynomial of degree t is irreducible is about $1/t$, and since there is a fast algorithm for testing irreducibility (see Ref. 1, Chapter 6), this selection would be easy to do. Next, the system designer produces a $k \times n$ generator matrix G for the code, which could be in canonical, for example row-reduced echelon, form.

Having generated G, the system designer now "scrambles" G by selecting a random dense $k \times k$ nonsingular matrix S, and a random $n \times n$ permutation matrix P. He then computes

$G' = SGP$, which generates a linear code with the same rate and minimum distance as the code generated by G. We call G' the public generator matrix, since it will be made known to the outside world.

The system designer then publishes the following data encryption algorithm, which is to be used by anyone desiring to communicate to him in a secure fashion.

Algorithm E

Let the data to be encrypted be divided into k-bit blocks. If $\mathbf{u}$ is such a block, transmit the vector $\mathbf{x} = \mathbf{u}G' + \mathbf{z}$, where G' is the public generator matrix, and $\mathbf{z}$ is a locally generated random vector of length n and weight t. ▨

Having received $\mathbf{x}$, the system designer can recover $\mathbf{u}$ efficiently by using the following decryption algorithm:

Algorithm D

Compute $\mathbf{x}' = \mathbf{x}P^{-1}$, where P^{-1} is the inverse of the permutation matrix P. $\mathbf{x}'$ will then be a codeword in the Goppa code previously chosen. Using Patterson's algorithm, one then computes $\mathbf{u}S = \mathbf{u}'$. Finally, $\mathbf{u}$ is computed by $\mathbf{u} = \mathbf{u}'S^{-1}$. ▨

III. Discussion

It is clear that algorithms D and E can be implemented quite simply. What remains to be studied is the security of the system. What we need to determine, essentially, is how difficult it will be for an eavesdropper who knows G' and intercepts $\mathbf{x}$ to determine $\mathbf{u}$. It appears that an eavesdropper has two basic attacks to try; first, to try to recover G from G' and so to be able to use Patterson's algorithm. Second, he might attempt to recover $\mathbf{u}$ from $\mathbf{x}$ without learning G.

The first attack seems hopeless if n and t are large enough because there are so many possibilities for G, not to mention the possibilities for S and P.

The second attack seems perhaps more promising but the basic problem to be solved is that of decoding a more or less arbitrary (n, k) linear code in the presence of t errors. In a recent paper Berlekamp, McEliece, and van Tilborg (Ref. 2) proved that the general decoding problem for linear codes is NP – complete, so one certainly expects that if the code parameters are large enough, that this attack too will be infeasible.

In particular, suppose we chose $n = 1024 = 2^{10}$, $t = 50$; then there will be about 10^{149} possible Goppa polynomials, and an astronomical number of choices for S and P. The dimension of the code will be about $k \geq 1024 - 50 \cdot 10 = 524$. Hence, a brute-force approach to decoding based on comparing $\mathbf{x}$ to each codeword has a work factor of about $2^{524} \approx 10^{158}$; and a brute-force approach based on coset leaders has a work factor of about $2^{500} \approx 10^{151}$. A more promising attack is to select k of the n coordinates randomly in hope that none of the k are in error, and based on this assumption, to calculate $\mathbf{u}$. The probability of no error, however, is about

$$\left(1 - \frac{t}{n}\right)^k,$$

and the amount of work involved in solving the k simultaneous equations in k unknown is about k^3. Hence, before finding $\mathbf{u}$ using this attack one expects a work factor of

$$k^3 \cdot \left(1 - \frac{t}{n}\right)^{-k}.$$

For $n = 1024, k = 524, t = 50$ this is about $10^{19} \approx 2^{65}$.

Of course, the above discussion proves nothing about other potential methods but it does suggest that this public key system is quite secure. One final remark: The algorithms E and D are very easy to implement using digital logic, and communication rates near 10^6 bits/second or more would be feasible. The number-theoretic system proposed by Rivest, et al. (Ref. 7) does not appear to be implementable at such speeds.

Finally we note that the decryption algorithm described in this article cannot be used as an encryption algorithm for producing unforgeable "signatures." This is because algorithm D will almost surely fail to produce any output at all unless its input is a vector within Hamming distance t of some codeword; and only a very small fraction of the 2^n possible binary vectors of length n have this property. For example, if $n = 1024, k = 524$, there are

$$2^{524} \cdot \sum_{k \leq 50} \binom{1024}{k} = 2^{808.41}$$

vectors within distance 50 of a codeword. Thus, the probability that a randomly selected length 1024 vector can be decoded successfully is only about $2^{-215.59}$.

References

1. Berlekamp, E. R., *Algebraic Coding Theory*, New York, McGraw-Hill, 1968.
2. Berlekamp, E. R., McEliece, R. J., and van Tilborg, H., "On the Inherent Intractibility of Certain Coding Problems," IEEE Trans. Inform. Theory, IT-24 (1978), *in press*.
3. Diffie, W., and Hellman, M., "New Directions in Cryptography," IEEE Trans. Inform. Theory, IT-22 (1976), pp. 644-654.
4. Kurzhals, P. R., "New Directions in Space Electronics," *Astronautics and Aeronautics*, Feb. 1977, pp. 32-41.
5. McEliece, R. J., *The Theory of Information and Coding*, (Vol. 3 of *The Encyclopedia of Mathematics and Its Applications*.) Reading, Mass., Addison-Wesley, 1977.
6. Merkle, R. C., and Hellman, M. E., "Hiding Information and Receipts in Trap-Door Knapsacks," paper presented at IEEE International Symposium on Information Theory, Cornell University, October, 1977.
7. Rivest, R. L., Shamir, A., and Adleman, L., "A Method for Obtaining Digital Signatures and Public-key Cryptosystems," Communications of the ACM 21 (1978), pp. 120-126.

N78-24227

Tracking Loop and Modulation Format Considerations for High Rate Telemetry

J. R. Lesh
Communications Systems Research Section

Tracking loops and modulation formats for DSN telemetry rates in the tens of megasymbols per second region are considered. It is shown that for high rate telemetry, subcarriers should not be used and suppressed carrier modulation should be used. It is then shown that the current DSN receivers can be used for tracking suppressed carrier signals with only minor modifications and that normal doppler tracking operations are unaffected by such changes. Finally, we show that the existing DSN, augmented by a megasymbol telemetry demodulator assembly can be used to process simultaneous high rate telemetry and ranging signals using an interplex modulation format which results in significant advantages to both telemetry and ranging.

I. Introduction

The DSN emerged at a time when weak signals and low data rates dominated. As a result, residual carrier phase modulation schemes with phase locked loops tracking the residual carrier component were employed. However, over the years technological advances in antennas, transmitters and signal processing have caused a marked increase in the available signal power and hence the achievable data rates. In fact essentially all of the current or near future deep space missions are already operating at or near the upper limit of the current DSN data rate capability.

The DSN, under the auspices of advanced systems, is currently involved in new high rate telemetry system designs which will push the DSN data rate capability into the tens of megabits per second region. Such telemetry reception capabilities would greatly enhance future missions such as Venus Orbiting Imaging Radar (VOIR) by greatly improving the attainable mapping resolution. However when designing any such system one should re-examine the assumptions upon which the earlier low rate system was based to see how many, or even if any, of them apply to the present problem. For example one should ask if subcarriers should still be used or if it is still necessary to retain a residual carrier for the purpose of tracking. In this paper we will examine the implications of such questions as well as assess the impacts of proposed new concepts on the current DSN.

II. Are Subcarriers Needed?

When the DSN operated at 8 bps using residual carrier modulation it was necessary to place the data modulation on subcarriers. This was necessary since without the subcarrier most of the data power would fall within the bandwidth of, and be tracked out by, the carrier phase locked loop. Also, at low data rates a carrier tracking loop is usually much closer to

threshold so that any additional disturbance in the loop can be quite serious.

At the higher data rates the picture is quite different. In order to support the higher data rates one must have more signal power. Thus the signal (and hence carrier power) to noise density ratio is very much larger. This results in a greatly improved carrier loop SNR. Also, the data signal spectrum is broad so that the part which is contained in the loop bandwidth (when subcarriers are not used) appears as white noise. Its effect is averaged out and degrades the tracking loop performance very little. This suggests that subcarriers are not needed in high data rate systems.

A much stronger statement can be made when considering the disadvantages of subcarriers. Consider a telemetry system which is to operate at 25 Mbps. Assume also that subcarriers are to be used. The DSN standard is for the subcarrier to be a square wave and have a frequency at least 1.5 times the data rate. Thus, a 37.5 MHz subcarrier is required. However, in order to keep the SNR degradation down to a tolerable level it is necessary to process a sufficient number of subcarrier harmonics; say to the fifth harmonic. In this example the resulting bandwidth is ±188 MHz on either side of the carrier and is larger than the current bandwidth allocation of 100 MHz at X-band. Therefore we see that subcarriers cannot be used at the higher data rates.

III. Is Residual Carrier Needed?

We saw in the last section that subcarriers should be eliminated in high rate systems. We will now consider the desirability of using residual carrier modulation.

Consider first a residual carrier signal of the form:

$$\chi(t) = \sqrt{2}\ A \cos\left[\omega_0 t - \theta D(t)\right] + n(t)$$

where A is the signal amplitude, ω_0 is the carrier angular frequency, θ the modulation angle ($\theta < 90°$), $D(t)$ is the binary data modulation (no subcarrier), and $n(t)$ is white gaussian noise. When this signal is tracked by a phase locked loop having a tracking error of ϕ, the resulting phase detector output $E(t)$ is (assuming ϕ is small):

$$E(t) = A(\cos\theta)\phi + A \sin\theta\, D(t) + n^1(t)$$

where $n^1(t)$ is the equivalent white gaussian noise at baseband. We note that the first term of $E(t)$ represents the phase error signal for tracking purposes, whereas the second term is the data dependent self noise resulting from the fact that no subcarrier was used. Since the data rate is high the energy of the data dependent interference will be spread over a wide bandwidth and hence over the tracking loop bandwidth will appear as a white noise. The equivalent two-sided spectral density $N_I(0)$ of this interference is given by:

$$N_I(0) = A^2 \sin^2\theta\, T_s = \frac{A^2\, T_s \sin^2\theta\, N_0}{N_0} = R\, N_0$$

where T_s is the symbol time duration, N_0 is the one-sided thermal noise spectral density and R is the symbol SNR. Then, if we compute the loop signal to noise ratio ρ_L we have that

$$\rho_L = \frac{A^2 \cos^2\theta}{2B_L\left(\frac{N_0}{2} + R N_0\right)} = \frac{A^2}{N_0 B_L}\left(\frac{\cos^2\theta}{1 + 2R}\right)\left(\begin{matrix}\text{Residual}\\ \text{Carrier}\end{matrix}\right)$$

where B_L is the one-sided loop bandwidth. We see that the loop SNR can be expressed as the product of the total signal power to noise in the loop bandwidth ratio and a degradation factor:

$$\beta = \left(\frac{\cos^2\theta}{1 + 2R}\right)$$

representing the effects of modulation format and self-noise interference. Note that if a subcarrier had been used the $2R$ term would have disappeared leaving the familiar result for the present phase locked loop performance.

We are interested in evaluating the degradation factor β for typical high rate applications. Table 1 lists the value of β for several values of SNR and for the case where $\theta = 80°$. Also shown in this table is a breakdown of the value of β into the contributing factors of self-interference and modulation loss.

From Table 1 we see that the penalty for using residual carrier is from 20 to 30 dB, 15 dB of which comes from the modulation loss.

Consider now a suppressed carrier signal of the form:

$$\chi(t) = \sqrt{2}\ A\, D(t) \cos\omega_0 t + n(t)$$

where $n(t)$ is narrow band white gaussian noise. Let $\chi(t)$ be applied to a Costas type tracking loop of the kind shown in

Fig. 1. Assume that the tracking reference signal has a phase error of ϕ radians as shown in the figure. The outputs of the arm filters $\chi_c(t)$ and $\chi_s(t)$ are given by:

$$\chi_c(t) = \sqrt{\alpha}\ A\ D(t) \cos\phi + n_c(t)$$

and

$$\chi_s(t) = -\sqrt{\alpha}\ A\ D(t) \sin\phi + n_s(t)$$

Here α represents the fraction of the data signal spectrum which is passed by the arm filters and $n_s(t)$ and $n_c(t)$ are the low pass quadrature noise terms, each with spectral density $N_0/2$ and one-sided bandwidth B. If the arm filters are ideal then:

$$\alpha = \frac{2}{\pi}\left\{\mathrm{Si}(2\pi BT_s) - \frac{\sin^2(\pi BT_s)}{\pi BT_s}\right\}$$

which depends on the symbol time-bandwidth product. Typical values for α are given in Table 2.

To produce an error control signal the cross product of χ_c and χ_s is taken. The resulting error signal is (assuming ϕ is small)

$$E(t) = \alpha A^2\phi + \sqrt{\alpha}\,AD(t)\,[n_c(t)\sin\phi - n_s(t)\cos\phi]$$

$$+ n_s(t)\,n_c(t) = \alpha A^2\,\phi + N_1(t) + N_2(t)$$

The first term represents the phase tracking signal whereas the second and third terms represent the data interference and thermal disturbance respectively. The null spectral density of $N_1(t)$ is:

$$S_{N1}(0) = \frac{\alpha A^2 N_0}{2}$$

Whereas the corresponding result for $N_2(t)$ is:

$$S_{N2}(0) = \frac{N_0^2 B}{2}$$

The tracking loop SNR is then found to be:

$$\rho_L = \frac{\alpha^2 A^4}{2B_L\left(\frac{\alpha N_0 A^2}{2} + \frac{N_0^2 B}{2}\right)}$$

$$= \frac{A^2}{N_0 B_L}\left(\frac{\frac{R\alpha^2}{BT_s}}{1+\frac{R\alpha}{BT_s}}\right) \quad \left(\begin{matrix}\text{Suppressed}\\ \text{Carrier}\end{matrix}\right)$$

Note that as in the case of residual carrier the loop SNR for the suppressed carrier system is the product of A^2/N_0B_L and the degradation term

$$\beta' = \frac{\frac{R\alpha^2}{BT_s}}{1+\frac{R\alpha}{BT_s}}$$

However, in this case the degradation factor depends on both the symbol SNR as well as the BT_s product. (α is also a function of BT_s.)

Table 3 lists the values of β' for several values of R and BT_s products.

Comparison of Table 3 with Table 1 shows that a significant improvement in tracking SNR results from suppressed carrier operation. For example, at $BT_s = 2$, the case of most practical interest, the suppressed carrier loop enjoys a 15 to 30 dB advantage over the residual carrier scheme.

IV. Is a New Receiver Needed?

To convert from residual to suppressed carrier modulation may be desirable from a technical performance standpoint but may not be economically feasible if a complete new receiver is needed. Fortunately it is possible to use the existing receivers for tracking suppressed carrier signals with only a slight modification. Figure 2a shows a block diagram of the block IV receiver. Similar results can be easily extended to the block III receiver if desired. The receiver transforms the received signal through a series of intermediate frequency conversions to an IF signal compatible with the final IF phase detector. The phase detector output is then filtered and used to control the VCO.

Consider now the block diagram shown in Fig. 2b. This shows how a megasymbol telemetry demodulator can be used along with the block IV receiver in a suppressed carrier mode. The receiver still makes the IF conversions as it did in the previous figure. However, the control of the VCO is accomplished now by the loop filter in the demodulator which operates from the 55 MHz IF. (This IF was selected since it has enough bandwidth to support megasymbol telemetry.) The only change to the receiver necessary for this configuration is the addition of the switch at the input to the VCO.

V. What About Doppler and Ranging?

Referring again to Fig. 2 we see that the receiver supplied signal to the doppler extraction equipment comes from the receiver VCO output. Since this VCO is common to both the residual and suppressed carrier configurations then no change is necessary in the hardware in order to maintain the doppler tracking capability. Actually the doppler tracking ability will be enhanced by the fact that the loop SNR will be greater, thus reducing the doppler jitter. There is, however, one minor impact to the doppler processing software as a result of going to suppressed carrier The present systems occasionally experience tracking cycle slips which result in phase jumps of ±360 degrees. In suppressed carrier systems there are two stable tracking lock points so that 1/2 cycle slips are possible. These, however, should be quite infrequent due to the improved tracking.

With regard to ranging we note first that at present, telemetry and ranging signals are sent in effectively a frequency division multiplexed format. This is accomplished by allowing the telemetry signal to occupy the lower region of the modulation spectrum and placing the ranging signal in the upper region. Actually, in more recent years the increasing telemetry rates have resulted in a significant degree of spectral overlap of these signals.

For suppressed carrier modulation this multiplexing method is not desirable, for two reasons; first of all the telemetry signal spectrum is quite broad and will most likely occupy all of the receiver IF bandwidth; second for suppressed carrier modulation this modulating signal would result in a transmitted signal with a nonuniform envelope which is undesirable from a power amplification standpoint. There is, however, an alternate method by which these two signals can be multiplexed which (1) eliminates interference between the telemetry and ranging signals, (2) allows complete freedom in selecting both the telemetry and ranging signal rates/frequencies (provided each one separately does not exceed the available IF bandwidth), and (3) allows processing with current DSN equipment. The technique simply involves modulating one component of a carrier with the telemetry signal and modulating a quadrature component of the carrier with the ranging signals. Both modulations are suppressed carrier in nature and the resulting signals are then summed using amplitudes appropriate for the necessary telemetry and ranging SNR requirements. Figure 3 shows the structure of the carrier modulator.

That this signal has the properties stated above can be seen quite easily. Interference resulting from spectral overlap is eliminated since the ranging and telemetry signals are in phase quadrature and can be easily isolated using a coherent receiver (even when their spectra overlap). Since they are isolated by phase then the presence of one does not in any way restrict the use of the other. Finally, with regard to processing, we note that the telemetry can be demodulated in the megabit-demodulator assembly as shown in Fig. 2b. Likewise the ranging signal *could* be demodulated on the other arm of the megabit-demodulator assembly. Unfortunately, this would result in a baseband ranging signal for which the DSN does not have a detector. However, recall that the receiver IF chain is still very much intact. As a result, the ranging signal can be processed from the 10 MHz IF in exactly the same way it is at present by simply ensuring that the reference in the Planetary Ranging Assembly (PRA) or MU II ranging machines are adjusted for the appropriate phase. This can easily be accomplished by a pretrack calibration.

The modulation scheme described above is really not a new scheme. It was originally developed at JPL as a suppressed carrier version of interplex modulation (Refs. 1 and 2). Its utility has been demonstrated on MVM-73 (in the residual carrier mode) and more recently has been used in the suppressed carrier mode on the Space Shuttle under the name of unbalanced quadraphase. It was demonstrated for MVM-73 that interplex modulation involving two telemetry signals could be processed by the existing DSN by proper phasing of the reference signals. Likewise, the interplex modulation of telemetry and ranging can be processed by the DSN with proper phasing. Finally, the suppressed carrier tracking configuration of Fig. 2b is also appropriate for tracking the suppressed carrier versions of interplex modulation (Refs. 1, 3 and 4).

VI. Conclusions

We have shown that to go to high data rates it is necessary to eliminate the use of subcarriers. We then demonstrated that a significant advantage in tracking loop SNR would result for changing from residual to suppressed carrier modulation. This gain in loop SNR is extremely desirable since it allows one to broaden the tracking loop bandwidth and hence simplifies the operational activities needed for signal acquisition without sacrificing tracking performance. Also a stronger loop SNR

means that the tracking loop is much less likely to be knocked out of lock by external RFI and results in improved navigation by means of reduced doppler jitter.

We next demonstrated that the current block IV receivers (or the block III receivers) could still be used in conjunction with the megasymbol demodulator assembly to track suppressed carrier signals. We next found that the doppler system was quite insensitive to the change to suppressed carrier with the only impact being the possibility of half cycle slips occurring, as well as full cycle slips. Finally we found that simultaneous telemetry and ranging, although impractical in the present format at high telemetry rates, could be easily handled by an unbalanced quadraphase signal format and that the resulting signal could be quite adequately processed by the existing DSN if simply augmented by the megasymbol demodulator assembly.

References

1. Butman, S., and Timor, U., "Suppressed Carrier Tracking for Two Channel Phase Modulated Telemetry" in Proceedings of the 1970 National Electronics Conference, pp. 758-761, 1970.
2. Butman, S., and Timor, U., "Interplex – An Efficient Multichannel PSK/PM Telemetry System", *IEEE Transactions on Communications*, Volume COM-20, No. 3, June 1972, pp. 415-419.
3. Levitt, B. K., Lesh, J. R., and Springett, J. C., "Shuttle/TDRSS Ku-Band Telemetry Study: Final Report" JPL internal report No. 900-742, Jet Propulsion Laboratory, Pasadena, California, April 5, 1976.
4. Lesh, J. R., "Costas Loop Tracking of Unbalanced QPSK Signals" submitted for presentation at the IEEE International Conference on Communications," Toronto, Canada, June 1978.

Table 1. Loop SNR degradation factor for residual carrier and $\theta = 60°$

R, dB	β, dB	$\frac{1}{1+2R}$, dB	$\cos^2\theta$, dB
0	-20.0	-4.8	-15.2
4	-23.0	-7.8	-15.2
10	-28.4	-13.2	-15.2

Table 2. Data power fraction α

BT_s	1	2	3	4	5
α	.903	.950	.966	.975	.980

Table 3. Loop SNR degradation factor for suppressed carrier tracking

R, dB	β', dB				
	$BT_s = 1$	$BT_s = 2$	$BT_s = 3$	$BT_s = 4$	$BT_s = 5$
0	-3.68	-5.14	-6.28	-7.19	-7.94
4	-2.03	-2.87	-3.65	-4.31	-4.90
10	-0.90	-1.05	-1.32	-1.60	-1.88

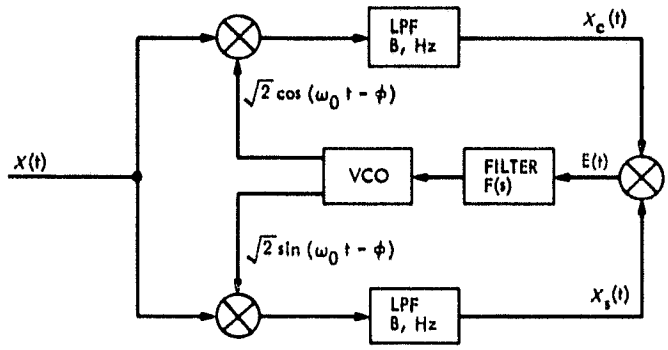

Fig. 1. Costas tracking loop

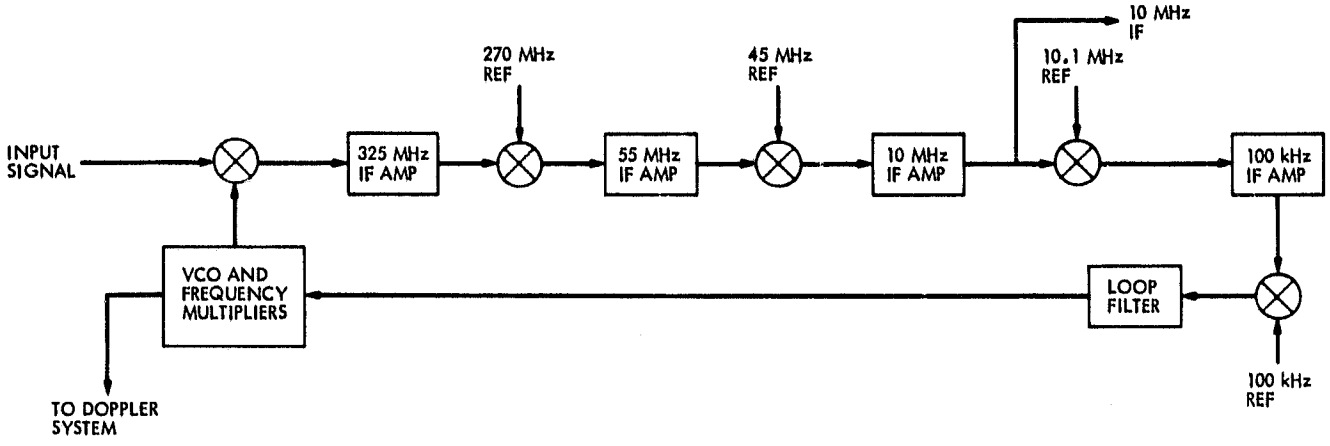

Fig. 2a. Simplified block IV receiver block diagram

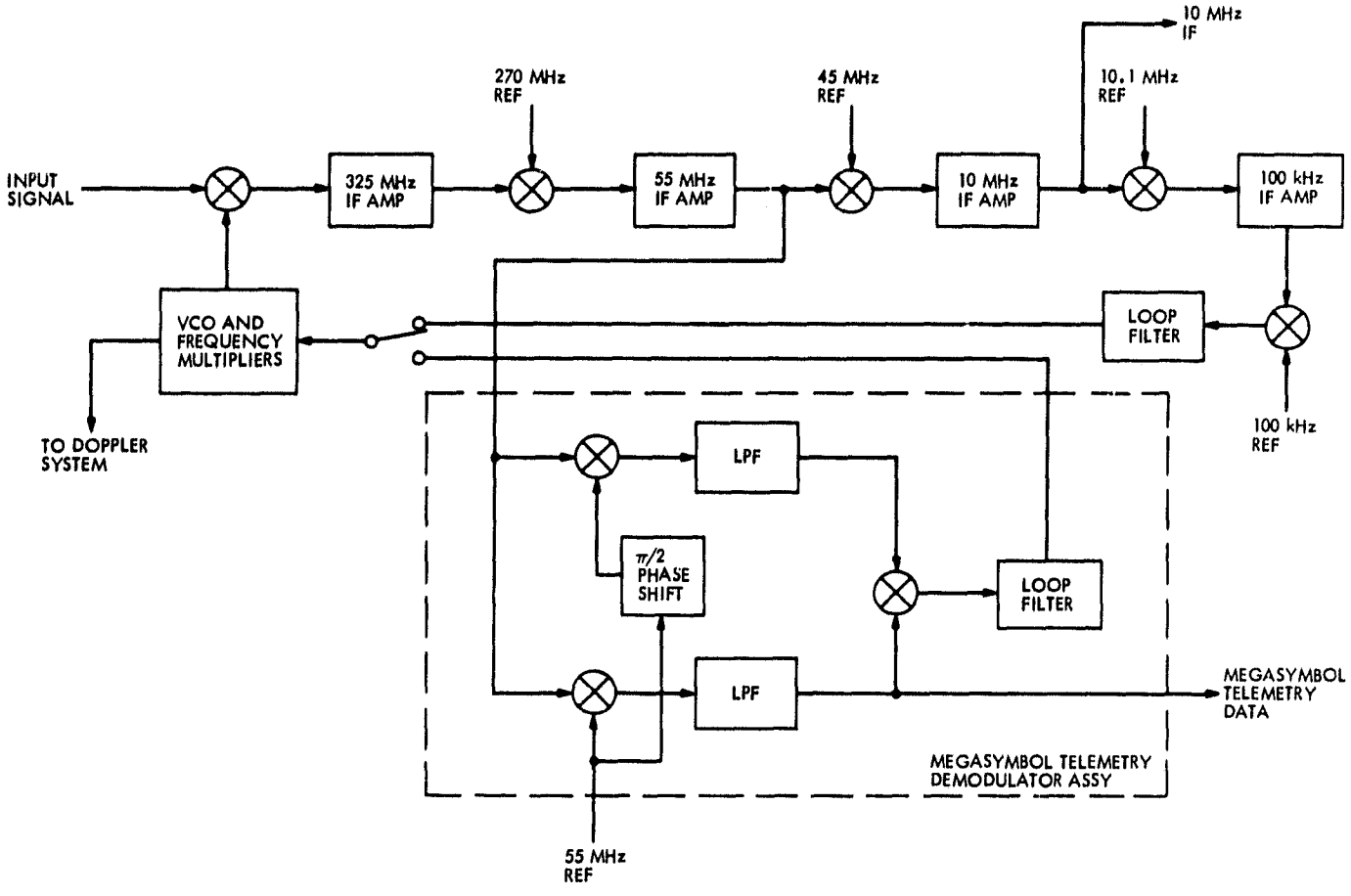

Fig. 2b. Modified block IV receiver block diagram for suppressed carrier

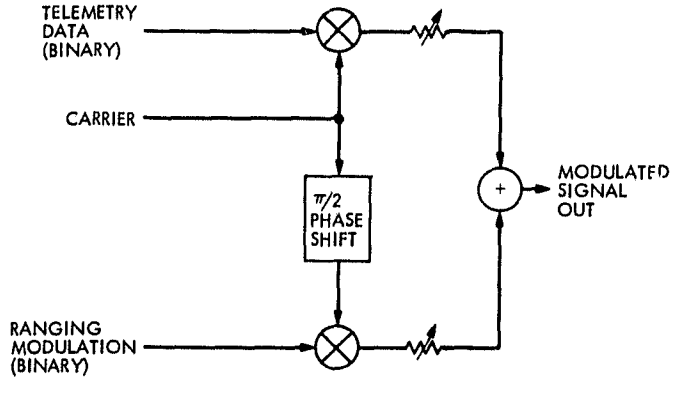

Fig. 3. Unbalanced QPSK modulator

ORIGINAL PAGE IS
OF POOR QUALITY

N78-24228

Developrnent Support — DSS 13 S-X Unattended Systems Development

E. B. Jackson
Radio Frequency and Microwave Subsystems Section

AT DSS 13 (the Venus Station), the subsystems necessary for telemetry reception from spacecraft have been placed under the control of an on-station supervisory computer (Station Controller) and various subsystem controllers, with control inputs originating from Network Operations Control Center (NOCC) at JPL, and monitor inputs from the various Station Subsystems available to the NOCC Operator. The controlled subsystems at DSS 13 include the Antenna and Servo, Microwave Configuration, Block III Receiver, and Subcarrier Demodulator Assembly.

System concepts, overall system description, computer controlled subsystem capabilities, and system testing are discussed. Testing, with control being exercised from NOCC at JPL, has been performed on both Helios and Voyager spacecraft. The test program is continuing.

I. System Concepts

The goal of the DSS 13 S-X Unattended Systems Development program is to demonstrate the capability to perform spacecraft tracking without the necessity for operator inputs at the station performing the tracking. Data are being collected and will be analyzed so as to obtain a measure of the cost effectiveness of station automation, including such factors as possible increased antenna user time availability and impact on station MTBF which may result from the added automatic equipment. Operation of the station is exercised from a remote location, such as Network Operations Control Center (NOCC) at JPL, using an overall supervisory computer (Station Controller), controlling subsystem microprocessors for each of the controlled subsystems. This supervisory computer and the subsystem microprocessors are located at the station. Control inputs from the operator at the remote location are minimal and communications with the Station Controller are via a High-Speed Data Line.

For the initial capability, it was decided to constrain the automatic capability to that required for the reception of spacecraft downlink telemetry, including Subcarrier Demodulation. (The remainder of the telemetry capability at a DSN Station is already computer controlled and could be made remote controlled with relatively minor development effort.) The subsystems chosen for modification at DSS 13 are the Antenna and Servo, Microwave Configuration, Block III Receiver and the Subcarrier Demodulator Assembly (SDA). The output of the DSS 13 SDA is transmitted to another DSN station at Goldstone for processing through the Symbol

Synchronizer Assembly (SSA) and Telemetry Processor Assembly (TPA). Subsequent transmission of telemetry data to NOCC is as now done.

These subsystems at DSS 13 have now been placed under computer control with capabilities which permit complete operation of these subsystems from a CRT Terminal located in NOCC, Bldg 230, at JPL. A block diagram of the system configuration is shown in Figure 1. The subsystem automatic control capabilities are described below.

II. System Description

A. Station Controller

The Station Controller, the supervisory computer in this system, is an 8080 based, JPL built, microprocessor, which communicates with the controlled subsystem controllers via a standard DSN star switch. All automatically controlled Subsystems, with the exception of the Antenna Controller, utilize a similar version of this 8080 based microprocessor. All communication between the NOCC Operator and the controlled subsystems is via the Station Controller, which accepts configuration, predict, and operational mode selection inputs. At the direction of the NOCC Operator, the Station Controller also controls the acquisition process.

B. 26-m Antenna and Servo

Starting with firm power on, but disconnected from the Servo Subsystem, the Antenna Controller, a MODCOMP II/25 Minicomputer, can automatically apply servo operating power, verify correct operation of the electrical and hydraulic components, and either move the antenna to any desired position or track any desired target using operator supplied pointing angle predicts. All movements are made in High-Speed Mode with controlled acceleration, at programmed speeds, until the antenna is at its desired pointing angle. The computer then automatically switches to Low-Speed Mode and tracks the computed target path. Several environmental and servo operational parameters are monitored continuously by the computer to ensure correct functioning. Table 1 "Servo Control Capabilities," Table 2 "Servo Parameters Monitored," and Table 3 "Antenna Movement Modes" list the automatic monitor and control capabilities of this subsystem.

This automated capability may be exercised either locally, using a Terminet as the computer I/O device, or remotely, using the CRT Operator Terminal in NOCC. In the latter case, the input is to the Station Controller and it directs and controls the actions taken by the Antenna Controller.

C. Block III Receiver

The Receiver Control Computer can control the receiver local oscillator frequency and provides initial conditions for the receiver tracking loop filter. Acquisition of the spacecraft downlink frequency is automatically accomplished by opening the receiver tracking loop, sweeping the local oscillator to the correct frequency, detecting the presence of the downlink, activating the tracking loop, stopping the sweep and phase-locking to the downlink carrier in a manner analogous to the actions taken manually by a skilled operator. The initial frequency, rate of sweep, acquisition time, start, and width of the sweep window are initially specified by the operator based on published predictions used by all DSN stations. These "predict" data are loaded into the Receiver Controller via the Station Controller.

D. Microwave Configuration

The configuration of the various microwave elements contained in the Cassegrain feedcone and antenna mounted electronics room is controlled by the positioning of three waveguide switches, two located in the feedcone and one located in the antenna electronics room. The positioning of these switches is under the control of the Microwave Configuration Controller and is specified by configuration information provided to the Microwave Configuration Controller by the NOCC Operator, through the Station Controller. Any possible switch position can be selected, based on configurations required by the track to be performed, e.g., "Transmitter Diplex" or "Low Noise Listen Only" modes.

E. Subcarrier Demodulator Assembly (SDA)

All of the front panel controllable, operational parameters of the Subcarrier Demodulator Assembly, whose selection is necessary for spacecraft subcarrier acquisition, are under the control of the SDA Controller. Table 4, "Controllable SDA Parameters," tabulates these parameters and their ranges. The value or position of these parameters is specified by the NOCC Operator to the Station Controller, which then directs the SDA Controller to effect selection. At the appropriate time, the Station Controller directs the SDA Controller to effect automatic acquisition of the spacecraft subcarrier.

III. System Operation

There are four modes through which the Unattended Operations Control will sequence to acquire spacecraft telemetry.

A. Station Controller Initialization

When the Station Controller Microprocessor is first initialized, it automatically enters a sequence wherein a diagnostic

routine checks that the input and output ports, and the controller memory are functioning correctly. The Controller then prompts the operator on input commands required to enter the next mode.

B. Controlled Subsystem Initialization

In this mode, selected by the Operator, each of the controlled subsystems is initialized, which includes verifying the communications link through the Star Switch, verifying memory operability, and verifying input and output ports. Successful completion of this mode substantiates, insofar as software diagnostics can determine, that the control microprocessors are functioning and are ready to accept configuration and predict data. The Station Controller then automatically enters the next mode.

C. Controlled Subsystem Configuration

In this mode, the Station Controller will accept, from the Operator, the configuration and predict information peculiar to the spacecraft to be tracked. This obviously includes antenna pointing, receiver operating frequency, microwave switch positions, and SDA data rate, bandwidth, and subcarrier frequency. Upon request, the Station Controller will display to the Operator the possible choices for each controlled subsystem. Upon completion of the input configuration and predict information, the Operator loads the various subsystems by instructing the Station Controller to "TRANSFER" the entered information. The Station Controller then automatically enters the next mode.

D. Controlled Subsystem Operate

Once in this mode, the Station Controller will respond to an Operator input command to "OPERATE," and the acquisition sequence begins.

IV. Acquisition Sequencing

Upon receipt of the message "ON POINT" from the 26-m Antenna Controller, the Station Controller automatically instructs the Block III Receiver Controller to commence acquisition of the spacecraft downlink carrier. Upon receipt of the message "RECEIVER IN LOCK," the Station Controller automatically instructs the SDA Controller to commence acquisition of the telemetry subcarrier. When the SDA completes acquisition of the telemetry subcarrier, it transmits the message "SDA IN LOCK" to the Station Controller and the acquisition sequence is complete. The base band spectrum output from the DSS 13 SDA is routed, via the microwave link, to another DSN station at Goldstone for symbol synchronization and decoding and transmission via HSDL to NOCC at bldg. 230, JPL. The NOCC Operator (DSN Controller), by observing the Station Controller generated messages displayed on his CRT Control Terminal, can monitor subsequent performance on his standard display, just as he would with any other DSN station.

V. System Testing

Commencing on 1 December 1977, the system as described above has been tested using Helios and Voyager spacecraft telemetry as test signals. Both DSS 11 and DSS 12 have been used as the DSN station with which telemetry processing is accomplished. Complete single point control, as described herein, has not yet been demonstrated as the 26-m Antenna Controller integration into the system is not yet completed. However, control, configuration, and predict loading of all other controlled subsystems have been repeatedly demonstrated successfully from NOCC with no operator input to these systems being accomplished locally at DSS 13.

Complete single point control, as described in this article, is anticipated to be demonstrated in the first week of March 1978. A description of the System Software will be reported in a later DSN Summary.

Table 1. Servo Control Capabilities

Function	Capability
Operating Power Management	Can either apply to start servo system or remove to shut down servo system.
Antenna Brakes	Can apply and release brakes selectively, on either axis, or can apply and release master brake (both axes simultaneously).
Antenna Speed	Can select, for either axis, either High or Low Speed as required by difference between antenna desired position and actual position.
Pre-limit	Can override a pre-limit warning.
Disable Condition	Can reset from Disable to Operate mode.

Table 2. Servo Parameters Monitored

Function	Type Monitor
Brake Status, both axes	Switch
Speed selected, both axes	Switch
Pre-limit Status, both axes	Switch
Final Limit Status, both axes	Switch
System Disable Status	Switch
Lubrication Available, Gearboxes	Flow Switch
Right Wrap-up of Cables	Switch
Left Wrap-up of Cables	Switch
Computer Control Selected	Switch
Differential Pressure, Elevation Low Speed Servo Valve	Transducer
Differential Pressure, Elevation High Speed Servo Valve, Left	Transducer
Differential Pressure, Elevation High Speed Servo Valve, Right	Transducer
Pressure, Elevation High Speed Hydraulic Fluid System Supply	Transducer
Pressure, Elevation Low Speed Hydraulic Fluid System Supply	Transducer
Differential Pressure, Azimuth High Speed Servo Valve	Transducer
Differential Pressure, Azimuth Low Speed Servo Valve	Transducer
Pressure, Azimuth High Speed Hydraulic Fluid System Supply	Transducer
Pressure, Azimuth Low Speed Hydraulic Fluid System Supply	Transducer
Fluid Level, System Hydraulic Fluid Supply Reservoir	Transducer
Wind Speed, South West Tower	Transducer
Wind Speed, South East Tower	Transducer
Wind Direction, South West Tower	Transducer
Wind Direction, South East Tower	Transducer
Temperature, Hydraulic Fluid Supply	Transducer
75 HP Starter In-Use?	Switch
125 HP Starter In-Use?	Switch
Volume Being Delivered, 75 HP Hydraulic Pump, Left	Transducer
Volume Being Delivered, 75 HP Hydraulic Pump, Right	Transducer
Volume Being Delivered, 125 HP Hydraulic Pump, Left	Transducer
Volume Being Delivered, 125 HP Hydraulic Pump, Right	Transducer

Table 3. Antenna Movement Modes

Mode	Description
RAMP (STOP)	Used to stop the antenna movement, without stowing, for whatever need.
AZIMUTH-ELEVATION	Used for positioning the antenna to some fixed coordinates, such as the near-field collimation tower or for maintenance purposes.
SIDEREAL	Used for tracking stars. Requires entry of current set of Right Ascension and Declination coordinates for desired target.
3-DAY FIT	Used for tracking spacecraft. Requires entry of three sets of Right Ascension and Declination coordinates, for the three successive days starting with day on which track is to be accomplished.

Table 4. Controllable SDA Parameters

Parameter	Range
INPUT SOURCE	Rcvr 1, Rcvr 2, Test, Tape
VCO LOOP FILTER SHORT	On, Off
VCO LOOP BANDWIDTH	Narrow, Medium, Wide
MODULATION INDEX	0 - 30 dB
SUBCARRIER FREQUENCY	100 - 1 × 10^6 Hz
SYMBOL RATE	5.6 - 270,000 symbols/second
OUTPUT PORT SELECTED	Demod, Test, Tape

ORIGINAL PAGE IS
OF POOR QUALITY

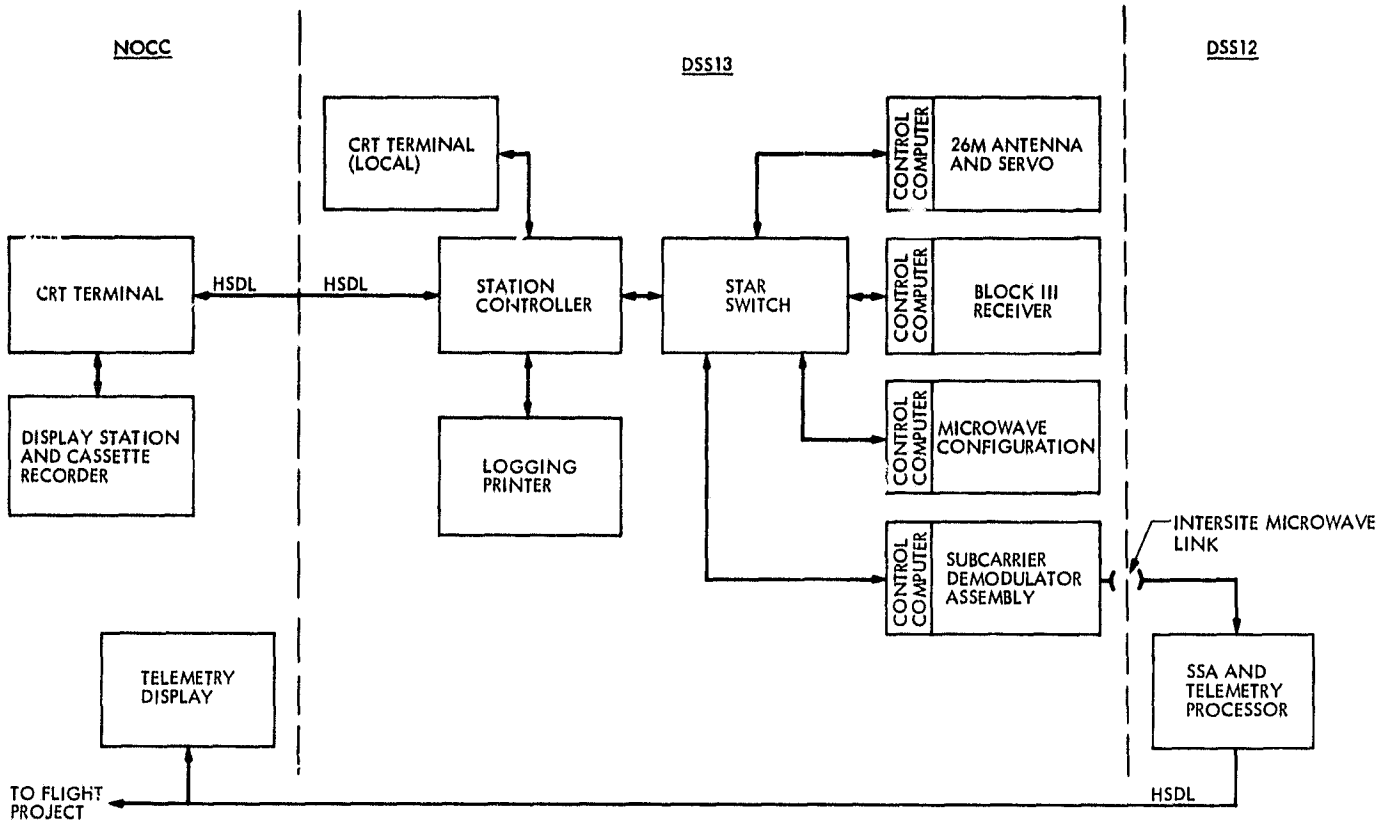

Fig. 1. DSS 13 unattended operations system configuration

N78-24229

The DSN Standard Real-Time Language

R. L. Schwartz, G. L. Fisher, and R. C. Tausworthe
DSN Data Systems Section

A set of requirements for the Deep Space Network Standard Real-Time Language has been recently drafted. This language will be a modern high-order programming language well-suited to the special needs of real-time programs developed for use in the Deep Space Stations and Network Operations and Control Center. Nearly all DSN real-time programming has, in the past, been done using assembly language. The implementation of a standard high-order language is being planned in order to promote the development of real-time programs with higher reliability, increased programmer productivity, language commonality, flexibility, and re-use potential, and to provide a means for reducing the current life-cycle costs of DSN software.

I. Introduction

The DSN real-time software includes tracking and data acquisition software and mission support software. These programs, typically driven by high-speed data interrupts, have rigid input/output format requirements and must interface with special-purpose external hardware.

Because of the serious time constraints imposed by the high-speed interrupts, and the strong dependencies on external data formats, these programs have in the past been written, for the most part, in assembly language. This practice has produced software with a high development and maintenance cost. As the hardware base has evolved over a period of years, and as different missions have imposed their differing constraints on the software, large existing programs have had to be almost completely redeveloped without substantial support from the earlier software.

The DSN system environment has in the past included a number of different small- to medium-size computers, with widely divergent characteristics. This diversified type of environment is expected to extend also into the foreseeable future. Future DSN capabilities, for example, are planned to include the use of single-chip microprocessors as part of the standard DSN set of Control and Computation Modules (CCMs).

A standard higher-order language specifically suited to the type of real-time programs developed by the DSN is needed to promote higher reliability, increased programmer productivity, language commonality, flexibility, and provide a means for reducing the current life-cycle cost of DSN software. A set of requirements for such a Deep Space Network standard real-time language has been recently drafted. This article summarizes that draft material. Work is continuing on refinements to these requirements, and completion of the language specification is scheduled for the end of this fiscal year.

II. Brief History of Language Design for Reliable Software

The development of higher-level computer programming languages is motivated by the desire to increase programmer productivity and make the process of programming independent of the particular machine used. The rapidly changing computer hardware, together with a rapidly expanding domain of problems to be handled by means of a digital computer, necessitates the viewing of a programming language as a vehicle for the expression of the problem in abstract terms, obviating a detailed machine-level specification of the algorithm. Thus, a programming language forms an interface between its users, who are concerned primarily with the ease of expression of a problem in abstract terms, and the instruction set on a particular real machine.

As the class of problems to be solved increases in scope and complexity, likewise does the necessary complexity of expression within the programming language. The ability of a user to understand and accurately communicate his intentions through the programming language necessarily becomes more difficult, yet at the same time becomes more crucial. The programming language must accept the burden of providing a vehicle for the expression of the problem in a conceptually clear manner in order to promote programmer understanding of what he has created.

This need has been recognized within the last decade, with various approaches being taken. After an early period, in which the development of extended assembly languages, such as FORTRAN, (Ref. 1) paralleled the development of computer architecture, the need for greater abstractions from the basic machine was recognized. The introduction of such languages as ALGOL 60 (Ref. 2) and LISP (Ref. 3) signalled the beginning of an age of higher-level languages primarily oriented toward the user. An attempt was made to formally express the semantics of these languages without reference to the concrete machine. This attempt at formalization of the semantics of a programming language was carried further by PL/1 (Ref. 4) and ALGOL 68 (Ref. 5) in very different manners. Both languages sought to increase the flexibility and universality of the language. ALGOL 68 chose to follow a course of greater orthogonality (using as few rules as possible, minimizing the number of special cases) and generalization of structure, leading to almost unbounded power being given to the bewildered programmer. PL/1 chose to increase the power of the language through a large set of constructs and specialized rules that the bewildered programmer needed to be aware of in order to express his or her problem.

Soon, a realization of the high cost of software production led to a methodology emphasizing a structured approach to the development of computer programs. This methodology initiated, among its supporters, a shift away from languages such as ALGOL 68 and PL/1, in favor of simpler languages with features encouraging more disciplined programming.

The programming language PASCAL (Ref. 6) was the earliest and perhaps the most successful of the languages to be designed at this time. PASCAL contains a minimum number of flow-of-control constructs, no default declarations or automatic type conversions, and a clear, concise syntax. PASCAL sought to treat language semantics in a manner that would allow both a precise implementation specification and a description of a formal (logical) system in which properties of the program could be derived (Ref. 7).

Various other languages, such as ALPHARD (Ref. 8), EUCLID (Ref. 9), GYPSY (Ref. 10), MADCAP-S (Ref. 11), STRUGGLE[1] (Ref. 12), and ALPO[1] (Ref. 13) have generally followed the same ideas of semantic description used by PASCAL, but each has proposed somewhat different sets of language features to increase program reliability, provability, power, etc.

The proliferation of programming languages and the resulting program incompatibilities which have occurred in the last five to ten years have spurred various large users of software toward the development of a standard programming language (cf. Ref. 14). The British government adopted the CORAL 66 (Ref. 15) programming language as its standard in 1975, the German government is now completing their standardization on the language PEARL (Ref. 16), and the French government is currently working on defining a French standard language. The U.S. Department of Defense has recently completed a study to define the requirements of a DOD standard real-time higher-order language (Refs. 17, 18), to be used in all defense system applications. The language, to be called DOD-1 (with PASCAL as its base language), is scheduled to be rigorously defined and a test translator for it implemented by early 1979. The DSN has patterned its draft requirements, summarized here, after the DOD requirements.

III. Goals for the DSN Standard Real-Time Language

This section lists and discusses a set of general goals to be met by the DSN standard real-time language. These are presented in their approximate order of importance.

A. Life Cycle Cost Effectiveness

The overriding goal of using the DSN standard higher-order language is to reduce the life cycle cost of DSN software,

[1]These languages have not been implemented.

including initial development cost, maintenance and operation cost over the system lifetime, and costs associated with retiring a program (de-implementation), if any.

A great deal of each new DSN software system development is a repetition of programming processes that have been written before. Yet, many DSN systems are started from scratch with little benefit from this previous work, other than what an individual programmer might remember having been a part of the previous project. Higher-order languages are preferred, of course, and used when possible, but the assembly language of the host machine is usually necessary at present. Even with the "same" higher-order language, differing dialects and local computer system alterations make it almost impossible to sustain a truly powerful production environment.

The DSN standard higher-order real-time language will remain stable (except under DSN Engineering Change Control Board direction) to ensure efficient reutilization of once-written software. Such stability will also tend to minimize the cost of sustaining an effective production environment.

B. Reliability

Real-time programs in the DSN control critical real-time processes in which there is a potentially severe penalty for faulty operation. DSN Software therefore must strive toward total reliability. The DSN standard real-time programming language will support a programming environment which fosters the creation of well-structured, readable, understandable, testable, manageable programs. Such characteristics in a program are known to promote program reliability through fewer design faults, decreased scope of error, and increased ease in fault detection, location, and repair.

C. Efficiency

For programs that demand it, the object code generated by the language translator must be efficient at run-time, mainly in terms of speed of execution, but also in terms of storage requirements. The handling of high-speed telemetry interrupts, for example, necessitates rapid response and processing speeds. The DSN real-time language must therefore provide users a means to optimize time-critical portions of their programs when necessary. Since such optimization is likely to be very machine-dependent, the real-time language must permit users to access low level features of the host machine in a way not conflicting with other goals of the language.

D. Maintainability

DSN programs written in any language must be maintainable. Recent industry studies (Ref. 19) and DSN qualitative studies have shown that program maintenance accounts for some 60% of the life-cycle costs of large programs.

Programs are made maintainable by modular construction, functional organization, localized scoping of data connections, simple control structures, the absence of special default features, easily understandable higher-level language constructs, and a stable, controlled programming environment. Additionally, maintainability relates to the availability of diagnostic tools and measurement aids which support the calibration, alteration, fault detection, fault isolation and location, and repair of the program. The DSN real-time language will form the kernel of a unified total programming system which will accommodate all of these needs.

E. Stability

The programming environment within which software is developed needs to be stable in order to provide reasonable assurances of the long-term reliability, validity, maintainability, and reusability of DSN Software. The programming system must have evolutionary potentials and avenues for change, lest it become inadequate for future missions. However, such evolution must be at a controlled, cost-effective pace.

The DSN standard real time language and its processor designs will be owned, implemented, and maintained by the DSN. Alterations will only be permitted as directed by DSN Engineering Change Control Board[2] action. Such changes will invariably require assessment of impacts, costs, and benefits prior to the implementation of new or altered features.

F. Training

The time required to learn the DSN standard real time language should be relatively short. In relation to this goal, the DSN standard real time language is required to be similar in certain ways with other languages being used in the DSN (principally MBASIC™ (Refs. 20, 21)). The features of the DSN language are meant to be English-like and self-descriptive. Nevertheless, the features will be well documented, with an accurate description of the language semantics oriented toward the understanding level of its users.

G. Transportability

Due to the range and diversity of programmable hardware in the DSN, reusability of software items relies on portability of program parts and transferability of personnel skills among the various machines used. Even among real-time programs with device and machine dependencies, there are a great number of operations, human and program, common among different software efforts on the different machines. The standard language will provide a means to isolate those portions of real-time programs which do and do not have an inherent

[2]Or other JPL or NASA responsible authority.

machine dependence, so that significant portions of programs may be reused as needed in other DSN applications.

The standard language will also increase the transportability of programmer knowledge and skill. The DSN standard real-time language is intended to allow each programmer to apply his or her skills among all machines and other tasks being done in the DSN.

IV. General Philosophy of Requirements

The DSN standard real-time language is intended to be a small, efficient, real-time-oriented, state-of-the-art, modern programming language for the DSN which can be adapted, via its extensible nature, to be useful for the entire spectrum of DSN real-time applications over the wide range of hardware characteristics projected for future use. The "smallness" of the language is meant to accommodate generality of expression while creating efficient programs using an affordable compiler (a few man-years per implementation).

The DSN real-time operational environment differs in important ways from machine to machine, and the needed features of DSN programs vary, depending on the particular machine and subsystem. Because of this, those facilities that can be better programmed as subsystem-dependent or hardware-dependent subroutines or macros have not been included in the real-time language requirements. The language therefore will have only very basic built-in input/output facilities, no specific mechanisms for parallel processing (other than interlocks), no co-routine syntax, and no built-in data types or constructs to handle the special and diversified hardware characteristics found in the present DSN hardware. All of these special characteristics will, however, be accommodatable by macros and subroutines written in the language which, by means of standard libraries, can be shared by groups of users.

A general principle that has been used in the formulation of the requirements is that the choice of syntax and semantics should follow the principle of "least astonishment." That is, there is probably a flaw in the language design if the "average programmer" is astonished to learn about some aspect of the language. The language is meant to appear sensible both to the average skilled programmer and the language specialist alike.

V. Language Requirements

The specific requirements of the language have been assembled in keeping with the general goals and requirements philosophy outlined above.

Briefly, the overall requirements to be satisfied by the language are:

(1) Statement-oriented.

(2) Supports top-down structured development of programs

(3) Strongly typed with full compile-time type checking

(4) Extensible, supporting data abstraction by means of a data definition facility

(5) Multi-layered language with several levels of definitional power

(6) Able to control non-standard external devices

(7) Allows separate compilation of program segments with full interface verification prior to execution

(8) Part of a total programming environment

(9) Compilable on DSN standard minicomputers

(10) Generates code for DSN standard minicomputers and CCM's

In this section we describe the salient features of the language which revolve around the data definition facility: its role in supporting data abstraction, its expanded definitional power, and its use in controlling real-time processes. We also briefly introduce the concept of a total programming environment for language support. Subsequent DSN Progress Report articles will describe these and other aspects of the language in more detail.

A. User Data Definition Facility

The DSN standard real-time language supports data abstraction by allowing the user to define new data types and operations within programs. New data types are defined by specifying the class of data objects comprising the type and the set of operations applicable to that class. The definition of the class of objects and operations on the objects is done by using the composition of previously defined data types and control structures, which, if required, can be augmented by the use of a medium-level, closer-to-machine-language layer described in section B below.

Once defined, these abstract data types may be used as one would use a built-in type; one may declare identifiers ranging over the data type, then operate on the data by means of the defined operations. By allowing access to the new object only by means of the pre-defined operators, an *encapsulation* of the data definition supporting the abstraction occurs, thereby guaranteeing the integrity of the object being defined; that is, no unauthorized modification of the representation may occur.

The number of specialized capabilities needed for a common language for all DSN real-time programming tasks is large and diverse. In many cases, there is no consensus as to the form these capabilities should take in a programming language. No higher-order language can build in all the features useful to a broad spectrum of applications, or which would anticipate future applications and requirements, or even provide a universally "best" capability in support of a single application area. Assembly language has had to serve as the main language tool for most existing DSN (and other) real-time programs because no higher order language has been available that can accommodate both the very low-level programming constructs as well as higher-order abstractions.

To require that a language be implemented which has only those primitives in the language required to handle current DSN applications is to build in obsolescence. Rather, the DSN real-time language must be robust in order to survive evolving hardware and software requirements. It must contain all the power necessary to satisfy current applications, yet, at the same time, contain the ability to extend that power to new and different application tasks.

A language with facilities for defining data and operations restricted to that data offers the capability to add new application-oriented structures and to use new programming techniques and mechanisms through descriptions written entirely within the language. It accommodates communication with non-standard external devices and diverse operating environments. The DSN standard real-time language definitions will have the appearance and costs of features which are built into the language while actually being catalogued as accessible application packages.

No single programming language can fulfill all the goals set forth earlier; but the DSN language, with its data and operation definition facilities, can adapt to meet changing requirements in a variety of areas while yet remaining very stable itself, thereby promoting efficiency, maintainability, reusability, etc.

B. Multi-Layered Language

The implementation of an abstract data type via the DSN standard real-time language data definition facility will be permitted to have more expressive power than will be allowed in the rest of the user program. Inside a data definition structure, the pointer data type may be used in order to implement the representation of linked structures or other data objects requiring the use of a pointer. Additional lower-level language features available only within the data definition facility include 1) a medium-level language layer which is closer to the machine language of the host computer, 2) calls to routines coded in other supported languages, and 3) operating system calls. Each of these capabilities is particularly important to support efficient control of real-time processes.

The medium-level, closer-to-the-machine-language layer will provide a machine-dependent method of accommodating those portions of DSN real-time programs which must absolutely have access to specific machine architecture or bit and byte level manipulations. The layer will consist of the normal high-level control constructs, a set of special machine-level data types (such as bit and byte), and a series of built-in functions which provide a one-to-one correspondence to the instructions present on the base machine. This medium-level language layer will thus provide machine-level access together with the high-level structuring tools present in high-level languages. A special machine-specific medium-level language will be required for each implementation.

Such a medium-level language concept is not new; it began with the medium-level language PL/360 (Ref. 22) developed by Niklaus Wirth for the IBM 360 in 1972. Since then, similar languages have been developed for many machines, following the style of PL/360.

The layered-language capability can be used, for example, to define a DSN standard (but not built-in) library data type called, say HIGH_SPEED_DATA_BLOCK, with data-accessing operations coded using the medium-level layer to unpack and retrieve the information as well as allocate and deallocate blocks as necessary.

C. Real-time Input/Output Control

The DSN standard real-time language will support control of real-time processes, both through generalized input/output operations and the use of its data definition facilities. The language will also provide an interlock construct as a primitive mechanism for programming data definitions used for synchronization of parallel and concurrent processes.

A large part of many DSN real-time programs is directly concerned with awkward or application-tailored input and output equipment, which have curious input/output instructions and special status words, and which deal with data in elaborate non-standard, machine-dependent formats, none of which can be clothed in the comfortable abstractions of a high-level programming language. As mentioned earlier, it is not possible for a single standard higher-level real-time language to contain efficient real-time constructs which are sufficiently general to be able to handle all, or even part, of the peripheral device interfaces likely to be seen in the DSN real-time environment.

Accordingly, any communication with external devices which is not possible via the built-in input/output constructs in the DSN standard real-time language can be handled by means of the data definition facility. The programmer will be able to define an abstract data type and operations which handle the necessary protocols and perform all the necessary communications. Inside the data definition structure, the programmer will have the use of the pointer data type, the medium-level language layer, calls to routines coded in other supported languages, and operating system requests.

D. The Total Programming Environment

The DSN standard real-time language will not necessarily require that the object machine have an operating system. The language implementations initially will be suitable for programming both the DSN standard minicomputer and the Control and Computation Modules (microprocessors). The language translator is currently planned for implementation on the DSN standard minicomputer, with a cross-compilation capability for compiling programs targeted for the Control and Computation Modules. There is no requirement for self-hosting on the CCMS.

The mere availability of a particular language processor by itself is not sufficient to satisfy the goals which have been set forth earlier. The time is past in which a modern language can be considered apart from the programming system in which it resides. The presence of synergistic tools to support program development is an essential factor in the cost-effective fabrication of programs of the complexity found in DSN tasks. For these reasons, and following the precedents of ECL (Ref. 23) and MBASIC™, the DSN real-time language will require a programming system designed specifically for the language. Among the elements of this programming system are (1) an intelligent text-editor, with features designed to aid in the coding of programs written in the language; (2) an intelligent linkage-editor (collection program) with facilities for resolving more of the module interfaces than just addresses; (3) a run-time support system that includes an intelligent, interactive test-probe capability; (4) an interactive mode of program development testing, with some emulation of the real-time environment; (5) a monitor capability which will provide performance measurement information, such as the total number of object code instructions, the machine cycle times required to support each of the statements in the standard language, the statement execution frequency counts, and the time-sampling statistics collected at run-time (either in interpretive or compiled-mode operation). Such performance measurements lead to programmer awareness of the time and storage characteristics of his code, and can substantially improve or optimize source code as required to meet applications constraints.

VI. Conclusion

The requirements reported in this article are, at this writing, in a preliminary state. Completion of the requirements and the endorsement of these by both programmatic and implementation organizations is required before the actual language and processor design activities begin. Liaison with institutional and flight-support computing efforts in their current quest for a JPL-wide standard real-time language may also be expected to influence the final set of requirements. (The current belief is that the DSN standard real-time language can form a kernel subset of the JPL standard real-time language, for the middle-to-large class of machines).

The authors do not mean to imply by this article that a new language must be invented to fulfill the requirements summarized here. However, since no higher-order languages currently implemented on DSN machines have been deemed adequate for DSN tasks (as borne out by the almost total reliance on assembly language), it seems fairly certain that whatever language is ultimately chosen (existing, adapted, or invented), the processor for that language will have to be designed, documented to DSN standards, and implemented. Current plans call for the completion of the DSN real-time language on the MODCOMP-II by the end of FY-80 and on the CCM's by the end of FY-81.

References

1. Engel, Jr., F., et al., "Draft Proposed ANS FORTRAN," *ACM SIGPLAN Notices*, 11(3), March 1976.

2. Naur, P. (ed.), "Revised Report on the Algorithmic Language ALGOL 60," *Comm. ACM 6*, pp. 1-17, 1963.

3. McCarthey, et al., *LISP 1.5 Programmer's Manual*, MIT Press, Cambridge, Mass., 1966.

4. IBM, "PL/1 Language Specification," Form GY33-6003-2, White Plains, New York.

5. van Wijngaarden, et al., "Revised Report on the Algorithmic Language ALGOL 68," *Acta Informatica* 5,1-3, January 1976 (also appeared in SIGPLAN Notices).

6. Wirth, N., "The Programming Language PASCAL," *Acta Informatica 1*, Vol. 1, pp. 35-63, 1971.

7. Hoare, C.A.R., N. Wirth, "An Axiomatic Definition of the Programming Language PASCAL," *Acta Informatica* 2, pp. 335-355, 1973.

8. Wulf, W. A., R. L. London, M. Shaw, "Abstraction and Verification in ALPHARD: Introduction to Language and Methodology," Computer Science Department, Carnegie Mellon University, June 1976.

9. Lampson, B. W., J. J. Horning, R. L. London, J. G. Mitchel, G. V. Popek, "Report on the Programming Language Euclid," ACM *SIGPLAN Notices*, 12(2), February 1977.

10. Ambler, A. L., et al., "Gypsy: A Language for Specification and Implementation of Verifiable Programs," Report ICSCA-CMP-2, University of Texas at Austin, January 1977.

11. Lauterback, C., C. Lucena, B. Moszkowski, "On the Use of MADCAP for the Development of Correct Programs," Computer Science Department, Internal Memorandum 132, UCLA, September 1974.

12. Berry, D. M., L. Chirica, Z. Erlich, C. Lucena, E. Walton, "STRUGGLE" Structured Generalized Goto-less Language," Internal Memo 147, Computer Science Department, UCLA, 1974.

13. Dembinski, P., G. Inglas, R. Schwartz, J. Takemura, "ALPO: A Language That's Proof Oriented," in R. Uzgalis (ed.), *Four Languages: Experiments in Computer Language Design*, UCLA-ENG-7544, Computer Science Department, UCLA, July 1975.

14. American National Standards Institute Inc., reports of periodic meetings of the committee in charge of Programming languages for the Control of Industrial Processes, ISO/TC97/SC5/WG1.

15. *Official Definition of CORAL* 66, Inter Establishment Committee on Computer Applications, ISBN 0 11 4702217, London, 1970.

16. PEARL Status as of October 1976, ANSI Committee Report ISO/TC97/SC5/WG1 N21, October 1976.

17. Fisher, D. A., "A Common Programming Language for the Department of Defense, Background and Technical Requirements," Institute for Defense Analysis, NTIS Distribution 77-000275, June 1976.

18. "Department of Defense Requirements for High Order Computer Programming Languages – Revised Ironman," July 1977 (appearing in ACM SIGPLAN Notices 12(12), December 1977).

19. Ross, D., "Homilies for Humble Standards," *Comm. ACM 9(11)*, pp. 1-14, 1976.

20. *MBASIC Fundamentals*, Vol. 1, Jet Propulsion Laboratory Internal Document 900-752, February 1974.

21. *MBASIC, Vol. 2, Appendices*, Jet Propulsion Laboratory, Internal Document 900-752, February 1974.

22. Wirth, N., "PL360-A Programming Language for the 360 Computers," *Journal of the ACM*, Vol. 15, No. 1, pp. 37-74.

23. Wegbreit, B., et al., "The ECL Programming System," *Proc. AFIPS* 39, pp. 253-262, 1971.

N78-24230

On Decoding of Reed-Solomon Codes Over GF(32) and GF(64) Using the Transform Techniques of Winograd[1]

I. S. Reed
Department of Electrical Engineering
University of Southern California

T. K. Truong and B. Benjauthrit
TDA Engineering

A new algorithm for computing a transform over GF(2^n), where $n = 5, 6$, is developed to encode and decode Reed-Solomon (RS) codes of length $2^n - 1$. Such an RS decoder is considerably faster than the conventional transform decoder over GF(2^n).

I. Introduction

Fast real-valued transforms over the group $(Z_2)^n$ were developed first by Green (Ref. 1) to decode the (32,6) Reed-Muller code (Ref. 2) used by JPL in the Mariner and Viking space probes. Recently Gore (Ref. 3) extended Mandelbaum's methods (Ref. 4) for decoding Reed-Solomon codes. He proposed to decode RS codes with a finite field transform over $GF(2^n)$, where n is an integer. Michelson (Ref. 5) implemented Mandelbaum's algorithm and showed that the decoder, using the transform over $GF(2^n)$, requires substantially fewer multiplications than a standard decoder (Refs. 6-8). The disadvantage of his transform method over $GF(2^n)$ is that the transform length is an odd number, so that the most efficient FFT algorithm cannot be used.

In this paper, a new algorithm based on the methods of Winograd (Refs. 9, 10) is developed to compute a transform over $GF(2^n)$ for $n = 5, 6$. This transform algorithm over $GF(2^n)$ for $n = 5, 6$ requires fewer multiplications than the conventional fast transform algorithm described by Gentleman (Ref. 11). The algorithm is presented in detail in this paper only for the cases $n = 5, 6$. This algorithm for RS codes over $GF(2^n)$, where $n = 2^m$, has been treated previously by the authors using similar procedures (Ref. 12).

[1]This work was supported in part by the U.S. Air Force Office of Scientific Research under Grant AFOSR-75-2798.

II. Cyclic Convolutions

The following algorithm for the cyclic convolution of two sequences is based on ideas due to Winograd (Refs. 9, 10). Let $GF(2^n)$ be the Galois field of 2^n elements. Observe first that if $X(u) = x_0 + x_1 u^m$, $Y(u) = y_0 + y_1 u^m$ for $m = 1, 2$, be two polynomials over $GF(2^n)$, then the product $T'(u) = X(u)Y(u)$ is computed as follows:

$$T'(u) = X(u)\,Y(u) = c_0 + c_1 u^m + c_2 u^{2m} \tag{1}$$

where $c_0 = x_0 \cdot y_0$, $c_1 = (x_0 + x_1) \cdot (y_0 + y_1) + x_0 \cdot y_0 + x_1 \cdot y_1$, and $c_2 = x_1 \cdot y_1$. Evidently there are exactly three multiplications required to compute (1).

It is well known (Ref. 9) that if

$$X(u) = \sum_{k=0}^{n-1} x_k u^k$$

and

$$Y(u) = \sum_{k=0}^{n-1} y_k u^k$$

are $(n-1)$-th degree polynomials, then the cyclic convolution of the coefficients of $X(u)$ and $Y(u)$ is given by the coefficients of

$$T(u) = X(u)\,Y(u) \equiv \sum_{k=0}^{n-1} Z_k u^k \bmod (u^n - 1).$$

Now factor the polynomial $u^n - 1$ over $GF(2^n)$ into irreducible relatively prime factors, i.e.,

$$u^n - 1 = \prod_{i=1}^{k} g_i(u),$$

where $(g_i(u), g_j(u)) = 1$ for $i \neq j$.

Then $T(u)$ mod $g_i(u)$ for $i = 1, 2, \ldots, k$ can be computed, using Eq. (1). To evaluate $T(u)$ from these residues the Chinese remainder theorem is used. To show this, consider first the cyclic convolution of 3 elements. This is given in matrix form as follows:

$$\begin{pmatrix} y_0 \\ y_1 \\ y_2 \end{pmatrix} = \begin{pmatrix} a_0 & a_1 & a_2 \\ a_1 & a_2 & a_0 \\ a_2 & a_0 & a_1 \end{pmatrix} \begin{pmatrix} x_0 \\ x_1 \\ x_2 \end{pmatrix} \tag{2}$$

where $y_i, a_i, x_i \in GF(2^n)$ for $i = 0, 1, 2$. The above convolution is obtained from the coefficients of

$$T(u) = (a_2 + a_0 u + a_1 u^2) \cdot (x_2 + x_1 u + x_0 u^2) \bmod (u + 1)(u^2 + u + 1) \tag{3}$$

where $(u + 1)$ and $(u^2 + u + 1)$ are the irreducible factors of $u^3 - 1$ over $GF(2)$.

To compute (3), let $m(u) = (u + 1)(u^2 + u + 1) = m_1(u)\, m_2(u) = m_1(u)\, M_1(u) = m_2(u)\, M_2(u)$. The system of congruences $T(u) = T_i(u) \bmod m_i(u)$ for $i = 1, 2$ is given by

$$T_1(u) \equiv (a_2 + a_0 u + a_1 u^2) \cdot (x_2 + x_1 u + x_0 u^2) \bmod (u - 1) = (a_2 + a_0 + a_1) \cdot (x_2 + x_1 + x_0)$$

and

$$\begin{aligned} T_2(u) &\equiv (a_2 + a_0 u + a_1 u^2) \cdot (x_2 + x_1 u + x_0 u^2) \bmod (u^2 + u + 1) \\ &\equiv [(a_2 + a_1) + (a_0 + a_1) u] \cdot [(x_2 + x_0) + (x_1 + x_0) u] \bmod (u^2 + u + 1) \end{aligned}$$

By (1), $T_2(u)$ is given by

$$\begin{aligned} T_2(u) \equiv\ & (a_2 + a_1) \cdot (x_2 + x_0) + [(a_2 + a_1 + a_0 + a_1) \cdot (x_2 + x_0 + x_1 + x_0) + (a_2 + a_1) \cdot (x_2 + x_0) \\ & + (a_0 + a_1) \cdot (x_1 + x_0)] u + (a_0 + a_1) \cdot (x_1 + x_0) u^2 \\ \equiv\ & (a_2 + a_1) \cdot (x_2 + x_0) + (a_0 + a_1) \cdot (x_1 + x_0) + [(a_2 + a_0) \cdot (x_2 + x_1) \\ & + (a_2 + a_1)(x_2 + x_0)] u \bmod (u^2 + u + 1) \end{aligned}$$

Evidently 3 multiplies are actually needed to compute $T_2(u)$. By Chinese remainder theorem for polynomials (Ref. 13), $T(u)$ can be reconstituted from $T_1(u)$ and $T_2(u)$ by

$$T(u) \equiv T_1(u)\, M_1(u)\, M_1^{-1}(u) + T_2(u)\, M_2(u)\, M_2^{-1}(u) \bmod u^3 - 1 \tag{4}$$

where $M_i^{-1}(u)$ uniquely satisfies the congruence

$$M_i(u)\, M_i^{-1}(u) \equiv 1 \bmod m_i(u) \text{ for } i = 1, 2.$$

These equations are satisfied by $M_1^{-1}(u) = 1$ and $M_2^{-1}(u) = u$. Hence

$$\begin{aligned} T(u) \equiv\ & (a_2 + a_0 + a_1) \cdot (x_2 + x_1 + x_0) + (a_2 + a_0) \cdot (x_2 + x_1) + (a_2 + a_1) \cdot (x_2 + x_0) + [(a_2 + a_0 + a_1) \cdot (x_2 + x_1 + x_0) \\ & + (a_2 + a_1) \cdot (x_2 + x_0) + (a_0 + a_1) \cdot (x_1 + x_0)] u + [(a_2 + a_0 + a_1) \cdot (x_2 + x_1 + x_0) + (a_0 + a_1) \cdot (x_1 + x_0) \end{aligned}$$

ORIGINAL PAGE IS
OF POOR QUALITY

$$+(a_2+a_0)\cdot(x_2+x_1)]\,u^2$$

$$\equiv y_0+y_1u+y_2u^2 \bmod (u^3-1)$$

where

$$\begin{aligned} y_0 &= (a_2+a_0+a_1)\cdot(x_2+x_1+x_0)+(a_2+a_0)\cdot(x_2+x_1)+(a_2+a_1)\cdot(x_2+x_0)\\ y_1 &= (a_2+a_0+a_1)(x_2+x_1+x_0)+(a_2+a_1)\cdot(x_2+x_0)+(a_0+a_1)\cdot(x_1+x_0)\\ y_2 &= (a_2+a_0+a_1)\cdot(x_2+x_1+x_0)+(a_0+a_1)\cdot(x_1+x_0)+(a_2+a_0)\cdot(x_2+x_1) \end{aligned} \tag{5}$$

If one lets

$$\begin{aligned} m_0 &= (a_2+a_0+a_1)\cdot(x_2+x_1+x_0)\\ m_1 &= (a_2+a_0)\cdot(x_2+x_1)\\ m_2 &= (a_2+a_1)\cdot(x_2+x_0)\\ m_3 &= (a_0+a_1)\cdot(x_1+x_0) \end{aligned} \tag{6}$$

Then (5) becomes

$$\begin{aligned} y_0 &= m_0+m_1+m_2\\ y_1 &= m_0+m_2+m_3\\ y_2 &= m_0+m_3+m_1 \end{aligned}$$

From (6) the total number of multiplications needed to perform (2) is exactly 4. Now consider cyclic convolutions of 5 elements of $GF(2^n)$. Again such a convolution can be represented in matrix form as

$$\begin{pmatrix} y_0\\ y_1\\ y_2\\ y_3\\ y_4 \end{pmatrix} = \begin{pmatrix} a_0 & a_1 & a_2 & a_3 & a_4\\ a_1 & a_2 & a_3 & a_4 & a_0\\ a_2 & a_3 & a_4 & a_0 & a_1\\ a_3 & a_4 & a_0 & a_1 & a_2\\ a_4 & a_0 & a_1 & a_2 & a_3 \end{pmatrix} \begin{pmatrix} x_0\\ x_1\\ x_2\\ x_3\\ x_4 \end{pmatrix} \tag{7}$$

where y_i, a_i, $x_i \in GF(2^n)$ for $i = 0, 1, 2, 3, 4$. The matrix in (7) is a 5×5 cyclic matrix. This matrix equation can be obtained also as the set of coefficients of

$$(a_4 + a_0u + a_1u^2 + a_2u^3 + a_3u^4)(x_4 + x_3u + x_2u^2 + x_1u^3 + x_0u^4) \bmod (u^5 - 1),$$

where $u^5 - 1$ factors into two irreducible factors over $GF(2)$ as follows,

$$u^5 - 1 = (u + 1)(u^4 + u^3 + u^2 + u + 1),$$

Let $m(u) = (u + 1)(u^4 + u^3 + u^2 + u + 1) = m_1(u)\, m_2(u) = m_1(u)\, M_1(u) = m_2(u)\, M_2(u)$. The system of congruences $T(u) \equiv T_i(u) \bmod m_i(u)$ for $i = 1, 2$ for this case is given by

$$T_1(u) \equiv (a_4 + a_0u + a_1u^2 + a_2u^3 + a_3u^4) \cdot (x_4 + x_3u + x_2u^2 + x_1u^3 + x_0u^4)$$

$$\equiv (a_4 + a_0 + a_1 + a_2 + a_3) \cdot (x_4 + x_3 + x_2 + x_1 + x_0) \bmod (u - 1) \tag{8a}$$

and

$$T_2(u) \equiv (a_4 + a_0u + a_1u^2 + a_2u^3 + a_3u^4) \cdot (x_4 + x_3u + x_2u^2 + x_1u^3 + x_0u^4)$$

$$\equiv [(a_4 + a_3) + (a_0 + a_3)\, u + (a_1 + a_3)\, u^2 + (a_2 + a_3)\, u^3]$$

$$\cdot [(x_4 + x_0) + (x_3 + x_0)\, u + (x_2 + x_0)\, u^2 + (x_1 + x_0)\, u^3] \bmod (u^4 + u^3 + u^2 + u + 1) \tag{8b}$$

In order to compute (8b), let $c_0 = (a_4 + a_3)$, $c_1 = (a_0 + a_3)$, $c_2 = (a_1 + a_3)$, $c_3 = (a_2 + a_3)$, $d_0 = (x_4 + x_0)$, $d_1 = (x_3 + x_0)$, $d_2 = (x_2 + x_0)$, $d_3 = (x_0 + x_1)$. Thus,

$$T_2(u) = [c_0 + c_1u + c_2u^2 + c_3u^3] \cdot [d_0 + d_1u + d_2u^2 + d_3u^3] \bmod (u^4 + u^3 + u^2 + u + 1) \tag{8c}$$

Now in (8c) let

$$C(u) = [c_0 + c_1u + c_2u^2 + c_3u^3] \cdot [d_0 + d_1u + d_2u^2 + d_3u^3]$$

$$= [(c_0 + c_1u) + u^2(c_2 + c_3u)] \cdot [(d_0 + d_1u) + u^2(d_2 + d_3u)]$$

ORIGINAL PAGE IS
OF POOR QUALITY

Next set $A_0 = (c_0 + c_1 u)$, $A_1 = (c_2 + c_3 u)$, $B_0 = (d_0 + d_1 u)$, $B_1 = (d_2 + d_3 u)$. Then

$$C(u) = (A_0 + u^2 A_1) \cdot (B_0 + u^2 B_1)$$

By (1) $C(u)$ is given by

$$C(u) = C_0 + C_1 u^2 + C_2 u^4$$

where

$$C_0 = A_0 \cdot B_0 = (c_0 + c_1 u) \cdot (d_0 + d_1 u)$$

$$C_2 = A_1 \cdot B_1 = (c_2 + c_3 u) \cdot (d_2 + d_3 u)$$

$$C_1 = D_1 - C_0 - C_2$$

where D_1 is defined to be

$$D_1 = (A_0 + A_1) \cdot (B_0 + B_1)$$

$$= [(c_0 + c_2) + (c_1 + c_3) u] \cdot [(d_0 + d_2) + (d_1 + d_3) u]$$

To compute C_0, C_2, D_1, use (1) again to obtain,

$$C_0 = (c_0 + c_1 u) \cdot (d_0 + d_1 u)$$

$$= c_0 \cdot d_0 + ((c_0 + c_1) \cdot (d_0 + d_1) - c_0 d_0 - c_1 d_1) u + c_1 \cdot d_1 u^2,$$

$$C_2 = (c_2 + c_3 u) \cdot (d_2 + d_3 u)$$

$$= c_2 \cdot d_2 + ((c_2 + c_3) \cdot (d_2 + d_3) - c_2 \cdot d_2 - c_3 \cdot d_3) u + c_3 \cdot d_3 u^2,$$

and

$$D_1 = [(c_0 + c_2) + (c_1 + c_3) u] \cdot [(d_0 + d_2) + (d_1 + d_3) u]$$

$$= (c_0 + c_2) \cdot (d_0 + d_2) + ((c_0 + c_2 + c_1 + c_3) \cdot (d_0 + d_2 + d_1 + d_3)$$

$$- (c_0 + c_2)(d_0 + d_2) - (c_1 + c_3)(d_1 + d_3)) u + (c_1 + c_3) \cdot (d_1 + d_3) u^2$$

Thus, finally

$$C(u) = c_0 \cdot d_0 + ((c_0 + c_1) \cdot (d_0 + d_1) - c_0 \cdot d_0 - c_1 \cdot d_1)\, u$$

$$+ ((c_0 + c_2) \cdot (d_0 + d_2) - c_0 \cdot d_0 - c_2 \cdot d_2 + c_1 \cdot a_1)\, u^2$$

$$+ ((c_0 + c_2 + c_1 + c_3) \cdot (d_0 + d_2 + d_1 + d_3) - (c_0 + c_2) \cdot (d_0 + d_2)$$

$$- (c_1 + c_3) \cdot (d_1 + d_3) - (c_0 + c_1) \cdot (d_0 + d_1) + c_0 \cdot d_0 + c_1 \cdot d_1$$

$$- (c_2 + c_3) \cdot (d_2 + d_3) + c_2 \cdot d_2 + c_3 \cdot d_3)\, u^3$$

$$+ ((c_1 + c_3)(d_1 + d_3) - c_1 \cdot d_1 - c_3 \cdot d_3 + c_2 \cdot d_2)\, u^4$$

$$+ ((c_2 + c_3) \cdot (d_2 + d_3) - c_2 \cdot d_2 - c_3 \cdot d_3)\, u^5 + c_3 \cdot d_3\, u^6$$

Hence $T_2(u) \equiv C(u) \bmod u^4 + u^3 + u^2 + u + 1$ is given by

$$T_2(u) = b_0 + b_1 u + b_2 u^2 + b_3 u^3 \tag{9}$$

where

$$b_0 = c_0 \cdot d_0 + (c_1 + c_3) \cdot (c_1 + d_3) + c_1 \cdot d_1 + (c_2 + c_3) \cdot (d_2 + d_3)$$

$$b_1 = (c_0 + c_1) \cdot (d_0 + d_1) + c_0 \cdot d_0 + (c_1 + c_3) \cdot (d_1 + d_3) + c_2 \cdot d_2$$

$$b_2 = (c_0 + c_2) \cdot (d_0 + d_2) + c_0 d_0 + (c_1 + c_3) \cdot (d_1 + d_3) + c_3 \cdot d_3$$

$$b_3 = (c_0 + c_2 + c_1 + c_3) \cdot (d_0 + d_2 + d_1 + d_3) + (c_0 + c_2) \cdot (d_0 + d_2)$$

$$+ (c_0 + c_1) \cdot (d_0 + d_1) + c_0 \cdot d_0 + (c_2 + c_3) \cdot (d_2 + d_3)$$

By the Chinese remainder theorem for polynomials (Ref. 13), $T(u)$ can be reconstituted from

$$T(u) \equiv T_1(u)\, M_1(u)\, M_1^{-1}(u) + T_2(u)\, M_2(u)\, M_2^{-1}(u) \bmod u^5 - 1 \tag{10}$$

where $M_1(u) = u^4 + u^3 + u^2 + u + 1$, $M_1^{-1}(u) = 1$, $M_2(u) = u + 1$, $M_2^{-1}(u) = u^3 + u$, and where $T_1(u)$ and $T_2(u)$ are given in (8a) and (9), respectively. By (10), $T(u)$ is

$$T(u) = y_0 + y_1 u + y_2 u^2 + y_3 u^3 + y_4 u^4 \tag{11}$$

where

$$\begin{aligned}
y_4 &= (a_0 + a_1 + a_2 + a_3 + a_4) \cdot (x_0 + x_1 + x_2 + x_3 + x_4) \\
&\quad + (a_0 + a_3) \cdot (x_3 + x_0) + (a_1 + a_3) \cdot (x_2 + x_0) + (a_0 + a_2) \cdot (x_3 + x_1) \\
&\quad + (a_2 + a_3) \cdot (x_1 + x_0) + (a_4 + a_0 + a_2 + a_1) \cdot (x_4 + x_3 + x_2 + x_1) \\
y_3 &= (a_0 + a_1 + a_2 + a_3 + a_4) \cdot (x_0 + x_1 + x_2 + x_3 + x_4) \\
&\quad + (a_0 + a_3) \cdot (x_3 + x_0) + (a_1 + a_2) \cdot (x_2 + x_1) \\
&\quad + (a_4 + a_0) \cdot (x_4 + x_3) + (a_1 + a_3) \cdot (x_2 + x_0) \\
&\quad + (a_4 + a_1) \cdot (x_4 + x_2) + (a_4 + a_3) \cdot (x_4 + x_0) \\
&\quad + (a_0 + a_2) \cdot (x_3 + x_1) + (a_2 + a_3) \cdot (x_1 + x_0) \\
y_2 &= (a_0 + a_1 + a_2 + a_3 + a_4) \cdot (x_0 + x_1 + x_2 + x_3 + x_4) \\
&\quad + (a_0 + a_3) \cdot (x_3 + x_0) + (a_4 + a_3) \cdot (x_4 + x_0) + (a_1 + a_3) \cdot (x_2 + x_0) \\
&\quad + (a_4 + a_0 + a_1 + a_2) \cdot (x_4 + x_3 + x_2 + x_1) + (a_4 + a_1) \cdot (x_4 + x_2). \\
y_1 &= (a_0 + a_1 + a_2 + a_3 + a_4) \cdot (x_0 + x_1 + x_2 + x_3 + x_4) \\
&\quad + (a_0 + a_3) \cdot (x_3 + x_0) + (a_4 + a_3) \cdot (x_4 + x_0) + (a_2 + a_3) \cdot (x_1 + x_0) \\
&\quad + (a_4 + a_0 + a_1 + a_2) \cdot (x_4 + x_3 + x_2 + x_1) + (a_4 + a_0) \cdot (x_4 + x_3), \\
y_0 &= (a_0 + a_1 + a_2 + a_3 + a_4) \cdot (x_0 + x_1 + x_2 + x_3 + x_4) \\
&\quad + (a_1 + a_3) \cdot (x_2 + x_0) + (a_4 + a_3) \cdot (x_4 + x_0) + (a_2 + a_3) \cdot (x_1 + x_0) \\
&\quad + (a_4 + a_0 + a_1 + a_2) \cdot (x_4 + x_3 + x_2 + x_1) + (a_1 + a_2) \cdot (x_2 + x_1)
\end{aligned}$$

If one lets

$$m_0 = (a_0 + a_1 + a_2 + a_3 + a_4) \cdot (x_0 + x_1 + x_2 + x_3 + x_4)$$

$$m_1 = (a_0 + a_3) \cdot (x_3 + x_0)$$

$$m_2 = (a_1 + a_3) \cdot (x_2 + x_0)$$

$$m_3 = (a_0 + a_2) \cdot (x_3 + x_1)$$

$$m_4 = (a_2 + a_3) \cdot (x_1 + x_0)$$

$$m_5 = (a_4 + a_0 + a_2 + a_1) \cdot (x_4 + x_3 + x_2 + x_1) \qquad (12a)$$

$$m_6 = (a_1 + a_2) \cdot (x_2 + x_1)$$

$$m_7 = (a_4 + a_0) \cdot (x_4 + x_3)$$

$$m_8 = (a_4 + a_1) \cdot (x_4 + x_2)$$

$$m_9 = (a_4 + a_3) \cdot (x_4 + x_0)$$

Then, (11) becomes

$$y_0 = m_0 + m_2 + m_9 + m_4 + m_5 + m_6$$

$$y_1 = m_0 + m_1 + m_9 + m_4 + m_5 + m_7$$

$$y_2 = m_0 + m_1 + m_9 + m_2 + m_5 + m_8 \qquad (12b)$$

$$y_3 = m_0 + m_1 + m_6 + m_7 + m_2 + m_8 + m_9 + m_3 + m_4$$

$$y_4 = m_0 + m_1 + m_2 + m_3 + m_4 + m_5$$

Hence, by (12), the total number of multiplications required to perform (7) is 10.

Theorem 1 below, due to Winograd (Ref. 10), will be needed in the following.

ORIGINAL PAGE IS
OF POOR QUALITY

Theorem 1: Let a and b be relatively prime positive integers and A be the cyclic $ab \times ab$ matrix, given by

$$A(x, y) = f(x + y \bmod a \cdot b), \qquad 0 \leq x, y < ab.$$

If π is a permutation of the set of integers $\{0, 1, \ldots, ab - 1\}$, let

$$B(x, y) = A(\pi(x), \pi(y)).$$

Then there exists a permutation π such that, if B is partitioned into $b \times b$ submatrices, each submatrix is cyclic and the submatrices form an $a \times a$ cyclic matrix.

In order to compute transforms of length $2^n - 1$ over $GF(2^n)$ for $n = 5$ it will be necessary to compute a convolution of 15 values over $GF(2^n)$. Such a cyclic convolution can again be expressed in matrix form as a 15×15 cyclic matrix. The permutation π in Theorem 1 for this 15×15 cyclic matrix is given by

$$\pi = \begin{pmatrix} 0 & 1 & 2 & 3 & 4 & 5 & 6 & 7 & 8 & 9 & 10 & 11 & 12 & 13 & 14 \\ 0 & 6 & 12 & 3 & 9 & 10 & 1 & 7 & 13 & 4 & 5 & 11 & 2 & 8 & 14 \end{pmatrix}$$

With this π the rows and columns of a 15×15 cyclic matrix can be partitioned into blocks of 5×5 cyclic matrices, such that each block forms a 3×3 cyclic matrix. This 15-point cyclic convolution in cyclic matrix form of 5×5 blocks is as follows:

$$\begin{pmatrix} E_0 \\ E_1 \\ E_2 \end{pmatrix} = \begin{pmatrix} A & B & C \\ B & C & A \\ C & A & B \end{pmatrix} \begin{pmatrix} Y_0 \\ Y_1 \\ Y_2 \end{pmatrix} \tag{13}$$

where

$$E_0 = \begin{pmatrix} y_0 \\ y_6 \\ y_{12} \\ y_3 \\ y_9 \end{pmatrix}, \quad E_1 = \begin{pmatrix} y_{10} \\ y_1 \\ y_7 \\ y_{13} \\ y_4 \end{pmatrix}, \quad E_3 = \begin{pmatrix} y_5 \\ y_{11} \\ y_2 \\ y_8 \\ y_{14} \end{pmatrix},$$

$$A = \begin{pmatrix} a_0 & a_6 & a_{12} & a_3 & a_9 \\ a_6 & a_{12} & a_3 & a_9 & a_0 \\ a_{12} & a_3 & a_9 & a_0 & a_6 \\ a_3 & a_9 & a_0 & a_6 & a_{12} \\ a_9 & a_0 & a_6 & a_{12} & a_3 \end{pmatrix}$$

$$B = \begin{pmatrix} a_{10} & a_1 & a_7 & a_{13} & a_4 \\ a_1 & a_7 & a_{13} & a_4 & a_{10} \\ a_7 & a_{13} & a_4 & a_{10} & a_1 \\ a_{13} & a_4 & a_{10} & a_1 & a_7 \\ a_4 & a_{10} & a_1 & a_7 & a_{13} \end{pmatrix}$$

$$C = \begin{pmatrix} a_5 & a_{11} & a_2 & a_8 & a_{14} \\ a_{11} & a_2 & a_8 & a_{14} & a_5 \\ a_2 & a_8 & a_{14} & a_5 & a_{11} \\ a_8 & a_{14} & a_5 & a_{11} & a_2 \\ a_{14} & a_5 & a_{11} & a_2 & a_8 \end{pmatrix} \qquad Y_0 = \begin{pmatrix} x_0 \\ x_6 \\ x_{12} \\ x_3 \\ x_9 \end{pmatrix}$$

$$Y_1 = \begin{pmatrix} x_{10} \\ x_1 \\ x_7 \\ x_{13} \\ x_4 \end{pmatrix}, \qquad Y_2 = \begin{pmatrix} x_5 \\ x_{11} \\ x_2 \\ x_8 \\ x_{14} \end{pmatrix}$$

Now make the correspondences: $a_0 \leftrightarrow A$, $a_1 \leftrightarrow B$, $a_2 \leftrightarrow C$, $y_0 \leftrightarrow E_0$, $y_1 \leftrightarrow E_1$, $y_2 \leftrightarrow E_2$, $x_0 \leftrightarrow Y_0$, $x_1 \leftrightarrow Y_1$, $x_2 \leftrightarrow Y_2$; then by a procedure precisely similar to that used to compute the cyclic convolution of 3 elements, defined in (2), one obtains

$$\begin{aligned} E_0 &= M_0 + M_1 + M_2 \\ E_1 &= M_0 + M_2 + M_3 \\ E_2 &= M_0 + M_3 + M_1 \end{aligned} \tag{14}$$

where

$$\begin{aligned} M_0 &= (A + B + C) \cdot (Y_0 + Y_1 + Y_2) \\ M_1 &= (C + A) \cdot (Y_1 + Y_2) \\ M_2 &= (C + B) \cdot (Y_2 + Y_0) \\ M_3 &= (A + B) \cdot (Y_0 + Y_1) \end{aligned}$$

Equation (14) requires 4 (5 × 5) cyclic matrix multiplies. To find M_i for $i = 0, 1, 2, 3$, one needs to multiply matrices of form $(A + B + C)$, $(C + A)$, $(C + B)$, and $(A + B)$ by vectors $(Y_0 + Y_1 + Y_2)$, $(Y_1 + Y_2)$, $(Y_2 + Y_0)$, and $(Y_0 + Y_1)$, respectively. For example consider $M_1 = (C + A) \cdot (Y_1 + Y_2)$

$$M_1 = \begin{pmatrix} f_0 \\ f_1 \\ f_2 \\ f_3 \\ f_4 \end{pmatrix} = \begin{pmatrix} a_0 + a_5, a_6 + a_{11}, a_{12} + a_2, a_3 + a_8, a_9 + a_{14} \\ a_6 + a_{11}, a_{12} + a_2, a_3 + a_8, a_9 + a_{14}, a_0 + a_5 \\ a_{12} + a_2, a_3 + a_8, a_9 + a_{14}, a_0 + a_5, a_6 + a_{11} \\ a_3 + a_8, a_9 + a_{14}, a_0 + a_5, a_6 + a_{11}, a_{12} + a_2 \\ a_9 + a_{14}, a_0 + a_5, a_6 + a_{11}, a_{12} + a_2, a_3 + a_8 \end{pmatrix} \begin{pmatrix} x_{10} + x_5 \\ x_1 + x_{11} \\ x_7 + x_2 \\ x_{13} + x_8 \\ x_4 + x_{14} \end{pmatrix}$$

Using the 5-point cyclic matrix in (7) and making the correspondences, $f_0 \leftrightarrow y_0$, $f_1 \leftrightarrow y_1$, $f_2 \leftrightarrow y_2$, $f_3 \leftrightarrow y_3$, $f_4 \leftrightarrow y_4$, $a_0 \leftrightarrow a_0 + a_5$, $a_1 \leftrightarrow a_6 + a_{11}$, $a_2 \leftrightarrow a_{12} + a_2$, $a_3 \leftrightarrow a_3 + a_8$, $a_4 \leftrightarrow a_9 + a_{14}$, $x_0 \leftrightarrow x_{10} + x_5$, $x_1 \leftrightarrow x_1 + x_{11}$, $x_2 \leftrightarrow x_7 + x_2$, $x_3 \leftrightarrow x_{13} + x_8$, $x_4 \leftrightarrow x_4 + x_{14}$, one obtains

$$M_1 = \begin{pmatrix} f_0 \\ f_1 \\ f_2 \\ f_3 \\ f_4 \end{pmatrix} = \begin{pmatrix} F_0 + F_2 + F_9 + F_4 + F_5 + F_6 \\ F_0 + F_1 + F_9 + F_4 + F_5 + F_7 \\ F_0 + F_1 + F_9 + F_2 + F_5 + F_8 \\ F_0 + F_1 + F_6 + F_7 + F_2 + F_8 + F_9 + F_3 + F_4 \\ F_0 + F_1 + F_2 + F_3 + F_4 + F_5 \end{pmatrix} \tag{15}$$

where

$$F_0 = (a_0 + a_5 + a_6 + a_{11} + a_{12} + a_2 + a_3 + a_8 + a_9 + a_{14}) \cdot (x_{10} + x_5 + x_1 + x_{11} + x_7 + x_2 + x_{13} + x_8 + x_4 + x_{14}),$$

$$F_1 = (a_0 + a_5 + a_3 + a_8) \cdot (x_{13} + x_8 + x_{10} + x_5),$$

$$F_2 = (a_6 + a_{11} + a_3 + a_8) \cdot (x_7 + x_2 + x_{10} + x_5),$$

$$F_3 = (a_0 + a_5 + a_{12} + a_2) \cdot (x_1 + x_{11} + x_{13} + x_8),$$

$$F_4 = (a_{12} + a_2 + a_3 + a_8) \cdot (x_{10} + x_5 + x_1 + x_{11}),$$

$$F_5 = (a_0 + a_5 + a_6 + a_{11} + a_{12} + a_2 + a_9 + a_{14}) \cdot (x_1 + x_{11} + x_7 + x_2 + x_{13} + x_8 + x_4 + x_{14})$$

$$F_6 = (a_6 + a_{11} + a_{12} + a_2) \cdot (x_1 + x_{11} + x_7 + x_2)$$

$$F_7 = (a_0 + a_5 + a_9 + a_{14}) \cdot (x_{13} + x_8 + x_4 + x_{14})$$

$$F_8 = (a_6 + a_{11} + a_9 + a_{14}) \cdot (x_7 + x_2 + x_4 + x_{14})$$

$$F_9 = (a_3 + a_8 + a_9 + a_{14}) \cdot (x_{10} + x_5 + x_4 + x_{14})$$

Equation (15) requires 10 multiplies. In a similar manner each of the matrices M_0, M_2, M_3 can be obtained using 10 multiplications. Thus by (14) the total number of multiplications needed to compute (13) is 40.

III. A New Algorithm for Computing a Transform over $GF(2^n)$ of $2^n - 1$ Points for $n = 5, 6$

Let $GF(2^n)$ be the finite field of 2^n elements. Assume that N is an integer that divides $2^n - 1$. Next, let the element $\gamma \epsilon GF(2^n)$ generate the cyclic subgroup of N elements, $G_N = \{\gamma, \gamma^2, \ldots, \gamma^N = 1\}$, in the multiplicative group of $GF(2^n)$. The transform over this subgroup G_N is defined by

$$A_j = \sum_{i=0}^{N-1} a_i \gamma^{ij} \quad \text{for} \quad 0 \leq j \leq N-1$$

ORIGINAL PAGE IS
OF POOR QUALITY

where $a_i \epsilon GF(2^n)$. Rewrite this in matrix form as

$$\bar{A} = W' \bar{a}, \tag{16}$$

where

$W' = (w'_{i,j})$ and $w'_{i,j} = \gamma^{ij}$.

Also let

$$A_0 = \sum_{i=0}^{N-1} a_i$$

and

$$A_j = A_0 + B_j \qquad \text{for} \qquad j = 1, 2, \ldots N-1$$

where

$$B_j = \sum_{i=1}^{N-1} a_i \gamma^{ij}$$

That is, let

$$\bar{B} = W\bar{a} \tag{17}$$

where W is the $(N-1) \times (N-1)$ matrix $(\gamma^{ij})_{i,j\neq 0}$ and $\bar{a}$, $\bar{B}$ are the column matrices (a_i) and (B_j), respectively.

If N is a prime number p, one can find an element $\alpha \epsilon GF(p)$ which generates the cyclic subgroup of $p-1$ elements. Hence a permutation or substitution σ can be defined by

$$\sigma = \begin{pmatrix} 1, 2, \ldots, p-2, p-1 \\ \alpha, \alpha^2, \quad , \alpha^{p-2}, \alpha^{p-1} = 1 \end{pmatrix} \bmod p$$

where all the elements of this substitution are taken modulo p.

Using the above permutation, by (Ref. 14), one can permute the indices of $\bar{B}$, $\bar{a}$, W defined in (17) so that matrix $\tilde{W} = (\gamma^{\sigma(i)\sigma(j)})_{i,j\neq 0}$ is cyclic. That is,

$$B_{\sigma(j)} = \sum_{i=1}^{p-1} a_{\sigma(i)} \gamma^{\sigma(i)\sigma(j)}$$

$$= \sum_{i=1}^{p-1} a_{\sigma(i)} \gamma^{\alpha^{i+j}}$$

$$= \sum_{i=1}^{p-1} a_{\sigma(i)} \gamma^{\sigma(i+j)} \qquad \text{for} \qquad j = 1, 2, \ldots, p-1 \tag{18a}$$

This is reexpressed in matrix form as

$$\tilde{B} = \tilde{W}\tilde{a} \tag{18b}$$

where

$\tilde{B} = (B_{\sigma(j)})$, $\tilde{W} = (\gamma^{\sigma(i+j)})_{i,j\neq 0}$, and $\tilde{a} = (a_{\sigma(i)})$.

By (18a), $B_{\sigma(j)}$ is a cyclic convolution of $a_{\sigma(i)}$ and $\gamma^{\sigma(i)}$ for $j = 1, 2, \cdots p-1$.

Let $p - 1 = p_1 \cdot p_2 \cdots p_r$ be the factorization of $p - 1$ into primes. If one lets $a_1 = p_1 \cdot p_2 \cdots p_{r-1}$ and $b_1 = p_r$, by Theorem 1 the cyclic matrix can be partitioned into $b_1^2 = p_r^2$ matrices of size $a_1 \times a_1$. Next let $a_1 = a_2 \times b_2$, where $a_2 = p_1 \cdots p_{r-2}$ and $b_2 = p_{r-1}$. If a_2 is not a prime, then $a_1 \times a_1$ cyclic matrix can be partitioned into b_2^2 matrices of size $a_2 \times a_2$. In general, $a_l = a_{l+1} \times b_{l+1}$, where b_{l+1} is a prime. If $a_{l+1} \neq 1$, then each $a_l \times a_l$ cyclic matrix can be partitioned into b_{l+1}^2 matrices of size $a_{l+1} \times a_{l+1}$. Otherwise, the procedure terminates. If the number of multiplications used to compute the cyclic convolution of p_l points is m_l for $l = 1, 2, \cdots, r$, then Winograd has shown (Ref. 10) that the number of multiplications needed to compute a $(p-1)$-point cyclic convolution is equal to $N = m_1 \cdot m_2 \cdots m_r$.

Let $N = N_1 N_2 \cdots N_k$, where $(N_i, N_j) = 1$ for $i \neq j$. Using the Chinese remainder theorem for integers it is shown by Winograd in Refs. 9, 10 that the transform matrix W' defined in (16) can be transformed into the direct product of W_1', W_2', $\cdots$, W_k', where W_l' is the matrix of an N_l-point transform. Assume that m_l is the number of multiplications needed to perform an N_l-point transform over $GF(2^n)$ for $l = 1, 2, \ldots, k$. Then, the number of multiplications required to compute an N-point transform is $m_1 \cdot m_2 \cdots m_k$.

A. Transform over $GF(2^5)$ of 31 Points

Consider the finite field $GF(2^5)$. Since $N = 2^5 - 1 = 31$ is a prime p, the cyclic convolution algorithm developed in the previous section can be used to calculate the transform of 15 points over $GF(2^5)$. For $N = 31$, the permutation σ is given by

$$\sigma = \begin{pmatrix} 1 & 2 & 3 & 4 & 5 & 6 & 7 & 8 & 9 & 10 & 11 & 12 & 13 & 14 & 15 & 16 & 17 & 18 & 19 & 20 \\ 3 & 9 & 27 & 19 & 26 & 16 & 17 & 20 & 29 & 25 & 13 & 8 & 24 & 10 & 30 & 28 & 22 & 4 & 12 & 5 \end{pmatrix}$$

$$\begin{pmatrix} 21 & 22 & 23 & 24 & 25 & 26 & 27 & 28 & 29 & 30 \\ 15 & 14 & 11 & 2 & 6 & 18 & 23 & 7 & 21 & 1 \end{pmatrix} \bmod 31$$

Let γ be a 31-st root of unity in $GF(2^5)$. Using the above permutation, one can permute the indices of $\tilde{B}$, $\tilde{a}$, W defined in (17) so that the matrix, $\tilde{W} = (\gamma^{\sigma(i+j)})_{i,j\neq 0}$ is cyclic for $i = 1, 2, \ldots, 30$ and $j = 1, 2, \ldots, 30$. By Theorem 1, the cyclic matrix $\tilde{W}$ can be first partitioned into 5×5 blocks as follows:

$$\tilde{W} = (A, B, C, \ldots)$$

In terms of this matrix the convolution (18b) is given by

$$\begin{pmatrix} T_1 \\ T_2 \\ T_3 \\ T_4 \\ T_5 \\ T_6 \end{pmatrix} = \begin{pmatrix} A & B & C & D & E & F \\ B & C & A & E & F & D \\ C & A & B & F & D & E \\ D & E & F & A & B & C \\ E & F & D & B & C & A \\ F & D & E & C & A & B \end{pmatrix} \begin{pmatrix} S_1 \\ S_2 \\ S_3 \\ S_4 \\ S_5 \\ S_6 \end{pmatrix} \tag{19}$$

where

$$T_1 = \begin{pmatrix} b_3 \\ b_{17} \\ b_{24} \\ b_{12} \\ b_6 \end{pmatrix}, \quad T_2 = \begin{pmatrix} b_{13} \\ b_{22} \\ b_{11} \\ b_{21} \\ b_{26} \end{pmatrix}, \quad T_3 = \begin{pmatrix} b_{15} \\ b_{23} \\ b_{27} \\ b_{29} \\ b_{30} \end{pmatrix}, \quad T_4 = \begin{pmatrix} b_{28} \\ b_{14} \\ b_7 \\ b_{19} \\ b_{25} \end{pmatrix},$$

$$T_5 = \begin{pmatrix} b_{18} \\ b_9 \\ b_{20} \\ b_{10} \\ b_5 \end{pmatrix}, \quad T_6 = \begin{pmatrix} b_{16} \\ b_8 \\ b_4 \\ b_2 \\ b_1 \end{pmatrix}, \quad A = \begin{pmatrix} \gamma^9 & \gamma^{20} & \gamma^{10} & \gamma^5 & \gamma^{18} \\ \gamma^{20} & \gamma^{10} & \gamma^5 & \gamma^{18} & \gamma^9 \\ \gamma^{10} & \gamma^5 & \gamma^{18} & \gamma^9 & \gamma^{20} \\ \gamma^5 & \gamma^{18} & \gamma^9 & \gamma^{20} & \gamma^{10} \\ \gamma^{18} & \gamma^9 & \gamma^{20} & \gamma^{10} & \gamma^5 \end{pmatrix}$$

$$B = \begin{pmatrix} \gamma^8 & \gamma^4 & \gamma^2 & \gamma^1 & \gamma^{16} \\ \gamma^4 & \gamma^2 & \gamma^1 & \gamma^{16} & \gamma^8 \\ \gamma^2 & \gamma^1 & \gamma^{16} & \gamma^8 & \gamma^4 \\ \gamma^1 & \gamma^{16} & \gamma^8 & \gamma^4 & \gamma^2 \\ \gamma^{16} & \gamma^8 & \gamma^4 & \gamma^2 & \gamma^1 \end{pmatrix}, \quad C = \begin{pmatrix} \gamma^{14} & \gamma^7 & \gamma^{19} & \gamma^{25} & \gamma^{28} \\ \gamma^7 & \gamma^{19} & \gamma^{25} & \gamma^{28} & \gamma^{14} \\ \gamma^{19} & \gamma^{25} & \gamma^{28} & \gamma^{14} & \gamma^7 \\ \gamma^{25} & \gamma^{28} & \gamma^{14} & \gamma^7 & \gamma^{19} \\ \gamma^{28} & \gamma^{14} & \gamma^7 & \gamma^{19} & \gamma^{25} \end{pmatrix}$$

$$D = \begin{pmatrix} \gamma^{22} & \gamma^{11} & \gamma^{21} & \gamma^{26} & \gamma^{13} \\ \gamma^{11} & \gamma^{21} & \gamma^{26} & \gamma^{13} & \gamma^{22} \\ \gamma^{21} & \gamma^{26} & \gamma^{13} & \gamma^{22} & \gamma^{11} \\ \gamma^{26} & \gamma^{13} & \gamma^{22} & \gamma^{11} & \gamma^{21} \\ \gamma^{13} & \gamma^{22} & \gamma^{11} & \gamma^{21} & \gamma^{26} \end{pmatrix}, \quad E = \begin{pmatrix} \gamma^{23} & \gamma^{27} & \gamma^{29} & \gamma^{30} & \gamma^{15} \\ \gamma^{27} & \gamma^{29} & \gamma^{30} & \gamma^{15} & \gamma^{23} \\ \gamma^{29} & \gamma^{30} & \gamma^{15} & \gamma^{23} & \gamma^{27} \\ \gamma^{30} & \gamma^{15} & \gamma^{23} & \gamma^{27} & \gamma^{29} \\ \gamma^{15} & \gamma^{23} & \gamma^{27} & \gamma^{29} & \gamma^{30} \end{pmatrix}$$

$$F = \begin{pmatrix} \gamma^{17} & \gamma^{24} & \gamma^{12} & \gamma^{6} & \gamma^{3} \\ \gamma^{24} & \gamma^{12} & \gamma^{6} & \gamma^{3} & \gamma^{17} \\ \gamma^{12} & \gamma^{6} & \gamma^{3} & \gamma^{17} & \gamma^{24} \\ \gamma^{6} & \gamma^{3} & \gamma^{17} & \gamma^{24} & \gamma^{12} \\ \gamma^{3} & \gamma^{17} & \gamma^{24} & \gamma^{12} & \gamma^{6} \end{pmatrix}, \quad S_1 = \begin{pmatrix} a_3 \\ a_{17} \\ a_{24} \\ a_{12} \\ a_6 \end{pmatrix}, \quad S_2 = \begin{pmatrix} a_{13} \\ a_{22} \\ a_{11} \\ a_{21} \\ a_{26} \end{pmatrix}$$

$$S_3 = \begin{pmatrix} a_{15} \\ a_{23} \\ a_{27} \\ a_{29} \\ a_{30} \end{pmatrix}, \quad S_4 = \begin{pmatrix} a_{28} \\ a_{14} \\ a_7 \\ a_{19} \\ a_{25} \end{pmatrix} \quad S_5 = \begin{pmatrix} a_{18} \\ a_9 \\ a_{20} \\ a_{10} \\ a_5 \end{pmatrix}, \quad S_6 = \begin{pmatrix} a_{16} \\ a_8 \\ a_4 \\ a_2 \\ a_1 \end{pmatrix}$$

Observe that the matrix equation (19) can be further reduced as follows:

$$N = \begin{pmatrix} F_0 \\ F_1 \end{pmatrix} = \begin{pmatrix} J & K \\ K & J \end{pmatrix} \begin{pmatrix} E_0 \\ E_1 \end{pmatrix} = \begin{pmatrix} J(E_0 + E_1) + (J + K) \cdot E_1 \\ J(E_0 + E_1) + (J + K) \cdot E_0 \end{pmatrix}$$

where

$$F_0 = \begin{pmatrix} T_1 \\ T_2 \\ T_3 \end{pmatrix}, \quad F_2 = \begin{pmatrix} T_4 \\ T_5 \\ T_6 \end{pmatrix}, \quad J = \begin{pmatrix} A & B & C \\ B & C & A \\ C & A & B \end{pmatrix},$$

ORIGINAL PAGE IS
OF POOR QUALITY

and

$$K = \begin{pmatrix} D & E & F \\ E & F & D \\ F & D & E \end{pmatrix}$$

Now let

$$\begin{aligned} U_1 &= (E_0 + E_1) \cdot J \\ U_2 &= (J + K) \cdot E_1 \\ U_3 &= (J + K) \cdot E_0 \end{aligned} \tag{20}$$

Then $F_0 = U_1 + U_2$, $F_1 = U_1 + U_3$. Thus, $3(15 \times 15)$ cyclic matrix multiplies are necessary to perform (20). By a procedure precisely similar to that used to compute the 15×15 cyclic convolution in (13), the number of multiplications needed to compute U_1 in (20) is 40. In a similar manner, each of the matrices U_2 and U_3 in (20) can be obtained with 40 multiplications. Thus, the total number of multiplications needed to perform (19) is $3 \times 40 = 120$.

B. Transform over $GF(2^6)$ of 63 Points

Since $N = 2^6 - 1 = 63 = N_1 \cdot N_2 = 7 \cdot 9$, by Winograd's algorithm one needs to compute an N_i-point transform over $GF(2^6)$ for $N_i = 7$ or 9. The algorithms for computing these transforms over $GF(2^6)$ are given in Appendix A. Let integer i for $0 \leq i < 63$ be represented by a pair $(i_1, i_2) = (i \bmod 3, i \bmod 5)$. Since 7 and 9 are relatively prime, by the Chinese remainder theorem,

$$i = i_1 \cdot 36 + i_2 \cdot 28 \bmod 63 \tag{21}$$

is the required representation.

Let γ be the 63rd root of unity in $GF(2^6)$. Also let $\gamma_1 = \gamma^9 \bmod 2$ and $\gamma_2 = \gamma^7 \bmod 2$ be the 7th and 9th roots of unity in $GF(2^6)$, respectively. The 63rd point transform over $GF(2^6)$ in i_1 and i_2 is

$$\begin{aligned} A_j &= \sum_{i=0}^{63} a_i \gamma^{ij} \\ A_{(j_1, j_2)} &= \sum_{i_1=0}^{6} \left[\sum_{i_2=0}^{8} a_{(i_1, i_2)} \gamma_2^{i_2 j_2} \right] \gamma_1^{i_1 j_1} \\ &= \sum_{i_1=0}^{6} a_{i_1}(j_2) \gamma_1^{i_1 j_1} \end{aligned} \tag{22}$$

where

$$a_{i_1}(j_2) = \sum_{i_2=0}^{8} a_{(i_1,i_2)}\, \gamma_2^{i_2 j_2} \qquad \begin{array}{l} \text{for } j_1 = 0, 1, 2, \ldots, 6 \\ \text{and } j_2 = 0, 1, 2, \ldots, 8 \end{array}$$

or in matrix notation

$$(a_{i_1}(j_2)) = W_2' \, \bar{a}_{i_1}$$

where

$$W_2' = \begin{pmatrix} \gamma_2^0 & \gamma_2^0 & \gamma_2^0 & \gamma_2^0 & \gamma_2^0 & \gamma_2^0 & \gamma_2^0 & \gamma_2^0 & \gamma_2^0 \\ \gamma_2^0 & \gamma_2^1 & \gamma_2^2 & \gamma_2^3 & \gamma_2^4 & \gamma_2^5 & \gamma_2^6 & \gamma_2^7 & \gamma_2^8 \\ \gamma_2^0 & \gamma_2^2 & \gamma_2^4 & \gamma_2^6 & \gamma_2^8 & \gamma_2^1 & \gamma_2^3 & \gamma_2^5 & \gamma_2^7 \\ \gamma_2^0 & \gamma_2^3 & \gamma_2^6 & \gamma_2^0 & \gamma_2^3 & \gamma_2^6 & \gamma_2^0 & \gamma_2^3 & \gamma_2^6 \\ \gamma_2^0 & \gamma_2^4 & \gamma_2^8 & \gamma_2^3 & \gamma_2^7 & \gamma_2^2 & \gamma_2^6 & \gamma_2^1 & \gamma_2^5 \\ \gamma_2^0 & \gamma_2^5 & \gamma_2^1 & \gamma_2^6 & \gamma_2^2 & \gamma_2^7 & \gamma_2^3 & \gamma_2^8 & \gamma_2^4 \\ \gamma_2^0 & \gamma_2^6 & \gamma_2^3 & \gamma_2^0 & \gamma_2^6 & \gamma_2^3 & \gamma_2^0 & \gamma_2^6 & \gamma_2^3 \\ \gamma_2^0 & \gamma_2^7 & \gamma_2^5 & \gamma_2^3 & \gamma_2^1 & \gamma_2^8 & \gamma_2^6 & \gamma_2^4 & \gamma_2^2 \\ \gamma_2^0 & \gamma_2^8 & \gamma_2^7 & \gamma_2^6 & \gamma_2^5 & \gamma_2^4 & \gamma_2^3 & \gamma_2^2 & \gamma_2^1 \end{pmatrix}$$

$$\bar{a}_{i_1} = \begin{pmatrix} a_{(i_1,0)} \\ a_{(i_1,1)} \\ a_{(i_1,2)} \\ a_{(i_1,3)} \\ a_{(i_1,4)} \\ a_{(i_1,5)} \\ a_{(i_1,6)} \\ a_{(i_1,7)} \\ a_{(i_1,8)} \end{pmatrix}$$

ORIGINAL PAGE IS
OF POOR QUALITY

Thus, (22) becomes

$$\overline{A}_{j_1} = \sum_{i_1=0}^{6} \gamma_1^{i_1 j_1} W_2' \overline{a}_{i_1} \quad \text{for } j_1 = 0, 1, 2, \ldots, 6$$

or

$$\begin{pmatrix} \overline{A}_0 \\ \overline{A}_1 \\ \overline{A}_2 \\ \overline{A}_3 \\ \overline{A}_4 \\ \overline{A}_5 \\ \overline{A}_6 \end{pmatrix} = \begin{pmatrix} W_2' & W_2' & W_2' & W_2' & W_2' & W_2' & W_2' \\ W_2' & W_2'\gamma_1^1 & W_2'\gamma_1^2 & W_2'\gamma_1^3 & W_2'\gamma_1^4 & W_2'\gamma_1^5 & W_2'\gamma_1^6 \\ W_2' & W_2'\gamma_1^2 & W_2'\gamma_1^4 & W_2'\gamma_1^6 & W_2'\gamma_1^1 & W_2'\gamma_1^3 & W_2'\gamma_1^5 \\ W_2' & W_2'\gamma_1^3 & W_2'\gamma_1^6 & W_2'\gamma_1^2 & W_2'\gamma_1^5 & W_2'\gamma_1^1 & W_2'\gamma_1^4 \\ W_2' & W_2'\gamma_1^4 & W_2'\gamma_1^1 & W_2'\gamma_1^5 & W_2'\gamma_1^2 & W_2'\gamma_1^6 & W_2'\gamma_1^3 \\ W_2' & W_2'\gamma_1^5 & W_2'\gamma_1^3 & W_2'\gamma_1^1 & W_2'\gamma_1^6 & W_2'\gamma_1^4 & W_2'\gamma_1^2 \\ W_2' & W_2'\gamma_1^6 & W_2'\gamma_1^5 & W_2'\gamma_1^4 & W_2'\gamma_1^3 & W_2'\gamma_1^2 & W_2'\gamma_1^1 \end{pmatrix} \begin{pmatrix} \overline{a}_0 \\ \overline{a}_1 \\ \overline{a}_2 \\ \overline{a}_3 \\ \overline{a}_4 \\ \overline{a}_5 \\ \overline{a}_6 \end{pmatrix}$$

Now by (21), one obtains $\overline{A_0}$ in terms of A_k as

$$\overline{A}_0 = \begin{pmatrix} A_{(0,0)} \\ A_{(0,1)} \\ A_{(0,2)} \\ A_{(0,3)} \\ A_{(0,4)} \\ A_{(0,5)} \\ A_{(0,6)} \\ A_{(0,7)} \\ A_{(0,8)} \end{pmatrix} = \begin{pmatrix} A_0 \\ A_{28} \\ A_{56} \\ A_{21} \\ A_{49} \\ A_{14} \\ A_{42} \\ A_7 \\ A_{35} \end{pmatrix}$$

Similarly

$$\overline{A}_1 = \begin{pmatrix} A_{(1,0)} \\ A_{(1,1)} \\ A_{(1,2)} \\ A_{(1,3)} \\ A_{(1,4)} \\ A_{(1,5)} \\ A_{(1,6)} \\ A_{(1,7)} \\ A_{(1,8)} \end{pmatrix} = \begin{pmatrix} A_{36} \\ A_{1} \\ A_{29} \\ A_{57} \\ A_{22} \\ A_{50} \\ A_{15} \\ A_{43} \\ A_{8} \end{pmatrix}, \quad \overline{A}_2 = \begin{pmatrix} A_{(2,0)} \\ A_{(2,1)} \\ A_{(2,2)} \\ A_{(2,3)} \\ A_{(2,4)} \\ A_{(2,5)} \\ A_{(2,6)} \\ A_{(2,7)} \\ A_{(2,8)} \end{pmatrix} = \begin{pmatrix} A_{9} \\ A_{37} \\ A_{2} \\ A_{30} \\ A_{58} \\ A_{23} \\ A_{51} \\ A_{16} \\ A_{44} \end{pmatrix},$$

$$\overline{A}_3 = \begin{pmatrix} A_{(3,0)} \\ A_{(3,1)} \\ A_{(3,2)} \\ A_{(3,3)} \\ A_{(3,4)} \\ A_{(3,5)} \\ A_{(3,6)} \\ A_{(3,7)} \\ A_{(3,8)} \end{pmatrix} = \begin{pmatrix} A_{45} \\ A_{10} \\ A_{38} \\ A_{3} \\ A_{31} \\ A_{59} \\ A_{24} \\ A_{52} \\ A_{17} \end{pmatrix}, \quad \overline{A}_4 = \begin{pmatrix} A_{(4,0)} \\ A_{(4,1)} \\ A_{(4,2)} \\ A_{(4,3)} \\ A_{(4,4)} \\ A_{(4,5)} \\ A_{(4,6)} \\ A_{(4,7)} \\ A_{(4,8)} \end{pmatrix} = \begin{pmatrix} A_{18} \\ A_{46} \\ A_{11} \\ A_{39} \\ A_{4} \\ A_{32} \\ A_{60} \\ A_{25} \\ A_{53} \end{pmatrix}$$

$$\overline{A}_5 = \begin{pmatrix} A_{(5,0)} \\ A_{(5,1)} \\ A_{(5,2)} \\ A_{(5,3)} \\ A_{(5,4)} \\ A_{(5,5)} \\ A_{(5,6)} \\ A_{(5,7)} \\ A_{(5,8)} \end{pmatrix} = \begin{pmatrix} A_{54} \\ A_{19} \\ A_{47} \\ A_{12} \\ A_{40} \\ A_{5} \\ A_{33} \\ A_{61} \\ A_{26} \end{pmatrix}, \quad \overline{A}_6 = \begin{pmatrix} A_{(6,0)} \\ A_{(6,1)} \\ A_{(6,2)} \\ A_{(6,3)} \\ A_{(6,4)} \\ A_{(6,5)} \\ A_{(6,6)} \\ A_{(6,7)} \\ A_{(6,8)} \end{pmatrix} = \begin{pmatrix} A_{27} \\ A_{55} \\ A_{20} \\ A_{48} \\ A_{13} \\ A_{41} \\ A_{6} \\ A_{34} \\ A_{62} \end{pmatrix}$$

$$\overline{a}_0 = \begin{pmatrix} a_0 \\ a_{28} \\ a_{56} \\ a_{21} \\ a_{49} \\ a_{14} \\ a_{42} \\ a_{7} \\ a_{35} \end{pmatrix}, \quad \overline{a}_1 = \begin{pmatrix} a_{36} \\ a_{1} \\ a_{29} \\ a_{57} \\ a_{22} \\ a_{50} \\ a_{15} \\ a_{43} \\ a_{8} \end{pmatrix}, \quad \overline{a}_2 = \begin{pmatrix} a_{9} \\ a_{37} \\ a_{2} \\ a_{30} \\ a_{58} \\ a_{23} \\ a_{51} \\ a_{16} \\ a_{44} \end{pmatrix}$$

$$\bar{a}_3 = \begin{pmatrix} a_{45} \\ a_{10} \\ a_{38} \\ a_3 \\ a_{31} \\ a_{59} \\ a_{24} \\ a_{52} \\ a_{17} \end{pmatrix}, \quad \bar{a}_4 = \begin{pmatrix} a_{18} \\ a_{46} \\ a_{11} \\ a_{39} \\ a_4 \\ a_{32} \\ a_{60} \\ a_{25} \\ a_{53} \end{pmatrix}, \quad \bar{a}_5 = \begin{pmatrix} a_{54} \\ a_{19} \\ a_{47} \\ a_{12} \\ a_{40} \\ a_5 \\ a_{33} \\ a_{61} \\ a_{26} \end{pmatrix}, \quad \bar{a}_6 = \begin{pmatrix} a_{27} \\ a_{55} \\ a_{20} \\ a_{48} \\ a_{13} \\ a_{41} \\ a_6 \\ a_{34} \\ a_{62} \end{pmatrix}$$

Using the 7-point transform in (1B) and making the correspondences, $\gamma^0 \longleftrightarrow W_2'$, $\gamma' \longleftrightarrow W_2'\gamma_1$, $\gamma^2 \longleftrightarrow W_2'\gamma_1^2$, $\gamma^3 \longleftrightarrow W_3'\gamma_1^3$, $\gamma^4 \longleftrightarrow W_2'\gamma_1^4$, $\gamma^5 \longleftrightarrow W_2'\gamma_1^5$, $\gamma^6 \longleftrightarrow W_2'\gamma_1^6$, one obtains

$$\begin{aligned}
A_0 &= M_0 \\
A_1 &= M_0 + M_1 + M_2 + M_3 + M_4 + M_5 + M_6 \\
A_2 &= M_0 + M_1 + M_7 + M_2 + M_4 + M_8 + M_5 \\
A_3 &= M_0 + M_1 + M_3 + M_7 + M_9 + M_{10} + M_{11} \\
A_4 &= M_0 + M_1 + M_3 + M_7 + M_4 + M_6 + M_8 \\
A_5 &= M_0 + M_1 + M_7 + M_2 + M_9 + M_{11} + M_{12} \\
A_6 &= M_0 + M_1 + M_2 + M_3 + M_9 + M_{12} + M_{10}
\end{aligned}$$

where

$$\begin{aligned}
M_0 &= W_2' \cdot (\bar{a}_0 + \bar{a}_1 + \bar{a}_2 + \bar{a}_3 + \bar{a}_4 + \bar{a}_5 + \bar{a}_6) \\
M_1 &= W_2' \cdot (\gamma^2 + \gamma^1 + \gamma^4 + 1) \cdot (\bar{a}_3 + \bar{a}_4 + \bar{a}_5 + \bar{a}_2 + \bar{a}_6 + \bar{a}_1) \\
M_2 &= W_2' \cdot (\gamma^2 + \gamma^1) \cdot (\bar{a}_5 + \bar{a}_2 + \bar{a}_3 + \bar{a}_4) \\
M_3 &= W_2' \cdot (\gamma^4 + \gamma^2)(\bar{a}_6 + \bar{a}_1 + \bar{a}_5 + \bar{a}_2) \\
M_4 &= W_2' \cdot (\bar{a}_3 + \bar{a}_5 + \bar{a}_6)
\end{aligned} \tag{23}$$

$$M_5 = W_2' \cdot (\gamma^2 + \gamma^5 + \gamma^1 + \gamma^6) \cdot (\bar{a}_5 + \bar{a}_3)$$

$$M_6 = W_2' \cdot (\gamma^4 + \gamma^3 + \gamma^2 + \gamma^5) \cdot (\bar{a}_6 + \bar{a}_5)$$

$$M_7 = W_2' \cdot (\gamma^4 + \gamma^1) \cdot (\bar{a}_6 + \bar{a}_1 + \bar{a}_3 + \bar{a}_4)$$

$$M_8 = W_2' \cdot (\gamma^4 + \gamma^3 + \gamma^1 + \gamma^6) \cdot (\bar{a}_6 + \bar{a}_3)$$

$$M_9 = W_2' \cdot (\bar{a}_4 + \bar{a}_2 + \bar{a}_1) \tag{23}$$

$$M_{10} = W_2' \cdot (\gamma^4 + \gamma^3 + \gamma^2 + \gamma^5) \cdot (\bar{a}_1 + \bar{a}_2)$$

$$M_{11} = W_2' \cdot (\gamma^4 + \gamma^3 + \gamma^1 + \gamma^6) \cdot (\bar{a}_1 + \bar{a}_4)$$

$$M_{12} = W_2' \cdot (\gamma^2 + \gamma^5 + \gamma^1 + \gamma^6) \cdot (\bar{a}_2 + \bar{a}_4)$$

Observe that all thirteen matrix multiplies in (23) are 9-point convolutions of exactly the same form as (8B). Thus one may compute M_j for $j = 0, 1, 2, 3, \ldots, 12$ in (23) with a procedure similar to that used to compute the convolution defined by (8B). Thus, the number of multiplications for computing M_j for $j = 0, 1, 2, \ldots, 12$ is 16, excluding multiplications by γ^0. Hence, the total number of multiplications needed is $13 \times 16 = 208$.

IV. Comparison of New Algorithm with Gentleman's Algorithm

If $N = 2^n - 1 = N_1 \cdot N_2 \cdots N_k$ where $(N_i, N_j) = 1$ for $i \neq j$, Gentleman shows in References 5 and 11 that an N-point transform of such an N requires $N(N_1 + N_2 + \cdots + N_k - k + 1)$ multiplications, including multiplications by unity. The present algorithm for computing the $(2^n - 1)$-point transform for $n = 5, 6$ and Gentleman's algorithm are compared in Table 1. The number of multiplications needed to perform these algorithms is given in both cases. Evidently for $n = 5$ and 6 the new algorithm for computing the $(2^n - 1)$-point transform requires considerably fewer multiplications than Gentleman's algorithm.

V. Transform Decoder for Reed-Solomon Codes

It is shown in References 12 and 15 that RS codes can be decoded with a fast transform algorithm over $GP(p^n)$ and continued fractions. There it was shown that the transform over $GF(p^n)$ where p is a prime and n is an integer can be used to compute the syndrome and error magnitudes. It follows from References 5 and 16 that the number of multiplications required to perform the syndrome and error magnitude calculations for the standard decoder is approximately $(N - 1)(d - 1) + t^2$, where N is the block length of the RS code in $GF(2^n)$, $d = 2t + 1$ is the minimum distance of the code and t is the number of allowable errors. (Note that the performance of the conventional decoder is dependent on the number of allowable errors.)

For (31, 15) and (63, 33) RS codes, the number of multiplications needed to compute the syndrome and the error magnitudes is given in Table 2. The new algorithm, Gentleman's algorithm, and the standard algorithm are compared in Table 2 in terms of the number of multiplications needed to compute the syndrome and the error magnitudes for decoding these RS codes.

ORIGINAL PAGE IS
OF POOR QUALITY

Appendix A

Consider $N_t = 7$. Let γ be a 7th root of unity in $GF(2^6)$. The transform over $GF(2^6)$ is expressible as

$$\begin{pmatrix} A_0 \\ A_1 \\ A_2 \\ A_3 \\ A_4 \\ A_5 \\ A_6 \end{pmatrix} = \begin{pmatrix} \gamma^0 & \gamma^0 & \gamma^0 & \gamma^0 & \gamma^0 & \gamma^0 & \gamma^0 \\ \gamma^0 & \gamma^1 & \gamma^2 & \gamma^3 & \gamma^4 & \gamma^5 & \gamma^6 \\ \gamma^0 & \gamma^2 & \gamma^4 & \gamma^6 & \gamma^1 & \gamma^3 & \gamma^5 \\ \gamma^0 & \gamma^3 & \gamma^6 & \gamma^2 & \gamma^5 & \gamma^1 & \gamma^4 \\ \gamma^0 & \gamma^4 & \gamma^1 & \gamma^5 & \gamma^2 & \gamma^6 & \gamma^3 \\ \gamma^0 & \gamma^5 & \gamma^3 & \gamma^1 & \gamma^6 & \gamma^4 & \gamma^2 \\ \gamma^0 & \gamma^6 & \gamma^5 & \gamma^4 & \gamma^3 & \gamma^2 & \gamma^1 \end{pmatrix} \begin{pmatrix} a_0 \\ a_1 \\ a_2 \\ a_3 \\ a_4 \\ a_5 \\ a_6 \end{pmatrix} \tag{A-1}$$

The permutation σ of $N = 7$ is given by

$$\sigma = \begin{pmatrix} 1 & 2 & 3 & 4 & 5 & 6 \\ 3 & 2 & 6 & 4 & 5 & 1 \end{pmatrix}$$

Applying the above permutation to (A-1), one obtains a 6×6 cyclic matrix equation. By Theorem 1, there exists a permutation π of rows and columns so that the 6×6 cyclic matrix can be partitioned into a 2×2 block matrix of 3×3 cyclic matrices as

$$\begin{pmatrix} B_3 \\ B_5 \\ B_6 \\ B_4 \\ B_2 \\ B_1 \end{pmatrix} = \begin{pmatrix} \gamma^2 & \gamma^1 & \gamma^4 & \gamma^5 & \gamma^6 & \gamma^3 \\ \gamma^1 & \gamma^4 & \gamma^2 & \gamma^6 & \gamma^3 & \gamma^5 \\ \gamma^4 & \gamma^2 & \gamma^1 & \gamma^3 & \gamma^5 & \gamma^6 \\ \gamma^5 & \gamma^6 & \gamma^3 & \gamma^2 & \gamma^1 & \gamma^4 \\ \gamma^6 & \gamma^3 & \gamma^5 & \gamma^1 & \gamma^4 & \gamma^2 \\ \gamma^3 & \gamma^5 & \gamma^6 & \gamma^4 & \gamma^2 & \gamma^1 \end{pmatrix} \begin{pmatrix} a_3 \\ a_5 \\ a_6 \\ a_4 \\ a_2 \\ a_1 \end{pmatrix} \tag{A-2}$$

or

$$\begin{pmatrix} E_1 \\ E_2 \end{pmatrix} = \begin{pmatrix} A & B \\ B & A \end{pmatrix} \begin{pmatrix} X_1 \\ X_2 \end{pmatrix}$$

$$= \begin{pmatrix} (X_1 + X_2) \cdot A + (B - A) \cdot X_2 \\ (X_1 + X_2) \cdot A + (B - A) \cdot X_1 \end{pmatrix}$$

$$= \begin{pmatrix} D + E \\ D + F \end{pmatrix}$$

where

$D = (X_1 + X_2) \cdot A$, $E = (B - A) \cdot X_2$, $F = (B - A) \cdot X_1$.

Since A and B are cyclic matrices, it is evident that the matrix $B - A$ is also a cyclic matrix. In (A-2), D is defined as

$$D = \begin{pmatrix} d_0 \\ d_1 \\ d_2 \end{pmatrix} = \begin{pmatrix} \gamma^2 & \gamma^1 & \gamma^4 \\ \gamma^1 & \gamma^4 & \gamma^2 \\ \gamma^4 & \gamma^2 & \gamma^1 \end{pmatrix} \begin{pmatrix} Y_0 \\ Y_1 \\ Y_2 \end{pmatrix}$$

where

$Y_0 = a_3 + a_4$, $Y_1 = a_5 + a_2$, and $Y_2 = a_6 + a_1$.

Using the 3-point cyclic convolution in (2) and making the correspondences, $a_0 \longleftrightarrow \gamma^2$, $a_1 \longleftrightarrow \gamma^1$, $a_2 \longleftrightarrow \gamma^4$, $x_0 \longleftrightarrow Y_0$, $x_1 \longleftrightarrow Y_1$, $x_2 \longleftrightarrow Y_2$, $y_0 \longleftrightarrow d_0$, $y_1 \longleftrightarrow d_1$, $y_2 \longleftrightarrow d_2$, one obtains

$$D = \begin{pmatrix} d_0 \\ d_1 \\ d_2 \end{pmatrix} = \begin{pmatrix} (\gamma^4 + \gamma^2 + \gamma^1) \cdot (a_3 + a_4 + a_5 + a_2 + a_6 + a_1) + (\gamma^4 + \gamma^2) \\ \cdot (a_6 + a_1 + a_2 + a_5) + (\gamma^4 + \gamma^1) \cdot (a_6 + a_1 + a_3 + a_4) \\ (\gamma^4 + \gamma^2 + \gamma^1) \cdot (a_3 + a_4 + a_5 + a_2 + a_6 + a_1) + (\gamma^4 + \gamma^1) \\ \cdot (a_6 + a_1 + a_3 + a_4) + (\gamma^2 + \gamma^1) \cdot (a_5 + a_2 + a_3 + a_4) \\ (\gamma^4 + \gamma^1 + \gamma^2) \cdot (a_3 + a_4 + a_5 + a_2 + a_6 + a_1) + (\gamma^2 + \gamma^1) \\ \cdot (a_5 + a_2 + a_3 + a_4) + (\gamma^4 + \gamma^2) \cdot (a_6 + a_1 + a_5 + a_2) \end{pmatrix} \quad \text{(A-3)}$$

Similarly,

$$E = \begin{pmatrix} e_0 \\ e_1 \\ e_2 \end{pmatrix} = \begin{pmatrix} \gamma^2 + \gamma^5\,\gamma^1 + \gamma^6\,\gamma^4 + \gamma^3 \\ \gamma^1 + \gamma^6\,\gamma^4 + \gamma^3\,\gamma^2 + \gamma^5 \\ \gamma^4 + \gamma^3\,\gamma^2 + \gamma^5\,\gamma^1 + \gamma^6 \end{pmatrix} \begin{pmatrix} a_4 \\ a_2 \\ a_1 \end{pmatrix}$$

$$= \begin{pmatrix} (\gamma^4 + \gamma^3 + \gamma^2 + \gamma^5 + \gamma^1 + \gamma^6) \cdot (a_4 + a_2 + a_1) + (\gamma^4 + \gamma^3 + \gamma^2 + \gamma^5) \cdot (a_1 + a_2) + (\gamma^4 + \gamma^3 + \gamma^1 + \gamma^6) \cdot (a_1 + a_4) \\ (\gamma^4 + \gamma^3 + \gamma^2 + \gamma^5 + \gamma^1 + \gamma^6) \cdot (a_4 + a_2 + a_1) + (\gamma^4 + \gamma^3 + \gamma^1 + \gamma^6) \cdot (a_1 + a_4) + (\gamma^2 + \gamma^5 + \gamma^1 + \gamma^6) \cdot (a_2 + a_4) \\ (\gamma^4 + \gamma^3 + \gamma^2 + \gamma^5 + \gamma^1 + \gamma^6) \cdot (a_4 + a_2 + a_1) + (\gamma^2 + \gamma^5 + \gamma^1 + \gamma^6) \cdot (a_2 + a_4) + (\gamma^4 + \gamma^3 + \gamma^2 + \gamma^5) \cdot (a_1 + a_2) \end{pmatrix} \tag{A-4}$$

and

$$F = \begin{pmatrix} f_0 \\ f_1 \\ f_2 \end{pmatrix} = \begin{pmatrix} \gamma^2 + \gamma^5\,\gamma^1 + \gamma^6\,\gamma^4 + \gamma^3 \\ \gamma^1 + \gamma^6\,\gamma^4 + \gamma^3\,\gamma^2 + \gamma^5 \\ \gamma^4 + \gamma^3\,\gamma^2 + \gamma^5\,\gamma^1 + \gamma^6 \end{pmatrix} \begin{pmatrix} a_3 \\ a_5 \\ a_6 \end{pmatrix}$$

$$= \begin{pmatrix} (\gamma^4 + \gamma^3 + \gamma^2 + \gamma^5 + \gamma^1 + \gamma^6) \cdot (a_3 + a_5 + a_6) + (\gamma^4 + \gamma^3 + \gamma^2 + \gamma^5) \cdot (a_6 + a_5) + (\gamma^4 + \gamma^3 + \gamma^1 + \gamma^6) \cdot (a_6 + a_3) \\ (\gamma^4 + \gamma^3 + \gamma^2 + \gamma^5 + \gamma^1 + \gamma^6) \cdot (a_3 + a_5 + a_6) + (\gamma^4 + \gamma^3 + \gamma^1 + \gamma^6) \cdot (a_6 + a_5) + (\gamma^4 + \gamma^3 + \gamma^1 + \gamma^6) \cdot (a_5 + a_3) \\ (\gamma^4 + \gamma^3 + \gamma^2 + \gamma^5 + \gamma^1 + \gamma^6) \cdot (a_3 + a_5 + a_6) + (\gamma^2 + \gamma^5 + \gamma^1 + \gamma^6) \cdot (a_5 + a_3) + (\gamma^4 + \gamma^3 + \gamma^2 + \gamma^5) \cdot (a_6 + a_5) \end{pmatrix} \tag{A-5}$$

Each of the Eqs. (A-3), (A-4), and (A-5) requires 4 multiplies.

Let

$$m_0 = 1 \cdot (a_0 + a_1 + a_2 + a_3 + a_4 + a_5 + a_6)$$

$$m_1 = (\gamma^2 + \gamma^1 + \gamma^4 + 1) \cdot (a_3 + a_4 + a_5 + a_2 + a_6 + a_1)$$

$$m_2 = (\gamma^2 + \gamma^1) \cdot (a_6 + a_2 + a_3 + a_4)$$

$$m_3 = (\gamma^4 + \gamma^2) \cdot (a_6 + a_1 + a_5 + a_2)$$

$$m_4 = 1 \cdot (a_3 + a_5 + a_6)$$

ORIGINAL PAGE IS
OF POOR QUALITY

$$m_5 = (\gamma^2 + \gamma^5 + \gamma^1 + \gamma^6) \cdot (a_5 + a_3)$$

$$m_6 = (\gamma^4 + \gamma^3 + \gamma^2 + \gamma^5) \cdot (a_6 + a_5)$$

$$m_7 = (\gamma^4 + \gamma^1) \cdot (a_6 + a_1 + a_3 + a_4)$$

$$m_8 = (\gamma^4 + \gamma^3 + \gamma^1 + \gamma^6) \cdot (a_6 + a_3)$$

$$m_9 = 1 \cdot (a_4 + a_2 + a_1)$$

$$m_{10} = (\gamma^4 + \gamma^3 + \gamma^2 + \gamma^5) \cdot (a_1 + a_2)$$

$$m_{11} = (\gamma^4 + \gamma^3 + \gamma^1 + \gamma^6) \cdot (a_1 + a_4)$$

$$m_{12} = (\gamma^2 + \gamma^5 + \gamma^1 + \gamma^6) \cdot (a_2 + a_4)$$

Thus, by (A-1), (A-2), (A-3), (A-4), and (A-5), one obtains

$$\begin{aligned}
A_0 &= m_0 \\
A_1 &= m_0 + m_1 + m_2 + m_3 + m_4 + m_5 + m_6 \\
A_2 &= m_0 + m_1 + m_7 + m_2 + m_4 + m_8 + m_5 \\
A_3 &= m_0 + m_1 + m_3 + m_7 + m_9 + m_{10} + m_{11} \\
A_4 &= m_0 + m_1 + m_3 + m_7 + m_4 + m_6 + m_8 \\
A_5 &= m_0 + m_1 + m_7 + m_2 + m_9 + m_{11} + m_{12} \\
A_6 &= m_0 + m_1 + m_2 + m_3 + m_9 + m_{12} + m_{10}
\end{aligned} \tag{A-6}$$

Thus, by (A-6), one observes that the number of multiplications needed to perform a 7-point transform over $GF(2^7)$ is 13, including the multiplications by unit $\gamma^0 = 1$.

Consider $N_i = 3^2$. Let γ be the 9th root of unity. Since 1, 2, 4, 5, 7, 8 are relatively prime to 9, the permutation σ is defined by

$$\sigma = \begin{pmatrix} 1, & 2, & 4, & 5, & 7, & 8 \\ 2, & 4, & 8, & 7, & 5, & 1 \end{pmatrix} \tag{A-7}$$

Rearranging the rows and columns of W defined in (17) in such a manner that the elements of matrix with indices relatively prime to 9 form a block, one has

$$\begin{pmatrix} b_1 \\ b_2 \\ b_4 \\ b_5 \\ b_7 \\ b_8 \\ b_3 \\ b_6 \end{pmatrix} = \begin{pmatrix} \gamma^{1\cdot1} & \gamma^{1\cdot2} & \gamma^{1\cdot4} & \gamma^{1\cdot5} & \gamma^{1\cdot7} & \gamma^{1\cdot8} & \gamma^{1\cdot3} & \gamma^{1\cdot6} \\ \gamma^{2\cdot1} & \gamma^{2\cdot2} & \gamma^{2\cdot4} & \gamma^{2\cdot5} & \gamma^{2\cdot7} & \gamma^{2\cdot8} & \gamma^{2\cdot3} & \gamma^{2\cdot6} \\ \gamma^{4\cdot1} & \gamma^{4\cdot2} & \gamma^{4\cdot4} & \gamma^{4\cdot5} & \gamma^{4\cdot7} & \gamma^{4\cdot8} & \gamma^{4\cdot3} & \gamma^{4\cdot6} \\ \gamma^{5\cdot1} & \gamma^{5\cdot2} & \gamma^{5\cdot4} & \gamma^{5\cdot5} & \gamma^{5\cdot7} & \gamma^{5\cdot8} & \gamma^{5\cdot3} & \gamma^{5\cdot6} \\ \gamma^{7\cdot1} & \gamma^{7\cdot2} & \gamma^{7\cdot4} & \gamma^{7\cdot5} & \gamma^{7\cdot7} & \gamma^{7\cdot8} & \gamma^{7\cdot3} & \gamma^{7\cdot6} \\ \gamma^{8\cdot1} & \gamma^{8\cdot2} & \gamma^{8\cdot4} & \gamma^{8\cdot5} & \gamma^{8\cdot7} & \gamma^{8\cdot8} & \gamma^{8\cdot3} & \gamma^{8\cdot6} \\ \gamma^{3\cdot1} & \gamma^{3\cdot2} & \gamma^{3\cdot4} & \gamma^{3\cdot5} & \gamma^{3\cdot7} & \gamma^{3\cdot8} & \gamma^{3\cdot3} & \gamma^{3\cdot6} \\ \gamma^{6\cdot1} & \gamma^{6\cdot2} & \gamma^{6\cdot4} & \gamma^{6\cdot5} & \gamma^{6\cdot7} & \gamma^{6\cdot8} & \gamma^{6\cdot3} & \gamma^{6\cdot6} \end{pmatrix} \begin{pmatrix} a_1 \\ a_2 \\ a_4 \\ a_5 \\ a_7 \\ a_8 \\ a_3 \\ a_6 \end{pmatrix} \tag{A-8}$$

Applying the permutation defined in (A-7) to the indices of the upper left 6×6 matrix of (A-8), one obtains

$$\begin{pmatrix} Y_2 \\ Y_4 \\ Y_8 \\ Y_7 \\ Y_5 \\ Y_1 \end{pmatrix} = \begin{pmatrix} \gamma^4 & \gamma^8 & \gamma^7 & \gamma^5 & \gamma^1 & \gamma^2 \\ \gamma^8 & \gamma^7 & \gamma^5 & \gamma^1 & \gamma^2 & \gamma^4 \\ \gamma^7 & \gamma^5 & \gamma^1 & \gamma^2 & \gamma^4 & \gamma^8 \\ \gamma^5 & \gamma^1 & \gamma^2 & \gamma^4 & \gamma^8 & \gamma^7 \\ \gamma^1 & \gamma^2 & \gamma^4 & \gamma^8 & \gamma^7 & \gamma^5 \\ \gamma^2 & \gamma^4 & \gamma^8 & \gamma^7 & \gamma^5 & \gamma^1 \end{pmatrix} \begin{pmatrix} a_2 \\ a_4 \\ a_8 \\ a_7 \\ a_5 \\ a_1 \end{pmatrix}$$

By Theorem 1, the above matrix can be partitioned into a 2×2 block matrix of 3×3 cyclic blocks as

$$\begin{pmatrix} Y_2 \\ Y_5 \\ Y_8 \\ Y_7 \\ Y_4 \\ Y_1 \end{pmatrix} = \begin{pmatrix} \gamma^4 & \gamma^1 & \gamma^7 & \gamma^5 & \gamma^8 & \gamma^2 \\ \gamma^1 & \gamma^7 & \gamma^4 & \gamma^8 & \gamma^2 & \gamma^5 \\ \gamma^7 & \gamma^4 & \gamma^1 & \gamma^2 & \gamma^5 & \gamma^8 \\ \gamma^5 & \gamma^8 & \gamma^2 & \gamma^4 & \gamma^1 & \gamma^7 \\ \gamma^8 & \gamma^2 & \gamma^5 & \gamma^1 & \gamma^7 & \gamma^4 \\ \gamma^2 & \gamma^5 & \gamma^8 & \gamma^7 & \gamma^4 & \gamma^1 \end{pmatrix} \begin{pmatrix} a_2 \\ a_5 \\ a_8 \\ a_7 \\ a_4 \\ a_1 \end{pmatrix} \tag{A-9}$$

ORIGINAL PAGE IS
OF POOR QUALITY

Now if one makes the correspondences, $\gamma^2 \leftrightarrow \gamma^4$, $\gamma^1 \leftrightarrow \gamma^1$, $\gamma^4 \leftrightarrow \gamma^7$, $\gamma^5 \leftrightarrow \gamma^5$, $\gamma^6 \leftrightarrow \gamma^8$, $\gamma^3 \leftrightarrow \gamma^2$, $B_3 \leftrightarrow Y_2$, $B_5 \leftrightarrow Y_5$, $B_6 \leftrightarrow Y_8$, $B_4 \leftrightarrow Y_7$, $B_2 \leftrightarrow Y_4$, $B_1 \leftrightarrow Y_1$, $a_3 \leftrightarrow a_2$, $a_5 \leftrightarrow a_5$, $a_6 \leftrightarrow a_8$, $a_4 \leftrightarrow a_7$, $a_2 \leftrightarrow a_4$, $a_1 \leftrightarrow a_1$ in (A-2), then by a procedure similar to that used to compute the matrix defined in (A-2), one obtains

$$
\begin{aligned}
Y_1 &= m_1 + m_2 + m_3 + m_4 + m_5 + m_6 \\
Y_4 &= m_1 + m_7 + m_2 + m_4 + m_8 + m_5 \\
Y_2 &= m_1 + m_3 + m_7 + m_9 + m_{10} + m_{11} \\
Y_7 &= m_1 + m_3 + m_7 + m_4 + m_6 + m_8 \\
Y_5 &= m_1 + m_7 + m_2 + m_9 + m_{11} + m_{12} \\
Y_8 &= m_1 + m_2 + m_3 + m_9 + m_{12} + m_{10}
\end{aligned}
$$

where

$$
\begin{aligned}
m_1 &= (\gamma^4 + \gamma^1 + \gamma^7) \cdot (a_2 + a_7 + a_5 + a_4 + a_8 + a_1) \\
m_2 &= (\gamma^4 + \gamma^1) \cdot (a_5 + a_4 + a_2 + a_7) \\
m_3 &= (\gamma^7 + \gamma^4) \cdot (a_8 + a_1 + a_5 + a_4) \\
m_4 &= 1 \cdot (a_2 + a_5 + a_8) \\
m_5 &= (\gamma^4 + \gamma^5 + \gamma^1 + \gamma^8) \cdot (a_5 + a_2) \\
m_6 &= (\gamma^7 + \gamma^2 + \gamma^4 + \gamma^5) \cdot (a_8 + a_5) \\
m_7 &= (\gamma^7 + \gamma^1) \cdot (a_8 + a_1 + a_2 + a_7) \\
m_8 &= (\gamma^7 + \gamma^2 + \gamma^1 + \gamma^8) \cdot (a_8 + a_2) \\
m_9 &= 1 \cdot (a_7 + a_4 + a_1) \\
m_{10} &= (\gamma^7 + \gamma^2 + \gamma^4 + \gamma^5) \cdot (a_1 + a_4) \\
m_{11} &= (\gamma^7 + \gamma^2 + \gamma^1 + \gamma^8) \cdot (a_1 + a_7) \\
m_{12} &= (\gamma^4 + \gamma^5 + \gamma^1 + \gamma^8) \cdot (a_4 + a_7)
\end{aligned}
\qquad \text{(A-10)}
$$

From (A-10), we know that the number of multiplications required to perform (32) is 10 excluding multiplications by γ^0

The last two columns of the matrix defined in (A-8) can be obtained by computing the following 2 X 2 cyclic matrix

$$\begin{pmatrix} X_1 \\ X_2 \end{pmatrix} = \begin{pmatrix} \gamma^3 & \gamma^6 \\ \gamma^6 & \gamma^3 \end{pmatrix} \begin{pmatrix} a_3 \\ a_6 \end{pmatrix} = \begin{pmatrix} \gamma^3 (a_3 + a_6) + (\gamma^3 + \gamma^6) a_6 \\ \gamma^3 (a_3 + a_6) + (\gamma^3 + \gamma^6) a_3 \end{pmatrix} \tag{A-11}$$

The last two rows of the matrix defined in (A-8) can be obtained by computing the following cyclic matrix

$$\begin{pmatrix} Z_1 \\ Z_2 \end{pmatrix} = \begin{pmatrix} \gamma^3 & \gamma^6 \\ \gamma^6 & \gamma^3 \end{pmatrix} \begin{pmatrix} a_1 + a_4 + a_7 \\ a_2 + a_5 + a_8 \end{pmatrix} \tag{A-12}$$

$$= \begin{pmatrix} \gamma^3 (a_1 + a_4 + a_7 + a_2 + a_5 + a_8) + (\gamma^3 + \gamma^6)(a_2 + a_5 + a_8) \\ \gamma^3 (a_1 + a_4 + a_7 + a_2 + a_5 + a_8) + (\gamma^3 + \gamma^6)(a_1 + a_4 + a_7) \end{pmatrix}$$

Note that the number of multiplications used to perform (A-11) or (A-12) is 3. Thus, the algorithm for computing the 9-point transform is

$$\begin{aligned}
b_0 &= 1 \cdot (a_0 + a_1 + a_2 + a_3 + a_4 + a_5 + a_6 + a_7 + a_8) \\
b_1 &= Y_1 + X_1 + 1 \cdot a_0 \\
b_2 &= Y_2 + X_2 + 1 \cdot a_0 \\
b_3 &= Z_1 + Z_2 + 1 \cdot a_3 + 1 \cdot a_6 + 1 \cdot a_0 \\
b_4 &= Y_4 + X_1 + 1 \cdot a_0 \\
b_5 &= Y_5 + X_2 + 1 \cdot a_0 \\
b_6 &= Z_2 + Z_1 + 1 \cdot a_3 + 1 \cdot a_6 + 1 \cdot a_0 \\
b_7 &= Y_7 + X_1 + 1 \cdot a_0 \\
b_8 &= Y_8 + X_2 + 1 \cdot a_0
\end{aligned} \tag{A-13}$$

ORIGINAL PAGE IS
OF POOR QUALITY

From (A-13), the total number of multiplications needed to perform a 9-point transform is 16, excluding multiplications by the unit $\gamma^0 = 1$.

Acknowledgement

The authors wish to thank Dr. N. A. Renzetti, Manager of Tracking and Data Acquisition Engineering, and the members of the Advanced Engineering Group in that organization at the Jet Propulsion Laboratory for their early support, suggestions, and encouragement of the research which led to this paper.

References

1. R. R. Green, "Analysis of a Serial Orthogonal Decoder," *Space Programs Summary 37-53*, Vol. III, 1968, pp. 185-187.
2. I. S. Reed, "A Class of Multiple-Error-Correcting Codes and the Decoding Scheme," *IRE Trans.*, PGIT-4, 1954, pp. 38-49.
3. W. C. Gore, "Transmitting Binary Symbols with Reed-Solomon Code," Johns Hopkins EE Report No. 73-5, April 1973.
4. D. Mandelbaum, "On Decoding Reed-Solomon Codes," *IEEE Trans. on Inform. Theory*, Vol. IT-17, No. 6, pp. 707-712, November 1971.
5. A. Michelson, "A New Decoder for the Reed-Solomon Codes Using a Fast Transform Technique," Systems Engineering Technical Memorandum, No. 52, Electronic Systems Group Eastern Division GTE Sylvania, August 1975.
6. W. W. Peterson, "Error-Correcting Codes," MIT Press, Cambridge, Mass., 1961, pp. 168-169.
7. S. Lin, "An Introduction to Error-Correcting Codes," Englewood Cliffs, N. J., Prentice-Hall, 1970.
8. J. Odenwalder, et al., "Hybrid Coding Systems Study Final Report," Linkabit Corp., NASA CR 114,486, Sept. 1972.
9. S. Winograd, "On Computing the Discrete Fourier Transform," *Proc. Nat. Acad. Sci. USA*, 1976, 73, pp. 1005-1006.
10. S. Winograd, "On Computing the Discrete Fourier Transform," Research Report, Math. Science Dept., IBM Thomas J. Watson Research Center, Yorktown Heights, New York, 10592.
11. W. M. Gentleman, "Matrix Multiplication and Fast Fourier Transforms," *Bell System Technical Journal*, 1968, pp. 1099-1103.
12. I. S. Reed, T. K. Truong, and B. Benjauthrit, "Transform Decoding of Reed-Solomon Codes over $GF(2^{2^n})$ Using the Techniques of Winograd," Submitted to *IEEE Trans. on Inform Theory.*
13. E. R. Berlekamp, Algebraic Coding Theory, New York, McGraw Hall, 1968.
14. I. S. Reed and T. K. Truong, "Fast Mersenne Prime Transforms for Digital Filters," to be published in the Proceedings of IEEE.
15. I. S. Reed, R. A. Scholtz, T. K. Truong, and L. R. Welch, "The Fast Decoding of Reed-Solomon Codes Using Fermat Theoretic Transforms and Continued Fractions," to be published in *IEEE Trans. Inform Theory.*
16. G. D. Forney, "On Decoding BCH Codes," *IEEE Transactions on Information Theory*, IT-11, October 1965.

Table 1. The Complexity of Transform over $GF(2^n)$ for n = 5, 6

$N = 2^n - 1$	Factors $N_1 \cdot N_2 \cdots N_k$	No. Mult. of New algorithm	No. Mult. of Gentleman's algorithm $N(N_1 + N_2 + \cdots + N_k - k + 1)$
$2^5 - 1$	31	120	961
$2^6 - 1$	7·9	$13 \cdot 16 = 208$	$63(7 + 9 - 1) = 945$

Table 2. The Complexity of Decoding RS of 2^n - 1 Points for n = 5, 6

N	Factors $N_1 \cdot N_2 \cdots N_k$	No. mult. of new algorithm	No. mult. of Gentleman's algorithm $2N(N_1 + N_2 + N_3 + \cdots - k + 1)$	No. mult. of the standard algorithm $(N - 1)(d - 1) + t^2$
31	31	$2 \times 120 = 240$	$2 \times 961 = 1922$	$30 \times 16 + 8^2 = 544$
63	7·9	$2 \times 208 = 416$	$2 \times 945 = 1890$	$62 \times 30 + 15^2 = 2085$

N78-24231

Electron Density and Doppler RMS Phase Fluctuation in the Inner Corona

A. L. Berman
TDA Engineering Office

Previous work has developed a self-consistent set of solar wind descriptors for the extended corona ($5\ r_\odot \leqslant r \leqslant 1$ AU). In this article, observations of the radial dependence of electron density and RMS phase fluctuation are used to construct a similar and symmetrical set of descriptors for the vastly different regime of the inner corona ($r_\odot \leqslant r \leqslant 5\ r_\odot$). The article concludes that the applicability of symmetrical coronal descriptors for both the inner and extended corona argues forcefully for the basic validity of the description.

I. Introduction

In a previous article (Ref. 1), extensive work by J. V. Hollweg (Refs. 2 through 4) was shown to provide a framework in which observations of the radial dependence of phase fluctuation and electron density in the extended corona ($5r_\odot \leqslant r \leqslant 1$ AU) could be combined with various assumptions and conservation of particle flow to produce an internally consistent set of solar wind descriptors. These are reproduced from Ref. 1 for the extended corona as follows:

$$\phi(a) \propto a^{-1.3}$$

$$N_e(r) \propto r^{-2.3}$$

$$L_t(r) \propto r$$

$$n(r) \propto r^{-2.3}$$

$$n/N_e = \epsilon;\ \epsilon \neq \epsilon(r)$$

$$v(r) \propto r^{0.3}$$

where

ϕ = RMS phase fluctuation

N_e = electron density

L_t = transverse fluctuation scale

n = electron density fluctuation

ϵ = ratio of electron density fluctuation to (mean) density

v = radial component of the solar wind velocity

a = signal closest approach distance

r = radial distance

$r_\odot$ = solar radius

ORIGINAL PAGE IS OF POOR QUALITY

It should be noted that the value for $\phi(a)$ assumes a signal path integration of $(-\infty,\infty)$ about the signal closest approach point; due to the finite limits of the Earth and the spacecraft, the observed radial dependence of actual data will always be somewhat steeper than $a^{-1.3}$.

The inner corona (here to be defined as $r_\odot \leqslant r \leqslant 5r_\odot$) forms a sharply distinct regime ("solar wind acceleration region") from the extended corona in regard to the radial dependence of electron density, solar wind radial velocity, etc., and hence provides an excellent opportunity for validating the extended corona description. It is therefore the purpose of this article to explore the relationship of the various coronal descriptors of the inner corona. Experimental observations of phase fluctuation and electron density in the inner corona will be shown to provide a self-consistent set of coronal descriptors which is symmetrical with those of the extended corona. The fact that the same description prevails in both (vastly distinct) coronal regimes is interpreted as compelling evidence for the validity of the description.

II. Phase Fluctuation Observations in the Inner Corona

The equatorial electron density model derived by Berman and Wackley (Refs. 5 through 7) from Viking Doppler noise and concurrent measurements of dual frequency (S minus X) range is:

$$N_e(r) = \frac{2.39 \times 10^8}{r^6} + \frac{1.67 \times 10^6}{r^{2.30}}, \text{ electrons/cm}^3$$

r = radial distance, solar radii

The doppler noise model ("ISEDC"; Ref. 5) which is the (signal path integrated) equivalent of the above electron density model is:

$$\text{ISEDC, Hz} = A_0 \left[\frac{\beta}{(\sin\alpha)^{1.30}}\right] F(\alpha,\beta) + A_1 \left[\frac{1}{(\sin\alpha)^5}\right]$$

$$F(\alpha,\beta) = 1 - 0.05 \left\{\frac{(\beta - \pi/2 + \alpha)^3 - (\alpha - \pi/2)^3}{\beta}\right\}$$

$$- 0.00275 \left\{\frac{(\beta - \pi/2 + \alpha)^5 - (\alpha - \pi/2)^5}{\beta}\right\}$$

where

α = Sun-Earth-probe (SEP) angle, radians

β = Earth-Sun-probe (ESP) angle, radians

$$A_0 = 1.182 \times 10^{-3}$$

$$A_1 = 4.75 \times 10^{-10}$$

For the above models, the electron density terms become equal valued at approximately $r = 4r_\odot$, while the corresponding Doppler noise terms become equal valued at approximately $r = 3r_\odot$. Doppler noise observations in the region $r < 4r_\odot$ are naturally quite sparse; however 20 pass average Doppler values have been accumulated for this inner coronal region from various Solar Conjunctions of Helios 1, Helios 2, and Viking. The method of computing "pass average" values is described in detail in Ref. 8. In deriving the ISEDC model, a three parameter (essentially simultaneous) least squares minimization was performed. The three parameters solved for were the inner corona term coefficient (A_1), and the extended corona term coefficient (A_0) and radial index (-1.30). Figure 1 presents the inner corona data as compared to the inner corona term, the extended corona term, and the combined ISEDC model. The data in the region $r < 4r_\odot$ are clearly seen to respond to the (integrated) inner coronal electron density term ($\propto a^{-5}$). Figure 2 presents the correlation between the data and the ISEDC model. Again the correlation is seen to be quite strong. The data in Figures 1 and 2 provide forceful evidence that $\phi(a) \propto a^{-5}$ in the inner corona.

III. Electron Density Observations in the Inner Corona

The radial dependence of electron density in the inner corona has been determined by eclipse photometry methods (van de Hulst, Ref. 9, Saito, Ref. 10, and Blackwell, Ref. 11) and via spacecraft range delays (Muhleman, Mariner 6, Ref. 12, Edenhofer, Helios 2, Ref. 13); in general these experiments have obtained consistent results which indicate a radially dependent electron density in the inner corona of the form $N_e(r) \propto r^{-6}$. Using the relationship derived by Hollweg (Ref. 2), one has for the assumption of a linear transverse scale[1]:

$$\phi^2(a) \propto \int_a^\infty \frac{1}{(r^6)^2} \frac{r^2\,dr}{\sqrt{r^2 - a^2}} \propto (a^{-5})^2$$

[1] The dependence with closest approach distance (a) is obtained by noting the integral:

$$\int_a^\infty \frac{r^\alpha\,dr}{\sqrt{r^2 - a^2}}$$

is transformed via the substitution:

$$r = a(\cos x)^{-1}$$

to:

$$a^\alpha \int_0^{\pi/2} (\cos x)^{-(1+\alpha)}\,dx$$

ORIGINAL PAGE IS
OF POOR QUALITY

Assuming conservation of particle flow in the corona (Cuperman and Harten, Ref. 14):

$$N_e(r)v(r)r^2 = K$$

and the proportionality between electron density and electron density fluctuation ($\epsilon = n/N_e$), one obtains an inner corona set of self-consistent descriptors symmetrical to those for the extended corona:

$$\phi(a) \propto a^{-5}$$

$$N_e(r) \propto r^{-6}$$

$$L_t(r) \propto r$$

$$n(r) \propto r^{-6}$$

$$n/N_e = \epsilon;\ \epsilon \neq \epsilon(r)$$

$$v(r) = r^4$$

This set of coronal descriptors is compared to those for the extended corona in Table 1.

IV. Discussion and Conclusions

Previously, observations of the radial dependence of phase fluctuation and electron density in the extended corona were seen to be consistent with the concept of a linear transverse fluctuation scale. The fact that a vastly different regime exists in the inner corona provides a powerful test bed to check the validity of the extended corona description. Observations of doppler noise and electron density in the inner corona, when combined with the assumption of a linear transverse fluctuation scale and conservation of particle flow, are seen to be self-consistent and symmetrical with the extended coronal description. It is hereby concluded that experimental observations in both the inner and extended corona provide compelling evidence for:

(1) The existence of a linear transverse fluctuation scale.

(2) The existence of proportionality between RMS phase fluctuation and integrated electron density.

References

1. Berman, A. L., "Electron Density in the Extended Corona: Two Views," in *The Deep Space Network Progress Report 42-41*, Jet Propulsion Laboratory, Pasadena, California, October 15, 1977.

2. Hollweg, J. V., "A Statistical Ray Analysis of the Scattering of Radio Waves by the Solar Corona," in *The Astronomical Journal*, Volume 73, Number 10, Part 1, December 1968.

3. Hollweg, J. V., and Harrington, J. V., "Properties of Solar Wind Turbulence Deduced by Radio Astronomical Measurements," in *The Journal of Geophysical Research, Space Physics*, Volume 73, Number 23, December 1, 1968.

4. Hollweg, J. V., "Angular Broadening of Radio Sources by Solar Wind Turbulence," in *The Journal of Geophysical Research, Space Physics*, Volume 75, Number 19, July 1, 1970.

5. Berman, A. L., and Wackley, J. A., "Viking S-Band Doppler RMS Phase Fluctuations Used to Calibrate the Mean 1976 Equatorial Corona," in *The Deep Space Network Progress Report 42-38*, Jet Propulsion Laboratory, Pasadena, California, April 15, 1977.

6. Berman, A. L., Wackley, J. A., Rockwell, S. T., and Kwan, M., "Viking Doppler Noise used to Determine the Radial Dependence of Electron Density in the Extended Corona," in *The Deep Space Network Progress Report 42-38*, Jet Propulsion Laboratory, Pasadena, California, April 15, 1977.

7. Berman, A. L., "Proportionality Between Doppler Noise and Integrated Signal Path Electron Density Validated by Differenced S-X Range," in *The Deep Space Network Progress Report 42-38*, Jet Propulsion Laboratory, Pasadena, California, April 15, 1977.

8. Berman, A. L., "Phase Fluctuation Spectra – New Radio Science Information to Become Available in the DSN Tracking System, Mark III-77," in *The Deep Space Network Progress Report 42-40*, Jet Propulsion Laboratory, Pasadena, California, August 15, 1977.

9. van de Hulst, H. C., "The Electron Density of the Solar Corona," *Bulletin of the Astronomical Institutes of The Netherlands*, Volume XI, Number 410, February 2, 1950.

10. Saito, K., "A Non-Spherical Axisymmetric Model of The Solar K Corona of The Minimum Type," *Annals of The Tokyo Astronomical Observatory*, University of Tokyo, Second Series, Volume XII, Number 2, Mitaka, Tokyo, 1970.

11. Anderson, J. D., Esposito, P. B., Martin, W. L., Thornton, C. L., and Muhleman, D. O., "Experimental Test of General Relativity Using Time Delay Data from Mariner 6 and Mariner 7," in *The Astrophysical Journal*, Volume 200, August 15, 1975.

12. Muhleman, D. O., Esposito, P. B., and Anderson, J. D., "The Electron Density Profile of the Outer Corona and the Interplanetary Medium from Mariner 6 and Mariner 7 Time Delay Measurements," *The Astrophysical Journal*, 211, February 1, 1977.

13. Edenhofer, P., Esposito, P. B., Hansen, R. T., Hansen, S. F., Lueneburg, E., Martin, W. L., and Zygielbaum, A. I., "Time Delay Occultation Data of the Helios Space-

crafts and Preliminary Analysis for Probing the Solar Corona," in the *Journal of Geophysics* 42, 1977.

14. Cuperman, S., and Harten, A., "Some Physical Implications of Recent Solar Wind Measurements" in *Solar Wind*, edited by Sonett, C. P., Coleman, P. J. Jr., and Wilcox, J. M., National Aeronautics and Space Administration, Washington, D. C., 1972.

Table 1. Coronal descriptions for the inner and extended corona

Parameter	Inner corona ($r_\odot \leqslant r \leqslant 5\ r_\odot$)	Extended corona ($5\ r_\odot \leqslant r \leqslant 1$ AU)
$\phi(a) \propto$	$a^{-5.0}$	$a^{-1.3}$
$N_e(r) \propto$	$r^{-6.0}$	$r^{-2.3}$
$L_t(r) \propto$	r	r
$n(r) \propto$	$r^{-6.0}$	$r^{-2.3}$
$n/N_e =$	$\epsilon;\ \epsilon \neq \epsilon(r)$	$\epsilon;\ \epsilon \neq \epsilon\ (r)$
$v(r) \propto$	$r^{4.0}$	$r^{0.3}$

ORIGINAL PAGE IS
OF POOR QUALITY

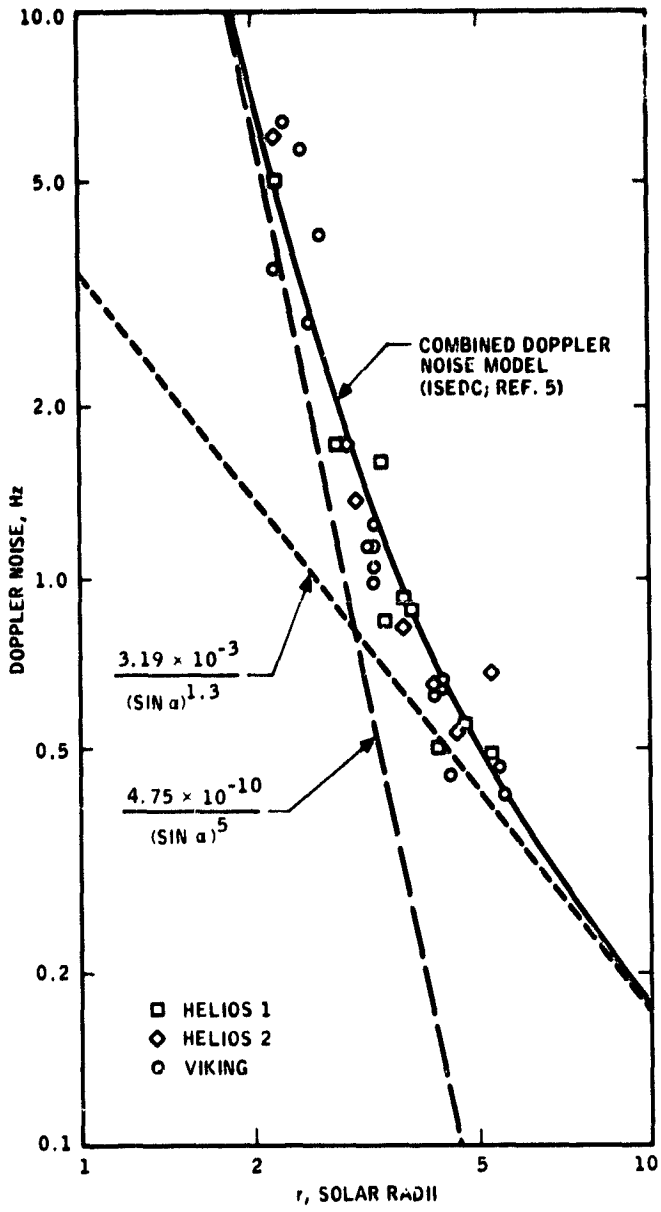

Fig. 1. Doppler noise vs radial distance in the inner corona

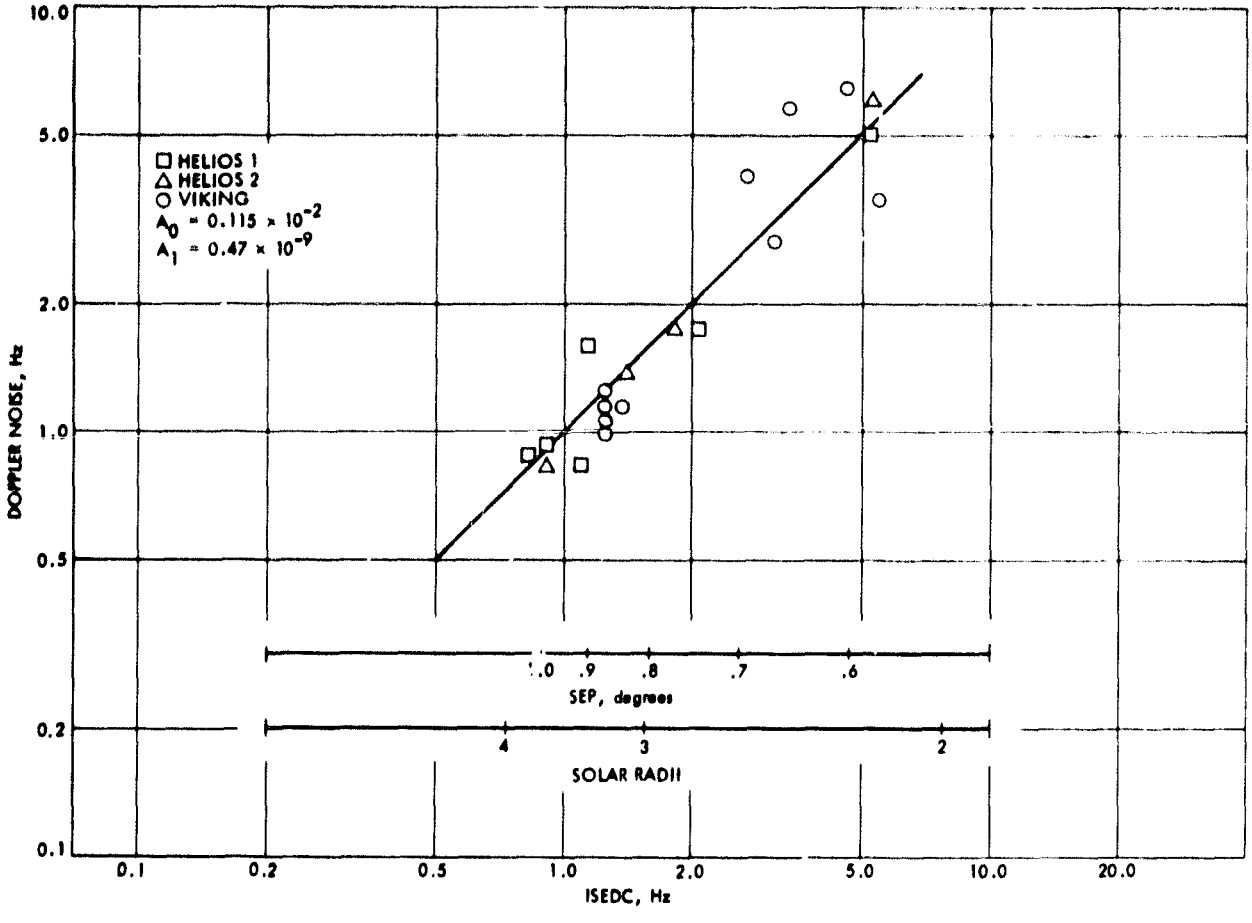

Fig. 2. Correlation of Viking and Helios doppler noise with the ISEDC model between 2 and 4 solar radii

N78-24232

The DSS Radio Science Subsystem—Real-Time Bandwidth Reduction and Wideband Recording of Radio Science Data

A. L. Berman
TDA Engineering Office

New radio science experiment requirements levied by the Pioneer Venus Project have resulted in the development of a multimission radio science subsystem at the 64-m subnet. Major functional capabilities of the DSS Radio Science Subsystem (DRSS) are real-time bandwidth reduction and wideband recording of radio science data. This article provides a functional description of the key characteristics, requirements, and operation of the DRS.

I. Introduction

The Pioneer Venus Mission, with launches scheduled in May 1978 (Pioneer Venus Orbiter) and August 1978 (Pioneer Venus Multiprobe) has two radio science experiments with major impact on The Deep Space Network (DSN). In December 1978 the Pioneer Venus Multiprobe Mission Spacecraft will encounter the planet Venus, and at that time, the Differential Long Baseline Interferometry (DLBI) experiment will attempt to measure wind velocities in the atmosphere of Venus as four probes descend through the atmosphere (Ref. 1). Also starting in December 1978, the Pioneer Venus Orbiter will undergo daily occultations by Venus for a period of approximately three months. In addition, a smaller period of occultations occurs in May 1979.

As the Pioneer Venus Mission planning evolved, it became clear that the DLBI experiment would require that the signals from the four descending probes and the (spacecraft) bus be received on one high phase stability, wideband (~2 MHz) open loop receiver, and that the output of this receiver be recorded on a high precision, very high rate recorder. In addition, it was also clear that costs associated with processing approximately 100 S- and X-band occultations of the Pioneer Venus orbiter by previously used techniques would be quite burdensome (Ref. 2). To reduce these costs, the idea was conceived of driving the open loop receiver first local oscillator with the predicted (atmospherically refracted) frequency, so that only a very narrow open loop receiver output bandwidth would need to be recorded. Since processing costs are approximately linear with recorded bandwidth, this procedure would be expected to result in substantial savings.

As a result of these new radio science experiment requirements, it became apparent that it would be appropriate for the DSN to create a Radio Science System (Ref. 3). The

equipment at the 64-meter subnet which will perform the "real-time bandwidth reduction"[1] and the wideband recording was combined to form the DSS Radio Science Subsystem (DRS). This article describes in detail the functional operation of the DSS Radio Science Subsystem. It should be emphasized that although the initial implementation of the DRS is geared toward the Pioneer Venus mission, the DRS provides multimission radio science capabilities, and will be extensively utilized in fulfillment of the radio science requirements of other projects, such as Viking, Voyager, Galileo, etc.

II. Functional Description of the DSS Radio Science Subsystem

A. Definition

The DSS Radio Science Subsystem, a dedicated and integral element of the DSN Radio Science System, performs the following functions:

(1) Receives programmed oscillator (PO) frequency predictions and uses an error detection algorithm to verify correctness of predictions transmission.

(2) Reduces required open-loop receiver bandwidth via automatic control of a programmed oscillator which centers the open-loop receiver about the predicted frequency profile.

(3) Digitizes and formats for high-speed data line (HSDL) transmission the narrowband open-loop receiver data and programmed oscillator data (radio science data).

(4) Digitizes and records wideband open-loop receiver data and associated timing information (wideband radio science data) on magnetic tape.

DSS Radio Science Subsystem functions and interfaces are presented in Fig. 1, while Fig. 2 presents functions and data flow.

B. Key Characteristics

The key characteristics of the DSS Radio Science Subsystem are listed below for functions of the Occultation Data Assembly (ODA) and the Digital Recording Assembly (DRA).

1. Real-time bandwidth reduction (ODA) key characteristics.

(1) Hardware and software compatibility with DSN Mark III configuration.

(2) Programmed oscillator frequency predictions reception via HSDL; transmission verification by an error detection algorithm.

(3) Frequency predictions conversion to frequency rates for automatic control of programmed oscillator that drives S- and X-band open-loop receivers.

(4) Availability of four analog-to-digital (A-D) conversion channels capable of being configured to digitize open-loop receiver data in the following channel vs maximum sample rate combinations:

(a) One channel at 80 k samples/second

(b) Two channels at 40 k samples/second

(c) Four channels at 20 k samples/second

(d) One channel at 60 k samples/second; one channel at 20 k samples/second

(5) Availability of 8-bit quantization level of digitized open-loop receiver data for the maximum rate; 12-bit level otherwise.

(6) Temporary storage of radio science data on magnetic tape at the DSS for subsequent transmission to the NOCC via HSDL.

2. Wideband recording (DRA) key characteristics.

(1) Hardware compatability with DSN Mark III configuration.

(2) A-D conversion of wideband open-loop receiver data with 3-bit quantization.

(3) Provision for 18-bit parallel user input interface.

(4) Provision for data recording at any discrete rate between 175 k bits/second and 50 M bits/second.

(5) Provision for data recording on magnetic tape at nominal tape speeds of 19.05, 38.1, 76.2, 152.4, and 304.8 cm centimeters/second.

(6) Provision for time-tagging of recorded data to one microsecond or better resolution.

(7) Provision for full reproduce capability (shared between two transports).

(8) Provision for tape copying capability.

(9) Provision for 18-bit parallel user output interface.

(10) Eighty-minute record capability at 76.2 centimeters/second (12.5 M bits/second).

(11) Internal monitoring of recording performance.

(12) Provision for final output in analog form for monitoring purposes.

[1]The expression "real-time bandwidth reduction" is here defined as the process of driving the open loop receiver local oscillator with frequency predictions, and subsequently filtering, digitizing, and recording a narrow bandwidth containing the (mixed) signal.

C. Functional Operation

1. Real-time bandwidth reduction. Frequency predictions that include planetary atmospheric effects are generated by the Network Control (NC) Support Subsystem PREDIK software program. Transmitted in the form of S-band frequencies at the programmed oscillator (PO) level, they reach the DRS via HSDL and are verified for correctness of transmission by an error detection algorithm before storage for subsequent use.

When initialized, the Occultation Data Assembly converts the time-tagged frequencies to frequency rate commands for the programmed oscillator control assembly; the programmed oscillator functions to drive narrowband S- and X-band open-loop receivers. Narrowband open-loop receiver data are received by the DRS, digitized, formatted, and stored on magnetic tape. Concurrently the programmed oscillator frequency is counted by the DRS, formatted, and stored on magnetic tape. Similarly, the ODA frequency rates to the Programmed Oscillator Control Assembly (POCA) and POCA frequency commands to the PO are received by the DRS, formatted, and stored on magnetic tape.

During DRS operation, manual inputs are made via the DSS Monitor & Control Subsystem (DMC), and, similarly, the DRS is monitored from the DMC.

The digitized open-loop receiver data and the various programmed oscillator frequency data are transmitted from the DSS to the NOCC via HSDL in nonreal time or via tape shipment. Users gain access to the radio science data via Intermediate Data Records (IDR) written by the Ground Communications Facility (GCF) Data Records Subsystem. Figure 3 presents a functional block diagram of the Occultation Data Assembly.

2. Wideband recording. Wideband open-loop receiver data from the Multimission Open-Loop Receiver (MMR), which may contain multiple probe signals and receiver calibration tones, are received by the Digital Recording Assembly. These data are digitized at a quantization level of 3 bits and are recorded on 18 tracks of magnetic tape at a nominal tape speed of 76.2 centimeters/second (12 M bits/second). Concurrently, timing information received from the Frequency and Timing Subsystem (FTS) is recorded on two additional tracks. During recording, performance is monitored internally within the DRA.

The DRA simultaneously records on two separate transports. Subsequent to these recordings, duplicate copies may be produced on the DRA. The recorded wideband tapes are subsequently shipped to the Compatibility Test Area (CTA 21) Radio Science Subsystem via Network Information Control (NIC).

III. Functional Requirements of the DSS Radio Science Subsystem

A. Functional Requirements for Real-Time Bandwidth Reduction

1. Programmed oscillator frequency predictions. The ODA shall accept via HSDL and store programmed oscillator frequency predictions in the form of time tagged S-band frequencies at the programmed oscillator level (~46 MHz).

2. Prediction error detection. The ODA shall include an error detection algorithm in conjunction with the NC Support Subsystem PREDIK software program. This shall be for the purpose of verifying prediction consistency from generation through the ODA.

3. Programmed oscillator frequency control. The ODA shall convert time-tagged frequency predictions to frequency rates, and provide the results to the Programmed Oscillator Control Assembly (POCA) for programmed oscillator control of narrowband S- and X-band open-loop receivers.

4. Signal presence and ODA operation verification. The ODA shall provide a reconstructed analog receiver signal to the Spectral Signal Indicator for real-time verification of signal presence in the receiver bandwidth and verification of ODA operation.

5. Occultation data processing and storage. The ODA shall receive, digitize, and store time-tagged narrowband S- and X-band open-loop receiver output. The following are mission period requirements:

(1) Pioneer Venus Orbiter

Channels: 1 S-band, 1 X-band
Bandwidths: 1 kHz S-band, 3 kHz X-band
5 kHz S-band, 15 kHz X-band
Quantization: 8-bit

(2) Pioneer Venus Orbiter (solar corona)

Channels: 1 S-band, 1 X-band
Bandwidths: 1000 Hz S- and X-band
500 Hz S- and X-band
100 Hz S- and X-band
Quantization: 8-bit

(3) Voyager (first Jupiter encounter)

Channels: 1 S-band, 1 X-band
Bandwidths: 2.5 kHz S-band, 7.5 kHz X-band
10 kHz S-band, 30 kHz X-band
Quantization: 8-bit

(4) Voyager (second Jupiter encounter and Saturn encounter)

Channels: 2 S-band, 2 X-band
Bandwidths: All channels 100 kHz
Quantization: 8-bit

6. Timing information and accuracy. The ODA shall time-tag data with the following timing accuracies:

(1) Time synchronization with station time shall be accurate to less than 10 microseconds.

(2) Sampling rate accuracy shall be within 3×10^{-10}

(3) Sampling jitter shall be less than:

(a) Two microseconds at 10-kHz bandwidth

(b) Twenty microseconds at 1-kHz bandwidth

7. Programmed oscillator frequency recording. The ODA shall time-tag and record the programmed oscillator frequency output as follows:

(1) The programmed oscillator frequency shall be counted and recorded at one-second intervals on the integer second.

(2) The recorded programmed oscillator frequency shall be accurate to 0.5 Hz at S-band (RMS).

Additionally, the ODA shall record:

(1) The POCA-commanded PO frequency at one-second intervals on the integer second.

(2) The ODA-commanded PO initial frequency, and subsequent frequency rates, at one-second intervals on the integer second.

8. Original Data Record (ODR) data content specification.

a. Systematic Data Errors. The ODR shall have a 99% probability of containing error-free data (exclusive of Paragraph *b* below) during any span of ODA operation up to 300 minutes duration.

b. Random Data Errors. The ODR bit error rate shall be less than 1×10^{-6}, exclusive of tape flaws.

9. Block I VLBI requirements (ODA). The Block I VLBI system requirements on the ODA are as follows:

(1) 8 channels multiplexed.

(2) 250-kHz bandwidth/channel.

(3) One bit/sample.

(4) 500 k bits/second data rate.

(5) 500 M bits data volume.

(6) 1×10^{-6} bit error rate.

(7) 2 nanosecond maximum sampling jitter of any bit with respect to station reference.

(8) 10-microsecond time tag accuracy.

B. Functional Requirements for Wideband Recording

1. Digitization and recording. The DRA shall accept, digitize, and record wideband open-loop receiver data.

2. Reproduction, tape copying, and recording continuity. The DRA shall provide:

(1) Full reproduce capability.

(2) Tape copying capability.

(3) Continuous recording (no gaps) capability.

3. Bit error rate. Exclusive of tape flaws, the DRA bit error rate shall be less than 1×10^{-6} at all required tape speeds.

4. Timing information and accuracy. The DRA shall time-tag recorded data with the following timing accuracies:

(1) Time synchronization with station time shall be less than 10 microseconds.

(2) Timing information shall have a resolution of one microsecond or better.

5. Analog Signal Regeneration and Delivery. The DRA shall regenerate an analog signal from the recorded input data and deliver the signal to the Spectral Signal Indicator of the DSS Receiver-Exciter Subsystem.

6. Pioneer Venus Recording. For the Pioneer Venus Multiprobe mission, the DRA shall record wideband data at a sample rate of $\geq$ 4-1/6 M samples/second with the following accuracies:

Sampling rate accuracy: 3×10^{-12}
Sampling jitter: $\leq$ 10 nanoseconds RMS
Quantization: 3-bit

The recording capability shall be continuous for a minimum of 80 minutes at a data rate of 12.5 M bits/sec.

7. Block II VLBI Requirements (DRA). Block II VLBI system requirements on the DRA are as follows:

(1) 8 channels.

(2) 2-MHz bandwidth/channel.

(3) 1 bit/sample.

(4) 32 M bits/second data rate.

(5) 10^{11} bits data volume.

(6) 1×10^{-6} bit error rate.

(7) 2 nanosecond maximum sampling jitter of any bit with respect to station reference.

(8) 5-microsecond time tag accuracy.

IV. DRS Planned Implementation Schedule

The planned implementation dates for the various DRS capabilities are presented below:

Digital Recording Assembly

DSS 14	Feb. 15, 1978
DSS 43	Feb. 15, 1978
DSS 63	Feb. 15, 1979

DSS Radio Science Subsystem

DSS 14	July 1, 1978
DSS 43	July 1, 1978
DSS 63 (ODA only)	Dec. 1, 1978

Programmed Oscillator Monitor

DSS 14	Oct. 1, 1978
DSS 43	Oct. 1, 1978
DSS 63	Dec. 1, 1978

Very Narrow Bandwidth Capability

DSS 63	Dec. 1, 1978
DSS 14	April 1, 1979
DSS 43	April 1, 1979

Four-channel Capability (Saturn Ring Experiment)

DSS 14	April 1, 1979
DSS 43	April 1, 1979
DSS 63	April 1, 1979

Spectral Signal Indicator Display Processing

DSS 14	July 1, 1979
DSS 43	July 1, 1979
DSS 63	July 1, 1979

DMC Interface

DSS 14	July 1, 1979
DSS 43	July 1, 1979
DSS 63	July 1, 1979

Wideband Interface

DSS 14	July 1, 1979
DSS 43	July 1, 1979
DSS 63	July 1, 1979

References

1. Berman, A. L., and Molinder, J. I., "The CTA 21 Radio Science Subsystem – Non-Real-Time Bandwidth Reduction of Wideband Radio Science Data," in *The Deep Space Network Progress Report 42-41*, Jet Propulsion Laboratory, Pasadena, California, October 15, 1977.

2. Berman, A. L., "Planetary Atmosphere Modeling and Predictions" in *The Deep Space Network Progress Report 42-42*, Jet Propulsion Laboratory, Pasadena, California, December 15, 1977.

3. Mulhall, B. D. L., "DSN Radio Science System Description and Requirements" in *The Deep Space Network Progress Report 42-39*, Jet Propulsion Laboratory, Pasadena, California, June 15, 1977.

ORIGINAL PAGE IS OF POOR QUALITY

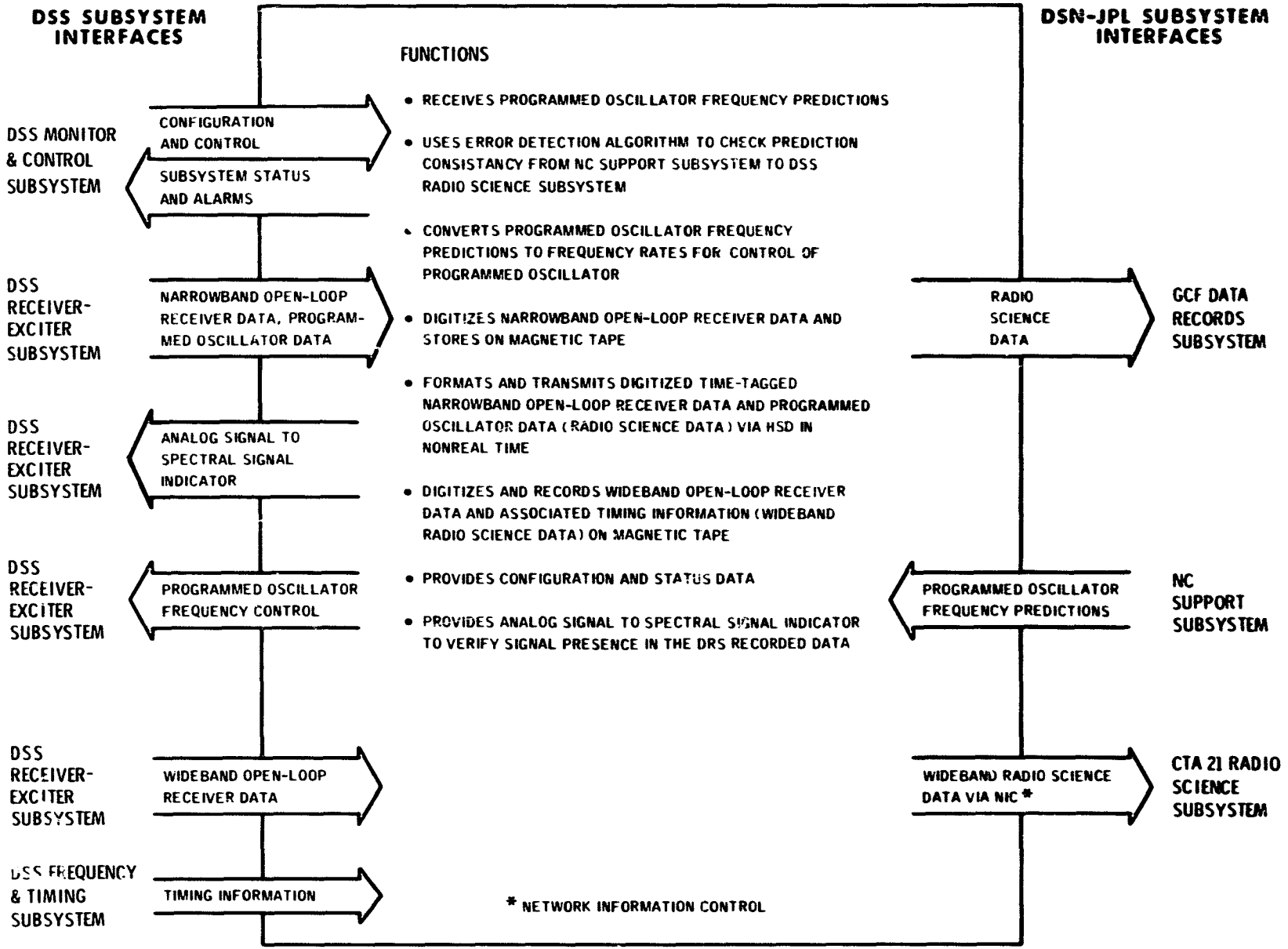
DSS SUBSYSTEM INTERFACES
FUNCTIONS
DSN-JPL SUBSYSTEM INTERFACES
DSS MONITOR & CONTROL SUBSYSTEM
CONFIGURATION AND CONTROL
SUBSYSTEM STATUS AND ALARMS
• RECEIVES PROGRAMMED OSCILLATOR FREQUENCY PREDICTIONS
• USES ERROR DETECTION ALGORITHM TO CHECK PREDICTION CONSISTANCY FROM NC SUPPORT SUBSYSTEM TO DSS RADIO SCIENCE SUBSYSTEM
• CONVERTS PROGRAMMED OSCILLATOR FREQUENCY PREDICTIONS TO FREQUENCY RATES FOR CONTROL OF PROGRAMMED OSCILLATOR
DSS RECEIVER-EXCITER SUBSYSTEM
NARROWBAND OPEN-LOOP RECEIVER DATA, PROGRAMMED OSCILLATOR DATA
• DIGITIZES NARROWBAND OPEN-LOOP RECEIVER DATA AND STORES ON MAGNETIC TAPE
RADIO SCIENCE DATA
GCF DATA RECORDS SUBSYSTEM
• FORMATS AND TRANSMITS DIGITIZED TIME-TAGGED NARROWBAND OPEN-LOOP RECEIVER DATA AND PROGRAMMED OSCILLATOR DATA (RADIO SCIENCE DATA) VIA HSD IN NONREAL TIME
DSS RECEIVER-EXCITER SUBSYSTEM
ANALOG SIGNAL TO SPECTRAL SIGNAL INDICATOR
• DIGITIZES AND RECORDS WIDEBAND OPEN-LOOP RECEIVER DATA AND ASSOCIATED TIMING INFORMATION (WIDEBAND RADIO SCIENCE DATA) ON MAGNETIC TAPE
DSS RECEIVER-EXCITER SUBSYSTEM
PROGRAMMED OSCILLATOR FREQUENCY CONTROL
• PROVIDES CONFIGURATION AND STATUS DATA
• PROVIDES ANALOG SIGNAL TO SPECTRAL SIGNAL INDICATOR TO VERIFY SIGNAL PRESENCE IN THE DRS RECORDED DATA
PROGRAMMED OSCILLATOR FREQUENCY PREDICTIONS
NC SUPPORT SUBSYSTEM
DSS RECEIVER-EXCITER SUBSYSTEM
WIDEBAND OPEN-LOOP RECEIVER DATA
WIDEBAND RADIO SCIENCE DATA VIA NIC *
CTA 21 RADIO SCIENCE SUBSYSTEM
DSS FREQUENCY & TIMING SUBSYSTEM
TIMING INFORMATION
* NETWORK INFORMATION CONTROL

Fig. 1. DSS Radio Science Subsystem functions and interfaces

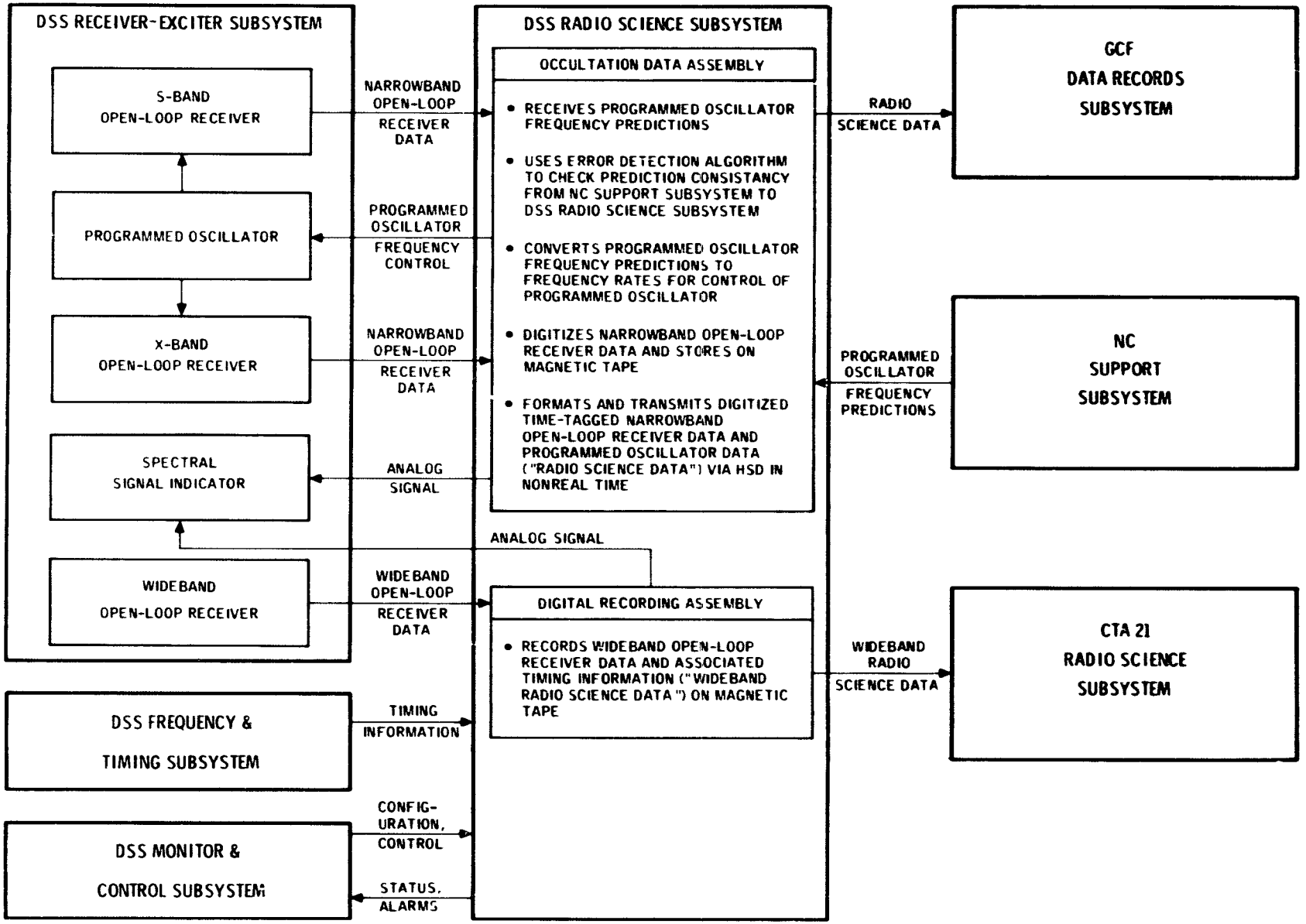
DSS RECEIVER-EXCITER SUBSYSTEM
S-BAND OPEN-LOOP RECEIVER
PROGRAMMED OSCILLATOR
X-BAND OPEN-LOOP RECEIVER
SPECTRAL SIGNAL INDICATOR
WIDEBAND OPEN-LOOP RECEIVER
DSS FREQUENCY & TIMING SUBSYSTEM
DSS MONITOR & CONTROL SUBSYSTEM
NARROWBAND OPEN-LOOP RECEIVER DATA
PROGRAMMED OSCILLATOR FREQUENCY CONTROL
NARROWBAND OPEN-LOOP RECEIVER DATA
ANALOG SIGNAL
WIDEBAND OPEN-LOOP RECEIVER DATA
TIMING INFORMATION
CONFIG-URATION, CONTROL
STATUS, ALARMS
DSS RADIO SCIENCE SUBSYSTEM
OCCULTATION DATA ASSEMBLY
• RECEIVES PROGRAMMED OSCILLATOR FREQUENCY PREDICTIONS
• USES ERROR DETECTION ALGORITHM TO CHECK PREDICTION CONSISTANCY FROM NC SUPPORT SUBSYSTEM TO DSS RADIO SCIENCE SUBSYSTEM
• CONVERTS PROGRAMMED OSCILLATOR FREQUENCY PREDICTIONS TO FREQUENCY RATES FOR CONTROL OF PROGRAMMED OSCILLATOR
• DIGITIZES NARROWBAND OPEN-LOOP RECEIVER DATA AND STORES ON MAGNETIC TAPE
• FORMATS AND TRANSMITS DIGITIZED TIME-TAGGED NARROWBAND OPEN-LOOP RECEIVER DATA AND PROGRAMMED OSCILLATOR DATA ("RADIO SCIENCE DATA") VIA HSD IN NONREAL TIME
ANALOG SIGNAL
DIGITAL RECORDING ASSEMBLY
• RECORDS WIDEBAND OPEN-LOOP RECEIVER DATA AND ASSOCIATED TIMING INFORMATION ("WIDEBAND RADIO SCIENCE DATA") ON MAGNETIC TAPE
RADIO SCIENCE DATA
PROGRAMMED OSCILLATOR FREQUENCY PREDICTIONS
WIDEBAND RADIO SCIENCE DATA
GCF DATA RECORDS SUBSYSTEM
NC SUPPORT SUBSYSTEM
CTA 21 RADIO SCIENCE SUBSYSTEM

Fig. 2. DSS Radio Science Subsystem functions and data flow

ORIGINAL PAGE IS
OF POOR QUALITY

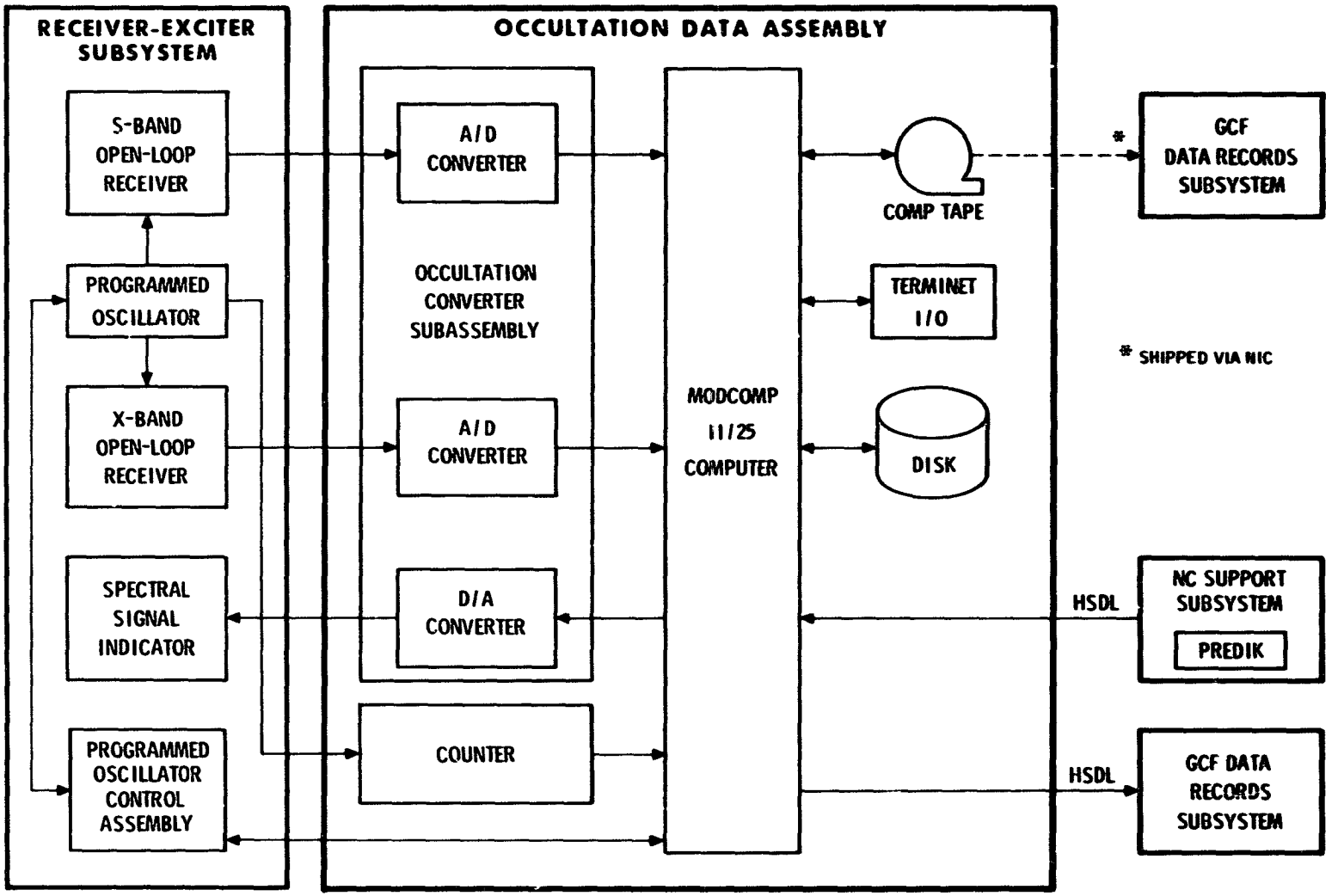

Fig. 3. Occultation Data Assembly functional block diagram

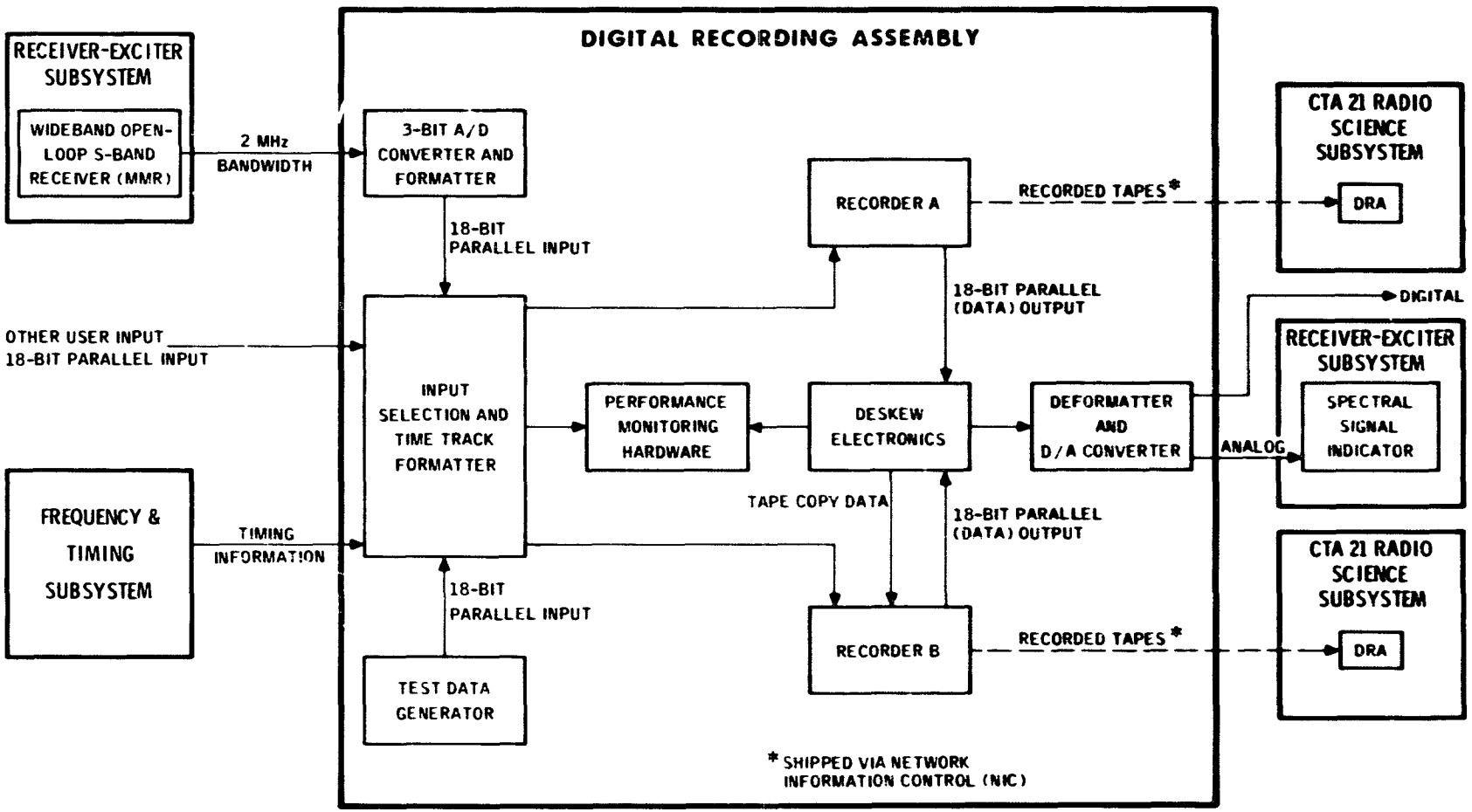

Fig. 4. Digital Recording Assembly functional block diagram

N78-24233

Solar Wind Density Fluctuation and the Experiment to Detect Gravitational Waves in Ultraprecise Doppler Data

A. L. Berman
TDA Engineering Office

The experiment to detect gravitational waves in ultraprecise Doppler data requires a total system (DSN Tracking System, spacecraft transponder, and media) fractional frequency fluctuation of approximately 1×10^{-15} for averaging times greater than 1000 seconds. At such levels, solar wind density fluctuation looms as a very difficult error source.

This article presents a detailed examination of solar wind electron (columnar) density fluctuation as it applies to the experiment to detect gravitational waves in ultraprecise doppler data. Expected two-way S-band fractional frequency fluctuation (due to solar wind density fluctuation) at a 1000-second averaging time is considered to be approximately 3×10^{-13}, while the optimum two-way X-band (X-band uplink and downlink) performance is predicted to be (also at a 1000-second averaging time) approximately 1×10^{-14}. The article concludes that both two-way S-band and X-band will be required (simultaneously) so that the predicted two-way X-band performance ($\sim 10^{-14}$) can be improved to a (defined) media goal of 3×10^{-16} via two-way dual frequency calibration of solar wind induced density fluctuation.

I. Introduction

In order to utilize two-way ultraprecise doppler data in the attempt to detect and measure various parameters of (hypothesized) gravitational waves (Refs. 1 and 2), one requires a total measurement system fractional frequency fluctuation on the order of 10^{-15}, over the averaging times of interest (approximately 50 to 5000 seconds). Major elements included in the total measurement system are:

(1) DSN Tracking System.

(2) Media (electron density fluctuation).

(3) Spacecraft transponder.

Since there are multiple elements in the DSN Tracking System which independently influence total system performance, a fractional frequency fluctuation goal of 3×10^{-16}

for each (independent) element will be adopted. At the present time, the two-way[1] S-band media (solar wind density) fractional frequency fluctuation performance appears to be approximately 3×10^{-13} (averaging times > 1000 seconds), or 3 orders of magnitude short of the desired 3×10^{-16} level. The steps which need to be taken (higher frequency band capability, dual frequency band capability) within the DSN Tracking System and on the spacecraft to significantly reduce media effects may begin to rival those necessary to put the DSN Tracking System on an overall fractional frequency fluctuation basis of less than 10^{-15}. Given the importance of solar wind density fluctuation in the usage of ultraprecise doppler data for the detection and measurement of gravitational waves, one requires accurate solar wind density fluctuation data for the design and implementation of such an ultraprecise doppler based gravitational wave detection experiment. It is the purpose of this article to present and analyze measured solar wind electron density fluctuation performance, appropriately formatted as fractional frequency fluctuation. Extensive two-way S-band doppler noise statistics acquired from a variety of spacecraft during 1975 and 1976 (Refs. 3 through 8) are used to construct average solar wind density fractional frequency fluctuation performance.

II. Solar Wind Density Fractional Frequency Fluctuation Performance

Two-way S-band doppler noise results obtained with the Viking spacecraft can be summarized (Refs. 5 and 6) as follows:

$$\sigma_f(\tau) = 1.182 \times 10^{-3} \left[\frac{\beta}{(\sin \alpha)^{1.3}}\right] F(\alpha, \beta) \left[\frac{60}{\tau}\right]^{0.29}$$

where:

$\sigma_f(\tau)$ = doppler noise, Hz

α = Sun-Earth-Probe angle, radians

β = Earth-Sun-Probe angle, radians

τ = doppler sample interval, seconds

$$F(\alpha, \beta) = 1 - 0.05 \left|\frac{(\beta - \pi/2 + \alpha)^3 - (\alpha - \pi/2)^3}{\beta}\right|$$

$$- 0.00275 \left|\frac{(\beta - \pi/2 + \alpha)^5 - (\alpha - \pi/2)^5}{\beta}\right|$$

The algorithm[2] used to calculate doppler noise (essentially) filters out fluctuation frequencies (ν) lower than ν_0 where (Ref. 8):

$$\nu_0 \approx (30\tau)^{-1}$$

Assuming a similar filtering out of (relatively) low frequency fluctuations in possible gravitational wave data reduction algorithms[3], the (given) doppler noise expression can be rather directly applied to the gravitational wave detection problem, with doppler sample interval approximately equal to averaging time.

Selecting a standard case of the spacecraft-Earth line perpendicular to the Sun-Earth line (with the spacecraft at infinity), so that:

$$\alpha = 90^\circ$$

$$\beta = 90^\circ$$

the doppler noise expression reduces to:

$$\sigma_f(\tau) = 1.60 \times 10^{-3} \left[\frac{60}{\tau}\right]^{0.29}, \text{ Hz}$$

which yields a fractional frequency fluctuation ($\sigma_f(\tau)/f$) for two-way S-band (uplink and downlink) of:

$$\sigma_f(\tau)/f = 2.28 \times 10^{-12}\, \tau^{-0.29}$$

Scaling by $(3/11)^2$, one obtains the equivalent expected two-way X-band performance:

$$\sigma_f(\tau)/f = 1.70 \times 10^{-13}\, \tau^{-0.29}$$

[1] For the remainder of this article, "two-way" will specifically connote "two-way (coherent) tracking mode, both uplink and downlink at the stated frequency".

[2] A "running" standard deviation computed from a least squares linear curve fit to 15 samples of actual minus predicted (average) doppler frequency.

[3] The design and implementation of algorithms to reduce and detect gravitational waves in ultraprecise doppler data will be a major part of the experiment.

ORIGINAL PAGE IS
OF POOR QUALITY

Figures 1 and 2 present average two-way S- and X-band fractional frequency fluctuation versus doppler sample interval.

Considering averaging periods of approximately 3 hours ("pass average"), Refs. 3, 4, and 6 found the average one standard deviation of (pass-average) doppler noise (σ_p) about a mean geometric value ($\bar{\sigma}_p$) established over several months of data to be (expressed in terms of $10 \log_{10}(\sigma_p/\bar{\sigma}_p)$):

$$\sigma(\sigma_p/\bar{\sigma}_p) = 1.92 \text{ dB } (-36\%, +56\%)$$

This value is applied as limits to the average fractional frequency fluctuation data presented in Figures 1 through 4.

III. Additional Factors in the Reduction of Solar Wind Density Fluctuation

Expected levels of fractional frequency fluctuation can be reduced somewhat by consideration of three additional circumstances:

(1) Density variations with solar cycle.

(2) Columnar density minimization in the antisolar direction ($\beta = 0°$).

(3) Columnar density fluctuation to (mean) density ratio minimization in the antisolar direction.

These conditions are briefly discussed below.

A. Density Variations with Solar Cycle

It is shown in Ref. 9 that the ratio of density and density fluctuation between solar cycle maximum and minimum (for Solar Cycle 20) was approximately 0.65 (value at maximum divided by value at minimum). The data used to derive the results of Section II were obtained at Solar Cycle minimum, hence one might expect to find at the next Solar Cycle (21) maximum (1979–1981) a reduction in average fractional frequency fluctuation by approximately 0.65.

B. Columnar Density Minimization in the Antisolar Direction ($\beta = 0°$)

The antisolar direction provide the minimum columnar density and hence (Ref. 7) the minimum columnar density fluctuation also. The columnar density reduction between the standard geometry chosen in Section II:

$$\alpha = 90°$$
$$\beta = 90°$$

and the antisolar direction:

$$\alpha = 180°$$
$$\beta = 0°$$

is approximately (assuming an r^{-2} density falloff for $r > 1$ AU):

$$2/\pi$$

and hence the density fluctuation can be expected to be reduced by a similar amount. Combination of this reduction with that from Subsection A yields a total reduction by a factor of 0.414. Figures 3 and 4 present the two-way S- and X-band average fractional frequency fluctuation for these conditions.

C. Columnar Density Fluctuation to (Mean) Density Ratio Minimization in the Antisolar Direction

Although columnar density (and hence columnar density fluctuation) is minimized in the antisolar direction, there may be a further reduction in the columnar density fluctuation because of a reduction in the columnar density fluctuation to (mean) density ratio (defined as ϵ', in Ref. 7). Quite simply, in the $\alpha = 90°$ case, density enhancements propagating radially cross the signal path perpendicularly near 1 AU (region of maximum density) with attendant (solar wind) velocities of approximately 440 km/second, as in Figure 5. As the antisolar direction is approached, the density enhancement propagation paths line up with signal path, and hence the density enhancements can be expected to move across the signal path with greatly reduced velocity (i.e., shifting the columnar fluctuation spectrum to lower frequencies).

The ground tracking system (with Rubidium frequency standard) doppler noise level for 60-second sample interval data is approximately (Ref. 5):

$$3 \times 10^{-3} \text{ Hz}$$

while the solar wind density S-band frequency fluctuation in the antisolar direction is expected to be:

$$1 \times 10^{-3} \text{ Hz}$$

It would therefore not have been previously possible to test this hypothesis (of a further reduction of density fluc-

tuation in the antisolar direction). However, with the current hydrogen maser frequency standard implementation at the 64-m subnet and the attendant large reduction in the ground tracking system noise level, it may now be possible to easily test this hypothesis.

IV. Conclusions

Two-way X-band (uplink and downlink), under even the most optimum conditions, results in a fractional frequency fluctuation of no better than 10^{-14} for averaging periods of at least 1000 seconds. To achieve the goal of 3×10^{-16}, it is here considered that solar wind density fluctuation will have to be further removed via dual frequency calibration. It may be possible to achieve the 1-1/2 orders of magnitude improvement from the two-way X-band performance level ($\sim 10^{-14}$) to the desired level (3×10^{-16}) via use of an additional S-band downlink (only) in combination with two-way X-band; in this regard, Wu, et al. (Ref. 10), have developed sophisticated techniques for calibration of uplink range when dual frequency is only available on the downlink. However, to more adequately guarantee the required improvement (to 3×10^{-16}) and to substantially reduce data reduction costs (i.e., by not requiring complex calibration algorithms such as the Wu uplink calibration technique) associated with the experiment, it seems reasonable to additionally require two-way S-band. It is thus here concluded that the implementation of a viable gravitational wave detection experiment based on ultraprecise doppler data will require simultaneous two-way X-band and two-way S-band capability.

References

1. Thorne, K. S., and Braginsky, V. B., "Gravitational-Wave Bursts from Nuclei of Distant Galaxies and Quasars: Proposal for Detection Using Doppler Tracking of Interplanetary Spacecraft," in *The Astrophysical Journal*, Volume 204: L1-L6, February 15, 1976.

2. Estabrook, F. B., and Wahlquist, H. D., "Response of Doppler Spacecraft Tracking to Gravitational Radiation," in *General Relativity and Gravitation*, Volume 6, No. 5, 1975.

3. Berman, A. L., and Wackley, J. A., "Doppler Noise Considered as a Function of the Signal Path Integration of Electron Density," in *The Deep Space Network Progress Report 42-33*, Jet Propulsion Laboratory, Pasadena, California, 15 June 1976.

4. Berman, A. L., Wackley, J. A., Rockwell, S. T., "The 1976 Helios and Pioneer Solar Conjunctions – Continuing Corroboration of the Link Between Doppler Noise and Integrated Signal Path Electron Density," in *The Deep Space Network Progress Report 42-36*, Jet Propulsion Laboratory, Pasadena, California, 15 December 1976.

5. Berman, A. L., "A Comprehensive Two-Way Doppler Noise Model for Near-Real-Time Validation of Doppler Data," in *The Deep Space Network Progress Report 42-37*, Jet Propulsion Laboratory, Pasadena, California, February 15, 1977.

6. Berman, A. L., Wackley, J. A., "Viking S-Band Doppler RMS Phase Fluctuations Used to Calibrate the Mean 1976 Equatorial Corona," in *The Deep Space Network Progress Report 42-38*, Jet Propulsion Laboratory, Pasadena, California, 15 April 1977.

7. Berman, A. L., "Proportionality Between Doppler Noise and Integrated Signal Path Electron Density Validated by Differenced S-X Range," in *The Deep Space Network Progress Report 42-38*, Jet Propulsion Laboratory, Pasadena, California, April 15, 1977.

8. Berman, A. L., "Phase Fluctuation Spectra: New Radio Science Information to Become Available in the DSN Tracking System Mark III-77," in *The Deep Space Network Progress Report 42-40*, Jet Propulsion Laboratory, Pasadena, California, August 15, 1977.

9. Berman, A. L., "Deep Space Telecommunications and the Solar Cycle: A Reappraisal," in *The Deep Space Network Progress Report 42-43*, Jet Propulsion Laboratory, Pasadena, California, February 15, 1978.

10. Wu, S. C., and Winn, B., "A Technique to Determine Uplink Range Calibration Due to Charged Particles," in *The Deep Space Network Progress Report 42-41*, Jet Propulsion Laboratory, Pasadena, California, October 15, 1977.

ORIGINAL PAGE IS
OF POOR QUALITY

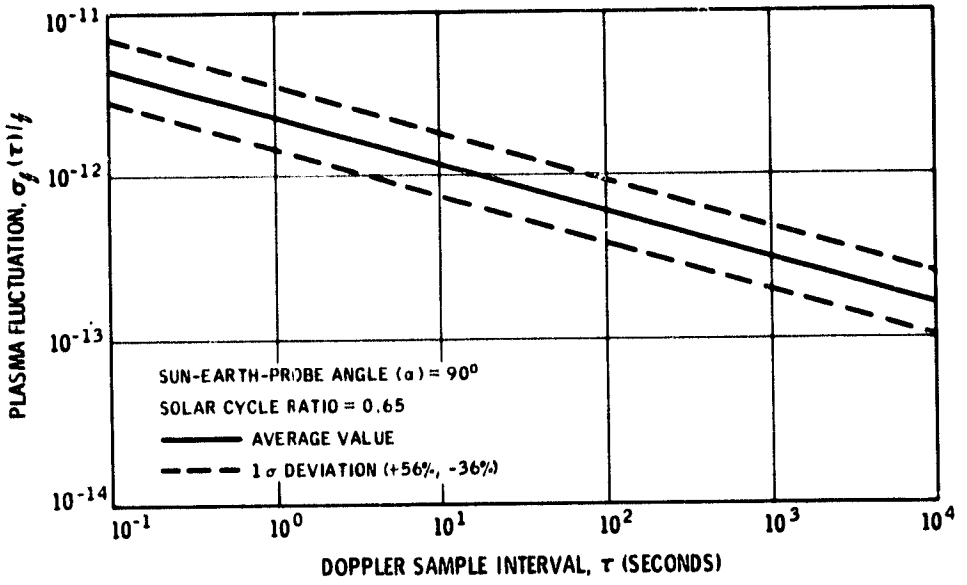

Fig. 1. Two-way S-band plasma fluctuation at solar cycle minimum

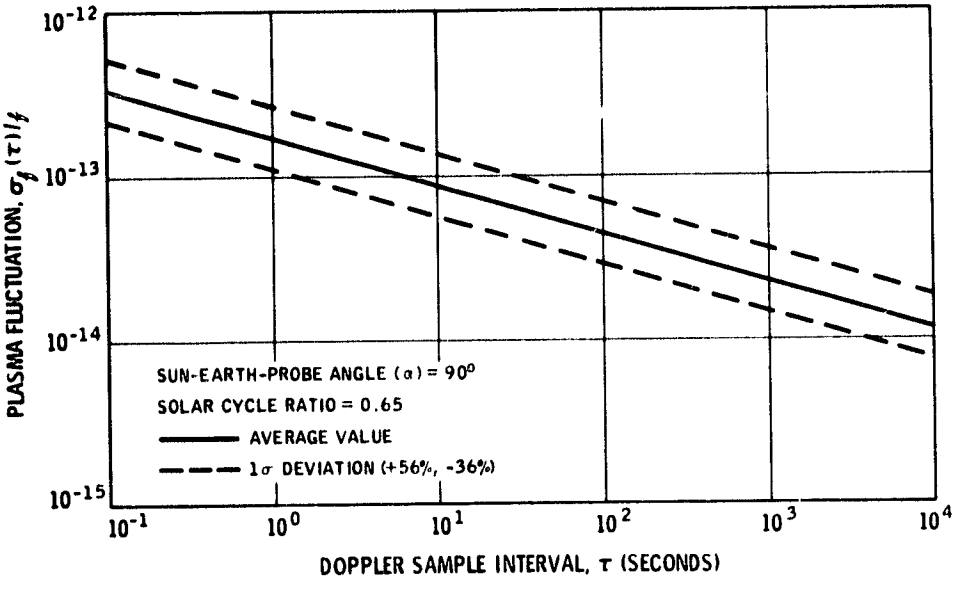

Fig. 2. Two-way X-band plasma fluctuation at solar cycle minimum

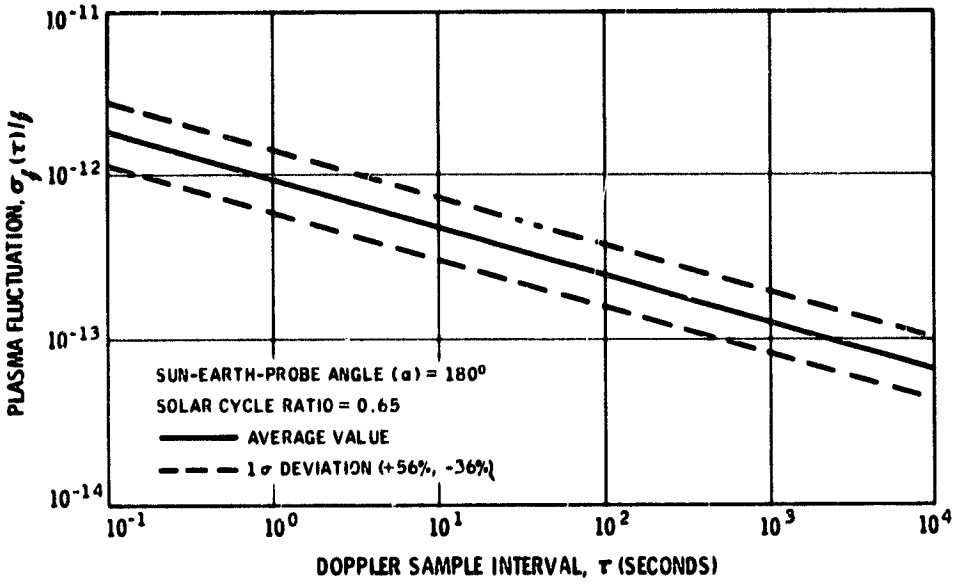

Fig. 3. Two-way S-band plasma fluctuation at solar cycle maximum

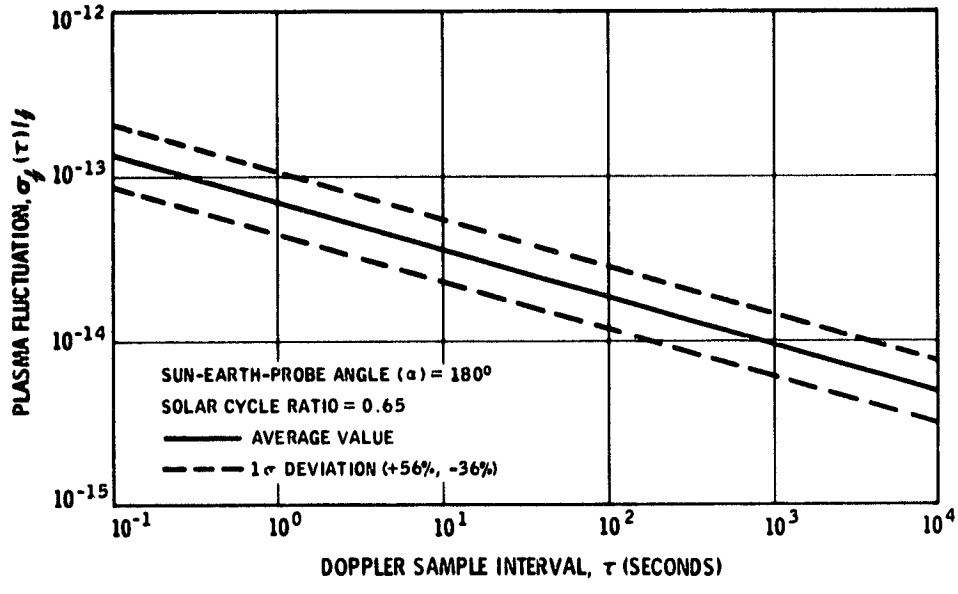

Fig. 4. Two-way X-band plasma fluctuation at solar cycle maximum

ORIGINAL PAGE IS
OF POOR QUALITY

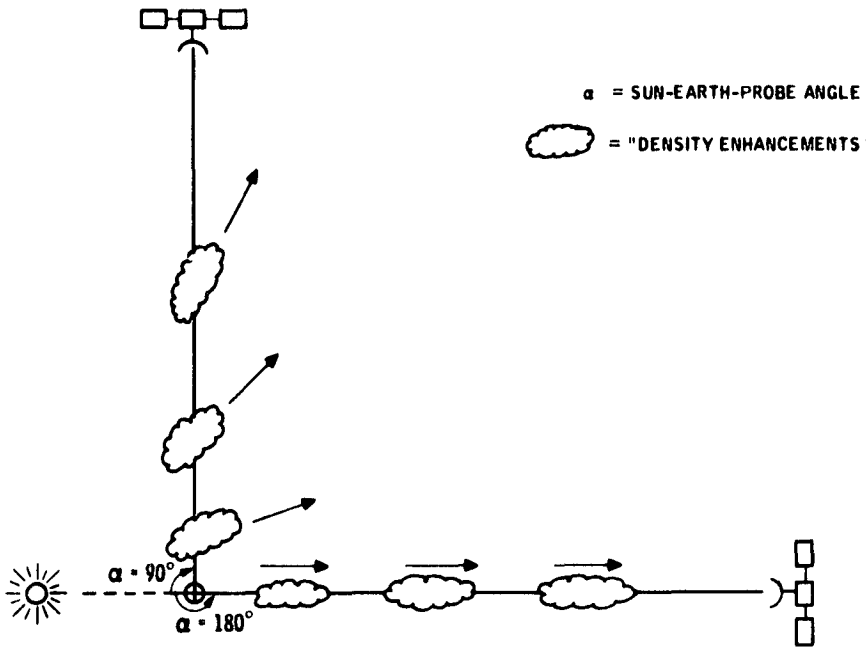

Fig. 5. Possible reduction in the (columnar) density fluctuation/density ratio in the antisolar direction

N78-24234

Solar Wind Turbulence Models Evaluated via Observations of Doppler RMS Phase Fluctuation and Spectral Broadening in the Inner Corona

A. L. Berman
TDA Engineering Office

The modelling of doppler noise (RMS phase fluctuation) has enjoyed considerable success via the experimentally observed proportionality between doppler noise and integrated electron density. Recently, theoretically derived models for doppler noise have been proposed. These models are broadly characterized as representing proportionality between doppler RMS phase fluctuation (ϕ) and particle flux. Under the assumptions of conservation of particle flux in the solar wind and proportionality between electron density and electron density fluctuation, these models yield a doppler noise dependence upon signal closest approach point (a) of:

$$\phi \propto a^{-1.5}$$

Doppler noise observations in the inner corona ($r_\odot \lesssim a \lesssim 5r_\odot$) are shown to conclusively demonstrate that doppler noise is proportional to integrated electron density ($\sim a^{-5}$), and not $a^{-1.5}$, as predicted by the particle flux models. Similarly, spectral broadening in the inner corona is seen to be proportional to integrated density. The article concludes that the particle flux models are in disagreement with the experimental observations of doppler noise to date, and hence are unlikely to be representative of actual solar wind processes.

I. Introduction

Berman and Wackley (1976, Ref. 1) have experimentally demonstrated that doppler noise (RMS phase fluctuation) is proportional to signal path integrated electron density. Recently, other investigators have derived theoretical expressions for the radial dependence of doppler noise. Callahan (Ref. 2) has derived such an expression for doppler noise, and Woo (Ref. 3) has both derived such an expression for and analyzed doppler noise ("Doppler Scintillation"). These independent efforts have resulted in somewhat similar models, which can be broadly characterized in terms of the dependence of doppler RMS phase fluctuation (ϕ) upon signal closest approach point (a) as:

$$\phi \propto \text{particle flux} \cdot a^{0.5}$$

applying the conservation of particle flux in the solar wind and assuming proportionality between electron density and electron density fluctuation, one directly obtains:

$$\phi \propto (a^{-2}) \cdot a^{0.5} = a^{-1.5}$$

This article examines the performance of these models (hereafter to be referred to as the "particle flux models") in respect to the experimental observations of doppler noise in both the extended corona ($5r_\odot \lesssim r \lesssim 1$ AU; $r_\odot$ = solar radius, r = radial distance) and inner corona ($r_\odot \lesssim r \lesssim 5r_\odot$), and concludes that the particle flux models are incompatible with the experimental observations to date. At the same time, these doppler noise observations continue to strongly support the proportionality between doppler noise and integrated electron density (hereafter to be referred to as the "integrated density model") as espoused by Berman and Wackley.

II. The Particle Flux Models

Evaluation of Eq. (24) from Callahan (Ref. 2) yields for the primary term:

$$\phi \propto n(a)v(a)a^{0.5}$$

where:

n = electron density fluctuation

v = solar wind radial velocity

If one assumes the conservation of particle flow in the solar wind (Cuperman and Harten, Ref. 4):

$$K = N_e(r)v(r)r^2$$

where:

N_e = electron density

in combination with the common assumption of proportionality between electron density and electron density fluctuation:

$$N_e(r) \propto n(r)$$

one directly obtains for doppler noise

$$\phi \propto (a^{-2}) \cdot a^{0.5} = a^{-1.5}$$

Simplification of Eq. (4) from Woo (Ref. 3) yields for doppler noise:

$$\phi \propto n(a)[v(a)]^{5/6} a^{0.5}$$

Considering $v^{5/6} \approx v$ (as Ref. 3 does) and assuming conservation of particle flow and proportionality between electron density and electron density fluctuation, one immediately obtains:

$$\phi \propto a^{-1.5}$$

By far the most interesting feature of these particle flux models is their absolute insensitivity to the radial dependence of (integrated) electron density! It is precisely this feature of the particle flux models which allows a straightforward evaluation via comparison to experimental observations of doppler noise in the vastly different regimes of the inner and extended corona. Briefly stated, the radial dependence of electron density is well known to change from r^{-6} to $\sim r^{-2.3}$ in the transition from the inner to the extended corona. The particle flux models predict that doppler noise will not "detect" this abrupt change in electron density; correspondingly, the integrated density model predicts that doppler noise will exactly mirror the sharp change in electron density.

III. Model Evaluation in the Extended Corona

To date, the only highly precise and mathematically objective determination of the radial dependence of doppler noise in the extended corona is Berman, Ref. 5. This study found the radial *index* to be -1.30 ($a^{-1.30}$), which corresponds to a $(-\infty, \infty)$ integration of $r^{-2.30}$. Since the average radial dependence of electron density in the extended corona found by a variety of experimentors is approximately $r^{-2.3}$ (Ref. 6), the results of Ref. 5 strongly support the integrated density model. Figure 1 (from Ref. 5) shows the results of a simultaneous two parameter least squares minimization to the (extended corona) coefficient and radial index. Although observations of doppler noise in the extended corona as portrayed in Fig. 1 clearly favor the integrated density model over the particle flux models, the difference between $a^{-1.30}$ and $a^{-1.5}$ is not large in absolute terms, and hence the extended corona results cannot be considered dramatically conclusive. Fortunately, the inner corona, with its abrupt shift

in the radial dependence of electron density, allows no such ambiguity. The data must conclusively favor one model over the other.

IV. Model Evaluation in the Inner Corona

Inner corona electron density observations via both eclipse photometry methods (van de Hulst, Ref. 7; Saito, Ref. 8; and Blackwell, Ref. 9) and spacecraft range delay measurements (Muhleman (Mariner 6) Ref. 10; Edenhofer (Helios 2), Ref. 11) show an extremely sharp change in electron density radial dependence at approximately $r = 4r_\odot$. The corresponding breakpoint for signal path integrated electron density is approximately $a = 3r_\odot$. Since the particle flux models are independent of electron density, one would expect no change in the doppler noise radial dependence at $a = 3r_\odot$. Figure 2 presents doppler noise observations for the region $2r_\odot \leqslant a \leqslant 6r_\odot$; included in Fig. 2 is the integrated density model of Berman (ISEDC) and the particle flux model of Callahan. There is no question but that experimental observations of doppler noise in the inner corona "sense" the sharp increase of integrated electron density at $a \approx 3r_\odot$. To this author it is an inescapable conclusion that the particle flux models simply do not correctly predict experimental observations of doppler noise, and hence their derivations cannot be considered representative of actual solar wind processes.

V. Spectral Broadening in the Inner Corona

Woo (Ref. 12) has derived a model for the spectral broadening (B) of a monochromatic spacecraft signal which is quite similar to the particle flux model of Ref. 3 (actually $\phi = B^{5/6}$ from Ref. 3). Therefore, just as for doppler noise, spectral broadening observations in the inner corona should not (according to Ref. 12) detect the onset of the inner corona electron density enhancement. To date, Rockwell (Ref. 13) has performed the only highly precise and mathematically objective study of spectral broadening radial dependence in the inner corona. Reference 13 achieved excellent results in fitting spectral broadening data via use of a model resembling integrated electron density. Figure 3 presents the data from Ref. 13; included in Fig. 3 are the individual "inner corona" and "extended corona" components from Rockwell's model. The important point is that the two components become equal valued at $a \approx 3r_\odot$, and hence spectral broadening data "sense" the change in electron density exactly as does doppler noise (and quite significantly, at the same radial distance). The clear fact that spectral broadening data are in good agreement with integrated electron density in the inner corona provides a most powerful refutation of the particle flux models for *both* RMS phase fluctuation and spectral broadening.

VI. Conclusions and Discussion

Recent attempts to theoretically derive the parametric form of doppler noise have produced ("particle flux") models which are independent of (integrated) electron density. The inner corona, with its vastly distinct electron density regimes, provides a most powerful test bed to assess the validity of the particle flux models. Experimental observations of doppler noise in the inner corona dramatically respond to the abrupt change in electron density regimes, and hence it must be concluded that the particle flux models do not model actual solar wind processes. Similarly, observations of spectral broadening in the inner corona mirror the doppler noise observations, and hence provide even further fortification of the negative evaluation of the particle flux models. It is an inexorable conclusion of this article that both RMS phase fluctuation and spectral broadening are proportional to integrated electron density, and not, as has been suggested, particle flux.

The importance of this conclusion should not be overlooked. With proportionality to integrated electron density, doppler noise represents a most powerful experimental tool for obtaining the radial dependence of both electron density and solar wind radial velocity; were the particle flux models correct, then doppler noise would be far less useful as a radio science data type.

References

1. Berman, A. L., and Wackley, J. A., "Doppler Noise Considered as a Function of the Signal Path Integration of Electron Density," in *The Deep Space Network Progress Report 42-33*, Jet Propulsion Laboratory, Pasadena, California, 15 June 1976.

2. Callahan, P. S., "A First-Principles Derivation of Doppler Noise Expected From Solar Wind Density Fluctuations," in *The Deep Space Network Progress Report 42-42*, Jet Propulsion Laboratory, Pasadena, California, December 15, 1977.

3. Woo, R., "Radial Dependence of Solar Wind Properties Deduced from Helios 1/2 and Pioneer 10/11 Radio Scattering Observations," in *The Astrophysical Journal*, 219, January 15, 1978.

4. Cuperman, S., and Harten, A., "Some Physical Implications of Recent Solar Wind Measurements," in *Solar Wind*, edited by Sonett, C. P., Coleman, P. J. Jr., and Wilcox, J. M., National Aeronautics and Space Administration, Washington, D.C., 1972.

5. Berman, A. L., Wackley, J. A., Rockwell, S. T., and Kwan, M., "Viking Doppler Noise Used to Determine the Radial Dependence of Electron Density in the Extended Corona," in *The Deep Space Network Progress Report 42-38*, Jet Propulsion Laboratory, Pasadena, California, 15 April 1977.

6. Berman, A. L., "Electron Density in the Extended Corona: Two Views," in *The Deep Space Network Progress Report 42-41*, Jet Propulsion Laboratory, Pasadena, California, October 15, 1977.

7. van de Hulst, J. C., "The Electron Density of the Solar Corona," *Bulletin of the Astronomical Institutes of The Netherlands*, Volume XI, Number 410, February 2, 1950.

8. Saito, K., "A Non-Spherical Axisymmetric Model of the Solar K Corona of the Minimum Type," *Annals of The Tokyo Astronomical Observatory*, University of Tokyo, Second Series, Volume XII, Number 2, Mitaka, Tokyo, 1970.

9. Anderson, J. D., Esposito, P. B., Martin, W. L., Thornton, C. L., and Muhleman, D. O., "Experimental Test of General Relativity Using Time Delay Data from Mariner 6 and Mariner 7," in *The Astrophysical Journal*, Volume 200, August 15, 1975.

10. Muhleman, D. O., Esposito, P. B., and Anderson, J. D., "The Electron Density Profile of the Outer Corona and the Interplanetary Medium from Mariner 6 and Mariner 7 Time Delay Measurements," *The Astrophysical Journal*, 211, February 1, 1977.

11. Edenhofer, P., Esposito, P. B., Hansen, R. T., Hansen, S. F., Lueneburg, E., Martin, W. L., and Zygielbaum, A. I., "Time Delay Occultation Data of the Helios Spacecrafts and Preliminary Analysis for Probing the Solar Corona," in the *Journal of Geophysics 42*, 1977.

12. Woo, R., Yang, F., and Ishimaru, A., "Structure of Density Fluctuations Near the Sun Deduced from Pioneer-6 Spectral Broadening Measurements," in *The Astrophysical Journal*, Vol. 210, No. 2, December 1, 1976.

13. Rockwell, S. T., "An Empirical Spectral Bandwidth Model for Superior Conjunction," in *The Deep Space Network Progress Report 42-43*, Jet Propulsion Laboratory, Pasadena, California, 15 February 1978.

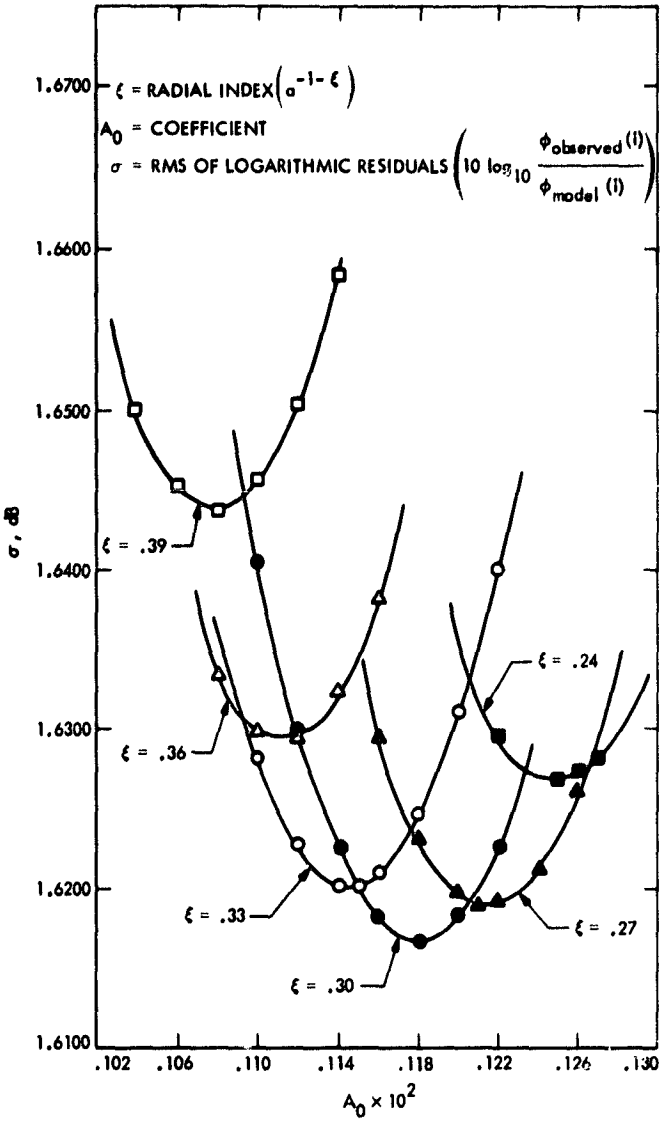

Fig. 1. Viking S-Band Doppler noise fit in the extended corona

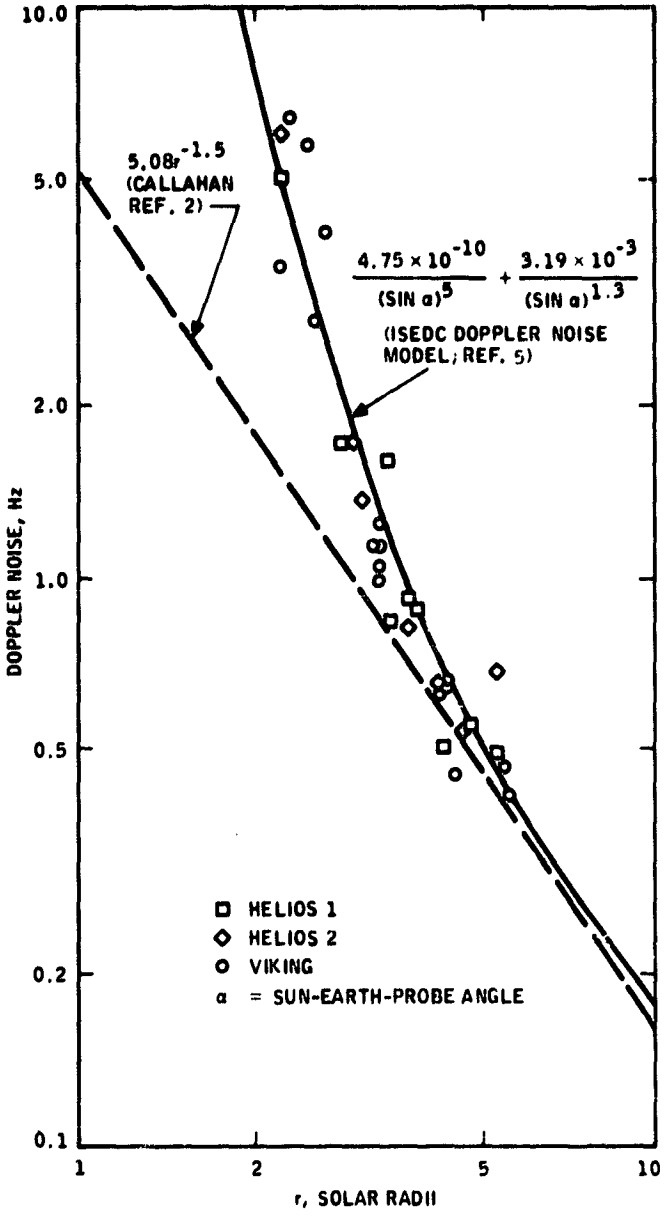

Fig. 2. Doppler noise models in the inner corona

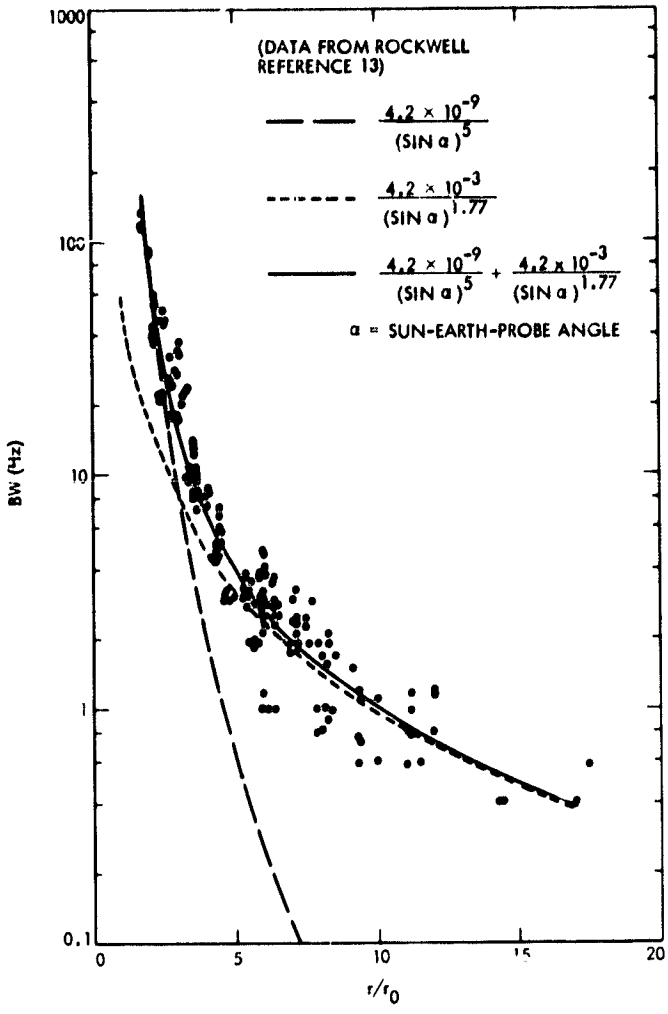

Fig. 3. Spectral broadening data in the inner corona

N78-24235

On the Suitability of Viking Differenced Range to the Determination of Relative Z-Distance

F. B. Winn
Navigation Systems Section

Radiometric differenced range residuals (10 Viking orbiting spacecraft observations) have been used to evaluate the current Deep Space Net adopted relative Z distance between Deep Space Station 43 and Deep Space Station 14. The $\Delta\rho$ noise is approximately twice the predicted noise: $\sigma_{\Delta\rho}$ is 3.4 m relative to a mean of -1 m. This scatter in the $\Delta\rho$ is most likely due to media calibration uncertainties and Deep Space Net hardware noise.

These 10 $\Delta\rho$ residuals yield an estimated Z distance between DSS 43 and DSS 14 of 7351803.6 m. The standard deviation of that estimate is 10.1 m.

I. Introduction

Radiometric differenced range residuals (10 Viking orbiting spacecraft observations) have been used to evaluate the current Deep Space Net adopted relative Z distance between Deep Space Station 43 and Deep Space Station 14. The Deep Space Net 'adopted Z coordinates' for Deep Space Stations are a product of the Goddard Space Flight Center. The adopted DSS 43 - DSS 14 relative Z distance is 7.351807×10^6 m. JPL has assigned a 15-m standard deviation to these Z coordinates. These 10 Viking differenced range observations, $\Delta\rho$, do not reveal a relative Z error of statistical significance: the ΔZ correction equals 1/3 the computed $\sigma_{\Delta Z}$. The relative Z correction is -3.4 m and the sigma is 10.1 m. Although this is encouraging, it is not definitive. This range sample is so small that systematic effects due to ΔZ, Deep Space Station longitude, and spacecraft declination errors may not have emerged above the range nosie.

The $\Delta\rho$ noise is approximately twice the predicted noise: $\sigma_{\Delta\rho}$ is 3.4 m relative to a mean of -1 m. This scatter in the $\Delta\rho$ is most likely due to media calibration uncertainties and Deep Space Net hardware noise. Additionally, the influences of ΔZ, Deep Space Station longitude, and spacecraft declination errors on $\Delta\rho$ are discussed.

II. The Differenced Range Data Set from the DSS 43—DSS 14 Baseline

Near simultaneous range measurements were obtained from the DSS 43–DSS 14 baseline (Ref. 2, Ref. 3): seven at an S-band frequency and three at an X-band frequency. The DSN acquired these observations from Viking-Mars orbiting spacecraft from January to April 1977 in a dual-station ranging demonstration. Usually only minutes separated the measurements of different DSSs (Figs. 1–6).

The positions and velocities of a spacecraft in the solar system are estimated usually by a least squares, differential correction technique (Orbit Determination Program, Ref. 4). The Doppler shift experienced by round-trip radio transmission from the earth to the spacecraft and back is the prime observable used in the least squares technique. A part of the procedure computes the difference between the observed range and the range computed from numerical integrations of the equations of motion of all the significant solar system bodies.

When compressed range residuals are computed from the raw range residuals (Fig. 1–6) and differenced, the compressed differenced range residuals do not show any systematic signatures in time (Fig. 7) or as a function of declination (Fig. 8). In these figures, a label of 'S' or 'X' indicates the frequency of the observation and the bar specified the one-sigma dispersion of each $\Delta\rho$ value. As previously stated, the dispersion of the combined 'S' and 'X' frequency $\Delta\rho$ is 3.4 m with a mean of -1 m. Alone 'S' band $\Delta\rho$ has a $\sigma_{\Delta\rho}$ = 2.6 m and a mean of -1 m.

III. Additional Australia—Goldstone Baseline Data

Besides these 10 $\Delta\rho$ observations, 4 additional $\Delta\rho$ observations were obtained from 3 different Canberra–Goldstone baselines: one from the DSS 42–DSS 14 baseline on 31 January; two from the DSS 43–DSS 11 baseline on 31 January and 16 February; and one from the DSS 42–DSS 11 baseline on 16 February.

Geodetic surveys within the Goldstone DSN complex have determined the relative $Z(\Delta Z)$ for the short baselines to <1 m (σ). The same is true for the DSS of the Canberra complex. Thus, all long baselines between the Canberra and Goldstone complexes should have a nearly common ΔZ error. Although a plot of all 14 $\Delta\rho$ points for the Canberra–Goldstone baselines is consistent with this view, the noise level is so high ($\sigma_{\Delta\rho}$ = 4.1 m) that little weight is given to this observation. To dramatize the noise level of this data, Fig. 9 exhibits what the signature in $\Delta\rho$ from an error in ΔZ (equal to 18 m, 3 times what the Voyager project specified as acceptable, Ref. 5) looks like.

IV. Error Analysis for $\Delta\rho$

This scatter in the $\Delta\rho$ values is most likely due to the 'media' calibration uncertainties (plasma, ionospheric ion, and atmospheric refraction calibration uncertainties) and DSN ranging system hardware perturbations. It can be shown that $\Delta\rho$ scatter seen in Fig. 9 does not stem from geometrical parameters, such as: relative Z distance (ΔZ); Mars declination (δ); DSS distance off the earth's spin axis (r_s); or, DSS longitude errors. Consider the following discussion.

The topocentric range from a DSS to a distant spacecraft may be approximated (Ref. 6) by

$$\rho(t) = R(t) - Z \sin\delta(t) - r_s \cos\delta(t) \cos[\omega t - \alpha(t) + \lambda]$$

where

$\rho(t)$ = the topocentric range at time 't'

$R(t)$ = geocentric range

Z = distance of DSS from earth's equator

δ = spacecraft declination

r_s = distance of DSS from earth's spin axis

ω = earth rotation rate

λ = DSS longitude

α = spacecraft right ascension

For differenced range from two DSS, which are time synchronized

$$\rho_2 - \rho_1 = (Z_1 - Z_2)\sin\delta - (r_{s_2} - r_{s_1})\cos\delta\,[\cos(\omega t - \alpha)\{\cos\lambda_2 - \cos\lambda_1\} + \sin(\omega t - \alpha)\{\sin\lambda_1 - \sin\lambda_2\}]$$

The errors in the differenced range per unit error in ΔZ, $\Delta\delta$, Δr_s, and λ are then

$$\frac{\epsilon(\Delta\rho)}{\epsilon(\Delta Z)} = \sin\delta$$

$$\frac{\epsilon(\Delta\rho)}{\epsilon(\Delta\delta)} = \Delta Z\cos\delta + \Delta r_s \sin\delta\,[\cos(\omega t - \alpha)\{\cos\lambda_2 - \cos\lambda_1\} + \sin(\omega t - \alpha)\{\sin\lambda_1 - \sin\lambda_2\}]$$

$$\frac{\epsilon(\Delta\rho)}{\epsilon(\Delta r_s)} = \cos\delta\ [\cos(\omega t - \alpha)\ \{\cos\lambda_2 - \cos\lambda_1\}$$

$$+ \sin(\omega t - \alpha)\ \{\sin\lambda_1 - \sin\lambda_2\}]$$

$$\frac{\epsilon(\Delta\rho)}{\epsilon(\lambda)} = -\ \ell_s \cos\delta\ [\cos(\omega t - \alpha)\ \{\sin\lambda_1 - \sin\lambda_2\}$$

$$+ \sin(\omega t - \alpha)\ \{\cos\lambda_1 - \cos\lambda_2\}]$$

For the DSS 43–DSS 14 baseline,

$$\Delta Z = 6 \times 10^6 \text{ m}$$

$$\Delta r_s = 1 \text{ m}$$

$$\lambda_1 = 149^\circ,\ \lambda_2 = 243^\circ,\ \Delta\lambda = 94^\circ$$

$$\epsilon(\Delta Z) = 15 \text{ m } (\sigma)$$

$$\epsilon(\Delta r_s) = 0.6\sqrt{2} = 0.8 \text{ m } (\sigma)$$

$$\epsilon(\lambda) = 2\sqrt{2} = 2.8 \text{ m } (\sigma)$$

and where $(\omega t - \alpha) = 196^\circ$. The spacecraft is over the subearth point equally distant from both DSS 43 and DSS 14 when $\omega t - \alpha = 196^\circ$. For a spacecraft declination of 20° and an $\epsilon(\delta)$ of 4×10^{-7} radians,[1] all the parameters of the $\Delta\rho$ equations are defined.

$$\epsilon(\Delta\rho) = f[\epsilon(\Delta Z)] = 5.1 \text{ m } (\sigma)$$

$$\epsilon(\Delta\rho) = f[\epsilon(\delta)] = 2.3 \text{ m } (\sigma)$$

$$\epsilon(\Delta\rho) = f[\epsilon(\Delta r_s)] = 0.5 \text{ m } (\sigma)$$

$$\epsilon(\Delta\rho) = f[\epsilon(\lambda)] = 1.4 \text{ m } (\sigma)$$

The root-sum-of-square of these error terms yields a combined $\sigma_{\Delta\rho} = 5.8$ m. A $\sigma_{\Delta\rho} = 5.6$ m results when only the $\sin\delta\ \epsilon(\Delta Z) + \Delta Z \cos\delta\ \epsilon(\delta)$ terms are considered. The diurnal terms are insignificant.

Since eight of the 10 DSS 43–DSS 14 $\Delta\rho$ (Fig. 8) involve a spacecraft at near constant δ (the declination is $-23^\circ \pm 1^\circ$ from 11 January through 31 January), it follows

$$\epsilon(\Delta\rho) = f[\Delta Z, \delta, \Delta r_s, \lambda] \approx \text{constant}$$

[1] 0.1 arc second is thought to be a reasonable Mars declination error for the JPL Developmental Ephemeris 96 (Ref. 7).

for these eight observations. Any declination error which might exist of the form '$a + bt$' (that is, a bias plus a drift rate) would be very small ($t < 20$ days) and not evident in the $\Delta\rho$.

The scatter in the $\Delta\rho$ set must stem from media calibration errors and hardware performance. Charged particle environments retard range transmission. The neutral particle atmosphere refracts and retards group propagations. DSS electrical hardware response times are included in range measurements. Different DSS frequency standards also distort $\Delta\rho$. These effects, via calibration, are removed from range data; however, each calibration process has its limitations. The uncertainties in a calibrated $\Delta\rho$ point are

$\sigma_{\Delta\rho} = 0.1\sqrt{2}$ m (σ) (plasma ion calibration, Ref. 8)

$\sigma_{\Delta\rho} = 0.5\sqrt{2}$ m (σ) (ionospheric ion calibration, Ref. 9)

$\sigma_{\Delta\rho} = 0.3\sqrt{2}$ m (σ) (trophospheric refraction calibration, Ref. 10)

$\sigma_{\Delta\rho} = 0.5$ m (σ) (frequency offset calibration, Ref. 11)

$\sigma_{\Delta\rho} = 1\sqrt{2}$ m (σ) (DSS hardware relay calibration, Refs. 12, 13)

These nongeometrical uncertainties RSS to 1.5 m. The $\sigma_{\Delta\rho}$ observed is 2.6 m for the S-band $\Delta\rho$ and 3.4 m for the S- and X-band $\Delta\rho$ combined – a noise level almost twice that predicted. This extra noise is detrimental to the determination of ΔZ. This is particularly true for low declination observations.

V. Accuracy of ΔZ Estimates

Each of the 10 $\Delta\rho$ observations (Fig. 8) independently provides an estimate of ΔZ (Fig. 10). The translation is $\Delta Z = \Delta\rho$ cosecant (δ). The mean ΔZ is −3.4 m with a standard deviation of 10 m. $\Delta Z = \Delta\rho/\sin\delta$; $\sigma_{\Delta\rho} = 3.4 \Rightarrow \delta_{\Delta Z} = 10$ for $\delta = 23^\circ$. The lower the declination, the greater the $\sigma_{\Delta Z}$ for a given $\sigma_{\Delta\rho}$.

Since spacecraft declinations are typically less than 20° for distant probes, the expectation that a $\sigma_{\Delta Z} \leqslant 6$ will be realized requires an expectation that $\sigma_{\Delta\rho} \leqslant 2$ m will be achieved.

VI. Range Quality

It is not known why $\sigma_{\Delta\rho}$ is at 3.4 meters for this sample. Maybe the sample is not representative. It certainly is a small sample. If the sample is fair, then the noise may result from 'media' or system perturbations not considered in the calibra-

ORIGINAL PAGE IS OF POOR QUALITY

tion process. The 'media' calibrations do not appear a likely explanation. Charged-particle calibrations for radiometric range and Doppler have been compared from such independent sources as Faraday polarimeter measurements (Ref. 9), S- and X-band dispersive Doppler and range measurements (Ref. 10), and S- and X-band DRVID measurements and found consistent to a few tenths of meters. Similarly, tropospheric refraction calibrations consistently yield conventional tracking data modelled to the 2 to 3 decimeter level. This is true even for observations below a 10° elevation angle (Ref. 10).

More $\Delta\rho$ data will provide the base needed to characterize the dependence of $\Delta\rho$ on $\epsilon(\Delta Z)$ and $\epsilon(\delta)$.

Differenced range data is being acquired from the Voyager spacecraft while the spacecraft are in heliocentric cruise. Although only four observations have been processed at this time, the Voyager $\Delta\rho$ appear even noisier than those of Viking. DSN and Voyager personnel are currently investigating the DSS fundamental calibration procedures in an effort to reduce the differenced range noise.

VII. Conclusions

DSN radiometric differenced range has been used to differentially correct the DSS 43–DSS 14 baseline relative Z distance. A correction of −3 m is indicated. However, the standard deviation of that correction is 10 m. The prior relative Z sigma was 15 m. The Voyager project requires a sigma of 6 m.

The 10 m sigma on relative Z stems from the differenced range noise ($\sigma_{\Delta\rho}$ = 3.4 m), the low declination angles for the spacecraft used ($\delta < 25°$), and transmission media calibrations.

For $\delta \leqslant 20°$, the $\Delta\rho$ must have a $\sigma_{\Delta\rho} \leqslant 2$ m if relative Z determinations to standard deviations of less than six meters are to be realized.

References

1. Marsh, J. G., "A Global Station Coordinate Solution Based Upon Camera and Laser Data GSFC 1973," presented at the First International Symposium (for) the Use of Artificial Satellites for Geodesy and Geodynamics, Athens, Greece, May 14–21, 1973.

2. Christensen, C. S., Green, D. W., Siegel, H. L., and Winn, F. B., "Dual Station Ranging Demonstrations," EM 314-141, Jet Propulsion Laboratory, Pasadena, Calif., October 27, 1977 (JPL internal document).

3. Siegel, H. L., Christensen, C. S., Green, D. W., and Winn F. B., "On Achieving Sufficient Dual Station Range Accuracy for Deep Space Navigation at Zero Declination," presented at AAS/AIAA Astrodynamics Specialist Conference, Jackson Hole, Wyoming, September 7–9, 1977.

4. Moyer, T. C., *Mathematical Formulation of the Double Precision Orbit Determination Program (DPODP)*, TR 32-1527, Jet Propulsion Laboratory, Pasadena, Calif., 15 May 1971.

5. *Support Instrumentation Requirements Document*, NASA, PD 618-501, National Aeronautics and Space Administration, Washington, D.C., June 1, 1976, pg. 2116 2.

6. Curkendall, D. W., and Ondrasik, V. J., "Analytic Methods of Orbit Determination," AAS/AIAA Astrodynamics Conference, Vail, Colorado, July 16–18, 1973.

7. Standish, E. M., etal., *JPL Development Ephemeris Number 96*, TR 32-1603, Jet Propulsion Laboratory, Pasadena, Calif., February 29, 1976.

8. Callahan, P. S., "Expected Range and Doppler Differences for Two-Station Tracking," IOM 315.1-134, Jet Propulsion Laboratory, Pasadena, Calif., May 26, 1977 (JPL internal document).

9. Yip, K. W., Winn, F. B., Reid, M. S., and Stelzried, C. T., "Decimeter Modeling of Ionospheric Columnar Electron Content at S-Band Frequencies," EM 391-620 Jet Propulsion Laboratory, Pasadena, Calif., February 7, 1975 (JPL internal document).

10. Madrid, G. A., et. al., *Tracking System Analytic Calibration Activities for the Mariner Mars 1971 Mission*, Technical Report 32-1587, Jet Propulsion Laboratory, Pasadena, Calif., March 1, 1974.

11. Chao, C. C., "Preliminary Report of Differenced Doppler Determination of Station Frequency Offset for Ranging Demonstration," IOM 314.7-102, Jet Propulsion Laboratory, Pasadena, Calif., July 28, 1977 (JPL internal document).

12. Spradlin, G. L., "DSS Range Delay Calibrations: Current Performance Level," *Deep Space Network Progress Report 42-36*, pp. 138, Jet Propulsion Laboratory, Pasadena, Calif., October 1976.

13. Koch, R. E., Chao, C. C., Winn, F. B., and Yip, K. W., "Conditioning of MVM'73 Radio-Tracking Data," presented at AIAA Mechanics and Control of Flight Conference, August 5–9, 1974.

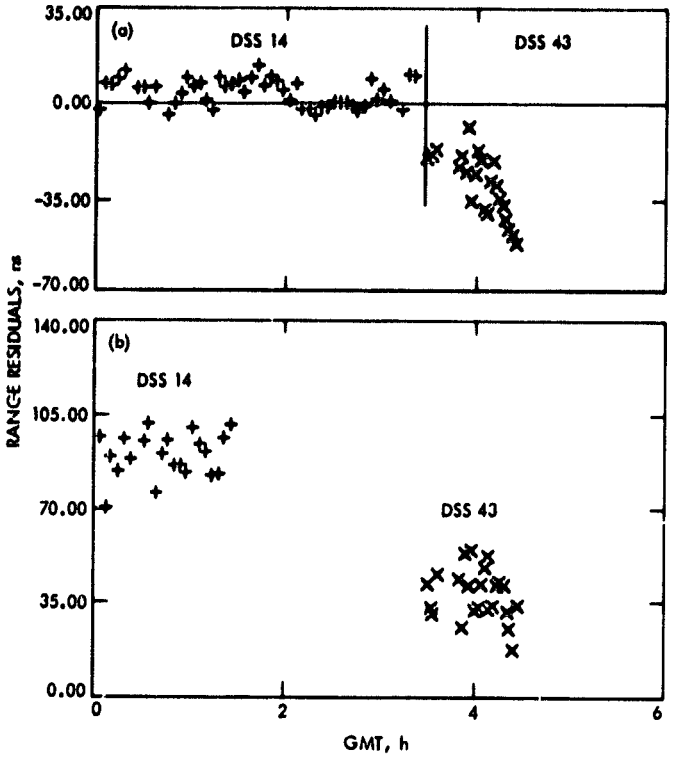

Fig. 1. Residuals as of January 11, 1977: (a) S-band, (b) X-band (1 m ≃ 7 ns)

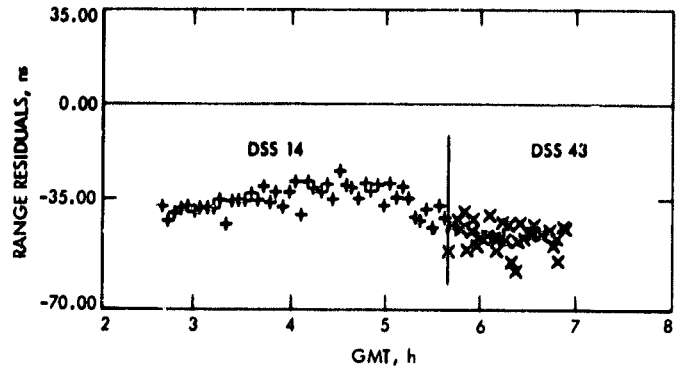

Fig. 2. S-band range residuals, January 19, 1977 (1 m ≃ 7 ns)

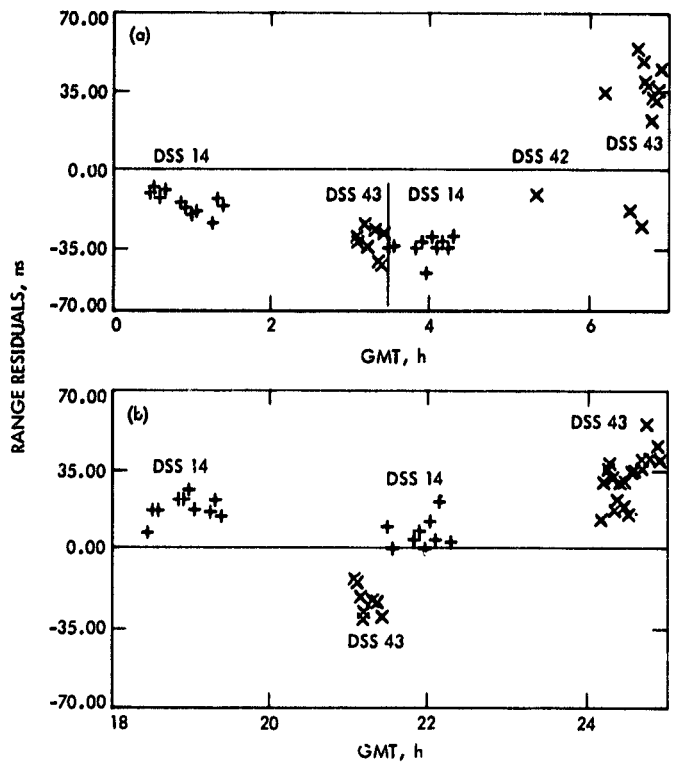

Fig. 3. Residuals as of January 20, 1977: (a) S-band, (b) X-band (1 m ≃ 7 ns)

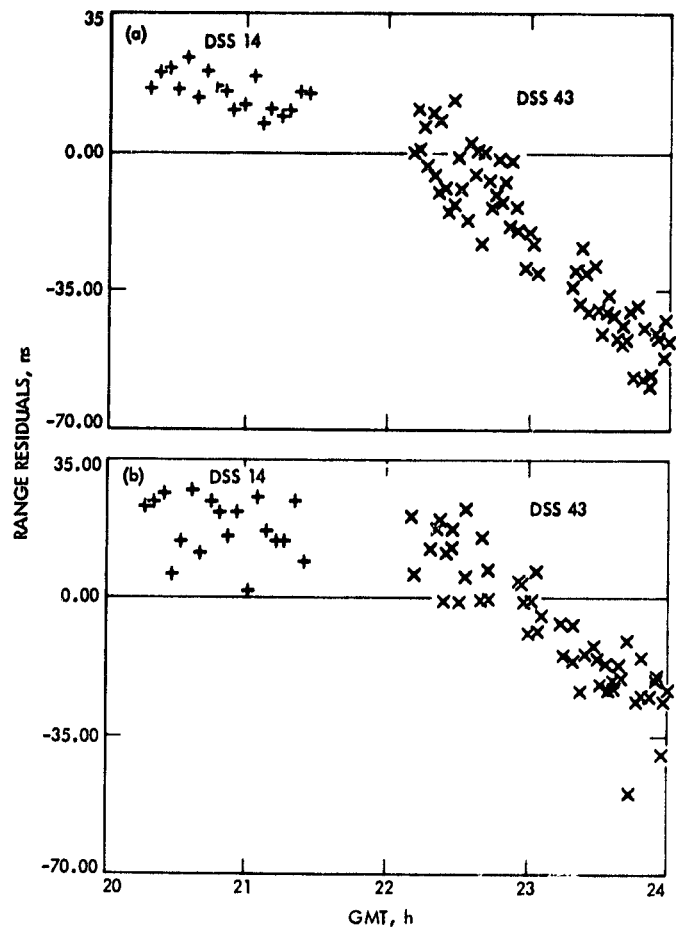

Fig. 4. Residuals as of January 22, 1977: (a) S-band, (b) X-band (1 m ≃ 7 ns)

ORIGINAL PAGE IS
OF POOR QUALITY

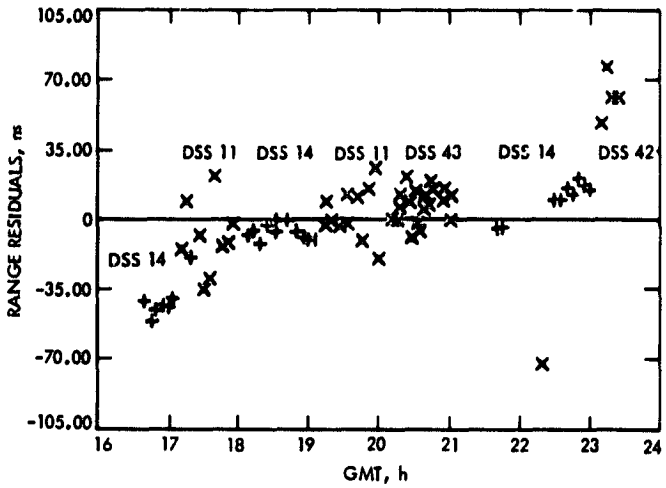

Fig. 5. S-band range residuals, January 31, 1977 (1 m ≈ 7 ns)

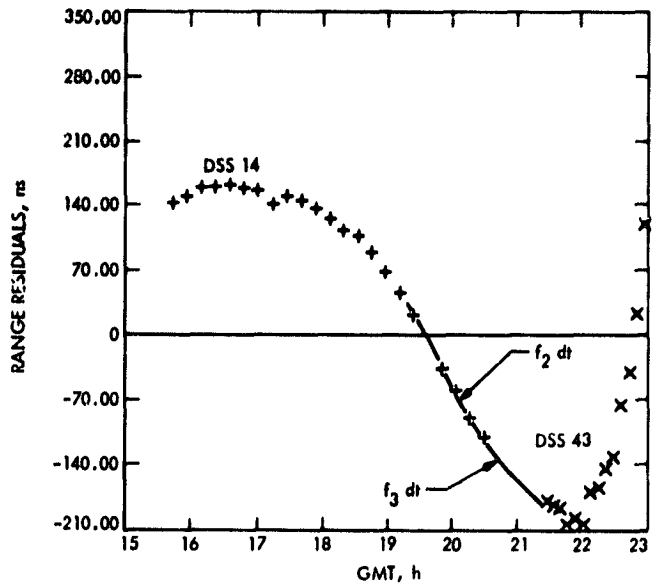

NOTE:

THE RANGE RESIDUAL SIGNATURE IS DUE TO UNMODELLED SPACECRAFT MOTION. INTEGRATED TWO-WAY AND THREE-WAY DOPPLER TRACKING DATA WERE USED TO MODEL THE SPACECRAFT TRAJECTORY ERROR DURING THE 56-MIN SEPARATION BETWEEN DSS 14 AND DSS 43 RANGE

Fig. 6. S-band range residuals, February 20, 1977 (1 m ≈ 7 ns)

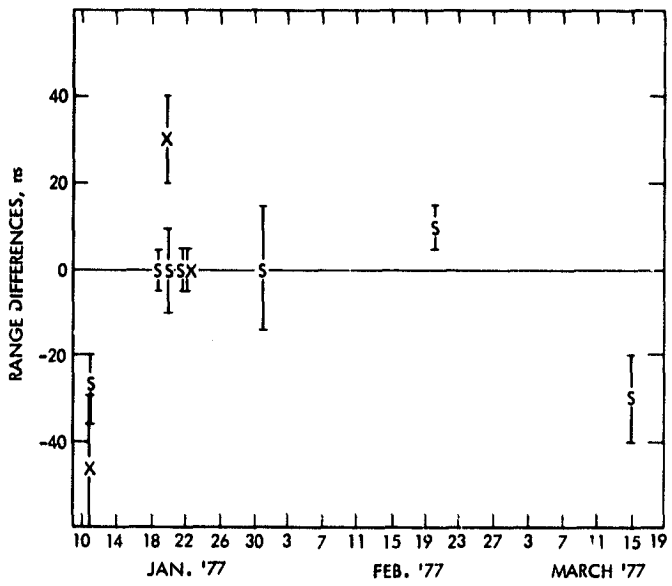

Fig. 7. DSS 43—DSS14 baseline range differences

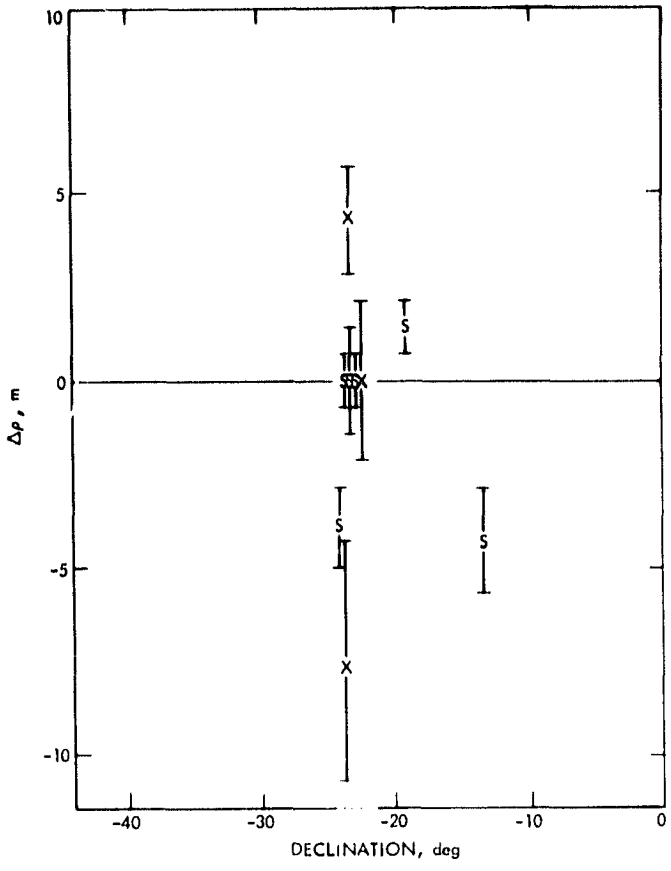

Fig. 8. $\Delta\rho$ as a function of declination

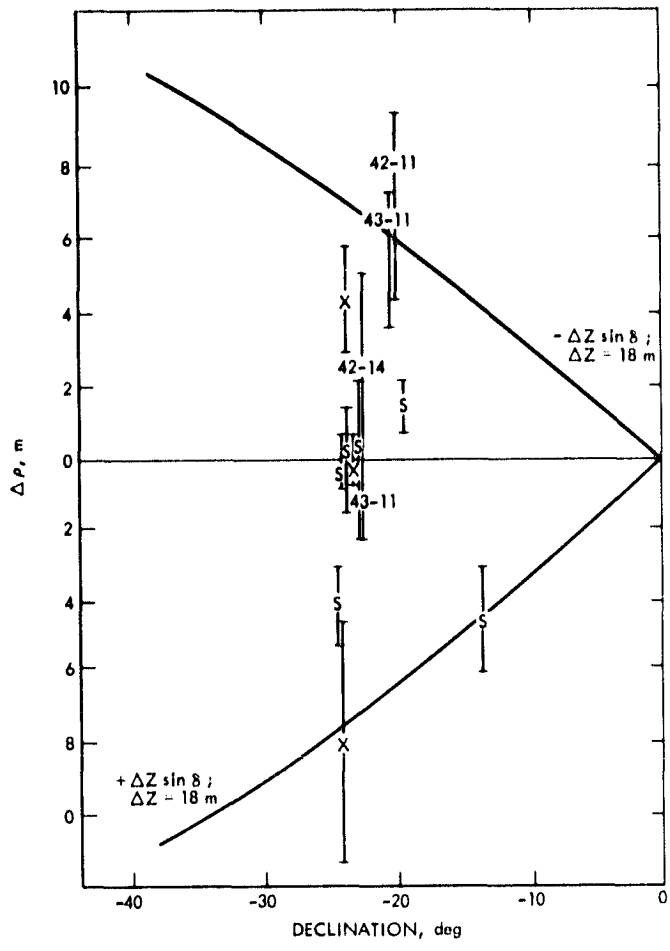

Fig. 9. All $\Delta\rho$ from Canberra—Goldstone Baselines

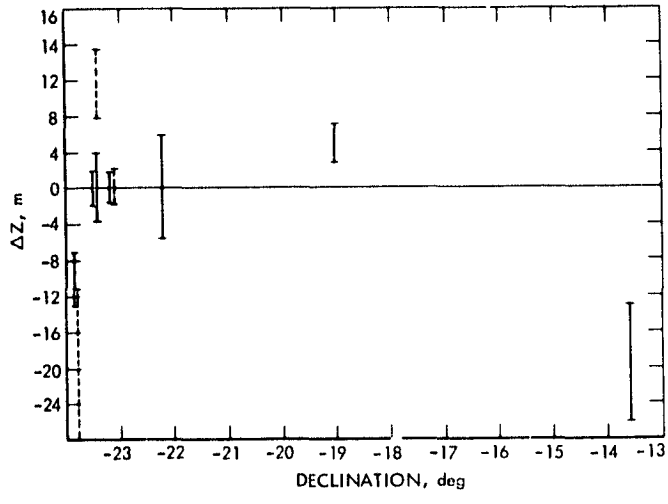

Fig. 10. ΔZ estimates for DSS 43—DSS 14 baseline

N78-24236

CCIR Papers on Telecommunications for Deep Space Research

N. F. deGroot
Telecommunications Systems Section

Three papers on telecommunications for deep space research have been adopted by Study Group 2 of the International Radio Consultative Committee (CCIR). In this article, we present the paper that considers the sharing of radio frequency bands between deep space research and other radio service.

I. Introduction

Study Group 2 of the International Radio Consultative Committee (CCIR) is concerned with the technical aspects of telecommunications for space research and radio astronomy. Three JPL papers on deep space research were submitted by the United States for consideration at a meeting held in Geneva during September, 1977. The papers were adopted and are:

Doc. 2/296 Telecommunication Requirements for Manned and Unmanned Deep Space Research

Doc. 2/269 Preferred Frequency Bands for Deep Space Research Using Manned and Unmanned Spacecraft

Doc. 2/279 Protection Criteria and Sharing Considerations Relating to Deep Space Research

The first of these papers was included in the September-October 1977 issue of the Deep Space Network Progress Report. Also in that report was a description of the role of CCIR papers in the establishment of worldwide regulations that determine the use of the radio frequency spectrum.

The paper on preferred frequency bands was included in the November-December 1977 issue.

This article presents the third paper, which considers interference protection and band sharing with other users.

Documents
CCIR Study Groups
Period 1974-1978

Doc. 2/279-E
23 September 1977

Original: English

UNITED STATES OF AMERICA

Draft New REPORT*
PROTECTION CRITERIA AND SHARING CONSIDERATIONS RELATING TO DEEP SPACE RESEARCH
(Draft Question 1/2 (Rev. 76))

1. Introduction

This report considers the sharing of frequency bands in the range 1-20 GHz between deep space research stations and stations of other services. Deep space earth and space station protection criteria are discussed. Potential interference is considered, and conclusions are drawn about the feasibility of sharing.

The 1-20 GHz range includes current allocations applicable to deep space research and some of the frequencies desired for future operational use. Preferred frequencies are given in Doc. 2/168. U.S. earth and space station characteristics are given in Doc. 2/167.

2. Earth station factors pertinent to sharing

The principal earth station parameters which pertain to interference and sharing are transmitter power, antenna gain and pointing, receiver sensitivity (including noise temperature) and bandwidth. Typical values of these parameters are given in Doc. 2/167. This section of the report considers some aspects of antenna pointing, and develops protection criteria for receivers at deep space earth stations. The section finishes with remarks about coordination. Consideration of transmitter power are given in a later section.

2.1 Intersections of satellite orbits and antenna beams from deep space earth stations.

The locations of the US deep space earth stations are given in Doc. 2/167. The stations are spaced approximately equally in longitude (120° apart) with two stations in the northern hemisphere, and the third in the southern hemisphere. Spacecraft in deep space currently remain in or near the plane of the ecliptic, which is tilted at 23-1/2° from the Earth's equatorial plane. The daily rotation of the Earth causes the antenna beam of at least one earth station to intersect the equatorial plane and hence the geostationary orbit when tracking a given spacecraft. The earth station may be subjected to interference from satellites within the antenna beam and operating in or near the allocated deep space bands.

Satellites that are not geostationary can pass through the one or more deep space tracking teams each day. Details of visibility statistics and in-beam duration times are contained in draft Report AH/2.

In the future the United States plans to deliver deep space probes into orbits out of the plane of the ecliptic. These missions will also result in some earth station tracking beams passing through the orbits of both geostationary and non-geostationary satellites.

2.2 Susceptibility of deep space earth station receivers to interference

A deep space telecommunication system is typically a phase-sensitive system. The earth station receiver utilizes phase-locked loops for carrier tracking and da a recovery. CW or noiselike interference in these loops can result either in degradation or loss of tracking and data. Report 544 contains information on the effects of interference in phase-locked loops. Report 545 presents information on the degradation of telemetering performance caused by interference.

*Proposed replacement for Report AL/2

ORIGINAL PAGE IS
OF POOR QUALITY

2.2.1 CW signal interference

2.2.1.1 Receiver capture. The changing Doppler shift of a received desired signal can cause the receiver pass band to move past a fixed frequency unwanted CW signal. Depending upon rate of motion and the amplitude of the unwanted signal, the receiver may lock to the interfering signal if R, the ratio of the CW signal power to the desired signal power, satisfies the relation:

$$R > \frac{df}{\pi f_n^2} \qquad (1)$$

where df is the rate of frequency change in Hz/s and f_n is the loop natural frequency in Hz.

An interfering CW signal that is 10 dB above a strong signal and is moving through the receiver passband at 100 Hz/s would cause the receiver to lock to the interfering signal. At a lower rate of movement, the required interfering signal level is proportionately lower until at a signal-to-interference ratio greater than one, the interfering signal will no longer capture the receiver, even if the movement rate is zero. Undesired CW signals not strong enough to cause receiver capture may cause interference to carrier tracking.

2.2.1.2 Carrier tracking degradation. An interfering CW signal can induce a phase modulation on the desired carrier signal when the frequency separation between the two signals is comparable to or less than the phase locked loop bandwidth. A maximum acceptable phase modulation of 10^{o} amplitude results from an interference-to-carrier power ratio of -15 dB. The design margin for carrier tracking is typically 10 dB with reference to the noise power in the carrier tracking loop bandwidth. For maximum acceptable carrier tracking degradation, the power in a CW interfering signal that may be within the phase locked loop bandwidth must not be greater than the amount shown in Table I.

TABLE I

CW interference with carrier tracking

Frequency (GHz)	Noise in 1 Hz Loop (dBW)	Minimum Carrier Power (dBW)	Maximum CW Interference (dBW)
2.3	-216.6	-206.6	-221.6
8.5	-215.0	-205.0	-220.0
15.0	-213.4	-203.4	-218.4

2.2.1.3 Telemetering degradation. Telemetering degradation is defined as the amount by which the signal-to-noise ratio must be increased to make the bit error rate, when an interfering signal is present, equal to what it would be if the interfering signal was absent. The maximum allowable degradation for deep space telemetering is 1 dB. For coded telemetering with a threshold signal-to-noise ratio of 2.3 dB, CW interference 6.8 dB below the noise power will result in 1 dB degradation. For uncoded telemetering with a threshold signal-to-noise ratio of 9.8 dB, CW interference 5 dB below the noise will result in 1 dB degradation. The noise power is proportional to the data bandwidth and the receiver noise spectral density. Examples of allowable level of CW interference are shown in Table II.

TABLE II

CW Interference with telemetering

Frequency (GHz)	Data (bits/s)	Noise Power in Data Bandwidth (dBW)	Interference-to-Noise Ratio for 1 dB Degradation (dB)	Maximum CW Interference (dBW)
2.3	40, uncoded	-200.6	-5.0	-205.6
8.4	40, coded	-200.0	-6.8	-206.8
	115k, coded	-164.4	-6.8	-171.2
15.0	40, coded	-197.4	-6.8	-204.2
	115k, coded	-162.8	-6.8	-169.6

2.2.2 Wideband interference

Wideband signals or noise that reduce the signal-to-noise ratio affect both the carrier tracking and the data channels. In the case of the telemetering channel, the spectral density of the interfering signal must be at least 5.9 dB below the spectral density of the receiver noise in order not to degrade the threshold performance by more than 1 dB. Maximum levels of wideband interference are shown in Table III.

TABLE III

Wideband interference with telemetering

Frequency (GHz)	Noise Spectral Density (dB(W/Hz))	Interference-to-Noise Ratio (dB)	Maximum Wideband Interference (dB(W/Hz))
2.3	-216.6	-5.9	-222.5
8.4	-215.0	-5.9	-220.9
15.0	-213.4	-5.9	-219.3

2.2.3 Interference to maser operation

Mixing of signals with the idler frequency of the maser pump can cause interference and saturation in the receiver passband. There are many frequencies at which such mixing can occur, all of which are far removed from the normal frequency of reception. Table IV gives possible interference frequencies for the two frequency bands currently used for reception at deep space research earth stations.

Interfering signals must be above -120 dBW in the idler bandwidth (which is very broad) at the maser input to be significant.

TABLE IV

Frequencies at which interference may be caused by mixing in the maser

Receiver frequency band	2 290 - 2 300 MHz	8 400 - 8 500 MHz
Maser pump frequency	12.7 GHz	19.3 and 24.0 GHz
Interference frequencies	15.0 GHz 10.4 7.5 5.2	32.4 GHz 27.8 15.6 10.9

2.2.4 Adjacent channel receiver saturation

The cryogenically cooled maser of the deep space receiver has a bandpass of approximately 50 MHz. Adjacent channel signals, if received at total power levels greater than

ORIGINAL PAGE IS OF POOR QUALITY

-120 dBW, can generate intermodulation products in the mixer and other receiver elements, causing saturation of the receiver.

2.2.5 Interference protection for Earth station receivers

Interruption of telecommunications can result from interference that is strong enough to cuase receiver capture or saturation. Weaker interference may result in degraded carrier tracking and telemetering performance. The level of interference that can be tolerated is determined by acceptable performance degradation. To protect Earth station receivers, the power spectral density of wideband interference, or the total power of CW interference, in any single band and all sets of bands 1 Hz wide, should not be greater than the values shown in Table V, for an aggregate of five minutes in any one day.* Table V also shows the maximum power flux density of interference, considering the effective area of a 70m earth station antenna.

TABLE V

Interference protection for earth station receivers

Band (GHz)	Maximum Power Spectral Density (dB (W/Hz))	Maximum Power Flux Density (dB (W/m^2 Hz))
2.3	-222.5	-256.2
8.4	-220.9	-253.8
15.0	-219.3	-250.2

2.3

2.3 Coordination considerations

The practicability of coordination is determined partially by the number of stations with which coordination must be effected. This is in turn controlled by the coordination distance. For deep-space research, the practicable coordination distance is currently considered to be 1,500 km.

Coordination distance may be calculated by the method of Appendix 28 of the Radio Regulations. An alternate method is given in Doc. 5/225 (Geneva, 1977). The two ways of determining distance give different results. For example, assuming a transhorizon station (i.e., 93 dB(W/10 kHz), in the 2.3 gHz band), the distances are 2,100 and 800 km, respectively.

A decision on the practicability of sharing with transhorizon stations is thus not possible, and further study is necessary.

3. Space station parameters and protection pertinent to sharing

The principal space station parameters which pertain to interference and sharing are antenna gain and pointing, transmitter power and receiver sensitivity. Details of these parameters are given in Doc. 2/167.

Space station and Earth station receivers for deep space research function in a similar manner, except that the space station does not include a maser. Space stations are susceptible to interference as described earlier for Earth stations.

The criterion for protection of space station receivers is that interference power must be no stronger than receiver noise power. Compared to Earth station criteria, this is less severe and is a consequence of generally larger performance margins on the Earth-to-space link. For protection of space stations, the power spectral density of wideband interference, or total power of CW interference, in any 1 kHz band should be no larger than the amount shown in Table VI for an aggregate of 5 minutes per day.

*Five minutes per day is generally taken as 0.001% of the time, as discussed in Report 546 (Geneva).

TABLE VI

Interference protection for space station receivers

Frequency (GHz)	Maximum Interference Level (dB(W/kHz))
2.1	-170.8
7.2	-169.6
15.0	-168.1

Space station e.i.r.p. is normally reduced while near Earth, minimizing the potential for interference to other stations.

4. Sharing considerations

The following paragraphs consider the possibility of interference between deep space research stations and those of other services. There are 8 possibilities to be considered, as shown in Table VII.

Table VII and the following paragraphs consider the possibility of interference in the deep space research Earth-to-space bands.

TABLE VII

Potential interference in Earth-to-space bands

Source	Receiver
Earth station	Terrestrial station
Earth station	Near Earth satellite
Terrestrial station	Earth station
Terrestrial station	Space station
Space station	Terrestrial station
Space station	Near Earth satellite
Near Earth satellite	Earth station
Near Earth satellite	Space station

4.1 Potential interference to terrestrial receivers from earth station transmitters

The normal maximum total power for current U.S. earth stations is 50 dBW. For a typical minimum elevation angle of 10 degrees, the e.i.r.p. directed towards the horizon does not exceed 57 dB(W/4 kHz), assuming the reference earth station antenna radiation pattern of Recommendation AA/2. For spacecraft emergencies, the maximum total power may be increased to 56 dBW, giving not more than 63 dB(W/4 kHz) at the horizon. These values of e.i.r.p. meet the requirements of RR 470F.

Aircraft stations within line-of-sight of a deep-space earth station will encounter total power flux densities as shown in Figure 1. For an aircraft altitude of 12 km, the maximum line-of-sight distance to an earth station is 391 km and the total power flux density at the aircraft can never be lower than -83 dB(W/m^2), again assuming the antenna pattern of Recommendation AA/2. Depending on distance and earth station antenna direction, the aircraft station may experience much higher flux densities and interference levels. Coordination with airborne stations is generally not practicable.

Tropospheric and rain scatter may couple deep-space earth station transmitting signals into trans-horizon, space system and other surface stations. When practicable, coordination should provide sufficient protection for terrestrial receivers and earth station receivers. See § 2.3 for coordination considerations.

4.2 Potential interference to satellite receivers from deep-space earth station transmitters

Satellites that come within the earth station beam will encounter power flux densities as shown in Figure 1. When an earth station is tracking a spacecraft such that the antenna beam passes through the geostationary satellite orbit, the flux density at a point on that orbit will vary with time as shown in Figure 2. For example, the total power flux density will be -95 dB(W/m^2) or more for 32 minutes. The figure assumes a transmitter power of 50 dBW, a 64 m antenna, and the reference earth station antenna pattern of Recommendation AA/2. An important observation is that the minimum flux density at the geostationary satellite orbit within line of sight of a deep space earth station is -122 dB (W/m^2), regardless of antenna pointing direction.

The duration and magnitude of signals from deep space earth station transmitters that may interfere with satellites in non-geostationary orbits depends on those orbits and the particular deep space tracking at that time.

4.3 Potential interference to deep-space station receivers from terrestrial or earth station transmitters

Terrestrial or earth station transmitters within sight of a deep space station are potential sources of interference. Figure 3 shows the space station distance at which interference power density from such a transmitter equals the receiver noise power density. For example, a transhorizon station with 93 dB(W/10 kHz) e.i.r.p. in the 2.1 GHz band could interfere with a space station receiver at ranges up to 4.1×10^9 km (600 K noise temperature, 3.7 m spacecraft antenna). The possibility of interference at such great distance poses a threat to space missions to planets as far away as Uranus. Stations with lower e.i.r.p or with antennae pointing away from the ecliptic plane will have less potential for interference.

4.4 Potential interference to space station receivers from near-Earth satellite transmitters

Near-Earth satellites typically have antennae directed at the Earth or at other satellites. Interference with deep-space station receivers may occur for those brief periods when the satellite antenna is directed near the ecliptic plane. As received at deep space stations, signals from satellites will usually be relatively weaker than those from earth stations.

5. Sharing considerations: space-to-Earth bands

Table VIII and the following paragraphs consider the possibility of interference in the deep space research space-to-Earth bands.

TABLE VIII

Potential interference in space-to-Earth bands

Source	Receiver
Deep space station	Terrestrial or earth station
Deep space station	Near Earth satellite
Terrestrial or earth station	Deep space earth station
Near Earth satellite	Deep space earth station

ORIGINAL PAGE IS OF POOR QUALITY

5.1 Potential interference to terrestrial or earth station receivers from deep-space station transmitters

Figure 4 shows power flux-density at the surface of the Earth caused by deep-space stations with characteristics as shown in Doc. 2/167. These stations typically use low gain, wide beam antennae while near Earth. After a time not exceeding six hours from launch, they are usually at a sufficient distance for the flux density at the surface of the Earth to be less than the maximum permitted by Radio Regulations for protection of line-of-sight radio-relay systems. For example, the Mariner Jupiter Saturn spacecraft is expected to use the low gain antenna until 4.2×10^7 km from Earth, at which time the flux density would be -198 dB(W/m^2) in 4 kHz after switching to the high gain antenna.

When the transmitting space station is using a higher gain directional antenna, there is the potential for interference with sensitive terrestrial receivers if their antennae are directed in the ecliptic plane. A space station operating at 2.3 GHz with an e.i.r.p. of 51 dBW at a distance of 5×10^8 km could create an input of -168 dBW to a transhorizon receiver (27 m antenna, main beam). The duration of such interference would be of the order of a few minutes because of the rotation of the Earth.

5.2 Potential interference to near-Earth satellite receivers from deep-space station transmitters

Considerations of this interference are similar to those for the space station to terrestrial receiver case, §5.1, with the exception of the path geometry. Depending on the changing conditions of that geometry, occasional brief interference is possible.

5.3 Potential interference to deep-space earth station receivers from terrestrial or earth station transmitters

Interference to deep-space earth station receivers may come from terrestrial or earth stations over line-of-sight paths, by tropospheric phenomena, or by rain scatter. For coordination considerations see § 2.3.

Other services with high power transmitters and high gain antennae are potential interference sources. Radiolocation stations are an example. Earth station transmitters are less likely sources of interference, depending on e.i.r.p. in the direction of the deep-space earth station. Coordination should provide adequate protection from radio-relay stations.

Aircraft transmitters within sight of a deep-space earth station may cause serious interference. At maximum line-of-sight distance in any direction (391 km for an aircraft at 12 km altitude), an e.i.r.p. of -26 dB(W/Hz) (for example, 10 dB(W/4 kHz) and 0 dBi antenna) will exceed the earth station interference limit by at least the amount shown in Table IX, assuming the reference earth station antenna pattern.

Coordination with airborne stations is generally not practicable.

TABLE IX

Interference from assumed aircraft transmitter

Frequency (GHz)	Deep-space Earth Station Interference Limit (dB (w/Hz))	Harmful interference from Aircraft* (dB)
2.3	-222.5	35.7
8.4	-220.9	22.1
15.0	-219.3	15.5

*Aircraft signal less deep-space earth station interference limit

5.4 Potential interference to deep-space earth station receivers from near Earth satellite transmitters

An analysis of the case for satellites in highly eccentric orbits may be found in Report AJ/2. It is concluded there that sharing is not feasible. This conclusion is also valid for satellites in circular and moderately eccentric orbits.

6. Discussion

Sharing with stations that are within line-of-sight (LOS) of deep-space earth stations is not feasible. Stations within LOS will create excessive interference to receivers of deep-space earth stations, or will be exposed to excessive interference from transmitters of these stations. Aeronautical mobile stations and near-Earth satellites frequently come within LOS of deep-space earth stations.

Sharing of deep-space Earth-to-space bands with stations utilizing high average e.i.r.p. is not feasible because of potential interference to stations in deep space. It is currently considered that stations with an e.i.r.p. that is more than 30 dB below the implemented or planned e.i.r.p. for space research earth stations do not pose a significant problem. From the data in 2/167, this means an average e.i.r.p. no greater than 82 dBW at 2 and 7 GHz. The deep-space earth station e.i.r.p. for other frequencies is not now known.

7. Conclusion

Criteria and considerations presented in this Report lead to the following conclusions:

7.1 Sharing of Earth-to-space bands

Deep-space research cannot share Earth-to-space bands with:

(a) receiving aeronautical mobile stations,

(b) receiving satellite stations, and

(c) transmitting terrestrial stations and earth stations utilizing high average e.i.r.p., for example, transmitting transhorizon stations, and transmitting fixed-satellite earth stations.

When coordination is practicable, sharing is feasible with other stations of all services. In some cases, coordination distance may be unacceptably great.

7.2 Sharing of space-to-Earth bands

Deep-space research cannot share space-to-Earth bands with:

(a) transmitting aeronautical mobile stations, and

(b) transmitting satellite stations.

When coordination is practicable, sharing is feasible with other stations of all services. In some cases, coordination distances may be unacceptably great.

The matter of unacceptably long coordination distance requires further study.

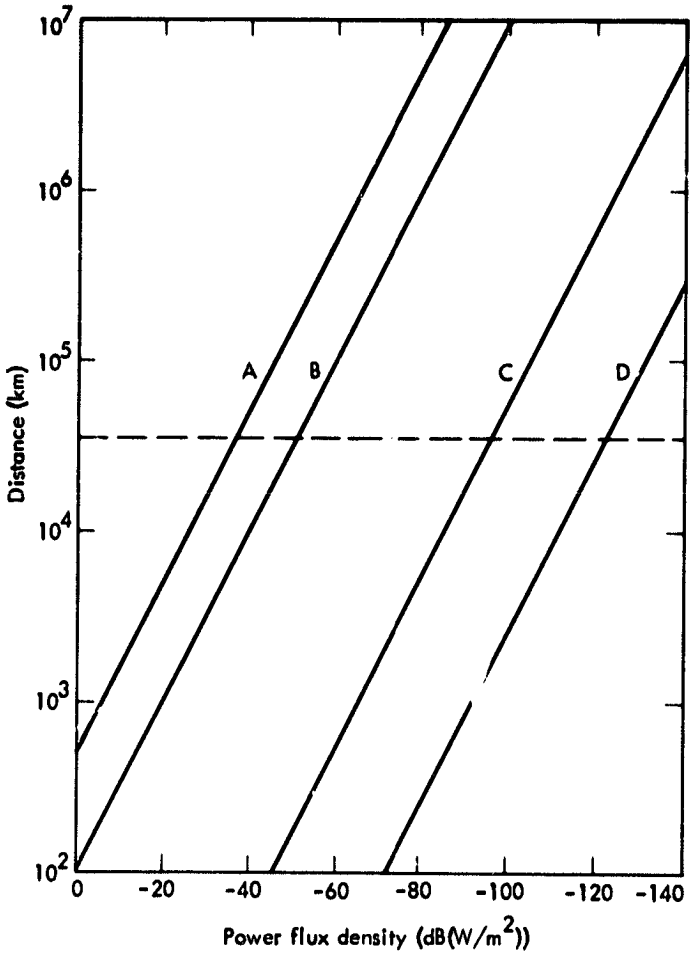

FIGURE 1.

Power flux density from Earth station transmitter
100 kW, 64 m antenna

A: Main beam, 15 GHz

B: Main beam, 2.1 GHz

C: 5 deg off axis
(14.5 dB gain, Rec. AA/2)

D: ≧ 48 deg off axis (-10 dB gain, Rec. AA/2)

— — : Altitude of geostationary satellite orbit, 3.56×10^4 km

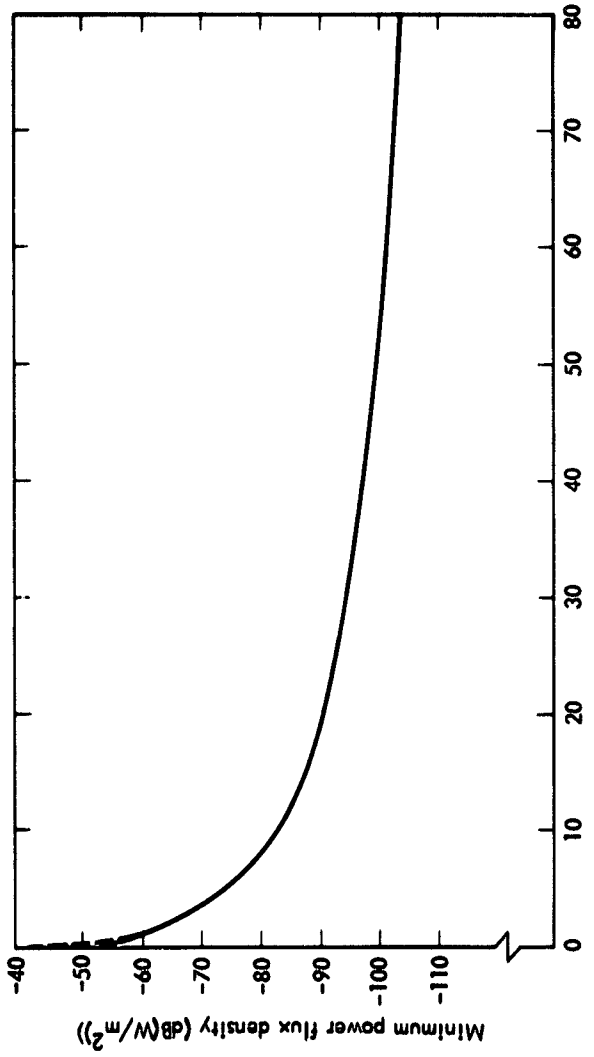

FIGURE 2.

Duration of potential interference to geostationary satellite intersecting beam axis from Earth station with 100 kW transmitter and 64 m antenna

——— : 2.1 GHz

— — — : 15 GHz

ORIGINAL PAGE IS
OF POOR QUALITY

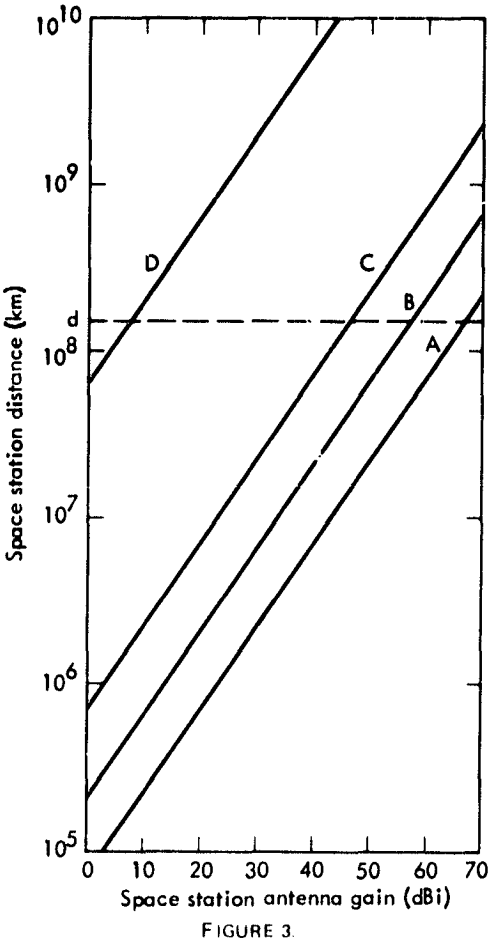

FIGURE 3

Space station distance from terrestrial transmitter for interference power equal to receiver noise power

A: 15 GHz relay transmitter, 55 dB(W/10 kHz); -168 dB(W/kHz) receiver noise power

B: 7.2 GHz relay transmitter, 55 dB(W/10 kHz); -170 dB(W/kHz) receiver noise power

C: 2.1 GHz relay transmitter, 55 dB(W/10 kHz); -171 dB(W/kHz) receiver noise power

D: 2.1 GHz transhorizon transmitter, 93 dB(W/10 kHz); -171 dB(W/kHz) receiver noise power

d: Space station range of 1 astronomical unit, 1.5×10^{8} km

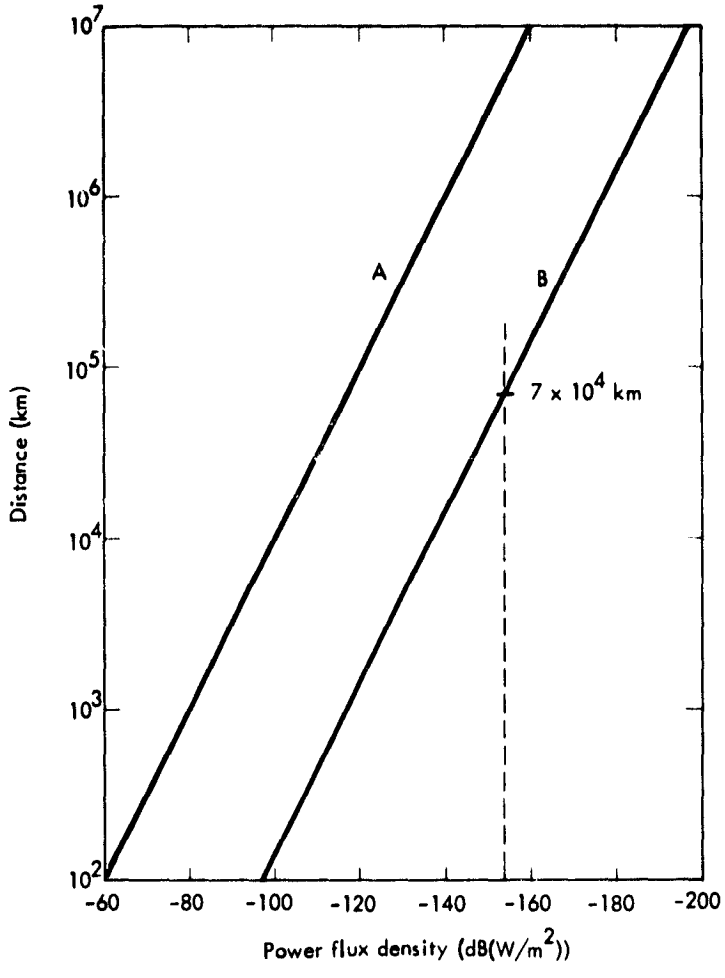

FIGURE 4.
Power flux density at surface of Earth from space station transmitter

A: 14 dBW transmitter, 37 dBi antenna

B: 14 dBW transmitter, 0 dBi antenna

— — —: -154 (dB(W/m^2)) (RR 470 NE)

N78-24237

Development of a Unified Criterion for Solar Collector Selection

F. L. Lansing
DSN Engineering Section

To assist in making engineering or management decisions, this article explores the possibility of building a single selection criterion to distinguish between different solar collector subsystems for a specific application or between different complete solar-powered systems. The development of two analogous criteria are discussed. The criteria combines both performance and unit area costs, and presents the dollar per unit power and the dollar per unit energy produced from a solar plant. Typical values for current focusing and nonfocusing solar collectors were included to support the discussion. The first phase development shows that the criteria evaluation is in need of more data about the annual dynamic behavior of the collector subsystem only, under the transient site-specific parameters such as solar flux, wind, and ambient temperature.

I. Introduction

It is a fact that the last decade has witnessed a great deal of research and development in nonfossil fuel energy sources to find a solution to the energy shortage problem. Many industrial organizations, academic institutes and research laboratories including the Jet Propulsion Laboratory, have started energy research and conservation programs Solar energy as one of the nondepletable sources has been under thorough investigation, and the solar collector component, as an entity, has occupied a major part of that investigation.

The above competitive efforts blossomed many collector concepts. Some concepts are still on paper while others are ahead in production phase. No bounds or standards are set to unify the parameters of module geometry, physical dimensions, weight, operating temperatures, optical properties of coatings or glazing, insulation thicknesses, heat loss rates, etc. Consequently, large collections of information and data regarding performance and cost of many "good" solar collectors were established. The differences in cost and performance are wide not only between collectors of different categories but also between collectors of the same category. Collector manufacturers enlarge this difference gap and support their own product selection rationale to obtain either high performance using expensive high grade materials or to sacrifice performance for a low cost product.

For a given application, the selection of the solar collector, whether it is a focusing or a nonfocusing type, affects the overall installation, operation and maintenance cost. For engineering or management decisions, the question that eventually will rise is which collector possesses the "best" score? The comparative adjective "best" means in engineer-

ORIGINAL PAGE IS OF POOR QUALITY

ing terms the one that not only scores highest in fulfilling its purpose at the required operating conditions with the least cost but also scores highest in reliability, durability, low risk, nonhazardous and low maintenance problems. Any cost methodology such as a life cycle cost analysis, a cost/benefit payback period analysis, or a cash flow analysis, may be used to support the selection rationale.

In the present article, the development of a single collector criterion combining performance and unit cost is explored to be used as a figure of merit. The other operational parameters of risk, maintenance, and reliability are not included for two reasons: (1) there is not enough data accumulated about collector failures, maintenance and durability to judge a newly developed solar collector, and (2) reliability and maintenance figures of merit using the probability theory are addressed elsewhere in detail and could be added to the total selection of analysis once a cost/performance criterion is established.

The main objectives of this study are set to (1) provide a means to distinguish between different solar collectors or integrated solar-powered systems for a given application combining only performance and unit cost, (2) reduce or eliminate the need for costly site-specific experimental tests once a good performance model is established at another site with different weather spectrum and (3) assist engineering and/or management in making decisions in system evaluation and cost effectiveness.

II. Collectors for Electric Power Generation

In comparing focusing collectors (such as parabolic troughs, parabolic dishes, fresnel lenses, etc.) with nonfocusing types (such as flatplate collectors) for electric power generation, the points in favor and against each type are as follows:

(1) Focusing collectors tend to have, in general, higher collection efficiency than nonfocusing types. This is caused by the reduction in heat losses as a result of small concentration areas which is much less than the increase in heat losses caused by high temperatures attained.

(2) Nonfocusing collectors have the ability to harness the diffuse radiation while focusing types do not have. Diffuse radiation can be as much as 20% of the total incident flux on clear days. This ratio goes up on cloudy days. On the other hand, nonfocusing collectors are generally nontracking and the radiation cosine losses due to their fixed oblique orientation (cosine the angle of incidence) exceeds the gain of the extra diffuse part. The result is a less peak and accumulated radiation intensity for clear days than tracking focusing collectors. The situation is reversed on cloudy days. However, it appears that this extra diffuse part plays an insignificant role in collection efficiency increase since nonfocusing collectors have generally higher efficiency as stated in item (1).

(3) Although tracking in focusing collectors is essential and adds an extra cost to the power plant, it is desirable in maintaining a constant collector efficiency for longer periods over the day. This is in contrast with nontracking nonfocusing types that possess an undesirable steep rate of efficiency decrease with operating temperature.

The above points indicate that collectors with high performance are accompanied by high cost and vice versa. The need for a selection methodology then follows as an essential tool for comparison of the various types.

The cost of a solar-electric power plant is greatly influenced by the overall conversion from solar-to-electric efficiency. If conversion is done via thermal power cycles, the efficiency is simply the product of collection efficiency times the power cycle thermal efficiency as shown in Fig. 1.

The efficiency trends shown in Fig. 1 for both the collector and the power cycle are general for any type of each. The collection efficiency always decreases with increasing operating temperature due to higher thermal losses and can reach zero when the incident radiation equals the losses at point B. The power cycle efficiency, on the other hand, increases with the operating temperature and starts from zero at ambient temperature, point A. The overall conversion efficiency will be zero at both points A and B and always possesses a maximum value in between A and B. The optimum operating temperature corresponding to maximum overall conversion efficiency should be the system design point.

III. Derivation of Maximum Solar/Electric Conversion Efficiency

The performance of solar collectors is generally the same whether they are focusing or nonfocusing types. The instantaneous collector efficiency (E_c) can be expressed approximately by the linear form

$$E_c = a_1 - b_1 \left(\frac{T - T_0}{I} \right) \qquad (1)$$

where

I = solar intensity per unit collector area

T_0 = ambient temperature

a_1 = collector constant representing its optical efficiency

b_1 = collector constant representing its thermal loss coefficient

T = Plate (receiver) temperature of the collector

Equation (1) can be put in the compact linear form:

$$E_c = a_2 - b_2 T \tag{2}$$

where a_2 and b_2 are collector constants given by

$$\left.\begin{aligned} a_2 &= a_1 + b_1 \frac{T_0}{I} \\ b_2 &= \frac{b_1}{I} \end{aligned}\right\} \tag{3}$$

The constants a_2, b_2 are considered collector "characteristic" constants to differentiate between shapes, geometry, optical and thermal properties for a given ambient temperature and solar intensity.

On the other hand, the thermal efficiency of power cycles can be expressed in general as a fraction of the corresponding Carnot's cycle working between the same source/sink temperature limits. This fraction is a function of many conditions, such as type of cycle, type of working fluid, pressure and temperature ranges, etc.

The ratio (λ) of real power cycle efficiency to Carnot's working between the same temperature limits, ranges in practice from 0.4 to 0.6 at full load. Accordingly, the thermal efficiency of a real power cycle working between a hot surface temperature T and an ambient temperature T_0 is approximated by

$$E_e = \lambda \left(1 - \frac{T_0}{T}\right) \tag{4}$$

The overall conversion from solar to electric efficiency (E_0) then follows as

$$E_0 = E_c \times E_e$$

or by combining Eqs. (2) and (4)

$$E_0 = \lambda \ (a_2 - b_2 T) \quad \left(1 - \frac{T_0}{T}\right) \tag{5}$$

The overall conversion efficiency from Eq. (5) can be zero at two positions:

(1) Where the collector efficiency is zero at a maximum temperature:

$$T_B = \frac{a_2}{b_2} \qquad \text{(point B on Fig. 1)}$$

(2) At a temperature $T_A = T_0$, or when the engine efficiency is zero at ambient temperature (point A on Fig. 1).

Assuming that the parameters a_2, b_2, and λ are unchanged with the collector temperature, the overall conversion efficiency will possess a maximum value $E_{0,max}$ at the optimum temperature T_{opt} given by differentiation as

$$T_{opt} = \sqrt{a_2 T_0 / b_2} \tag{6}$$

$$E_{0,max} = \lambda a_2 \left(1 - \frac{T_0}{T_{opt}}\right)^2 \tag{7}$$

Equations (5) and (7) show that at the optimum operating temperature

$$E_c = \frac{a_2}{\lambda} \cdot E_e \tag{8}$$

This means that if the value of (a_2) is equal to (λ) the optimum temperature (T_{opt}) will be the intersection point between the engine efficiency and collector efficiency curves. The location of the optimum temperature will be lower than the intersection temperature or higher depending on whether the value of (a_2/λ) is larger or smaller than 1, respectively.

The optimum operating temperature for the combined collector-engine system as calculated from Eq. (6) is dependent on the slope (b_2) and ordinate intersection (a_2) of the collector efficiency line. Smaller slopes and larger ordinate intersection produce higher overall conversion efficiency $E_{0,max}$ and higher optimum temperature. This explains why focusing collectors are offering a superior performance compared to nonfocusing types.

IV. First Selection Criterion for Solar-Electric Plant ($/kWe)

From an engineering viewpoint, a solar-electric plant should be combining good performance (presented by the maximum overall conversion efficiency) and low cost to compete with conventional fossil-fuel or nuclear power plants. Before rating different collectors or different energy conversion systems, the following parameters and assumptions will be fixed for all candidates under investigation:

(1) Operating temperature will be the optimum value corresponding to the maximum overall conversion efficiency.

(2) Site and location with its topography and geography is the same to each candidate.

(3) Weather spectrum, ambient temperature, humidity, wind speed, and direction are the same to each candidate.

(4) Cloud cover, thickness, height, dispersion, and frequency of appearance are the same to each candidate.

(5) Clear day solar insolation spectrum is the same for all candidates. Even though focusing and nonfocusing collectors receive different proportions of direct, diffuse, and ground reflected parts, the conversion efficiency is assumed to be independent of the intensity of input energy. In other words, each collector will be scored and judged according to its ability to collect and transfer to the working fluid the solar energy which was harnessed.

(6) Maintenance and operation costs (M&O) will be assumed in direct proportionality to the unit collector cost ($/m^2). This means that expensive collectors will have larger M&O costs than inexpensive ones. These annual costs will constitute a fixed percentage (of order 10% for example) of the installation cost.

The collection surface area can be calculated from the simple equation:

$$\text{collector area (m}^2\text{)} = \frac{\text{electric power output (kWe)}}{\text{solar radiation intensity (kWt/m}^2\text{)} \times \text{overall solar-electric conversion efficiency } (E_{0,max})} \tag{9}$$

The electric power output in the numerator and the solar radiation intensity in the denominator should be computed during the same time interval. The latter could be a 15-min peak, a daily average, a monthly average, a seasonal average or a yearly average. The overall solar-electric conversion efficiency is determined by using Eq. (7), with fixed solar radiation and ambient conditions.

The installation cost in dollars of the whole solar power plant including energy collection, conversion, storage, and transport subsystems can be divided by the total collection area (in m^2) to yield a unit installation cost in ($/m^2). The operation and maintenance cost when added as a fixed percentage of the installation cost will facilitate the comparison, so that we need only to speak about the unit plant cost.

The total plant (or collector) cost per kW$_e$ output can thus be given by:

$$\text{plant (or collector) \$/kWe} = \frac{\text{unit plant (or collector) cost (\$/m}^2\text{)}}{\text{solar radiation intensity (kWt/m}^2\text{)} \times \text{overall solar-electric conversion efficiency } (E_{0,max})} \tag{10}$$

Equation (10) applies to any solar-electric plant whether it is an indirect thermal-electric conversion via power cycles or a direct solar-electric conversion such as photovoltaic cells. Also, Eq. (10) can be used in comparing collectors only for solar-electric application by using the unit collector cost $/m^2 instead of the unit plant cost ($/m^2).

A common reference value of the solar radiation intensity is one "sun" defined as a peak intensity of 1 kWt/m^2 (0.1 W/cm^2 or 317 Btu/h ft^2) at solar noon. For tracking collectors, the intensity of 1 kWt/m^2 is considered a suitable incident radiation reference. But for nontracking collectors, a radiation reference of 0.8 kWt/m^2 will be chosen as a

radiation reference to account for the cosine of the angle of incidence losses. Under these radiation references, the cost of any solar-electric plant (or collector) per electric kilowatt at the bus bar can be given by substituting in Equation (10). For solar-electric power plants with tracking solar collectors,

$$\text{total plant (or collector cost) \$/kWe} = \frac{\text{unit plant (or collector) cost \$/m}^2}{\text{overall conversion efficiency } (E_{0,max})} \tag{11a}$$

For solar-electric power plants with nontracking solar collectors,

$$\text{total plant (or collector) cost \$/kWe} = \frac{\text{unit plant (or collector) cost \$/m}^2}{0.8 \times \text{overall conversion efficiency } (E_{0,max})} \tag{11b}$$

Equations (11a, b) present the first figure of merit (\$/kWe) which differentiates between the different solar-electric conversion systems combining both performance and cost. Other figures of merit representing maintainability, risk, durability, etc., can be added to complete the selection criteria.

Table 1 lists typical results for some current solar collectors. The instantaneous efficiency curves are plotted as shown in Fig. 2 versus the average collector temperature. The heat engine efficiency working at 50% of Carnot's between the collector temperature and ambient temperature 25°C (77°F) is also plotted for reference. Some cost and efficiency data were abstracted from Refs. 1 through 12.

Equations (6) and (7) are used to calculate the optimum operating temperature and the maximum overall conversion efficiency, respectively. The unit collector cost (\$/m^2) figures were either abstracted from manufacturer data or estimated from past experience. Equations (11a, b) are used to estimate the \$/kWe figures as given in Table 1. The maximum overall conversion efficiencies were in good agreement with some of the values reported in Refs. 13 and 14 using other derivations.

It is apparent from Table 1 that focusing collectors with their high temperature capability, in spite of their high cost, are favored for solar-electric conversion. However, the rate of decreasing costs by mass production in focusing and nonfocusing types can change the selection procedure. Table 2 for example, shows how the competition between solar collectors can be tough. The three hypothetical solar collectors presented in Table 2 have different optimum performance figures as presented by 3%, 8%, and 16% conversion efficiency and different unit cost as given by \$60, \$200, and \$400/m^2. According to Eq. (11), the collector cost alone per kWe output is the same for all of them and equals \$2500/kWe which appears to make the selection process not decisive. The first collector could be a typical flat plate collector as evidenced in Table 1. Also, the second collector could be a low performance parabolic trough, and the third collector could be a paraboloid, dish or a heliostat power tower collector. Furthermore, if the rest of the subsystems such as energy transport, conversion, and storage subsystems, excluding the collector subsystem, cost the same when producing 1 kWe, then the choice will still be narrowed down to that collector which requires the least land area for the given output. Table 2 shows that collection areas range from 6 to 42 m^2/kWe for the above cases depending on the overall conversion efficiency as given in Eq. (9). This collection area should further allow for shadowing effects, module spacing, etc., which means larger land areas and more installation cost. For these nondecisive cases, knowledge of collector performance over longer periods of time is very important, which leads to the second analogous criterion in the next section.

V. Second Selection Criterion for Solar-Electric Plants (\$/kWhe)

The unit plant (or collector) cost in \$/kWe derived in the last section cannot stand alone as the sole criterion for comparing different types of collectors. The "\$/kWe" figure has been derived based on "instantaneous" collector efficiencies measured at noon time with a fixed value of solar insolation and assuming a quasi-steady-state operation (1 kWt/m^2 for tracking collectors or 0.8 kWt/m^2 for nontracking types). In practice, solar collectors do not actually operate at their steady-state conditions since they are subject to many site-specific time varying variables such as solar flux, ambient temperatures and wind speed.

A collector response time, defined as the time taken to reach 99% of its steady-state temperature under a step change of the solar flux, is known to vary from a few minutes to about one hour according to the collector thermal capacitance. It appears, therefore, that a criterion based on a performance measure integrated (or accumulated) over a day, a month, or a year period would be more suitable in comparing different solar-electric power plants

ORIGINAL PAGE IS OF POOR QUALITY

encompassing these transient conditions. The unit energy cost ($/kWhe) produced by a solar-electric plant with performance integrated over one year could act as a second selection criterion to represent the effects of the dynamic and site-specific performance. The derivation of this criterion can be simplified as follows:

Let the annual electrical energy generated from a solar-electric power plant (W^*) in kWhe be given by

$$W^* = I^* \times A_c \times E_c^* \times E_e^* \times E_s^* \times E_T^* \qquad (12a)$$

or

$$W^* = I \times A_c \times E_0^* \qquad (12b)$$

where

I^* = accumulated annual solar flux, kWht/year

A_c = collectors area, m^2

E_c^* = accumulated annual collection efficiency

E_e^* = annual engine efficiency

E_s^* = annual storage subsystem efficiency

E_T^* = annual energy transport subsystem efficiency

E_0^* = annual overall solar-electric efficiency

The annual cost (C) in dollars could be calculated using the cost recovery factor (CRF) of the borrowed money in a lifetime mortgage plan as

$$\text{annual cost } (C) = \begin{bmatrix}\text{collector subsystem cost} \\ + \text{storage subsystem cost} \\ + \text{energy conservation subsystem cost} \\ + \text{energy transport subsystem cost}\end{bmatrix} \times \left[\text{cost recovery factor } (CRF)\right] + \text{annual maintenance and operation cost} \qquad (13)$$

In most applications, the energy storage, transport, and conversion subsystems cost will be assumed to be a fixed fraction of the collector subsystem cost. Also, the annual maintenance and operation cost will be assumed in proportion to the total installation cost. Consequently, Eq. (13) could be rewritten as

$$C \simeq A_c \times C_c \times R \qquad (14)$$

where C_c is the collector cost per unit area ($/m^2), and R is the ratio of the total annual cost to the total collector cost. For example, if the collectors lifetime is taken as 20 years and the interest rate on the borrowed money is 8%, the (CRF) will be 0.10185 $/yr With approximately a 4:1 ratio between total installation to collector cost, the ratio R is found to be around 0.4.

The cost per unit electrical energy output then follows by combining Eqs. (12b) and (14) as

$$\text{cost/kWhe} = \frac{C}{W^*} = \frac{C_c \cdot R}{I^* \cdot E_0^*} \qquad (15)$$

For example, if a paraboloid solar collector is built with 450 $/$m^2$, a ratio of R of 0.4, an annual overall solar-electric conversion of 0.18, and an accumulated annual insolation of 3126 kWht/m^2 (a daily average direct normal flux of 8.7576 kWht/m^2 such as that measured at Goldstone area, California) the cost per kWhe produced would be approximately 0.31 dollars.

The cost/kWhe criterion expressed mathematically in Eq. (15) indicates that in order to generate low cost electrical energy, the parameters, C_c, R, I^* and E_0^* should be in harmony with each other and not separately optimized. For instance, if a flat plate collector, having a unit cost of 60 $/$m^2$, an annual conversion efficiency of 0.03 and an annual solar flux of 2604 kWht/m^2, is compared with the above paraboloid dish example with the same ratio of R of 0.4, the cost of energy produced would be 0.307 dollars/kWhe which is approximately the same for both types. The first collector (paraboloid dish) has a high unit cost (C_c), receives high solar flux as a result of tracking, and has a high conversion efficiency because of its high operation temperature. The second collector is completely opposite to the first, but both produce energy with the same cost. The final selection in this case should be guided by other factors such as durability, maintainability, land areas, visibility etc.

The second criterion shows clearly the important need of accurate site-specific transient analyses to predict the annual conversion efficiency (E_0^*) of different solar-electric systems to support the first criterion which is not site-specific.

VI. Solar-Cooling Application

To use the solar energy as a driving force for cooling devices, several well-known concepts can be coupled with a heat source. Shown in Fig. 3 are the coefficient of performance trends versus the collection fluid temperature leaving the collector subsystem for some of the above concepts. Superimposed on Fig. 3 is the general behavior of the collector efficiency. The overall coefficient of performance (*OCOP*) is defined as the ratio between the refrigeration effect (Q_3) and the incident solar flux (Q_1) as illustrated in Fig. 3. Thus

$$OCOP = \frac{Q_3}{Q_1} = \frac{Q_3}{Q_2} \times \frac{Q_2}{Q_1} \tag{16}$$

or

$$\left[OCOP\right] = \begin{bmatrix}\text{collector}\\ \text{subsystem}\\ \text{efficiency}\end{bmatrix} \times \begin{bmatrix}\text{cooling}\\ \text{subsystem}\\ COP\end{bmatrix} \tag{17}$$

The overall system performance possesses always a maximum value at an optimum temperature in between the ambient temperature (*A*) (where the coefficient of performance of the cooling subsystem is zero) and the equilibrium collector temperature (*B*) (where the collector thermal losses are equal to the incident solar flux). The point of maximum *OCOP* should be the selected design point, and is usually determined by curve plotting instead of analytical expressions.

Similar to the discussion presented in Section IV, the unit power cost (\$/kWe) for solar-electric application will be replaced here by the unit power cost (\$/Tons of refrigeration[1]) for solar-cooling devices. The overall solar-electric conversion efficiency (E_0, max) will also be replaced by the overall-solar-cooling effect coefficient of performance $(OCOP)_{max}$. All other parameters bear the same meaning.

The first criterion, presented in Equations (11a, b) for solar-electric conversion, could be rewritten then for solar-driven refrigeration devices as follows:

For tracking solar collectors (intensity = 1 kWt/m^2):

$$\begin{bmatrix}\text{total plant}\\ \text{(collector)}\\ \text{cost \$/Ton}\end{bmatrix} = 3.516 \times \frac{\text{unit plant (or collector) cost \$/m}^2}{\left[\begin{matrix}\text{overall coefficient of performance}\\ (OCOP)_{max}\text{ from}\\ \text{solar-refrigeration effect}\end{matrix}\right]} \tag{18a}$$

For nontracking solar collectors (at intensity of 0.8 kWt/m^2)

$$\begin{bmatrix}\text{total plant}\\ \text{(collector)}\\ \text{cost \$/Ton}\end{bmatrix} = 4.4 \times \frac{\text{unit plant (or collector) cost \$/m}^2}{\left[\begin{matrix}\text{overall coefficient of performance}\\ (OCOP)_{max}\text{ from}\\ \text{solar-refrigeration effect}\end{matrix}\right]} \tag{18b}$$

Also, for the second criterion, the cost per unit "cooling" energy or \$/(Ton·h) could be derived by the same procedure used for solar-electric plants. Analogous to Eq. 15, the (\$/Ton·h) could be written as:

$$\text{cost (Ton·h)} = \frac{3.516 \cdot C_c \cdot R}{I^* \cdot (OCOP)^*} \tag{19}$$

where $(OCOP)^*$ is the accumulated annual overall coefficient of performance (from solar flux-to-refrigeration effect). All the other parameters bear the same meaning as before. Again, the transient response to the fluctuating solar flux, ambient conditions and wind speed, etc., are very necessary in order to estimate the annual performance before comparing different refrigeration schemes.

VII. Solar-Heating Application

For this particular application, the first criterion does not apply and only the second one does. The estimated unit cost of thermal energy collected (\$/kWht) is the key number needed for comparison with other conventional heating devices such as fuel-fired boilers, electric heaters, or heat pumps. Analogous to Eq. (15), the (\$/kWht) is written for solar heating as

$$\text{unit energy cost \$/kwht} = \frac{C_c \cdot R}{I^* \cdot E_H^*} \tag{20}$$

where E_H^* is the combined annual efficiency of the collectors and storage subsystems. All other parameters bear the same

[1]One ton of refrigeration = 12000 Btu/h = 3.516 kWt cooling energy.

ORIGINAL PAGE IS
OF POOR QUALITY

meaning as used before. Only in solar heating applications, the value of the operating fluid temperature has to be specified in advance before calculating E_H^*. For example, if the solar heating application is for space heating then the E_H^* would be estimated with the candidate collectors producing a uniform temperature of 49°C (120°F), which is enough for this application. For domestic hot water use, a temperature ranging from 60 to 82°C (140 to 180°F) is adequate, and shall be used for estimating E_H^*. This means that the evaluation of E_H^* is assumed to be done at a single value of collector temperature, for all competing collectors, irrespective of the possible ranges of higher temperature beyond this value that each collector can reach. Therefore, each collector will be judged on how much annual energy was collected from the sun and transferred to the end point at a prespecified heating temperature. Once more, for heating application, the collectors transient behavior and their sensitivity to time-varying input data, is of great value to any comparison process.

VIII. Summary

The following points summarize the present study:

(1) To make a good engineering or management decision as to which collector or solar-conversion device should be used in a given solar application, two analogous selection criteria are presented. The first criterion gives the unit cost per unit power produced, based on instantaneous solar radiation or noon-time flux. The ($/kWe) for solar-electric application and the ($/Ton) for solar-refrigeration devices, are two examples of the first criterion. The second criterion gives the unit cost per unit energy accumulated (or integrated) over a year period and taking into consideration the fluctuating nature of the solar flux, ambient temperature, wind speed and the thermal capacitance of the collector itself. The ($/kWhe) for solar-electric conversion, the ($/Ton·h) for solar-refrigeration conversion and the ($/kWht) for solar-heating are examples of the second criterion.

(2) The first criterion was tested for solar-thermal-electric conversion and for 13 types of available collectors (Table 1). The ($/kWe) figure was found lowest among tracking and focusing collectors and highest among flat-plate, nonfocusing, nontracking collectors. However, the need for transient performance data for the second criterion ($/kWhe) is found very essential before a final selection process can be made.

References

1. Simon, F., *Solar Collector Performance Evaluation with the NASA-Lewis Solar-Simulator–Results for an All-Glass-Evacuated Tubular Selectively-Coated Collector with a Diffuse Reflector*, NASA TMX-71695. NASA Lewis Research Center, Cleveland, Ohio. April 1, 1975.

2. Ari Rabl, *Optical and Thermal Properties of Compound Parabolic Concentrators*, Argonne National Lab, Argonne, Illinois, February 1975.

3. *Performance Study of the Compound Parabolic Concentrator Solar Collector*, report prepared by Environmental Consulting Services Inc., Boulder, Colorado, for the Argonne National Laboratory, September 1974.

4. *Corning Tubular Evacuated Collector*, Corning Glass Works, Lighting Products Division, Corning, New York., January 1975.

5. Simon, F., *Flat-Plate Solar-Collector Performance Evaluation with a Solar Simulator as a Basis for Collector Selection and Performance Prediction*, NASA TMX-71793, NASA Lewis Research Center, Cleveland, Ohio.

6. Kleinkauf, W., Kohne, R., Lindner, F. and Simon, M., "A Solar Power Plant in the 10 KWe Range with Focusing Collectors", International Aerospace Abstracts by Technical Information Service of AIAA, paper No. A76-45995, American Institute of Astronautics and Aeronautics, New York, New York, March 1976.

7. Ramsey, J.W., Sparrow, E.M., and Eckert, E.R.G., "Solar Thermal Electric Power Generation Using a System of Distributed Parabolic Trough Collectors", in International Aerospace Abstracts issued by Technical Information Service AIAA, paper No. A75-47511, American Institute of Astronautics and Aeronautics, New York, New York, August 1975.

8. *Solar Energy Program Semiannual Review Report*, Sandia Laboratories, Albuquerque, New Mexico, July 1976.

9. *Northrup Collector*, Northrup Incorporated, 302 Nichols Drive, Hutchins, Texas, 1975.

10. Shimada, K., Swerdling, M., *Terrestrial Solar Thermonic Energy Conversion Systems Concept*, JPL Technical Memorandum 33-744, Jet Propulsion Laboratory, Pasadena, California, November 1975.

11. Lansing, F., and Dorman, J., "High Efficiency Solar Concentrator," *Deep Space Network Progress Report 42-35*, Jet Propulsion Laboratory, Pasadena, California, October 1976, pp. 99–109.

12. Anderson, D. E., and Stickley, R. A., "A Line Focus Segmented Mirror Concentrator", SPIE Vol. 85 *Optics in Solar Energy Utilization II*, 1976 pp. 121–127.

13. Athey, R. E., "Evaluation of the Flat Plate Solar Collector System for Electric Power Generation", *Solar Energy*, Vol. 18, 1976, pp 143–147.

14. Barber, R. E., "Solar Powered Organic Rankine Cycle Engines – Characteristics and Cost", 11th Intersociety Energy Conversion Engineering Conference, IECEC, Vol. 2, 1976, pp. 1151–1156, Society of Automotive Engineers, New York.

Table 1. Typical results for some current collectors[a]

No.	Collector	Tracking	$E_{0,max}$, %[a]	Collector, $/m^2	C...ctor,	Optimum temperature, °C(°F)
1.	Owens-Illinois (Refs. 1 and 5)	No	3.50	200	71...	135 (275)
2.	Winston (compound parabolic) (Refs. 2 and 3)	No	3.93	140	4450	133 (271)
3.	Croning (tubular evaculated) (Ref. 4)	No	9.96	140	1763	191 (376)
4.	Parabolic trough (Refs. 6, 7, and 8)	Yes	11.9-12.7	175	1380-1470	316-430 (600-805)
5.	Northrup collector (Fresnel lens) (Ref. 9) (Corning tube tested)	Yes	13.3	135-240	1020-1810	433 (812)
6.	Northrup collector (black paint) (Ref. 9)	Yes	5.8	135	2340	123 (253)
7.	Parabolic dish (or power tower) Ref. 10)	Yes	18-28	250-450	800-2500	1400 (2560)
8.	NASA-Honeywell, black nickel (Ref. 5) 2 Ar-double glazing (flat plate)	No	5.21	170	4125	108 (227)
9.	NASA-Honeywell, black nickel (Ref. 5) Double glazing (flat plate)	No	4.4	100	2812	111 (231)
10.	Double glazing (general collector) Flat plate, nonselective	No	3.12	100	4000	92 (197)
11.	Liquid lens concentrator (Ref. 11)	Yes	12.2	150	1220	358 (676)
12.	Sheldal (slats) fixed receiver, tracking reflector (Ref. 12)	Yes	13.7	180	1310	428 (803)
13.	General Atomics fixed mirror receiver	Yes	11.9	160	1340	431 (808)

[a] At 25°C ambient temperature.

Table 2. Comparison between three hypothetical collectors

Parameter	Collector (type 1) flatplate	Collector (type 2) parabolic trough	Collector (type 3) paraboliod dish
$E_{0,max}$, %	3	8	16
Collector cost $/$m^2$	60	200	400
Reference intensity, kwt/m^2	0.8	1.0	1.0
Power collected cost $/kWe	2500	2500	2500
Surface area m^2/kWe	41.6	12.5	6.2

ORIGINAL PAGE IS
OF POOR QUALITY

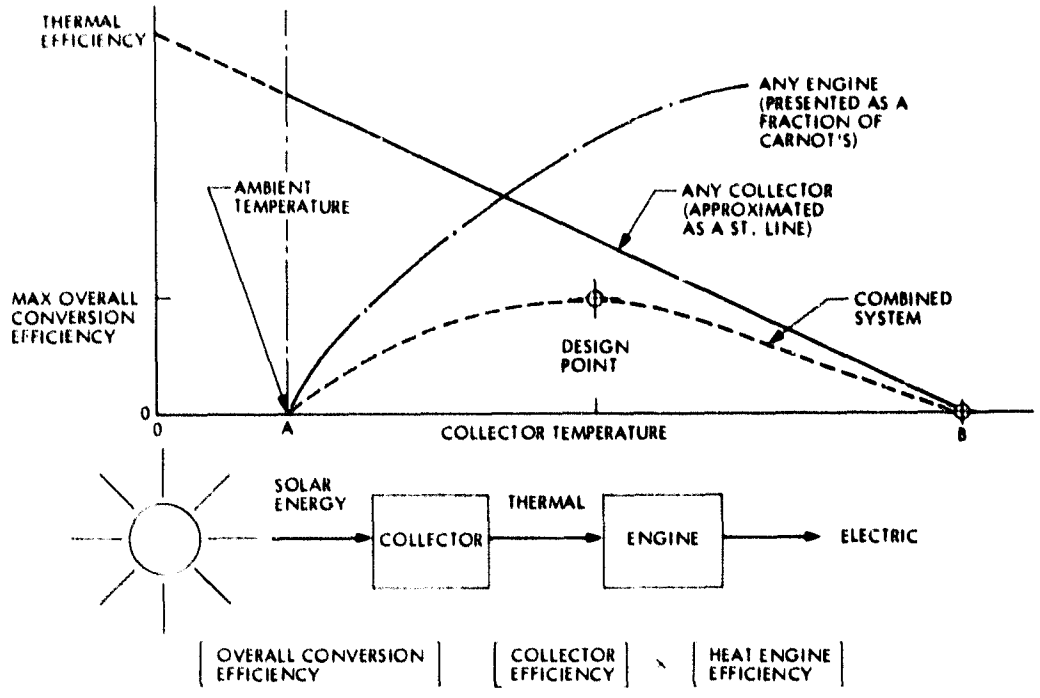

Fig. 1. Optimization of solar thermal-electric conversion

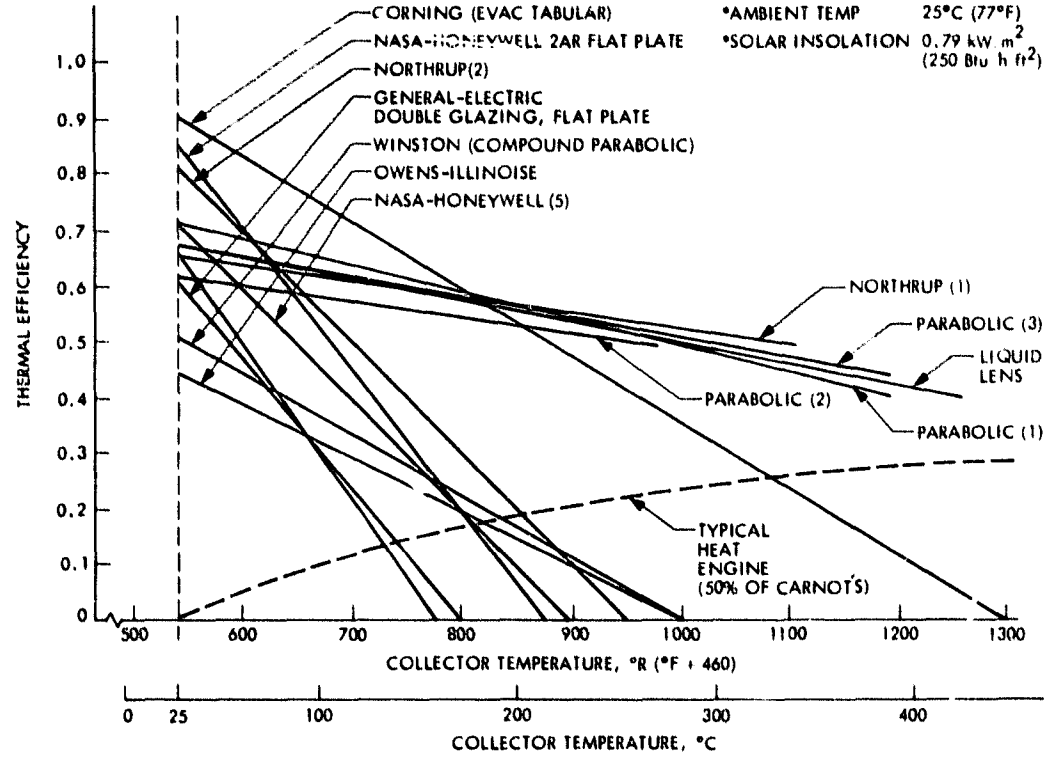

Fig. 2. Performance curves for some current solar collectors

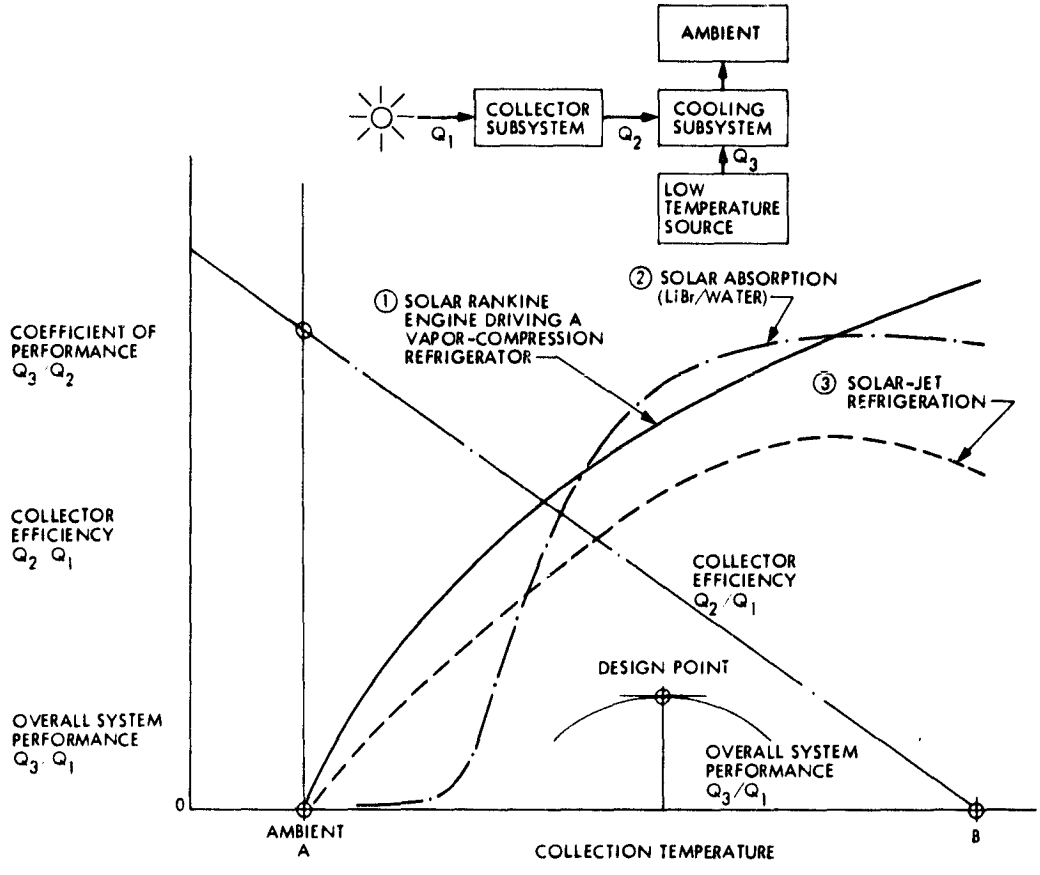

Fig. 3. Optimization of solar-thermal cooling systems

ORIGINAL PAGE IS OF POOR QUALITY

N78-24238

Implementation of Automated Fault Isolation Test Programs for Maximum Likelihood Convolutional Decoder (MCD) Maintenance

M. E. Alberda
DSN Data Systems Section

This article describes the automated fault isolation test programs that have been developed to support rapid turn-around factory (or depot) level maintenance of the Maximum Likelihood Convolutional Decoder (MCD). Functional requirements and detailed design characteristics are described, along with a summary of the evaluation and testing completed so far.

I. Introduction

Test programs, run on a computerized Logic Card tester, have been developed to support rapid turn-around factory (or depot) level maintenance for the MCD, which is currently being installed throughout the DSN as a part of the Telemetry Subsystem. The MCD requirements and design characteristics are described in a previous DSN Report (Ref. 1).

These programs were entirely developed based on the use of existing design test equipment and support software in order to realize maximum economy with minimum development time, and at the same time achieve excellent overall fault isolation capability and extensive computer generated documentation.

One program for each of the two MCD plug-in circuit cards has been developed. In size and complexity, the MCD Interface Board contains 59 Integrated Circuits (IC's) while the Decoder Board contains 92 IC's.

These programs were developed specifically to support a guaranteed maximum repair time of 30 calendar days, at the repair facility, regardless of the nature or extent of the failure (excepting, of course, unforeseen catastrophic cases where a whole circuit board would have to be replaced). Also, a condition was added that if the expected repair effort, to be accomplished on a "time-and-material" cost basis, exceeded a predetermined threshold level, then the 30 day maximum period was to begin after receiving formal authorization to proceed with the repair effort from JPL.

In acceptance testing, the Interface Board program correctly identified 92% of the random customer selected faults manually inserted, while the Decoder Board program correctly identified 98% of the faults inserted (50 faults per board).

II. Specific Functional Requirements

The definition of the required performance characteristics for these programs is contained in the JPL Technical Requirements Document (Ref. 2).

The salient functional requirements, and the factors used in their selection, are discussed briefly below.

A. Logic Tester

The Mirco Model 530 Tester was selected as the test unit to be used for the following reasons:

(1) Readily available (a standard catalog item).

(2) Reasonable cost.

(3) Rapid processing speed (200 KHz. Instruction rate).

(4) Ease of Maintenance and Operation.

(5) Availability of powerful support software, i.e., the FLASH (Fault Location And Simulation Hybrid) Simulator (Ref. 6), which offers greatly reduced programming time, improved testing comprehensiveness, and also provides computer generated program documentation.

B. Fault Isolation Capability

Each test program was required to be capable of identifying a circuit fault to within one IC (as a design goal) but in any event to within a group of not more than ten IC's, as an upper limit design goal.

The TRD also specified that, of the total number of faults simulated by FLASH (which includes shorts, opens, grounds, etc. for all circuit nodes on the board) at least 85% shall be correctly identified by each program.

Furthermore, all undetected (or incorrectly identified) faults were required to be isolatable using the available manual procedures called "Scope Trace" and/or "Time-Nodal-Test" transition counting.

C. Program Acceptance Test Procedure (PATP)

A specific PATP was required for each program. These procedures each contained a requirement that fifty (50) random customer selected faults (grounds) be inserted on each known good board, one fault at a time, and the test programs should correctly identify at least 85% of these known faults.

III. Design Approach

The basic approach used for this development effort was selected based on an awareness of commonly used digital test techniques and test equipment, including various types of test stimuli generation (psuedo-random, manually generated, etc.).

The utilization of FLASH was selected because of its ability to methodically and rapidly simulate all possible faults, of all types, by use of its software modeling capability. This was considered to be far more complete, and economical, than other approaches involving more conventional manual techniques, of test stimuli generation and hardware testing (destructive and non-destructive).

Additionally, FLASH offered the advantages of reduced development time and effort, since it was fully developed and checked out, and had been successfully used on several previous test program developments of a similar type. FLASH offered the most complete and effective approach known, it was felt, because in addition to the primary automated mode of operation, it provided the data necessary for the two manual back-up modes called SCOPE TRACE and Time-Nodal-Test (TNT) Counts. By use of these back-up modes, fully non-ambiguous fault isolation can be achieved, involving minimal time, effort and operator skill.

IV. Design Description

A brief description of the Tester hardware and of the test software development, documentation and utilization is presented below. Detailed descriptions covering these subjects are provided in Refs. 3 through 10. The Tester and the test software are designed to evaluate circuit boards which contain all digital (i.e. 2-level) circuit devices.

A. Tester Description

The Tester used is the Mirco Model 530. This unit is portable, totally self-contained, includes all operator controls and displays on its top surface, and the boards to be tested mount directly to it via customized Interface Adaptor connection units, one for each of the two board types to be tested and one to be used with the Tester itself in its Self-Test mode.

The physical characteristics for this unit are listed below.

(1) Input Power – 270 Watts (115 V.A.C., 60 Hz)

(2) Size – 22.86 cm high
58.42 cm wide
40.64 cm deep

(3) Weight – 24.9 kilograms

(4) Operating Environment – 10°C (50°F) to 49°C (120°F), with 10 – 90% relative humidity.

(5) Operator Panel – See Figure 1 (for more detail, see Ref. 8).

The Tester contains a microprogrammed test processor to execute the stored test program and to monitor and evaluate the test results. The processor instructions are implemented

using a combination of hardware and microcode, which provides for fast execution speed and the desired degree of flexibility.

The following basic modules are contained within the Tester:

(1) Memory – Random access, 8K bytes (8 bits/byte)

(2) Central Processor – Microprogrammed control.

(3) Driver/Sensor Modules (3) – Each contain 32 lines which can be used as inputs to/or outputs from the board under test, under program control. Connections to the board are made via the board connector and also via eight (8) chip-clips which attach directly to specified IC's on the board.

(4) Paper Tape Reader (Optical and Interface) – Used for program loading to the tester. Speed – 130 bytes/second.

(5) Interface Adaptors (3) – Cable interconnection panels containing all unique wiring and cabling, including chip-clip connector cables which attach directly to specified IC's on the boards, one for each board and one for Tester Self-Test.

(6) TNT (Transition Node Time) Probe and Processor – A probe which can be used to count the level changes that occur, at any circuit node, while the test program is run, and the result is displayed on the Tester. The result, or TNT signature, is a function of total changes in each direction.

B. Test Program Development

The test programs were developed based on full use of the capabilities provided by the FLASH support software, which was contractor developed and owned. These programs include NETGEN, MBUILD, FLASH, MSCOPE, DICT, MRPOST, and MCODE, each providing a specific function in the program development cycle. All support software is resident on a General Automation SPC-16 host computer (see Figure 2).

Initially, the programmer analyzed the logic design of the circuit board to be tested to become aware of all of its functional operating characteristics. He then developed a set of input stimuli patterns which are the series of tests that are incorporated into the final test program. For each test, a set of stimuli were provided as inputs to the board and the corresponding board outputs were monitored, all under program control. The input test patterns were extensive enough to drive all circuit nodes high and low one or more times during the test program.

The programmer provided information about each board that was used to develop a computerized model of the board. Inputs included an input/output pin assignment list, a device (IC) assignment list (IC's listed by standard type number) and an IC interconnection list. FLASH included a sub-routine library containing a subroutine model for each different IC type used. From these lists, NETGEN was used to create a logic image file of the board, and this file was in turn used by MBUILD to create a computer IMAGE of the board.

The programmer generated input stimuli patterns and the board IMAGE were used as inputs to FLASH, which also contains a simulator (or model) of the actual Model 530 Tester, and simulation runs were made using these three components. A sub-program within FLASH, called AUTO FAULT, automatically inserted all possible faults (opens, shorts, grounds, and incorrect timing delays to simulate faulty one-shots, etc.) into the board IMAGE, one at a time, and the test sequence was run until the fault was detected and an identifying entry, or fault signature, was stored. Faults not detected were stored in a No-Find list. In response to the stimuli contained within each test, another sub-program called SCOPE FILE monitors and records the state of all the circuit output nodes in the board image, at the end of each test in the test program. These data were used by MSCOPE to generate the SCOPE TRACE section of the documentation.

The DICT program sorted, tabulated and outputted all of the fault signature data (mentioned above) to generate the Fault Dictionary section of the documentation. Entries in this Dictionary are tabulated by test number and light numbers, which correspond to numbered lights on the Tester. When a fault is detected by the Tester, it shows the test number and one (or more) light numbers, and the corresponding entry in the Dictionary shows the one (or more) probably defective IC's on the board.

The MRPOST and MCODE programs were used to generate the test program object code tape, which is loadable directly into the Tester.

The test programs were evaluated using known good boards, operating with the Tester, to verify that the simulation software developed and used is accurate and correctly models the actual hardware.

The documentation package for each program contains the following:

(1) Fault Dictionary

(2) Scope Trace

(3) No-Find List

(4) Source and Object Programs Listings

(5) Interface Adaptor Wire List

(6) TNT Counts – for all circuit nodes.

(7) Statistics Summary Sheet (See Figures 3 and 4)

The Statistics sheet shows the comprehensiveness, or percentage of total faults found, and also the fault isolation achieved, or percentage of isolation to one, vs. two or more, IC's. As indicated, 93% comprehensiveness was achieved for the MCD Interface board and 94.9% for the Decoder board. Thus most faults (93 – 95%) will be detected on the first run of the test program. Run time is less than 0.2 second for each program. For resolving undetected faults, or for improving fault isolation (if needed), two approaches are available. One is to evaluate each fault in the No-Find list, and by searching the Scope-Trace table, find a test where the subject circuit node should have changed state, then monitor this node with a separate oscilloscope and probe to determine whether or not the node is changing as shown by the Scope Trace. The other approach is to use the TNT probe, with the Tester, to count transitions at various suspect circuit nodes, based on general knowledge of the board operation and on the known symptoms of the malfunctions. Correct counts have been tabulated for all circuit nodes for each board. Many nodes can be checked in a short time because total run time is so short. Each repaired MCD will be re-tested using the MCD Acceptance Test Procedure (Ref. 1) to verify operational readiness.

V. Testing and Evaluation

The testing done so far consists of the Program Acceptance Tests which were completed at the end of the development cycle. As indicated above, fifty random faults (grounds) per board were selected by the customer and inserted, one at a time, on each board and the appropriate test program was run on the Tester, after the board had been mounted to the Tester via its Interface Adaptor.

(1) Interface Board
46 of 50 faults were detected and correctly identified, giving an accuracy of 92%. Of the 4 remaining faults, 3 were detected as test failures by the program, but the program did not identify the actual location of the faults by IC number and pin number. The program failed to detect the other fault and showed a PASS condition.

(2) Decoder Board
49 of 50 faults were detected and correctly identified, giving an accuracy of 98%. The one remaining fault was detected by the program, but not correctly identified to the actual location.

The back-up fault detection and isolation procedures using Scope Trace and TNT counting were not evaluated at the time of the Acceptance tests, but will be exercised and evaluated in the near future. These procedures will be used to verify the fault location, as indicated by the Fault Dictionary, following a normal run of the test program. In this way faults will be positively identified before any IC's are replaced.

Through Dec. 1977, there have been two MCD units repaired at the factory, using these programs, and their use was entirely satisfactory. Additional performance data will be accumulated as these programs continue to be used for MCD repairs, in supporting the 33 MCD units which have been delivered to the DSN, since the last delivery from the factory in April 1976.

VI. Conclusion

The entire development of these programs proceeded as initially planned, on schedule and within budget, and the final performance quality exceeded the fixed, and the design goal, requirements specified in the TRD.

References

1. Alberda, M. E., "Implementation of a Maximum Likelihood Convolutional Decoder in the DSN", in The Deep Space Network Progress Report 42-37, pp. 176-183, Jet Propulsion Laboratory, Pasadena, Calif., Feb. 15, 1977.

2. Alberda, M. E., Technical Requirements Document for MCD Maintenance Test Programs, JPL TRD 338-339, Rev. A, Sept. 1976 (JPL Internal Document).

3. MCD Test Software Operations Manual, Linkabit Corp., March 1977, JPL Tech. Manual No. TM14005 (JPL Internal Document).

4. MCD Decoder Board (UUT 6803) Test Document, Mirco, Feb. 1977, JPL Tech. Manual No. TM14006 (JPL Internal Document).

5. MCD Interface Board (UUT 3023) Test Document, Mirco, Jan. 1977, JPL Tech. Manual No. TM14007 (JPL Internal Document).

6. Programming Manual, FLASH Test Generation Software, SPC-16, Release 1.0, Mirco, Jan. 1975, JPL Tech. Manual No. TM14008 (JPL Internal Document).

7. Mirco 500 Series Logic Circuit Tester, Programmer's Manual, No. 500-P-506, Jan. 1975, JPL Tech. Manual No. TM14009 (JPL Internal Document).

8. Mirco 500 Series Logic Circuit Tester, Operator's Manual, Mirco No. 500-0-511, Jan. 1975, JPL Tech. Manual No. TM14011 (JPL Internal Document).

9. Mirco 500 Tester Schematics and PWB Drawings, Mirco Manual No. 500-DWG-511, Jan. 1975, JPL Tech. Manual No. TM14010 (JPL Internal Document).

10. Mirco 500 Series Logic Tester, Maintenance Manual, Mirco No. 500-MD-512, Jan. 1975, JPL Tech. Manual No. TM14012 (JPL Internal Document).

ORIGINAL PAGE IS
OF POOR QUALITY

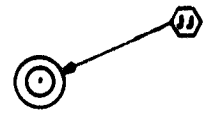

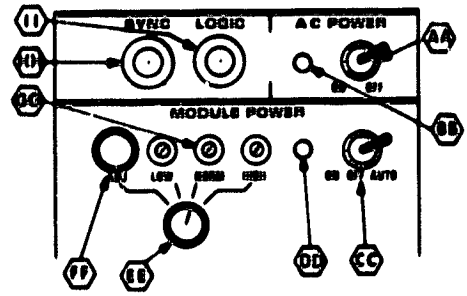

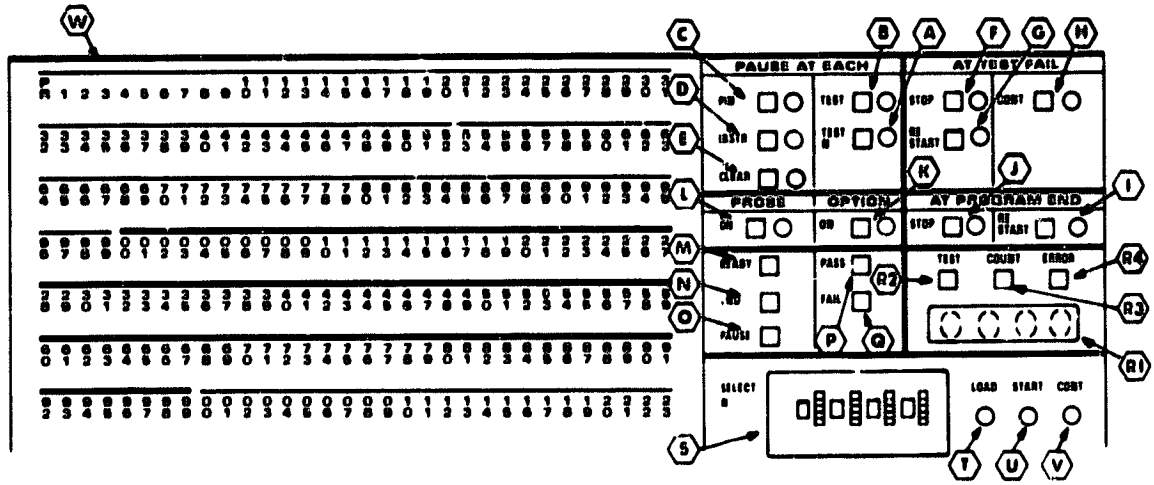

Fig. 1. Operator control test panel diagram

ORIGINAL PAGE IS
OF POOR QUALITY

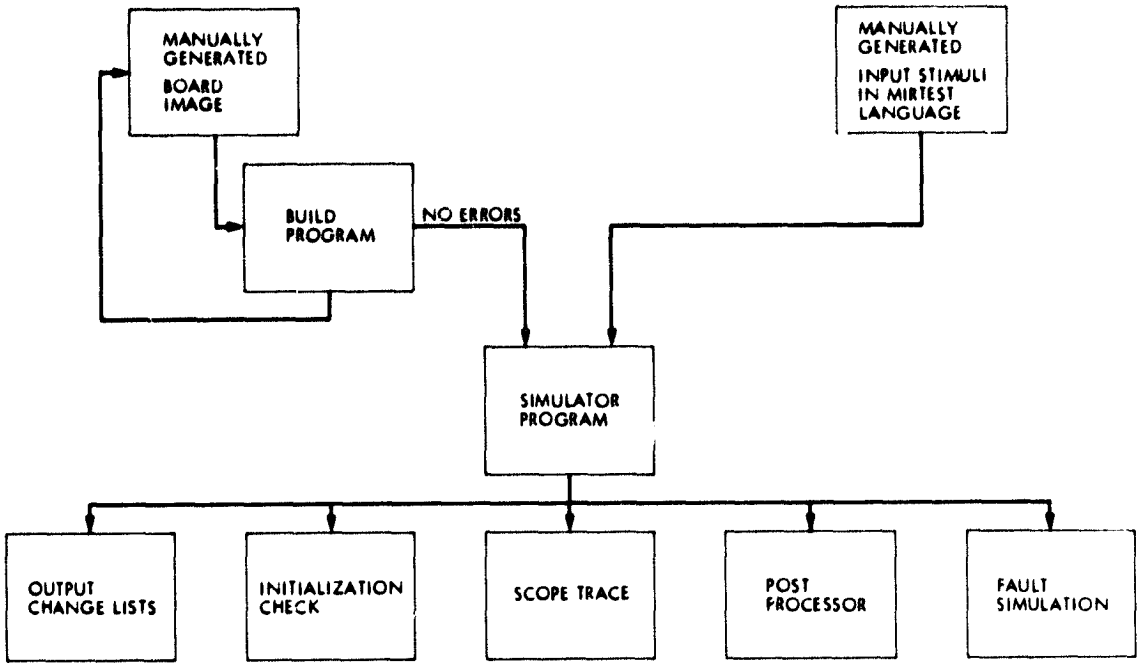

Fig. 2. Use of flash test generation software

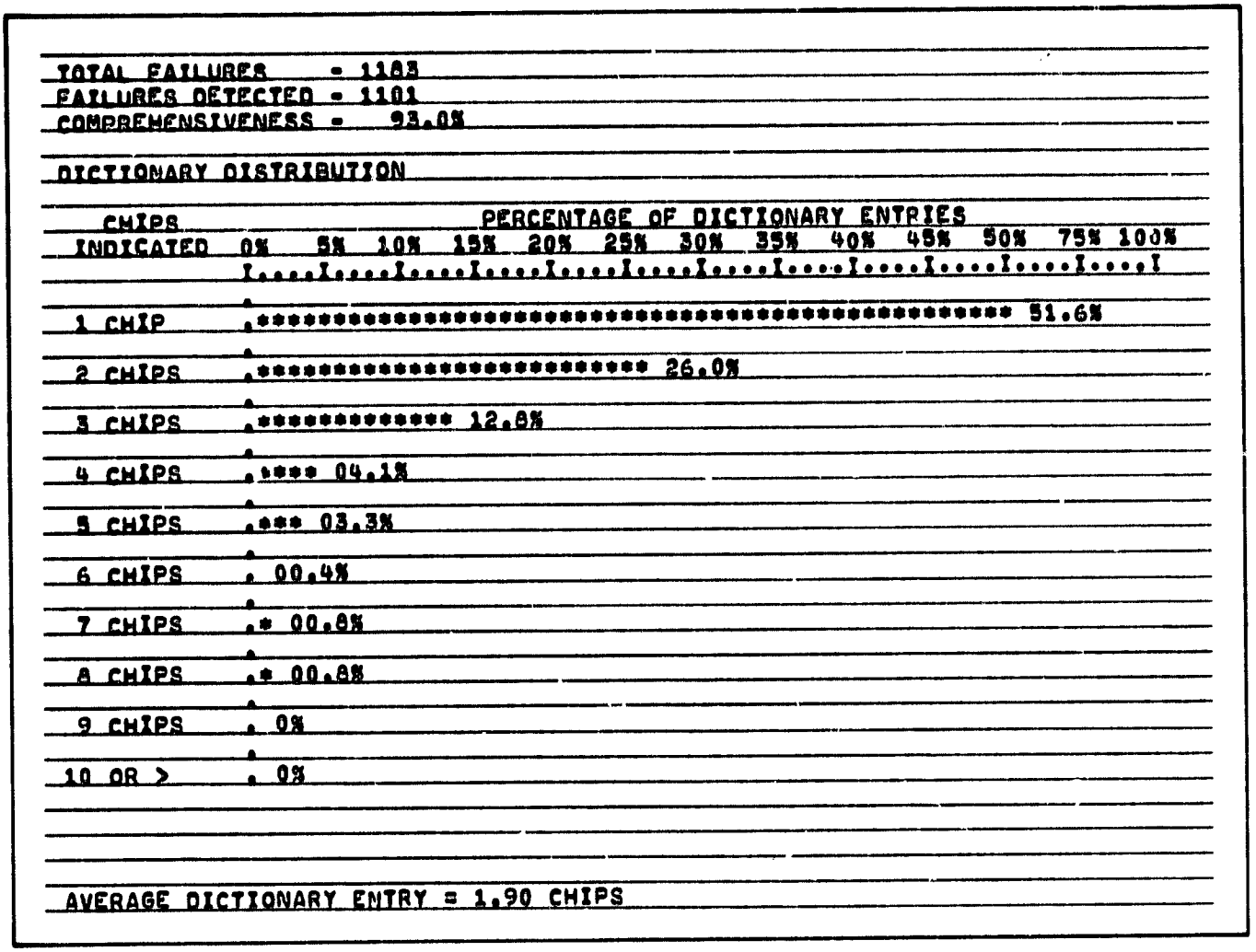

Fig. 3. MCD interface board program, statistic sheet UUT No. 3023

ORIGINAL PAGE IS
OF POOR QUALITY

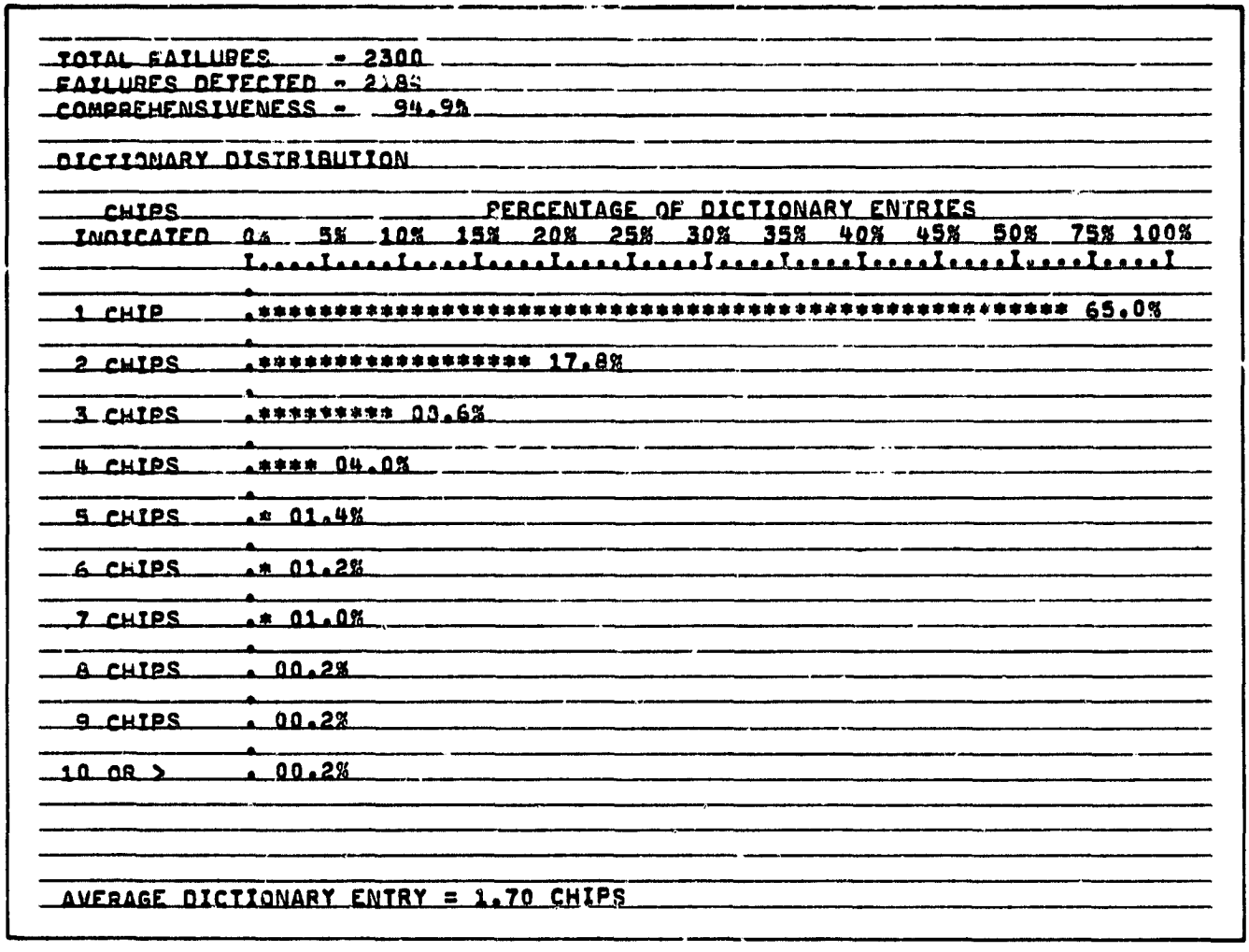

Fig. 4. MCD decoder board program, statistic sheet UUT No. 6803

N78-24239

Performance of Solar-Powered Vapor-Jet Refrigeration Systems with Selected Working Fluids

V. W. Chai and F. L. Lansing
DSN Engineering Section

The performance of the solar-powered vapor-jet refrigeration scheme is compared with five selected working fluids: R-11, R-12, R-113, Butane and Water These fluids were selected among those able to suit both a power cycle and a refrigeration cycle. The results indicated that water has the highest coefficient of performance and differs by a wide margin compared to the other compound organic fluids at all boiler and evaporator temperatures considered.

I. Introduction

One of the objectives of the on-going DSN Energy Conservation Project at the Deep Space Communication Complex (GDSCC), Goldstone, California, is to reduce the purchased energy by using alternate nondepletable sources such as solar energy. Heating, ventilation, and air-conditioning (HVAC) systems consume about 30 percent of the total energy consumption and their coupling with solar energy presents a potential saving. It has been shown earlier (Ref. 1) that the solar-powered vapor-jet refrigeration system (Fig. 1) possesses an overall coefficient of performance comparable with that obtained from solar-absorption systems or solar-powered Rankine turbo-compressor systems. However, little has been done in the literature to explore the potential use of solar-jet refrigeration systems, and it is the intent of this article to help shed some light on the subject. Conceptually, the solar-jet refrigeration scheme as sketched in Fig. 1 is similar to solar-powered Rankine turbo-compressor scheme in which a Rankine-power cycle drives a vapor-compression refrigeration cycle. The former scheme uses a nozzle-diffuser ejector for the expansion-compression processes instead of the combined turbine compressor unit used in the latter scheme.

Another important difference between the two schemes is that the ejector scheme can only operate with a single type fluid while the turbine-compressor scheme can work with dual fluid loops. Consequently, it is very important to carefully select the working fluid which best obtains not only a high power cycle efficiency, but a high coefficient of performance (COP) for the refrigeration cycle also. Other than water as the working fluid (Ref. 1), Anderson (Ref. 2) used butane gas while Kakabaev and Davletov (Ref. 3) used freon refrigerant 12 in their jet refrigeration studies. Neither stated the rationale behind using the chosen chemical as the working fluid.

In the literature, various working fluids for Rankine power cycle alone or refrigeration cycles alone have been studied extensively (Ref. 4, 5, 7). However, the selection of fluids to suit both a power cycle and a refrigeration cycle has not been explored enough, despite the recent interest in solar Rankine turbo-compressor refrigeration systems.

II. Criteria for Working Fluid Selection

There are literally hundreds of organic compounds that can be used as working fluids. Some are only suitable for power cycles which require chemical stability at high boiler temperature while others are only suitable for refrigeration cycles that operate at very low temperature ranges without freezing. Before selecting the candidate fluids that have properties suitable to both a power cycle and a refrigeration cycle to be used in the solar jet refrigeration system analysis, it is worthwhile to consider the selection criteria. The fluid thermal behavior which maximizes the system coefficient of performance (COP) and satisfies these criteria will be selected. The selection criteria are listed as follows:

First, the availability of the fluid and the associated cost. A fluid which may result in a very high performance, but has limited resources or is scarcely found would mean a high cost for the system.

Second, candidate fluids should have a relatively high critical temperature and pressure which raises the high limit for the boiler temperature. A boiler temperature of 93.3°C (200°F) for example, means that many fluids having low critical temperatures such as refrigerant-13 (T critical = 29°C) would be operating at supercritical conditions. Supercritical operation requires a careful nozzle/diffuser design. The boiler to evaporator pressure ratio will also affect the nozzle design. For example, for superheated steam, if the back pressure is lower than 54.6 percent of the boiler stagnation pressure, the nozzle must be convergent-divergent with supersonic flow. Without a proper nozzle/diffuser design, under-expansion or over-expansion will occur, which decreases the isentropic efficiency.

Third, thermal and chemical stability under cycling between hot and cold regions is another criterion controlling the highest boiler temperature for longer operation.

Fourth, for safe operation candidate fluids should be compatible with surrounding materials such as copper, iron, rubber seals, etc.

Fifth, fluids should not have excessive boiler pressures or too low condensing pressures. For a particular boiler temperature, the saturation pressure should not be too high, to prevent leakage problems, and eliminate the need for heavy components. Also, condenser or evaporator pressures should not be too low in order to avoid air leakage into the system. The condenser to evaporator pressure ratio should be within allowable limits to assist in an efficient diffuser design.

Sixth, the slope of the vapor saturation curve on the temperature-entropy diagram should be as steep as possible. This slope defines the exit conditions of the expansion and compression processes, and consequently affects the flow rates of the system. For isentropic expansion or compression, with fluid having a negative slope, exit conditions will be wet vapor at the end of the expansion process and superheated vapor at the end of the compression process as shown in Fig. 2a. Conversely, for a positive slope vapor saturation curve as shown in Fig. 2b, the opposite conditions take place. It is therefore preferable to use a fluid having a steep slope for its vapor saturation curve. The slope should not be greatly deviated from the vertical to avoid extreme conditions.

Seventh, include other operational safety criteria such toxicity, flammability, and chemical reactions with air or water. Finally, the candidate fluid should have high heat transfer coefficient within the temperature range of operation. This property reduces the heat transfer area required for the solar collector, condenser and evaporator heat exchangers.

III. Selected Working Fluids

Based on the above criteria mentioned, five fluids are chosen for investigation, and their properties are listed in Table 1. These selected fluids are known to be suitable in other solar-powered air-conditioning schemes. Steam jet refrigeration is a well known technology and it has been widely used in industry for some time before the use of mechanically-driven vapor-compression refrigeration. Water has its well known advantages. However, it is limited to temperatures above its freezing temperature. Also, evaporator operation, with water, at low temperature and pressure has resulted in high specific volumes which required bulky equipment. Refrigerant-12 was used later in the freon ejector solar cooler reported by Kakabaev and Davletov (Ref. 3). With a boiler temperature ranging from 70 to 80°C, a condenser temperature at 38°C and an evaporation temperature of 18°C, the coefficient of performance (COP) ranged from 0.3 to 0.7 depending on the cooling load and the mass flow ratio between the high pressure vapor into the nozzle and the low pressure vapor from the evaporator. Accordingly, R-12 is selected in this work as a prospective candidate to be compared with water.

Biancardi, Mender, Blecher and Hall (Ref. 6) used refrigerant-11 in their turbo-compressor unit. A COP of about 1.0 was achieved with turbine inlet temperature of 115.55°C (240°F). Refrigerant-11 resulted in not only a high COP but also proved itself adequate in both power cycle and refrigeration cycle combination. Therefore, R-11 is selected in this study as another candidate fluid to be added to the above list.

Barber (Ref. 4) used both refrigerant-12 and refrigerant-113 for the dual fluid solar-powered Rankine turbocompressor

cycle. Refrigerant-113 is often considered as a power cycle fluid (Ref. 5) for its high critical temperature. Refrigerant-113 is then added to the list since it has also a high thermal stability at temperatures up to 500°C.

Finally, after Anderson (Ref. 2), butane is considered a candidate fluid for the study. With butane, the performance was shown in Reference 2 to be comparable with that of the Rankine turbocompressor system and the ejector system can operate at lower supply temperatures than that for solar absorption system.

IV. Performance Comparison With the Selected Working Fluids

The five working fluid candidates namely; water, R-11, R-12, R-113 and Butane are tried each in a jet refrigeration cycle under identical evaporator, condenser and boiler temperatures. The objectives were set to determine the trend of the cycle coefficient of performance with (1) various boiler temperatures keeping all other parameters the same and (2) various evaporator temperatures keeping all other parameters the same.

The isentropic efficiency for each of the nozzle and the diffuser is kept unchanged in the study. Since the condenser temperature can vary only with the type of cooling medium whether it is air or water, and ambient conditions, the condenser temperature was considered a fixed parameter not affecting the final fluid choice. On the other hand, the boiler temperature is considered an important parameter since it is controlled by the maximum stable temperature the fluid can handle. The evaporator temperature is also important since it is controlled by the fluid freezing temperature.

The results of the parametrization study are plotted in Figures 3 and 4 using the fluid thermodynamic properties in Reference 8 and the nomogram methodology previously reported in Reference 1. Figure 3 shows the coefficient of performance (COP) versus the evaporator temperature for the five working fluids with all other parameters fixed. Since water cannot operate below 0°C, the evaporator temperature range was taken between 4.44°C (40°F) and 15.56°C (60°F). From Fig. 3, the higher the evaporator temperature, the higher the COP which is an expected result derived from the ideal Carnot's performance.

It is also evident from Fig. 3 that the COP for fluids R-11, R-12, R-113 and Butane lie within a narrow band much lower than that for water. For example, at 10°C (50°F) evaporator temperature, the COP for the organic fluids tested varied from 0.4 to R-11 to 0.47 for R-113 compared to 0.85 for water at the same conditions: a result which makes water a fluid with excellent performance.

In Fig. 4, the COP results were plotted with fixed evaporator temperature versus the boiler temperature. Boiler temperatures were chosen between 80°C (176°F) and 110°C (230°F) to suit most low cost flat-plate collectors. Theoretically for the Carnot refrigeration cycle, the COP increases with increasing the high source temperature (boiling temperature) and the trends in Fig. 4 for water follow the theoretical trend. However, for refrigerant-11 and refrigerant-113, the COP reaches a maximum at about 95°C with COP at about 0.35 for R-113 and 0.32 for R-12. For refrigerant-12 the COP increases with increasing boiler temperature, but its relatively low critical temperature (~110°C) prevents it from operating at higher temperature values.

Also from Fig. 4, steam has the highest COP among the fluids selected, which is contributed mainly by its large latent heat of vaporization. On the other hand, steam required bulky components to handle the large volumes of flow since it has a very large specific volume compared to organic compounds at the same temperature.

V. Summary and Findings

From this study, the following findings can be drawn:

1. The performance of the solar-powered vapor-jet refrigeration scheme was tested with five selected working fluids: R-11, R-12, R-113, Butane and water, using the nomogram methodology constructed earlier in Reference 1.
2. The proper selection of the working fluid is subject to many selection criteria such as (1) fluid availability and low cost, (2) high critical temperature (3) thermal and chemical stability under hot/cold cycling (4) compatibility with other surrounding materials (5) low saturation pressures, (6) steep slope of vapor-saturation curve on temperature-entropy diagram (7) nonflammability, toxicity properties, and (8) high heat transfer coefficient.
3. All five working fluids selected have an increasing trend of COP with the evaporator temperature. The increasing trend could be reasoned by the similar Carnot's behavior. However, the resulting COP had two distinct bands separated by a large margin: water performance in one side and all the other organic compounds in a narrow band. Water was shown superior than the other organic fluids with a (COP) almost double the value obtained from the other fluids.
4. With the boiler temperature as a parameter, refrigerants R-11 and R-113 reached a maximum (COP) value at about 95°C but water and R-12 had a monotonic trend. Again,

the water (COP) was superior compared to other organic compounds. The large latent heat of vaporization that the water possesses in addition to the odd-shaped and small vapor curve slopes that the organic compounds have on the temperature-entropy diagram contributed to the water performance superiority.

Although water, as a fluid, has the disadvantage of large specific volume at low temperatures which tend to increase the component size, besides its low freezing temperature which requires careful handling and design, it is foreseen that water will be selected as the only candidate in future studies of solar-powered vapor-jet refrigeration schemes.

References

1. Lansing, F. L., Chai, V. W., "A Thermodynamic Analysis of a Solar-powered Jet Refrigeration System". DSN Progress Report 42-41, Jet Propulsion Laboratory, Oct. 15, 1977, pp. 209-217.
2. Anderson, H., "Assessment of Solar Powered Vapor Jet Air-conditioning System". Presented at 1975 International Solar Energy Congress and Exposition (ISES) held at UCLA, Los Angeles, California, p 408.
3. Kakabaev, A., Davletov, A., "A Freon Ejector Solar Cooler". Geliotekhnika, vol. 2, No. 5, pp. 42-48, 1966.
4. Barber, R. E., "Solar Air Conditioning System Using Rankine Power Cycles – Design and Test Results of Prototype Three Ton Unit". Institute of Environmental Science, 1975, pp. 170-179.
5. Miller, D. R., "Rankine Cycle Working Fluids for Solar-to-electrical Energy Conversion". Final report for Sandia Laboratory, Albuquerque, New Mexico, January, 1974.
6. Biancardi, F. R., Meader, M. D., Blecher, W. A., and Hall, J. B., "Design and Operation of Solar-powered Turbocompressor Air-conditioning and Heating System" IECEC '75 Record, pp. 186-194.
7. Allen, R. A., Stiel, L. I., "Working Fluids for Solar Rankine Heat Pumps". Solar Energy Heat Pump Systems for Heating and Cooling Buildings. ERDA Doc. coo-2560-1, 1975, pp. 98-105.
8. ASHRAE Handbook of Fundamentals, American Society of Heating, Refrigerating and Air Conditioning Engineers, Inc., New York, New York 1972.

ORIGINAL PAGE IS
OF POOR QUALITY

Table 1. Some properties of the selected fluids

Selected Working Fluids	Critical Temperature (°C)	Critical Pressure (atm)	Molecular Weight (gm/gm-mole)	1 Boiler Pressure (atm)	2 Condenser Pressure (atm)	3 Evaporator Pressure (atm)	Specific Volume at Condenser Temperature (m^3/kg)	Flammable or explosive units in air (% by volume)
Steam	374	218	18.02	.78	.034	.0008	12.80	non-flammable
Refrigerant-11	198	43.2	137.38	6.97	1.10	.48	.098	non-flammable
Refrigerant-12	112	40.6	120.93	29.26	6.73	3.51	.014	non-flammable
Refrigerant-113	214	33.7	187.39	3.72	.47	.18	.208	non-flammable
Butane	152	37.46	58.13	13.25	2.53	1.20	.085	1.6 to 6.5

1 Boiler Temperature 93.3°C(200°F)
2 Condenser Temperature 26.67°C(80°F)
3 Evaporator Temperature 4.44°C(40°F)

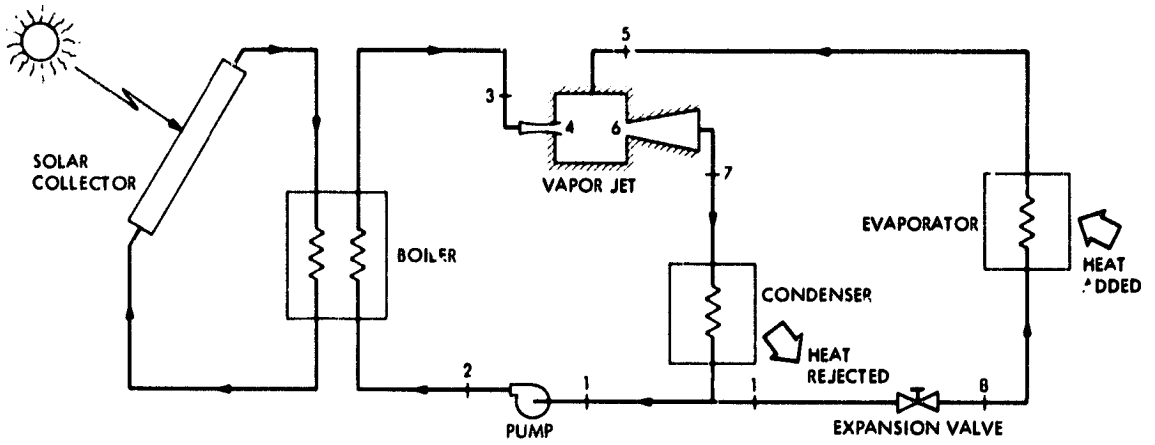

Fig. 1. Vapor jet refrigeration system driven by solar energy

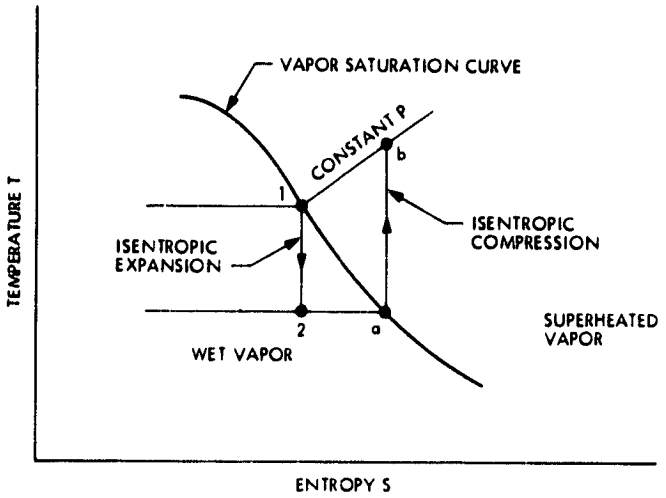

Fig. 2a. Negative slope of a vapor-saturation curve

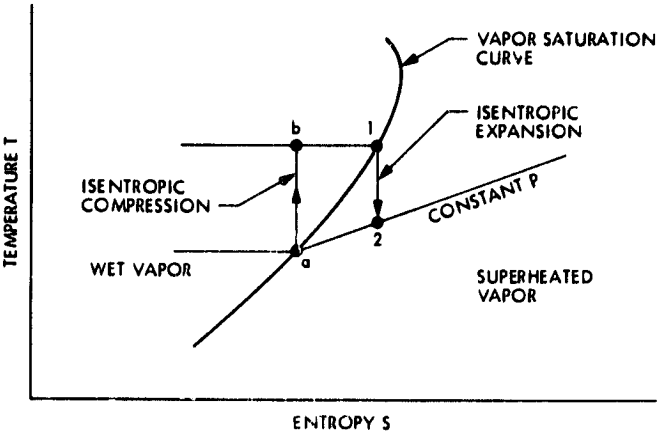

Fig. 2b. Positive slope of a vapor-saturation curve

ORIGINAL PAGE IS
OF POOR QUALITY

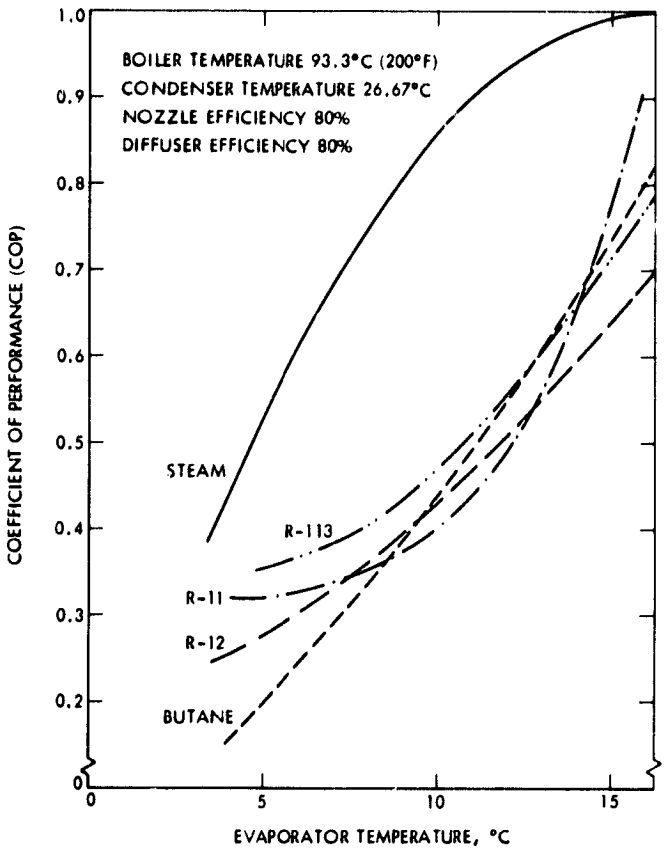

Fig. 3. Effect of the evaporation temperature on the coefficient of performance

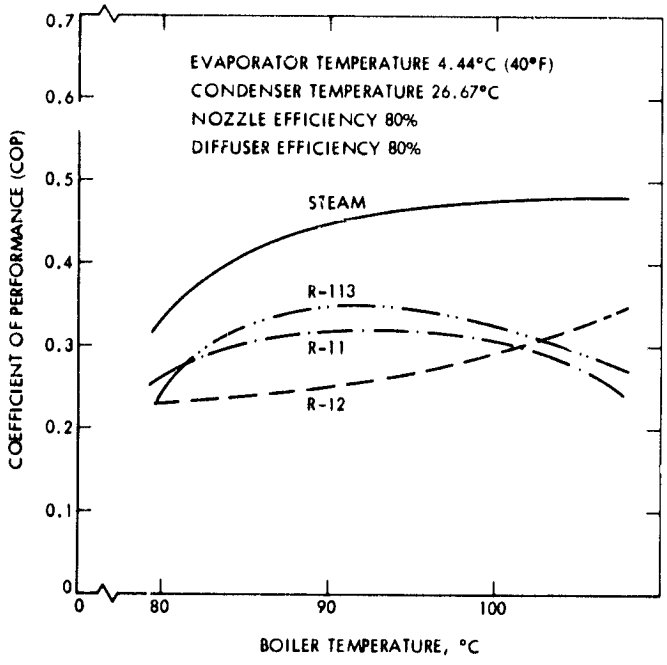

Fig. 4. Effect of the boiler temperature on the coefficient of performance

ORIGINAL PAGE IS
OF POOR QUALITY

N78-24240

Voyager Near Simultaneous Ranging Transfers

G. L. Spradlin
Deep Space Network Operations Section

During testing of near simultaneous ranging techniques, a major shortcoming of the standard DSN uplink transfer procedure was uncovered. Use of the standard procedure resulted in loss of phase coherence between received and reference range codes for the round trip light time following a transfer. It is the intent of this article to report on the philosophy behind, and the operational procedure developed for near simultaneous range transfers, a new uplink transfer procedure that will enable the DSN to generate good range data during the interval from transmitter off to loss of the coherent downlink.

I. Introduction

A unfortunate geometry, zero declination, will exist at Saturn encounter for both Voyagers. This geometry will make it impossible to solve for the spacecraft's declination by fitting doppler data as is normally done in the orbit determination process. An alternative technique for deriving the spacecraft's declination is by use of range data taken near simultaneously from stations at widely separated latitudes, and triangulating to solve for the needed declination angle. This dependence upon range data will require that highly accurate range measurements and range delay calibration information be available to the navigators and radio scientists. It has been towards this end that countless hours have been (and continue to be) spent proving and refining network ranging procedures and analytical techniques for data quality verification.

Periodic tests of the near simultaneous ranging (NSR) technique were conducted during late 1976 and early 1977. The purpose of these tests was to verify that the range accuracy requirements for Voyager navigation could be met, and also to develop the operational procedures that would be imposed on the DSN by this new data collection scheme. The results of these tests are the subject of Reference 1.

As a result of analysis of the data collected during the near simultaneous ranging tests (and noted in Ref. 1), it was discovered that standard DSN procedures for station-to-station uplink handovers had resulted in loss of range code phase coherence, and hence loss of range data during the round trip light time following a handover. It was suggested that phase compensatory tuning might be utilized by the network to solve this problem, and prevent the loss of range data after uplink handovers.

In support of the near simultaneous range data collection effort, the DSN has accepted the phase compensatory tuning recommendation, and developed operational procedures for carrying it out. The remainder of this article describes this plan, and presents the operational procedure that the network will be utilizing in support of the near simultaneous ranging effort.

II. NSR Transfer Philosophy

Every two weeks, once a month per spacecraft, the Voyager Project is planning to gather navigation and radio science data (S-band doppler and range data, and X-band doppler and range

when available) by means of a "tracking cycle". The tracking cycle consists of four consecutive 64-meter antenna tracks beginning with DSS 43 and ending with DSS 43. It should be noted, however, that an attempt to collect NSR data may be made whenever two DSSs are scheduled simultaneously to track a single Voyager spacecraft; this includes colocated stations, and stations of the same general view period (64-meter and/or 26-meter antennas).

The data of prime importance during the tracking cycles (or other simultaneous tracking periods) are the NSR data. During these overlaps, attempts will be made to maximize the return of high quality two- and three-way doppler and NSR measurements. Since two stations cannot concurrently have sustained uplinks with a single spacecraft, collection of the NSR data will require that numerous uplink transfers be made during the overlaps to provide data redundancy and hence data confidence.

These numerous transfers present more of a problem for the network than a cursory glance might reveal. The "standard" DSN transfer, where: (1) the incoming DSS and the outgoing DSS both tune to the spacecraft's receiver VCO center frequency, XA, (adjusted for one-way doppler and light time); (2) the incoming DSS turns on its transmitter and the outgoing DSS turns its off two seconds later; and (3) the DSSs both tune to their respective Track Synthesizer Frequencies (TSFs) and remain there until the end of the track or the next transfer, cannot generally be used for uplink transfers while NSR data are being generated. This tuning pattern, while adequate to transfer the uplink, will change the phase relationship of the ground reference and received range codes, and will thus result in the loss of range data from the outgoing DSS for the round trip light time. To avoid this loss of NSR data, an alternate tuning procedure has been developed.

The new transfer procedure that has resulted from analysis of the problem will, upon completion of all required tuning, restore both the frequency and code phase relationships required for good ranging throughout the round trip light time following an uplink transfer. The only data loss is that during the period of the tuning. This transfer procedure, dubbed the NSR transfer, takes advantage of the programming and precision tuning capabilities of the Programmed Oscillator Control Assembly (POCA) available at the 64-meter DSSs. The procedure calls for both incoming and outgoing DSSs to execute precision symmetrical tuning patterns between specified limits, at fixed rates, and at specific times. Figure 1 graphically depicts a NSR transfer and its related events.

In Fig. 1, it can be seen that the transfer procedure requires utilization of four ramps to achieve the desired symmetrical tuning pattern. All ramps are done at the same rate, 5 Hz/sec (POCA); the initial direction of the first ramp is dependent upon whether XA is above or below TSF. The distance tuned, ΔHZ, is simply

$$\Delta HZ = XA - TSF$$

Since the XA is a doppler dependent frequency, it constantly changes. Therefore the ΔHZ for any given transfer time will be different. That is, sometimes a sweep of +30 HZ will be required, or +2.1 HZ or - 12.4 HZ, etc. It is for this reason that the upper and lower limit registers of the POCA are used; otherwise, new rates and ramp start times would have to be determined for each transfer to account for the different distances to be tuned, and to retain the desired symmetry. As four frequencies are needed for POCA limits: TSF + ΔHZ, TSF, TSF - ΔHZ, TSF, and they must be encountered in this sequence, it will be necessary to reload each POCA limit once during the transfer sequence. Nominal times for these updates have been indicated at transfer + 1 min. 20 sec., and at transfer + 2 min. 40 sec.

In Fig. 1, UL1 and LL1 represent the initial upper and lower limits respectively. (Note: if ΔHZ is a negative number the first sweep will be in the direction of a lower frequency and LL1.) UL2 and LL2 represent the updated POCA limits. The Ts and Rs represent the contents of the four POCA rate/time registers with all rates at either plus or minus 5 Hz/sec. (POCA) (as appropriate) and times as follows:

T0 = Time of transfer minus 1 minute
T1 = Time of transfer plus 1 minute
T2 = Time of transfer plus 2 minutes
T3 = Time of transfer plus 4 minutes

The total time to execute the entire transfer and tuning pattern is approximately 5 minutes with the time changing by a few seconds depending upon the magnitude of ΔHZ.

Other events indicated are the actual transfer time, and the incoming and outgoing range modulation on/off times. Transmitter on at the incoming DSS is at the even minute followed by transmitter off two seconds later at the outgoing DSS. Transfer time is defined as the time of transmitter on at the incoming station. Range data prior to the first ramp start time may be of value; therefore, range modulation at the outgoing station will not be turned off until a convenient time after the start of tuning (range modulation off at transfer - 20 sec, nominally). Similarly, range modulation at the incoming DSS is not applied until tuning is complete (nominally, range modulation on at transfer + 4 min. 10 sec.).

Clearly, the NSR transfer requires the use of a POCA. When transfers are required for the collection of NSR data where a POCA is not available a "standard" transfer is to be executed. Or, in the unique case of DSS 12 and DSS 14, a TSF transfer is to be used. (DSS 12 and DSS 14 are unique in that they are each equipped with a ranging subsystem unlike DSSs 42/43 and 61/63 where ranging systems are shared, also DSSs 12 and 14 are close enough that tuning for transfer is unnecessary, i.e., almost identical doppler shifts.)

While it is unfortunate that the network must adapt to a new transfer procedure in support of NSR data collection, it should be noted that development of a fixed procedure has been one of the design goals in an effort to make the required adaptation as painless as possible.

The uplink tuning rate selected, 240 Hz/sec (S-band), is compatible with Voyager Telecommunications provided signal level estimates for Jupiter Encounter (and beyond). Ground receiver tuning will be avoided by:

(1) Selection of the 30-Hz-wide bandwidth at the Block IV Receiver-Exciter Subsystem, and,

(2) Zeroing the Static Phase Error (SPE) of the receivers prior to beginning the NSR transfer sequence.

III. NSR Transfer Procedure

To aid in the transfer of information, a new transfer message, the NSR TRANSFER MESSAGE (Fig. 2) has been designed. This form provides all needed information (frequencies and event times) for both incoming and outgoing stations. The blanks on the NSR TRANSFER MESSAGE are to be filled in by the Network Operations Control Team (NOCT). To assist in completing the form, an HP 9810 calculator program has been written that, given the inputs necessary for a "standard" transfer, will convert these to (also, output) NSR transfer information required to complete the form. Section IV provides an example of how the program and transfer message are to be utilized.

The same considerations utilized for determining an optimal tuning strategy were also used in determining a ranging strategy. It is not anticipated that ranging parameters will be altered prior to encounter. Arrangements have been made to provide these inputs through the Sequence of Events (SOE). A line item will be provided that will warn of an approaching overlap period, and provide some general reminders including the necessary range parameters. It is of paramount importance that the Planetary Ranging Assembly (PRA) not be interrupted during the overlap period; this is regardless of the transmitter or range modulation status. Any and all inputs, such as a round-trip light time (RTLT) update, must be made prior to the critical data collection period.

The SOE items will include, in addition to the above mentioned ranging parameters:

(1) A statement that announces the beginning of the NSR data collection period, and provides initial conditions.

(2) A warning of an approaching period of NSR transfers that should be a trigger to the NOCT to prepare the necessary NSR TRANSFER MESSAGE(S).

(3) A statement to commence multiple NSR transfers, the GMT of this statement should coincide with the first transfer.

(4) A statement that announces the end of a NSR transfer period.

The following items should be remembered as they directly impact the NSR data:

(1) Frequent uplink transfers will result in frequent doppler mode (two-way vs. three-way) changes; the NOCT must be careful that the correct mode is indicated to avoid extensive data editing.

(2) The good/bad doppler switch (manual) should be set to indicate bad doppler data during uplink tuning, and one RTLT later when the tuning is received in the downlink. This will again eliminate the need for data editing.

(3) The doppler sample rate should be set to one sample per ten seconds during all transfer periods. It should be left at one sample per ten seconds continuously at 64-meter DSSs throughout the tracking cycle.

(4) NSR transfers should be performed on thirty-five minute centers:

(a) Beginning at ten degrees elevation (64-meter antennas) or at the indicated SOE start time whichever is later,

(b) At the midpoint of the DSS 43/63 overlap until the overlap exceeds approximately two hours (three NSR transfers),

(c) And an odd number of NSR transfers *always* must be completed (3, 5 etc.),

(d) And no more than five transfers are to be attempted during 64-meter overlaps. More transfers may be requested during DSS 12/14 NSR data collection periods. The maximum number may later be reduced to three transfers during 64-meter overlaps.

In addition to providing the NOCT with the aforementioned HP 9810 program, a program copy will be provided to each 64-meter DSS. This should help expedite the transfer of NSR transfer information. It is not necessary for each DSS to have the XA and TSF of the other involved DSS. Zeros may be entered in the program for inputs relative to the other station; this will not affect the NSR transfer information output for the station utilizing the program. It is further suggested that the DSSs adopt the NSR TRANSFER MESSAGE form as a recording medium.

IV. Example

A SOE item that indicates the beginning of a NSR multiple transfer period has been noted. At a convenient time, about an hour prior to the noted SOE item the NSR TRANSFER MESSAGE for the first transfer is prepared. This first transfer time is to be 235000; this is somewhat later than the event time of the SOE, but is the first predicts data point available after ten degrees (10°) of elevation angle has been reached. DSS 14 is outgoing and is currently at a TSF of 44028500 Hz. The transfer will be to DSS 43 whose TSF will also be 44028500 Hz. From the tracking predicts the respective transfer time (23:50:00) XAs are found to be:

XA (14) = 44028546.7 Hz

XA (43) = 44028490.9 Hz

Now load the NSR TRANSFER PROGRAM into the HP 9810 calculator, and simply enter the data requested by the program (Fig. 3) as follows:

(1) "XFER GMT =" enter the transfer time, 23:50:00

(2) "OUTGOING TSF =" enter DSS 14's TSF, 44028500

(3) "OUTGOING XA =" enter DSS 14's XA, 44028546.7

(4) "INCOMING TSF =" enter DSS 43's TSF, 44028500

(5) "INCOMING XA =" enter DSS 43's XA, 44028490.9

(6) The NSR TRANSFER MESSAGE is now filled out from the program output, and then either read or faxed or both to the involved DSSs. The DSSs should be reminded of the notes at the bottom of the form (Fig. 4) as they are important to the successful completion of the NSR transfer.

Once the program card becomes available at the 64-meter DSSs, it may prove most expeditious to simply verify that the DSSs have arrived at the same frequencies as those computed by the NOCT. Each DSS will have available its own TSF and XA, but not those of the other involved DSS; therefore, comparison of results will be limited to only those items that directly apply to that DSS.

Reference

1. H. L. Siegel, C. S. Christensen, D. W. Green, F. B. Winn, "On Achieving Sufficient Dual Station Range Accuracy for Deep Space Navigation at Zero Declination," AIAA/AAS Astrodynamic Specialists Conference, Jackson Hole, Wyoming, September 7-9, 1977.

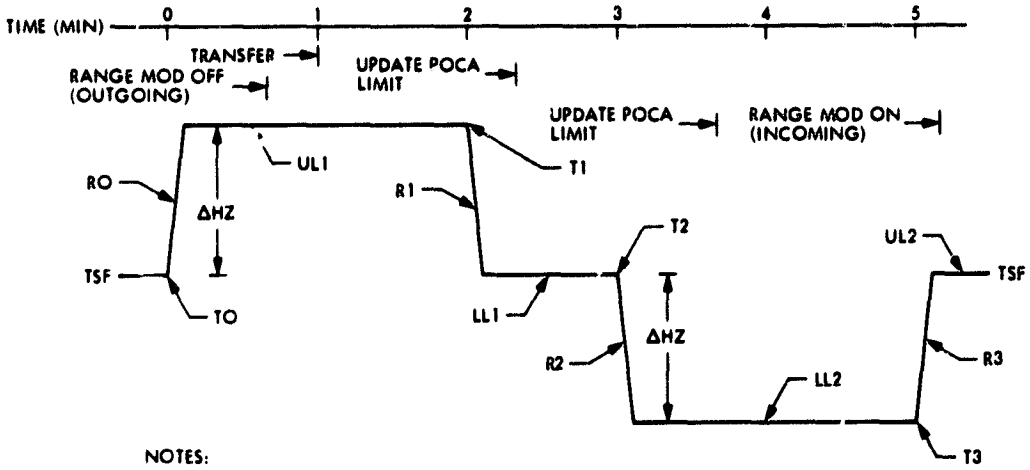

NOTES:

1. ΔHz = XA (OF TRANSFER) - TSF, COMPUTED TO ONE TENTH Hz
2. ALL TUNING RATES ARE 5 Hz/sec, THE SIGN ON R0 & R3 IS THE SAME AS THAT OF ΔHz
   THE SIGN ON R1 & R2 IS OPPOSITE THAT OF ΔHz
3. UL1 = POCA INITIAL UPPER LIMIT FREQUENCY = TSF + (ΔHz)
4. LL1 = POCA INITIAL LOWER LIMIT FREQUENCY = TSF = UL2
5. LL2 = TSF - (ΔHz)
6. T0 = TIME OF TRANSFER - 1 min
7. T1 = TIME OF TRANSFER + 1 min
8. T2 = TIME OF TRANSFER + 2 min
9. T3 = TIME OF TRANSFER + 4 min
10. PRA MUST NOT BE INTERRUPTED REGARDLESS TRANSMITTER OR RANGE MOD STATUS
11. DOPPLER SAMPLE INTERVAL = 10 sec
12. RECEIVER BANDWIDTHS SET 30 Hz-WIDE, NO TUNING AT TRANSFER REQUIRED
13. TRANSFERS TO OCCUR ON 35 min CENTERS

Fig. 1. NSR transfer and related events

NSR TRANSFER MESSAGE

TRANSFER NUMBER _____

S/C _____
DAY _____
OUTGOING DSS _____
INCOMING DSS _____
PRDX SET ID _____
CONTROLLER _____

OUTGOING DSS TSF: _____ HZ

ITEM	GMT	ACTION
A.	_____	TUNE FROM TSF TO _____ HZ
B.	_____	RANGE MOD OFF
C.	_____	TRANSMITTER OFF
D.	_____	TUNE TO TSF
E.	_____	TUNE FROM TSF TO _____ HZ
F.	_____	TUNE TO TSF

INCOMING DSS TSF: _____ HZ

A.	_____	TUNE FROM TSF TO _____ HZ
B.	_____	TRANSMITTER ON
C.	_____	TUNE TO TSF
D.	_____	TUNE FROM TSF TO _____ HZ
E.	_____	TUNE TO TSF
F.	_____	RANGE MOD ON

NOTES:
1. ALL TUNING RATES ARE "PLUS" OR "MINUS" 5 HZ/SEC.
2. UNLESS A PRA FAILURE OCCURS, THE PRA SHOULD REMAIN UNINTERRUPTED REGARDLESS OF TRANSMITTER OR RANGE MODULATION STATUS.
3. RECEIVER SPE SHOULD BE NULLED PRIOR TO EACH TRANSFER.
4. TRK AND LIMIT ENABLE (POCA) MUST BE RESET PRIOR TO EACH RAMP.
5. A NEW POCA UPPER OR LOWER LIMIT MUST BE ENTERED AT TRANSFER PLUS ONE MINUTE-TWENTY SECONDS, AND AGAIN AT TRANSFER PLUS TWO MINUTES-FORTY SECONDS.

Fig. 2. NSR transfer message form

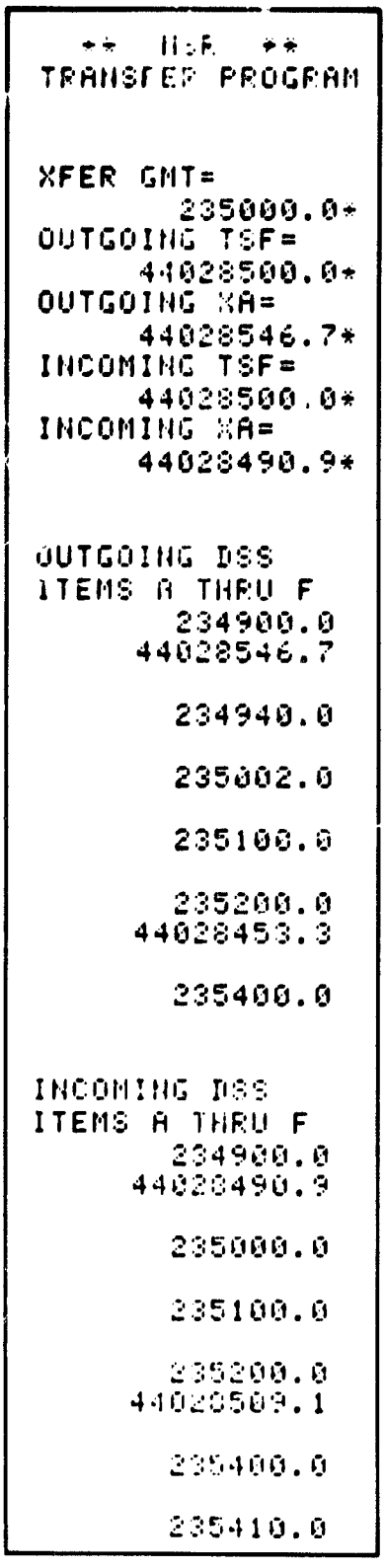

Fig. 3. Example of program output

ORIGINAL PAGE IS
OF POOR QUALITY

NSR TRANSFER MESSAGE

TRANSFER NUMBER 1

S/C 99
DAY 000
OUTGOING DSS 14
INCOMING DSS 43
PRDX SET ID XXXX
CONTROLLER GLS

OUTGOING DSS TSF: 44028500 HZ

ITEM	GMT	ACTION
A.	234900	TUNE FROM TSF TO 44028546.7 HZ
B.	234940	RANGE MOD OFF
C.	235002	TRANSMITTER OFF
D.	235100	TUNE TO TSF
E.	235200	TUNE FROM TSF TO 44028453.3 HZ
F.	235400	TUNE TO TSF

INCOMING DSS TSF: 44028500 HZ

A.	234900	TUNE FROM TSF TO 44028490.9 HZ
B.	235000	TRANSMITTER ON
C.	235100	TUNE TO TSF
D.	235200	TUNE FROM TSF TO 44028509.1 HZ
E.	235400	TUNE TO TSF
F.	235410	RANGE MOD ON

NOTES:
1. ALL TUNING RATES ARE "PLUS" OR "MINUS" 5 HZ/SEC.
2. UNLESS A PRA FAILURE OCCURS, THE PRA SHOULD REMAIN UNINTERRUPTED REGARDLESS OF TRANSMITTER OR RANGE MODULATION STATUS.
3. RECEIVER SPE SHOULD BE NULLED PRIOR TO EACH TRANSFER.
4. TRK AND LIMIT ENABLE (POCA) MUST BE RESET PRIOR TO EACH RAMP.
5. A NEW POCA UPPER OR LOWER LIMIT MUST BE ENTERED AT TRANSFER PLUS ONE MINUTE-TWENTY SECONDS, AND AGAIN AT TRANSFER PLUS TWO MINUTES-FORTY SECONDS.

Fig. 4. Completed NSR transfer message

N78-24241

Some Data Relationships Among Diverse Areas of the DSN and JPL

R. M. Smith
DSN Support Section

A logical-level data model is used to represent real-world relationships among diverse areas of the Deep Space Network (DSN) and non-DSN areas. The possibility for reduction of data redundancy is addressed.

I. Introduction

Section 377 (Deep Space Network Support) maintains an operational database containing data for managing equipment used in Deep Space Network operations. The types of data maintained are: description, identification, location and several kinds of status including data on failures, modifications and shipments. During the past few years, work conducted on the database has revealed and emphasized the existence of relationships in the data domain among diverse elements of the DSN and JPL.

II. Data Relationships

This article presents a cursory analysis of some of the data relationships that exist among various DSN (and JPL, non-DSN) activities. The data elements used in this article are representative of existing real-world attributes. Data element sets, representing existing real-world entities, are presented in this article in the form of third-normal-form relations (defined in Ref. 1). The relations and data elements are not necessarily used as-is in existing databases, rather the intent of these representations is to show the existence of real relationships in the data domain; hence the possibility for communication and coordination among the databases of apparently diverse organizations. The lists of data elements and relations are not exhaustive.

Seven separate functions in the DSN and two non-DSN functions are represented by collections of relations to illustrate interrelationships within and beyond the bounds of the DSN.

Table 1 lists all the data elements used in this article and defines each, as used in the article. Tables 2 through 10 depict relations applicable to the functions indicated by the table titles. Each table may be viewed as a separate, limited logical database or the entire collection may be viewed as representative of a larger, global logical database.

Within each table can be seen one or more data elements used repeatedly, as common keys, among the relations. These common keys provide logical links among *relations*. Were these relations properly established in a database, a user could make use of the existence of the common keys to produce useful information. For instance, using relations 3 and 27 with CON NUMBER as a common key a user could determine the location of an item of equipment with a specific JPL Property

Number *or* he could obtain a listing of all property-controlled equipment at a given location.

Similar logical links exist among *tables* (therefore, between JPL activities). For instance, CON NUMBER is common to Tables 2, 6 and 7; JPL DWG is common to Tables 2, 3, 7 and 4 (where DOCUMENT is equivalent to JPL DWG). As a final example of the existence of logical links: If the relations were integrated in a database, the location of all equipment authorized under a given ADP (Automatic Data Processing) Plan could be determined; using ADP ID as an access key in relation 98; using PO NUMBER as a common key between relations 98 and 1; using CON NUMBER as a common key between relations 1 and 3; deriving resultant location data from LOCATION in relation 3. Casual inspection will reveal other, similar relationships.

III. Redundancies

It is interesting to note the amount of redundancy that exists throughout Tables 2 through 10. By integrating all 99 of the relations in Tables 2 through 10, 26 duplicate relations may be deleted. An additional 7 relations may be removed because of the existence of multiple inferred relationships. This amounts to approximately 33 percent reduction in redundancy as a result of integrating the diverse data sets. This is probably typical of the degree of reduction that could be achieved in an actual integration.

Reference

1. Date, C. J., *An Introduction to Database Systems*, Addison-Wesley Publishing Company, Inc., Reading, Mass., 1975.

Table 1. Definitions of data elements used in tables 2 through 10

DATA ELEMENT NAME	DATA ELEMENT DEFINITION
1-ACCEPTANCE	ACCEPTANCE STATUS OF ECO FIRST INSTALLATION
2-ACQ DATE	DATE ON WHICH PROPERTY WAS ACQUIRED BY JPL
3-ADDRESS	ADDRESS OF A MANUFACTURER
4-ADP ID	ADP PLAN IDENTIFICATION
5-APPLIC FAC	FACILITY TO WHICH AN ENGINEERING CHANGE IS APPLICABLE
6-CATEGORY	USAGE CATEGORY OF EQUIPMENT
7-CDE	COGNIZANT DEVELOPMENT ENGINEER
8-CERT STATUS	EMPLOYEE QA TRAINING STATUS
9-CERT SUBJECT	SUBJECT IN WHICH AN EMPLOYEE IS CERTIFIED
10-COE REC DATE	DATE ON WHICH A COE RECEIVED AN ECO KIT
11-COE SHIP DATE	DATE ON WHICH A COE SHIPPED AN ECO KIT
12-COE	COGNIZANT OPERATIONS ENGINEER
13-CON NUMBER	DSN EQUIPMENT CONTROL NUMBER
14-COST	COST OF AN ITEM
15-CSE	COGNIZANT SUSTAINING ENGINEER
16-DATE FUNCTIONAL	DATE ON WHICH MODIFIED EQUIPMENT IS FUNCTIONAL
17-DATE	DATE OF AN EVENT OR CONDITION
18-DELEGATION	FACILITY TO WHICH EQUIPMENT MAINTENANCE IS DELEGATED
19-DESCRIPTION	DESCRIPTION OF AN ITEM
20-DESIGN FINISH	DATE THAT ECO DESIGN IS FINISHED
21-DEST FAC	FACILITY TO WHICH AN ITEM IS BEING SHIPPED
22-DISCREPANCY	DISCREPANCY DISCOVERED DURING INSPECTION
23-DISPOSITION	FINAL DISPOSITION OF MATERIAL AFTER INSPECTION
24-DOCUMENT	CONTROLLING IDENTIFICATION OF A DOCUMENT
25-DUE DATE	DATE ON WHICH AN EVENT OR CONDITION IS DUE
26-EC COST	ESTIMATED TOTAL COST TO IMPLEMENT AN ECO
27-EC EXCEPTION	EXCEPTION TO AN ECO FIRST INSTALLATION
28-EC STATUS	EC STATUS OF AN ITEM OF EQUIPMENT
29-ECI	ENGINEERING CHANGE INSTRUCTION
30-ECO	ENGINEERING CHANGE ORDER
31-ECR	ENGINEERING CHANGE REQUEST
32-EMP NUMBER	JPL EMPLOYEE NUMBER
33-EMP ORGANIZATION	NUMERIC DIVISION-SECTION IDENTIFIER
34-EST DESIGN FINISH	ESTIMATED ECO DESIGN FINISH DATE
35-EST FAB FINISH	ESTIMATED ECO FABRICATION FINISH DATE
36-FAB FINISH	DATE THAT ECO FABRICATION IS FINISHED
37-FAC COMP DATE	DATE OF ECO COMPLETION AT A FACILITY
38-FAC EST COMP	ESTIMATED DATE OF ECO COMPLETION AT A FACILITY
39-FAC REC DATE	DATE OF ECO KIT RECEIPT AT A FACILITY
40-FACILITY	DSN OPERATIONAL OR SUPPORT FACILITY
41-FAIL DATE	DATE OF EQUIPMENT FAILURE
42-FAIL TIME	TIME OF EQUIPMENT FAILURE
43-ICE	IMPLEMENTATION COORDINATION ENGINEER
44-INSP DATE	DATE ON WHICH AN INSPECTION WAS COMPLETED
45-INSP NUMBER	UNIQUE NUMBER ASSIGNED TO AN INSPECTION ACTIVITY
46-INSP STATUS	STATUS OF AN INSPECTION

Table 1 (contd)

47-INSP TYPE	TYPE OF INSPECTION
48-ISSUE UNIT	UNIT OF ISSUE FROM SUPPLY
49-JPL DWG	JPL DRAWING NUMBER
50-LANGUAGE	NAME OF A PROGRAMMING LANGUAGE
51-LEAD TIME	LEAD TIME FOR RECEIPT OF MATERIAL AFTER ORDER
52-LOCATION	DSN OPERATIONAL OR SUPPORT FACILITY
53-MA NAME	NAME OF A MAJOR ASSEMBLY
54-MFR	MANUFACTURER
55-MODEL	MODEL IDENTIFICATION
56-NAME	NAME OF A MANUFACTURER
57-NOMENCLATURE	DESCRIPTIVE EQUIPMENT NAME
58-NSE	NETWORK SYSTEMS ENGINEER
59-NSN	NATIONAL STOCK NUMBER
60-OPSTAT	OPERATIONAL STATUS OF EQUIPMENT
61-OWNER	FACILITY TO WHICH EQUIPMENT IS ASSIGNED
62-PART NUMBER	MANUFACTURER'S PART NUMBER
63-PO NUMBER	PURCHASE ORDER NUMBER
64-PRIORITY	PRIORITY OF AN ENGINEERING CHANGE ASSESSMENT
65-PROCEDURE	CONTROLLING IDENTIFICATION OF A PROCEDURE
66-PROGRAM	CONTROLLING IDENTIFICATION OF A COMPUTER PROGRAM
67-PROJECT	FLIGHT PROJECT
68-PROP NUMBER	JPL PROPERTY NUMBER
69-QUANTITY	QUANTITY OF SPARES REQUIRED
70-RACK	SUBSYSTEM RACK IDENTIFIER
71-REC DATE	DATE OF RECEIPT AT A FACILITY
72-REF DES	SUBSYSTEM REFERENCE DESIGNATOR
73-REFER TO	PARTY TO WHICH AN ECR IS REFERRED FOR REVIEW
74-RELEASE DATE	DOCUMENT OR PROGRAM RELEASE DATE
75-REPAIR TIME	TIME EXPENDED IN REPAIRING AN ITEM
76-REQ COMP DATE	REQUIRED COMPLETION DATE
77-REVISION	REVISION LETTER OF A JPL DRAWING
78-SCOE	SYSTEM COGNIZANT OPERATIONS ENGINEER
79-SERIAL NUMBER	MANUFACTURER'S EQUIPMENT SERIAL NUMBER
80-SERVICE DATE	DATE ON WHICH EQUIPMENT WAS SERVICED
81-SERVICE FAC	FACILITY THAT PERFORMED SERVICE ON EQUIPMENT
82-SERVICE INTERVAL	PRESCRIBED TIME INTERVAL BETWEEN SERVICES
83-SHIP DATE	DATE OF SHIPMENT
84-SHIP FAC	FACILITY THAT SHIPPED AN ITEM
85-SS NAME	SUBSYSTEM NAME
86-SSE	SUBSYSTEM ENGINEER
87-SSMA	SUBSYSTEM-MAJOR ASSEMBLY CODE
88-STADIR	STATION DIRECTOR
89-SUBSYSTEM	SUBSYSTEM CODE
90-SYSTEM NAME	SYSTEM NAME
91-SYSTEM	SYSTEM CODE
92-TA EXCEPTION	TRANSFER AGREEMENT EXCEPTION
93-TA STATUS	TRANSFER AGREEMENT STATUS
94-TEST TIME	TIME EXPENDED IN TESTING AN ITEM
95-TITLE	TITLE OF A DOCUMENT OR COMPUTER PROGRAM
96-VENDOR	NAME OF AN EQUIPMENT VENDOR

ORIGINAL PAGE IS
OF POOR QUALITY

Table 2. Examples of relations pertinent to DSN operations

	RELATION NAME	DATA ELEMENTS
1)	ACQUISITION	(CON NUMBER,COST,PO NUMBER,ACQ DATE)
2)	AC DESIGNED	(FACILITY,SSMA,RACK,REF DES,NSN)
3)	ASSIGNMENT	(CON NUMBER,OWNER,LOCATION,OPSTAT,REC DATE)
4)	CDE	(SSMA,CDE)
5)	COE	(SSMA,COE)
6)	CSE	(SSMA,CSE)
7)	DELEGATION	(NSN,SERVICE INTERVAL,DELEGATION,PROCEDURE)
8)	DESCRIPTION	(CON NUMBER,NSN,CATEGORY)
9)	EC APPLICABILITY	(ECO,APPLIC FAC,SSMA,REQ COMP DATE)
10)	EC COST EST	(ECO,EC COST)
11)	EC DESCRIPTION	(ECR,DESCRIPTION)
12)	EC EXCEPTION	(ECO,FACILITY,EC EXCEPTION)
13)	EC PROCEDURE	(ECO,PROCEDURE)
14)	ECI	(ECI,JPL DWG)
15)	ECO DWG	(ECO,JPL DWG)
16)	ECO ECI	(ECO,ECI)
17)	ECO MILESTONES	(ECO,COE REC DATE,COE SHIP DATE,DEST FAC,FAC REC DATE FAC EST COMP,DATE FUNCTIONAL,FAC COMP DATE)
18)	ECO EQUIPMENT	(CON NUMBER,ECO,EC STATUS)
19)	ECR OPEN	(ECR,DATE,PRIORITY)
20)	ENROUTE	(CON NUMBER,SHIP DATE,SHIP FAC,DEST FAC)
21)	FAILURE	(CON NUMBER,FAIL DATE,FAIL TIME,FACILITY)
22)	FIRST INST	(ECO,DATE,ACCEPTANCE)
23)	IMPLEMENTATION ENG	(FACILITY,ICE)
24)	MAJOR ASSEMBLY ID	(SSMA,MA NAME)
25)	MANUFACTURER	(MFR,NAME,ADDRESS)
26)	NSN	(NSN,MFR,MODEL,JPL DWG)
27)	PROPERTY	(CON NUMBER,PROP NUMBER)
28)	REFER ECR	(ECR,REFER TO)
29)	SERVICE DUE	(CON NUMBER,DUE DATE)
30)	SERVICE HISTORY	(CON NUMBER,SERVICE DATE,SERVICE FAC,TEST TIME, REPAIR TIME)
31)	SPARES REQ	(NSN,QUANTITY,FACILITY)
32)	SSE	(SUBSYSTEM,SSE)
33)	STATION DIRECTOR	(FACILITY,STADIR)
34)	SUBSYST COORD	(FACILITY,SSMA,RACK,REF DES,CON NUMBER)
35)	SUBSYSTEM ID	(SUBSYSTEM,SS NAME)
36)	SYST TA STATUS	(SYSTEM,TA STATUS)
37)	SYSTEM CDE	(SYSTEM,SCDE)
38)	SYSTEM ENGINEER	(SYSTEM,NSE)
39)	SYSTEM ID	(SYSTEM,SYSTEM NAME)
40)	TA EXCEPTIONS	(SSMA,TA EXCEPTION)
41)	TA STATUS	(SSMA,FACILITY,TA STATUS)

Table 3. Examples of relations pertinent to DSN engineering change management

	RELATION NAME	DATA ELEMENTS
42)	EC APPLICABILITY	(ECO,APPLIC FAC,SSMA,REQ COMP DATE)
43)	EC COST EST	(ECO,EC COST)
44)	EC DESCRIPTION	(ECR,PROJECT,DESCRIPTION,REQ COMP DATE)
45)	EC EXCEPTIONS	(ECO,FACILITY,EC EXCEPTION)
46)	ECO MILESTONE	(ECO,CDE REC DATE,CDE SHIP DATE,DEST FAC,FAC REC DATE, FAC EST COMP,DATE FUNCTIONAL,FAC COMP DATE)
47)	EC PROCEDURE	(ECO,PROCEDURE)
48)	EC SUBSYSTEM	(ECR,SUBSYSTEM)
49)	ECI	(ECI,JPL DWG)
50)	ECO DWG	(ECO,JPL DWG)
51)	ECO ECI	(ECO,ECI)
52)	ECO FORECAST	(ECO,EST DESIGN FINISH,EST FAB FINISH)
53)	ECO KIT	(ECO,DESIGN FINISH,FAB FINISH)
54)	ECR OPEN	(ECR,DATE,PRIORITY)
55)	FIRST INST	(ECO,DATE,ACCEPTANCE)
56)	REFER ECR	(ECR,REFER TO)

Table 4. Examples of relations pertinent to DSN maintenance and operation documentation

	RELATION NAME	DATA ELEMENTS
57)	COST	(DOCUMENT,REVISION,COST)
58)	RELEASE DATE	(DOCUMENT,REVISION,RELEASE DATE)
59)	TITLE	(DOCUMENT,TITLE)

Table 5. Examples of relations pertinent to the DSN program library

	RELATION NAME	DATA ELEMENTS
60)	APPLICABILITY	(PROGRAM,SSMA)
61)	PROGRAM ID	(PROGRAM,LANGUAGE,TITLE)
62)	RELEASE DATE	(PROGRAM,RELEASE DATE)
63)	TA STATUS	(PROGRAM,TA STATUS,DATE)

Table 6. Examples of relations pertinent to DSN logistics

	RELATION NAME	DATA ELEMENTS
64)	COST	(NSN,COST)
65)	IDENTIFICATION	(NSN,MFR,MODEL,PART NUMBER,NOMENCLATURE)
66)	LEAD TIME	(NSN,LEAD TIME)
67)	LOCATION	(CON NUMBER,LOCATION)
68)	SERVICE DELEGATION	(NSN,DELEGATION)
69)	SOURCE	(NSN,VENDOR)
70)	UNIT OF ISSUE	(NSN,ISSUE UNIT)

Table 7. Examples of relations pertinent to DSN workmanship assurance

	RELATION NAME	DATA ELEMENTS
71)	DISCREPANCY	(INSP NUMBER,DISCREPANCY)
72)	ECO INSPECTION	(INSP NUMBER,ECO,INSP STATUS)
73)	EMP CERT STATUS	(EMP NUMBER,CERT STATUS,CERT SUBJECT)
74)	EQUIPMENT ID	(CON NUMBER,MFR,MODEL,NOMENCLATURE,SERIAL NUMBER)
75)	EQUIPMENT DWG	(CON NUMBER,JPL DWG)
76)	INSPECT DATE	(INSP NUMBER,DISPOSITION,DATE)
77)	INSPECTION	(CON NUMBER,INSP DATE,LOCATION,INSP NUMBER,INSP TYPE)
78)	SUBSYSTEM APPLIC	(INSP NUMBER,SUBSYSTEM)

Table 8. Examples of relations pertinent to DSN subsystem status and assignments

	RELATION NAME	DATA ELEMENTS
79)	CDE	(SSMA,CDE)
80)	CDE	(SSMA,CDE)
81)	IMPLEMENTATION ENG	(FACILITY,ICE)
82)	MAJOR ASSEMBLY ID	(SSMA,MA NAME)
83)	SSE	(SUBSYSTEM,SSE)
84)	STATION DIRECTOR	(FACILITY,STADIR)
85)	SUBSYSTEM ID	(SUBSYSTEM,SS NAME)
86)	SYST TA STATUS	(SYSTEM,TA STATUS)
87)	SYSTEM CDE	(SYSTEM,SCDE)
88)	SYSTEM ENGINEER	(SYSTEM,NSE)
89)	SYSTEM ID	(SYSTEM,SYSTEM NAME)
90)	TA EXCEPTIONS	(SSMA,TA EXCEPTION)
91)	TA STATUS	(SSMA,FACILITY,TA STATUS)

ORIGINAL PAGE IS
OF POOR QUALITY

Table 9. Examples of relations pertinent to JPL property control

	RELATION NAME	DATA ELEMENTS
92)	ACQUISITION	(PROP NUMBER,COST,ACQ DATE,PO NUMBER)
93)	EMP RESPONSIBILITY	(PROP NUMBER,EMP NUMBER)
94)	EMPLOYEE ORG	(EMP NUMBER,EMP ORGANIZATION)
95)	EQUIP SERIAL	(PROP NUMBER,SERIAL NUMBER)
96)	EQUIPMENT ID	(PROP NUMBER,MFR,MODEL,NOMENCLATURE)
97)	LOCATION	(PROP NUMBER,LOCATION)

Table 10. Examples of relations pertinent to the management of automatic data processing equipment

	RELATION NAME	DATA ELEMENTS
98)	ADP PLAN	(ADP ID,PO NUMBER)
99)	LOCATION	(PO NUMBER,PROP NUMBER,MFR,MODEL,LOCATION)

N78-24242

A New, Nearly Free, Clock Synchronization Technique

W. H. Hietzke
DSN Operations Section

A new, near real-time, method for intercomplex clock synchronization is proposed. The method consists of transmitting a symmetric frequency ramp to a spacecraft and determining the time at which the received ramp (in doppler residuals) occurs at overlapping stations. Adjusted preliminary data suggest that the accuracy of the method may be better than 0.7 microseconds. The method requires no additional hardware and can be done during normal tracks. Other, perhaps more accurate, variations of the method are under investigation.

I. Introduction

Interstation clock synchronization is extremely important in both spacecraft navigation and in the ultimate accuracy of scientific data obtained from the spacecraft. Several methods of clock synchronization are either in use or have been proposed. Most precise methods utilize radio signals from extraterrestrial objects – either originating there (Very Long Baseline Interferometry) or bounced from them (Moon Bounce). There are several contributors to the ultimate accuracy of the synchronization which all such methods have in common. These are: 1) station location uncertainty, 2) atmospheric delays, and 3) electronic (station) delays. The new method proposed below is no exception. These three factors, however, can be measured to an accuracy which translates to less than 10 ns synchronization uncertainty.

Currently the DSN synchronizes its clocks via the "Moon Bounce" method. The ultimate accuracy of this method is approximately 5 microseconds. This system requires additional antennas and related hardware, an operator at each site, the generation of special "Moon Bounce" predicts, and the data must be collected and reduced. The method proposed below can accomplish clock synchronization to a similar (and even better) accuracy, using existing data outputs – but it does not require special antennas, predicts, or additional operators. Also, real-time programs can be written to compute certain parameters which will reduce analysis time and give ultimately near-real-time synchronization. A variation of the method can also be utilized for Very Long Baseline Interferometry (VLBI) clock synchronization. This will be discussed later.

II. Description of Method

The method consists of transmitting a symmetric sawtooth frequency ramp to a spacecraft. This ramp can be identical to those currently employed for Pioneer ramp ranging. The transmit time should be such that the ramp is received approximately in the middle of the overlap interval of two DSS whose clock off-sets are to be determined Both DSS must be locked to the signal throughout the duration of the ramp.

The ramp, unmodeled in predicts, will appear inverted in the doppler residuals. This will be the data base for the synchronization. Doppler residuals are computed by the Real

Time Monitor (RTM) by differencing actual received (DSN) doppler and predicted doppler. For most tracks this difference will be small – a few Hz. For the purpose of this synchronization, the actual magnitude is unimportant. However, the residuals may vary in a nonlinear manner. This is likely when the spacecraft experiences non-constant accelerations. These orbit modeling uncertainties will produce large nonlinear doppler residuals when the doppler changes rapidly. Choosing spacecraft which undergo constant acceleration during the ramp duration will eliminate this problem. Also, this effect can easily be seen in the data so that the data can be corrected or rejected. The Voyager spacecrafts are good candidates for this procedure.

If the transmitted ramp is of the form:

$$f(t) = \begin{cases} a't + f_0 & t'_0 \leq t < t'_1 \\ -a't + b' & t'_1 \leq t < t'_2 \\ a't + c' & t'_2 \leq t < t'_3 \\ f_0 & t'_3 \leq t \end{cases}$$

where:

a' = magnitude of the rate of change of frequency

f_0 = initial frequency

and b' and c' are constants, the form of the doppler residuals when the ramp is received at each DSS is:

$$R(t) = \begin{cases} R_0 & t < t_0 \\ a_1 t + b_1 & t_0 \leq t < t_1 \quad (1) \\ a_2 t + b_2 & t_1 \leq t < t_2 \quad (2) \\ a_3 t + b_3 & t_2 \leq t < t_3 \quad (3) \\ R_1 & t_3 < t \end{cases}$$

For a symmetrical sawtooth frequency ramp (and $R_0 = R_1$), $a_1 = -a_2 = a_3$.

III. Data Analysis

Analysis of the data proceeds as follows: A least squares linear fit is made to $R(t)$ for each segment (indicated 1, 2, 3). For the fit, a total of four points are not used – these are the first and last points of each segment. For each segment 1, 2 and 3, a RMS deviation is computed. For an equation of the form:

$$R(t) = at + b$$

$$\sigma_R = \sqrt{\frac{\sum_{i=1}^{n} (\Delta R_i)^2}{n}}$$

where ΔR_i is the difference between the actual R and the fit R at t_i, and n is the number of data points obtained (see Figure 1).

The uncertainty of the coefficients a and b is given by

$$\sigma_a = \sqrt{\frac{n}{n \sum_{i=1}^{n} (t_i)^2 - \left(\sum_{i=1}^{n} t_i \right)^2}}\ \sigma_R$$

$$\sigma_b = \sqrt{\frac{\sum_{i=1}^{n} (t_i^2)}{n \sum_{i=1}^{n} (t_i)^2 - \left(\sum_{i=1}^{n} t_i \right)^2}}\ \sigma_R$$

The points of interest are the times at which the peaks occur. These are:

$$t_1^* = \frac{b_1 - b_2}{a_1 - a_2}$$

and

$$t_2^* = \frac{b_2 - b_3}{a_2 - a_3}$$

ORIGINAL PAGE IS
OF POOR QUALITY

The accuracy with which these times are known is given by:

$$\sigma_{t_1^*} = \left\{ \left(\sigma_{b_1}^2 + \sigma_{b_2}^2\right) \left(\frac{1}{a_1 - a_2}\right)^2 \right.$$

$$\left. + \left(\frac{b_2 - b_1}{(a_1 - a_2)^2}\right)^2 \left(\sigma_{a_1}^2 + \sigma_{a_2}^2\right) \right\}^{1/2}$$

and a similar equation for $\sigma_{t_2^*}$. The equation can be put in a form containing σ_R and n (the number of data points for each segment) by approximating the sums in the σ_a and σ_b equations by integrals

$$\sum t_i \rightarrow \int t dt; \quad \sum t_i^2 \rightarrow \int t^2 \, dt.$$

The result – for a sawtooth frequency ramp with a 20 minute period – is:

$$\sigma_{t_1^*} \cong \frac{\sigma_R}{(a_1 - a_2)\, n^{1/2}} \left\{ \left(\frac{3.67}{n}\right)^2 \right.$$

$$\left. + (2.45)^2 \left(\frac{b_1 - b_2}{a_1 - a_2}\right)^2 \right\}^{1/2}$$

As can be seen from the equation, a large slope will reduce the uncertainty in t_1^*. Thus, using X-band will improve the accuracy of t^* by a factor of about 4.8 over S-band. Although choosing large n (short sample times) will increase the σ_R somewhat, since σ_t^* is proportional to $n^{-1/2}$, large n will reduce the uncertainty of t^* (approximately as $n^{-0.2}$). For example, 1 second data will reduce the uncertainty in t^* by a factor of about 1.6 over 10 second data.

For large n, the uncertainty in t^* is approximately:

$$\sigma_{t_1^*} \cong \frac{2.45\,|b_1 - b_2|}{(a_1 - a_2)^2\, n^{1/2}}\, \sigma_R$$

Thus, minimizing b_i is also important. No attempt was made below to minimize b_1, b_2 or b_3, but this is easily done.

I have gone through this analysis using ramp ranging data for Pioneer 10, taken at DSS 14 on DOY 209 (1977). The exciter VCO was increased at a rate of 2.083 Hz/sec. (This rate can be increased somewhat in future tests, without fear of losing lock on the ramp's return.) The received S-band slope is

$$\left(\frac{240}{221} \times 48 \times 2.083\right) + C_0 \cong 108.6.$$

The constant C_0 is a term involving the spacecraft motion. The results of the analysis are shown in Table 1, below, for 10 second data, and Table 2 shows the uncertainty of the time of the peaks.

For this day, the "Doppler Noise" (computed for 60 second data) was 0.007. This is high, noise levels of 0.003 are the rule and values slightly lower can be obtained using a Hydrogen maser. Thus, an improvement by a factor of 2 is expected for σ_t^* for standard data. This translates to specification of the event (the peak) to 0.49 μs at each station (1 second X-band data) resulting in a clock offset measurement accuracy of 0.7 μs (excluding other correction uncertainties).

All of the above calculations may be incorporated into the RTM – including a check of the doppler residuals to automatically activate the subroutine when a ramp occurs. What remains then is to apply corrections to the measured clock offset for 1) the difference in signal path length (divided by C), 2) the difference in electronic delays, and 3) the difference in atmospheric delays.

As mentioned previously, this method is compatible with VLBI. Several schemes can be used to correlate the data, and these are under investigation.

The advantage of this system will be a reduction of data processing time with considerable cost savings rather than an improvement of accuracy over the currently proposed VLBI clock sync method. This is possible because the spacecraft can be considered a coherent point source – thus, circumventing some correlation problems associated with the transverse coherence length of stellar radio sources. (This will allow similar accuracies with less data.) The signal level will be high and the time change of the frequency can be computed before the fact. This last point will allow the use of more narrow receiver bandwidths, driven by programmable local oscillators.

Table 1. Ten second data

Region	a_f (Hz/Sec)	b_f (Hz)	σ_R (X 10^{-3})	σ_a (X 10^{-6})	σ_b (X 10^{-4})
1	-108.60002	329.0453	7.59	5.06	0.835
2	108.60002	-65484.6439	9.61	0.436	4.71
3	-108.60002	130636.9870	10.02	6.68	70.4

Table 2. Uncertainty of the time of the peaks

Peak	σ_t^* (10 sec. S-band)	σ_t^* (1 sec. S-band)	σ_t^* (1 sec. X-band)
t_1^*	7.42 μs	4.67 μs	0.97 μs
t_2^*	33.8 μs	21.3 μs	4.4 μs

ORIGINAL PAGE IS
OF POOR QUALITY

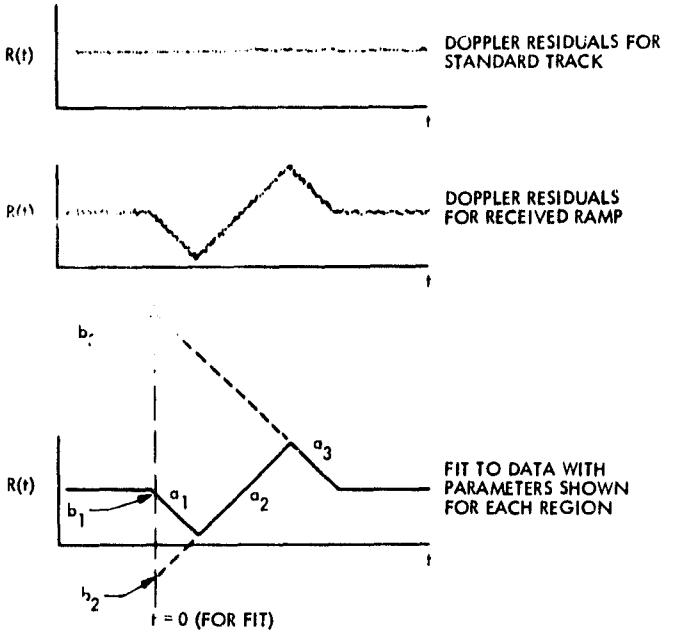

Fig. 1. Typical doppler residual plots

N78-24243

Tracking Operations During the Voyager 2 Launch Phase

J. A. Wackley and G. L. Spradlin
DSN Operations Section

The Voyager 2 launch phase tracking operational procedures were carefully studied and conservatively designed to accommodate any launch contingency. This launch phase was marked by the first use of the Goldstone complex, including the 64 meter antenna, as the initial acquisition location. The following report details the pre-launch planning for and subsequent analysis of tracking operations during the Voyager 2 launch phase.

I. Introduction

On August 20, 1977 at 14:29:44.27 Greenwich Mean Time (GMT), Voyager 2 lifted off from the Kennedy Space Center signaling the somewhat unsure start of the Voyager mission. The purpose of this mission is to study the regions of Jupiter, Saturn, and possibly Uranus, as well as the interplanetary media.

To begin this investigation, Voyager 2 was launched at an azimuth of 124.09 degrees aboard a Titan 3E/Centaur D1T launch vehicle with insertion into the trans-Jupiter orbit occurring over Southeast Asia. The geometry of the parking orbit and subsequent Jupiter transfer orbit was such that the Goldstone Deep Space Communications Complex, specifically Deep Space Station (DSS) 12, became the prime initial acquisition station. This launch marked the first use of a Goldstone station for the initial acquisition as well as the first use of a 64 meter station during the initial pass.

This report details the pre-launch planning for the initial acquisition pass and presents an analysis of the events of that pass.

II. Trajectory Considerations

The open window launch trajectory for 20 August presented angle and frequency rates which were comparable to other recent parking orbit ascent launches (Ref. 1). Specifically, these rates were:

Hour Angle (HA) = -0.049 degrees/second
One Way Doppler (D1) = +82.6 Hz/second
$\dot{X}_A$ = 68 Hz/second (S-Band)

The trajectory for Voyager 2 also had the following characteristics:

(1) The angle and frequency rates were highest at open window of any particular launch date

(2) The highest maximum elevation angle was achieved for open window launch

(3) The declination of the spacecraft was very high (41°) and would remain so for many weeks after launch

Of these three items, only the high declination angle required special planning which is detailed in Section VII.

Figure 1 stereographically illustrates the initial pass over DSS 12 while Figure 2 depicts the elevation angle during this pass. Additionally, Figure 2 serves as a timeline for significant tracking events that occurred during the pass.

An important facet in the design of an initial acquisition strategy is the effect of an anominal launch in the spacecraft trajectory. To this end, 3σ launch trajectories were provided by the Voyager Navigation team. Examination of these trajectories yielded the following 3σ uncertainties in the tracking parameters at the rise of DSS 12:

3σ Hour Angle = 0.31 degrees
3σ D1 = 300 Hz (S-Band)
3σ D2 = 600 Hz (S-Band)
3σ XA = 182 Hz (S-Band)

These figures are somewhat smaller than those encountered in other recent launch phases. For example, for the Helios 2 launch (Ref. 2) the 3σ uncertainties were:

3σ Hour Angle = 1.15 degrees
3σ D1 = 3500 Hz (S-Band)
3σ XA = 1632 Hz (S-Band)

These data were, however, somewhat incomplete in that there exist many different possibilities for non-standard trajectories which could result in (possibly) larger errors. In light of this and in order to insure complete success, the initial acquisition strategy was developed from an extremely conservative approach.

III. Tracking Subsystem Software

This launch, unlike any other launch, was to be supported using a plethora of newly implemented software as well as much new hardware. Since the last (Helios 2) launch, new Antenna Pointing Subsystem (APS) and Planetary Ranging Assembly (PRA) software had been implemented, the tracking prediction software had been extensively changed, the Metric Data Assembly (MDA) and its associated software had been newly implemented and the Block III Network Support Controller (NSC) had come into use. As this software and equipment underwent extensive pre-launch testing, many flaws and failures were discovered; in fact, every one of the above mentioned components underwent some degree of modification during the last few months before launch.

A. Tracking Predictions

In March of 1977, the DSN tracking prediction system was completely changed. The previous system relied wholly on topocentric trajectory data in the form of a polynomial coefficient tape (PCT) generated by the project navigation team. This PCT was then evaluated by the PREDIK software to produce tracking predictions.

The new (and currently used) system requires as input a probe ephemeris tape (PET) containing the probe trajectory in terms of a central body. The PET then becomes the input to the Fast Phi-factor Generator Program (FPGP) which translates these data to topocentric observables and generates the PCT input to PREDIK.

In the course of generating the many predicts sets required to characterize the launch trajectories, it was found that FPGP could not quickly or accurately produce launch phase predictions. These problems obviously caused concern that FPGP could not be used at all during the launch phase of Voyager. To improve the running time of FPGP there were extensive changes to the program files. These changes resulted in the elimination of two tapes and much operator intervention. This streamlining allowed the running time to be reduced significantly.

It was also discovered that FPGP tended to over fit when the observables were undergoing a high rate of change. To correct this situation FPGP was modified to allow user control of the minimum span duration thereby diminishing the tendency toward overfitting.

In later testing (in fact, within three weeks of launch), it was found that the time from launch (TFL) option did not function correctly. While copies of the predicts produced at JPL had the proper time field, those received at the stations did not. Since this was an important launch phase predicts option, (see Section IV) the cause of the problem (one line of the program had been inadvertently omitted) was quickly isolated and corrected.

The NSC is the Σ5 computer used to generate and transmit tracking and telemetry predictions as well as other products such as the sequence of events and schedule. During pre-launch testing it was found that the NSC software used in the construction of transmission files would not accept the Voyager spacecraft identifiers. It was also discovered during the testing cycle that the Metric Data Assembly (MDA) would not permit reception of a single pass of predictions. During the launch phase predictions are, of course, generated on a single pass basis. Both programs were quickly modified to correct these anomalies.

Thus, after a less than encouraging start, the prediction system was finally ready for launch support with less than three weeks to spare.

B. APS II Drive Tape Verification

With the implementation of the APS II software in early 1976, the format of the antenna drive tape was changed thereby nullifying the drive tape verification software. This left only a check sum computation for verification of the drive tape. It was believed that this method of verification was wholly inadequate for support during this critical phase. The original APS drive tape verification program was therefore quickly modified and brought into operational usage just weeks before the Voyager 2 launch.

C. Planetary Ranging Assembly

In late May analysis of ranging data from DSS 12 revealed a one second error in the range acquisition (T_0) time as reported by the MDS version of the Planetary Ranging Assembly (PRA) software. Like the other previously discussed problems, this one was quickly corrected and the PRA was made ready for launch support.

IV. Angle Drive Strategy

The angle drive strategy for the Voyager 2 was essentially the same strategy successfully used during previous launches and was based upon the following considerations:

(1) It was desired that the uplink be acquired shortly after rise,

(2) Usage of a drive tape was required during the one-way to two-way transition,

(3) Acquisition of early (near earth) auto track data was desired, and

(4) It was desired to lock the receiver coupled to the S-Band Cassegrain antenna as well as the S-Band Acquisition Aid Antenna (SAA) connected receiver prior to initiation of the uplink sweep.

It was planned that at least four and possibly five drive tapes would be generated to assure the station of the best available drive tape. The antenna drive strategy then became:

(1) At launch minus seven days (or L-24 hours if the launch date slipped) open, mid and close window drive tapes were to be generated. These tapes would be in TFL format and would be used as back ups for drive tapes to be produced during the final countdown. To use these tapes, a time offset (Δt) equal to the actual lift-off time would be entered into the APS. Which tape to use would be specified by the Tracking Network Operations Analyst (NOA).

(2) At L-105 minutes a new drive tape with times in GMT format would be generated. It had been determined previously that (based upon an analysis of angle rates) the SCM antenna beam width would tolerate an error of up to three seconds in lift-off time before it would become extremely difficult to lock the receivers. The L-105 minute predicts would then be prime if launch was within three seconds of expected.

(3) At L-4 minutes, a contingency predicts set based upon a lift-off plus three second trajectory would be generated. If lift-off was more than three seconds late, these predicts would be transmitted to the station for use in punching a drive tape.

(4) Finally, if none of the previously mentioned drive tapes were adequate, a prediction set based on the actual lift-off time would be generated as soon as that time became known. A drive tape based on these predictions would become prime.

Following the uplink acquisition, as early as practicable the antenna drive mode would be changed to auto track. This switch would be done in three steps: the signal on the SAA receiver would be peaked using offsets to the latest available drive tape, auto track would then be accomplished on the SAA, and finally, auto track would be accomplished on the SCM.

V. Initial Uplink Acquisition

The Voyager initial uplink acquisition had been designed with the following criteria in mind:

(1) The uplink should be acquired at the earliest practicable time based on station capabilities and spacecraft trajectory constraints,

(2) The uplink acquisition sweep should span a frequency range and be at a rate that best guarantees acquisition on the first sweep, and

(3) The uplink acquisition should be complete in time to have all stations (particularly DSS 14) ready to receive the critical 7.2 kbps telemetry data.

The following uncertainty information pertaining to the uplink was made available by the Voyager project:

3σ Trajectory	~ 192 Hz (S-Band)
3σ Measurement	~ 1000 Hz (S-Band)
3σ Receiver "Random Walk"	~ 2000 Hz (S-Band)
3σ S/C Temperature	~ 1500 Hz (S-Band)

Combining the above, one arrives at a total 3σ uncertainty of:

3σ Total	~ 2700 Hz (S-Band)
or	~ 28 Hz (VCO)

This uncertainty was extremely small with respect to uncertainties for previous missions (for instance 3σ for Viking was 5300 Hz), therefore, to be extremely conservative (and hence allow for any sort of abnormal launch vehicle or spacecraft performance) and since there was no real impact on tuning duration, the previously described 3σ uncertainty was more than tripled resulting in a sweep of approximately XA ± 9600 Hz (S-Band) or XA ± 100 Hz (VCO).

The Voyager spacecraft receiver tuning rates are bounded by:

$$60 \text{ Hz/sec} < \text{tuning rate} < 1000 \text{ Hz/sec (S-Band)}$$
$$(0.6 \text{ Hz/sec} < \text{tuning rate} < 10 \text{ Hz/sec (VCO)})$$

under the strong signal (-100 dBm) conditions that were to be encountered during the initial pass. For the initial acquisition a sweep rate of 3 Hz/sec (VCO; or 288 Hz/sec at S-Band level) was selected because:

(1) The rate was well above the push limit of the receiver and thus would result in a successful acquisition.

(2) Should it become necessary to manually tune the exciter, it was believed that the station could not accurately tune at a higher rate than the chosen rate.

(3) A rate of 288 Hz/sec (S-Band) would result in an effective (Doppler rates considered) tuning rate of approximately 238 Hz/sec at the spacecraft receiver. This rate was very nearly the geometric mean of the upper and lower sweep rate limits (245 Hz/sec).

The sweep was to start at lift-off plus 78 minutes, approximately 5 minutes after the spacecraft would have risen. This allowed sufficient time for the necessary sideband/sidelobe searches before starting the uplink acquisition.

Finally, the sweep was to consist of a single upleg in the direction of the change of XA, with the ending frequency becoming the TSF for the remainder of the pass. This was advantageous in that no additional tuning to reduce static phase error (SPE) would be required during the remainder of the pass.

Incorporating the preceding information, the general uplink acquisition procedure was:

(1) Transmitter connected to the S-Band Acquisition Aid Antenna (SAA) and set to radiate at 10 kw.

(2) Transmitter on at start of uplink sweep minus 20 seconds.

(3) Radiometric data to be flagged two way at start of sweep minus 10 seconds. (This would enable the NOCT to know when (and if) two-way lock was achieved and whether lock was on the main carrier or a sideband.)

(4) Sweep to start at L+78 minutes or approximately 5 minutes after spacecraft rise.

(5) Sweep to cover at least XA ± 100 Hz (VCO) at a rate of 3 Hz/sec (VCO).

(6) Sweep duration to be approximately 80 seconds.

If the first sweep failed a contingency sweep encompassing a region 50 percent larger (XA ± 150 Hz (VCO)) than the original sweep would be performed, starting 2 minutes and 30 seconds after completion of the first sweep. The contingency sweep would consist of a downleg and an upleg followed by a sweep back to TSF executed continuously with no pauses between legs. (Of course, if two-way was achieved anytime during the contingency sweep the station was to stop tuning, lock the receivers and then tune directly to TSF.) The tuning instructions for both sweeps were to be provided to DSS 12 well before lift-off via a sweep message similar to that shown in Fig. 3.

VI. Ranging

Range data collection for Voyager was to begin shortly after the initial acquisition at DSS 12. Additionally, plans were made to transfer the uplink from DSS 12 to DSS 14 so that ranging could continue for as long as possible.

Originally, it had been planned that the ranging would be done with eighteen component acquisitions interspersed with ten component acquisitions. After the risks inherent in changing range parameters (i.e., possibly significant losses of data) were pointed out to the Voyager project, it was decided to pipeline fifteen component ranging acquisitions separated by three differenced range versus integrated doppler (DRVID) measurements.

The following parameters were to be used:

(1) T1 = 59 seconds

(2) T2 = 2 seconds

(3) T3 = 60 seconds

(4) T0 = 3CCEE

(5) RTLT = 0 seconds

(6) Number of components = 15

(7) Carrier Suppression = 3 dB

VII. Downlink Acquisition at DSS 62

Because of the high declination (41°) of the Voyager 2 trajectory, it was found that DSS 62 would be unable to acquire the spacecraft downlink until the spacecraft reached an elevation of approximately 16°, this being the minimum elevation at which the antenna could be pointed at this declination. On the first pass, this constraint would cause a more than fifty minute gap between the end of track at DSS 44 and the start of track at DSS 62. However, because of the strong signal levels expected during that time, it would be possible to narrow the gap considerably using the SAA. From available information, the threshold of the SAA was computed to be:

-164.4 dBm in the 48 Hz RF Bandwidth

-170.4 dBm in the 12 Hz RF Bandwidth

The signal level at the time of DSS 44 set was expected to be at least -161.4 dBm. Thus, there would be from three to nine decibels of downlink margin. From (very old!) SAA antenna patterns it was found that the angular offsets necessary to reduce the signal level to threshold were:

~8° for threshold in the 48 Hz RF Bandwidth

~15° for threshold in the 12 Hz RF Bandwidth

These offsets translated (assuming sidereal angle rates) to an increase of from 32 to 61 minutes in the view period of DSS 62. Thus, the obvious conclusion was that, by judicious use of the receiver, the downlink could be acquired using the broad (16°) beam of the SAA and at a much lower elevation than that at which the main antenna could even point, thereby reducing the gap in the tracking of the spacecraft and possibly eliminating it completely. The extended coverage is stereographically illustrated in Fig. 4.

It was decided to attempt to close the downlink gap (the gap in the uplink would be tolerated) using the following procedure:

(1) Two sets of predicts would be generated for DSS 62. One set, to be used for driving the antenna, would have the actual horizon mask. The other set would have a zero degree elevation horizon and would be used to compute frequencies for the SAA receiver sweep.

(2) DSS 62 would drive to the specified rise point (as defined by the antenna limits) at least by the time that the spacecraft would reach zero degrees elevation.

(3) At the time of the earliest possible acquisition, DSS 62 personnel would slowly sweep the receiver in the 12 Hz RF bandwidth and attempt to acquire the downlink.

(4) When the spacecraft reached the rise point the SCM receiver would be locked and normal tracking, including an uplink acquisition, would begin.

The coverage gap would continue for several weeks after launch but, unfortunately, this use of the SAA would be restricted to (because of signal level constraints) the first pass.

VIII. Post Launch Analysis

A. Tracking Predictions

1. Prediction Generation. Minutes before the scheduled 14:25:00 GMT lift-off time the Voyager 2 countdown went into a hold that was to last four minutes and 44 seconds. This delay made it imperative that tracking predictions based on the actual lift-off time be generated and made available to the initial acquisition stations prior to spacecraft rise, approximately 70 minutes after launch.

Because of the suddenness with which the hold was initiated and terminated, there was much confusion about what the actual lift-off time was to be. This confusion resulted in the required lift-off PET being delivered approximately fifteen minutes after lift-off.

Thanks in large part to the pre-launch streamlining (Section IIIA), predicts were available approximately twenty minutes before the expected spacecraft rise.

2. Prediction Accuracy. The accuracy of the launch phase predictions (as measured by pseudo-residuals) was very good. The pseudo-residuals, computed in near real-time by differencing radiometric data with the lift-off tracking predictions in the NOCC Tracking Real Time Monitor (RTM), had the following average values during the early portions of the launch pass at DSS 12:

$\Delta HA \cong -0.085$ degrees

$\Delta D2 \cong -130$ Hz (S-Band)

$\Delta XA \cong 8.9$ Hz (VCO)

These differences may be compared to the 3σ uncertainties presented in Sections II and V:

$3\sigma\ \Delta HA \cong 0.309$ degrees

$3\sigma\ \Delta D2 \cong 588$ Hz (S-Band)

$3\sigma\ \Delta XA \cong 30$ Hz (VCO)

As can be seen, all residuals were well within the 3σ uncertainties. The small Hour Angle residual was especially significant in that it facilitated the spacecraft acquisition at DSS 14 by being less than the beamwidth of the 64 meter antenna.

The two way doppler residual continued to increase throughout the pass attaining a value of approximately -169 Hz (S-Band) late in the pass at DSS 12.

The value of the ΔXA was very small considering the many possible sources of error, both trajectory and temperature. The 3σ uncertainty provided by Voyager telecom was thus shown to be very accurate.

B. Initial Downlink Acquisition

The initial downlink acquisition at DSS 12 proceeded very smoothly with acquisition occurring at 15:41:31 GMT or approximately one minute before the expected spacecraft rise time. As can be seen in Figure 5, the receiver was swept through a very wide (approximately 12 KHz) range of frequencies apparently centered at the downlink frequency expected at spacecraft rise and commencing well before rise.

The early acquisition is due to the fact that because of the high declination angle, spacecraft rise was dictated by the antenna mechanical limits (see Figure 1) rather than the local horizon. Thus, it was possible for the SAA to "see" the spacecraft below the antenna limits. Additionally, because of the high signal levels present during this phase it was possible to lock the SCM receiver as the spacecraft passed through the sidelobes of the SCM antenna resulting in acquisition approximately 40 seconds earlier than planned.

C. Initial Two-Way Acquisition at DSS 12

Shortly after lift-off an apparent problem with the spacecraft inertial reference unit gyros was detected by the project. Because of the nature of the problem (the attitude control computer had changed gyro pairs several times), project requested that the DSN acquire the uplink at the earliest possible time to allow for emergency commanding, if it became necessary Since the initial uplink sweep had already been designed to start at the earliest possible time (see Section V) it was decided not to depart from the current (familiar) plan.

The uplink acquisition parameters provided to DSS 12 were:

(1) Transmitter on:	15:47:40	GMT
(2) Transmitter power:	10	KW
(3) Frequency:	22014140.0	Hz (VCO)
(4) Start tuning:	15:48:00	GMT
(5) Tuning rate:	180	Hz/min (VCO)
(6) Tune to:	22014380.0	Hz (VCO)

A comparison of the instructed sweep with the sweep actually performed at DSS 12 is shown in Figure 6. As can be seen, the sweep was performed excellently and closely followed the expected tuning pattern.

The spacecraft receiver was acquired at 15:48:36 GMT, within 10 seconds of the expected time.

The acquisition of the two way downlink did not, unfortunately, proceed as smoothly as that of the uplink. The receiver was quickly relocked (in about 3 seconds) to the coherent downlink. It was soon noticed that the doppler residuals were larger than expected (almost six times the 3σ magnitude) and changing very quickly (see Table 1 and Figure 7).

At 15:49:57 GMT, receiver lock was broken and a sideband search performed. Upon reacquisition of the downlink the doppler residuals showed that the receiver had again locked to a spurious signal. This time, however, the doppler residuals indicated a positive bias but with the same magnitude as those calculated before the sideband search. Additionally, the signal was very noisy with doppler noise averaging more than 11 Hz.

At approximately 16:00:00 GMT, DSS 12 was instructed to perform yet another sideband search. During this search the receiver was swept through a frequency range of approximately 170 KHz (S-Band level) around the expected carrier. When the receiver was relocked at 16:00:30 GMT, the carrier was finally acquired as indicated by a doppler residual of approximately -130 Hz and doppler noise of approximately 0.030 Hz.

The cause of the spurious signals has not been precisely determined. However, it is believed that since:

(1) No other station experienced the same problem

(2) The spurious signals were spaced evenly (approximately 4 KHz) on both sides of the expected carrier frequency

(3) The station reported that they returned to the original frequency after the sideband search

the spurious signals may have been an artifact of the effect of the high signal level on the DSS 12 receiver.

D. Angle Tracking

In accordance with the plan outlined in Section IV, tracking predictions based on the actual lift-off time were generated and transmitted to DSS 12 prior to the expected spacecraft rise time. These predictions were in turn used in the generation of the antenna drive tape used by DSS 12 during the early portion of its pass.

At 15:49:27 GMT, immediately following the completion of the two-way acquisition, DSS 12 went to auto track. However, partly because of the receiver lock on the erroneous frequency, the antenna quickly drifted off point driving a maximum of two degrees from the predicted pointing angle. At 15:49:57 GMT DSS 12 returned to aided track.

After locking to the carrier the drive mode was returned to auto track successfully at 16:02:21 GMT.

Because of a change in the attitude of the spacecraft DSS 12 returned to aided track shortly after 17:11:00 GMT when the signal level fell below the auto track threshold. The station continued to track in this mode for the remainder of the pass.

E. Ranging at DSS 12

Ranging data at DSS 12 was found to be invalid shortly after the ranging sequence was started. Several unsuccessful attempts were made to locate and correct the problem but no obvious problem could be found during the pass.

Later, extensive investigation revealed that the fault was in the rate-aiding circuitry of the Planetary Ranging Assembly and was therefore not detectable in the testing configuration used during the initial Voyager 2 pass.

The loss in ranging data from DSS 12 was somewhat compensated for by the short period of ranging at DSS 14.

F. Summary of Events at DSS 14

DSS 14 became the first 64 meter station to acquire the Voyager spacecraft at 15:41:52 GMT, within 20 seconds of the acquisition by DSS 12. The ease of the lock-up allayed fears that, because of the narrow beamwidth of the antenna and the large uncertainties in the near earth trajectory, DSS 14 would not acquire in time to receive the high rate (7.2 KB/s) telemetry data.

Due to an error in entering the correct subcarrier demodulator assembly (SDA) frequency during the generation of the tracking predictions, the major portion of this data was lost. DSS 14 was able to lock the SDA after approximately 28 minutes after discovering a 40 KHz error in the frequency. During the data outage at DSS 14, the MIL 71 tracking station provided the high rate telemetry data.

Following the transfer of the uplink from DSS 12, DSS 14 began ranging at 19:47:00 GMT. The ranging data was good and provided the project with important near earth data.

DSS 14 continued tracking until 22:05:00 GMT.

G. Downlink Acquisition at DSS 62

The attempt to close the downlink gap between DSS 44 and DSS 62 by using the SAA met with only marginal success. During the Titan burn, the spacecraft switched to its secondary attitude control processor. Because of this unexpected change, the project decided to delay the acquisition of the stellar reference, Canopus, until the contents of the processor could be examined. This decision left the spacecraft in a less than optimum attitude. The resultant degradation in signal level severely impacted the "off point" tracking scheme described in Section VII.

The antenna at DSS 62 was driven to the antenna mechanical prelimits well before the expected time of spacecraft rise. At 22:57:00 GMT, approximately five minutes earlier than expected, the downlink signal was detected but at too low a level to maintain receiver lock. Continuous receiver lock was finally achieved at 23:27:00 GMT but at a signal level (-170 dBm) well below telemetry threshold. At the time of continuous receiver lock, the spacecraft was still nine degrees away from the main beam of the SCM antenna. Because of the unfavorable attitude of the spacecraft, telemetry was not received until the SCM receiver could be locked at 00:02:00 GMT.

It is apparent, then, that had the spacecraft been aligned as planned, the SAA could have been successfully used to close the gap between DSS 44 and DSS 62.

IX. Conclusion

The Voyager 2 launch and near earth phases were marked by spacecraft and data acquisition problems resulting in an inauspicious beginning for the Voyager mission.

The DSN tracking procedures and in particular the initial acquisition procedures, having been conservatively designed to encompass any launch contingency, significantly contributed to the successful completion of this phase of the Voyager mission.

References

1. Berman, A.L. and J.A. Wackley, "Tracking Operations During the Viking 1 Launch Phase," in *The Deep Space Network Progress Report*, 42-30, pp. 273-290, Jet Propulsion Laboratory, Pasadena, Calif., December 15, 1975.

2. Bright, L.E., "Tracking Operations During the Helios 2 Launch Phase," in *The Deep Space Network Progress Report*, 42-32, pp. 277-295, Jet Propulsion Laboratory, Pasadena, Calif., April 15, 1976.

Table 1. DSS 12 doppler residuals

GMT	Doppler Residual, Hz	Comment
15:47:29	+1077.1	Last good one-way residual
15:48:00	−11947.7	Start uplink tuning
15:48:36	−1571.8	Two-way uplink acquired
15:48:37	−1958.9	Receiver out of lock
15:49:25	−3325.1	Tuning completed; in lock on spurious signal
15:49:46	−3499.9	In lock on spurious signal
15:50:05	−14533.9	Sideband search; maximum excursion
15:50:33	+3192.6	Receiver in lock on spurious signal following first sideband search
15:52:00	+3025.8	Still on spurious signal
15:54:00	+2976.7	Still on spurious signal
15:56:00	+2944.5	Still on spurious signal
15:58:00	+2909.2	Still on spurious signal
16:00:01	−9789.1	Start second sideband search
16:00:06	−162635.9	Maximum negative excursion
16:00:17	+172736	Maximum positive excursion
16:00:29	−130.5	Receiver in lock on carrier
16:01:00	−134.3	Receiver in lock on carrier
16:03:00	−145.4	Receiver in lock on carrier

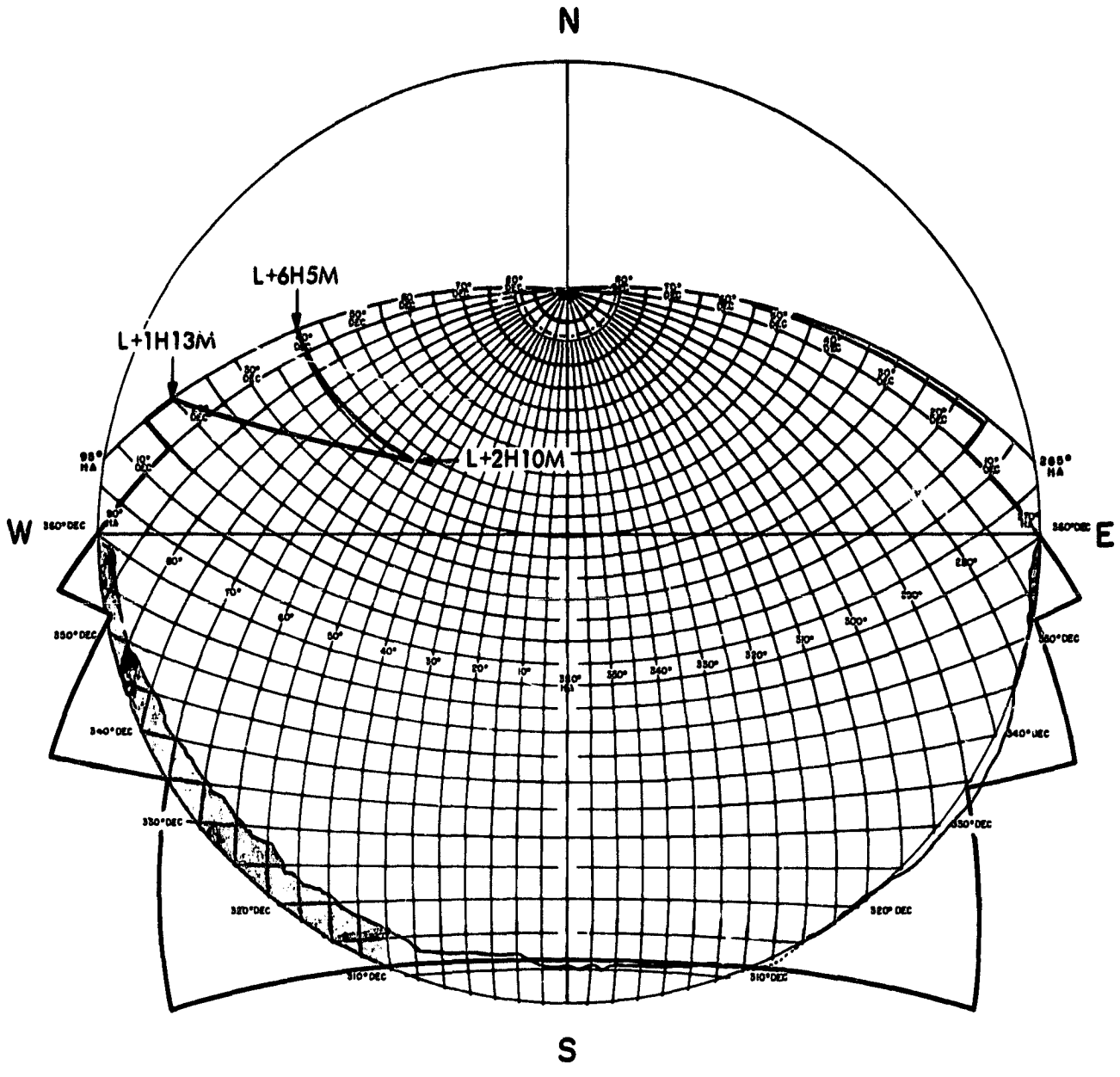

Fig. 1. DSS 12 Voyager 2 launch, 20 August 1977

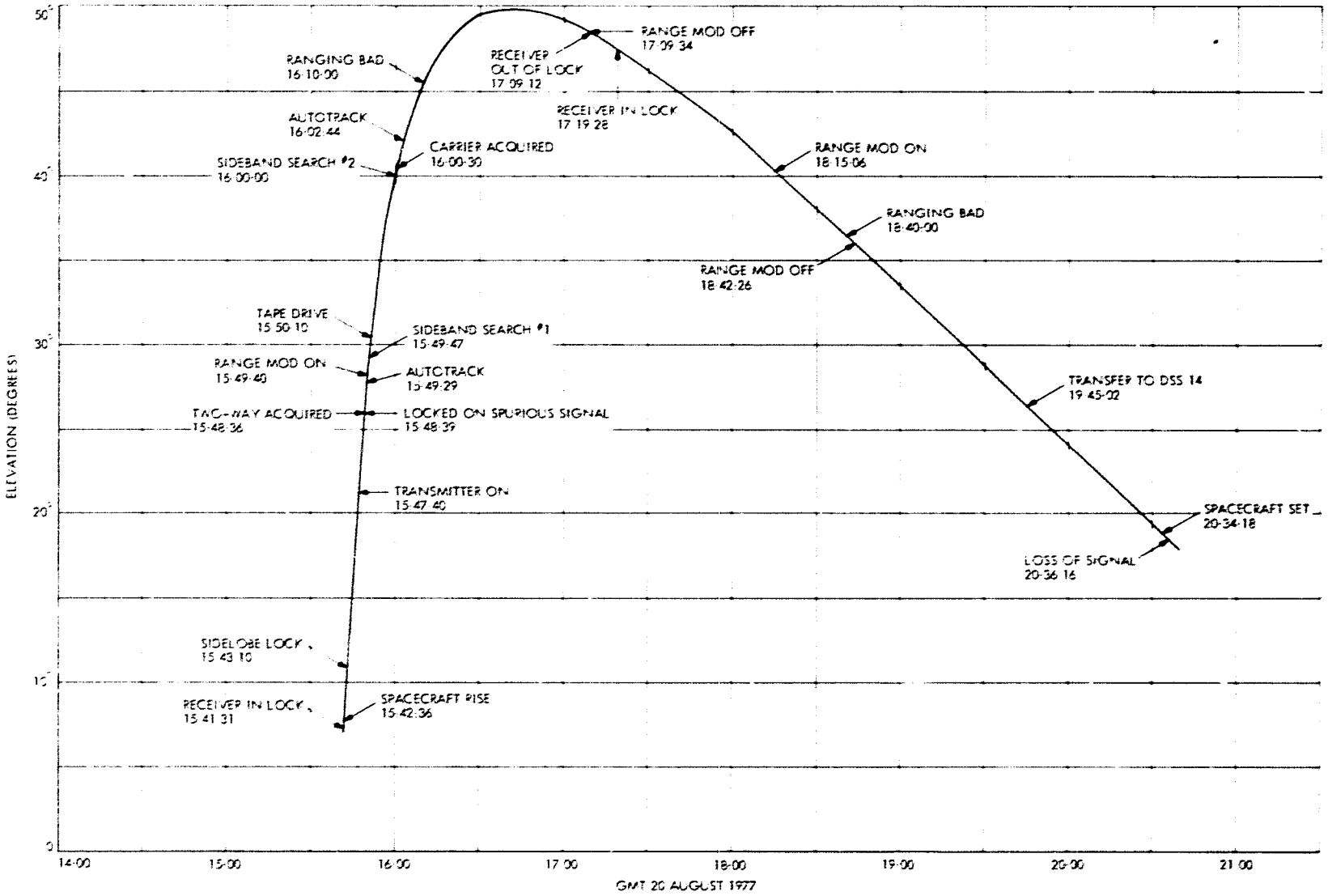

Fig. 2. Spacecraft elevation at DSS 12, Voyager 2 launch

ORIGINAL PAGE IS
OF POOR QUALITY

VOYAGER 2 INITIAL ACQUISITION DSS-12 VERSION 3

A. PREDICTS			
1. TEXT:	X205		IS PRIME
2. DRIVE TAPE:	X205		IS PRIME
3. HA BIAS:	—		DEG
4. DEC BIAS:	—		DEG
5. MAX HA RATE:	−2.84	DEG/MIN AT 15:42:48	GMT
6. MAX DEC RATE:	+2.17	DEG/MIN AT 15:42:48	GMT
7. APS TIME BIAS:	—	H — M — S	
B. INITIAL UPLINK ACQUISITION			
8. TXR ON:	15:47:40		GMT
9. TXR PWR:	10		KW
10. TSF 1:	22014140.0		HZ
11. START TUNING:	15:48:00		GMT
12. TUNING RATE:	+180		HZ/MIN (VCO)
13. TSF 2:	22014380.0		HZ
14. CMD MOD ON:	15:49:30		GMT
15. RNG MOD ON:	15:49:40		GMT
C. CONTINGENCY SWEEP: EXECUTE ONLY IF DIRECTED			
16. START TUNING:	15:52:00		GMT
17. TUNING RATE:	180		HZ/MIN (VCO)
18. SWEEP DOWN TO:	22014180.0		HZ
19. SWEEP UP TO:	22014500.0		HZ
20. SWEEP DOWN TO TSF:	22014380.0		HZ
21. CMD MOD ON:	15:51:00		GMT

D. RANGING PARAMETERS

TO: 3CCEE T1: 59 T2: 2 T3: 60

RTLT: 0 COMPONENTS: 15

SPECIAL INSTRUCTIONS: CARRIER SUPPRESSION = 3dB

Fig. 3. Actual uplink acquisition message, Voyager 2 launch

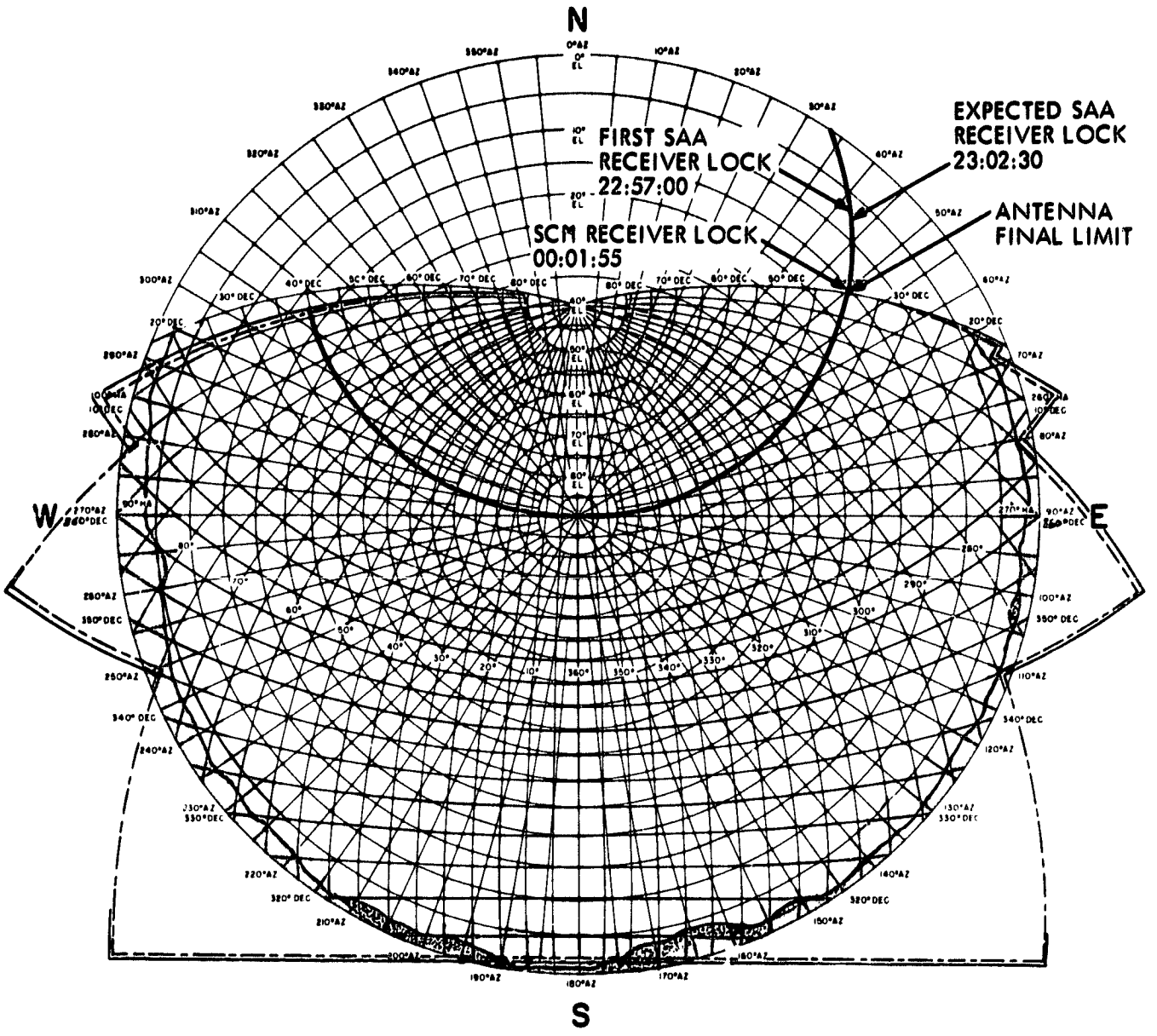

Fig. 4. DSS 62 Voyager 2 launch, 21 August 1977

ORIGINAL PAGE IS
OF POOR QUALITY

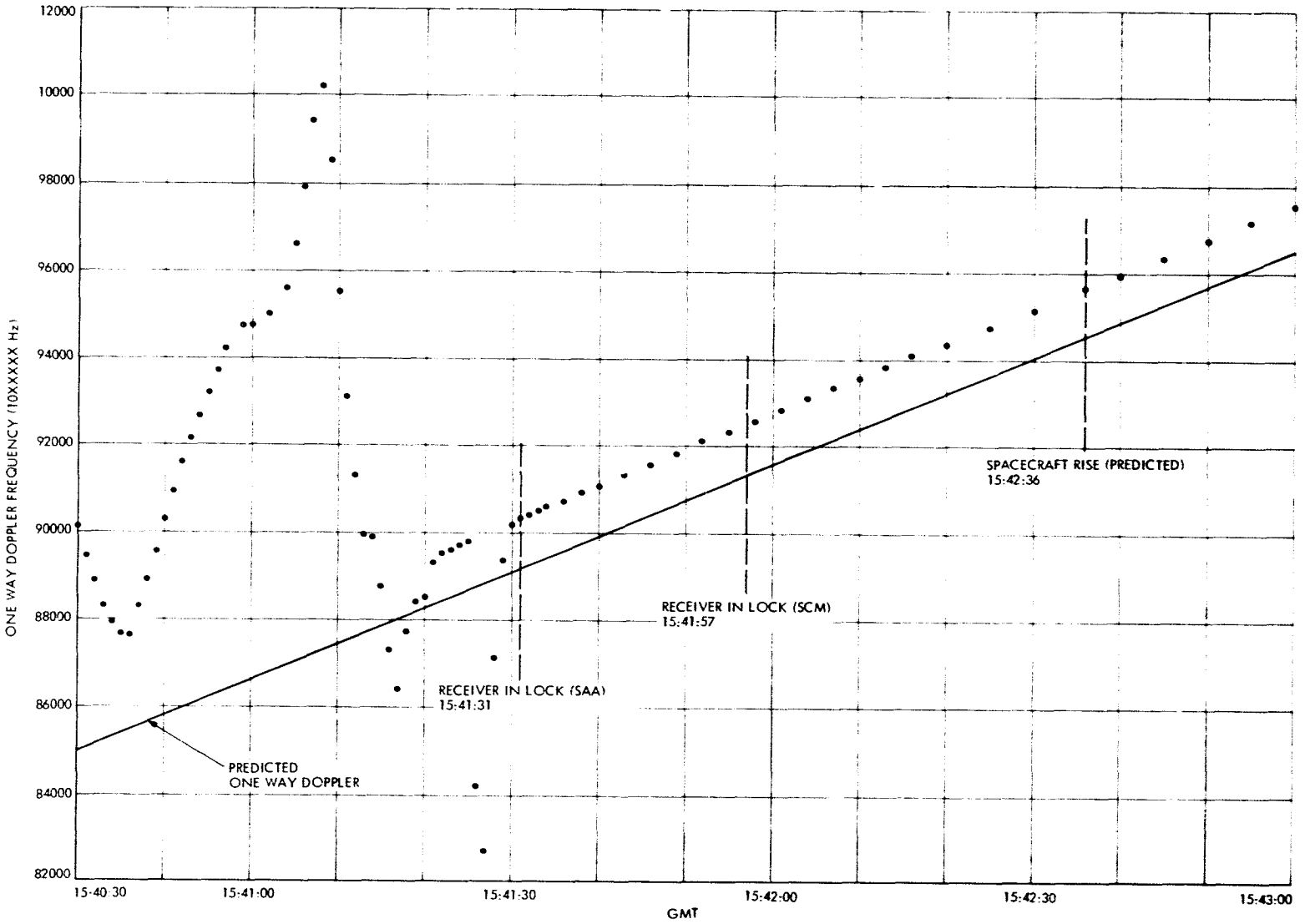

Fig. 5. Initial downlink acquisition at DSS 12, Voyager 2 launch

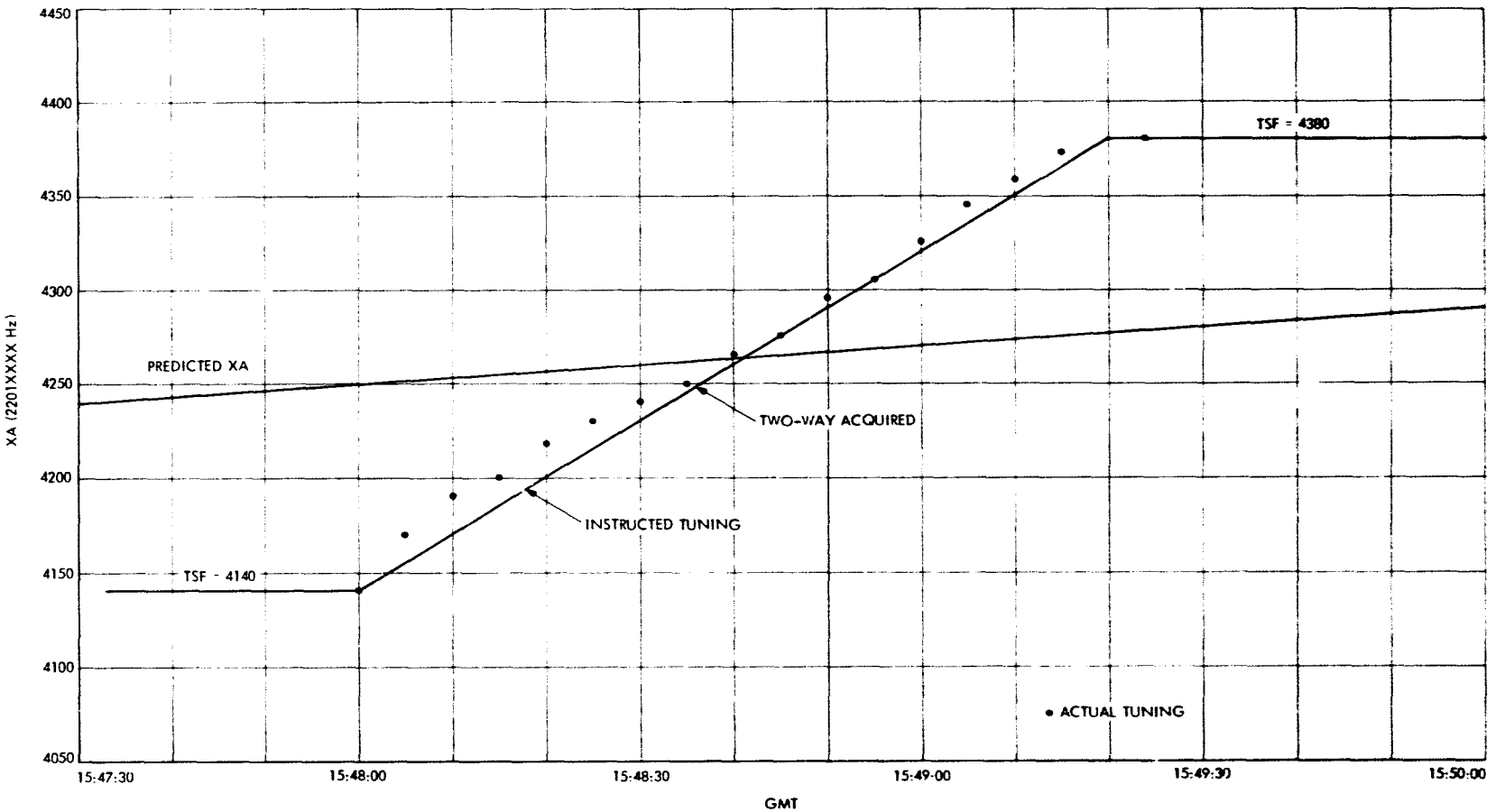

Fig. 6. Comparison of actual versus instructed tuning at DSS 12 Voyager 2 launch

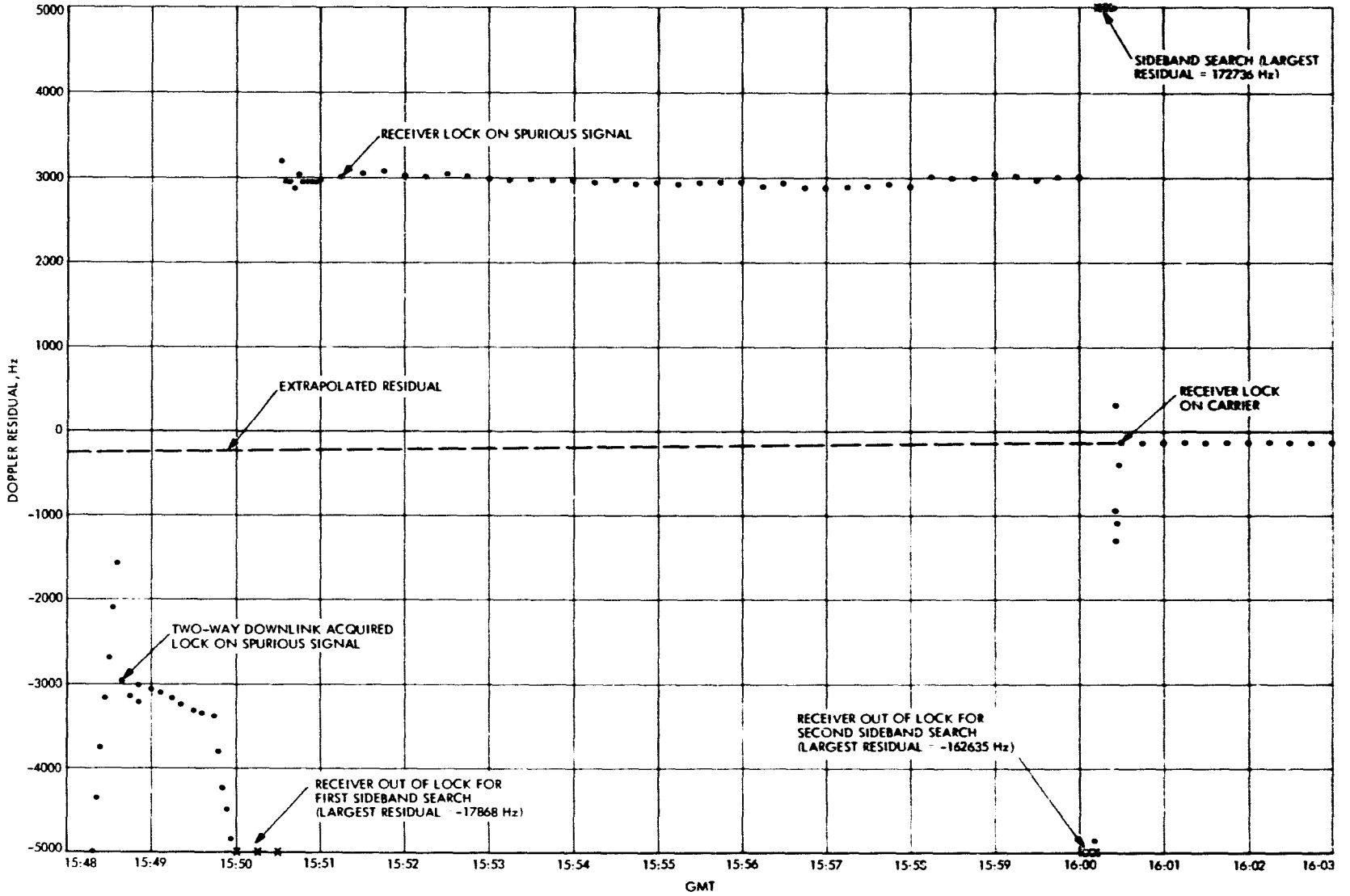

Fig. 7. Two-way doppler residuals at DSS 12, Voyager 2 launch

N78-24244

An Effective Procurement and Financial Management Reporting System

J. B. Rozek and F. R. Maiocco
Deep Space Network Support Section

This article describes the existing computerized Goldstone Procurement and Financial (GPF) management data base system. Sample management analysis reports are included and discussed along with estimated cost savings and anticipated benefits of the computerized system. In general, the system structure and procedures contained in this article are relevant to any company's financial and procurement data acquisition and information handling system. Test data are used throughout this report to demonstrate the capability of the GPF system of programs.

I. Introduction

The general view of the existing computerized GPF Data Management System is shown in Fig. 1 and discussed in Ref. (1). Figure 1 briefly indicates that the GPF user has the capability to input pertinent data to the data base and receive various GPF reports via a remote computer terminal. All information handling, updating, sorting, searching of files, storage and report generation is performed by the computer. The table, report, and figure numbers noted in Fig. 1 pertain to the respective items in this article.

Several major files are required to accommodate the GPF data and to provide the essential statistics for a requested management report. The pertinent files are a Purchase File, Cost Center File (COC), Budget File, Vendor File, JPL File, Stock Issue File (SIS) and Disbursement File (DISB). The record structure of these respective files are shown in Tables 1 to 7 and sample computer status codes for Purchase Requisitions (PR) and Purchase Orders (PO) are listed in Table 8.

The developed system of programs (file generator, updating and report writers) is user oriented. Prompting information for the user is available to minimize development of an extensive user training program and permits front-end editing to improve data base integrity.

The subsequent sections of this article discuss the management application programs. Initially nine application programs were developed for monitoring procurement and financial matters at Goldstone; and they are:

(1) GDSCC Procurement Accomplishment Report:

Part I: Purchase Requisition Report
Part II: Purchase Order Report.

(2) Commitment Category Summary Report.

(3) Business Subcontracting Report:

Part I: Small Business Report
Part II: Large Business Report.

(4) Purchase Requisition Status Report.

(5) Monthly Specified Account Report.

(6) Monthly Specified Cost Center Report.

(7) Specified Account Budget Report.

(8) Specified Cost Center Budget Report.

(9) An All Account Budget Report.

These report programs satisfy the requirements of Ref. (1), and utilization of these reports by the managers/users insures that they will gain better visibility in procurement and financial matters of their particular cost center, account, and/or budget.

II. Description of Report Writer Programs

The first four reports noted above essentially are workload related and summarize the activity performed by the GPF group during a particular reporting period. The remaining five reports (numbers 5 through 9) are financial type reports in that monies are related to specific accounts, cost centers, and budgets.

A. The GDSCC Procurement Accomplishment Report

This two-part report contains PR and PO information in reference to PRs received, outstanding PRs, POs processed and outstanding POs for any specified period of time.

The following detail information is provided to the user for the specified reporting period.

1. Part I: Purchase Requisition Report (Fig. 2).

(1) The total number of PRs received in a given month with further breakdown by PR Number and Status (routine, urgent, etc.)

(2) The total number of outstanding PRs with further breakdown by PR number and Status (routine, urgent, etc.)

(3) The committed dollar value per outstanding PR.

PRs that have committed dollar values of $0.00 indicate as a minimum that the PR is either cancelled or the received PR became a PO or at the time of data entry the dollar value of the outstanding PR was unknown.

(4) The total committed dollar value.

This report briefly informs the user of input transactions to the GPF unit and identifies additional workload for both the procuring agent and the data entry clerk. A cursory view of Fig. 2 informs the user, for example, that three urgent PRs are outstanding and eight outstanding PRs were written prior to the reporting period under investigation. Should an outstanding PR have no dollar value listed, further investigation by the user is required in order to determine the accuracy of the estimated total committed dollar value. Management may view that a significant number of outstanding PRs indicate potential problems in workload, personnel or training, and thus institute policies and procedures to improve organizational efficiency.

2. Part II: Purchase Order Report (Figs. 3 and 4).

a. Purchase orders released (Fig. 3). This part of the report identifies the total number of POs written in a given month. It highlights a further subcategorization by status to five (5) classes of Purchase Orders per management's request (Routine, Urgent, Blanket Contract, Subcontract, and Petty Cash). It identifies a portion of the procuring agent's work load, the individual dollar value per PO and the total dollar value handled per reporting period.

b. Outstanding purchase orders (Fig. 4). This portion of the report identifies the total number of outstanding POs per reporting period, the identical subcategorization by status as described above, the individual dollar value per PO and the total obligated dollar value per reporting period.

The buyer should follow up on POs where dollar values are missing in order to insure proper data base updating. This is essential for accurate financial reports.

Reviewing Figs. 2 and 3, the manager/user can assess the GPF work unit's efficiency by creating an efficiency ratio (outputs to inputs), i.e., POs processed to PRs received or outstanding. A closer review of Figs. 3 and 4 indicates that three (3) Purchase Orders (222222, 338620, 888888) were written in March '76 and closed out. Therefore they do not appear on the outstanding PO report.

B. The Commitment Category Summary Report (Fig. 5)

This report contains procurement commitments in various dollar value categories. The following detail information is provided to the user:

(1) The number and dollar value of transactions valued from $0 – 500.

(2) The number and dollar value of transactions valued from $501 – 1,000.

(3) The number and dollar value of transactions valued from $1,001 – 2,500.

(4) The PO number, PO date, Vendor name and dollar value of the respective contract valued from $2,501 – 10,000.

(5) The PO number, PO date, Vendor name and dollar value of the respective contract valued from $10,001 – 25,000.

(6) The PO number, PO date, Vendor name and dollar value of the respective contract valued from $25,001 – 100,000.

(7) The PO number, PO date, Vendor name and dollar value of the respective contract valued over $100,000.

(8) The total obligated dollar value per reporting period.

The sample printout also indicates to the user that there exists in the data base possible erroneous vendor codes for certain PO numbers. This part of the printout is an editing clue to the user that either (1) the Vendor file must be updated to include the noted vendor codes or (2) the vendor code for the particular PO number identified must be corrected. Hence once these corrections are made an accurate report can then be recreated.

C. The Business Subcontracting Report (Figs. 6 and 7)

This two-part report reflects the number of contracts and their dollar value above and below $10,000 with respect to large and small businesses. The category of a business, large or small, is determined before data is entered into the Vendor File (see Table 4). This report satisfies a NASA requirement for the GDSCC Contractor.

The following information is provided to the user:

1. Part I: Small Business Subcontracting Report (Fig. 6).

a. Contracts under $10,000. The number of contracts and total dollar value under $10,000 awarded to small businesses with a further breakdown by Purchase Order number, Vendor name and the respective dollar amount are identified.

b. Contracts over $10,000. The number of contracts and total dollar value over $10,000 awarded to small businesses with a further breakdown by Purchase Order number, Vendor name, and the respective dollar amount are identified.

The total number of contracts and the total dollar value awarded to small businesses are summarized at the end of this part of the report.

2. Part II: Large Business Subcontracting Report (Fig. 7).

a. Contracts under $10,000. The number of contracts and total dollar value under $10,000 awarded to large businesses with a further breakdown by Purchase Order number, Vendor name and the respective dollar amount are identified.

b. Contracts over $10,000. The number of contracts and total dollar value over $10,000 awarded to large businesses with a further breakdown by Purchase Order number, Vendor name and the respective dollar amount are identified.

The following summary items are tabulated at the end of Part II of this report.

(1) The total number of contracts and the total dollar value awarded to large businesses.

(2) The combined total number of contracts and the overall total dollar value awarded in the reporting period to both small and large businesses.

(3) The percentage of total contracts awarded to small businesses.

(4) The percentage of total contracts awarded to large businesses.

(5) The percentage of total dollar amount awarded to small businesses.

(6) The percentage of total dollar amount awarded to large businesses. Notice the similar data base error message for the user (see comment in Subsection B).

D. Purchase Requisition Status Report (Fig. 8)

This report gives the status of a specific PR as documented in the data base. The following information is provided to the user:

The number of items on the specified PR and the cost center involved. The PR Status Report is divided into three parts. It is possible, depending on the number of items and the procurement status of each item on the PR, that any combination of the following three parts of this printout can occur.

Part 1: If no Purchase Order has been written for a particular line item then this portion of the printout identifies PR data such as: the total cost, the item's status (routine, urgent, etc.), quantity requested, date Purchase Requisition was received and the account involved.

Part 2: If a Purchase Order was written for a particular line item but the item has not been received, this portion identifies

the status of the item (routine, urgent, etc.); the total cost, quantity ordered, Vendor promised date, Purchase Order date, Purchase Order number, PR and PO item numbers, Vendor's name, phone number and appropriate contact.

Part 3: If a particular line item was received or partial shipment of an item was received, this portion identifies the status of the item, quantity ordered, quantity received, receiving date, Receiving Report number, Purchase Order number, and PR and PO item numbers. For partial shipments received, the Vendor's name, phone number and appropriate contact are identified per PR item.

Figure 8 is a sample Status report for a PR as of 15 December 1977. Three items were on the original PR. The Status Report indicates that item 2 has not been placed on a PO, and items 1 and 3 were procured, i.e., POs were written. The example further indicates a partial shipment of PR item 1 and a possible overshipment of PR item 3.

E. Monthly Specified Account Report (Fig. 9)

This report provides the financial status of a specific account for a given month. The following information is provided to the user:

The total of committed, obligated and incurred dollar values of the specified account for a given month with a further breakdown of each cost center charging to that specific account. With this type of data, management becomes cognizant of the total financial activities per account and cost center. For example, the Carpenter Shop was charged with $1,230 worth of Stock Issues. This amount is approximately 43 percent of the total financial activity for account 11122.

F. Monthly Specified Cost Center Report (Fig. 10)

This report provides the total of committed, obligated and incurred dollar values of a specified cost center for a given month. Obviously, if more than one account is used by the particular cost center, the individual accounts would contain similar type of information.

G. Budget Reports

The following three reports (Figs. 11, 12 and 13) provide the cost center manager, administrative assistant, or section manager status information of accounts and budgets under his (her) cognizance. In a very succinct format these reports display the burdened budget, its balance in actual dollar value, the balance in projected dollar value and the balance in estimated dollar value, i.e. the pertinent data required by a manager to make sound financial decisions.

To determine the balance in actual dollar value (ADV) for a particular cost center's budget (Bc), Lab Burden (LB) and G & A, in percent, are required inputs to the program. Hence the balance in actual dollar value (column 8 of the printouts) is determined as follows:

$$ADV = Bc - \{ DISB \cdot \alpha + (DSIS + DJPL) \cdot \beta \}$$

where:

DISB = total disbursements via M&O Contractor (col 5)

DSIS = total disbursements of Stock Issues (col 3)

DJPL = total disbursement via JPL (col 4)

$$\alpha = \left(1 + \frac{G\&A + LB}{100}\right)$$

$$\beta = \left(1 + \frac{LB}{100}\right)$$

Having determined the balance in ADV for any cost center's budget, the balance in projected dollar value PDV (col 9), is determined as follows:

$$PDV = ADV - \text{obligated dollar value}$$
$$= \text{col (8)} - \text{col (6)}$$

where the obligated dollar value is defined as the cumulative dollar value of unpaid purchase orders for the particular cost center.

This number essentially tells the user that if customer billing and company disbursements were made instantaneously, the actual amount of the budget left for other procurement is PDV.

The balance in estimated dollar value, EDV col (10), is determined as follows:

$$EDV = PDV - \text{committed dollar value}$$
$$= \text{col (9)} - \text{col (7)}$$

where the committed dollar value is defined as the cumulative dollar value of outstanding purchase requisitions for the particular cost center.

Similar procedures are followed to determine the results for a specific account or all accounts. Obviously the user will quickly determine whether or not a particular budget is (can be) overrun by observing EDV.

1. The Specified Account Budget Report (Fig. 11). This report provides the financial condition of a specified-account in reference to its budget.

The following detail information is provided to the user for each cost center charging to the specific account:

- Cost Center Identification Code
- Burden Budget
- Incurred Dollar Value
  - Stock Issue (SIS) dollar value
  - JPL Purchase dollar value
  - Disbursement charges
- Obligated Dollar value
- Committed Dollar value
- Balance
  - Actual Balance of the cost center budget
  - Projected Balance of the cost center budget
  - Estimated Balance of the cost center budget

Having printed the above information per cost center, the following summary information is provided to the user for the specified account.

- Total Burden Budget
- Total Stock Issue (SIS) dollar value
- Total JPL Purchase dollar value
- Total Disbursement charges
- Total Obligated dollar value
- Total Committed dollar value
- Total Actual Balance of the account budget
- Total Projected Balance of the account budget
- Total Estimated Balance of the account budget

For example, one will note that 10 percent (133,576 actual $ value) of the total budget for account 111222 was spent as of the report date. Approximately 4.8 percent of 133,576 was used for SIS, 1.3 percent for JPL disbursements, and 3.5 percent for M&O Contractor disbursements. The carpenter shop spent 40 percent of its budget (3 months into fiscal year) while the Repro shop only disbursed four percent of its budget.

At the end of the report, the cost centers are identified for the benefit of the user.

2. The Specified Cost Center Budget Report (Fig. 12). This report identifies the financial condition of a specified Cost Center in reference to its budget. The following detail information is provided to the user:

- Account Number(s)
- Burden Budget per account
- Incurred Dollar Value
  - Total Stock Issue (SIS) dollar value
  - Total JPL Purchase dollar value
  - Total Disbursement (DISB) charges
- Total Obligated dollar value
- Total Committed dollar value
- Balance
  - Total Actual Balance of the account budget
  - Total Projected Balance of the account budget
  - Total Estimated Balance of the account budget

3. All Accounts Budget Report (Fig. 13). This report summarizes the financial condition of all accounts in reference to their respective budgets for which GDSCC Procurement/ Financial Planning is responsible. This report will be extensively used during budget iterations and financial planning at Goldstone.

The following information is provided to the user by accounts:

- Cost Center Identification Code
- Burden Budget
- Incurred Dollar Value
  - Stock Issue (SIS) dollar value
  - JPL Purchase dollar value
  - Disbursement charges
- Obligated dollar value
- Committed dollar value
- Balance
  - Actual Balance of the cost center budget
  - Projected Balance of the cost center budget
  - Estimated Balance of the cost center budget

ORIGINAL PAGE IS
OF POOR QUALITY

Summarized at the end of each account's printout is the following account information:

Total Burden Budget

Total Stock Issue (SIS) dollar value

Total JPL Purchase dollar value

Total Disbursement charges

Total Obligated dollar value

Total Committed dollar value

Total Actual Balance of the account budget

Total Projected Balance of the account budget

Total Estimated Balance of the account budget

This report is a true reflection of the budgets from the beginning of the fiscal year to date. To assist the user in appropriate financial planning decisions, a printout of outstanding PRs and POs are available at the user's request, see Figs. 14 and 15. Similar backup information is available to the user upon termination of reports 5 and 7. To reiterate, the purpose of such backup printouts is to assist the Section manager, cost center supervisor or administrative assistant in their financial management decision making process. Obviously the above reports, Figs. 11, 12 and 13, give the overview of a particular budget – i.e. overspent, underspent, or balanced. The utility of these backup printouts are left to the GPF financial and management users to establish.

III. Estimated Preliminary Savings and Anticipated Benefits

The manual procurement and financial data management system as documented in Ref. (1), consisted of 2 JPL personnel and 4 Contractor personnel. Discussions with GDSCC's Administrative Assistant reveals that plans for conversion to the computerized GPF data base system has resulted in a manpower reduction of one JPL and one Contractor type effective FY 78. Reduction was in Senior type personnel. Estimated annual burdened manpower savings is $80k which is based on $50k per JPL MY and $30k per M&O Contractor MY.

Operations costs for the GPF unit, however, must increase by approximately $12k per year to account for computer services on the Univac 1108 system plus an additional $3k per year for Software maintenance and support.

It was determined during FY 77 by GPF Contractor management that it took approximately two people one week (1/2MM) to prepare an average financial/procurement report. This time includes file searching, sorting, data acquisition, data verification, processing and report preparation. The burdened hourly rate for M&O Contractor manhours is approximately $14.42/hr. Eight reports are required four (4) times a year and the average cost per report is $1154. The annual preparation cost for these eight GPF financial reports, four times per year, is approximately $37k.

Average report preparation time in the current automated GPF data base system and the computerized Facility Management System is four to five minutes. The maximum cost of a report generated in the Facility Management System according to users was $50. Assuming that the average cost per report in the GPF data base does not exceed $50 then the estimated cost of preparing the identical reports four times a year is $1600 (approximately $2k per year). The $35k or equivalent manhour savings due to computer generated reports can then be applied to other necessary tasks.

From a marginal cost analysis point of view, the net annual dollar savings are shown below.

$ 80k	Manpower Reduction – Annual cost savings
+35k	Est. Annual Report Preparation cost savings ($37k-$2k)
$115k	Subtotal Annual Savings
-15k	Additional Annual Cost for Computer Services
$100k	Est. Net Annual Savings

In noninflated dollars this estimated net savings is equivalent to $1.0 million over a ten-year life time of the system. Actual development costs of this computerized data base system is approximately $90k. The software package is operational and has been demonstrated during the past year. For the GPF System to be operational, certain essential data files must be generated and the PR files updated as required. It is estimated that initial cost to create the basic files for a viable GPF data base is less than $10k. Hence, indications are that the computerized GPF data management system will pay for itself in less than one year once the decision has been made to proceed with final implementation.

Notably, there are other benefits at present which cannot be quantified monetarily. These anticipated benefits are as follows:

(1) Basically nonexisting computational errors.

(2) An inherently reliable data base.

(3) Timely and pertinent procurement and financial information for management decisions.

(4) Expanded financial reporting capabilities not previously available in the GPF manual data management system.

(5) Improved control and visibility of budget and accounts data.

Reference

1. Maiocco, F. R. and J. B. Rozek, "An Approach to Improve Management Visibility Within the Procurement and Financial Group at Goldstone," in *The Deep Space Network Progress Report 42-35*, pp. 171-179, Jet Propulsion Laboratory, Pasadena, California, October 15, 1976.

Table 1. Purchase Requisition, purchase order and Receiving Report record layout

Item	Array name	Field size	Format
Account[a]	ACC	5	N
Cost center	COC	4	A/N
Purchase requisition number	PRN	6	N
Purchase requisition date	PRD	6	N
Purchase requisition receiving date	RED	6	N
Quantity requested[a]	QRE	7	N
Unit of measurement[a]	UNM	2	A
Item number	ITE	2	N
Unit price[a]	UPR	10	N
Status[a]	STA	1	A/N
Revision	REV	1	N
Purchase order number[a]	PON	6	N
Purchase order date	POD	6	N
Vendor promise date	VPD	6	N
Vendor code	VEN	4	A/N
Quantity ordered[a]	QOR	7	N
Unit of measurement[a]	UMO	2	A
Purchase order item number	ITM	2	N
Purchase order unit price[a]	UPO	10	N
Receiving report number	RRN	6	N
Receiving date	RCD	6	N
Quantity received	QRC	7	N
Unit of measurement	UMR	2	A

[a]Stored date of record items can be updated.

Table 2. Cost center record layout

Item	Array name	Field size	Format
Cost center[a]	COC	4	A/N
Cost center name[a]	CCN	22	A
Account[a]	ACC	5	N
Cost center status[a]	CCS	1	A

[a]Stored data of record items can be updated.

Table 3. Budget record layout

Item	Array name	Field size	Format
Cost center[a]	COC	4	A/N
Cost center name[a]	CCN	22	A
Account[a]	ACC	5	N
Budget[a]	FYB	8	N
Budget entry date[a]	BED	6	A
Budget revision date[a]	BRD	4	A
Cost center status[a]	CCS	1	A

[a]Stored data of record items can be updated.

Table 4. Vendor record layout

Item	Array name	Field size	Format
Vendor code[a]	VC	4	A/N
Vendor name[a]	VN	36	A
Address[a]	VA	36	A/N
Zip code[a]	VZ	5	N
Vendor size[a]	VS	1	A
Vendor rating[a]	VR	2	A/N
Vendor phone number[a]	VP	10	N
Vendor contact[a]	VCT	15	A

[a]Stored data of record items can be updated.

Table 5. JPL record layout

Item	Array name	Field size	Format
Account	ACC	5	N
Cost center	COC	4	A/N
Dollar amount	DOL	9	N
Date of entry	DOE	6	A

ORIGINAL PAGE IS
OF POOR QUALITY

Table 6. SIS record layout

Item	Array name	Field size	Format
Account	ACC	5	N
Cost center	COC	4	A/N
Dollar amount	DOL	9	N
Date of entry	DOE	6	A

Table 7. Disbursement record layout

Item	Array name	Field size	Format
Purchase order number	PON	6	N
Cost center	COC	4	A/N
Invoice number	INU	10	A
Invoice date	IDA	6	N
Freight charges	FCH	8	N
Check number	CNU	8	A
Date paid	DAP	6	N
Dollar value	DOV	11	N

Table 8. Status codes

Status code	Description
0	Routine
1	Urgent
2	Fixed price contract
3	Blanket contract
4	Construction contract
5	Time material contract
6	Labor hours contract
7	Contract
8	Petty cash
9	Quotation
X	Cancellation

ORIGINAL PAGE IS
OF POOR QUALITY

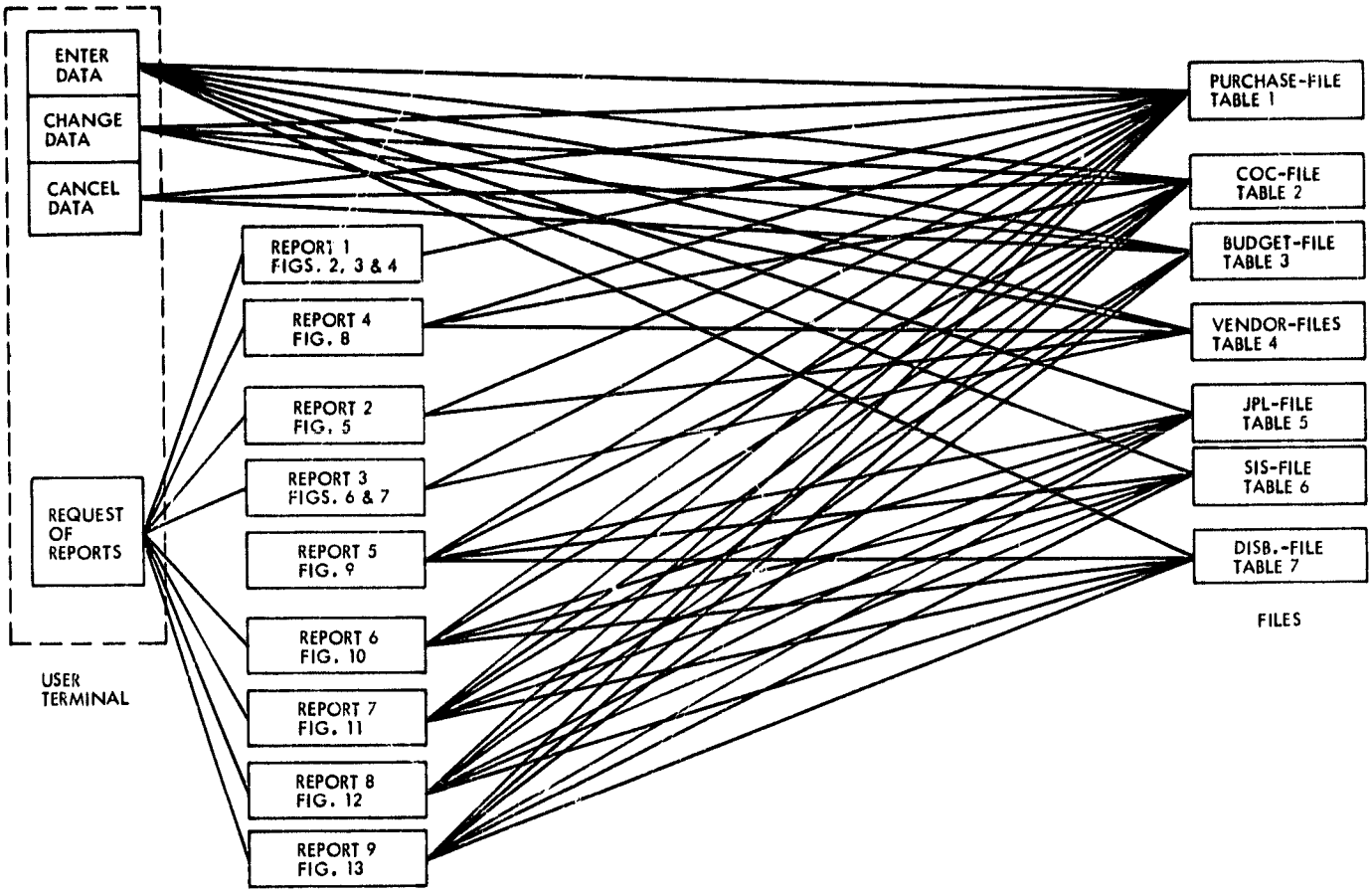

Fig. 1. An overall profile of the automated GDSCC financial/procurement system

TODAYS DATE: 15 DEC. 77

GDSCC PROCUREMENT ACCOMPLISHMENT REPORT

BEGINNING PERIOD:0176 ENDING PERIOD:0376

PART I: PURCHASE REQUISITION REPORT

PURCH.REQ.S RECEIVED IN: 0376 XXXXXX OUTSTANDING PURCH.REQ.S OF TOT.PERIOD

PURCH. REQ. NUMBER	RTN	URGENT	CANC	RTN	URGENT	OUOT	COMMITTED DOLLAR VALUE
111342	0	0	1	0	0	0	0.00
118833	1	0	0	1	0	0	3.35
156822	1	0	0	0	0	1	975.20
235489	0	0	0	1	0	0	277.69
238933	1	0	0	1	0	0	1282.71
254823	0	0	0	1	0	0	7.50
312142	0	0	0	1	0	0	630.00
313155	0	0	0	1	0	0	362.64
341871	1	0	0	0	0	0	0.00
381648	1	0	0	0	0	0	0.00
416281	1	0	0	0	0	1	2050.78
444555	0	1	0	0	1	0	134.75
517297	0	0	0	1	0	0	2.00
565924	1	0	0	0	0	0	0.00
575757	0	0	0	0	1	0	567.84
624113	0	0	0	1	0	0	345.00
648211	0	0	0	0	1	0	5.00
816412	1	0	0	0	0	0	0.00
TOTAL	8	1	1	8	3	2	

TOTAL PURCHASE REQUISITIONS RECEIVED IN 0376 : 10
NUMBER OF OUTSTANDING PURCHASE REQUISITIONS INCL 0376: 13
TOTAL COMMITTED DOLLAR VALUE IN K-DOLLARS: 6.644

Fig. 2. GDSCC Procurement Accomplishment Report

ORIGINAL PAGE IS
OF POOR QUALITY

PART II: PURCHASE ORDER REPORT

A: PURCHASE ORDERS RELEASED (WRITTEN) IN: 0376

PURCH. ORDER NUMBER	RTN	URGT	BLANK CONTR	$ VALUE	SUB. CONTR	$ VALUE	PETTY CASH	$ VALUE	SUBTOTAL $ VALUE RELEASED
222222	0	1	0	0	0	0	0	0	30.12
338620	1	0	0	0	0	0	0	0	37.50
339966	0	0	0	0	1	10276	0	0	10275.60
449928	0	0	0	0	0	0	1	243	243.12
666229	0	0	1	11060	0	0	0	0	11060.00
882051	0	0	0	0	1	158	0	0	158.16
888888	1	0	0	0	0	0	0	0	29.25
TOTAL	2	1	1	11060	2	10434	1	243	

TOTAL NBR.OF PURCHASE ORDERS RELEASED DURING 0376 : 7
SUBTOTAL DOLLAR VALUE RELEASED IN K-DOLLARS 21.834

Fig. 3. Purchase Order Report

B: OUTSTANDING PURCHASE ORDERS OF TOTAL PERIOD

PURCH. ORDER NUMBER	RTN	URGT	BLANK CONTR	$ VALUE	SUB. CONTR	$ VALUE	PETTY CASH	$ VALUE	OBLIGATED DOLLAR VALUE
128934	0	1	0	0	0	0	0	0	2.54
222243	1	0	0	0	0	0	0	0	149.40
261888	1	0	0	0	0	0	0	0	64.68
339966	0	0	0	0	1	10276	0	0	10275.60
449928	0	0	0	0	0	0	1	243	243.12
523742	1	0	0	0	0	0	0	0	429.24
666229	0	0	1	11060	0	0	0	0	11060.00
666441	1	0	0	0	0	0	0	0	67.20
882051	0	0	0	0	1	158	0	0	158.16
TOTAL	4	1	1	11060	2	10434	1	243	

NUMBER OF OUTSTANDING PURCHASE ORDERS INCL 0376 : 9
TOTAL OBLIGATED DOLLAR VALUE IN K-DOLLARS: 22.450

Fig. 4. Outstanding Purchase Order Report

TODAYS DATE: 02 NOV. 77

BEGINNING PERIOD:0176 ENDING PERIOD:0376

COMMITMENT CATEGORY SUMMARY REPORT

$ 0 - 500

PURCH. ORDER NUMBER	PURCH. ORDER DATE	VENDOR NAME	NUMBER OF TRANS-ACTIONS	$ AMOUNT IN K-DOLLARS
			7	.474

$ 10,001 - 25,000

PURCH. ORDER NUMBER	PURCH. ORDER DATE	VENDOR NAME	NUMBER OF TRANS-ACTIONS	$ AMOUNT IN K-DOLLARS
339966	32376	ARCCO SANDBLASTING		10.276
666229	32776	A-1 GLC CTG&TNG		11.060

TOTAL OBLIGATED DOLLAR VALUE IN K-DOLLARS PER REPORTING PERIOD: 21.810

---NOTE---

THE FOLLOWING VENDOR CODE(S) DOES(DO) NOT EXIST IN VENDOR-FILE

VENDOR CODE	PO NUMBER
A003	523742
A003	449928
B059	261888

Fig. 5. Commitment Category Summary Report

ORIGINAL PAGE IS OF POOR QUALITY

TODAYS DATE: 01 NOV. 77

BUSINESS SUBCONTRACTING REPORTS

BEGINNING PERIOD:0176 ENDING PERIOD:0376

PART I: SMALL BUSINESS REPORT

A: CONTRACTS UNDER 10,000 DOLLARS

PO NR.	VENDOR NAME	$ VALUE
888888	ABR ENTERPRISES INC	29.25
222222	ABR ENTERPRISES INC	30.12
338620	ABR ENTERPRISES INC	37.50
666441	ABR ENTERPRISES INC	67.20
222243	AACCO SANDBLASTING	149.40
882051	ABR ENTERPRISES INC	158.16

TOTAL AMOUNT IN K-DOLLARS: .472
TOTAL CONTRACTS UNDER $10,000 AWARDED TO SMALL BUSINESSES: 6

B: CONTRACTS OVER $10,000

PO NR.	VENDOR NAME	$ VALUE
339966	AACCO SANDBLASTING	10275.60
666229	A-1 GLS CTG&TNG	11060.00

TOTAL AMOUNT IN K-DOLLARS: 21.336
TOTAL CONTRACTS OVER $10,000 AWARDED TO SMALL BUSINESSES: 2

TOTAL CONTRACTS AWARDED TO SMALL BUSINESSES: 8
TOTAL AMOUNT IN K-DOLLARS AWARDED TO SMALL BUSINESSES 21.807

Fig. 6. Small Business Subcontracting Report

PART II: LARGE BUSINESS REPORT

A: CONTRACTS UNDER 10,000 DOLLARS

PO NR.	VENDOR NAME	$ VALUE
128934	NAT CASH REGSTR	2.54

TOTAL AMOUNT IN K-DOLLARS: .003
TOTAL CONTRACTS UNDER $10,000 AWARDED TO LARGE BUSINESSES: 1

B: CONTRACTS OVER $10,000

---NOTE---

NO CONTRACTS OVER $10,000 AWARDED TO LARGE BUSINESSES DURING REPORTING PERIOD

TOTAL CONTRACTS AWARDED TO LARGE BUSINESSES: 1
TOTAL AMOUNT IN K-DOLLARS AWARDED TO LARGE BUSINESSES .003
TOTAL CONTRACTS AWARDED IN REPORTING PERIOD: 9
TOTAL AMOUNT IN K-DOLLARS AWARDED IN REPORTING PERIOD 21.810

88.89 PERCENT OF TOTAL AWARDS WENT TO SMALL BUSINESSES
11.11 PERCENT OF TOTAL AWARDS WENT TO LARGE BUSINESSES
99.99 PERCENT OF TOTAL AMOUNT IN K-DOLLARS WENT TO SMALL BUSINESSES
.01 PERCENT OF TOTAL AMOUNT IN K-DOLLARS WENT TO LARGE BUSINESSES

---NOTE---

THE FOLLOWING VENDOR CODE(S) DOES(DO) NOT EXIST IN VENDOR-FILE

VENDOR CODE	PO NUMBER
A003	523742
A003	449928
B059	261888

Fig. 7. Large Business Subcontracting Report

TODAYS DATE: 15 DEC. 77

STATUS OF PURCHASE REQUISITION: 444555 HAVING: 3 ITEMS
FOR COST CENTER: 101A REPRO SHOP

P.R. ITEM	ACCOUNT	PURCHASE REQ. RECEIVING DATE	QUANTITY REQUESTED	TOTAL COST	STATUS
2	11122	81276	55.00	134.75	1

NO PURCHASE ORDERS HAVE BEEN WRITTEN FOR THE ABOVE ITEMS

P.R. ITEM	P.O. ITEM	PURCHASE ORDER NUMBER	RECEIVING REPORT NUMBER	RECEIVING DATE	QUANTITY ORDERED	QUANTITY RECEIVED	STATUS
1	3	681423	438135	41676	55.00	24.00	1
3	2	222222	888888	22376	8.00	11.00	1

NOTE 1:ABC LETTERING ART 21373391410

◆◆ NOTE NUMBERS CORRESPOND TO P.R. ITEM NUMBER

Fig. 8. Purchase Requisition Status Report

TODAYS DATE: 16 DEC. 77

FINANCIAL REPORT OF ACCOUNT: 11122 FOR MONTH OF MAR. 76

COST CNTR	COST CENTER NAME	COMMIT $VALUE	OBLIG. $VALUE	INCURRED $ VALUE SIS	JPL	DISB	TOTAL $VALUE
100A	PHOTO LAB	0	290	269	0	0	559
101A	REPRO SHOP	135	41	0	0	0	176
332A	CARPENTER SHOP	0	0	1230	0	0	1230
408A	MACHINE SHOP	3	0	553	0	0	556
412K	COMPLEX SUPPLY	0	0	367	0	0	367
TOTAL		138	331	2419	0	0	2888

Fig. 9. Monthly Specified Account Report

TODAYS DATE: 14 OCT. 77

FINANCIAL REPORT FOR COST CENTER: 408A(MACHINE SHOP
FOR MONTH OF: MAR. 76

ACCOUNT	COMMIT. $ VALUE	OBLIG. $VALUE	INCURRED $ VALUE SIS	JPL	DISB.	TOTAL $VALUE
11122	3	0	553	0	0	556

Fig. 10. Monthly Specified Cost Center Report

ORIGINAL PAGE IS
OF POOR QUALITY

TODAYS DATE: 16 DEC. 77

BUDGET REPORT FOR ACCOUNT: 11122

COST CNTR	BURDENED BUDGET	INCURRED $ VALUE SIS	JPL	DISB.	OBLIG. $VALUE	COMM. $VALUE	ACTUAL $VALUE	BALANCE PROJEC. $VALUE	ESTIM. $VALUE
100A	8500	330	109	22	517	8	7988	7471	7463
101A	6000	0	89	123	568	412	5760	5192	4780
332A	12000	2585	1167	563	0	0	7194	7194	7194
408A	19500	3122	221	4019	67	711	11187	11120	10409
412K	102000	367	132	0	0	7	101447	101447	101440
TOTAL	148000	6404	1718	4727	1152	1138	133576	132424	131286

100A PHOTO LAB
101A REPRO SHOP
332A CARPENTER SHOP
408A MACHINE SHOP
412K COMPLEX SUPPLY

Fig. 11. Specified Account Budget Report

TODAYS DATE: 14 OCT. 77

BUDGET REPORT FOR COST CENTER: 408A(MACHINE SHOP)

ACCT.	BURDENED BUDGET	INCURRED $ VALUE SIS	JPL	DISB.	OBLIG. $VALUE	COMM. $VALUE	ACTUAL $VALUE	BALANCE PROJEC. $VALUE	ESTIM. $VALUE
11122	19500	3122	221	4019	67	708	11187	11120	10412

Fig. 12. Specified Cost Center Budget Report

ORIGINAL PAGE IS
OF POOR QUALITY

TODAYS DATE: 16 DEC. 77

BUDGET REPORT FOR ACCOUNT: 33119

COST CNTR	BURDENED BUDGET	INCURRED $ VALUE SIS	JPL	DISB.	OBLIG. $VALUE	COMM. $VALUE	ACTUAL $VALUE	BALANCE PROJEC. $VALUE	ESTIM. $VALUE
309D	14000	0	450	0	11060	2051	13501	2441	390
TOTAL	14000	0	450	0	11060	2051	13501	2441	390

309D COM.CENTER

TODAYS DATE: 16 DEC. 77

BUDGET REPORT FOR ACCOUNT: 45219

COST CNTR	BURDENED BUDGET	INCURRED $ VALUE SIS	JPL	DISB.	OBLIG. $VALUE	COMM. $VALUE	ACTUAL $VALUE	BALANCE PROJEC. $VALUE	ESTIM. $VALUE
233A	10000	0	0	0	3	0	10000	9997	9997
TOTAL	10000	0	0	0	3	0	10000	9997	9997

233A FOOD SERVICE

TODAYS DATE: 16 DEC. 77

BUDGET REPORT FOR ACCOUNT: 55666

COST CNTR	BURDENED BUDGET	INCURRED $ VALUE SIS	JPL	DISB.	OBLIG. $VALUE	COMM. $VALUE	ACTUAL $VALUE	BALANCE PROJEC. $VALUE	ESTIM. $VALUE
976W	2600	0	0	0	0	568	2600	2600	2032
TOTAL	2600	0	0	0	0	568	2600	2600	2032

976W CUSTODIAL

Fig. 13. All Account Budget Report

OUTSTANDING PURCHASE REQUISITIONS
AS OF 16 DEC. 77

COST CENTER	ACCOUNT	PR.NUMBER	PR.DATE	STATUS	TOTAL $VALUE
100A	11122	254823	12276	0	7.50
100P	22341	238933	31876	0	1282.71
101A	11122	235489	12376	0	277.69
101A	11122	444555	31876	1	134.75
101S	11122	312142	11176	0	630.00
309D	33119	416281	32376	9	2050.78
408A	11122	118833	31276	0	3.35
408A	11122	313155	12376	0	362.64
408A	11122	624113	22376	0	345.00
409D	66622	156822	32376	9	975.20
412K	11122	517297	11276	0	2.00
412K	11122	648211	11676	1	5.00
976W	55666	575757	22376	1	567.84

Fig. 14. Outstanding PR Report

ORIGINAL PAGE IS
OF POOR QUALITY

OUTSTANDING PURCHASE ORDERS
AS OF 16 DEC. 77

COST CENTER	ACCOUNT	PO.NUMBER	PO.DATE	STATUS	TOTAL $VALUE
100A	11122	222243	21476	0	149.40
100A	11122	261888	22676	0	64.69
100A	11122	449928	32376	8	243.12
101A	11122	523742	21976	0	429.24
101A	11122	681423	41676	1	74.58
233A	45219	128934	21376	1	2.54
309D	33119	666229	32776	3	11060.00
408A	11122	666441	21276	0	67.20
409D	66622	339966	32376	5	10275.60
409D	66622	882051	32376	5	158.16

IF YOU WISH ADDITIONAL INFORMATION ABOUT
A SPECIFIC PURCHASE REQUISITION--PLEASE LOAD--
377♦GPF.PR-STAT-PRGM

Fig. 15. Outstanding PO Report

NASA—JPL—Coml., L.A., Calif.